Modélisation multi-échelles de la contraction musculaire : De la dynamique stochastique des moteurs moléculaires à la mécanique des milieux continus

François Kimmig

université PARIS-SACLAY

NNT : 2019SACLX071

Thèse de doctorat

Multi-scale modeling of muscle contraction

From stochastic dynamics of molecular motors to continuum mechanics

Thèse de doctorat de l'Université Paris-Saclay
préparée à École polytechnique

École doctorale n°579 Sciences mécaniques et énergétiques, matériaux et géosciences (SMEMaG)
Spécialité de doctorat : Mécanique

Thèse présentée et soutenue à Palaiseau, le 6 décembre 2019, par

FRANÇOIS KIMMIG

Composition du Jury :

Christophe Clanet Directeur de recherche CNRS, École polytechnique	Président
Lev Truskinovsky Directeur de recherche CNRS, ESPCI	Rapporteur
Luca Dede' Professeur assistant, Politecnico di Milano	Rapporteur
Marie-Christine Ho Ba Tho Professeur, Université technologique de Compiègne	Examinateur
Marco Linari Professeur, Università degli Studi di Firenze	Examinateur
Vittorio Sansalone Professeur, Université Paris-Est	Examinateur
Dominique Chapelle Directeur de recherche Inria	Directeur de thèse
Matthieu Caruel Maître de conférence, Université Paris-Est	Co-directeur de thèse
Philippe Moireau Directeur de recherche Inria	Invité

à Cécile C.,
à mes grands-parents
Jacqueline et Jean-Louis, Marthe et Dieter

Remerciements

J'ai eu la chance au cours de ces trois années de thèse de travailler avec trois éminents chercheurs Dominique Chapelle, Matthieu Caruel et Philippe Moireau, qui, en plus d'exceller dans leurs domaines de recherche, sont aussi des personnes humainement exceptionnelles. Je souhaite leur adresser mes plus chaleureux remerciements. Merci Dominique pour ta confiance, tes encouragements[1], de m'avoir guidé scientifiquement dans ce travail en me considérant dès le début comme un collègue scientifique et pour ton optimisme réconfortant face aux difficultés. Philippe m'avait bien dit au début de ma thèse "quand tu as un problème, parles-en à Dominique" mais je dois reconnaitre que je n'avais pas tout de suite pris la mesure de la puissance de ce conseil. Merci Matthieu pour ta disponibilité, ton soutien et tes conseils pour naviguer sur l'océan des connaissances des physiologistes sur la contraction musculaire, ta bienveillance dans les moments difficiles et les séances devant un tableau toujours remplies de bonne humeur et desquelles sont sorties beaucoup d'idées de cette thèse. Merci Philippe d'avoir cru en moi, de m'avoir communiqué cette confiance avec force et de tes efforts pour m'aider à mettre en perspective et apprécier mon travail. Merci aussi de m'avoir permis d'élargir les horizons de cette thèse et de lui donner une coloration mathématique qui était si importante pour moi. C'était un réel plaisir de travailler avec vous trois. L'étendue du spectre de vos connaissances suscite chez moi une profonde admiration et constitue une importante source de motivation pour me dépasser. Vous m'avez beaucoup appris et je me réjouis beaucoup de nos futures aventures.

J'aimerais aussi remercier Luca Dede' et Lev Truskinovsky qui m'ont fait l'honneur d'accepter d'être rapporteurs de ce manuscrit. Je remercie Luca Dede' pour sa lecture attentive de mon travail et ses commentaires. Les idées de Lev Truskinovsky sur la contraction musculaire sont au coeur de mon travail. Son impact sur ce manuscrit va donc bien au dela des précieux conseils qui m'ont permis de l'améliorer puisque qu'il a constitué une grande source d'inspiration scientifique.

Je remercie également chaleureusement les membres du jury : Marie-Christine Ho Ba Tho, Vittorio Sansalone, Christophe Clanet et Marco Linari d'avoir pris le temps de s'interesser à mon travail et de venir assister à ma soutenance (et ce malgré les conditions particulièrement difficiles au début du mois de décembre). To Marco Linari and your colleagues Vincenzo Lombardi, Pascale Bianco, Gabriella Piazzesi, Marco Caremani and Massimo Reconditi and all other members of the PhysioLab, thank you for having given me the opportunity to work in your team and the fruitful interactions that we have had all along this work. I received the warmest welcome possible in your team and this period will definitely stay in my mind as one of the highlights of my PhD.

La thèse est le dernier étage de la formation académique. Elle ne peut donc être réussie sans des bases solides. J'aimerais donc profiter de cette occasion pour remercier d'autres personnes importantes qui, avant ma thèse, ont eu un impact décisif sur mon cursus, ont nourri mon goût pour les sciences et ont façonné ce que je suis. J'aimerais citer no-

[1] "allez, ça ira mieux après un bon weekend à la montagne", et c'est allé mieux !

tamment Michel Courtieu – c'est avec vous que j'ai découvert les mathématiques et vos encouragements à poursuivre dans cette voie auront été le point de départ de mon parcours académique – , Jean-Pierre Lièvre – votre rigueur et votre passion pour les sciences m'ont profondément marqué – , et enfin Olivier Moynot – votre gentillesse est toujours pour moi une grande source d'inspiration et vos préceptes auront été présents chaque jour dans mon esprit au cours de cette aventure. I would like also to thank Professor Simon D. Guest and Professor Christian Cyron for having guided me in my first experiences of academic research, triggering in me and then sustaining the desire to go further in this path.

Cette thèse n'est pas un accomplissement uniquement personnel mais le fruit des efforts de tout un environnement ; et quel environnement ! Je souhaite donc remercier toutes les personnes qui contribuent à l'ambiance agréable et dynamique du Laboratoire de Mécanique du Solide de l'École polytechnique et de l'équipe MΞDISIM et à leur fonctionnement.

Je dois bien sûr commencer par mes deux compères Arthur Le Gall et Federica Caforio. Ce fut un immense plaisir de partager cette aventure avec vous. Votre intelligence et votre gentillesse m'impressionnent et sont une grande source d'inspiration. Federica, ma wingwoman à bien des égards, ton optimisme dans la capacité des calculs – même ceux qui paraissent les plus horribles – à finalement donner quelque chose d'exploitable aura contribué à quelques succès dans l'accélération de mon code. Merci pour toutes nos discussions sur la linguistique, la politique, les sciences et la cuisine. Arthur, le médecin avec lequel on peut discuter de convergence L^2 d'estimateur, ta générosité, ta curiosité et ta capacité à t'intéresser et à comprendre les mathématiques sont exceptionnelles, merci pour tes cours particuliers de physiologie et mon baptême de voile. Je remercie aussi Radek Chabiniok pour sa bonne humeur indéfectible et ses conseils sur les modèles cardiovasculaires, Fabrice Vallée, l'infatigable générateur d'idées et non moins infatigable partenaire de tennis, Frédérique Robin, pour nos pauses musicales matinales, Cécile Patte, qui aura supporté de travailler dans la même pièce que moi pendant ma période rédaction[2] et Francesco Regazzoni pour nos interactions sur nos sujets de thèse respectifs. Je souhaite également remercier Cécile Della Valle de m'avoir initié à des sujets passionnants et pour nos discussions sur nos théorèmes préférés, la philosophie et nos podcasts favoris. Je pense également à Bruno Burtschell et Alexandre Laurin qui m'ont donné envie de venir travailler dans cet environnement lorsque je réfléchissais à mon sujet de thèse, à Sébastien Gilles[3], Gautier Bureau et Jérôme Diaz pour les conseils algorithmiques et informatiques, à Sébastien Imperiale et Frédérique Clément qui m'ont encouragé et enrichi scientifiquement et enfin à Sophie Ramananarivo, Eric Charkaluk, Eric Lorentz, Didier Clouteau, Martin Genet et Jean-Marc Allain avec qui j'ai eu la chance de pouvoir travailler pour mes missions d'enseignement. Merci à tous les doctorants et stagiaires du LMS et de MΞDISIM, ceux que j'ai eu la joie de rencontrer : Ludovic Gil, Camille Guévenoux, Nicole Tueni, Jérémie Chichignou, Jessica Manganotti, Yanis Balit, Othmane Zerhouni, Filippo Agnelli, Florent Wijanto, Ustim Khristenko, Anchal Goyal, Marija Gusseva et ceux que j'ai eu le plaisir de retrouver : Alexandre Jouan, Jean-Pierre Voropaieff et Laurent Guin. Je n'oublie pas non plus Alexandra Joly et Anna Johnsson que je remercie pour leur capacité à résoudre les problèmes plus vite qu'ils n'arrivent. Enfin, je remercie vivement Philippe Moireau et Patrick Le Tallec, qui oeuvrent beaucoup pour créer et entretenir la précieuse dynamique du laboratoire en faisant en sorte de toujours donner aux doctorants les meilleures conditions pour réaliser leur travail, en soutenant leurs initiatives et en ayant toujours un mot gentil pour chacun. Je me souviens aussi que les cours de Patrick Le Tallec ont grandement participé à mon développement scientifique, et que c'est lui qui m'a mis en contact avec

[2] il parait que je râle avec le sourire et que du coup, ça va

[3] mon maître Git

Dominique au début de cette aventure.

Bien sûr, je ne serais pas là où je suis aujourd'hui sans mes amis, avec qui j'ai passé tant de bons moments et qui par leur soutien dans les phases difficiles auront aussi contribué à la réussite de cette thèse. Je leur en suis extrêmement reconnaissant. Je souhaite remercier particulièrement Robin Scherrer, mon plus vieil ami, Thibault Asselborn, Valentin Wiederhirn, Alexis Morfin et Marion Ulmann. Merci Jérémie Laurent de m'avoir encouragé à me lancer dans l'aventure de la thèse, pour les moments passés à partager nos théories sur le monde, les gens, le second principe et bien sûr merci pour ton amitié. Dix ans ont passé depuis nos premières colles sous les toits d'un lycée lyonnais et nous voilà bientôt tous les deux docteurs ! Je remercie aussi Cédric Bourdais, Benoît de Laitre, Hugo Ghiron, Paula Alemany Ripoll, Aude Nyadanu – ta bonne humeur particulièrement communicative n'a d'égal que ton talent à faire vivre tes projets[4]– , Arturo Ruano San Martin, Robin Larrieu, Milena Suarez-Castillo, Mathilde Pierre, Louis Hénaux, Leopold Shaabani Ardali, Matthieu Xémard, Quentin Laudreau, Laurent Cornaggia et Sisi Li, ma première research team mate. Merci à la team Munich : Arthur Gautier, Emmanuel Siefert – il y aurait tant à dire que je me contenterais de mentionner qu'à bien des égards tu me montres la voie – , Irène Cucchi – ton intelligence, ton optimisme et ta sagesse sont au plus haut dans mon estime[5]– , Stanislas Chambon, la gentillesse incarnée, Hélène Dreyfuss, Madeleine Devys et Paul Coupier ; et bien sûr merci à mon excellent colocataire Jean-Philippe Boucher[6]. Je pense aussi avec une certaine émotion à Marie-Pierre et Jean-Philippe, merci pour votre bienveillance et votre confiance.

Enfin, et surtout, j'aimerais remercier ma famille, ma soeur Claire-Marie et ceux à qui je dois le plus, mes parents, qui ont cru en moi et m'ont soutenu depuis toujours et m'ont encouragé sur le chemin du travail et de la connaissance.

[4] dont je m'efforce de m'inspirer

[5] et je n'oublierai pas que tu étais là pour me donner du chocolat au point le plus bas

[6] dont les talents de cuisinier auront adouci mes derniers jours de rédaction

Table des matières

Introduction (English)

This PhD thesis has been prepared in the MΞDISIM team at Inria and École polytechnique, funded by École polytechnique, under the supervision of Dr. Dominique Chapelle and Dr. Matthieu Caruel. I have also been co-advised by Dr. Philippe Moireau throughout this project.

Context

This thesis deals with the mathematical description of the micro-scale muscle contraction mechanisms with the aim of proposing and integrating our models into a multiscale heart simulation framework.

Digital medicine

This thesis is part of a worldwide trend towards the development of a so-called *digital medicine* through the use of numerical tools and in particular numerical models. The hopes raised by this set of technologies are enormous: a personalized medicine with more accurate treatments and an early detection of diseases, which is associated with a reduced mortality but also the safer and faster development of new drugs. A wide array of research programs are conducted on this topic.

Following the development of technologies, medical data acquisition tools have long been developed. Milestones in this process are the invention of the electrocardiogram (ECG) [Waller, 1887; Einthoven, 1895], the sonography, the CT-scan [Cormack, 1963; Hounsfield, 1973], and MR imaging [Lauterbur, 1973; Mansfield & Maudsley, 1977]. The development of computing power and information systems, which make the data more easily available and useable along with the development of physiological signal measurement tools take this approach to a new level of development.

These research and development efforts in digital medicine aim at taking up the triple challenge of improving the understanding of the physiology and the pathologies, enhancing the diagnosis and optimizing the treatment of patients.

- The understanding of the physiology can be improved by numerically testing physiological hypotheses and see which ones correspond to the reality. Moreover, well calibrated models allow to obtain *in silico* the reconstruction of data that are difficult or impossible to measure on living subjects. Naturally, this challenge can only be achieved with models that are able to establish causal links between physiological events.

- The enhancement of diagnosis is believed to be achieved through a quantification of the patient analysis enabling the physicians to take more informed and more objective decisions. The models are here used as a filter to look at the data and augment the amount of information that can be extracted from these data and present them in a more meaningful way.

- The optimization of treatment is probably the most difficult step. The ability to model not only the basal behavior but also to capture the effects of the treatment – impact of drugs, change of the organ geometry – is a prerequisite to the implementation of a this procedure.

Note that in all three challenges, the need of quantitative *predictive* models and their proper calibration are crucial. Another central point is the interaction between the model and the measured data. The latter are used to patient-specifically calibrate the models so that personalized model outputs can be obtained.

The complex nature of physiological mechanisms make the process of building models intrinsically multi-disciplinary mixing biology, chemistry, physics, mathematics and computer science.

An important point is the diversity of models that are required in this process. Indeed, the choice of the modeling ingredients to address a specific physiological or clinical question has to be carefully made. It results from the trade-off between the accuracy of the model prediction, the associated computational cost and the availability of the measurements required to feed the model in order to get a relevant calibration. For instance, an analysis targeting global indicators of an organ may be performed on a reduced geometry, especially if the conditions on the boundary of the geometry cannot be assessed specifically. On the contrary, if propagation phenomena or localized physiological parameter variations are studied, the use of a geometrically extended model is required.

The research efforts in digital medicine resulted for instance in development of models of the lungs [Howatson Tawhai et al., 2000; Roth et al., 2017] or the growth of tumors [Quaranta et al., 2005; Clatz et al., 2005; Ribba et al., 2006; Enderling & Chaplain, 2014]. Some outstanding breakthroughs have also already been achieved in the fields of drug discovery where models help predict the effects of molecules [Sliwoski et al., 2013; Tanrikulu et al., 2013]. Moreover, in the process of drug development, numerical tools have already been accepted by regulators as a substitute to pre-clinical animal testing in the context of diabetes treatment design [Dalla Man et al., 2014; Visentin et al., 2017].

The cardiovascular system has not escaped the trend of personalized medicine.

The pioneer work of Hodgkin & Huxley [1952] for the description of the action potential and of Huxley [1957a] for the striated muscle contraction led the way to more global and specific descriptions of the cardiovascular system. One can cite here, the early work of Noble [1962] for the description of the muscle cell membrane electrophysiological activity along with the Purkinje fibers (see next section), of Mirsky [1969]; Ghista et al. [1973] and P.J. Hunter [Hunter, 1975; Hunter & Smaill, 1988] on the modeling of the heart muscle tissue and C.S. Peskin for both the tissue modeling [Peskin, 1975] and the blood flow modeling [Peskin, 1972, 1977].

Since then, many research teams have engaged in the development of heart and vascular physical models [Guccione & McCulloch, 1993; Nash & Hunter, 2000; Chapelle et al., 2001; Sainte-Marie et al., 2006; Taylor & Figueroa, 2009; Nordsletten et al., 2011; Trayanova, 2011; Chapelle et al., 2012; Sugiura et al., 2012; Caruel et al., 2013b; Baillargeon et al., 2014; Pant et al., 2014; Hirschvogel et al., 2017; Quarteroni et al., 2017]. A review of the development of cardiovascular models and their applicability to clinical questions is presented in [Chabiniok et al., 2016].

Models of subpart of the heart have also been developed to target specific phenomena such as the growth and remodeling of the muscle tissue [Rodriguez et al., 1994; Humphrey & Rajagopal, 2002], which have then been applied in the context of aortic aneurysms [Cyron et al., 2014] or the growth and remodeling of the whole heart [Kroon et al., 2009; Kerckhoffs et al., 2012]. The function of the valves and the flow around them [Astorino et al., 2009; Stella & Sacks, 2007], the blood flow in the arteries [Quarteroni et al., 2002; Formaggia et al., 2003] and the behavior of the arterial wall [Gasser et al., 2005] have been specifically studied as well. These model elements can naturally be used as a part of a whole organ model if required.

The community focusing on the cardiovascular system has presented promising proofs of concept for the three main challenges of the digital medicine. Models have proven to be able to give a better insight into the physiology [Hyde et al., 2015; McDowell et al., 2013]. Regarding the improvement of diagnosis, the estimation from MRI data using data assimilation techniques of the arterial wall contractility [Chabiniok et al., 2012; Genet

et al., 2015] or the aortic wall stiffness [Bertoglio et al., 2014] could be achieved. In the domain of electrophysiology, the evaluation of the electrical state in a heart beat contraction [Corrado et al., 2015] was performed. Some research works also deal with the challenge of optimizing the treatment as a theoretical analysis or even completed by a validation on real in vivo data. In the first category, one can mention the work of Rausch et al. [2017] displaying the theoretical ability of a heart model to help select the design of implantable mitral annuloplasty rings. An example of the latter category is the work of Sermesant et al. [2012] who presented a computational framework able to find *a priori* the optimal position of pacemaker electrodes, therefore having the potential to replace the current practice of trial and error and thus shorten the duration of the procedure and increase safety.

The promises of the academic research have already started to translate into the clinical practice. Indeed, companies such as HeartFlow and Arterys have already received clearance from the public health authorities to commercialize products relying on cardiovascular models to assess blood flows in the cardiovascular tree.

The human heart

The heart is the main object of study of this thesis. We give here a brief presentation of its structure and functioning. A more complete description of the heart can be found for instance in [Silverthorn et al., 2009].

The heart is an organ located in the thorax between the lungs. It is integrated into the cardiovascular circulatory system, which allows the movement of blood through the body to supply the organs with oxygen, nutriments and hormones and to handle the transport of waste products. The heart serves as a blood pump in this circulatory system. There are three distinct blood circulations:

- the pulmonary circulation, which corresponds to the part of the blood traveling through the lungs so that gas exchanges can be performed leading to the blood oxygenation;
- the coronary circulation, which supplies blood to the heart itself through the coronary arteries;
- the systemic circulation, which provides blood to the rest of the body.

A presentation of the heart structure is given in Figure 1. It is composed of four chambers: the left and right *atria* and the left and right *ventricles*. The *septum* separates the left and right ventricles. The valves are the interface between the ventricles and the atria on the one hand, and from the circulatory system on the other hand. They also allow to give a direction to the blood circulation. The *triscupid valve* is located between the right atrium and the right ventricle; the pulmonary valve separates the right ventricle from the pulmonary artery. The left ventricle is also connected with adjacent elements by two valves: the *mitral valve* for the left atrium and the *aortic valve* for the aorta.

The heart tissue, called *myocardium*, is contractile, which allows to generate pressure in the cavities and to eject blood. It is composed of fibers coiled around the cavities. This arrangement of fibers creates a twist in the ventricle, which enhances the contraction. At a microscopic scale, these fibers form a branching network (see Figure 2). The muscle contraction is triggered by an electrical signal originating from the right atrium. This signal travels in the whole heart through the Purkinje fibers and by means of a propagation from one contractile cell to another.

In a cardiac cycle, the blood from the systemic circulation (that contains less oxygen) enters the heart through the right atrium, while the oxygenated blood coming from the

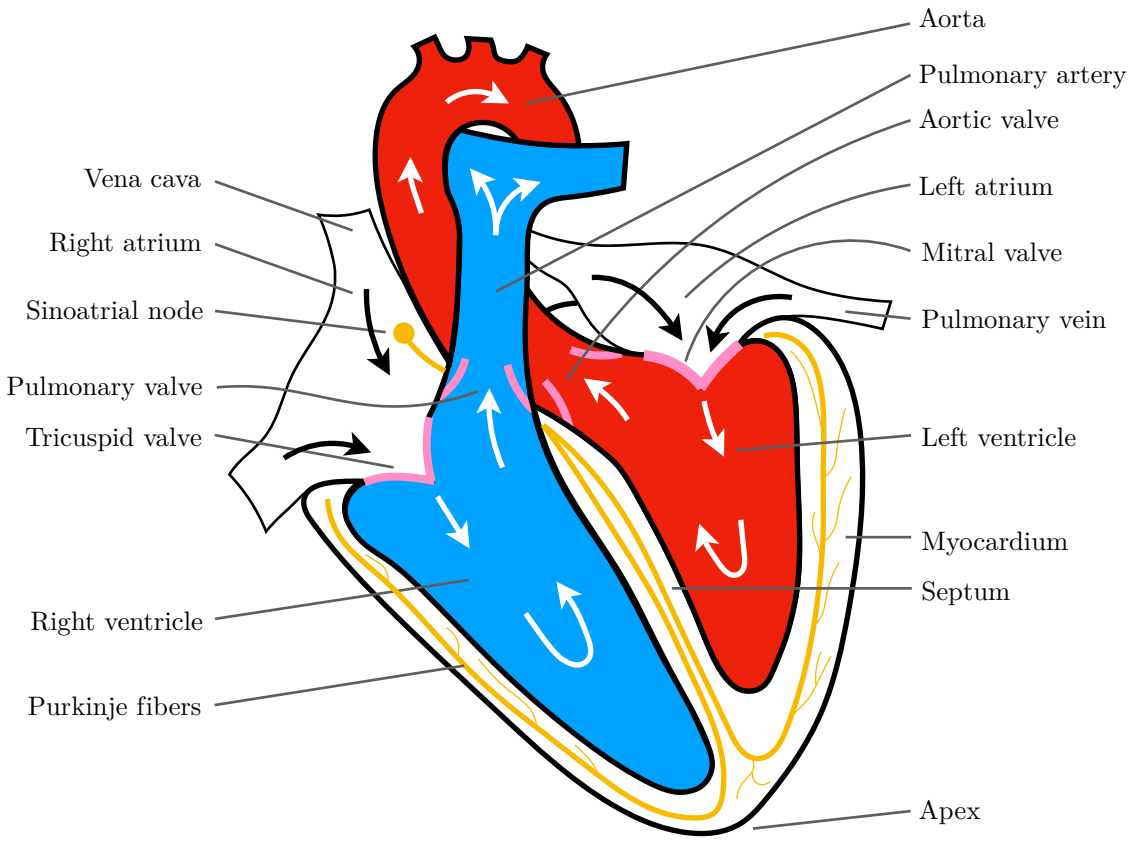

Figure 1 – Schematic representation of the heart. Oxygenated blood is depicted in red and deoxygenated blood in blue.

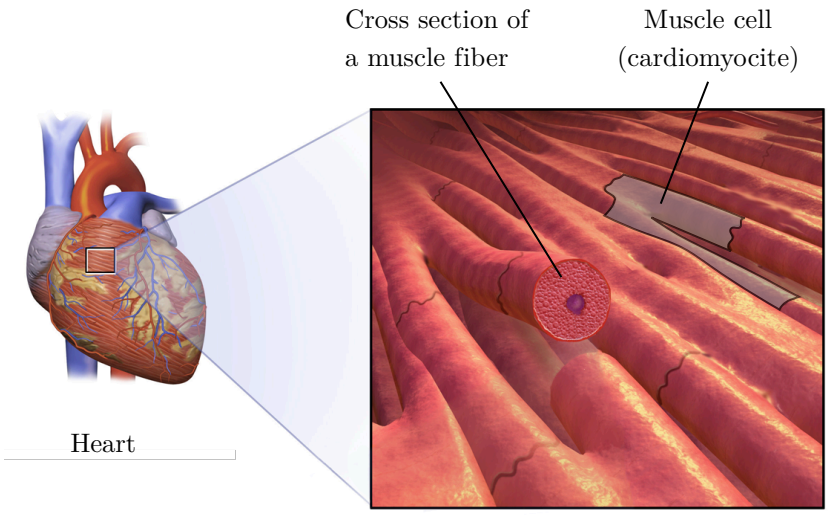

Figure 2 – Cardiac muscle fiber network. This illustration is a modification of *Cardiac Muscle* by BruceBlaus, licensed under CC BY 4.0.

lungs enters in the left atrium. The atria contraction is triggered first ensuring the filling of the ventricles. The contraction triggering signal then reaches the ventricles, which eject the blood into the pulmonary artery towards the lungs and into the aorta towards the rest of the body. The fluxes of blood inside the heart are illustrated in Figure 1. The main cavity of interest is the left ventricle. We present the typical evolution of its pressure and its volume in a cardiac cycle in Figure 3. At the beginning of the cycle, the left atrium contracts, its pressure increases and blood flows inside the ventricle. Then, the ventricle starts to contract and the pressure inside the cavity increases and the mitral valve closes. When the ventricular pressure reaches the aortic pressure, the aortic valve opens and the blood is ejected into the aorta. Simultaneously, the cavity volume decreases. After reaching a peak, the ventricular pressure decreases. The relaxation begins and the aortic valve closes. When the ventricular pressure falls to the level of the atrium pressure, the mitral valve opens and a new cycle can take place. The function of heart as a pump is illustrated here. Indeed, the left ventricle brings a volume of blood from a low atrium pressure to a high aortic pressure. A useful representation of these data for the understanding of the cardiac function is the pressure-volume relation. It forms a loop due to the cyclic nature of the heart functioning. An illustration is presented in Figure 4. The contraction period of the cycle is called *systole* and the relaxation period is called *diastole*. Note that the diastole and systole are not synchronized for atria and ventricles.

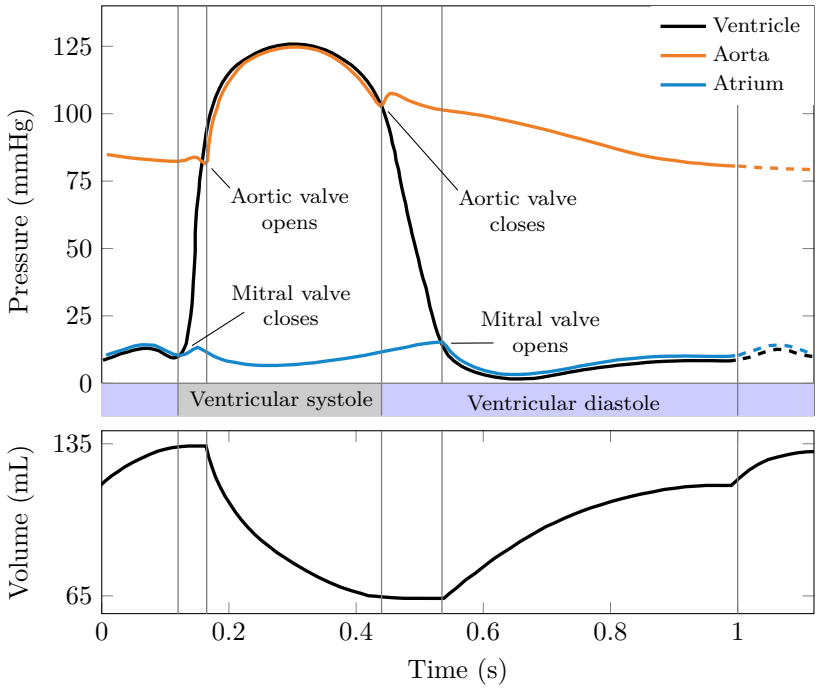

Figure 3 – Typical evolution of the left ventricle pressure and volume in a cardiac cycle.

Cardiac muscles being the main point of interest of this thesis, we give here a quick anatomy description. The muscle fibers are composed of a series arrangement of small ($\sim$2 µm) contractile units called *sarcomeres*. The latter are mainly made of two arrays of protein filaments: myosin filament (thick filament) and actin filament (thin filament). Components of myosin filament, *myosin heads*, interact with the actin monomers (also called *actin sites*) in a cyclic manner while consuming metabolic fuel provided by ATP hydrolysis. The myosin head attaches to an actin site forming a so-called *cross-bridge*. While a myosin head is attached, a fast conformation change occurs leading to the gener-

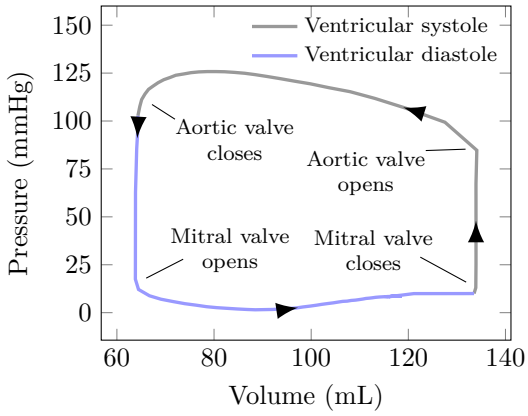

Figure 4 – Typical left ventricle pressure-volume loop (PV loop) in a cardiac cycle.

ation of a contraction force. This phase is called the *power stroke*. The force generated by cross-bridges is said to be an *active force* as the force generation process involves energy consumption. As a result of the force development, the sarcomere may shorten by the relative sliding between the actin and myosin filaments.

Modeling of muscle contraction

The study and modeling of the muscle behavior started over a century ago and has been very active in the last fifty years. A historical review, written by one of the main protagonist, H.E. Huxley, is available [Huxley, 2004]. We refer to [Caruel & Truskinovsky, 2018] for a review of recent theoretical modeling work.

From the pioneer work of A.V. Hill [Hill, 1938], immense efforts have been made by biologists and physiologists to experimentally characterize the structure of muscle, the mechanism of muscle contraction and its regulations. The scientific community can be decomposed in two groups. The first one, led by A.F. Huxley and H.E. Huxley from the 50's, and then in particular by V. Lombardi, focuses on the fine characterization of the structure and the microscopic interactions underlying the macroscopic contraction in skeletal muscle, and recently applies their experimental protocol to cardiac muscles. The second one, led by H.E.D.J. ter Keurs and P.P. de Tombe from the 80's and 90's, respectively, concentrates on the characterization of cardiac muscles contraction and the associated regulation mechanisms.

Modelers have worked in parallel of the experimental breakthroughs, taking advantage of the latest physiological discoveries to enhance the models. The first model of muscle contraction was formulated by A.V. Hill in 1938 alongside his landmark experimental work on the macroscopic thermodynamics of muscle contraction [Hill, 1938]. He observed the relation between the muscle shortening speed and the developed force, along with the associated heat fluxes. This force-velocity relation is the main feature of the actin-myosin interaction. It is now often termed the *Hill's curve*. The model that A.V. Hill proposed to account for his experimental observations is a simple rheological model composed of a spring and an "active element" having the force-velocity relation as a constitutive equation. This model targets the muscle macro-scale. It is still used nowadays because of its simplicity [Quarteroni et al., 2017].

In the early 50's, it was believed that the contraction occurs as a results of the coiling of a single actomyosin filament. A change of paradigm started in 1954. The group of A.F. Huxley (in Cambridge, England) and the group of H.E Huxley (in Cambridge,

Massachusetts) publish, in the same issue of *Nature*, two experimental studies observing the variations of the striations in skeletal muscle with the muscle stretch [Huxley & Niedergerke, 1954; Huxley & Hanson, 1954]. From these results emerges the idea that muscle shortening originates from the relative sliding of the myosin and actin filaments and that a force is created by the interaction between these components. This constitutes the *sliding filament theory*.

Based on a (at the time speculative) mechanism involving the formation of cross-bridges by myosin heads and actin sites Huxley [1957a] proposed a new model of muscle contraction. This model describes the behavior of a population of myosin heads interacting with localized actin sites. Each myosin head is modeled as a linear spring. The rates at which the myosin heads attach and detach vary with the distance between the myosin head and the actin site. The generation of a force results from the modeling assumption that the myosin heads attach preferentially in a position where the spring is stretched, while detachment occurs when the spring is compressed. Despite the simple assumptions chosen here, the Huxley'57 model is already able to account for the essential feature of the actin-myosin interaction: the force-velocity curve first observed by [Hill, 1938]. This model was later extended, in particular by Podolsky et al. [1969], by Julian [1969] to incorporate the calcium activation process, and also by Deshcherevskiĭ [1971], who, conversely to the original model, considers non-localized actin binding sites. The Huxley'57 model remains today the basis for the modeling of muscle contraction.

In the same year, H.E. Huxley obtained the first observation of cross-bridges as part of a high resolution observation of the actin and myosin filaments that definitely confirms the sliding filament theory as the correct mechanism underlying muscle contraction [Huxley, 1957b].

A decade later, H.E. Huxley's structural measurements suggest that the attached myosin heads change their angle of attachment during the contraction process. This change between two stable conformations is now named *power stroke* [Huxley, 1969]. The initial and final conformations are called *pre-power stroke* and *post-power stroke* conformations, respectively.

In 1971, A.F. Huxley and R.M. Simmons observe the behavior of skeletal muscles under a quick change of length (the time scale considered here is below 1 ms and is thus shorter than the time scale of the attachment-detachment process, which is around 100 ms in their experimental conditions). The response in force displays several phases: an instantaneous force drop followed by a quick force recovery. These experiments suggest that phenomena with different time scales occur in the interaction between myosin heads and actin sites. A.F. Huxley and R.M. Simmons proposed a model to account for this experimental observation [Huxley & Simmons, 1971]. Their description assumes that cross-bridges behave like a bistable snap-spring. The energy of the bistable element is modeled as two infinitely narrow energy wells of different depth. If the spring is stretched enough the bistable element can transition from one state to the other recreating a positive force generation capability. This model thus incorporates the idea of the power stroke suggested by experimental results of H.E. Huxley two years before. Note that this model does not include the attachment-detachment dynamics and only focuses on the description of the cross-bridges.

The same year, a basic cycle for the interaction in solution between actin, myosin and the energy supply in the form of ATP in this interaction was presented [Lymn & Taylor, 1971]. It consists in two attached and two detached states. The transition between the two attached states can be identified with the power stroke. The detachment is associated with the hydrolysis of ATP and thus with an input of energy.

One issue raised by the Huxley-Simmons'71 model is the dynamics of the transition between the two states of the bistable element. Indeed, the transition occurs when the

energy of the current state is equal to the energy of the future state (after transitioning). During the transition, an exchange of energy between the bi-stable element and the spring occurs, the total energy remaining constant. It is equivalent to define the energy barrier between the two states as the energy depth of the current energy well. This energy has to be provided by the thermal fluctuations and this results in a slow transition between the two states compared to that observed experimentally.

This issue was solved by T.L. Hill in the 70's through his tremendous effort of model formalization [Hill, 1974, 1976, 1977]. He proposed to describe the transition between the two discrete states by an independent energy landscape that defines the transition energy barrier. At the level of discrete chemical states, it is equivalent to say that the transition rates (or equivalently the transition energy landscape) can be chosen arbitrarily. The consistency with thermodynamics is maintained by considering for each transition a reverse whose rate that is defined by the detailed balance

$$\frac{k}{k^{\text{rev}}} = \exp\left[\frac{-\Delta w}{k_B T}\right]$$

where k is the transition rate of the forward reaction, k^{rev} the transition rate of the reverse reaction, Δw is the free energy difference between the final state and the initial state for the forward reaction, k_B is the Boltzmann constant and T is the absolute temperature. The change between states of the cross-bridge is thus analogous to transition between chemical states. With this "purely chemical" formalism, it is natural to incorporate, in a single model, the idea of the attachment-detachment dynamics proposed by Huxley [1957a] and the description of the power stroke introduced by Huxley & Simmons [1971]. This class of model is called *chemico-mechanical models.* Based on his framework, T.L. Hill and his co-authors formulated a model that is capable of capturing the behavior in response to fast length changes– with the correct dynamics – along with the force-velocity relation [Eisenberg & Hill, 1978; Eisenberg et al., 1980]. The power stroke is modeled by the transition between two discrete states.

Since then, many modeling ingredients have been incorporated in the class of chemico-mechanical models to embed additional aspects of the muscle contraction physiology discovered experimentally. Piazzesi & Lombardi [1995] added an intermediate state in the power stroke from which the complete cycle can be aborted to improve the energy consumption prediction of the model. The idea of a series of discrete chemical states to represent the power stroke was extended using up to five chemical states [Linari et al., 2009] (in this case without the attachment-detachment process). Moreover, some model refinements integrating the cycle of ATP to the actin-myosin interaction have been developed [Linari et al., 2010; Caremani et al., 2015]. The family of chemico-mechanical models is the most used in the community of physiologists to analyze a growing corpus of experimental results. These models became very complex to remain comprehensive.

An effort of simplification was undertaken by G.I. Zahalak from the 80's. He introduced the idea that computing the probability of all the myosin head configurations may not be always necessary since the main quantity of interest – the active force – only depends on one moment of this probability. He showed that, under a hypothesis on the spatial variation of attachment probability, the force evolution could be computed from the dynamics of a few moments of this probability only [Zahalak, 1981]. The set of partial differential equations governing the chemico-mechanical models becomes here a set of ordinary differential equations. Building on a similar idea but using a slightly different assumption – based on the spatial variation of the transition rates, which then affect the binding states probabilities of all the myosin heads – Bestel et al. [2001] proposed a relevant reduction of the Huxley'57 model. G.I. Zahalak also suggested to take advantage

from the different time scales to derive simplified models [Zahalak, 2000]. His procedure aggregates the – possibly many – transitions representing the power stroke into a single transition through relevant approximations.

Note that another broad family of models called *Brownian ratchets* has been developed by a physics community to study collective effects with a high level of abstraction in parallel of the development of new experimental techniques on single myosin heads [Kron & Spudich, 1986; Molloy et al., 1995; Veigel et al., 1998]. The idea here is to use the representation of molecules subjected to thermal fluctuations diffusing in a periodic energy potential [Magnasco, 1993; Prost et al., 1994]. These purely mechanical models were originally targeting the behavior of molecular motors but have then been applied to muscle contraction [Jülicher et al., 1997; Wang & Oster, 2002; Esaki et al., 2003].

The most recent improvement of muscle contraction models came from the work of L. Truskinovsky and his collaborators. The succession of discrete chemical states representing the power stroke in chemico-mechanical is here replaced by a continuous manifold [Marcucci & Truskinovsky, 2010; Caruel et al., 2013a]. In a sense, this is an approach that is parallel to the description of T.L. Hill and his collaborators. The latter assume that the discrete states are separated by an arbitrary energy landscape, which is associated with the conformation changes occurring between the discrete states and which then only appears in the model through the transition rates between the discrete states. The model is purely chemical but the evolution between the discrete states is governed by a hidden mechanical energy. With the continuous power stroke models, the whole energy landscape of the system is directly provided. It is constructed from the coupling of a quadratic mechanical energy – representing the linear elastic behavior of the cross-bridges – with a mechanical double-well potential associated with the myosin head pre- and post-power stroke stable conformations. Note that additional energy wells could be added to represent additional stable conformations [Marcucci et al., 2016]. The models are purely mechanical without discrete chemical states.

The continuous power stroke models were first restricted to the description of the power-stroke (as the Huxley-Simmons'71 model). They were then extended to also take into account the attachment-detachment process by Caruel et al. [2019] who model attachment and detachment as jump processes between two energy landscapes (possibly associated with a simultaneous myosin head position change). This approach has the particularity to reconcile a fully mechanical approach for the description of the power stroke and a chemical description of the attachment-detachment process. The models proposed and studied in this manuscript fall within this sub-family of models.

An alternative approach to incorporate the formation and destruction of cross-bridges to the continuous description of the power stroke was proposed by Sheshka [2012]; Sheshka & Truskinovsky [2014] extending the Brownian ratchets models. The resulting model is purely mechanical description of the actin-myosin interaction.

Very recently, the fine properties of cardiac muscles have been measured [Caremani et al., 2016].

Despite the abundant research on muscle contraction conducted in the last sixty years, this field is still very active. Experiments using X-ray diffraction patterns (using the regular structure of the sarcomere as a diffractor) allow to better understand the structural variations occurring in the contraction [Reconditi et al., 2003; Piazzesi et al., 2007; Reconditi et al., 2014; Ait-Mou et al., 2016], pathologies [Ait-Mou et al., 2018] or to better identify the various chemical states appearing in the cycle [Houdusse & Sweeney, 2016]. In particular, a new state of the myosin head, called *off-state*, has recently been discovered in skeletal muscle [Reconditi et al., 2011; Linari et al., 2015] and cardiac muscles [Reconditi et al., 2017]. This opens new opportunities for the development of dedicated models and

the refinement of existing ones.

Theoretical challenges

Despite the large amount of efforts already put into the modeling of muscle contraction, many questions remain open.

First, the sixty years of actin-myosin model developments have not succeeded in making the model predictions match with all experimental data. In particular, the energetics aspects of the actin-myosin interaction remain difficult to reconcile with the kinetics aspects, the ATP consumption predicted with classical models being usually higher than that actually measured.

Secondly, most of the fine description of the actin-myosin interaction at the origin of muscle contraction has been performed for skeletal muscles, the development of model targeting specifically cardiac muscles being only very recent. Experimental data with cardiac muscles show similar qualitative behavior but the quantitative results differ. This discrepancy may be explained by intrinsic differences between skeletal and cardiac muscle, by differences between species but also by the fact that the experiments with cardiac muscles are usually performed at higher temperatures. There is thus a need for models specifically targeting the behavior of cardiac muscles.

Thirdly and most importantly, the need of modeling elements for medical applications does not imply a search of a single model that could capture many different aspects of the studies phenomenon. It is rather a collection of models having different degrees of complexity that is required. For each particular application, the rightful model, which best satisfies the trade-off between ability of the model to bring meaningful elements to solve the investigated question and the computational cost, should be selected. The issue of computational cost is crucial for medical applications because real-time simulations may be required in some cases, for instance if the model is embedded in a tool used to assist a surgical intervention. Note that faster-than-real-time may be the relevant simulation time scale, if for instance several scenarios have to be tested or if the quantification of uncertainties is furthermore performed. The consistency between the different models is a decisive point. Indeed, to transfer a calibration made with one model to another or to bridge space and time scales, the models need to be rigorously and systematically related. For instance, in the framework of heart modeling, a detailed analysis of a pathology may be performed with a refined model and *ex vivo* data so that the model of the pathology may be used in a more global description at the tissue level or the heart level, where using of this refined model is impossible. The ability to link the models and to control the conservation and loss of properties through this transition from one model to another is therefore an essential feature that should be sought in modeling efforts within the framework of digital medicine. This gives rise to the first goal of this thesis that can be stated as follows:

Propose a hierarchical modeling framework of the cardiac actin-myosin interaction underlying cardiac muscle contraction.

To tackle this issue, we pursue the following strategy. We start from a complex model, which was only validated for skeletal muscle [Caruel et al., 2019], and we show the applicability of this model to cardiac muscles, trying to match as many physiological indicators as possible. This model is governed by stochastic differential equations (SDEs). Then, we perform the adiabatic elimination of the faster internal variable, which corresponds to the power stroke, obtaining from the Fokker-Planck equation associated with the stochastic model a description of the state of the myosin head under the form of a partial differential equation (PDE). Finally, building on the ideas of Zahalak [2000] and Bestel et al. [2001],

we propose, under a specific assumption for the spatial variability of the attachment and detachment rates, further simplifications of the model by considering only the moments of the PDE solution that are of interest for the computation of the force and the stiffness. The dynamics is then only governed by ordinary differential equations (ODEs). The calibration of the models, that may look like a secondary element, should not be neglected. It is indeed a key element to prove the validity of the proposed models and is a highly time consuming process.

The proposed models describe a situation where all myosin heads and all actin sites are available for the formation of cross-bridges (we say equivalently that the thick and thin filament are fully activated). This is not the case in the living heart. To be able to use the models in the context of heart modeling, these regulation mechanisms taking place *in vivo* have to be incorporated in the model. This motivates the introduction of our second goal:

Enhance the classical actin-myosin interaction models to incorporate the regulation mechanisms taking place at the heart level.

Our approach here is to establish new PDEs describing the system dynamics from the conservation of matter. It is used to handle both varying availability of myosin heads and actin sites.

Finally, these complete models have to be properly coupled with a model of tissue so that they can eventually used in an organ model. The third goal of this work is thus naturally defined as:

Link these newly proposed models in a heart multi-scale simulation framework.

The goal is two-fold: it consists in linking the continuous equations of the microscopic model and that of the macroscopic (organ model) from a theoretical standpoint, but also to propose adapted numerical methods to carry out the organ simulation in a rigorous way. Here, thermodynamics will play a crucial role serving as a guideline for the design of the link between scales and the development of numerical methods.

To achieve the three goals presented above, several challenges have to be addressed. There is first a challenge of understanding the nature and the functioning of the system we are trying to describe. The second challenge concerns the multi-scale nature of the considered problems. Indeed, the heart contraction from the actin-myosin interaction to the organ response involves time scales spanning over four orders of magnitude (from 100 µs to 1 s) and space scales covering eight orders of magnitude (from 1 nm to 10 cm).

Structure of this work

This thesis is composed of five chapters.

Chapter 1 – Review of muscle contraction physiology

This chapter tackles the first challenge identified for this work, namely the understanding of the physiology. We review the elements of the muscle contraction physiology available in the literature that are of interest for the development of actin-myosin interaction models and the incorporation of the contraction regulation mechanisms. No experiment has been performed for this work; there are therefore no new experimental data among that presented in this chapter. However, some interpretations of experimental data are original. Moreover, to the best of my knowledge, a recent global physiology review with the focus on the relevant elements for the development of heart models did not exist before.

Chapter 2 – Thermodynamic properties of muscle contraction models and associated discrete-time principles

In Chapter 2, we reformulate the chemico-mechanical models, which have as a common root the Huxley'57 model [Huxley, 1957a], into a unifying framework. We establish some mathematical properties with a particular emphasis on the thermodynamical properties. The first main contribution of this work is the introduction of a new rheological scheme to incorporate the micro-scale chemico-mechanical model into a macroscopic mechanical tissue model and the establishment of the thermodynamical properties of the coupled system. This part was already well advanced before the beginning of my PhD work and I have only a contribution in the establishment of some properties of the coupled system. The second main contribution is the design of numerical methods for chemico-mechanical models satisfying the thermodynamics and the enhancement of previously proposed methods for the coupled system so that the discrete thermodynamics balance can be tracked from the micro to the macro-scale.

The chapter takes the form of an article co-authored by François Kimmig, Dominique Chapelle and Philippe Moireau, published in AMSES and entitled *Thermodynamics properties of muscle contraction models and associated discrete-time principles.* It is referred to as [Kimmig et al., 2019a] in the rest of the manuscript. Note that the appendix presented in this chapter is not part of the published article.

Chapter 3 – Hierarchical modeling of force generation in cardiac muscle

In this chapter, we present the derivation of a hierarchy of actin-myosin interaction models. We start from a refined stochastic model [Caruel et al., 2019] and display the ability of this model to describe the behavior of cardiac muscles before applying several steps of simplification.

A strong emphasis is put on the calibration process of these models that take advantage of the hierarchical structure in which they are embedded. The models outputs are evaluated against data obtained on rat cardiac cells at 25 °C. The proposed calibration allows the most refined model to match many physiological indicators, while simplified models are restricted to the indicators that correspond to their time scale of validity. This validates the relevance of the proposed models and their predictive ability. This chapter takes the form of a pre-print article co-authored by François Kimmig and Matthieu Caruel, entitled *Hierarchical modeling of force generation in cardiac muscle.* It is referred to as [Kimmig & Caruel, 2019] in the rest of the manuscript.

Chapter 4 – Activation-contraction coupling in a multiscale heart model capturing the Frank-Starling effect

This chapter concerns the incorporation into the model of a first regulation mechanism: the variation of the myosin heads availability. We consider two groups of myosin heads (available and not available). Using the conservation of myosin heads, we establish the PDE that governs the system dynamics. It is an extension of that of the Huxley'57 model with additional terms accounting for the exchanges between the two groups of myosin heads. The numerical methods proposed in Chapter 2 are extended to take the additional terms into account. The activation of the thin filament is, in this chapter, treated phenomenologically. Linking the newly proposed models to a cardiac simulation environment, we perform heartbeat simulations and demonstrate the ability of our model to capture the key features of the Frank-Starling mechanism, which takes place at the organ level and originates from the myosin and actin availability variations.

This chapter takes the form of a pre-print article co-authored by François Kimmig, Philippe Moireau and Dominique Chapelle, entitled *Activation-contraction coupling in a*

multiscale heart model capturing the Frank-Starling effect. It is referred to as [Kimmig et al., 2019b] in the rest of the manuscript.

Chapter 5 – Varying thin filament activation in the framework of the Huxley'57 model

To complete our modeling framework, we need to properly integrate the activation of actin sites into the model. Applying a similar strategy as in Chapter 4, we obtain a system of equations describing the actin-myosin interaction and the variation of activation of the thick and thin filament. The calibration of the model is performed with *ex vivo* data. Our model has the capability of producing important physiological data.

Main contributions

To conclude this introduction, an overview of the scientific productions during this thesis is given. This work was also presented in several conferences in poster sessions or oral presentations.

Published articles and pre-prints

- Kimmig, F., Chapelle, D., and Moireau, P. (2019). Thermodynamic properties of muscle contraction models and associated discrete-time principles. *Advanced Modeling and Simulation in Engineering Sciences*, 6(1), 6.
- Kimmig, F., and Caruel, M. Hierarchical modeling of force generation in cardiac muscle. *Pre-print*
- Kimmig, F., Moireau, P., and Chapelle, D. Activation-contraction coupling in a multiscale heart model capturing the Frank-Starling effect. *Pre-print*

Oral communications

- 8th World Congress of Biomechanics – WCB 2018 – Dublin, Ireland
  Poster session: *Multi-scale modeling of muscle contraction.*
- 6ème rencontre du GDR Mécabio – Université Montpellier 2, France
  Oral presentation: *Multi-scale modeling of muscle contraction.*
- 6th International conference on computational and mathematical biomedical engineering – CMBE 2019 – Tohoku University, Sendai City, Japan
  Oral presentation: *Activation-contraction coupling in a multi-scale heart model.*
- Symposium Jean Mandel 2019 – École Polytechnique, Palaiseau, France
  Oral presentation: *Activation-contraction coupling in a multi-scale heart model.*

Software development The models presented in chapters 3, 4 and 5 have been implemented in the heart simulation library *CardiacLab*, which is developed internally in the MΞDISIM team. This library has been used to perform all cardiac simulations presented in this thesis.

Moreover, the chemico-mechanical contraction model developed by [Piazzesi & Lombardi, 1995] has also been implemented into this environment. Altogether, these contributions represent about 10 000 lines of codes.

Bibliography

Ait-Mou, Y., Hsu, K., Farman, G.P., Kumar, M., Greaser, M.L., Irving, T.C., & de Tombe, P.P. (2016). Titin strain contributes to the Frank–Starling law of the heart by structural rearrangements of both thin- and thick-filament proteins. *Proceedings of the National Academy of Sciences*, *113*(8), 2306–2311.

Ait-Mou, Y., Lacampagne, A., Irving, T., Scheuermann, V., Blot, S., Ghaleh, B., de Tombe, P.P., & Cazorla, O. (2018). Altered myofilament structure and function in dogs with Duchenne muscular dystrophy cardiomyopathy. *Journal of molecular and cellular cardiology*, *114*, 345–353.

Astorino, M., Gerbeau, J.-F., Pantz, O., & Traoré, K.-F. (2009). Fluid–structure interaction and multi-body contact: Application to aortic valves. *Computer Methods in Applied Mechanics and Engineering*, *198*(45-46), 3603–3612.

Baillargeon, B., Rebelo, N., Fox, D.D., Taylor, R.L., & Kuhl, E. (2014). The Living Heart Project: A robust and integrative simulator for human heart function. *European Journal of Mechanics / A Solids*, *48*(C), 38–47.

Bertoglio, C., Barber, D., Gaddum, N., Valverde, I., Rutten, M., Beerbaum, P., Moireau, P., Hose, R., & Gerbeau, J.-F. (2014). Identification of artery wall stiffness: in vitro validation and in vivo results of a data assimilation procedure applied to a 3D fluid-structure interaction model. *Journal of Biomechanics*, *47*(5), 1027–1034.

Bestel, J, Clément, F, & Sorine, M (2001). A Biomechanical Model of Muscle Contraction. In *Medical Image Computing and Computer-Assisted Intervention – MICCAI 2001*, (pp. 1159–1161). Berlin, Heidelberg: Springer, Berlin, Heidelberg.

Caremani, M., Melli, L., Dolfi, M., Lombardi, V., & Linari, M. (2015). Force and number of myosin motors during muscle shortening and the coupling with the release of the ATP hydrolysis products. *The Journal of Physiology*, *593*(15), 3313–3332.

Caremani, M., Pinzauti, F., Reconditi, M., Piazzesi, G., Stienen, G.J.M., Lombardi, V., & Linari, M. (2016). Size and speed of the working stroke of cardiac myosin in situ. *Proceedings of the National Academy of Sciences*, *113*(13), 3675–3680.

Caruel, M., Allain, J.-M., & Truskinovsky, L. (2013a). Muscle as a Metamaterial Operating Near a Critical Point. *Physical review letters*, *110*(24), 248103.

Caruel, M., Chabiniok, R., Moireau, P., Lecarpentier, Y., & Chapelle, D. (2013b). Dimensional reductions of a cardiac model for effective validation and calibration. *Biomechanics and Modeling in Mechanobiology*, *13*(4), 897–914.

Caruel, M., Moireau, P., & Chapelle, D. (2019). Stochastic modeling of chemical-mechanical coupling in striated muscles. *Biomechanics and Modeling in Mechanobiology*, *18*(3), 563–587.

Caruel, M., & Truskinovsky, L. (2018). Physics of muscle contraction. *Reports on Progress in Physics*, (pp. 1–98).

Chabiniok, R, Moireau, Philippe, Lesault, P F, Rahmouni, A, Deux, J F, & Chapelle, Dominique (2012). Estimation of tissue contractility from cardiac cine-MRI using a biomechanical heart model. *Biomechanics and Modeling in Mechanobiology*, *11*(5), 609–630.

Chabiniok, R., Wang, V.Y., Hadjicharalambous, M., Asner, L., Lee, J., Sermesant, M., Kuhl, E., Young, A.A., Moireau, P., Nash, M.P., Chapelle, D., & Nordsletten, D.A. (2016). Multiphysics and multiscale modelling, data-model fusion and integration of organ physiology in the clinic: ventricular cardiac mechanics. *Interface focus*, *6*(2), 20150083.

Chapelle, D., Clément, F., Génot, F., Le Tallec, P., Sorine, M., & Urquiza, J.M. (2001). A Physiologically-Based Model for the Active Cardiac Muscle Contraction. In *Functional Imaging and Modeling of the Heart*, (pp. 128–133). Berlin, Heidelberg: Springer, Berlin, Heidelberg.

Chapelle, D., Le Tallec, P., Moireau, P., & Sorine, M. (2012). Energy-preserving muscle tissue model: formulation and compatible discretizations. *Journal for Multiscale Computational Engineering*.

Clatz, O., Sermesant, M., Bondiau, P.Y., Delingette, H., Warfield, S.K., Malandain, G., & Ayache, N. (2005). Realistic simulation of the 3-D growth of brain tumors in MR images coupling diffusion with biomechanical deformation. *IEEE Transactions on Medical Imaging*, *24*(10), 1334–1346.

Cormack, A.M. (1963). Representation of a function by its line integrals, with some radiological applications. *Journal of applied physics*, *34*(9), 2722–2727.

Corrado, Cesare, Gerbeau, Jean-Frédéric, & Moireau, Philippe (2015). Identification of weakly coupled multiphysics problems. application to the inverse problem of electrocardiography. *Journal of Computational Physics*, *283*, 271–298.

Cyron, C.J., Wilson, J.S., & Humphrey, J.D. (2014). Mechanobiological stability: a new paradigm to understand the enlargement of aneurysms? *Journal of The Royal Society Interface*, *11*(100), 20140680–11.

Dalla Man, C., Micheletto, F., Lv, D., Breton, M., Kovatchev, B., & Cobelli, C. (2014). The UVA/PADOVA Type 1 Diabetes Simulator. *Journal of Diabetes Science and Technology*, *8*(1), 26–34.

Deshcherevskiĭ, V I (1971). A kinetic theory of striated muscle contraction. *Biorheology*, *7*(3), 147–170.

Einthoven, W. (1895). Ueber die Form des menschlichen Electrocardiogramms. *Pflügers Archiv - European Journal of Physiology*, *60*(3-4), 101–123.

Eisenberg, E., & Hill, T.L. (1978). A cross-bridge model of muscle contraction. *Progress in biophysics and molecular biology*, *33*(1), 55–82.

Eisenberg, E., Hill, T.L., & Chen, Y. (1980). Cross-bridge model of muscle contraction. Quantitative analysis. *Biophysical Journal*, *29*(2), 195–227.

Enderling, H., & Chaplain, M.A.J. (2014). Mathematical modeling of tumor growth and treatment. *Current pharmaceutical design*, *20*(30), 4934–4940.

Esaki, S., Ishii, Y., & Yanagida, T. (2003). Model describing the biased Brownian movement of myosin. *Proceedings of the Japan Academy, Series B*, *79B*(1), 9–14.

Formaggia, Luca, Lamponi, Daniele, & Quarteroni, Alfio (2003). One-dimensional models for blood flow in arteries. *Journal of Engineering Mathematics*, *47*(3-4), 251–276.

Gasser, T.C., Ogden, R.W., & Holzapfel, G.A. (2005). Hyperelastic modelling of arterial layers with distributed collagen fibre orientations. *Journal of The Royal Society Interface*, *3*(6), 15–35.

Genet, M., Lee, LC, Ge, L., Acevedo-Bolton, G., Jeung, N., Martin, A., Cambronero, N., Boyle, A., Yeghiazarians, Y., Kozerke, S., & Guccione, J.M. (2015). A Novel Method for Quantifying Smooth Regional Variations in Myocardial Contractility Within an Infarcted Human Left Ventricle Based on Delay-Enhanced Magnetic Resonance Imaging. *Journal of Biomechanical Engineering*, *137*(8), 081009.

Ghista, D.N., Patil, K.M., Gould, P., & Woo, K.B. (1973). Computerized left ventricular mechanics and control system analyses models relevant for cardiac diagnosis. *Computers in Biology and Medicine*, *3*(1), 27–46.

Guccione, J.M., & McCulloch, A.D. (1993). Mechanics of Active Contraction in Cardiac Muscle: Part I—Constitutive Relations for Fiber Stress That Describe Deactivation. *Journal of Biomechanical Engineering*, *115*(1), 72–81.

Hill, A.V. (1938). The heat of shortening and the dynamic constants of muscle. *Proc. R. Soc. Lond. B*, *126*(843), 136–195.

Hill, T.L. (1974). Theoretical formalism for the sliding filament model of contraction of striated muscle Part I. *Progress in biophysics and molecular biology*, *28*, 267–340.

Hill, T.L. (1976). Theoretical formalism for the sliding filament model of contraction of striated muscle part II. *Progress in biophysics and molecular biology*, *29*, 105–159.

Hill, T.L. (1977). *Free Energy Transduction in Biology*. Academic Press.

Hirschvogel, M., Bassilious, M., Jagschies, L., Wildhirt, S.M., & Gee, M.W. (2017). A monolithic 3D-0D coupled closed-loop model of the heart and the vascular system: Experiment-based parameter estimation for patient-specific cardiac mechanics. *International Journal for Numerical Methods in Biomedical Engineering*, *84*(3), e2842–22.

Hodgkin, A.L., & Huxley, A.F. (1952). A quantitative description of membrane current and its application to conduction and excitation in nerve. *The Journal of Physiology*, *117*(4), 500–544.

Houdusse, A., & Sweeney, H.L. (2016). How Myosin Generates Force on Actin Filaments. *Trends in Biochemical Sciences*, *41*(12), 989–997.

Hounsfield, G.N. (1973). Computerized transverse axial scanning (tomography): Part 1. Description of system. *The British journal of radiology*, *46*(552), 1016–1022.

Howatson Tawhai, M., Pullan, A.J., & Hunter, P.J. (2000). Generation of an anatomically based three-dimensional model of the conducting airways. *Annals of Biomedical Engineering*, *28*(7), 793–802.

Humphrey, J.D., & Rajagopal, K.R. (2002). A constrained mixture model for growth and remodeling of soft tissues. *Mathematical models and methods in applied sciences*, *12*(03), 407–430.

Hunter, P.J. (1975). *Finite Element Analysis of Cardiac Muscle Mechanics.*. Ph.D. thesis, University of Oxford.

Hunter, P.J., & Smaill, B.H. (1988). The analysis of cardiac function: a continuum approach. *Progress in biophysics and molecular biology*, *52*(2), 101–164.

Huxley, A.F. (1957a). Muscle structures and theories of contraction. *Progr. Biophys. Chem.*.

Huxley, A.F., & Niedergerke, R. (1954). Structural changes in muscle during contraction; interference microscopy of living muscle fibres. *Nature*, *173*(4412), 971–973.

Huxley, A.F., & Simmons, R.M. (1971). Proposed mechanism of force generation in striated muscle. *Nature*.

Huxley, H.E. (1957b). The double array of filaments in cross-striated muscle. *The Journal of biophysical and biochemical cytology*, *3*(5), 631–648.

Huxley, H.E. (1969). The mechanism of muscular contraction. *Science*, *164*(3886), 1356–1365.

Huxley, H.E. (2004). Fifty years of muscle and the sliding filament hypothesis. *European Journal of Biochemistry*, *271*(8), 1403–1415.

Huxley, H.E., & Hanson, J. (1954). Changes in the cross-striations of muscle during contraction and stretch and their structural interpretation. *Nature*, *173*(4412), 973–976.

Hyde, E.R., Behar, J.M., Claridge, S., Jackson, T., Lee, A.W.C., Remme, E.W., Sohal, M., Plank, G., Razavi, R., Rinaldi, C.A., & Niederer, S.A. (2015). Beneficial Effect on Cardiac Resynchronization From Left Ventricular Endocardial Pacing Is Mediated by Early Access to High Conduction Velocity Tissue: Electrophysiological Simulation Study. *Circulation. Arrhythmia and electrophysiology*, *8*(5), 1164–1172.

Julian, Fred J (1969). Activation in a skeletal muscle contraction model with a modification for insect fibrillar muscle. *Biophysj*, *9*(4), 547–570.

Jülicher, F., Ajdari, A., & Prost, J. (1997). Modeling molecular motors. *Reviews of Modern Physics*, *69*(4), 1269–1282.

Kerckhoffs, R.C.P., Omens, J.H., & McCulloch, A.D. (2012). A single strain-based growth law predicts concentric and eccentric cardiac growth during pressure and volume overload. *Mechanics research communications*, *42*, 40–50.

Kimmig, F., & Caruel, M. (2019). Hierarchical modeling of muscle contraction. *submitted*.

Kimmig, F., Chapelle, D., & Moireau, P. (2019a). Thermodynamic properties of muscle contraction models and associated discrete-time principles. *Advanced Modeling and Simulation in Engineering Sciences*, *6*(1), 6.

Kimmig, F., Moireau, P., & Chapelle, D. (2019b). Activation-contraction coupling in a multiscale heart model, an element for capturing the frank-starling effect. *to be submitted*.

Kron, Stephen J, & Spudich, James A (1986). Fluorescent actin filaments move on myosin fixed to a glass surface. *Proceedings of the National Academy of Sciences*, *83*(17), 6272–6276.

Kroon, W., Delhaas, T., Arts, T., & Bovendeerd, P. (2009). Computational modeling of volumetric soft tissue growth: application to the cardiac left ventricle. *Biomechanics and Modeling in Mechanobiology*, *8*(4), 301–309.

Lauterbur, P.C. (1973). Image Formation by Induced Local Interactions: Examples Employing Nuclear Magnetic Resonance. *Nature*, *242*(5394), 190–191.

Linari, M., Brunello, E., Reconditi, M., Fusi, L., Caremani, M., Narayanan, T., Piazzesi, G., Lombardi, V., & Irving, M. (2015). Force generation by skeletal muscle is controlled by mechanosensing in myosin filaments. *Nature*, *528*(7581), 276–279.

Linari, M., Caremani, M., & Lombardi, V. (2010). A kinetic model that explains the effect of inorganic phosphate on the mechanics and energetics of isometric contraction of fast skeletal muscle. *Proceedings. Biological sciences*, *277*(1678), 19–27.

Linari, M., Piazzesi, G., & Lombardi, V. (2009). The Effect of Myofilament Compliance on Kinetics of Force Generation by Myosin Motors in Muscle. *Biophysj*, *96*(2), 583–592.

Lymn, R.W., & Taylor, E.W. (1971). Mechanism of adenosine triphosphate hydrolysis by actomyosin. *Biochemistry*, *10*(25), 4617–4624.

Magnasco, M.O. (1993). Forced thermal ratchets. *Physical review letters*, *71*(10), 1477–1481.

Mansfield, P., & Maudsley, A.A. (1977). Medical imaging by NMR. *The British journal of radiology*, *50*(591), 188–194.

Marcucci, L., & Truskinovsky, L. (2010). Mechanics of the power stroke in myosin II. *Physical Review E*, *81*(5), 051915–8.

Marcucci, L., Washio, T., & Yanagida, T. (2016). Including thermal fluctuations in actomyosin stable states increases the predicted force per motor and macroscopic efficiency in muscle modelling. *PLoS Computational Biology*, *12*(9).

McDowell, K.S., Vadakkumpadan, F., Blake, R., Blauer, J., Plank, G., MacLeod, R.S., & Trayanova, N.A. (2013). Mechanistic Inquiry into the Role of Tissue Remodeling in Fibrotic Lesions in Human Atrial Fibrillation. *Biophysj*, *104*(12), 2764–2773.

Mirsky, I. (1969). Left ventricular stresses in the intact human heart. *Biophysj*, *9*(2), 189–208.

Molloy, J E, Burns, J E, Kendrick-Jones, J, Tregear, R T, & White, DCS (1995). Movement and force produced by a single myosin head. *Nature*, *378*(6553), 209.

Nash, M.P., & Hunter, P.J. (2000). Computational Mechanics of the Heart. *Journal of elasticity and the physical science of solids*, *61*(1), 113–141.

Noble, D. (1962). A modification of the Hodgkin—Huxley equations applicable to Purkinje fibre action and pacemaker potentials. *The Journal of Physiology*, *160*(2), 317–352.

Nordsletten, D.A., Niederer, S.A., Nash, M.P., Hunter, P.J., & Smith, N.P. (2011). Coupling multi-physics models to cardiac mechanics. *Progress in biophysics and molecular biology*, *104*(1-3), 77–88.

Pant, S., Fabrèges, B., Gerbeau, J.-F., & Vignon-Clementel, I. (2014). A methodological paradigm for patient-specific multi-scale CFD simulations: from clinical measurements to parameter estimates for individual analysis. *International Journal for Numerical Methods in Biomedical Engineering*, *30*(12), 1614–1648.

Peskin, C.S. (1972). Flow patterns around heart valves: a numerical method. *Journal of Computational Physics*, *10*(2), 252–271.

Peskin, C.S. (1975). *Mathematical aspects of heart physiology*. Courant Institute of Mathematical Sciences.

Peskin, C.S. (1977). Numerical analysis of blood flow in the heart. *Journal of Computational Physics*, *25*(3), 220–252.

Piazzesi, G., & Lombardi, V. (1995). A cross-bridge model that is able to explain mechanical and energetic properties of shortening muscle. *Biophysical Journal*, *68*, 1966–1979.

Piazzesi, G., Reconditi, M., Linari, M., Lucii, L., Bianco, P., Brunello, E., Decostre, V., Stewart, A., Gore, D.B., Irving, T.C., Irving, M., & Lombardi, V. (2007). Skeletal muscle performance determined by modulation of number of myosin motors rather than motor force or stroke size. *Cell*, *131*(4), 784–795.

Podolsky, R J, Nolan, A C, & Zaveler, S A (1969). Cross-bridge properties derived from muscle isotonic velocity transients. *Proceedings of the National Academy of Sciences*, *64*(2), 504–511.

Prost, J., Chauwin, J.-F., Peliti, L., & Ajdari, A. (1994). Asymmetric pumping of particles. *Physical review letters*, *72*(16), 2652–2655.

Quaranta, V., Weaver, A.M., Cummings, P.T., & Anderson, A.R.A. (2005). Mathematical modeling of cancer: The future of prognosis and treatment. *Clinica Chimica Acta*, *357*(2), 173–179.

Quarteroni, A., Lassila, T., Rossi, S., & Ruiz-Baier, R. (2017). Integrated Heart-Coupling multiscale and multiphysics models for the simulation of the cardiac function. *Computer Methods in Applied Mechanics and Engineering*, *314*, 345–407.

Quarteroni, A., Veneziani, A., & Zunino, P. (2002). Mathematical and numerical modeling of solute dynamics in blood flow and arterial walls. *SIAM*, *39*(5), 1488–1511.

Rausch, M.K., Zöllner, A.M., Genet, M., Baillargeon, B., Bothe, W., & Kuhl, E. (2017). A virtual sizing tool for mitral valve annuloplasty. *International Journal for Numerical Methods in Biomedical Engineering*, *33*(2).

Reconditi, M., Brunello, E., Fusi, L., Linari, M., Martinez, M.F., Lombardi, V., Irving, M., & Piazzesi, G. (2014). Sarcomere-length dependence of myosin filament structure in skeletal muscle fibres of the frog. *The Journal of Physiology*, *592*(5), 1119–1137.

Reconditi, M., Brunello, E., Linari, M., Bianco, P., Narayanan, T., Panine, P., Piazzesi, G., Lombardi, V., & Irving, M. (2011). Motion of myosin head domains during activation and force development in skeletal muscle. *Proceedings of the National Academy of Sciences*, *108*(17), 7236–7240.

Reconditi, M., Caremani, M., Pinzauti, F., Powers, J.D., Narayanan, T., Stienen, G.J.M., Linari, M., Lombardi, V., & Piazzesi, G. (2017). Myosin filament activation in the heart is tuned to the mechanical task. *Proceedings of the National Academy of Sciences*, (pp. 3240–3245).

Reconditi, M., Koubassova, N., Linari, M., Dobbie, I., Narayanan, T., Diat, O., Piazzesi, G., Lombardi, V., & Irving, M. (2003). The conformation of myosin head domains in rigor muscle determined by X-ray interference. *Biophysj*, *85*(2), 1098–1110.

Ribba, B., Saut, O., Colin, T., Bresch, D., Grenier, E., & Boissel, J.P. (2006). A multiscale mathematical model of avascular tumor growth to investigate the therapeutic benefit of anti-invasive agents. *Journal of Theoretical Biology*, *243*(4), 532–541.

Rodriguez, E.K., Hoger, A., & McCulloch, A.D. (1994). Stress-dependent finite growth in soft elastic tissues. *Journal of Biomechanics*, *27*(4), 455–467.

Roth, C.J., Ismail, M., Yoshihara, L., & Wall, W.A. (2017). A comprehensive computational human lung model incorporating inter-acinar dependencies: Application to spontaneous breathing and mechanical ventilation. *International Journal for Numerical Methods in Biomedical Engineering*, *33*(1).

Sainte-Marie, J., Chapelle, D., Cimrman, R., & Sorine, M. (2006). Modeling and estimation of the cardiac electromechanical activity. *Computers & Structures*, *84*(28), 1743–1759.

Sermesant, M., Chabiniok, R., Chinchapatnam, P., Mansi, T., Billet, F., Moireau, P., Peyrat, J.M., Wong, K., Relan, J., Rhode, K., Ginks, M., Lambiase, P., Delingette, H., Sorine, M., Rinaldi, C.A., Chapelle, D., Razavi, R., & Ayache, N. (2012). Patient-specific electromechanical models of the heart for the prediction of pacing acute effects in CRT: A preliminary clinical validation. *Medical Image Analysis*, *16*(1), 201–215.

Sheshka, Raman (2012). *The power stroke driven muscle contraction*. Ph.D. thesis, École polytechnique.

Sheshka, R, & Truskinovsky, L (2014). Power-stroke-driven actomyosin contractility. *Physical review. E, Statistical, nonlinear, and soft matter physics*, *89*(1), 012708.

Silverthorn, D.U., Ober, W.C., Garrison, C.W., & Silverthorn, A.C. (2009). *Human physiology: an integrated approach*. Pearson.

Sliwoski, G., Kothiwale, S., Meiler, J., & Lowe, E.W. (2013). Computational Methods in Drug Discovery. *Pharmacological Reviews*, *66*(1), 334–395.

Stella, J.A., & Sacks, M.S. (2007). On the Biaxial Mechanical Properties of the Layers of the Aortic Valve Leaflet. *Journal of Biomechanical Engineering*, *129*(5), 757–10.

Sugiura, S., Washio, T., Hatano, A., Okada, J., Watanabe, H., & Hisada, T. (2012). Multi-scale simulations of cardiac electrophysiology and mechanics using the University of Tokyo heart simulator. *Progress in biophysics and molecular biology*, *110*(2-3), 380–389.

Tanrikulu, Y., Krüger, Bj., & Proschak, E. (2013). The holistic integration of virtual screening in drug discovery. *Drug Discovery Today*, *18*(7-8), 358–364.

Taylor, C.A., & Figueroa, C.A. (2009). Patient-specific modeling of cardiovascular mechanics. *Annual Review of Biomedical Engineering*, *11*, 109–134.

Trayanova, N.A. (2011). Whole-heart modeling: applications to cardiac electrophysiology and electromechanics. *Circulation Research*, *108*(1), 113–128.

Veigel, Claudia, Bartoo, Marc L, White, David CS, Sparrow, John C, & Molloy, Justin E (1998). The stiffness of rabbit skeletal actomyosin cross-bridges determined with an optical tweezers transducer. *Biophysj*, *75*(3), 1424–1438.

Visentin, R., Campos-Náñez, E., Schiavon, M., Lv, D., Vettoretti, M., Breton, M., Kovatchev, B.P., Dalla Man, C., & Cobelli, C. (2017). The UVA/Padova Type 1 Diabetes Simulator Goes From Single Meal to Single Day. *Journal of Diabetes Science and Technology*, *12*(2), 273–281.

Waller, A.D. (1887). A Demonstration on Man of Electromotive Changes accompanying the Heart's Beat. *The Journal of Physiology*, *8*(5), 229–234.

Wang, H., & Oster, G. (2002). Ratchets, power strokes, and molecular motors. *Applied Physics A*, *75*(2), 315–323.

Zahalak, G.I. (1981). A distribution-moment approximation for kinetic theories of muscular contraction. *Elsevier*, *55*(1-2), 89–114.

Zahalak, G I (2000). The two-state cross-bridge model of muscle is an asymptotic limit of multi-state models. *Journal of Theoretical Biology*.

Introduction (Français)

Cette thèse a été préparée dans l'équipe Inria MΞDISIM et à l'École polytechnique, financée par l'École polytechnique, sous la direction de Dominique Chapelle et Matthieu Caruel. Philippe Moireau m'a également conseillé tout au long de ce projet.

Contexte

Cette thèse s'intéresse à la modélisation mathématique des mécanismes de contraction musculaire à l'échelle microscopique, dans le but de proposer et d'intégrer nos modèles à un environnement de simulation cardiaque multi-échelles.

Médecine numérique

Ce travail s'inscrit dans un mouvement mondial de développement d'une médecine dite *numérique* à travers l'utilisation d'outils numériques et notamment de modèles. Les espoirs suscités par cet ensemble de technologies sont énormes : une médecine personnalisée avec des traitements plus précis et un dépistage précoce des maladies, qui est associée à une réduction de la mortalité mais également au développement plus sûr et plus rapide de nouveaux traitements. Un large éventail de programmes de recherche sont menés sur ce sujet.

Le développement de technologies nouvelles a depuis longtemps conduit à la mise au point d'outils d'acquisition de données médicales innovants [Chapelle *et al.*, 2012]. Des étapes clés de ce processus sont l'invention de l'électrocardiogramme (ECG) [Waller, 1887 ; Einthoven, 1895], de l'échographie, du scanner [Cormack, 1963 ; Hounsfield, 1973] et de l'imagerie par résonance magnétique [Lauterbur, 1973 ; Mansfield et Maudsley, 1977]. L'augmentation de la puissance de calcul et des systèmes d'information, qui rendent les données plus facilement disponibles et exploitables, ainsi que la multiplication des outils de mesure de signaux physiologiques amènent cette approche à un nouveau niveau de développement.

Les efforts de recherche et développement dans le domaine de la médecine numérique visent à relever le triple défi d'améliorer la compréhension de la physiologie et des pathologies, d'améliorer le diagnostic et d'optimiser le traitement des patients.

- La compréhension de la physiologie peut être améliorée en testant numériquement des hypothèses physiologiques afin de déterminer lesquelles correspondent à la réalité. De plus, des modèles bien calibrés permettent d'obtenir *in silico* la reconstruction de données difficiles ou impossibles à mesurer sur des sujets vivants. Naturellement, ce défi ne peut être atteint qu'avec des modèles capables d'établir des liens de causalité entre des événements physiologiques.

- Nous pensons que l'amélioration du diagnostic passe par une quantification de l'analyse du patient permettant aux médecins de prendre des décisions plus informées et plus objectives. Les modèles servent ici de filtres à travers lesquels les données sont examinées augmentant ainsi la quantité d'information pouvant en être extraite et permettant de donner plus de sens à ces données.

- L'optimisation du traitement est probablement le défi le plus difficile. La capacité de modéliser non seulement le comportement basal, mais également de capturer dans le modèle les effets du traitement (l'impact des médicaments ou de la modification de la géométrie de l'organe par exemple) est une condition préalable à la mise en œuvre de cette procédure.

Notons que, dans les trois défis, le besoin de modèles quantitatifs *prédictifs* et leur calibration sont des éléments cruciaux. Un autre point central concerne l'interaction entre le

modèle et les données, ces dernières étant utilisées pour calibrer les modèles de manière spécifique à un patient afin d'obtenir des prédictions personnalisées.

La complexité des mécanismes physiologiques rend le processus de construction de modèles intrinsèquement multidisciplinaire mêlant biologie, chimie, physique, mathématiques et informatique, et impose le développement d'une large variété des modèles. En effet, le choix des ingrédients de modélisation pour répondre à une question physiologique ou clinique spécifique doit être soigneusement défini. Ce choix résulte d'un compromis entre la précision de la prédiction du modèle, le coût de calcul associé et la disponibilité des mesures nécessaires à la calibration de ce modèle. Par exemple, une analyse ciblant les indicateurs globaux d'un organe peut être effectuée sur une géométrie réduite, en particulier si les conditions sur les limites de la géométrie ne peuvent pas être évaluées spécifiquement. Au contraire, si l'on étudie des phénomènes de propagation ou des variations de paramètres physiologiques localisés, l'utilisation d'un modèle géométriquement étendu est nécessaire.

Les efforts de recherche en médecine numérique ont abouti, par exemple, au développement de modèles de poumons [Howatson Tawhai *et al.*, 2000 ; Roth *et al.*, 2017] ou à la croissance de tumeurs [Quaranta *et al.*, 2005 ; Clatz *et al.*, 2005 ; Ribba *et al.*, 2006 ; Enderling et Chaplain, 2014]. Des avancées remarquables ont également déjà été réalisées dans les domaines de la découverte de médicaments, où les modèles permettent de prédire les effets de molécules [Sliwoski *et al.*, 2013 ; Tanrikulu *et al.*, 2013]. De plus, dans le processus de développement de médicaments, les régulateurs ont déjà validé l'utilisation d'outils numériques en remplacement de tests pré-cliniques sur les animaux pour la conception d'un traitement du diabète [Dalla Man *et al.*, 2014 ; Visentin *et al.*, 2017].

Le système cardiovasculaire n'a pas échappé au développement de la médecine personnalisée. Le travail précurseur de Hodgkin et Huxley [1952] pour la description du potentiel d'action et de Huxley [1957a] pour la contraction des muscle striés ont ouvert la voie à des descriptions plus globales et spécifiques du système cardiovasculaire. Nous pouvons citer ici les travaux de Noble [1962] pour la description de l'activité électrophysiologique de la membrane des cellules musculaires ainsi que des fibres de Purkinje (voir section suivante), de Mirsky [1969] ; Ghista *et al.* [1973] et P.J. Hunter [Hunter, 1975 ; Hunter et Smaill, 1988] sur la modélisation du tissu musculaire cardiaque et C.S. Peskin pour la modélisation des tissus [Peskin, 1975] et le flux sanguin [Peskin, 1972, 1977].

Depuis lors, de nombreuses équipes de recherche se sont consacrées à la mise au point de modèles physiques cardiaques et vasculaires [Guccione et McCulloch, 1993 ; Nash et Hunter, 2000 ; Chapelle *et al.*, 2001 ; Sainte-Marie *et al.*, 2006 ; Taylor et Figueroa, 2009 ; Nordsletten *et al.*, 2011 ; Trayanova, 2011 ; Chapelle *et al.*, 2012 ; Sugiura *et al.*, 2012 ; Caruel *et al.*, 2013b ; Baillargeon *et al.*, 2014 ; Pant *et al.*, 2014 ; Hirschvogel *et al.*, 2017 ; Quarteroni *et al.*, 2017]. Nous faisons référence également à Chabiniok *et al.* [2016] qui présentent une synthèse du développement des modèles cardiovasculaires et de leur applicabilité aux questions cliniques.

Des modèles de sous-parties du cœur ont également été développés pour cibler des phénomènes spécifiques tels que la croissance et le remodelage du tissu musculaire [Rodriguez *et al.*, 1994 ; Humphrey et Rajagopal, 2002], qui ont ensuite été appliqués dans le contexte des anévrismes aortiques [Cyron *et al.*, 2014] ou la croissance et le remodelage du coeur entier [Kroon *et al.*, 2009 ; Kerckhoffs *et al.*, 2012]. La fonction des valves et le flux qui les entoure [Astorino *et al.*, 2009 ; Stella et Sacks, 2007], le flux sanguin dans les artères [Quarteroni *et al.*, 2002 ; Formaggia *et al.*, 2003] et le comportement de la paroi artérielle [Gasser *et al.*, 2005] ont également été spécifiquement étudiés. Ces éléments de modèle peuvent naturellement être utilisés en tant que partie d'un modèle d'organe complet si nécessaire.

La communauté travaillant sur le système cardiovasculaire a elle aussi présenté des

preuves de concept prometteuses pour les trois principaux défis de la médecine numérique. Les modèles se sont révélés capables de mieux faire comprendre la physiologie [Hyde *et al.*, 2015 ; McDowell *et al.*, 2013]. En ce qui concerne l'amélioration du diagnostic, l'estimation à partir de données IRM utilisant des techniques d'assimilation de données de la contractilité [Chabiniok *et al.*, 2012 ; Genet *et al.*, 2015] ou de la raideur de la paroi aortique [Bertoglio *et al.*, 2014] a été réalisée. Dans le domaine de l'électrophysiologie, l'évaluation de l'état électrique dans une contraction de battement de coeur [Corrado *et al.*, 2015] a été réalisée. Certains travaux de recherche traitent également du défi de l'optimisation du traitement, d'un point de vue uniquement théorique ou complétés par une validation sur des données réelles *in vivo*. Dans la première catégorie, on peut mentionner le travail de Rausch *et al.* [2017], qui montre la capacité théorique d'un modèle cardiaque à aider à sélectionner le design des implants pour une annuloplastie mitrale. Un exemple de la second catégorie est le travail de Sermesant *et al.* [2012], qui ont présenté un cadre de calcul capable de trouver *a priori* la position optimale des électrodes de stimulateur cardiaque, pouvant ainsi remplacer la pratique actuelle fonctionnant par essais et erreurs et donc raccourcir la durée de la procédure et augmenter les taux de succès.

Les promesses de la recherche universitaire ont déjà commencé à se traduire dans la pratique clinique. En effet, des entreprises telles que HeartFlow et Arterys ont déjà reçu l'autorisation de la part des autorités régulatrices de commercialiser des produits s'appuyant sur des modèles cardiovasculaires pour évaluer les flux sanguins dans le réseau cardiovasculaire.

Le cœur humain

Le cœur est l'objet principal de cette thèse. Nous donnons ici une brève présentation de son anatomie et de son fonctionnement. Une description plus complète du coeur peut être trouvée par exemple chez [Silverthorn *et al.*, 2009].

Le cœur est un organe situé dans le thorax, entre les poumons. Il est intégré dans le système circulatoire cardiovasculaire, permettant au sang de circuler dans le corps pour alimenter les organes en oxygène, en nutriments et en hormones, et d'assurer le transport des déchets. Le cœur pompe le sang dans ce système circulatoire. Il y a trois circulations sanguines distinctes :

- la circulation pulmonaire, qui correspond à la partie du sang circulant dans les poumons afin de permettre des échanges gazeux conduisant à l'oxygénation du sang ;
- la circulation coronaire qui alimente le coeur lui-même en sang par les artères coronaires ;
- la circulation systémique, qui fournit du sang au reste du corps.

L'anatomie du cœur est présentée sur la Figure 5. Il est composé de quatre chambres : les deux *oreillettes* (nommées droite et gauche) et les deux *ventricules* (nommés droit et gauche égalenent). Le *septum* sépare les deux ventricules. Les valves constituent l'interface entre les ventricules et les oreillettes d'une part, et les ventricules et le système circulatoire de l'autre. Elles permettent également de donner une direction à la circulation sanguine. La *valve triscupide* est située entre l'oreillette droite et le ventricule droit ; la *valve pulmonaire* sépare le ventricule droit de l'artère pulmonaire. Le ventricule gauche est également relié aux éléments voisins par deux valves : la *valve mitrale* pour l'oreillette gauche et la *valve aortique* pour l'aorte.

Le tissu cardiaque, appelé *myocarde*, est contractile, ce qui permet de générer une pression dans les cavités et ainsi d'éjecter le sang. Il est composé de fibres enroulées autour des cavités. Cet arrangement de fibres crée une torsion dans le ventricule, ce qui améliore

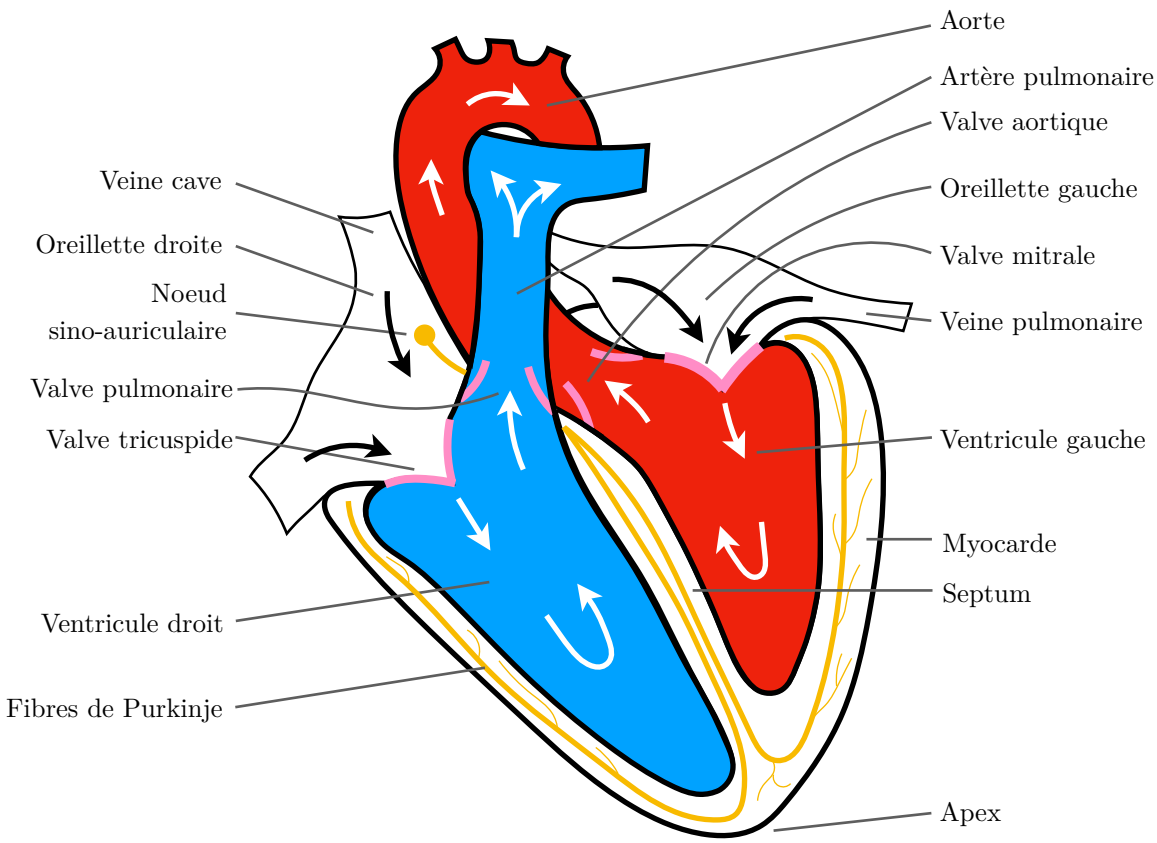

FIGURE 5 – Représentation schématique du coeur. Le sang oxygéné est représenté en rouge et le sang désoxygéné en bleu. Les flux sanguins sont représentés par des flèches noires et blanches.

la contraction. À l'échelle microscopique, ces fibres forment un réseau de ramifications (voir la Figure 6). La contraction musculaire est déclenchée par un signal chimique et

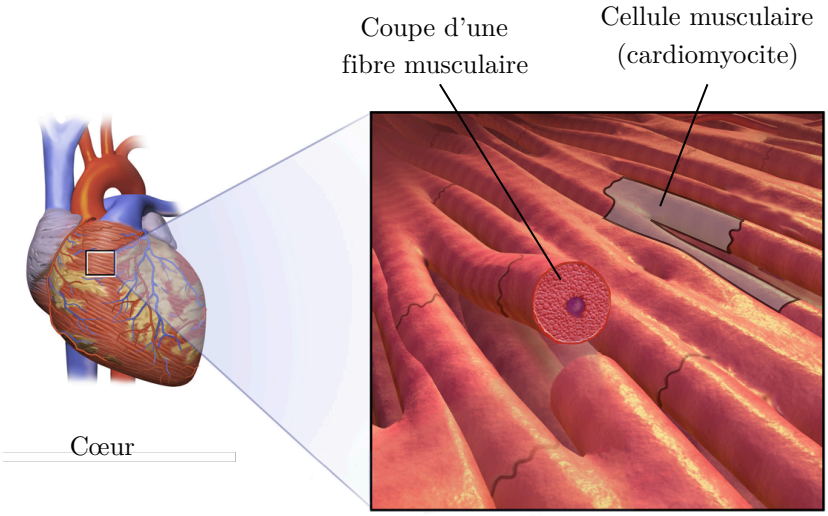

FIGURE 6 – Réseau de fibres musculaires cardiaques. Cette illustration est une modification de *Cardiac Muscle* par BruceBlaus, sous licence CC BY 4.0.

électrique provenant de l'oreillette droite. Ce signal traverse tout le cœur à travers les fibres de Purkinje et se propage d'une cellule contractile à une autre.

Dans un cycle cardiaque, le sang désoxygéné pénètre dans le cœur par l'oreillette droite, tandis que le sang oxygéné provenant des poumons entre dans l'oreillette gauche. La contraction atriale se déclenche la première, permettant le remplissage des ventricules. Le signal déclenchant la contraction atteint ensuite les ventricules, qui éjectent le sang dans l'artère pulmonaire en direction des poumons et dans l'aorte vers le reste du corps. Les flux de sang dans le cœur sont illustrés à la Figure 5. La principale cavité d'intérêt pour notre étude est le ventricule gauche. Nous présentons l'évolution typique de sa pression et de son volume dans un cycle cardiaque à la Figure 7. Au début du cycle, l'oreillette gauche se contracte, sa pression augmente et le sang coule dans le ventricule. Ensuite, le ventricule commence à se contracter, la pression à l'intérieur de la cavité augmente et la valve mitrale se ferme. Lorsque la pression ventriculaire atteint la pression aortique, la valve aortique s'ouvre et le sang est éjecté dans l'aorte. Simultanément, le volume de la cavité diminue. Après avoir atteint un pic, la pression ventriculaire diminue. La relaxation commence et la valve aortique se ferme. Lorsque la pression ventriculaire tombe au niveau de la pression de l'oreillette, la valve mitrale s'ouvre et un nouveau cycle peut avoir lieu. La fonction du cœur en tant que pompe est illustrée ici. En effet, le ventricule gauche amène un volume de sang d'une pression auriculaire basse à une pression aortique élevée. Une représentation utile de ces données pour la compréhension de la fonction cardiaque est la relation pression-volume. Cette relation forme une boucle en raison de la nature cyclique du fonctionnement du cœur. Une illustration est présentée à la Figure 8. La période de contraction du cycle s'appelle la *systole* et la période de relaxation s'appelle la *diastole*. Notons que la diastole et la systole des oreillettes et des ventricules ne sont pas synchronisées.

Les muscles cardiaques étant l'objet d'étude principal de cette thèse, nous donnons ici une description de leur anatomie. Les fibres musculaires sont composées d'une série de petites unités contractiles appelées *sarcomères* ($\sim$2 µm). Ces derniers sont principalement constitués de deux réseaux de filaments de protéines : le filament de myosine (filament

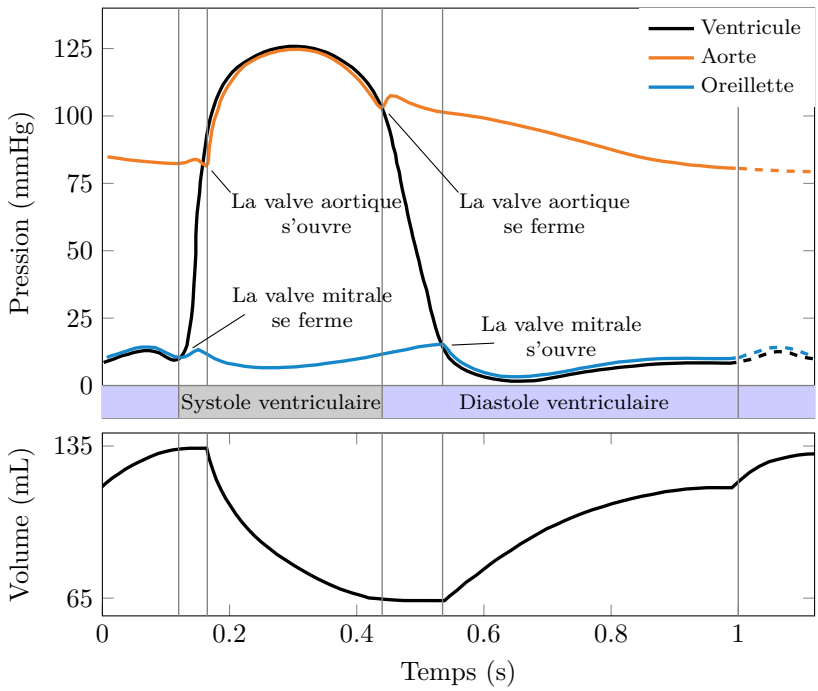

FIGURE 7 – Évolution typique de la pression et du volume du ventricule gauche dans un cycle cardiaque.

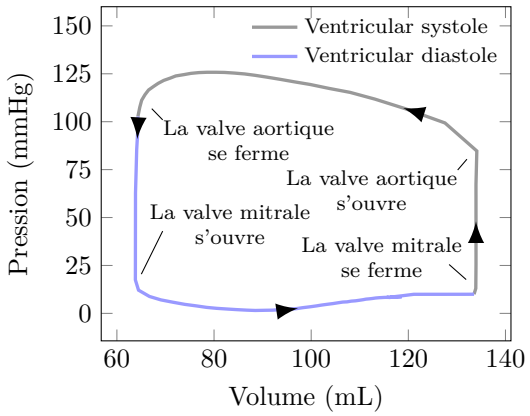

FIGURE 8 – Boucle pression-volume typique du ventricule gauche (boucle PV) dans un cycle cardiaque.

épais) et le filament d'actine (filament fin). Des composants spécifiques du filament de myosine, les *têtes de myosine*, interagissent avec les monomères d'actine (également appelés *sites d'actine*) de manière cyclique entraînant la consommation de carburant métabolique fourni par l'hydrolyse de l'ATP. La tête de myosine se fixe à un site d'actine formant un *pont*. Lorsqu'une tête de myosine est attachée, un changement rapide de conformation se produit, conduisant à la génération d'une force de contraction. Cette phase est appelée le *power stroke*. La force générée par les ponts actine-myosine est dite *active* car le processus de génération de cette force implique une consommation d'énergie. Une conséquence du développement de cette force est le raccourcissement de la longueur du sarcomère – si les conditions limites le permettent – via le glissement relatif des filaments d'actine et de myosine.

Modélisation de la contraction musculaire

L'étude et la modélisation du comportement musculaire ont débuté il y a plus d'un siècle et a été très active au cours des cinquante dernières années. Un compte-rendu historique a été écrit par l'un des principaux protagonistes : H.E. Huxley [Huxley, 2004]. Nous renvoyons vers [Caruel et Truskinovsky, 2018] pour une synthèse de travaux de modélisation théoriques récents.

Après les travaux précurseurs de A.V. Hill [Hill, 1938], les biologistes et physiologistes ont déployé des efforts considérables pour caractériser de manière expérimentale la structure du muscle, le mécanisme de contraction musculaire et ses régulations. La communauté scientifique peut être décomposée en deux groupes. Le premier, conduit par A.F. Huxley et H.E. Huxley depuis les années 50, puis notamment par V. Lombardi, s'intéresse à la caractérisation fine de la structure et des interactions microscopiques sous-jacentes à la contraction macroscopique du muscle squelettique, et les protocoles expérimentaux développés ont récemment été appliqués aux muscles cardiaques. Le second, mené par H.E.D.J. ter Keurs et P.P. de Tombe depuis les années 80 et 90 respectivement, se concentre sur la caractérisation de la contraction des muscles cardiaques et des mécanismes de régulation associés.

Les modélisateurs ont travaillé en parallèle des avancées expérimentales, tirant parti des dernières découvertes physiologiques pour améliorer les modèles. Le premier modèle de contraction musculaire est formulé par A.V. Hill en 1938, parallèlement à ses travaux expérimentaux sur la thermodynamique macroscopique de la contraction musculaire [Hill, 1938]. Il observe la relation entre la vitesse de raccourcissement musculaire et la force développée, ainsi que les flux de chaleur associés. Cette relation force-vitesse est la caractéristique principale de l'interaction actine-myosine. Elle est aujourd'hui souvent nommée *courbe de Hill*. Le modèle proposé par A.V. Hill pour rendre compte de ses observations expérimentales est un modèle rhéologique simple composé d'un ressort et d'un "élément actif" ayant la relation force-vitesse comme équation constitutive. Ce modèle cible la macro-échelle musculaire. Il est toujours utilisé dans des travaux récent en raison de sa simplicité [Quarteroni *et al.*, 2017].

Au début des années 50, la théorie dominante suppose que la contraction résulte de l'enroulement d'un seul filament d'actomyosine. Un changement de paradigme commence en 1954. Le groupe d'A.F. Huxley (à Cambridge en Angleterre) et le groupe d'H.E. Huxley (à Cambridge dans le Massachusetts) publient, dans le même numéro de *Nature*, deux études expérimentales observant les variations des stries du muscle squelettique avec l'étirement musculaire [Huxley et Niedergerke, 1954 ; Huxley et Hanson, 1954]. De ces résultats émerge l'idée que le raccourcissement musculaire provient du glissement relatif des filaments de myosine et d'actine et qu'une force est créée par l'interaction de ces composants. Ceci constitue la *théorie des filaments glissants*.

En utilisant un mécanisme (spéculatif à l'époque) impliquant la formation de ponts

actine-myosine entre les têtes de myosine et les sites d'actine Huxley [1957a], propose un nouveau modèle de contraction musculaire. Ce modèle décrit le comportement d'une population de têtes de myosine en interaction avec des sites d'actine localisés. Chaque tête de myosine est modélisée par un ressort linéaire et la vitesse à laquelle les têtes de myosine s'attachent et se détachent varie en fonction de la distance entre la tête de myosine et le site d'actine. La génération d'une force résulte de l'hypothèse de modélisation selon laquelle les têtes de myosine s'attachent préférentiellement dans une position où le ressort est tendu, tandis qu'un détachement se produit lorsque le ressort est comprimé. Malgré les hypothèses simples choisies ici, le modèle Huxley'57 est déjà en mesure de prendre en compte la caractéristique essentielle de l'interaction actine-myosine : la courbe force-vitesse de Hill [1938]. Ce modèle a ensuite été étendu, en particulier par Podolsky *et al.* [1969], par Julian [1969] pour intégrer le processus d'activation par le calcium, et également par Deshcherevskiĭ [1971], qui, à l'inverse du modèle d'origine, considère les sites d'actine non localisés. Le modèle Huxley'57 reste aujourd'hui la base de la modélisation de la contraction musculaire.

Au cours de la même année, H.E. Huxley a obtenu la première observation de ponts actine-myosine dans le cadre d'une observation à haute résolution des filaments d'actine et de myosine, ce qui a confirmé la théorie des filaments glissants [Huxley, 1957b].

Une décennie plus tard, les mesures structurelles de H.E. Huxley suggèrent que les têtes de myosine attachées changent d'angle d'attachement pendant le processus de contraction. C'est ce changement entre deux conformations stables qui est maintenant appelé *power stroke* [Huxley, 1969]. Les conformations initiales et finales sont respectivement appelées conformations *pré-power stroke* et *post-power stroke*.

En 1971, A.F. Huxley et R.M. Simmons observent le comportement des muscles squelettiques à la suite d'un changement de longueur rapide (l'échelle de temps considérée ici est inférieure à 1 ms et est donc plus courte que l'échelle de temps du processus d'attachement-détachement, qui est d'environ 100 ms dans leurs conditions expérimentales). La réponse en force affiche plusieurs phases : une chute de force instantanée suivie d'une récupération de force rapide. Ces expériences suggèrent que des phénomènes à différentes échelles de temps se produisent dans l'interaction entre les têtes de myosine et les sites d'actine. A.F. Huxley et R.M. Simmons proposent un modèle pour prendre en compte cette observation expérimentale [Huxley et Simmons, 1971]. Leur description suppose que les ponts actine-myosine se comportent comme un ressort bistable. L'énergie de l'élément bistable est modélisée comme deux puits d'énergie infiniment étroits de profondeurs différentes. Si le ressort est suffisamment étiré, l'élément bistable peut passer d'un état à l'autre, créant ainsi une capacité de génération de force positive. Ce modèle intègre donc l'idée du power stroke suggérée par les résultats expérimentaux de H.E. Huxley deux ans plus tôt. Notons que ce modèle n'inclut pas la dynamique attachement-détachement et se concentre uniquement sur la description des ponts actine-myosine.

La même année, un cycle de base pour l'interaction en solution entre l'actine, la myosine et l'alimentation en énergie sous forme d'ATP dans cette interaction est proposé [Lymn et Taylor, 1971]. Il comprend deux états attachés et deux états détachés. La transition entre les deux états attachés peut être identifiée au power stroke. Le détachement est associé à l'hydrolyse de l'ATP et donc à un apport d'énergie.

Une difficulté du modèle Huxley-Simmons'71 est la dynamique de la transition entre les deux états de l'élément bistable. En effet, la transition se produit lorsque l'énergie de l'état actuel est égale à l'énergie de l'état futur (après la transition). Pendant la transition, il se produit un échange d'énergie entre l'élément bi-stable et le ressort, l'énergie totale restant constante. Cela revient à définir la barrière d'énergie entre les deux états comme la profondeur d'énergie du puits d'énergie actuel. Cette énergie doit être fournie par les fluc-

tuations thermiques, ce qui entraîne une transition lente entre les deux états par rapport à celle observée expérimentalement.

Ce problème a été résolu par T.L. Hill dans les années 70 grâce à son formidable effort de formalisation du modèle [Hill, 1974, 1976, 1977]. Il propose de décrire la transition entre les deux états discrets par un paysage énergétique indépendant définissant la barrière énergétique de transition. Au niveau des états chimiques discrets, cela revient à dire que les taux de transition (ou le paysage énergétique de transition) peuvent être choisis de manière arbitraire. La cohérence avec la thermodynamique est maintenue en considérant pour chaque transition un retour dont le taux est défini par la balance détaillée

$$\frac{k}{k^{\text{rev}}} = \exp\left[\frac{-\Delta w}{k_B T}\right]$$

où k est le taux de transition de la réaction directe, k^{rev} le taux de transition de la réaction inverse, Δw est la différence d'énergie libre entre l'état final et l'état initial état pour la réaction directe, k_B est la constante de Boltzmann et T est la température absolue. Le changement entre les états du pont actine-myosine est donc analogue à la transition entre des états chimiques. Avec ce formalisme "purement chimique", il est naturel d'intégrer, dans un même modèle, l'idée de la dynamique d'attachement-détachement proposée par Huxley [1957a] et la description du power stroke introduit par Huxley et Simmons [1971]. Les modèles de cette classe sont dits *modèles chimico-mécaniques.* Sur la base de son formalisme, T.L. Hill et ses co-auteurs formulent un modèle capable de capturer le comportement en réponse à des changements rapides de longueur – avec la bonne dynamique – ainsi que la relation force-vitesse [Eisenberg et Hill, 1978 ; Eisenberg *et al.*, 1980]. Le power stroke est modélisé ici par la transition entre deux états discrets.

Depuis, de nombreux ingrédients de modélisation ont été incorporés à la classe des modèles chimico-mécaniques afin d'intégrer d'autres aspects de la physiologie de la contraction musculaire découverts expérimentalement. Piazzesi et Lombardi [1995] ajoutent un état intermédiaire dans le power stroke à partir duquel le cycle complet peut être interrompu pour améliorer la prévision de consommation d'énergie du modèle. L'idée d'une série d'états chimiques discrets pour représenter le power stroke est étendue en utilisant jusqu'à cinq états chimiques [Linari *et al.*, 2009] (dans ce cas, sans processus d'attachement-détachement). De plus, certaines améliorations de modèle intégrant le cycle de l'ATP à l'interaction actine-myosine sont développées [Linari *et al.*, 2010 ; Caremani *et al.*, 2015]. La famille des modèles chimico-mécaniques est la plus utilisée dans la communauté des physiologistes pour analyser un corpus croissant de résultats expérimentaux. Ces modèles sont devenus très complexes pour rester complets.

Un effort de simplification a été entrepris par G.I. Zahalak à partir des années 80. Il a introduit l'idée que le calcul de la probabilité de toutes les configurations des têtes de myosine peut ne pas être toujours nécessaire, car la principale quantité d'intérêt – la force active – ne dépend que des premiers moments de cette probabilité. Il montre que, sous une hypothèse sur la variation spatiale de la probabilité d'attachement, l'évolution de la force peut être calculée à partir de la dynamique de quelques moments de cette probabilité seulement [Zahalak, 1981]. L'ensemble des équations aux dérivées partielles régissant les modèles chimico-mécaniques devient ici un ensemble d'équations différentielles ordinaires. S'appuyant sur une idée similaire mais en utilisant une hypothèse légèrement différente – fondée sur la variation spatiale des taux de transition, qui affectent ensuite les probabilités d'états de toutes les têtes de myosine – Bestel *et al.* [2001] proposent une autre réduction pertinente du modèle Huxley'57. G.I. Zahalak suggère également de tirer parti des différentes échelles de temps pour obtenir des modèles simplifiés [Zahalak, 2000]. Pour cela, il regroupe les transitions représentant le power stroke en une seule transition par des approximations pertinentes.

Notons qu'une autre famille de modèles appelée *cliquets browniens* a été développée par une communauté de physiciens pour étudier les effets collectifs avec un niveau d'abstraction élevé suite au développement de nouvelle techniques expérimentales sur des têtes de myosine individuelles [Kron et Spudich, 1986 ; Molloy *et al.*, 1995 ; Veigel *et al.*, 1998]. L'idée est ici d'utiliser la représentation de molécules soumises à des fluctuations thermiques diffusant dans un potentiel d'énergie périodique [Magnasco, 1993 ; Prost *et al.*, 1994]. Ces modèles purement mécaniques ciblaient à l'origine le comportement des moteurs moléculaires, mais ont ensuite été appliqués à la contraction musculaire [Jülicher *et al.*, 1997 ; Wang et Oster, 2002 ; Esaki *et al.*, 2003].

L'amélioration la plus récente des modèles de contraction musculaire provient des travaux de L. Truskinovski et de ses collaborateurs. La succession d'états chimiques discrets représentant le power stroke dans les modèles chimico-mécaniques est ici remplacée par une variété continue [Marcucci et Truskinovsky, 2010 ; Caruel *et al.*, 2013a]. En un sens, il s'agit d'une approche parallèle à la description de T.L. Hill et de ses collaborateurs. Ces derniers supposent que les états discrets sont séparés par un paysage énergétique arbitraire, qui est associé aux changements de conformation qui se produisent entre les états discrets et qui n'apparaît alors dans le modèle que via les taux de transition entre les états discrets. Le modèle est purement chimique mais l'évolution entre les états discrets est régie par une énergie mécanique cachée. Avec les modèles à power stroke continu, tout le paysage énergétique du système est directement fourni. Il est construit à partir du couplage d'une énergie mécanique quadratique – représentant le comportement élastique linéaire des ponts actine-myosine – avec un potentiel mécanique à double puits associé aux conformations stables de la tête de myosine avant et après le power stroke. Notons que des puits d'énergie supplémentaires pourraient être ajoutés pour représenter des conformations stables supplémentaires [Marcucci *et al.*, 2016]. Ces modèles sont purement mécaniques sans états chimiques discrets.

Les modèles de power stroke continus ont d'abord été restreints à la description du power stroke (comme le modèle Huxley-Simmons'71). Ils ont ensuite été étendus pour prendre également en compte le processus d'attachement-détachement par Caruel *et al.* [2019] qui modélisent l'attachement et le détachement sous forme de processus de saut entre deux paysages énergétiques (éventuellement associés à un changement simultané de la position de la tête de myosine). Cette approche a la particularité de réconcilier une approche entièrement mécanique pour la description de le power stroke et une description chimique du processus de attachement-détachement. Les modèles proposés et étudiés dans ce manuscrit appartiennent à cette sous-famille de modèles.

Sheshka [2012] ; Sheshka et Truskinovsky [2014] proposent une autre approche pour incorporer la formation et la destruction de ponts actine-myosine à la description continue du power stroke, en élargissant les modèles à cliquet brownien. Le modèle résultant est une description purement mécanique de l'interaction actine-myosine.

Récemment, les propriétés fines des muscles cardiaques ont été mesurées expérimentalement [Caremani *et al.*, 2016].

Malgré l'abondante recherche sur la contraction musculaire menée au cours des soixante dernières années, ce domaine est toujours très actif. Des expériences utilisant des motifs de diffraction de rayons X (en utilisant la structure régulière du sarcomère comme diffracteur) permettent de mieux comprendre les variations structurelles se produisant dans la contraction [Reconditi *et al.*, 2003 ; Piazzesi *et al.*, 2007 ; Reconditi *et al.*, 2014 ; Ait-Mou *et al.*, 2016], les pathologies [Ait-Mou *et al.*, 2018] ou de mieux identifier les différents états chimiques apparaissant dans le cycle [Houdusse et Sweeney, 2016]. En particulier, un nouvel état de la tête de myosine, appelé *off-state*, a récemment été découvert dans les muscles squelettiques [Reconditi *et al.*, 2011 ; Linari *et al.*, 2015] et dans les muscles cardiaques

[Reconditi *et al.*, 2017]. Cela ouvre de nouvelles opportunités pour le développement de modèles dédiés et le raffinement des modèles existants.

Enjeux théoriques

Malgré les efforts considérables déjà déployés dans la modélisation de la contraction musculaire, de nombreuses questions restent ouvertes.

Premièrement, les soixante années de développement de modèles d'actine-myosine n'ont pas permis de faire correspondre les prévisions du modèle avec toutes les données expérimentales. En particulier, les aspects énergétiques de l'interaction actine-myosine restent difficiles à concilier avec les aspects cinétiques, la consommation d'ATP prédite par les modèles classiques étant généralement supérieure à celle réellement mesurée.

Deuxièmement, la majeure partie de la description détaillée de l'interaction actine-myosine à l'origine de la contraction musculaire a été réalisée pour les muscles squelettiques, le développement de modèles ciblant spécifiquement les muscles cardiaques n'étant que très récents. Les données expérimentales sur les muscles cardiaques montrent un comportement qualitatif similaire, mais les résultats quantitatifs diffèrent. Cette différence peut s'expliquer par les différences intrinsèques entre le muscle squelettique et le muscle cardiaque, par les différences entre les espèces animales utilisées pour les expériences, mais également par le fait que les expériences sur les muscles cardiaques sont généralement effectuées à des températures plus élevées. Il existe donc un besoin de modèles ciblant spécifiquement le comportement des muscles cardiaques.

Troisièmement et de manière plus importante encore, le besoin d'éléments de modélisation pour des applications médicales n'implique pas la recherche d'un modèle unique capable de prendre en compte de nombreux aspects du phénomène des études. Il s'agit plutôt d'obtenir une collection de modèles ayant différents degrés de complexité. Pour chaque application particulière, le modèle adéquat, qui propose le meilleur compromis entre la capacité du modèle à apporter des éléments pertinents pour résoudre la question examinée et le coût de calcul, doit être sélectionné. La question du coût de calcul est cruciale pour les applications médicales car des simulations en temps réel peuvent être nécessaires dans certains cas, par exemple si le modèle est intégré à un outil utilisé pour faciliter une intervention chirurgicale. Notons que l'échelle de temps de simulation pertinente peut être plus rapide que le "temps réel", par exemple si plusieurs scénarios doivent être testés ou si la quantification des incertitudes est par ailleurs effectuée. La cohérence entre les différents modèles est un point décisif. En effet, pour transférer un étalonnage réalisé avec un modèle à un autre ou pour relier les échelles d'espace et de temps, il est nécessaire de relier les modèles de manière rigoureuse et systématique. Par exemple, dans le cadre de la modélisation du cœur, une analyse détaillée d'une pathologie peut être réalisée avec un modèle raffiné et des données *ex vivo* afin que le modèle de la pathologie puisse être utilisé dans une description plus globale au niveau tissulaire, où l'utilisation de ce modèle raffiné est impossible car trop couteuse en temps de calcul. La capacité de lier les modèles et de contrôler la conservation et la perte de propriétés à travers la transition d'un modèle à l'autre est donc une caractéristique essentielle à rechercher dans les efforts de modélisation dans le cadre de la médecine numérique. Cela donne lieu au premier objectif de cette thèse qui peut être formulé comme suit :

Proposer un cadre de modélisation hiérarchique de l'interaction cardiaque actine-myosine sous-jacente à la contraction du muscle cardiaque.

Pour résoudre ce problème, nous poursuivons la stratégie suivante. Nous partons d'un modèle complexe, qui n'a été validé que pour les muscles squelettiques [Caruel *et al.*,

2019], et nous montrons l'applicabilité de ce modèle aux muscles cardiaques, en essayant de faire correspondre avec les données expérimentales autant d'indicateurs physiologiques que possible. Ce modèle est régi par des équations différentielles stochastiques (EDS). Nous effectuons ensuite l'élimination adiabatique des variables internes les plus rapides, qui correspondent à la paramétrisation du power stroke, en obtenant à partir de l'équation de Fokker-Planck associée au modèle stochastique une description de l'état de la tête de myosine sous la forme d'une équation aux dérivées partielles (EDP). Enfin, en nous fondant sur les idées de Zahalak [2000] et de Bestel *et al.* [2001], nous proposons, sous une hypothèse spécifique sur la variation spatiale des taux d'attachement et de détachement, des simplifications supplémentaires de ce modèle en considérant uniquement les moments de la solution de l'EDP qui présentent un intérêt pour le calcul de la force et de la raideur. La dynamique n'est alors régie que par des équations différentielles ordinaires (EDO). La calibration des modèles, qui peut sembler être un élément secondaire, ne doit pas être négligée. Il s'agit en effet d'un élément clé pour prouver la validité des modèles proposés et d'un processus complexe.

Les modèles proposés décrivent une situation dans laquelle toutes les têtes de myosine et tous les sites d'actine sont disponibles pour la formation de ponts actine-myosine (nous disons de manière équivalente que les filaments épais et fins sont complètement activés). Ce n'est pas le cas dans le cœur. Pour pouvoir utiliser les modèles dans le contexte de la modélisation cardiaque, les mécanismes de régulation prenant place *in vivo* doivent être incorporés dans le modèle. Ceci motive l'introduction de notre deuxième objectif :

Améliorer les modèles classiques d'interaction actine-myosine pour incorporer les mécanismes de régulation ayant lieu à l'échelle du cœur.

Notre approche consiste ici à établir de nouvelles EDPs décrivant la dynamique du système à partir de la conservation de la matière. Elle est utilisée pour gérer la disponibilité variable des têtes de myosine et des sites d'actine.

Enfin, ces modèles complets doivent être correctement couplés à un modèle de tissu afin de pouvoir finalement être utilisés dans un modèle d'organe. Le troisième objectif de ce travail est donc naturellement défini comme suit :

Lier les nouveaux modèles proposés dans un environnement de simulation multi-échelle de cœur.

L'objectif ici est double : il consiste à relier d'un point de vue théorique les équations continues du modèle microscopique et celles du macroscopique (modèle d'organe), mais aussi à proposer des méthodes numériques adaptées pour réaliser la simulation de l'organe de manière rigoureuse. La thermodynamique joue ici un rôle crucial en tant que guide pour la conception du lien entre les échelles et le développement des méthodes numériques.

Pour atteindre les trois objectifs présentés ci-dessus, plusieurs défis doivent être relevés. Il nous faut d'abord comprendre la nature et le fonctionnement du système que nous essayons de décrire. Le deuxième défi concerne la nature multi-échelle des problèmes examinés. En effet, la contraction cardiaque depuis l'interaction actine-myosine jusqu'à la réponse de l'organe implique des échelles de temps couvrant quatre ordres de grandeur (de 100 µs à 1 s) et des échelles d'espace couvrant huit ordres de grandeur (de 1 nm à 10 cm).

Structure du manuscrit

Cette thèse est composée de cinq chapitres.

Chapter 1 – Physiologie de la contraction musculaire

Ce chapitre aborde le premier défi identifié pour ce travail, à savoir la compréhension de la physiologie. Nous passons en revue les éléments de la physiologie de la contraction musculaire disponibles dans la littérature qui présentent un intérêt pour le développement de modèles d'interaction actine-myosine et l'intégration des mécanismes de régulation de cette interaction. Aucune expérience n'a été réalisée pour ce travail, il n'y a donc pas de nouvelles données expérimentales parmi celles présentées dans ce chapitre. Cependant, certaines interprétations des données expérimentales sont originales. De plus, à ma connaissance, il n'existait pas de bilan physiologique global récent mettant l'accent sur les éléments pertinents pour le développement de modèles cardiaques.

Chapter 2 – Propriétés thermodynamiques des modèles de contraction musculaire et principes discrets associés

Au Chapitre 2, nous reformulons les modèles chimico-mécaniques, qui ont pour racine commune le modèle Huxley'57 [Huxley, 1957a], dans un cadre unifié. Nous établissons des propriétés mathématiques avec une attention particulière pour les propriétés thermodynamiques. Le première contribution principale de ce travail est l'introduction d'un nouveau schéma rhéologique visant à incorporer le modèle chimico-mécanique microscopique dans un modèle tissulaire macroscopique et l'établissement des propriétés thermodynamiques du système couplé. Cette partie était déjà bien avancée avant le début de ma thèse et je n'ai contribué qu'à établir certaines propriétés du système couplé. La deuxième contribution principale est la conception de méthodes numériques pour les modèles chimico-mécaniques satisfaisant la thermodynamique et l'amélioration des méthodes précédemment proposées pour le système couplé, de sorte que l'équilibre thermodynamique discret puisse être vérifié de l'échelle microscopique à l'échelle macroscopique.

Le chapitre se présente sous la forme d'un article co-écrit par François Kimmig, Dominique Chapelle et Philippe Moireau, publié dans AMSES et intitulé *Thermodynamics properties of muscle contraction models and associated discrete-time principles.* Il est référencé par [Kimmig *et al.*, 2019a] dans le reste du manuscrit. Notons que l'annexe présentée dans ce chapitre ne fait pas partie de l'article publié.

Chapter 3 – Modélisation hiérarchique du développement de la force dans les muscles cardiaques

Dans ce chapitre, nous présentons une hiérarchie de modèles d'interaction actine-myosine. Nous partons d'un modèle stochastique fin [Caruel *et al.*, 2019] et montrons la capacité de ce modèle à décrire le comportement des muscles cardiaques avant d'effectuer plusieurs étapes de simplification.

Nous nous intéressons particulièrement au processus de calibration de ces modèles qui tirent parti de la structure hiérarchique dans laquelle ils sont intégrés. Les prédictions de ces modèles sont évaluées par rapport aux données obtenues sur des muscles cardiaques de rat à 25 °C. L'étalonnage proposé permet au modèle le plus raffiné de correspondre à de nombreux indicateurs physiologiques, tandis que les modèles simplifiés se limitent aux indicateurs correspondant à leur domaine de validité. Ceci valide la pertinence des modèles proposés et leur capacité prédictive. Ce chapitre prend la forme d'un article à soumettre co-écrit par François Kimmig et Matthieu Caruel, intitulé *Hierarchical modeling of force generation in cardiac muscle.* Il est appelé [Kimmig et Caruel, 2019] dans le reste du manuscrit.

Chapter 4 – Couplage activation-contraction dans un modèle multi-échelle de cœur reproduisant l'effet Frank-Starling

Ce chapitre traite de l'incorporation dans nos modèles d'un premier mécanisme de régulation : la variation de la disponibilité des têtes de myosine. Nous considérons deux groupes de têtes de myosine (disponibles et non disponibles). En utilisant la conservation des têtes de myosine, nous établissons l'EDP qui régit la dynamique du système. Nous obtenons une extension du modèle Huxley'57 avec des termes supplémentaires rendant compte des échanges entre les deux groupes de têtes de myosine. Les méthodes numériques proposées au Chapitre 2 sont étendues pour prendre en compte ces termes supplémentaires. L'activation du filament fin est, dans ce chapitre, traitée de manière phénoménologique. En reliant les modèles nouvellement proposés à un environnement de simulation cardiaque, nous effectuons des simulations de battements cardiaques et démontrons la capacité de notre modèle à saisir les principales caractéristiques du mécanisme de Frank-Starling, qui se manifeste au niveau de l'organe et provient des variations de disponibilité des têtes de myosine et des sites d'actine.

Ce chapitre prend la forme d'un article à soumettre co-écrit par François Kimmig, Philippe Moireau et Dominique Chapelle, intitulé *Activation-contraction coupling in a multiscale heart model capturing the Frank-Starling effect*. Il est référencé par [Kimmig *et al.*, 2019b] dans le reste du manuscrit.

Chapter 5 – Variation du l'activation du filament fin dans le cadre des modèles Huxley'57

Pour compléter notre cadre de modélisation, nous devons intégrer rigoureusement l'activation des sites d'actine dans le modèle. En appliquant une stratégie similaire à celle du Chapitre 4, nous obtenons un système d'équations décrivant l'interaction actine-myosine et la variation d'activation des filaments épais et minces. La calibration du modèle est effectuée avec les données *ex vivo*. Notre modèle a la capacité de produire des données physiologiques importantes.

Contributions principales

Pour conclure cette introduction, nous donnons un aperçu des productions scientifiques réalisées au cours de cette thèse. Ce travail a également été présenté lors de plusieurs conférences sous forme de posters ou de présentations orales.

Articles publiés et à soumettre

- Kimmig, F., Chapelle, D., and Moireau, P. (2019). Thermodynamic properties of muscle contraction models and associated discrete-time principles. *Advanced Modeling and Simulation in Engineering Sciences*, 6(1), 6.
- Kimmig, F., and Caruel, M. Hierarchical modeling of force generation in cardiac muscle. *à soumettre*
- Kimmig, F., Moireau, P., and Chapelle, D. Activation-contraction coupling in a multiscale heart model capturing the Frank-Starling effect. *à soumettre*

Conférences

- 8th World Congress of Biomechanics – WCB 2018 – Dublin, Ireland
  Session posters : *Multi-scale modeling of muscle contraction.*
- 6ème rencontre du GDR Mécabio – Université Montpellier 2, France
  Présentation orale : *Multi-scale modeling of muscle contraction.*

- 6th International conference on computational and mathematical biomedical engineering – CMBE 2019 – Tohoku University, Sendai City, Japan
  Présentation orale : *Activation-contraction coupling in a multi-scale heart model.*

- Symposium Jean Mandel 2019 – École polytechnique, Palaiseau, France
  Présentation orale : *Activation-contraction coupling in a multi-scale heart model.*

Dévelopment logiciel Les modèles présentés dans les chapitres 3, 4 et 5 ont été implémentés dans la librairie de simulation de coeur *CardiacLab*, qui est développée en interne dans l'équipe MΞDISIM. Cette librairie a été utilisée pour effectuer toutes les simulations cardiaques présentées dans cette thèse.

De plus, le modèle de contraction chimico-mécanique développé par Piazzesi et Lombardi [1995] a également été implémenté dans cet environnement. Au total, ces contributions représentent environ 10 000 lignes de codes.

Bibliographie

Ait-Mou, Y., Hsu, K., Farman, G., Kumar, M., Greaser, M., Irving, T. et de Tombe, P. (2016). Titin strain contributes to the Frank–Starling law of the heart by structural rearrangements of both thin- and thick-filament proteins. *Proceedings of the National Academy of Sciences*, 113(8) :2306–2311.

Ait-Mou, Y., Lacampagne, A., Irving, T., Scheuermann, V., Blot, S., Ghaleh, B., de Tombe, P. et Cazorla, O. (2018). Altered myofilament structure and function in dogs with Duchenne muscular dystrophy cardiomyopathy. *Journal of molecular and cellular cardiology*, 114 :345–353.

Astorino, M., Gerbeau, J.-F., Pantz, O. et Traoré, K.-F. (2009). Fluid–structure interaction and multi-body contact : Application to aortic valves. *Computer Methods in Applied Mechanics and Engineering*, 198(45-46) :3603–3612.

Baillargeon, B., Rebelo, N., Fox, D., Taylor, R. et Kuhl, E. (2014). The Living Heart Project : A robust and integrative simulator for human heart function. *European Journal of Mechanics / A Solids*, 48(C) :38–47.

Bertoglio, C., Barber, D., Gaddum, N., Valverde, I., Rutten, M., Beerbaum, P., Moireau, P., Hose, R. et Gerbeau, J.-F. (2014). Identification of artery wall stiffness : in vitro validation and in vivo results of a data assimilation procedure applied to a 3D fluid-structure interaction model. *Journal of Biomechanics*, 47(5) :1027–1034.

Bestel, J., Clément, F. et Sorine, M. (2001). A Biomechanical Model of Muscle Contraction. *In Medical Image Computing and Computer-Assisted Intervention – MICCAI 2001*, pages 1159–1161. Springer, Berlin, Heidelberg, Berlin, Heidelberg.

Caremani, M., Melli, L., Dolfi, M., Lombardi, V. et Linari, M. (2015). Force and number of myosin motors during muscle shortening and the coupling with the release of the ATP hydrolysis products. *The Journal of Physiology*, 593(15) :3313–3332.

Caremani, M., Pinzauti, F., Reconditi, M., Piazzesi, G., Stienen, G., Lombardi, V. et Linari, M. (2016). Size and speed of the working stroke of cardiac myosin in situ. *Proceedings of the National Academy of Sciences*, 113(13) :3675–3680.

Caruel, M., Allain, J.-M. et Truskinovsky, L. (2013a). Muscle as a Metamaterial Operating Near a Critical Point. *Physical review letters*, 110(24) :248103.

Caruel, M., Chabiniok, R., Moireau, P., Lecarpentier, Y. et Chapelle, D. (2013b). Dimensional reductions of a cardiac model for effective validation and calibration. *Biomechanics and Modeling in Mechanobiology*, 13(4) :897–914.

Caruel, M., Moireau, P. et Chapelle, D. (2019). Stochastic modeling of chemical-mechanical coupling in striated muscles. *Biomechanics and Modeling in Mechanobiology*, 18(3) :563–587.

Caruel, M. et Truskinovsky, L. (2018). Physics of muscle contraction. *Reports on Progress in Physics*, pages 1–98.

Chabiniok, R., Moireau, P., Lesault, P. F., Rahmouni, A., Deux, J. F. et Chapelle, D. (2012). Estimation of tissue contractility from cardiac cine-MRI using a biomechanical heart model. *Biomechanics and Modeling in Mechanobiology*, 11(5) :609–630.

Chabiniok, R., Wang, V., Hadjicharalambous, M., Asner, L., Lee, J., Sermesant, M., Kuhl, E., Young, A., Moireau, P., Nash, M., Chapelle, D. et Nordsletten, D. (2016). Multiphysics and multiscale modelling, data-model fusion and integration of organ physiology in the clinic : ventricular cardiac mechanics. *Interface focus*, 6(2) : 20150083.

Chapelle, D., Clément, F., Génot, F., Le Tallec, P., Sorine, M. et Urquiza, J. (2001). A Physiologically-Based Model for the Active Cardiac Muscle Contraction. *In Functional Imaging and Modeling of the Heart*, pages 128–133. Springer, Berlin, Heidelberg, Berlin, Heidelberg.

Chapelle, D., Le Tallec, P., Moireau, P. et Sorine, M. (2012). Energy-preserving muscle tissue model : formulation and compatible discretizations. *Journal for Multiscale Computational Engineering*.

Clatz, O., Sermesant, M., Bondiau, P., Delingette, H., Warfield, S., Malandain, G. et Ayache, N. (2005). Realistic simulation of the 3-D growth of brain tumors in MR images coupling diffusion with biomechanical deformation. *IEEE Transactions on Medical Imaging*, 24(10) :1334–1346.

Cormack, A. (1963). Representation of a function by its line integrals, with some radiological applications. *Journal of applied physics*, 34(9) :2722–2727.

Corrado, C., Gerbeau, J.-F. et Moireau, P. (2015). Identification of weakly coupled multiphysics problems. application to the inverse problem of electrocardiography. *Journal of Computational Physics*, 283 :271–298.

Cyron, C., Wilson, J. et Humphrey, J. (2014). Mechanobiological stability : a new paradigm to understand the enlargement of aneurysms ? *Journal of The Royal Society Interface*, 11(100) :20140680–11.

Dalla Man, C., Micheletto, F., Lv, D., Breton, M., Kovatchev, B. et Cobelli, C. (2014). The UVA/PADOVA Type 1 Diabetes Simulator. *Journal of Diabetes Science and Technology*, 8(1) :26–34.

Deshcherevskiĭ, V. I. (1971). A kinetic theory of striated muscle contraction. *Biorheology*, 7(3) :147–170.

Einthoven, W. (1895). Ueber die Form des menschlichen Electrocardiogramms. *Pflügers Archiv - European Journal of Physiology*, 60(3-4) :101–123.

Eisenberg, E. et Hill, T. (1978). A cross-bridge model of muscle contraction. *Progress in biophysics and molecular biology*, 33(1) :55–82.

Eisenberg, E., Hill, T. et Chen, Y. (1980). Cross-bridge model of muscle contraction. Quantitative analysis. *Biophysical Journal*, 29(2) :195–227.

Enderling, H. et Chaplain, M. (2014). Mathematical modeling of tumor growth and treatment. *Current pharmaceutical design*, 20(30) :4934–4940.

Esaki, S., Ishii, Y. et Yanagida, T. (2003). Model describing the biased Brownian movement of myosin. *Proceedings of the Japan Academy, Series B*, 79B(1) :9–14.

Formaggia, L., Lamponi, D. et Quarteroni, A. (2003). One-dimensional models for blood flow in arteries. *Journal of Engineering Mathematics*, 47(3-4) :251–276.

Gasser, T., Ogden, R. et Holzapfel, G. (2005). Hyperelastic modelling of arterial layers with distributed collagen fibre orientations. *Journal of The Royal Society Interface*, 3(6) :15–35.

Genet, M., Lee, L., Ge, L., Acevedo-Bolton, G., Jeung, N., Martin, A., Cambronero, N., Boyle, A., Yeghiazarians, Y., Kozerke, S. et Guccione, J. (2015). A Novel Method for Quantifying Smooth Regional Variations in Myocardial Contractility Within an Infarcted Human Left Ventricle Based on Delay-Enhanced Magnetic Resonance Imaging. *Journal of Biomechanical Engineering*, 137(8) :081009.

Ghista, D., Patil, K., Gould, P. et Woo, K. (1973). Computerized left ventricular mechanics and control system analyses models relevant for cardiac diagnosis. *Computers in Biology and Medicine*, 3(1) :27–46.

Guccione, J. et McCulloch, A. (1993). Mechanics of Active Contraction in Cardiac Muscle : Part I—Constitutive Relations for Fiber Stress That Describe Deactivation. *Journal of Biomechanical Engineering*, 115(1) :72–81.

Hill, A. (1938). The heat of shortening and the dynamic constants of muscle. *Proc. R. Soc. Lond. B*, 126(843) :136–195.

Hill, T. (1974). Theoretical formalism for the sliding filament model of contraction of striated muscle Part I. *Progress in biophysics and molecular biology*, 28 :267–340.

Hill, T. (1976). Theoretical formalism for the sliding filament model of contraction of striated muscle part II. *Progress in biophysics and molecular biology*, 29 :105–159.

Hill, T. (1977). *Free Energy Transduction in Biology*. Academic Press.

Hirschvogel, M., Bassilious, M., Jagschies, L., Wildhirt, S. et Gee, M. (2017). A monolithic 3D-0D coupled closed-loop model of the heart and the vascular system : Experiment-based parameter estimation for patient-specific cardiac mechanics. *International Journal for Numerical Methods in Biomedical Engineering*, 84(3) :e2842–22.

Hodgkin, A. et Huxley, A. (1952). A quantitative description of membrane current and its application to conduction and excitation in nerve. *The Journal of Physiology*, 117(4) :500–544.

Houdusse, A. et Sweeney, H. (2016). How Myosin Generates Force on Actin Filaments. *Trends in Biochemical Sciences*, 41(12) :989–997.

Hounsfield, G. (1973). Computerized transverse axial scanning (tomography) : Part 1. Description of system. *The British journal of radiology*, 46(552) :1016–1022.

Howatson Tawhai, M., Pullan, A. et Hunter, P. (2000). Generation of an anatomically based three-dimensional model of the conducting airways. *Annals of Biomedical Engineering*, 28(7) :793–802.

Humphrey, J. et Rajagopal, K. (2002). A constrained mixture model for growth and remodeling of soft tissues. *Mathematical models and methods in applied sciences*, 12(03) : 407–430.

Hunter, P. (1975). *Finite Element Analysis of Cardiac Muscle Mechanics.* Thèse de doctorat, University of Oxford.

Hunter, P. et Smaill, B. (1988). The analysis of cardiac function : a continuum approach. *Progress in biophysics and molecular biology*, 52(2) :101–164.

Huxley, A. (1957a). Muscle structures and theories of contraction. *Progr. Biophys. Chem.*

Huxley, A. et Niedergerke, R. (1954). Structural changes in muscle during contraction ; interference microscopy of living muscle fibres. *Nature*, 173(4412) :971–973.

Huxley, A. et Simmons, R. (1971). Proposed mechanism of force generation in striated muscle. *Nature*.

Huxley, H. (1957b). The double array of filaments in cross-striated muscle. *The Journal of biophysical and biochemical cytology*, 3(5) :631–648.

Huxley, H. (1969). The mechanism of muscular contraction. *Science*, 164(3886) : 1356–1365.

Huxley, H. (2004). Fifty years of muscle and the sliding filament hypothesis. *European Journal of Biochemistry*, 271(8) :1403–1415.

Huxley, H. et Hanson, J. (1954). Changes in the cross-striations of muscle during contraction and stretch and their structural interpretation. *Nature*, 173(4412) :973–976.

Hyde, E., Behar, J., Claridge, S., Jackson, T., Lee, A., Remme, E., Sohal, M., Plank, G., Razavi, R., Rinaldi, C. et Niederer, S. (2015). Beneficial Effect on Cardiac Resynchronization From Left Ventricular Endocardial Pacing Is Mediated by Early Access to High Conduction Velocity Tissue : Electrophysiological Simulation Study. *Circulation. Arrhythmia and electrophysiology*, 8(5) :1164–1172.

Julian, F. J. (1969). Activation in a skeletal muscle contraction model with a modification for insect fibrillar muscle. *Biophysj*, 9(4) :547–570.

Jülicher, F., Ajdari, A. et Prost, J. (1997). Modeling molecular motors. *Reviews of Modern Physics*, 69(4) :1269–1282.

Kerckhoffs, R., Omens, J. et McCulloch, A. (2012). A single strain-based growth law predicts concentric and eccentric cardiac growth during pressure and volume overload. *Mechanics research communications*, 42 :40–50.

Kimmig, F. et Caruel, M. (2019). Hierarchical modeling of muscle contraction. *submitted*.

Kimmig, F., Chapelle, D. et Moireau, P. (2019a). Thermodynamic properties of muscle contraction models and associated discrete-time principles. *Advanced Modeling and Simulation in Engineering Sciences*, 6(1) :6.

Kimmig, F., Moireau, P. et Chapelle, D. (2019b). Activation-contraction coupling in a multiscale heart model, an element for capturing the frank-starling effect. *to be submitted*.

Kron, S. J. et Spudich, J. A. (1986). Fluorescent actin filaments move on myosin fixed to a glass surface. *Proceedings of the National Academy of Sciences*, 83(17) :6272–6276.

Kroon, W., Delhaas, T., Arts, T. et Bovendeerd, P. (2009). Computational modeling of volumetric soft tissue growth : application to the cardiac left ventricle. *Biomechanics and Modeling in Mechanobiology*, 8(4) :301–309.

Lauterbur, P. (1973). Image Formation by Induced Local Interactions : Examples Employing Nuclear Magnetic Resonance. *Nature*, 242(5394) :190–191.

Linari, M., Brunello, E., Reconditi, M., Fusi, L., Caremani, M., Narayanan, T., Piazzesi, G., Lombardi, V. et Irving, M. (2015). Force generation by skeletal muscle is controlled by mechanosensing in myosin filaments. *Nature*, 528(7581) :276–279.

Linari, M., Caremani, M. et Lombardi, V. (2010). A kinetic model that explains the effect of inorganic phosphate on the mechanics and energetics of isometric contraction of fast skeletal muscle. *Proceedings. Biological sciences*, 277(1678) :19–27.

Linari, M., Piazzesi, G. et Lombardi, V. (2009). The Effect of Myofilament Compliance on Kinetics of Force Generation by Myosin Motors in Muscle. *Biophysj*, 96(2) :583–592.

Lymn, R. et Taylor, E. (1971). Mechanism of adenosine triphosphate hydrolysis by actomyosin. *Biochemistry*, 10(25) :4617–4624.

Magnasco, M. (1993). Forced thermal ratchets. *Physical review letters*, 71(10) : 1477–1481.

Mansfield, P. et Maudsley, A. (1977). Medical imaging by NMR. *The British journal of radiology*, 50(591) :188–194.

Marcucci, L. et Truskinovsky, L. (2010). Mechanics of the power stroke in myosin II. *Physical Review E*, 81(5) :051915–8.

Marcucci, L., Washio, T. et Yanagida, T. (2016). Including thermal fluctuations in actomyosin stable states increases the predicted force per motor and macroscopic efficiency in muscle modelling. *PLoS Computational Biology*, 12(9).

McDowell, K., Vadakkumpadan, F., Blake, R., Blauer, J., Plank, G., MacLeod, R. et Trayanova, N. (2013). Mechanistic Inquiry into the Role of Tissue Remodeling in Fibrotic Lesions in Human Atrial Fibrillation. *Biophysj*, 104(12) :2764–2773.

Mirsky, I. (1969). Left ventricular stresses in the intact human heart. *Biophysj*, 9(2) : 189–208.

Molloy, J. E., Burns, J. E., Kendrick-Jones, J., Tregear, R. T. et White, D. (1995). Movement and force produced by a single myosin head. *Nature*, 378(6553) :209.

Nash, M. et Hunter, P. (2000). Computational Mechanics of the Heart. *Journal of elasticity and the physical science of solids*, 61(1) :113–141.

Noble, D. (1962). A modification of the Hodgkin—Huxley equations applicable to Purkinje fibre action and pacemaker potentials. *The Journal of Physiology*, 160(2) :317–352.

Nordsletten, D., Niederer, S., Nash, M., Hunter, P. et Smith, N. (2011). Coupling multi-physics models to cardiac mechanics. *Progress in biophysics and molecular biology*, 104(1-3) :77–88.

Pant, S., Fabrèges, B., Gerbeau, J.-F. et Vignon-Clementel, I. (2014). A methodological paradigm for patient-specific multi-scale CFD simulations : from clinical measurements to parameter estimates for individual analysis. *International Journal for Numerical Methods in Biomedical Engineering*, 30(12) :1614–1648.

Peskin, C. (1972). Flow patterns around heart valves : a numerical method. *Journal of Computational Physics*, 10(2) :252–271.

Peskin, C. (1975). *Mathematical aspects of heart physiology*. Courant Institute of Mathematical Sciences.

Peskin, C. (1977). Numerical analysis of blood flow in the heart. *Journal of Computational Physics*, 25(3) :220–252.

Piazzesi, G. et Lombardi, V. (1995). A cross-bridge model that is able to explain mechanical and energetic properties of shortening muscle. *Biophysical Journal*, 68 : 1966–1979.

Piazzesi, G., Reconditi, M., Linari, M., Lucii, L., Bianco, P., Brunello, E., Decostre, V., Stewart, A., Gore, D., Irving, T., Irving, M. et Lombardi, V. (2007). Skeletal muscle performance determined by modulation of number of myosin motors rather than motor force or stroke size. *Cell*, 131(4) :784–795.

Podolsky, R. J., Nolan, A. C. et Zaveler, S. A. (1969). Cross-bridge properties derived from muscle isotonic velocity transients. *Proceedings of the National Academy of Sciences*, 64(2) :504–511.

Prost, J., Chauwin, J.-F., Peliti, L. et Ajdari, A. (1994). Asymmetric pumping of particles. *Physical review letters*, 72(16) :2652–2655.

Quaranta, V., Weaver, A., Cummings, P. et Anderson, A. (2005). Mathematical modeling of cancer : The future of prognosis and treatment. *Clinica Chimica Acta*, 357(2) :173–179.

Quarteroni, A., Lassila, T., Rossi, S. et Ruiz-Baier, R. (2017). Integrated Heart-Coupling multiscale and multiphysics models for the simulation of the cardiac function. *Computer Methods in Applied Mechanics and Engineering*, 314 :345–407.

Quarteroni, A., Veneziani, A. et Zunino, P. (2002). Mathematical and numerical modeling of solute dynamics in blood flow and arterial walls. *SIAM*, 39(5) :1488–1511.

Rausch, M., Zöllner, A., Genet, M., Baillargeon, B., Bothe, W. et Kuhl, E. (2017). A virtual sizing tool for mitral valve annuloplasty. *International Journal for Numerical Methods in Biomedical Engineering*, 33(2).

Reconditi, M., Brunello, E., Fusi, L., Linari, M., Martinez, M., Lombardi, V., Irving, M. et Piazzesi, G. (2014). Sarcomere-length dependence of myosin filament structure in skeletal muscle fibres of the frog. *The Journal of Physiology*, 592(5) : 1119–1137.

Reconditi, M., Brunello, E., Linari, M., Bianco, P., Narayanan, T., Panine, P., Piazzesi, G., Lombardi, V. et Irving, M. (2011). Motion of myosin head domains during activation and force development in skeletal muscle. *Proceedings of the National Academy of Sciences*, 108(17) :7236–7240.

Reconditi, M., Caremani, M., Pinzauti, F., Powers, J., Narayanan, T., Stienen, G., Linari, M., Lombardi, V. et Piazzesi, G. (2017). Myosin filament activation in the heart is tuned to the mechanical task. *Proceedings of the National Academy of Sciences*, pages 3240–3245.

Reconditi, M., Koubassova, N., Linari, M., Dobbie, I., Narayanan, T., Diat, O., Piazzesi, G., Lombardi, V. et Irving, M. (2003). The conformation of myosin head domains in rigor muscle determined by X-ray interference. *Biophysj*, 85(2) :1098–1110.

Ribba, B., Saut, O., Colin, T., Bresch, D., Grenier, E. et Boissel, J. (2006). A multiscale mathematical model of avascular tumor growth to investigate the therapeutic benefit of anti-invasive agents. *Journal of Theoretical Biology*, 243(4) :532–541.

Rodriguez, E., Hoger, A. et McCulloch, A. (1994). Stress-dependent finite growth in soft elastic tissues. *Journal of Biomechanics*, 27(4) :455–467.

Roth, C., Ismail, M., Yoshihara, L. et Wall, W. (2017). A comprehensive computational human lung model incorporating inter-acinar dependencies : Application to spontaneous breathing and mechanical ventilation. *International Journal for Numerical Methods in Biomedical Engineering*, 33(1).

Sainte-Marie, J., Chapelle, D., Cimrman, R. et Sorine, M. (2006). Modeling and estimation of the cardiac electromechanical activity. *Computers & Structures*, 84(28) : 1743–1759.

Sermesant, M., Chabiniok, R., Chinchapatnam, P., Mansi, T., Billet, F., Moireau, P., Peyrat, J., Wong, K., Relan, J., Rhode, K., Ginks, M., Lambiase, P., Delingette, H., Sorine, M., Rinaldi, C., Chapelle, D., Razavi, R. et Ayache, N. (2012). Patient-specific electromechanical models of the heart for the prediction of pacing acute effects in CRT : A preliminary clinical validation. *Medical Image Analysis*, 16(1) :201–215.

Sheshka, R. (2012). *The power stroke driven muscle contraction.* Thèse de doctorat, École polytechnique.

Sheshka, R. et Truskinovsky, L. (2014). Power-stroke-driven actomyosin contractility. *Physical review. E, Statistical, nonlinear, and soft matter physics*, 89(1) :012708.

Silverthorn, D., Ober, W., Garrison, C. et Silverthorn, A. (2009). *Human physiology : an integrated approach.* Pearson.

Sliwoski, G., Kothiwale, S., Meiler, J. et Lowe, E. (2013). Computational Methods in Drug Discovery. *Pharmacological Reviews*, 66(1) :334–395.

Stella, J. et Sacks, M. (2007). On the Biaxial Mechanical Properties of the Layers of the Aortic Valve Leaflet. *Journal of Biomechanical Engineering*, 129(5) :757–10.

Sugiura, S., Washio, T., Hatano, A., Okada, J., Watanabe, H. et Hisada, T. (2012). Multi-scale simulations of cardiac electrophysiology and mechanics using the University of Tokyo heart simulator. *Progress in biophysics and molecular biology*, 110(2-3) : 380–389.

Tanrikulu, Y., Krüger, B. et Proschak, E. (2013). The holistic integration of virtual screening in drug discovery. *Drug Discovery Today*, 18(7-8) :358–364.

Taylor, C. et Figueroa, C. (2009). Patient-specific modeling of cardiovascular mechanics. *Annual Review of Biomedical Engineering*, 11 :109–134.

Trayanova, N. (2011). Whole-heart modeling : applications to cardiac electrophysiology and electromechanics. *Circulation Research*, 108(1) :113–128.

Veigel, C., Bartoo, M. L., White, D. C., Sparrow, J. C. et Molloy, J. E. (1998). The stiffness of rabbit skeletal actomyosin cross-bridges determined with an optical tweezers transducer. *Biophysj*, 75(3) :1424–1438.

Visentin, R., Campos-Náñez, E., Schiavon, M., Lv, D., Vettoretti, M., Breton, M., Kovatchev, B., Dalla Man, C. et Cobelli, C. (2017). The UVA/Padova Type 1 Diabetes Simulator Goes From Single Meal to Single Day. *Journal of Diabetes Science and Technology*, 12(2) :273–281.

Waller, A. (1887). A Demonstration on Man of Electromotive Changes accompanying the Heart's Beat. *The Journal of Physiology*, 8(5) :229–234.

Wang, H. et Oster, G. (2002). Ratchets, power strokes, and molecular motors. *Applied Physics A*, 75(2) :315–323.

Zahalak, G. (1981). A distribution-moment approximation for kinetic theories of muscular contraction. *Elsevier*, 55(1-2) :89–114.

Zahalak, G. I. (2000). The two-state cross-bridge model of muscle is an asymptotic limit of multi-state models. *Journal of Theoretical Biology*.

CHAPTER 1

Physiology of muscle contraction

In this chapter, we present a literature review of the experimental works targeting the actin-myosin interaction and its regulations with the aim of compiling the relevant information for the development of the models. We first give a general qualitative review of the heart function and the associated underlying mechanisms following a top-down approach. In a second part, we focus on the quantitative properties of the cardiac muscle. We first analyze the experimental results aiming at characterizing the interaction between myosin heads and actine sites and then focus on the characterization of the regulation mechanisms.

Contents

In this chapter, we give a synthetic review of the structure of muscles in animals and the physiology of muscle contraction with some personal interpretation.

Our presentation will be organized in two main parts. We will start by a qualitative description of the muscle excitation-contraction mechanism, mainly focused on the physiology of cardiac muscles. Skeletal muscles, which share essential features with cardiac muscles, will be briefly introduced as a variation of the cardiac muscle and sometimes used as a benchmark for cardiac muscles, although the characterization of skeletal muscles has historically been performed first. Then, we will present the state of the art on the quantitatively properties of cardiac muscles.

A particular emphasis will be put on the levels of physiology that will be used to support the development of our models (actin-myosin interaction, thin filament activation, microscopic mechanisms underlying the Frank-Starling macroscopic regulation).

Our presentation of general physiology mainly relies on [Silverthorn et al., 2009]. For more details on the sarcomere structure we refer to [Craig and Padrón, 2004] and to [Craig and Woodhead, 2006] for a detailed description of the myofilaments. A presentation of the excitation mechanisms can by found in [Bers, 2002]. Our review of the quantitative properties of the excitation will be two-fold. First, to present the actin-myosin interaction, we use the extensive work of the group of Vincenzo Lombardi at the University of Florence. Second, the description of the thick and thin filaments activation and the associated regulation is mainly supported by the works of Henk ter Keurs, Peter de Tombe and their co-authors (see e.g. [de Tombe et al., 2010; de Tombe and ter Keurs, 2016]). The physiological latter mechanisms are at the origin of one of the main regulation at organ level called the *Frank-Starling mechanism*, which makes the left ventricular pressure at the end of the contraction vary as a function of the ventricular volume. For a general presentation on this topic, we refer to the reviews by Allen and Kentish [1985], ter Keurs [1996] de Tombe et al. [2010] and Sequeira and Velden [2017].

1.1 Description of muscle contraction

To qualitatively present the various mechanisms involved in muscle contraction, we follow a top-down approach from the macroscopic description of the tissue to the nanometric events occurring at the level of individual proteins.

1.1.1 Anatomy of muscles

Muscles are one of the four types of soft tissues in animals along with connective tissues, nervous tissues and epithelial tissues. Their function is to transform a signal from the nervous system into a mechanical force. They are made of the association of proteins taking care of the structure integrity, the generation of force and the regulation of the generated force. There are two categories of muscles in animals: striated muscles and smooth muscles.

1.1.1.1 Different types of muscles in human body

Striated muscles, which group together cardiac and skeletal muscles, contract in response to electrical pulse signals resulting from conscious or unconscious control. Their normal functioning is a succession of contraction and relaxation phases paced by the electrical stimulations. Smooth muscles are found in the walls of organs such as the stomach or blood vessels. As opposed to striated muscles, they contract under unconscious control and generate near permanent contractions. Only striated muscles will be studied in this

manuscript and we will restrict the presentation to this type of muscle, and in particular to cardiac muscles, in what follows.

1.1.1.2 Multiscale structure of striated muscle in space

Cardiac muscle are a multi-scale structure in space. They are made of an arrangement of cardiac cells, called *cardiomyocytes*, which form an array of branching fibers. The cells are branching in an irregular way (see Figure 1.1). They are linked between each other by intercalated disks which allow the force developed to be transferred throughout the whole muscle. Muscle fibers are themselves composed of a bundle of myofibrils. The myofibrils are made up of a small contraction unit, called sarcomere, which is periodically repeated along the fibre. The sarcomeres are linked together by protein structures called Z-disks. The length of the sarcomere is typically 2 µm. The very ordered structure of the sarcomeres gives rise to bands that can be seen when observing myofibrils under the microscope, which gave their name to this type of muscle. Inside the sarcomere, two protein filaments – myosin filaments and actin filaments – interact with each other creating bonds between myosin heads and actin sites. The contraction originates from a protein conformational change whose size is typically 10 nm (see Section 1.1.2). The structure of striated muscle thus allows the transformation of nanometric displacements at the protein scale into the observed macroscopic contraction at the organ scale.

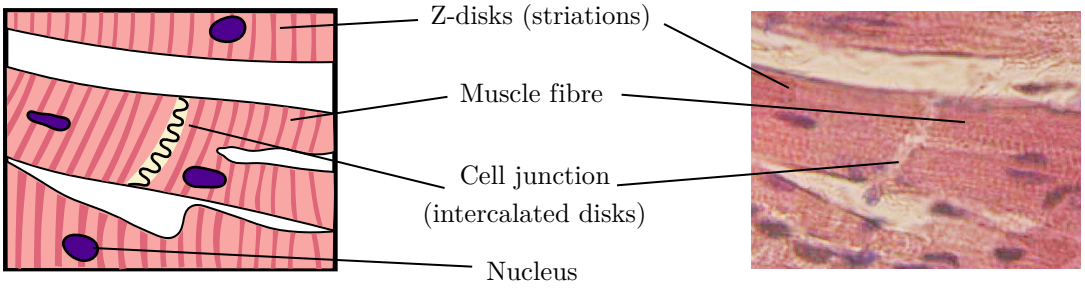

Figure 1.1 – Cardiac fibers organization. (a) Schematic. (b) Microscope image. The cells are linked together by the junctions called intercalated disks. They form an array of branching fibers. The striation appearing on the image originate from the sarcomeres. The right panel is a modification of the work of Dr. S. Girod, Anton Becker, licensed under CC BY 2.5.

1.1.1.3 Anatomy of a cardiomyocyte

Cardiomyocytes contain all the materials needed to perform the *activation-contraction coupling* (also called the excitation-contraction coupling). It is the transformation of a local electrical signal into a mechanical force.

The cell membrane contains ion channels and ion exchangers that allow the transfer of ions inwards and outwards. These elements react as a function of the membrane electrical potential and are affected by the ions concentrations on both sides of the membrane. The ions exchangers of interest for the muscle contraction are the calcium sodium exchangers (denoted NCX). They exchange one Ca^{2+} ion against three Na^{+} ions. The NCX has a threshold potential that depends on the calcium and sodium concentrations. When the membrane potential is higher than the NCX potential, calcium is brought into the cell, and vice versa.

The sarcomeres in series span across the cell and are linked on the boundaries to the intercalated disks in order to transmit the force to the neighboring cells.

The cell is also equipped with a reservoir of calcium ion called the *sarcoplasmic reticulum* (sarcoplasmic reticulum). It captures calcium ions from the cell cytosol with ATP-driven Ca^{2+}-pumps and releases them quickly and in a large amount when activated. The activation is triggered by inwards calcium fluxes detected by receptors denoted RyRs. The RyRs also act as release channels for calcium ions. The released calcium ions are captured by the sarcomere, where they trigger the contraction. Under the action of the calcium Ca^{2+}-pumps, calcium is liberated by the sarcomere and uptaken by the sarcoplasmic reticulum. The transfer of ions through the membranes is an active process in the sense that it consumes energy brought by ATP. It uses between 30% and 40% of the energy consumed by the cell [Barclay, 2015].

The structure of a cardiomyocyte is schematically displayed in Figure 1.2.

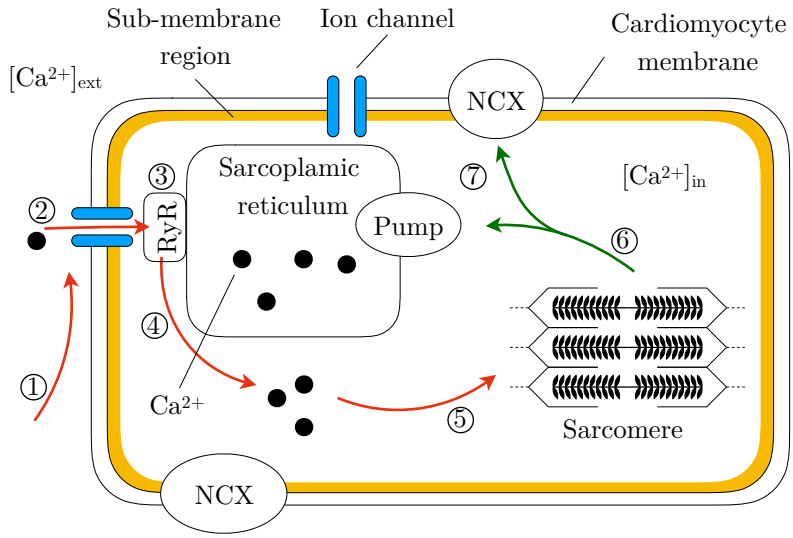

Figure 1.2 – Schematic of a cardiomyocyte. The sequence of events occurring during activation (red arrows) and relaxation (green arrows) is also presented: (1) the action potential travels on the membrane, (2) calcium ion channels are activated and let calcium ions in, (3) this calcium flux triggers the sarcoplasmic reticulum, (4) calcium is released in the cytosol, (5) calcium ions are captured by the sarcomere, (6) calcium ions are taken from the sarcomere, (7) calcium ions are uptaken by the sarcoplasmic reticulum or removed from the cells by the exchangers.

We now define the calcium concentrations that will be used through the entire manuscript. The external calcium concentration is denoted by $[Ca^{2+}]_{ext}$. In the cell, we distinguish between the membrane ion concentration, which is related to the ions linked to the membrane and the intracellular calcium concentration depending on the amount of ion in the cytosol. The intracellular calcium concentration is denoted by $[Ca^{2+}]_i$.

1.1.1.4 Anatomy of a sarcomere and the myofilaments

The elementary unit of the contractile apparatus is the sarcomere. The sarcomere is a highly organized structure (see Figure 1.3). It has a longitudinal symmetry and can thus be seen as two half-sarcomeres contracting in opposite directions. A sarcomere is delimited by protein components appearing as thick black lines on microscope images called *Z-disks*. Our description of the sarcomere structure relies on Craig and Padrón [2004], completed by [Kobayashi et al., 2008] for the description of the thin filament.

The sarcomere is mainly composed of two family of parallel filaments overlapping themselves in a crystalline-like arrangement (see Figure 1.3). The first family is made

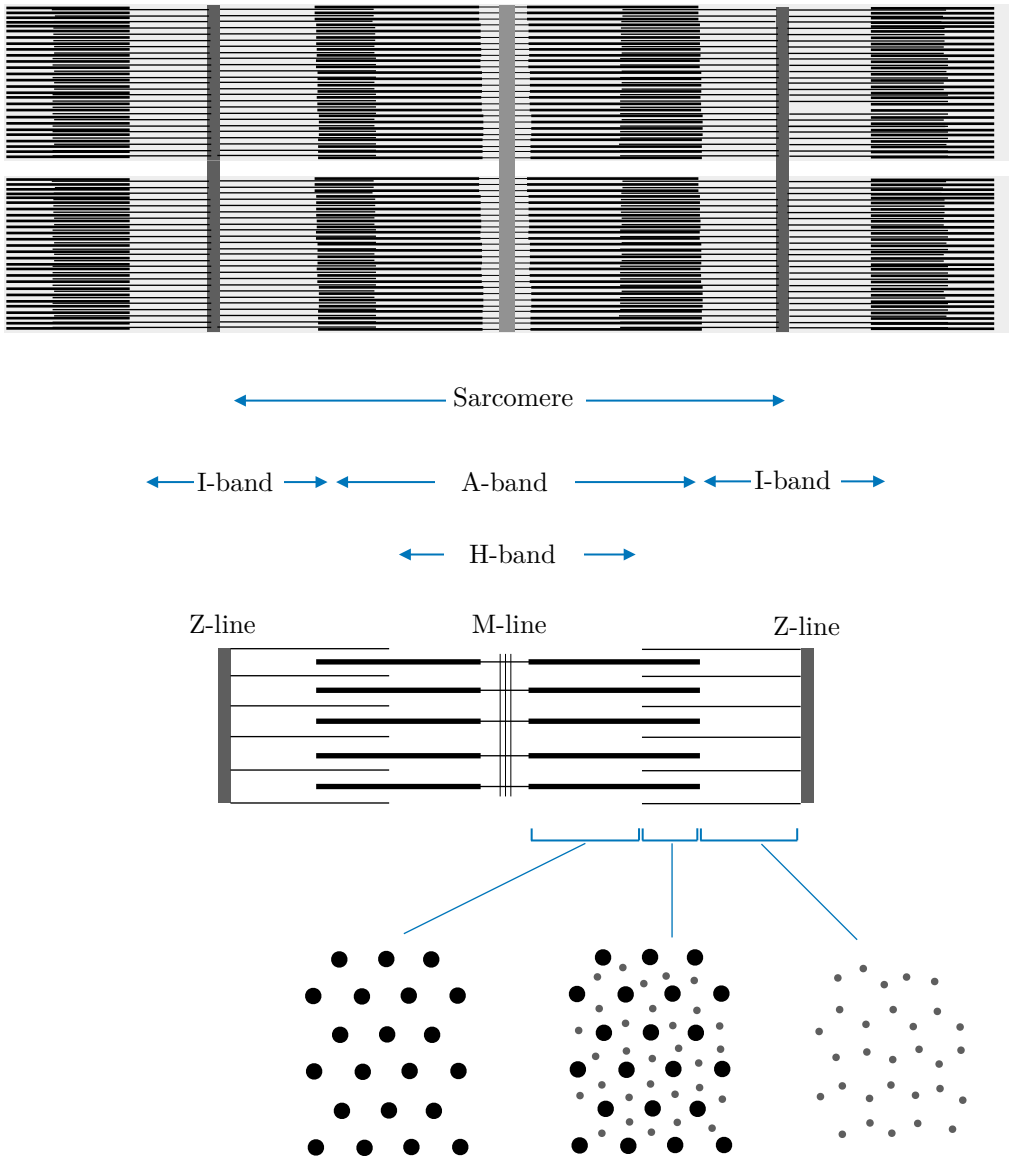

Figure 1.3 – Illustration of the sarcomere and of its structure. The crystalline structure of the sarcomere appears. The link between the thick filaments appears in the M-line. Inspired from [Craig and Padrón, 2004].

of the actin filaments, which are anchored on the Z-disks. The second family is made of myosin filaments spanning in both directions from the sarcomere median plan on which they are linked. In the middle of the sarcomere, a protein structure connects the thick filaments. It is the M-line that appears in the microscope image.

The actin filaments form the so-called *thin filaments*, which are polymers made of actin monomers forming a double helix (see illustration in Figure 1.4.). The spatial periodicity of the double helix is 37–40 nm, while the actin monomer is 5.5 nm long. Each actin monomer has a myosin binding site. At rest, these binding sites are covered by a tropomyosin molecule (Tm), which prevents myosin binding. Tm is a 40 nm long polymer that is wrapped around the actin filaments. The thin filament is thus covered by a set of Tm that overlap in their head and tail regions. The part of the thin filament that is covered by one Tm molecule is called a *Regulatory Unit* (RU). A regulatory unit thus includes seven actin monomers and has a length of 38.5 nm. In each RU, a troponin complex (Tn) is bound to Tm and block its position in front of the actin sites. The troponin complex is made of three proteins: the troponin-T (TnT) that actually binds to Tm, the troponin-C (TnC) that binds to calcium and a troponin-I (TnI). At rest, a domain of TnI binds to actin, which strongly fixes the Tm with respect to actin. In the presence of calcium, the affinity of TnI for another part of the troponin complex increases, TnI detaches from the actin filament. The tropomyosin is liberated and this allows the access to some actin sites of the regulatory unit for the myosin heads. Note that due to the varying orientation of the actin site along the actin filament helix, it is likely that the myosin head can not bind to all actin sites but only to those that have the appropriate orientation. The question of how many actin sites actually have the "appropriate orientation" remains open.

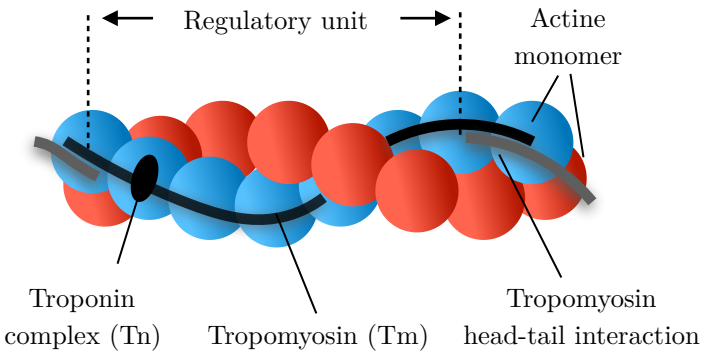

Figure 1.4 – Schematic of an actin filament.

The myosin filaments form the the so-called *thick filaments*. They contain 294 myosin molecules [Reconditi et al., 2017], each of which is made of a *head*, which is exposed towards the outside of the filaments, and a *tail*, which is anchored in the backbone of the filament. The heads are organized in a regular array forming helices. The periodicity of the helix is 43 nm, meaning that the myosin heads are separated by this distance along the longitudinal direction. Along the helix direction, the myosin heads are separated by 14.3 nm [Craig and Padrón, 2004] (see Figure 1.5). In the central region of the thick filament, there is no myosin head; it is called the bare zone. The density of thick filament in a cross section is 424 filaments/m^2 [Pinzauti et al., 2018]. The thin and thick filaments are regrouped under the term *myofilaments*.

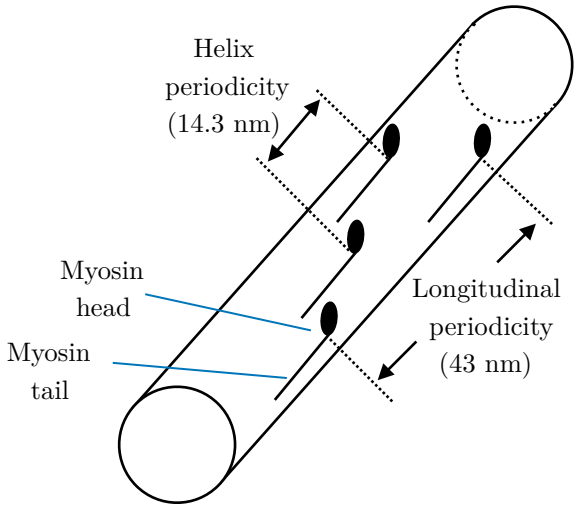

Figure 1.5 – Schematic of a myosin filament.

In addition to these two types of filaments, another element, called *titin*, plays an important role in muscle contraction. It is a giant protein spanning from the Z-disks, wrapping around the thin filament and anchored in the M-line. Titin allows the sarcomere to recover its original length in the relaxation phase. Titin also contributes to the passive stiffness of the tissue [Fukuda et al., 2008; Mateja et al., 2013; Methawasin et al., 2014]. In addition, it may play a role in many regulatory mechanisms such as the on-off transition (see Section 1.4.2.2) and the modulation of the thin filament sensitivity to calcium (see Section 1.4.2.3).

The rest length of the sarcomere is called the *slack length*. The slack length of cardiac sarcomeres, is commonly reported to be 1.85 µm [ter Keurs et al., 1980] for rat and 1.70 µm for humans [van der Velden et al., 2000]. We can note that a negligible stiffness is measured around the slack length which explains the difficulty to define the stress-free state of cardiac fibers [Caruel et al., 2013].

1.1.1.5 Anatomy of a myosin head

As already mentioned above, the myosin has two main components: its tail and its head. The head is named the S1 domain and the tail can itself be split into two parts: the light meromyosin (LMN), which is anchored in the myosin filament, and the S2 domain that sticks out of the filament core (see Figure 1.6). Electron-microscopy and X-ray crystallographic analyses reveal the complex 3D structure of the myosin heads [Rayment et al., 1993; Irving et al., 2000]. The myosin head has two stable positions corresponding to two conformations of the protein. The angle between the head and the tail changes between these two conformations by 70°. It corresponds to a longitudinal displacement (projected along the filament direction) of 11 nm [Irving et al., 2000] (see Figure 1.6). Note that this value is sometimes also reported to be 8 nm [Kaya and Higuchi, 2010].

When bound together the actin site and the myosin head form a *cross-bridge*. Experiments on individual molecules show that the cross-bridge has elastic properties. The compliance is concentrated in the head or at the connection point between the actin site and the myosin head, the tail part of the myosin being much stiffer [Kaya and Higuchi, 2010].

When a myosin head is attached, the change between the two stable conformations generates a force and the transition is then called the *power stroke*. The initial and

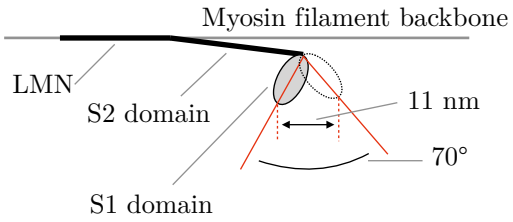

Figure 1.6 – Two stable angular positions of the myosin head. These positions are separated by an angle of 70°, which corresponds to a longitudinal displacement of 11 nm

final conformation are naturally referred to as *pre-power stroke* and *post-power stroke*, respectively.

1.1.2 Origin of contraction - the actin-myosin interaction

The actin-myosin interaction occurs in a cyclic manner. A commonly accepted description of this cycle has been proposed by Lymn and Taylor [1971]. It is illustrated in Figure 1.7. The Lymn-Taylor cycle is composed of four stages:

- in the first stage, the myosin head in the pre-power stroke conformation attaches to an actin site.
- in the second stage, the myosin undergoes a conformation change, which generate a force. This is the power stroke.
- in the third stage, the myosin head, which is now in the post-power stroke conformation, detaches. The use of chemical energy brought by ATP molecules is necessary for the detachment. In each cycle, this consumes an energy of 100 zJ [Barclay, 2015].
- in the fourth stage, the detached myosin head recovers its power stroke capability by transitioning back to the pre-power stroke conformation. The myosin head can then enter in a new cycle.

Note that experiments in solution indicate that the power stroke is a fast step – its duration is of the order of 1 ms – compared to the whole cycle duration, which is of the order of 100 ms [Linari et al., 2010]. Conclusions drawn for experiments in solution must be transposed with care to intact muscle, where geometric and mechanical constraints are drastically different. Nevertheless, this still shows a separation of time scales between a fast power stroke stage compared to the rest of the cycle comprising the attachment-detachment process. A confirmation of this property is given by mechanical experiments on individual cardiac muscle cells, which display the same separation of time scales (see Section 1.3.2.1). The Lymn-Taylor cycle gives a correct picture of the interaction between myosin heads and actin sites but there is still a lot of unknowns in this molecular interaction. Intense research activities are dedicated to the description of all the structural changes occurring during this cycle [Houdusse and Sweeney, 2016].

1.1.3 Thick filament activation

In the above presentation of the interaction between a myosin head and an actin site, we suppose that the myosin head is always available for attachment and that the actin site is always accessible for the myosin head. However, in physiological conditions, this may not be the case.

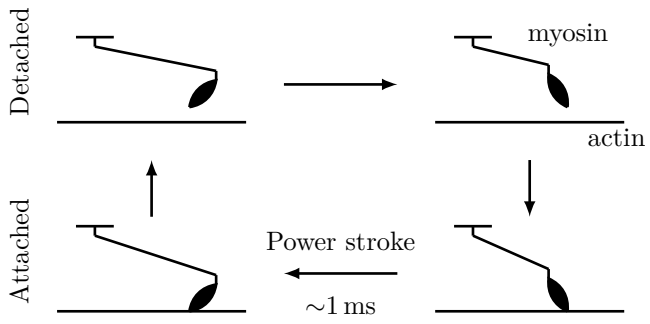

Figure 1.7 – Illustration of the Lymn-Taylor cycle [Lymn and Taylor, 1971].

It has recently been observed in skeletal muscles with X-ray crystallographic measurements, that the myosin head can be in a position where the S2 domain does not point out of the thick filament backbone anymore, but is instead aligned along the filament backbone [Reconditi et al., 2011] and the myosin heads is folded back towards the M-line. This state is called *off-state*, as opposed to *on-states* when the S2 domain points towards the thin filament. Additional investigation with skeletal muscles, showed that the on-off transition is triggered by a mechanosensing mechanism [Linari et al., 2015]. More recently, the off-state was also observed in cardiac muscles but only at rest and in isometric conditions [Reconditi et al., 2017].

Moreover, when stretching the sarcomere, the level of activation of the thick filament varies (see Section 1.4.2.2).

1.1.4 Thin filament activation

As for the myosin filament, the level of activation of the thin filament is controlled and regulated. The cardiac cycle is an alternation of contractions and relaxations, both of which are solely triggered, in physiological conditions, by the presence or the absence of Ca^{2+} ions in the cytosol, which serve to activate the thin filament. Pacemaker cells in the atria create a depolarization wave that propagates in the heart in a controlled manner. When the depolarization wave reaches a cardiomyocyte, it induces the release of calcium in the cytosol of the contractile cells. The calcium ions then interact with the thin filament to activate the actin sites and allow the binding of myosin heads. This activation signal transduction is regulated extrinsically by the neuroendocrine system (see Section 1.1.5) and intrinsically by the extension at the scale of the sarcomere (see Section 1.4.2.3).

The variations of the level of thin filament activation act as a command to switch the muscle cell between the contraction and relaxation phases.

In this section we present the different stages of the signal transduction between the pacemaker signal to the activation of the actin site keeping our top-down approach. We then introduce the regulation mechanisms. Note that an illustration of the events of the activation process occurring at the cell level is presented in Figure 1.2.

1.1.4.1 Macroscopic activation signal propagation

We will first consider the basal behavior, that is in the absence of the extrinsic regulation (see [Bers, 2002] for more details). At the level of the sinoatrial node (in the right atrium) special cardiac muscles cells, called pacemaker cells, generate an electrical signal. The proteins across the cell membrane allow a inflow of calcium which results in increasing the

amount of positive charges inside the cell. As a result, the originally negative membrane potential is increasing. When the potential reaches a threshold, the membrane depolarizes. In response to depolarization, a sequence of events involving the movement of ions into and out of the cell occurs, thus changing the membrane potential. This behavior is spontaneous (is not necessarily triggered by a signal from the nervous system) and occurs at a constant frequency (60–80 bpm). The sinoatrial mode is a natural pacemaker.

As part of the sequence of events resulting from the depolarization, ion currents appear toward the neighboring cells thus changing their own membrane potential. At some point the potential reaches a threshold and the neighboring cells depolarizes. The depolarization of the pacemaker cells thus triggers the depolarization of the surrounding cells in the atrium. The depolarization wave propagates and reaches the atrioventricular node which acts like a synchronizer.

The depolarization wave propagates then through the bundle of His and the Purkinje fibers to the apex of the heart and triggers the depolarization of the contractile cells. From the apex, the depolarization spreads to the ventricular contracting cells and travels to the top of the ventricle (towards the valves).

1.1.4.2 Interactions at the cell membrane - the action potential

We will now describe in more detail the sequence of events occurring in the contractile cells leading to the action potential.

At rest, the contractile cell membrane is polarized. It contains more negative charges inside the cell than the outside environment which creates a negative potential. ATP-fueled pumps maintain this potential by bringing sodium and calcium ions out and potassium ions in.

The activation is initiated from the Purkinje fibers or a neighboring cell. In response to the stimulation, the sodium ion channels open causing a large flux of sodium ions towards the inside of the cell. The potential increases; the cell is depolarizing (phase 0). Following the depolarization (phase 1), the potassium channels open and a small amount of potassium ions goes out of the cell, and causes a slight decreases of the potential. It is the early repolarization (phase 2). In a subsequent step, the fluxes of calcium ions into the cell and potassium ions out of the cell balance, causing a plateau phase in the evolution of the membrane potential (phase 3). In the last phase, calcium channels close and potassium ions keep leaving the cell. The potential decreases to its original value; this is the repolarization of the cell (phase 4). The shape of the action potential in a contractile cell is presented in Figure 1.8(a). Note that the action potential in pacemakers cell has a different shape. Note also that the superposition of the action potentials gives rise to the macroscopic ECG signal.

The sodium channels that intervene in the early phase of the action potential need time after being activated to reach their initial configuration and be active again [Silverthorn et al., 2009]. The time during which the sodium channel cannot be activated is called the *refractory period*. In this period an electrical stimulation will have no effect on the sodium channels and thus will not trigger an action potential. In cardiac muscles the refractory period ends as the force relaxation is well advanced. Therefore, a new contraction cannot be initiated until the current contraction is finished. As a result, tetanus is prevented under physiological conditions. Preventing tetanus in cardiac muscle is physiologically relevant because the cardiac cycle consists in alternating periods of contraction (ejection phase) and relaxation (filling phase). A tetanised state would thus stop the cardiac cycle. However, note that under specific non-physiological conditions, a tetanised state is still possible in cardiac muscle (see Section 1.1.6.1).

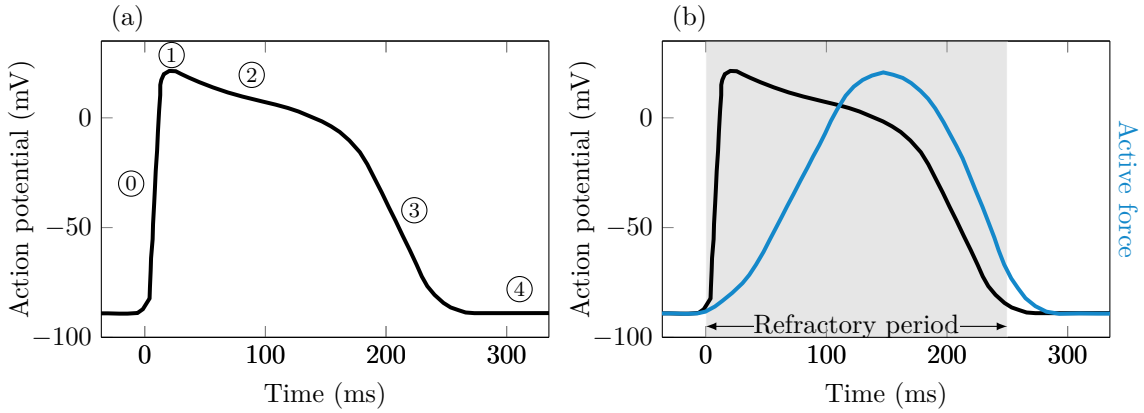

Figure 1.8 – Membrane action potential and force developed in cardiac muscle cells. (a) Action potential of a contractile cardiac muscle cell. (b) Action potential and force development by a cardiomyocyte. Reproduced from [Silverthorn et al., 2009].

1.1.4.3 Ion fluxes in the bulk cytosol

We will now look in more detail at the mechanisms underlying the different phases of the action potential with a focus on the parts that are involved in the activation-contraction coupling.

Two elements are of particular importance for muscle contraction and relaxation: the Ca^{2+}-channels and the Na^{+}-Ca^{2+}-exchangers (NCX). The depolarization of the membrane leads to the opening of Ca^{2+}-channels creating an inward current of calcium ions.

Calcium ions release in the cytosol In the first phase of the action potential, Na^{+} ions enter the cell leading to the increase of the membrane potential, which becomes positive. As a result, the NCX and the Ca^{2+}-channels work in "calcium-intake mode". The amount of calcium brought into the cell by the Ca^{2+}-channels and the NCXs is not sufficient to induce the activation of the thin filament. As it has been revealed by [Fabiato, 1983], the flux of calcium through the membrane is actually only a triggering signal for the release of calcium contained in the sarcoplasmic reticulum in large quantities. It is thus a Ca^{2+}-induced-Ca^{2+}-release. The sarcoplasmic reticulum release is fast; it reaches its peak in 2 ms - 3 ms [Puglisi et al., 1999]. The activation mechanisms of the calcium release has been understood but, conversely, the origin of the termination of the release remains subject to debate [Bers, 2002]. The closing of the RyRs is not fully elucidated.

Calcium ions uptake in the sarcoplasmic reticulum Once the release of calcium is completed, the dominant effect regarding calcium ions in the cytosol is the removal from the cytosol trough different paths: re-uptake in the sarcoplasmic reticulum or outwards flux from the cell through the Na/Ca^{2+} exchangers. The relative importance of these paths for calcium uptake varies among species and can be affected by diseases [Bers, 2002].

1.1.4.4 Mechanisms at sarcomere-level

We will now describe how calcium interacts with the thin filament to make the actin sites available for myosin attachment.

Actin site activation In the presence of calcium, Ca^{2+} binds to TnC, which induces a structural change leading to the exposition of a site on TnC of high affinity for the switch

domain of TnI. The switch domain of TnI attaches to TnC and the inhibitory part of TnI, which was bound to an actin site, is moved. This prevents its attachment to actin. The troponin complex is now detached from the actin filament and so is the tropomyosin, which is linked to the troponin complex by the TnT. When the tropomyosin is free to move, some actin sites become available for the formation of cross-bridges with myosin heads [Gordon et al., 2000].

Note that TnC has three actin binding sites (2 high affinity sites and 1 low affinity site) [Kobayashi et al., 2008]. According to Kobayashi et al. [2008], the two high-affinity sites do not contribute to contraction regulation so that the contraction is only regulated through the binding to the low-affinity binding site.

Actin site de-activation The detachment of the calcium ions from the troponin complex is less understood than its attachment. Two paths are possible: either calcium detaches first from the TnC while the myosin head stays attached or the myosin heads detaches before calcium. Sun and Irving [2010] state that the two paths are possible, the choice of one or another being determined by their respective kinetics, i.e. whether myosin head or calcium detach faster. The rates of those dynamics depend on the amount of elements in each state (attached or detached for the myosin head and attached to an actin site or in the cytosol for calcium ions) and the respective transition rates between these states. For instance the more calcium ions are attached to the thin filament, the higher is the detachment rate towards the cytosol.

1.1.4.5 Length-dependent activation

Some of the cell elements involved in the transduction of the calcium-induced calcium release by the sarcoplasmic reticulum to the activation of the actin sites are length sensitive. It results in a higher level of thin filament activation when the sarcomere is stretched. This effect is called the *length dependent activation* (LDA). The length dependent activation is analyzed in more details in Section 1.4.2.3.

1.1.5 Neuroendocrine regulation

The behavior described above occurs spontaneously in the presence of the required ions, but at the constant frequency imposed by the pacemaker cells. This is the basal functioning of the heart. The actual functioning of the heart is regulated by the autonomous nervous system, which produces two antagonist effects acting simultaneously. The relative importance of these two regulation mechanisms sets the actual state of the heart contraction.

The sympathetic (or orthosympathetic) nervous system "enhances" the activity of the heart, increasing the beating pace and the inotropic state. It acts through two pathways: a neuronal pathway and an endocrine pathway. In the neuronal pathway, the signal is transported by action potential in the nerves ultimately leading to the liberation of neuromediator at the vicinity of the contractile cell. In the endocrine pathway, the sympathetic system activates the adrenal cortex which liberates catecholaminergic endocrines in the blood. Both neurotransmitter and endocrines interacts with receptors located on the outer surface of the muscle cell, triggering a signaling cascade inside the cell. Typical catecholamine endocrines involved in the sympathetic system are the adrenaline (also called epinephrine) and the noradrenaline (also called norepinephrine).

As opposed to the sympathetic nervous system, the parasympathetic nervous system activation results in a reduction of the heart rate and a decrease in contractility. It works only through a neuronal pathway. A typical neuromediator of the parasympathetic system

is acetylcholine. We insist again on the fact that the neuromediators and endocrines of the sympathetic nervous system and the neuromediators of the parasympathetic nervous system are present at the same time but a group dominates the other.

In pacemaker cells, the signaling cascade induced by both sympathetic and parasympathetic systems modifies the functioning of the ion channels, thus changing the ions fluxes, which ultimately impacts the produced paced action potential. The sympathetic system also acts on the contractile cells. In reaction to its activation, the dynamics of Ca^{2+}-channels and exchangers is modified, increasing the amount of calcium brought inside the cell. Simultaneously, the activity of the ATP-driven Ca^{2+}-pumps of the sarcoplasmic reticulum is enhanced. Combined with the increased amount of calcium present inside the cell, the amount of calcium stored in the sarcoplasmic reticulum is increased. Therefore, more calcium is available to be released in the cell. This leads to a higher activation level and thus an increased contractility. Moreover, the enhanced activity of the Ca^{2+}-pumps of the sarcoplasmic reticulum results in a more efficient calcium re-uptake. Therefore, the twitch duration is reduced [Silverthorn et al., 2009]. Each modification of the ion fluxes through the membrane will induce a change in the action potential. These changes can then be observed in the general ECG.

Note also that the action of the neuroendocrine regulation is not restricted to variations of the amount of calcium released inside the cell. It also directly affects proteins that are involved in the activation-contraction coupling (see Section 1.4.3).

1.1.6 Additional information

1.1.6.1 Tetanus in intact cardiac cells

We have seen that, in normal physiological conditions, cardiac muscles cells cannot be tetanised. However, it is possible to artificially induce a tetanus in intact cells, for instance with high excitation frequency in the presence of chemical agent impairing the functioning of the sarcoplasmic reticulum [Schouten et al., 1990; ter Keurs et al., 2008; Gao et al., 1998]. Alternatively, one can block the Ca^{2+}-channel of the sarcoplasmic reticulum in the open position or inhibit the Ca^{2+}-pump of the sarcoplasmic reticulum [Pery-Man et al., 1993]. Note also that a treatment with caffeine allows to trigger the complete release of the calcium ions contained in the sarcoplasmic reticulum, which leads to a large concentration of calcium in the cytosol [Fabiato and Fabiato, 1975].

1.1.6.2 Rigor state

The *rigor* is the state of the muscle in the absence of ATP. It has been suggested that in this state, all 294 heads of each half-thick filament are attached [Cooke and Franks, 1980]. The energy needed for detachment, which is normally brought by ATP, is indeed missing.

Knowing that all heads are attached allows to perform stiffness measurements [Linari et al., 1998; Piazzesi et al., 2007; Pinzauti et al., 2018].

Note that in rigor state the molecular structure of the myosin head is different from the cycling myosin head (the angle of between the S1- and the S2-domains can reach greater values than that observed in physiological conditions) [Reconditi et al., 2003].

1.1.6.3 Skinned cells

Skinned cells are cells whose membrane has been degraded and in which only the contractile apparatus remains. They are used in experimental protocols because they allow to have a perfectly controlled ionic environment. The drawback is that this environment is,

at best, only an approximation of the physiological conditions. The calcium environment corresponds to the intracellular calcium concentration in intact cells, we will thus denote it $[Ca^{2+}]_i$ as well.

An extensive review of the properties of skinned cells compared to intact cells and the methods that can be used to produce them is given by Kentish et al. [1986].

1.1.7 Skeletal muscles

Skeletal and cardiac muscles differ in their function. Indeed, skeletal muscle must be able to move the body and maintain the posture while cardiac muscles have to fulfill their role as a blood pump. Moreover, cardiac muscle should be able to work without any interruption throughout the course of life (without fatigue).

Similarly to cardiac muscles, skeletal muscles are organized in sarcomeres. They thus also belong to the group of striated muscles. The organization of the sarcomere is qualitatively similar in cardiac and skeletal muscles cells, and in both case, the contraction originates from the interaction between actin and myosin filaments.

However, important differences can be observed. In terms of anatomy, skeletal muscle cells are much longer and may have several nuclei. Their structure is more regular than cardiac muscles as they are organized in long parallel cylindrical fibers without branching.

The main difference between skeletal and cardiac muscles lies in the activation signal transduction. The activation is mediated, like cardiac muscles, by a Ca^{2+}-induced-Ca^{2+}-release, ultimately liberating the actin site for myosin heads binding. The triggering of the activation signal occurs, however, in a much different way. In skeletal muscles, the cells receive a signal from motor neurons, which triggers an action potential that propagates inside the cells. In the cascade of events following the initiation of this action potential, calcium ions enter the cells, triggering the release of the calcium ions stored in the sarcoplasmic reticulum. Unlike cardiac cells, the activation signal does not propagate between the cells; each cell is in contact with motor neurons. Moreover, there is no neuroendocrine regulation by the autonomous nervous system in the skeletal muscle cells.

Unlike cardiac muscles, skeletal muscles often work a the maximum level of thin filament activation, conditions in which variations of the sensitivity to calcium do not matter. Moreover, skeletal muscles express a different form of the TnI, which makes the thin filament activation less sensitive to the sarcomere length [Tachampa et al., 2007]. The developed force is thus less sensitive to variation in the sarcomere length.

The force development also display differences in skeletal compared to cardiac muscles. It is faster in skeletal muscles. Furthermore, the refractory period is shorter in skeletal muscles, which allows to re-activate the muscle before the end of the contraction. When doing so, other action potentials are generated, triggering contraction twitches that add up to each other. At sufficiently high activation frequency, the developed tension reaches a maximal value which is maintained continuously in a so called *tetanised state* or *tetanus*.

1.2 Passive properties of muscle cells

The passive mechanical behavior corresponds to the muscle response in the absence of calcium activation, that is, when no cross-bridge is formed.

In this work, the focus is put on the modeling of the active component of muscle contraction. Therefore, we will only briefly present the passive properties.

We present in Figure 1.9 the passive force with respect to the sarcomere length measured on cardiac muscle samples along the fibre direction by different groups [ter Keurs et al., 1980; Van Heuningen et al., 1982; Caremani et al., 2016]. Several general comments

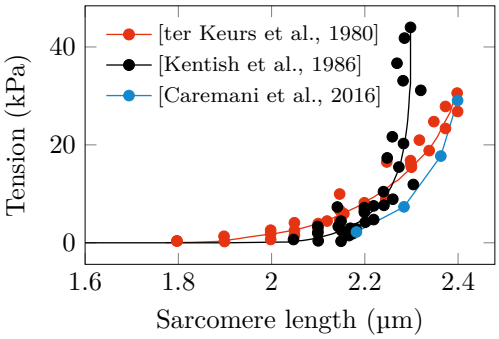

Figure 1.9 – Passive properties of muscle samples along the fibre direction. Data from [Caremani et al., 2016] (rat cardiac cell at 27 °C), [Kentish et al., 1986] (rat cardiac cell at 22–24 °C) and [ter Keurs et al., 1980] (rat cardiac cells at 25 °C).

can be made from these experimental data. First, all experiments present a strong increase in the passive force when the sarcomere is stretched at lengths greater than 2.3 µm. Muscles display non-linear elastic properties. Second, one can note that the stiffness near zero passive force is very low. This explains that measuring the sarcomere slack length is a difficult challenge.

The main components of the muscle cell that contribute the the passive behavior are collagen fibers embedded into a polymer matrix and the titin filaments in the sarcomeres. Passive muscles can thus be seen as a fibre reinforced material. The soft increase in passive force corresponds to the stretch of the polymer matrix, which uncoils the collagen fibers. The steep increase in passive force starts with the stretching of the collagen fibers themselves, which are much stiffer than the matrix [Holzapfel and Ogden, 2009]. Recently, a substantial number of works have also highlighted the contribution of titin to the passive properties of the cardiac muscle cells [Fukuda et al., 2008; Mateja et al., 2013; Methawasin et al., 2014].

In physiological conditions during a heart cycle, the sarcomere length spans on average between 1.90 µm and 2.20 µm although lower or higher values may also be observed at special locations in the tissue [Rodriguez et al., 1992]. The range of sarcomere lengths is limited by the passive force in tension for large sarcomere lengths. One can add that *in vivo* the pericardium (fibrous bag in which the heart is located) also limits the extension of the ventricles and thus of the sarcomere length.

Additionally to its elastic properties, muscles also display a viscous behavior [Hill, 1938; Noble, 1977; de Tombe and ter Keurs, 1992].

1.3 Characterization of fast muscles activation-contraction coupling

We now quantitatively characterize the elements of the activation-contraction coupling that are of interest for the development of our models. In this section, we want to describe the baseline behavior, that is, independently from the regulation mechanisms. We thus consider experiments in which the mechanisms modulating the force are maintained constant through the duration of the measurement of interest. In particular, the sarcomere length must be properly maintained constant.

In a first part, we give a macroscopic description of the cardiac muscle cell contraction. Then, we present in detail experiments characterizing the actin-myosin interaction.

Finally, we present the state of the art knowledge on the thin filament activation.

This presentation is based on experiments performed *ex vivo* on isolated cells, which are therefore disconnected from the autonomous nervous system. The behaviors characterized in these experiments thus correspond to the basal functioning of the cell. Some comments about the impact of the neuroendocrine system are presented in Section 1.4.3. This is a limitation for our goal of modeling the contraction in the context of heart modeling since we have seen in Section 1.1.5 that this impacts many step of the excitation-contraction process.

1.3.1 Muscle twitch contraction

The first way to characterize the contraction is to observe a muscle cell contracting as a response to an excitation signal. Three types of control can be applied on muscle samples. In *fixed ends* (FE) conditions, the sample of muscle is maintained between clamps that do not move. The sarcomere length in the central region of the sample is measured through time. In *length clamped* (LC) conditions, the measurement of the sarcomere length is used to apply a feedback signal to the clamps position controlling system such that the length of the sarcomeres remains constant. Instead, by controlling the length at certain scales of the muscle sample, one can also control the after-load that the muscle must sustain [Lecarpentier et al., 1979]. We call the latter condition *after-load control*.

A typical cardiac muscle twitch contraction in length clamped conditions is presented in Figure 1.10. The twitch contraction can be decomposed into two phases. The first phase

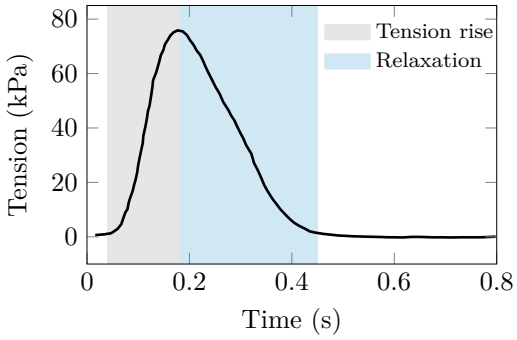

Figure 1.10 – Cardiac muscle twitch contraction obtain on rat cardiomyocyte at 23–24 °C. Data from [Janssen and Hunter, 1995]. The sarcomere length is maintained constant throughout the experiment by a feedback loop and is equal to 2.00 µm. The extracellular calcium concentration $[Ca^{2+}]_{ext}$ is equal to 2 mM.

from the excitation of the cell to the peak is the *tension rise* and lasts about 100 ms. The remaining part is called *relaxation*. The latter phase lasts about 200 ms.

Note that the use of twitch contraction measurements is not adapted to the characterization of the actin-myosin interaction because it mixes many other mechanisms: the dynamics of calcium uptake and release in the cell, the thin filament activation dynamics, the attachment-detachment process. More specific experiments isolating the dynamics of the actin-myosin interaction have been designed (see Section 1.3.2). The twitch contraction measurement can nevertheless be used as an element to understand the thin filament activation because dedicated experiments do not exist (see Section 1.3.3).

Comparing the maximum twitch force with passive experiments presented in Figure 1.9, one can note that the passive force is negligible with respect to the active force for the most part of the contraction twitch. Indeed, at the sarcomere length used in this

experiment (SL = 2.00 µm), the average passive tension among the experiments presented in Section 1.2 is 2 kN. It is much smaller than the active tension of 76 kPa measured at the twitch peak. We will see in Section 1.4 that this observation remains true for all physiological regulation conditions.

1.3.2 Actin-myosin interaction

In this section we review several classes of experiments targeting the different processes composing the actin-myosin interaction. It is here essential to note that these different processes occur at vastly different time scales.

We distinguish two classes of experiments. First, the so-called fast transient response to quick load or length changes provides the main set of data to investigate the actin-myosin interaction. The idea of this type of experiment is to observe molecular processes whose characteristic time scales are short compared to the typical time of completion of the Lymn-Taylor cycle. For that, a load change, whose timescale is short enough to reveal the finest time scales, is applied.

On the contrary, the second class of experiments aims at longer time scales phenomena, which involve the whole actin-myosin interaction cycle. We can distinguish first the protocols aiming at the steady-state dynamics and second the protocols aiming at the transient dynamics.

Note that the viscous intrinsic properties may play a role in the responses to all experiments.

1.3.2.1 Fast time scale response to fast load changes (phase 1, phase 2)

To investigate the fast time scales of the muscle contraction mechanism, two "dual" experimental protocols have been designed. Both protocols use as an initial condition an activated isometric muscle sample under length clamped conditions. The preparation contracts and generates a steady-state isometric force. From this initial steady-state, two different maneuvers may be used. In one case, a step in length is applied and the tension response is measured [Huxley and Simmons, 1971; Piazzesi and Lombardi, 1995]. In the other case, a step in force is applied and the length response per half-sarcomere (hs) is measured [Piazzesi et al., 2002; Caremani et al., 2016]. In both experimental setups, the step is performed quickly with respect to the cross-bridge fastest response time scale (∼100 µs in length control and ∼200 µs in force control). Applying a step allows to synchronize the myosin heads so that their individual behavior can be investigated with the measured macroscopic response immediately following the applied step [Lombardi et al., 1992].

A typical response following a step in force from the isometric tension T_0 to a tension $T_c = 0.6T_0$ for skeletal muscles is shown in Figure 1.11(a). The initial response displays two phases:

- an initial elastic phase (phase 1);
- a fast shortening phase, corresponding to the power stroke (phase 2) [Huxley and Simmons, 1971];
- a pause in the shortening (phase 3);
- a slow shortening phase, which involves the attachment-detachment dynamics (phase 4) [Piazzesi et al., 2002].

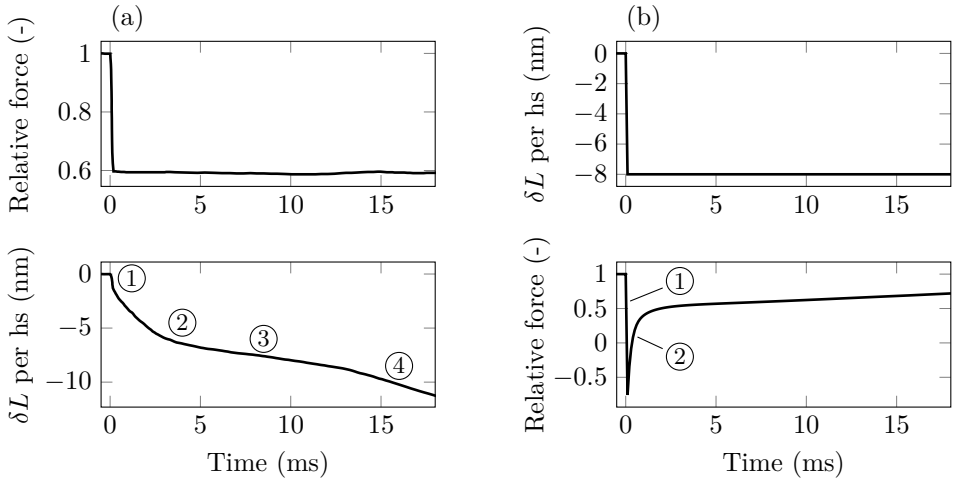

Figure 1.11 – Typical transient responses obtained experimentally from frog skeletal muscle at 4 °C in both force control (a) and length control (b) conditions. The different phases of the response are indicated by circled numbers. Data from (a) [Piazzesi et al., 2002] and (b) [Piazzesi and Lombardi, 1995].

Phase 1 and phase 2 are characterized by the amount of shortening at the end of the respective phases. These shortening are denoted L_1 and L_2, respectively. The steady-state dynamics in phase 4 corresponds to the regime from which the force-velocity curve – first observed by Hill [1938] – is constructed. More details are given in Section 1.3.2.2.

The response following a length step per half-sarcomere δL for skeletal muscles is presented in Figure 1.11(b). The response displays two fast phases: first an abrupt drop in force – up to a level T_1 – almost synchronized with the step itself, and second a partial recovery towards the initial tension – up to a level T_2 – within $\sim 2\,\text{ms}$. The equivalence between the force-length relation at the end of phases 1 and phase 2 with the two experimental setups has been demonstrated experimentally. Piazzesi et al. [2002] show with skeletal muscles that the curves $L_1(T_c/T_0)$ and $T_1(\delta L)/T_0$, on the one hand, and $L_2(T_c/T_0)$ and $T_2(\delta L)/T_0$, on the other end, are superimposed. We insist, that the equivalence only concerns the force-length relation at the end of the phases. The dynamics in phase 2, which is not instantaneous, is not the same in length control and in force control conditions.

For cardiac muscle, the characterization of phase 1 and phase 2 has been first performed by [Caremani et al., 2016] with rat cardiac muscles cells at 25 °C using the force control setup (see Figure 1.12). Cardiac muscles differ from measurements for frog skeletal muscle at 4 °C by the absence of phase 3. Note that a first characterization of rat cardiac muscle cells in length control conditions was also performed by [Pinzauti et al., 2018]. The signature of phase 1 and phase 2, namely the curves $L_1(T_c/\check{T}_c)$ and $L_2(T_c/\check{T}_c)$, are presented in Figure 1.13(a). The rate of shortening in phase 2 (which is the inverse of the time between the end of phase 1 and the end of phase 2 and is denoted by r_2) is presented in Figure 1.13(b).

1.3.2.2 Steady-state properties

Isometric state Substantial information about the molecular contraction mechanism can be recovered from the analysis of isometric contractions. Note that a sustained isometric contraction state does not exist in intact cardiac muscles in physiological conditions (see Figure 1.10). We refer to isometric conditions when the developed force reaches its

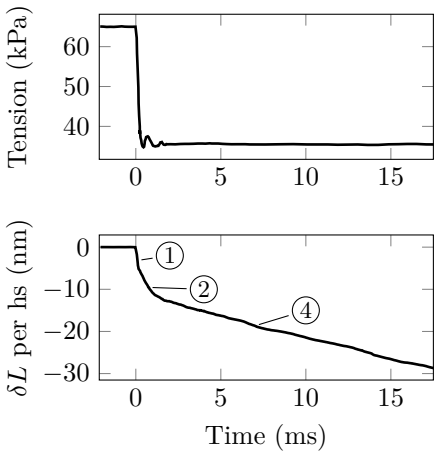

Figure 1.12 – Transient response obtained experimentally with rat cardiac muscle at 27 °C in force control conditions. Data from [Caremani et al., 2016].

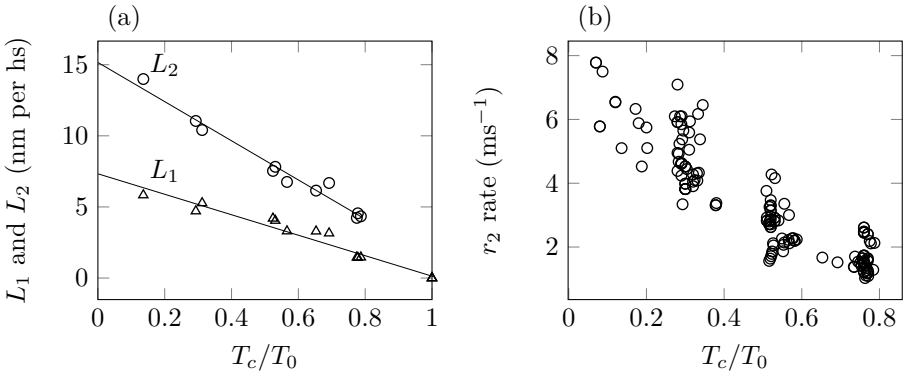

Figure 1.13 – (a)Shortening at the end of phase 1 and 2 in fast load change experiments. (b) Rate of shortening in phase 2. (a) & (b) Experimental data obtained by Caremani et al. [2016] with rat cardiac muscles cell at 27 °C. Figure reproduced from [Caremani et al., 2016].

peak in a twitch contraction in which the length of the fibre is maintained constant (specific experimental apparatus have been designed for that purpose [ter Keurs et al., 1980; Van Heuningen et al., 1982; Caremani et al., 2016]).

The isometric force developed by cardiac muscles cells depends on the level of sarcomere stretch and thin filament activation. In maximal activation conditions, the force can reach the value 118 kPa [Caremani et al., 2016]. On the contrary, the force per attached head does not depend on the thick and thin filament activation. From the ratio of attached head in several activation conditions [Pinzauti et al., 2018], we can derive the ratio of attached heads when the developed force is maximal (see Table 1.1).

In addition to the force measurement, energetics measurements can be performed in isometric conditions. A quantity of interest, that we call the ATP tension cost and that we denote A_T, corresponds to the energy flux consumed per myosin head in the sarcomere per unit of force produced (note that some myosin heads may not contribute to the force production). To compute this quantity, one can use the ATP consumption per unit volume measured by de Tombe and Stienen [2007] at 25 °C. Reconditi et al. [2017] provide geometrical data, which allow to derive a density of myosin heads per unit volume of 1.246×10^{23} heads/m^3 (choosing a reference length of 1 µm for the half sarcomere). Note that "per head" means here per heads in the half-sarcomere and not per cycling head. Neglecting the ATP consumption in the relaxed state, we obtain from the data of [de Tombe and Stienen, 2007] a tension cost of 0.0928 /s/head/kPa. Note that these measurements use skinned cells. The ATP consumption is thus exclusively related to the actin-myosin interaction, whereas 30% to 40 % of the energy brought by ATP is used to pump ions through the different membranes in intact cells [Barclay, 2015].

The isometric indicators are summarized in Table 1.1.

Isometric indicators	symbol	Exp. value	Reference
Maximal ratio of attached heads	$\check{n}_{\text{att}}$	0.15	[Pinzauti et al., 2018]
Force per attached head	$\check{\tau}_c^{th}$ / $\check{n}_{\text{att}}$	6.14 pN	[Pinzauti et al., 2018]
Maximal total stress	T_0	118 kPa	[Caremani et al., 2016]
Energetics indicator			
ATP tension cost	A_T	0.0928 /s/head/kPa	[de Tombe and Stienen, 2007]

Table 1.1 – Properties of rat cardiac muscle cells in isometric conditions at 27 °C.

Steady-state shortening The force-velocity curve is defined as the signature of the phase 4 of the response following a step in force (see Figure 1.12). However, it is also possible to measure a force-velocity curve in length control conditions by imposing a constant shortening velocity and measuring the steady-state force developed by the muscle (note that this is not part of the transient response following a step in length). For the force-velocity curve as well, the equivalence between length control and force control setups has been established experimentally. Daniels et al. [1984] registered the force-velocity curve in both control conditions with the same cardiac sample and obtain a single master curve. The dynamics of phase 4 involves to the attachment and detachment processes.

The force-velocity curve of cardiac muscles has been measured by several groups in various levels of sarcomere stretch and thin filament calcium activation conditions [Van Heuningen et al., 1982; Daniels et al., 1984; de Tombe and ter Keurs, 1990, 1992; Caremani et al., 2016]. A comparison of the experimental data obtained on rat cardiac muscles at 25 °C, with all curves scaled by the individual isometric tension T_0, is presented in Figure 1.14. The different experimental works display a good level of consistency, considering

the possibility of inter-individual variability. All curves scale to a single master curve. Note that in a finer analysis, de Tombe and ter Keurs [1992] observe that the unloaded shortening velocity decreases when the isometric tension T_0 is low. This effect may be due to the viscous load that is relatively more important when the overall active force is low (since it is itself independent on the active force).

One can note that, in a physiological cycle, the heart is always working against an external load – namely, the blood pressure inside the ventricle. Therefore, the low load regime of the force-velocity curve is not of primary importance in the context of organ modeling.

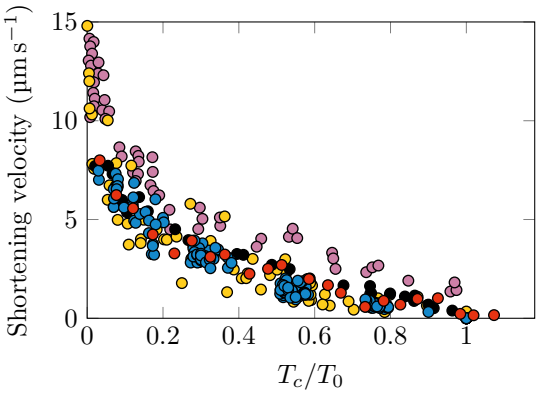

Figure 1.14 – Summary of experimental force-velocity curve measured on rat cardiac muscles. The steady-state force is denoted by T_c and the isometric force by T_0. We collect here all data points obtained in various sarcomere stretch and thin filament activation conditions. All experiments are performed on rat trabeculae. Data from (black) [Van Heuningen et al., 1982] at 25 °C, (yellow) [Daniels et al., 1984] at 25 °C, (lilac) [de Tombe and ter Keurs, 1990] at 25 °C, (orange) [de Tombe and ter Keurs, 1992] at 25 °C, (blue) [Caremani et al., 2016] at 27 °C.

1.3.2.3 Slow time transients

As we explain in Section 1.3.1, the tension rise does not straightforwardly give insight into the actin-myosin interaction because it is also affected by the thin filament activation. However, if the myosin heads can be detached while the thin filament remains activated, the tension evolution can be linked to the attachment and detachment transition rates. The following experimental setup has been designed to achieve this aim. Starting from an isometric condition, a release quickly followed by a restretch of the sample allows to break most of the cross-bridges, which sets the force to zero, while *a priori* letting the thin filament activation unchanged. The evolution of the force after this maneuver is thus linked to the attachment and detachment transition rates that can be extracted from the data through a model. As opposed to the load and length step experiments (see Section 1.3.2.1), this transient experiment targets the events of the actin-myosin interaction occurring at slow time scales.

A typical experimental time evolution obtained with skinned rat cardiac cells [de Tombe and Stienen, 2007] are presented in Figure 1.15(a). The rate of force development can then be computed for various values of the initial tension (see Figure 1.15(b)).

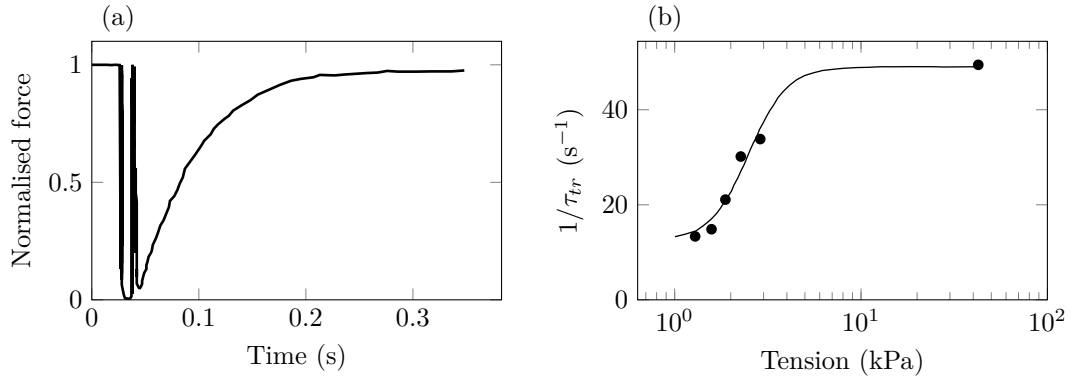

Figure 1.15 – (a) Typical tension redevelopment after a quick release-restretch maneuver. Data obtained with skinned rat cardiac cells at 20 °C with $[Ca^{2+}]_i = 3.16$ mM. Note that the sarcomere length was not controlled throughout the experiment. (b) Rate of tension redevelopment as a function of the isometric force. Data measured at 25 °C for skinned rat cardiac cells, the various level of force are obtained by varying the environment calcium concentration. (a) & (b) Data from [de Tombe and Stienen, 2007].

1.3.2.4 Concluding remarks

The above presented experimental data show that muscles are not only a multi-scale structure in space but are also multi-scale in time. Indeed, for cardiac muscles the transient response to force steps displays three different time scales: an instantaneous elastic response (phase 1), a quick shortening response corresponding to a synchronized power stroke performance of the attached heads, which has a characteristic time of ∼2 ms (phase 2), and a slow shortening response of time scale ∼10 ms involving the attachment and detachment of the myosin heads (phase 4). The shortening velocity in phase 2 is one order of magnitude higher than that registered in phase 4 [Caremani et al., 2016].

1.3.3 Activation of the thin filament

The thin filament activation is triggered by the binding of calcium on the troponin-C ultimately freeing the actin site for the attachment of myosin heads. This mechanism involves several intermediate stages and regulations mechanisms.

The difficulty to quantitatively characterize the thin filament activation relies in the fact that it cannot be isolated from other phenomena in the measurements. The variations of the calcium concentration in the cytosol or the average force can be measured but none of them is directly linked to the level of activation of the thin filament (the ratio of actin sites that are available to form cross-bridges with myosin heads). The evolution of the intracellular calcium concentration $[Ca^{2+}]_i$ depends on the uptake and release of calcium by the thin filament but also by the other cellular elements: sarcoplasmic reticulum, ion channels and ion exchangers.

Structural changes in the thin filament can be tracked with the addition of fluorescent elements [Sun et al., 2009; Ait-Mou et al., 2016] but here again the link with the activation of thin filament is not straightforward (the observed structural changes may only be intermediate steps towards the actin site activation). An option could be the use of X-ray diffraction patterns as for the characterization of the thick filament properties [Linari et al., 2015; Reconditi et al., 2017]. However, the size of the thin filament structure

and the time scale of its activation dynamics are not compatible with the use of X-rays[1].

A possibility to address this difficulty of isolating the level of thin filament activation is to consider the steady-state behavior. We will start our presentation with these experiments that reveal the presence of cooperativity effects in the activation process. We will thus discuss the hypotheses proposed to explain the observed behavior. Finally, the dynamics of the thin filament activation will be investigated.

1.3.3.1 Steady-state conditions

To get access to the thin filament activation level with force measurement, muscle can be observed in steady-state conditions. In this way, the dynamical effects coming from the actin-myosin interaction and the thin filament activation dynamics are removed and the force relates to the number of activated actin sites – we will see in Section 1.4.2.1 that the force per attached head is independent from the calcium supply; the relation between the level of thin filament activation and the force is thus linear.

To obtain steady-state conditions, one needs to block the thin filament in the activated state. It can be obtained by using skinned cells or tetanised intact cells (see Section 1.1.6.3 and Section 1.1.6.1, respectively). To vary the level of thin filament activation, experiments at various surrounding calcium concentrations are performed (intracellular calcium concentration for skinned cell and extracellular calcium concentration for intact tetanised cells). Typical results for skinned cells and tetanised intact cells are presented in Figure 1.16. The relation between the calcium supply and the developed force – or equiva-

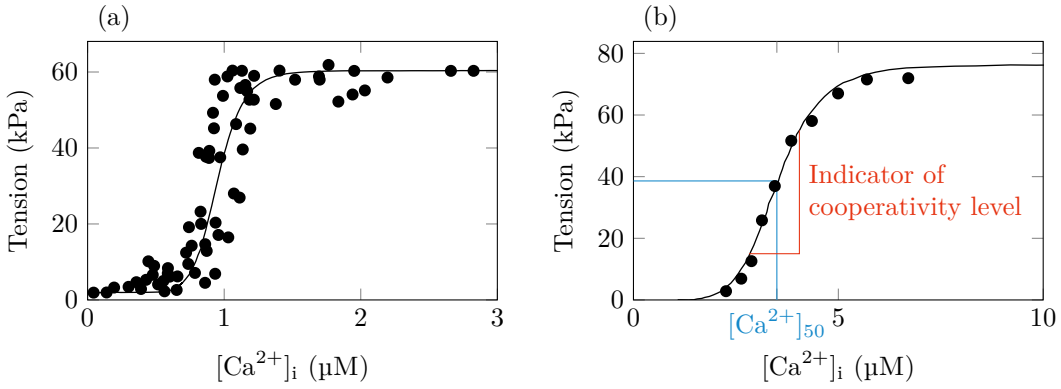

Figure 1.16 – Force developed by cardiomyocytes in steady-state conditions. (a) Tetanised intact cells from mice trabeculae at room temperature (20–22 °C). From [Gao et al., 1998]. The extracellular calcium concentration $[Ca^{2+}]_{ext}$ is controlled and the resulting intracellular calcium concentration $[Ca^{2+}]_i$ is measured. The sarcomere length is set to 2.1–2.2 µm but not strictly maintained constant. (b) Skinned cells from rat at 15 °C at various level of myofilaments compression. From [Dobesh et al., 2002]. Here the intracellular calcium concentration $[Ca^{2+}]_i$ is directly imposed, the sarcomere length is maintained at 2.25 µm

lently the thin filament activation – is strongly non-linear. At a certain level of calcium supply, the force sharply increases. The experimental curve has the shape of a sigmoid. It can be fitted by a function of the form

$$\text{Force} \propto \frac{[Ca^{2+}]^{n_H}}{[Ca^{2+}]_{50}^{n_H} + [Ca^{2+}]^{n_H}}. \tag{1.1}$$

[1] Vincenzo Lombardi, personal communication

This particular relation is the indication of the presence of *cooperativity* effects, i.e. the fact that an actin site is more easily activated or a cross-bridge is more easily formed if the neighboring actin sites are already activated or involved in the formation of cross-bridges.

Evidence of cooperativity The activation of the thin filament involves a binding process of calcium on the troponin-C. The troponin has 3 binding sites but two have a very high affinity with calcium resulting in an actual one site binding reaction (see Section 1.1.4.4). We now consider an analogy with the Hill equation, which originally describes the cooperative binding of oxygen to hemoglobin (see Appendix 1.6.1). In this model, the static solution is also of the form of (1.1). The parameter n_H is called the Hill number and is interpreted as an indicator of the level of cooperativity of the binding process. It corresponds to the number of oxygen binding sites. The parameter $[Ca^{2+}]_{50}$ is an indicator of the sensitivity to calcium. It corresponds to the intracellular calcium concentration that allows to develop half of the maximal tension. Note that an increase in sensitivity to calcium is represented by a decrease of the parameter $[Ca^{2+}]_{50}$. The sensitivity and the cooperativity are different concepts and can vary independently.

Applying this model to the binding of calcium to troponin, a static ($[Ca^{2+}]_i$, Force) curve with a Hill number of one is predicted. Experimental data fitting the force-calcium relation with the sigmoid equation (1.1) show a large discrepancy in the value obtained for the Hill number. With skinned cells, Gao et al. [1994] obtain a Hill number of 2.7, Dobesh et al. [2002] find 7, Konhilas et al. [2002a] find 6, Sun et al. [2009] obtain 3.1 and Kentish et al. [1986] find values around 4. With tetanised intact cells, Gao et al. [1994] obtain a Hill number of 5 or 7. Despite the large variability, two trends can be noticed:

- apart from the data obtained by Dobesh et al. [2002], it seems that the level of cooperativity is higher in tetanised intact cells than in skinned cells. This was also observed by Gao et al. [1994] although Dobesh et al. [2002] notice that the significance of their results may be undermined by the absence of rigorous sarcomere length control;
- the Hill number is always greater than one.

Interpreting these results in the light of the Hill equation, the cooperativity effects are stronger than that expected for the binding of calcium to troponin. It is commonly admitted in the literature [de Tombe et al., 2010] that this analogy with the Hill equation is valid and that it demonstrates the presence of cooperativity mechanisms in the thin filament activation that add to the binding cooperativity. It means that the activation of the thin filament involves positive feedbacks loops leading to a magnification of the level of activation.

Another observation that can be made when comparing intact and skinned cells is the difference in the calcium concentrations. In intact cells, the force saturates at $[Ca^{2+}]_i \sim 2\,\mu M$ while in saturates at $[Ca^{2+}]_i \sim 8\,\mu M$ in skinned cells. Naturally, the skinned cells solution is only "an approximation" of the physiological intracellular solution so it is not surprising that differences appear. It can be noted that a compression of the myofilaments lattice in skinned cells reduces the discrepancy between intact and skinned cells [Kentish et al., 1986; Konhilas et al., 2002b]. Results obtained with this type of cells remain nevertheless valuable to get insight into the cell physiology.

1.3.3.2 Origin of the cooperativity

Static experiments let appear that cooperativity effects are at play in the activation of the thin filament. In this section, we investigate the potential origins of this cooperativity

effect. In general, the underlying mechanisms can be regrouped in four categories:

- Ca^{2+}-Ca^{2+}cooperativity in which the binding of a calcium ion on an actin site increase the rate of binding to the neighboring actin sites. A possible mechanism could be that when tropomyosin is not blocked by the troponin C (event that follows the binding of calcium on the troponin C), it destabilizes the neighboring tropomyosin and indirectly the troponin C through tropomyosin head-tail interactions increasing the affinity for calcium of the neighboring actin sites. Electromagnetic interactions could also be at play.

- Ca^{2+}-RU cooperativity in which the binding of a calcium ion increases the probability of activating the neighboring sites (maybe without a calcium binding). A possible mechanism could be that when tropomyosin is not blocked by the troponin C (event that follows the binding of calcium on the troponin C) through tropomyosin head-tail interactions, it destabilizes the neighboring tropomyosin enabling the attachment on the neighboring RU without calcium binding.

- Xb-Ca^{2+}cooperativity in which the attachment of a myosin head increases the probability of binding of calcium on the neighboring actin site. A possible mechanism could be that an attached myosin head pushes the tropomyosin further and through tropomyosin head-tail interactions changes the structure of the troponin C on the neighboring RU increasing the affinity for calcium.

- Xb-RU cooperativity in which the attachment of a myosin head increases the probability of attachment on the neighboring actin site without calcium binding on the actin sites. A possible mechanism could be that an attached myosin head pushes the tropomyosin further and through tropomyosin head-tail interactions destabilizes the neighboring tropomyosin enabling the attachment on the neighboring RU.

To investigate the origin of cooperativity, one has to decompose the different steps of the thin filament activation. A possible intermediate measure is the structural changes of the TnC, using the cardiomyocyte having a modified TnC such that it has fluorescent properties and that structural changes can be observed by mean of changes in the polarization of the light emitted. With this technique, and using blebbistatin to prevent myosin binding, Sun et al. [2009] showed that the myosin heads attachment has only a very limited effect on the thin filament activation cooperativity for rat skinned trabeculae. Indeed, the level of cooperativity observed in the relation between the force and the calcium concentration and that observed in the relation between the average structural indicator (computed through a structural model from the fluorescence data) are the same: the Hill numbers are respectively 3 and 2.85. One can note that several papers reporting that the binding of myosin heads contribute to the thin filament activation using cross-bridges in rigor conditions [Robinson et al., 2004]. These works are not in contradiction with the above mentioned results. Indeed, [Sun et al., 2009] demonstrate that in rigor, cross-bridges contribute to the thin filament cooperative activation. Therefore, it seems that the Xb-$Ca^{2+}$and Xb-RU cooperativity mechanisms are excluded in physiological conditions and that the thin filament cooperativity is an intrinsic property [Sun et al., 2009; Sun and Irving, 2010].

Moreover, Ait-Mou et al. [2016] state that "there is no indication of cooperativity" in the binding of $Ca^{2+}$to TnC. It would mean that the cooperativity mechanism is positioned in the interaction between TnC and Tm or between adjacent Tm. The cooperativity is thus most probably related to Ca^{2+}-RU mechanisms although no definitive conclusion can be drawn yet [de Tombe and ter Keurs, 2016; Ait-Mou et al., 2016].

1.3.3.3 In dynamical conditions

Steady-state analysis is not enough to get a full picture of the thin filament activation, which is a dynamical process. Dynamical experiments, such as twitch contractions, have thus to be used to fully characterize it. Using fluorescent proteins that interact with calcium, a measure of the intracellular calcium concentration $[Ca^{2+}]_i$ can be obtained. The fluorescent proteins (fura-2 [Backx et al., 1995; Janssen et al., 2002; Gao et al., 1998] or fluo-3 [Caputo et al., 1994]) bind to calcium, which results in a change of their emission spectrum. After excitation, the emitted light signal is measured and is converted into the calcium concentration by solving the dynamical equation governing the binding and unbinding of the protein to calcium. Typical results from [Janssen et al., 2002] are presented in Figure 1.17. Note that this experiment is not performed with a proper sarcomere length control feedback loop. Therefore, their quantitative significance is limited. Similar results are also obtained by Backx et al. [1995] and Gao et al. [1998]. The transient evolution of

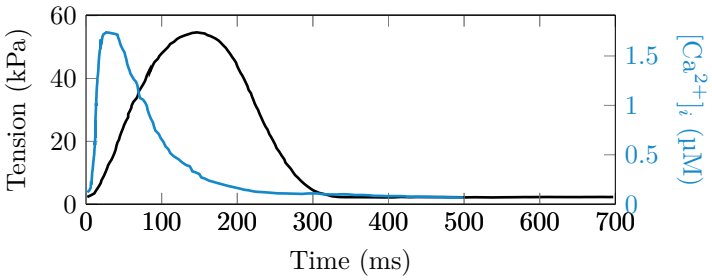

Figure 1.17 – Typical force and intracellular calcium concentration evolution in twitch contractions. Note that here the sarcomere length is not properly maintained constant. Data from [Janssen et al., 2002] from rat cardiac cells at 30 °C.

the calcium concentration is faster than the force evolution and almost exclusively occurs in the tension rise phase of the twitch contraction.

The interpretation of the twitch contraction signal in terms of information on the thin-filament activation is difficult. Indeed, the observed cytosolic calcium concentration transient is the result of competing dynamics:

- the calcium release and uptake from the sarcoplasmic reticulum,
- the calcium flow inwards and outwards through the channels and exchangers and the interaction between the membrane concentration and and the cytosolic concentration,
- the calcium binding and unbinding to and from the thin filament, which involves not well characterized cooperativity effects (see Section 1.3.3.2).

Therefore, a low concentration does not imply anything on the flux of calcium trough the cytosol, it only means that there is no storage of calcium in the cytosol.

The main part of the calcium ions released in the cytosol are then captured by the actin filament. The cytosolic calcium concentration $[Ca^{2+}]_i$ observed during the release is thus only the part of the released calcium that is not captured by the thin filament. Indeed, the full activation of the thin filament requires 120 µM of calcium [ter Keurs, 1996] (allowing to generate an active tension of 120 kPa). Even if we consider a sub-maximal level of thin filament activation, the peak calcium concentration observed in the cytosol (∼1 µM) remains much lower the amount of calcium linked to the filament.

With this element in mind, a possible interpretation of the calcium transient is the following. The release of calcium by the sarcoplasmic reticulum is brutal, peaking in less than 5 ms (see Section 1.1.4.3). Simultaneously, calcium ions are being captured by the thin filament in a fast manner – also with a time scale of 1 ms [Allen and Kentish, 1985]. These two antagonist phenomena equilibrate when the calcium transient peaks. Later, the release of calcium stops and the action of Ca^{2+}-pumps start, which take calcium ions back to the sarcoplasmic reticulum and the calcium concentration decreases. The calcium that is liberated by the actin sites in the relaxation process is either regularly liberated or quickly captured in the sarcoplasmic reticulum so that is does not change the trend in the calcium evolution. Note that the actin sites are not necessarily immediately activated, there may also be an internal dynamics between the calcium binding and the actin site activation.

However, some properties have been inferred experimentally. The thin filament activation and not the actin-myosin interaction is the limiting reaction in the tension rise phase of a twitch contraction [Regnier et al., 2004], except in maximal calcium supply conditions where the attachment dynamics dominates [de Tombe et al., 2006; Campbell, 2014]. In the relaxation phase, it seems more likely that the two mechanisms contribute together to the tension evolution [Davis et al., 2007]. The time between the peak of calcium release and the peak of force is thus probably an estimation of the activation dynamics.

An important point is that, in a twitch contraction, the force does not have time to reach what would be its steady-state value[2]. This can be explained by the fact that the amount of calcium released by the sarcoplasmic reticulum allows a sub-saturating activation only, or by the fact that the activation dynamics is not fast enough before calcium starts to be up-taken in the sarcoplasmic reticulum or transferred outside of the cell. This point is illustrated in Figure 1.29, which compares the peak force obtained in a twitch contraction in "large activation conditions" and the steady-state force in maximal activation conditions (tetanus).

The characterization of the cooperativity effects is non resolved in steady-state conditions and the interpretability of dynamical measurements is difficult. Therefore, characterization of the potential dynamical effects of cooperativity have not been investigated yet. Moreover experiments with a simultaneous strict sarcomere length control and a measurement of the transient calcium concentration have never been performed to the best of my knowledge. As a result, the interpretability of the dynamical measurements of the force and the calcium concentration in terms of the level of activation of the thin filament remains limited. To be able to get a full understanding of the thin filament activation (which would then allow to build models), a dynamic measurement of the calcium released in the cytosol or captured by the thin filament would be required.

1.4 Characterization of the muscle active contraction regulation

We have so far presented the baseline functioning of the actin-myosin interaction and the thin filament activation. We now characterize the regulation mechanisms that are at play in the cell through the variation of the sarcomere length and the neuroendocrine system.

In a first step, we will present the manifestation of the regulation mechanisms at the scale of the sarcomere. The effect of varying calcium supply, which is a path of action for the neuroendocrine regulation, will be described as well. In a second step, we will focus on the origin of the contraction regulation mechanisms starting from the impact of

[2]Pieter P. de Tombe, personal communication

sarcomere length extension on both the thick and the thin filaments. The effect of the neuroendocrine regulation as a modulation of protein activity will only be briefly discussed at the end because this aspect is not considered in our models.

1.4.1 Effect of the regulation at the scale of the sarcomere

As a first step, we focus on the regulation of the developed force by the sarcomere length. We present the effect of this regulation and then analyze the mechanisms underlying this regulation.

1.4.1.1 Developed force

From the pioneer work of ter Keurs et al. [1980], who first measured twitch contractions at constant sarcomere length, several groups have investigated the relation between the twitch peak force and the sarcomere length. Additional measurements with steady-state contraction can also be considered. We present in Figure 1.18 (closed symbols) the variation of the developed force as a function of the sarcomere length at various levels of calcium supply. Different experimental setups are presented: measure of the peak force in intact cell twitch contractions (panels (a)-(d)), measure of the steady-state force in tetanised intact cells (panel (e)) and skinned cells (panel (f)). In each of these setups, the sarcomere length is carefully maintained constant until at least the measure of the force. All of these experiments consistently display an increase of the force with increasing sarcomere length. The force is thus regulated by the sarcomere length. The presence of this relation is for all experiment types show that this regulation is intrinsic to the sarcomere.

Furthermore, this regulation is dependent on the calcium activation. An increase in the calcium supply is consistently correlated with an increase of the force and there is a unique force-length relation for each level of calcium supply. It is important to note that the force-length relations obtained at various level of calcium supply do not scale to a single master curve. This is particularly clear on the data obtained with skinned cells (in panel (f)). The non-scalability property indicates that the regulation results from complex mechanisms mixing the variations of sarcomere length, the recruitment of myosin heads and the calcium induced activation of the thin filament.

On panel (b), (c) and (d), the passive force is also represented. We see here that the passive force is negligible with respect to the peak active force in the physiological range of sarcomere length

To analyze more closely the interaction between the regulation and the calcium supply, we present in Figure 1.19 the variation of the force developed by cardiac skinned cells as a function of the environment calcium concentration at various sarcomere lengths. Here again, we see that increasing the calcium supply does not result in a simple scaling of the force. An increase in sarcomere length is thus correlated with changes in the handling of calcium by the cell. The same conclusion is also drawn by other experimental works [Kentish et al., 1986; Konhilas et al., 2002a; Farman et al., 2010].

1.4.1.2 Force dynamics

Sarcomere length also has an impact on the force development dynamics. We present in Figure 1.20 contraction twitches obtained at different sarcomere lengths in various calcium supply conditions. In each experiment, the sarcomere length is maintained constant throughout the contraction twitch.

The experimental results show a clear correlation between the sarcomere length and the duration of the relaxation phase. At higher sarcomere length, which is associated with

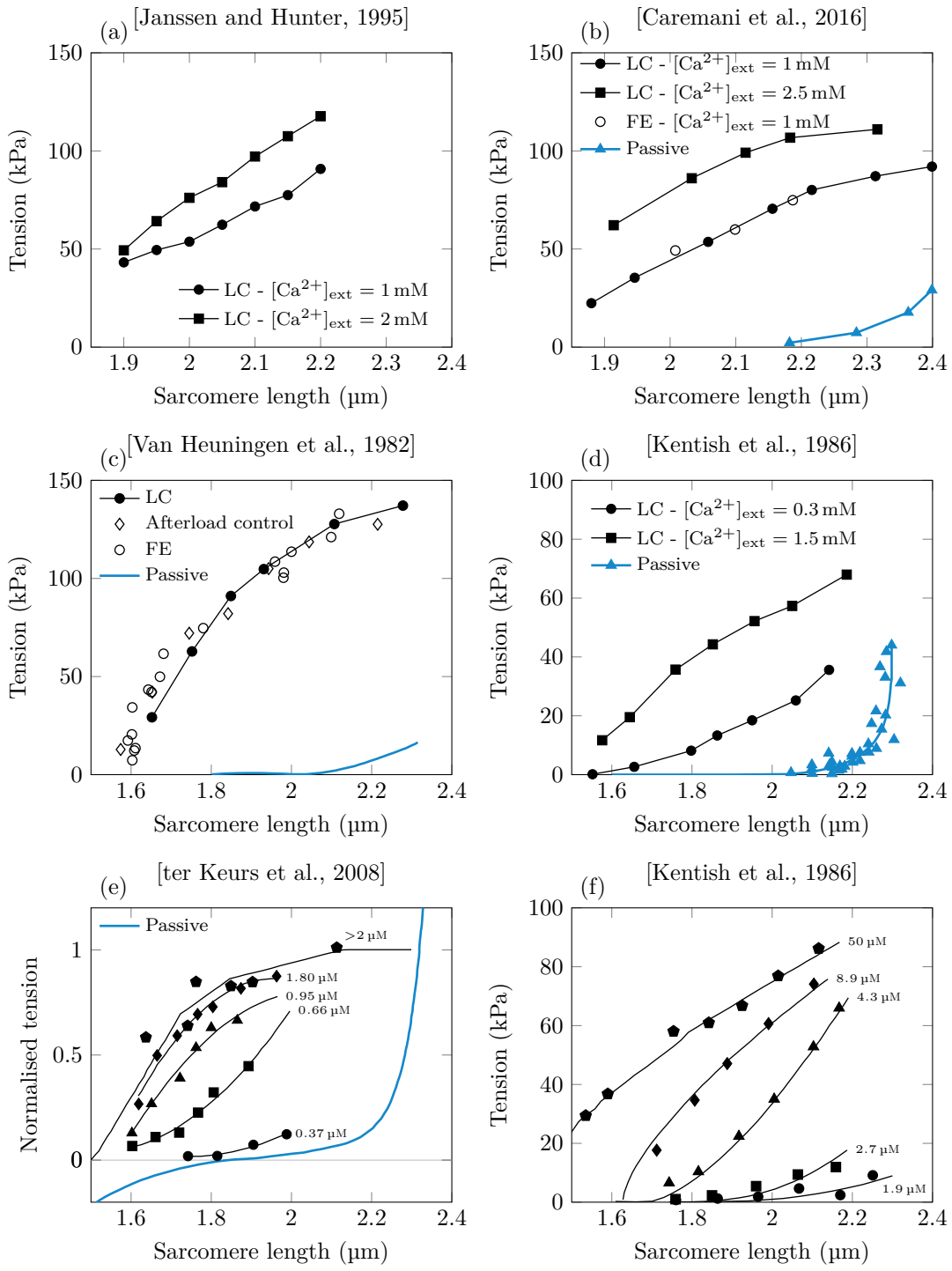

Figure 1.18 – Relation between force and sarcomere length in cardiac muscle cells. Data point represented by closed symbols correspond to experiments in length clamped conditions (LC), open symbols represent experiments in fixed ends conditions (FE), see Section 1.3.1. (a) - (d) Measure of the peak force in intact cardiac cell twitch contractions; (a) data from [Janssen and Hunter, 1995] from rat cells at 25 °C, (b) data from [Caremani et al., 2016] from rat cells at 27 °C, (c) data from [Van Heuningen et al., 1982] from rat cells at 25 °C, (d) data from [Kentish et al., 1986] from rat cells at 22–24 °C. (e) Steady-state force in tetanised intact cardiac cells. Data from [ter Keurs et al., 2008] from rat cells at 26 °C. Several sets of data points are obtained using different levels of extracellular calcium concentration, the corresponding intracellular calcium concentration are indicated next to each set of data point. (f) Steady-state force in skinned cardiac cells from [Kentish et al., 1986] from rat cells at 22–24 °C. The environment calcium concentration is indicated next to each data set. (a) - (f) Note that the tension presented here is the active tension only, that is, the measured tension minus the passive tension.

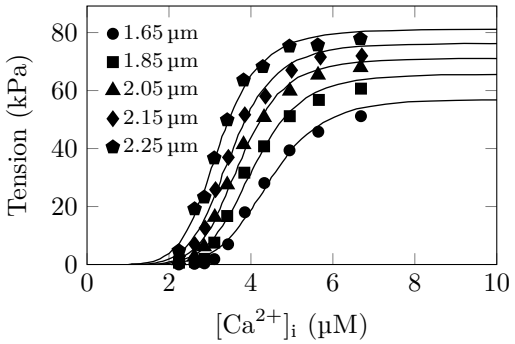

Figure 1.19 – Relation between the force developed by skinned cardiac cells with respect to the environment calcium concentration at different sarcomere lengths. Data from [Dobesh et al., 2002] obtained with rat skinned cell at 15 °C.

a higher force, the relaxation lasts longer. A small increase of the tension rise duration with increasing sarcomere length is also observed in the data from [Janssen and Hunter, 1995]. This effect is however not present in the data from [Van Heuningen et al., 1982].

When the sarcomere length is not maintained constant, the actin and myosin filaments slide past each other. This shortening is associated with a drop in force according to the force-velocity curve (see Section 1.3.2.2). This adds up to the reduction of force following the force-length relation (see Section 1.3.2.2). Twitch contractions illustrating this situation are presented in Figure 1.21. As expected, when the sarcomere length reduces during the twitch, the peak force is reduced and the twitch duration is shortened.

1.4.1.3 Time scale of the length dependent regulation

An important element to investigate the regulation of the force with sarcomere length is its dynamics.

Comparing the peak force obtained at a given – instantaneous – sarcomere length in various experimental conditions gives insight into the dynamics of the regulation mechanism. Indeed, we can compare whether the history of sarcomere length evolution matters or if the force depends only on the instantaneous sarcomere length. Caremani et al. [2016] and Van Heuningen et al. [1982] performed twitch contractions in both length clamped and fixed ends – i.e. with varying sarcomere length. In Figure 1.18(b) and (c), data points represented by closed circles are obtained in length clamped conditions and data points represented by open circles with fixed end conditions.

Moreover, Van Heuningen et al. [1982] also performed experiments in which the muscle sample contracts against a fixed after-load. The minimum sarcomere length that allows the muscle to sustain the load is measured. The data points corresponding to these experimental conditions are represented in the panel (c) by open diamonds.

We observe that with all three types of experimental conditions, the points lie on the same force-length relation. First, this supports the idea that the regulation is an intrinsic direct link between the force and the sarcomere length. Second, it shows that the regulation quickly adapt to the current sarcomere length at the time scale of the contraction twitch.

Note that, although they display the same force-length relation, the length clamped, fixed end (and probably the after-load control) setups are not equivalent when dealing with the dynamical aspects as shown in Section 1.4.1.2.

Additional investigation by Mateja and de Tombe [2012] endorse the same conclusion

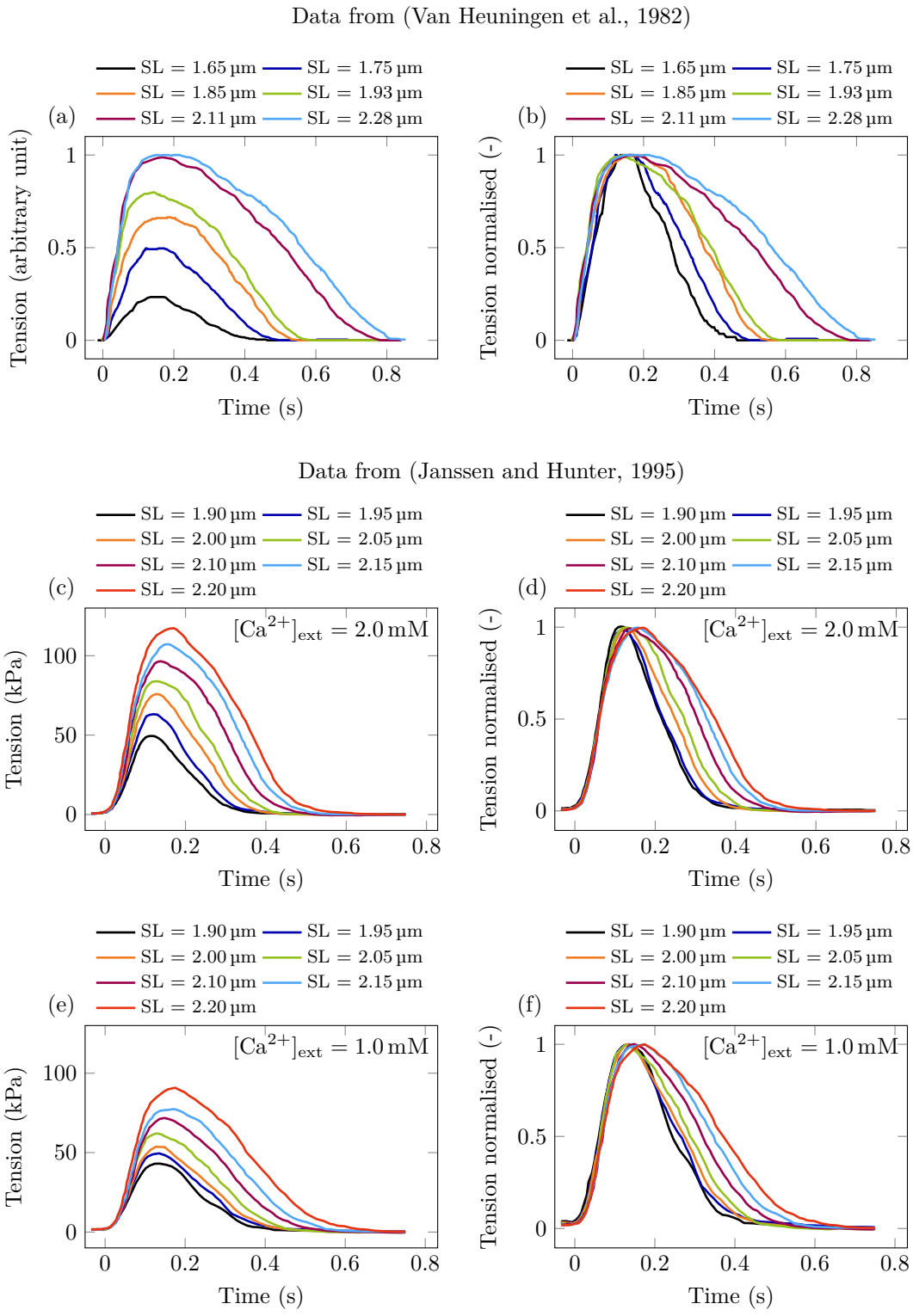

Figure 1.20 – Twitch contraction of rat trabeculae at 25 °C. (a) & (b) Respectively absolute and normalized data from [Van Heuningen et al., 1982]. The extracellular calcium concentration is unspecified. (c) & (d) Respectively absolute and normalized data from [Janssen and Hunter, 1995] with an extracellular calcium concentration of 2.0 mM. (e) & (f) Respectively absolute and normalized data from [Janssen and Hunter, 1995] obtained with an extracellular calcium concentration of 1.0 mM.

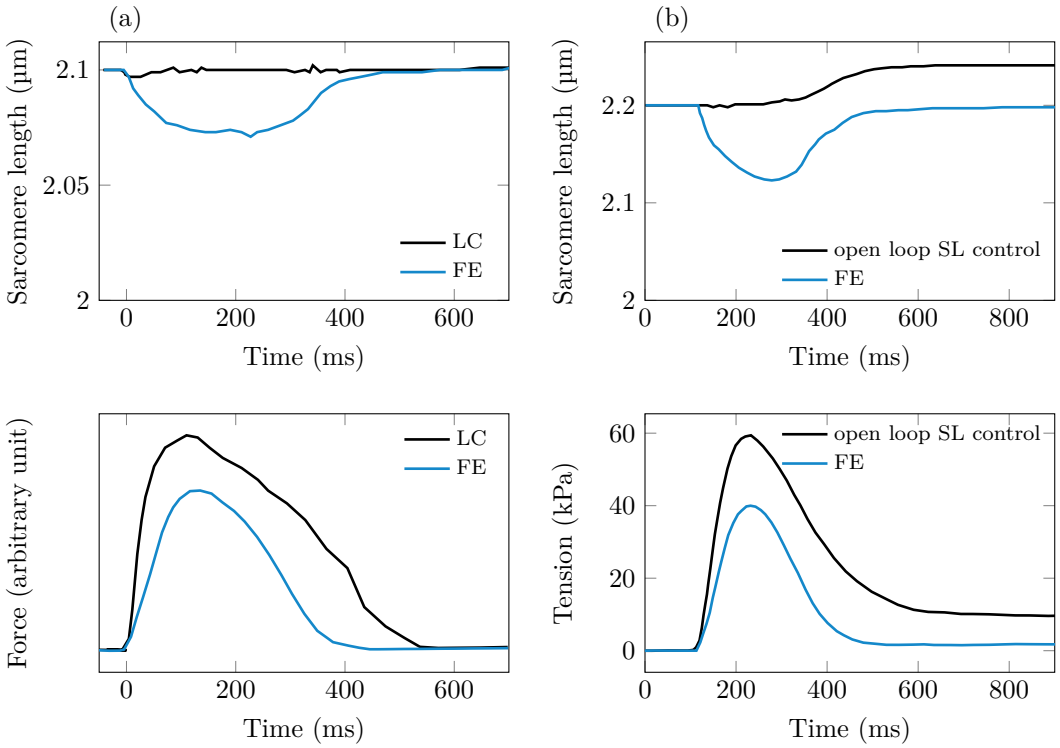

Figure 1.21 – Twitch contraction of cardiac muscle with various boundary conditions. (a) Sarcomere length variation and twitch contraction in length clamped conditions (LC, black curve) and in fixed ends conditions (FE, blue curve) starting from the same initial condition (see Section 1.3.1). Data from [ter Keurs et al., 1980] with rat cardiac cells at 25 °C. (b) Sarcomere length variation and twitch contraction in open loop sarcomere length control (resulting in a clamped conditions followed by an active increase of the sarcomere length) (black curve) and in fixed ends conditions (blue curve) starting from the same initial condition. Note that in the first conditions, the stretch of the sarcomere lead to a non-zero passive force that remains at the end of the twitch. Data from [Caremani et al., 2016] from rat cardiac cells at 27 °C. Note that the tension presented here is the active tension only, that is, the measured tension minus the passive tension.

that regulation is "virtually instantaneous". In their work, they observe the tension rise dynamics in two case: in the first case the initial sarcomere length is maintained at the initial value long before the contraction start, in the second case, the sarcomere length is brought to the initial sarcomere length by a quick sarcomere length ramp (lasting 5 ms) just before the contraction start. With this time scale for sarcomere length variations, they observe no differences in the time evolution of the tension between the two experimental conditions. They thus state that 5 ms is an upper bound for the regulation time scale. However, the fact that no differences could be observed suggests that the actual time may be much shorter than this upper bound.

In summary, the regulation of the muscle developed force appears to be instantaneous at the time scale of a contraction twitch and is probably also very fast compared to the attachment-detachment time scale, which is, in the fastest case, of the order of 5 ms. In particular, in the heart the regulation is able to adapt in a beat-to-beat manner.

Note that there exists a second variation of the force with the sarcomere length observed *ex vivo* at the time scale of 10 min [Allen and Kentish, 1985]. It consists of an increase in the amount of calcium released in the cytosol when the tissue is stretched leading to an increase of the developed force. The origin of this effect is only partly understood [Cingolani et al., 2013]. At the scale of the heart, this regulation translates into the so-called *Anrep effect*.

1.4.1.4 Summary of the intrinsic force regulation effects

At the sarcomere level, the force is regulated by a mechanism that makes it directly linked to the stretch of the sarcomere. The force increases monotonically with the sarcomere length (up to a sarcomere length of about 2.4 µm). The force-length relation depends on the level of calcium supply, a higher amount of calcium made available in the cell being associated with an increase of the force.

This regulation of the force occurs at a fast time scale with respect to the attachment detachment time scale and thus a fortiori with respect to the contraction twitch time scale.

1.4.2 Origin of the observed regulation mechanisms

We have seen in Section 1.4.1 that in cardiac muscle the force-length relation combines a double dependency on the sarcomere length and the calcium supply. Although many studies have been conducted on this topic for the last four decades, the origin of the force-length relation in cardiac muscles remains partially unsolved [de Tombe and ter Keurs, 2016; de Tombe et al., 2010; Sequeira and Velden, 2017].

In all generality, the variation of the force with sarcomere length may come from an increase of the force developed per attached myosin heads, from an increase in the number of attached myosin heads or from both. The latter factor itself may result from the combination of an increase in the number of available myosin heads, and an increase in the level of activation of the thin filament.

In this section, we will give a review of the different directions that have been explored to account for the observed behaviors that we then use as a guideline for the choice of our modeling ingredients in the following chapters.

1.4.2.1 Variation of the force developed per cross-bridge

We first consider the assumption that the variation of force with sarcomere length results from a variation of the average force developed by each attached head. Note that a change of the average force per attached head would come from an alteration of the actin-myosin

interaction. Information on the actin-myosin interaction with varying sarcomere length or the level of calcium supply can thus be used to investigate the impact of the variation in force per attached head on the force-length relation.

Some elements of answer are given by Amiad Pavlov and Landesberg [2016], who show, with experiments targeting the force redevelopment time after a length step, that the cycling rate, and thus *a priori* the attachment and detachment rates, of the cross-bridges is independent of the sarcomere length. Similarly, de Tombe and Stienen [2007] show that the detachment rate in independent on the level of calcium supply. Moreover, studies based on ATPase rate measurement concluded that the rate of detachment was not sarcomere length dependent [Wannenburg et al., 1997]. These works do not measure the force per attached head but would thus tend to indicate that the force per attached head does not vary with sarcomere length since other myosin head properties are not affected.

An additional element supporting the same conclusion – with accurate sarcomere length and $[Ca^{2+}]_{ext}$ control – is given by Caremani et al. [2016] who show that the "mechanokinetic properties of the motors" do not depend on the sarcomere length and the extracellular calcium concentration. Indeed, we know from Section 1.3.2 that the four phases of the transient mechanical response in force or length control conditions can be used to characterize the actin-myosin interaction. In particular, phase 2 is a reflexion of the power stroke and phase 4 originates from the attachment-detachment mechanism. In [Caremani et al., 2016], the shortening after a step in force in force control conditions is recorded for various initial sarcomere length and extracellular calcium concentration. The variation of $L_T = L_2 - L_1$ – which is the signature of the power stroke – and the shortening velocity in phase 4 as a function of the normalized force are presented in [Caremani et al., 2016, Fig. 3C] and in Figure 1.14, respectively. We can observe that, in both phases, the data for all conditions lie on the same master curve showing that the intrinsic behavior is the same. These observations thus support the idea that the dynamics of the cross-bridges is not affected by changes in sarcomere length or contractile state. One should note that in force control conditions, the sarcomere undergo shortening, therefore its length varies during the experiment. However, the magnitude of the variations remains below 30 nm (see Figure 1.12) leading to a relative variation of the force of 4 %, which is probably of the order of the uncertainty on the force in the data.

A definitive answer is brought by Pinzauti et al. [2018] regarding the role of the contractile state. Indeed they directly show that when changing the contractile state (with a change of extracellular calcium concentration), the average force per myosin head remains constant. Considering the results of [Caremani et al., 2016] it is likely that the same would be observed with variations of the sarcomere length.

We should nevertheless mention that some other groups obtained opposite results. Milani-Nejad et al. [2013] and Adhikari et al. [2004] measure a decrease of the cycling rate with increasing sarcomere length. However de Tombe and ter Keurs [2016] attribute these results to unadapted experimental conditions (in particular lacking of a correct control of the sarcomere length).

In conclusion, experimental results show that the myosin head properties are not affected by the sarcomere length nor by the calcium supply. The assumption that the force-length relation originates from a variation of the force per attached head is thus rejected. The variation of the force with sarcomere length and the contractile state is only the result of a change in the number of attached myosin heads.

1.4.2.2 Variation of the thick filament activation

A first way to vary the number of attached heads is to change the availability of the myosin heads (we will also say the activation level of the thick filament).

Quantification of the thick filament contribution To investigate the part of the force-length relation that is due to the variation of the number of available myosin heads, we need to isolate this effect from other contributions and in particular, from the variation of the thin filament activation level and transient effects that may not allow the force to reach its maximum value.

To do so, the thin filament needs to be saturated with calcium, so that an increase in the calcium sensitivity would have no effect. We know that the cardiac cell is not "designed" to work in a thin filament maintained activation. Several techniques can be used to overcome this difficulty. A first option is to perform experiments on skinned cells, so that the calcium concentration surrounding the thin filaments can be directly controlled (see Section 1.1.6.3). A second option is to artificially induce the saturation of the thin filament in intact cells (see Section 1.1.6.1)

The first characterization of force variation with sarcomere length was performed by [Kentish et al., 1986] and [Dobesh et al., 2002]. The muscle fibers are directly activated by a high – unphysiological – increase of the calcium concentration $[Ca^{2+}]_i$ to "saturate" the thin filament with calcium. The statement that the thin filament is saturated with calcium is supported by the fact that the obtained force-length relation is not further enhanced with increasing environment calcium concentration. Other groups also worked with skinned cells Fabiato and Fabiato [1975] and with intact tetanised cells [ter Keurs et al., 2008]. In the latter experiments, the saturation of thin filament is ensured by checking that an increase of the extra-cellular calcium concentration does not lead to an increase in the force. The results are presented in Figure 1.22.

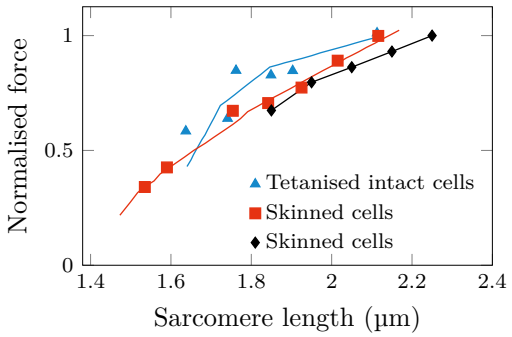

Figure 1.22 – Variation of force with sarcomere length in saturation thin filament activation conditions. (Triangle) intact tetanised rat cardiac cell at 26 °C [ter Keurs et al., 2008], (Square) skinned rat cardiac cells at 22–24 °C [Kentish et al., 1986], (Diamond) skinned rat cardiac cells at 15 °C [Dobesh et al., 2002]. The solid lines trend lines of the data.

In the experimental conditions presented here, the force can only be varied by a change in the number of available myosin heads. These experiments thus demonstrate that the sarcomere length has a direct impact on the myosin heads availability.

Origin of the thick filament activation variations Several mechanisms have been proposed to explain the variation of the thick filament activation with sarcomere length.

Overlap effect The first mechanism imagined to account for variations of the myosin availability with the sarcomere length has been proposed by Gordon et al. [1966], originally for skeletal muscles. It explains the change in force by the variations of the size of the overlap region between the actin and the myosin filament. It is motivated by the fact that the overlap between the filaments is visibly changed when the sarcomere length varies (see Figure 1.23).

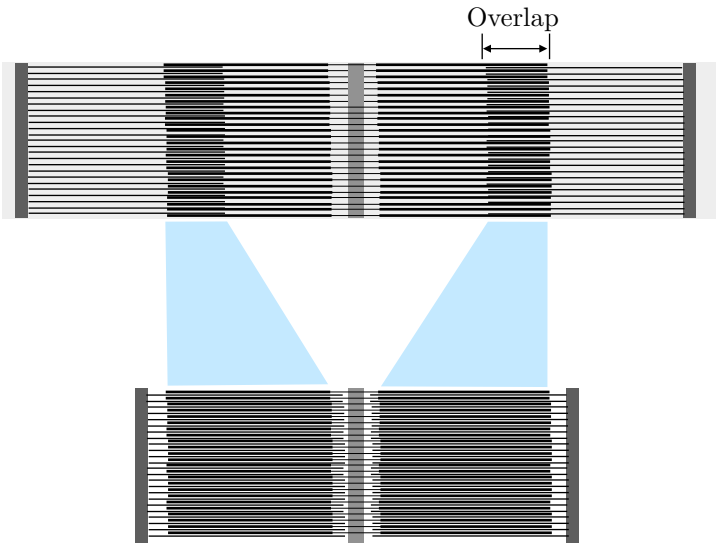

Figure 1.23 – Illustration of the variation of overlap with the sarcomere length for skeletal muscles. (Top) Extended sarcomere. (Bottom) Shortened sarcomere. Here a shortening of the sarcomere leads to a increase of the overlap region.

The overlap is defined as the ratio of the thick filament which is "covered"' by the thin filament. It can be analytically computed from the length of the different filaments. The various regimes of this models are presented in Figure 1.24. Each state corresponding to a transition between two "regimes of overlap" is numbered as presented in the figure. To relate the overlap to the force, Gordon et al. [1966] assume that the force is proportional to the size of the *single overlap region*, that is, the region of the thick filament that is covered by one and only one actin. In particular, they make the assumption that in double overlap region the myosin heads generate no force on average. Two explanations may support this assumption:

- in the double overlap region the myosin heads attach in a non-specific manner on a thin filament link either to the left or the right Z-disc of the sarcomere, which will result in the generation of a positive or negative active force. This leads to an average zero force.

- due to some steric constraints, there is no attachment possible in the double overlap region.

Note that the first hypothesis would be disadvantageous from an efficiency point of view because in the double overlap region the zero force would be generated with an non-zero ATP consumption. For sarcomere length corresponding to a state between state 5 and state 4, increasing the sarcomere length reduces the degree of double overlap between the thin filaments which increases the number of available myosin heads allowing to generate

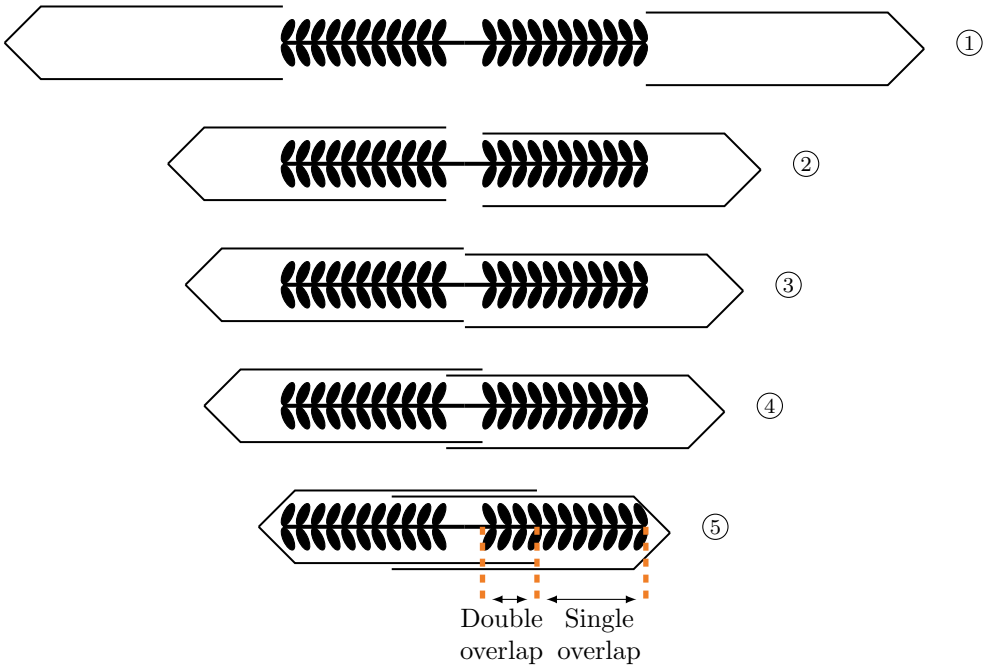

Figure 1.24 – Variation of overlap with sarcomere length. Each state corresponding to a transition between two "regimes of overlap" are indexed by a number as presented in Figure. Inspired from [Gordon et al., 1966]. For sarcomere length lower than that corresponding to index 5, the thick filament is compressed by the Z-discs. The overlap model cannot describe alone the variation of force because of the contribution of compression forces.

a higher tension. When further increasing the sarcomere length (between state 4 and state 2), the overlap between the thin filaments is only located in the central region of the sarcomere in which there is no myosin head. The number of available myosin heads thus stays constant and the developed force reaches a plateau. In the last range of sarcomere lengths (between state 2 and state 1), a region, where the thin and thick filaments do not overlap, appears. The number of available cross-bridges is reduced and so is the force. For sarcomere lengths lower than that of the state indexed by 5, the overlap alone cannot explain the variation of the force because the thick filament is compressed between the Z-discs and the resulting compression forces have to be taken into account.

The hypothesis of varying overlap to account for the variation of force with sarcomere length can be transposed to cardiac muscles, which have a similar structure. The comparison between the analytical overlap, computed from cardiac filament length measurements taken from [ter Keurs et al., 2008], and the experimental force-length relations in saturated thin filament activation conditions (presented in Figure 1.22) is displayed in Figure 1.25(a). The overlap variation correlates to a certain extend with the force variations but the predicted plateau of force that is not really observed experimentally. Therefore, no clear conclusion can be drawn. Moreover, some limitations to the approach can be mentioned. The overlap model does not truly account for the three-dimensional nature of the sarcomere, where the notion of "double overlap" is not as clearly defined as in a 2D representation. Moreover, the behavior of the myosin head in the double overlap region is only speculative.

To put this results in perspective, we present in Figure 1.25(b) the comparison of the analytical overlap computed from skeletal muscle data of [Gordon et al., 1966]. In skeletal muscle, the sarcomere length is not limited by the passive force and a larger range

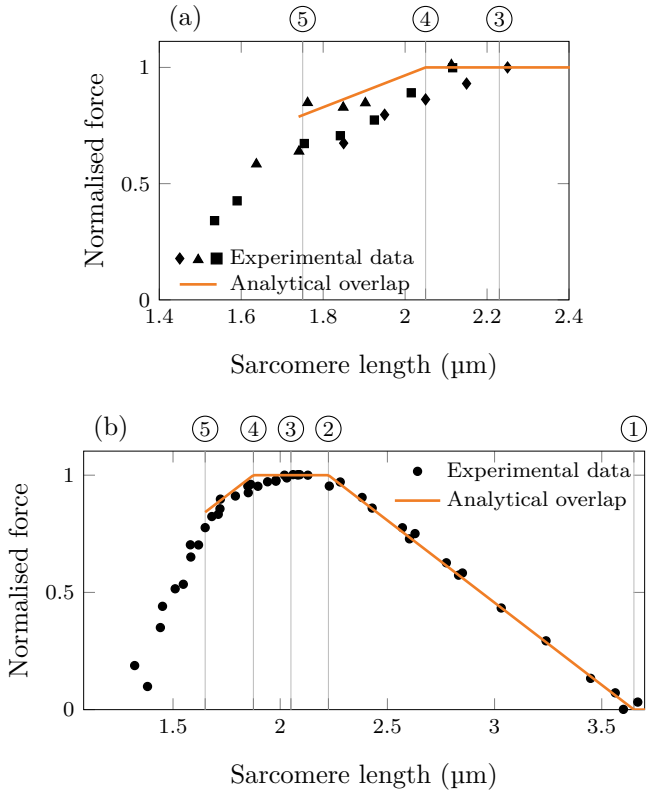

Figure 1.25 – Comparison between the overlap model prediction with experimental data in saturated thin filament activation conditions. Each state corresponding to a transition between two "regimes of overlap" are indexed by a number as presented in Figure 1.24. (a) Data from cardiac muscle. (Triangle) intact tetanised rat cell at 26 °C [ter Keurs et al., 2008], (Square) skinned rat cells at 22–24 °C [Kentish et al., 1986], (Diamond) skinned rat cells at 15 °C [Dobesh et al., 2002]. (Orange line) Analytical overlap computed from cardiac myofilament measurements from [ter Keurs et al., 2008]. (b) Data from frog skeletal muscle at 3–5 °C. Data and analytical overlap from [Gordon et al., 1966].

of sarcomere lengths can be explored. The experimental curve shows three regimes: an ascending limb, a plateau, and a descending limb. As stated by the authors of the original paper [Gordon et al., 1966], the analytical variation of overlap is only able to precisely account for the variation of force in the plateau region and in the descending limb of the force-length relation. The prediction regarding the ascending limb, which corresponds to the double overlap regime, has a lower quality. The good adequacy of the overlap model with the data on specific regimes led the community to accept the variation of filament overlap as the origin of the force-length relation in skeletal muscles, and by extension, it popularized the idea that the myosin heads in the double overlap region do not contribute to the force. However, the latter assumption is not clearly validated by the experimental results.

In conclusion, the variation of overlap between the thick and thin filament with sarcomere length may have an impact on the observed force-length relation but no definitive conclusion can be drawn without additional experimental studies.

Inter-filament spacing The inter-filament spacing has long been considered as a possible explanation of the force variation with the sarcomere length. Indeed, when the muscle is stretched the global Poisson effect creates a compression in the radial directions. This compression of the muscle implies a compression of the sarcomeres, bringing the actin and myosin filaments closer together and potentially changing the component structure (see Figure 1.26). Note that, since it is linked to both the thin and the thick filament, titin may also play a role in bringing them closer together [Sequeira and Velden, 2017].

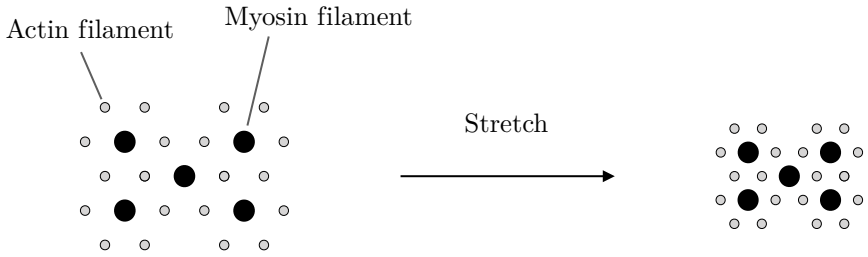

Figure 1.26 – Stretching reduces the lateral spacing. Figure reproduced from [Shiels and White, 2008].

First experiments using dextran to compress the structure and assessing the level of compression from the muscle width found a correlation between the level of compression and the calcium sensitivity [Godt and Maughan, 1981; Fuchs and Wang, 1996]. However, more recent work measuring directly the inter-filament spacing with X-ray measurements, drew the opposite conclusion showing that the inter-filament spacing has no impact on the force-length relation [Konhilas et al., 2002b].

This finding has been recently confirmed by Ait-Mou et al. [2016]. They show that no correlation could be found between the movement of the myosin head towards the thin filament and the developed force on the one hand and between the filament spacing and the developed force on the other hand.

Transition between the on- and the off-state The transition between the off- and on-states of the myosin head (see Section 1.1.3) has also been proposed to explain the variation of the thick filament activation with the sarcomere length [Reconditi et al., 2017; Piazzesi et al., 2018], but no definitive conclusion can be drawn at this time. A reason for that is that the dynamical tracking of the on-off transition has never been performed with

cardiac muscle cells. Therefore, it is still unknown whether the on-off transition dynamics would be compatible with the dynamics of the myosin filament activation variations observed when stretching the sarcomere.

This mechanism is believed to be the limiting stage of the tension rise implying that its operating time scale is the order of the time scale of the tension rise (100 ms) [Linari et al., 2015]. This seems *a priori* incompatible with the fast time scale observed for the regulation of the force with sarcomere length (see Section 1.4.1.3).

Note however that this mechanism could work as an amplifier of another mechanism leading to the recruitment of myosin heads with increasing sarcomere length. Indeed, an increase in the number of available myosin heads will result in an increase of the force further increasing the number of available heads through the transition from the off-state to the on-state (the transition being affected by the force in the thick filament).

Structural rearrangement of the filament Generally, experiments using X-ray diffraction measurements have proven that increasing sarcomere length causes rearrangements in the thick filament structure [Ait-Mou et al., 2016]. These rearrangements are different from that observed in the transition between the on- and off-states. They may be related to titin, which is a natural candidate to explain the link between the sarcomere length and the structural rearrangements. It is indeed linked to the Z-disks and connects to the M-line (and thus to the thick filament). Titin is thus extended when the sarcomere is stretched and simultaneously the apparition of a passive force is induced. This extension and the force are transmitted to the thick filament, whose structure may as a result be affected.

Conclusion on the thick filament contribution analysis The thick filament alone contributes to the variations of the active force with the sarcomere length. Several mechanisms may explain this phenomenon: a variation of the single overlap between the actin and myosin filaments or structural rearrangements of the thick filaments induced by the stretch of titin.

Note that cardiac muscle has a less regular structure than skeletal muscle. The branchings between the cells give a two-dimensional nature to the structure that is never considered when interpreting the experimental results. This may explain why it is more difficult to transfer individual sarcomere theory to macroscopic force values.

1.4.2.3 Variation of the thin filament activation

Experimental data show a variation of the force-length relation with the level of calcium supply (see Figure 1.18) in a way that excludes the possibility of a simple scaling effect.

This variation may originate from changes in the number of available myosin heads, although myosin heads do not directly interact with calcium, through a positive feedback of the myosin heads. In this case, an increase in calcium supply, which leads to an increase in the thin filament activation and thus in the number of attached myosin heads, would result in an even higher number of attached heads.

However, having concluded from Section 1.3.3.2 that the cooperativity mechanisms in the thin filament activation do not involve a contribution from formed cross-bridges and having *a priori* excluded the on-off transition as a possible origin of the thick filament activation variation with the sarcomere length (see Section 1.4.2.2), this hypothesis is not probable. We will thus assume that there is not effect of calcium on the thick filament and that the alteration of the force-length relation with the calcium supply only results from variations in the thin filament level of activation.

Quantification of the thin filament contribution In this section, we will quantify the thin filament activation variations with the sarcomere length and investigate its origin. As we have seen in Section 1.3.3, the level of thin filament activation cannot be directly accessed with the current experimental techniques making it difficult to draw definitive conclusions.

Static case As in Section 1.3.3, a first step is to consider the impact of sarcomere length variations on the steady-state behavior.

If the thin filament activation were not affected by the sarcomere length (i.e. it depends only on the surrounding calcium concentration), then the curves at different level of calcium activation could be scaled to a single master curve. We see in the experimental data that this is not the case, showing that the level of calcium activation is indeed, modulated by the sarcomere length.

To better see the impact of variations in sarcomere length on the level of activation of the thin filament, we try to decorrelate the contribution of the change in the number of available myosin heads from the level of thin filament activation. We assume, as justified in Section 1.4.2.1, that the steady-state force is proportional to the number of available myosin heads and the number of activated actin sites. We denote the level of thick filament activation by n_0 and the level of thin filament activation by n_a. In steady-state conditions, they are both functions of the sarcomere length ℓ_{hs}. We estimate the function $n_0(\ell_{hs})$ from the data from [Kentish et al., 1986; Dobesh et al., 2002; ter Keurs et al., 2008] in maximal thin filament conditions (see Figure 1.27(a)). We then consider the data from intact tetanised rat cells obtained by ter Keurs et al. [2008] at sub-maximal levels of calcium supply. We obtain an estimation of n_a at different level of calcium supply (see Figure 1.27(b)). At each sub-maximal calcium supply level, the force per available myosin

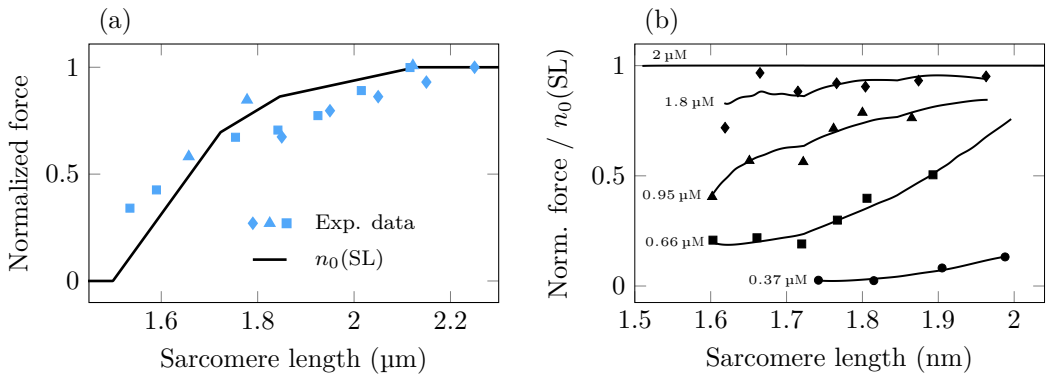

Figure 1.27 – (a) Estimation of the thick filament activation function n_0 with respect to sarcomere length. (Triangle) intact tetanised rat cardiac cell at 26 °C [ter Keurs et al., 2008], (Square) skinned rat cardiac cells at 22–24 °C [Kentish et al., 1986], (Diamond) skinned rat cardiac cells at 15 °C [Dobesh et al., 2002]. (b) Normalized force per available myosin head as a function of the sarcomere length for tetanised intact cardiomyocytes at various level of calcium supply. Data from [ter Keurs et al., 2008] obtained with tetanized rat cardiac cells at 26 °C.

head increases with the increase in sarcomere length while the intracellular calcium concentration remains constant. This estimation shows that independently from the variation of the availability of the myosin heads, the force is also increased by an enhancement of the thin filament activation when the sarcomere length increases.

We have seen in Section 1.3.3.1 that the thin filament activation is characterized by the sensitivity to calcium and the level of cooperativity. They thus constitute a good metric

to investigate the impact of the sarcomere length on the thin filament activation.

Performing experiments on skinned cells with a control of the sarcomere length during the contraction, Konhilas et al. [2002a,b]; Dobesh et al. [2002] report that the sensitivity to calcium is increased with increasing sarcomere length while the level of cooperativity remains unchanged (see Figure 1.28). This conclusion has later been confirmed by Farman

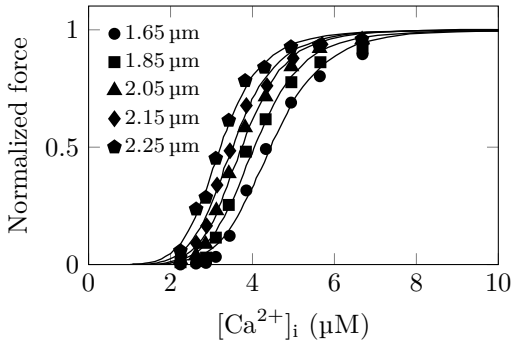

Figure 1.28 – Variation of the normalized force as a function of the sarcomere length at various $[Ca^{2+}]_i$ for rat cardiac skinned cardiomyocytes at 15 °C. Data from [Dobesh et al., 2002]. Note that the raw data used here are the same as in Figure 1.19.

et al. [2010].

Dynamical case The sarcomere length has an impact on the dynamics of the twitch contraction (see Section 1.4.1.2). The duration of the twitch is indeed longer at higher sarcomere length. This variation comes from a variation in the thin filament activation dynamics since the myosin head dynamics is not affected by the sarcomere length (see Section 1.4.2.1).

We conclude from the previous paragraphs that the level of thin filament activation is varied with the sarcomere length statically and dynamically. We will now present the different direction that have been explored to account for this variation.

To better understand the impact of the thin filament transient activation on the twitch peak force, we compare, at various sarcomere lengths, the force obtained in maximal thin filament activation steady state conditions and the peak force obtained in twitch contraction at "high" level of calcium supply.

Assuming that these "high" levels of calcium supply would correspond to a full thin filament activation in steady-state conditions, this comparison give an indication of the level of activation actually reached at the peak of a twitch. The results are presented in Figure 1.29. The peak force is always lower than the steady-state counterpart. Since the thin filament activation is the limiting reaction in the tension rise phase, it strongly suggests that, in a twitch contraction, the thin filament does not have time to reach the asymptotic level of activation that the environment conditions would allow in a steady-state contraction.

Origin of the thin filament activation variations

Variation of the calcium fluxes through the cellular membrane A first mechanism that can vary the level of thin filament activation is a variation of the amount of calcium that enters the cells, that could possibly then affect the calcium induced calcium release or directly contribute to the thin filament activation. Such a change of calcium

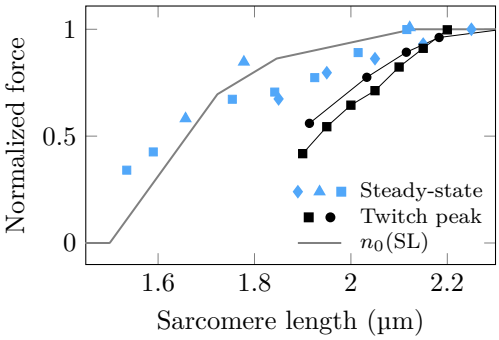

Figure 1.29 – Comparison of steady-state force in saturation calcium conditions with twitch contraction peak force at high level of calcium supply. (Black closed circle) Peak force in twitch contractions for intact rat cardiac cells at 27 °C with $[Ca^{2+}]_{ext} = 2.5\,mM$. Data from [Caremani et al., 2016]. (Black closed square) Peak force in twitch contractions for intact rat cardiac cells at 23–24 °C with $[Ca^{2+}]_{ext} = 2.0\,mM$. Data from [Janssen and Hunter, 1995]. (Gray line) Estimation of the thick filament activation function n_0 with respect to sarcomere length. (Blue triangle) intact tetanised rat cardiac cell at 26 °C [ter Keurs et al., 2008], (Blue square) skinned rat cardiac cells at 22–24 °C [Kentish et al., 1986], (Blue diamond) skinned rat cardiac cells at 15 °C [Dobesh et al., 2002].

flux through the cell membrane would affect the action potential. Allen [1977] show that the action potentials do not significantly vary after changes of sarcomere length, thus disproving this hypothesis.

Moreover, the increase in calcium sensitivity with sarcomere length is also observed with skinned cells (see Section 1.4.1.1). It is therefore unlikely, that the mechanism underlying the variations of the thin filament activation involves the cell membrane.

Variation of the calcium fluxes inside the cell A second mechanism may lie on the fact that the calcium released from the sarcoplasmic reticulum to the cytosol is increased with increasing sarcomere length allowing a higher amount of calcium to bind to the thin filament. Backx and ter Keurs [1993] show that the evolution of $[Ca^{2+}]_i$ observed in a twitch contraction is not significantly affected by the sarcomere length (see Figure 1.30). In the intracellular calcium concentration rising phase, the evolutions of $[Ca^{2+}]_i$ at long and short sarcomere lengths are the same and they reach the same peak concentration. In the decrease phase, variations between different sarcomere length conditions are observed but they are of a much lower order than differences in the force, showing that they are probably not significant. The same observation was also obtained by [Allen and Kurihara, 1982]. This observation can be explained by two mechanisms: either the release of calcium in the cytosol and the binding of calcium to the thin filament vary in a similar manner (in this case, a potential increase in the amount of calcium released induced by the variation of sarcomere length could be compensated by an increase in the amount of calcium captured by the thin filament) or they are both unaffected by the sarcomere length.

The first mechanism is advocated by ter Keurs [1996], who thus assumes that the affinity of calcium for troponin-C is increased with increasing sarcomere length. This explanation is coherent with the fact that a muscle length release during the twitch is associated with an immediate small increase of $[Ca^{2+}]_i$, directly linking the sarcomere length and the number of calcium ions bound on the thin filament [Allen and Kurihara, 1982; Backx and ter Keurs, 1993].

However, more recent experimental data show that the affinity of calcium for troponin-

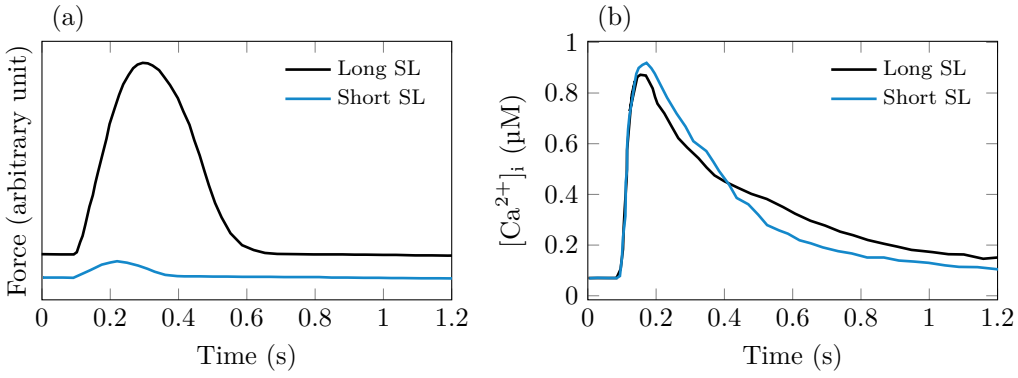

Figure 1.30 – Intracellular calcium concentration transient in a twitch contraction performed on rat cardiomyocytes at two different sarcomere lengths (1.6 µm and 2.15 µm) at 22 °C. Note that these experiments are not performed in length clamped condition. From [Backx and ter Keurs, 1993].

C is not affected by sarcomere length [Ait-Mou et al., 2016] making unlikely, in my opinion, that the net uptake and release of calcium at different sarcomere lengths vary and exactly compensate. Therefore, the variation of the thin filament activation level most probably relies on a variation of its response to calcium.

Variation of the sensitivity to calcium A second mechanism that can change the level of thin filament activation is the variation of the sensitivity to calcium, which has been observed experimentally.

To understand the variation of sensitivity, Farman et al. [2010] observed the thin filament structural changes while blocking myosin head binding at various sarcomere lengths. It appears that the variations in sensitivity are not affected by the formation of cross-bridges. Cross-bridge binding is not involved in the increase in sensitivity [Farman et al., 2010]. The length-dependent activation is thus intrinsic to the thin filament.

Furthermore, Ait-Mou et al. [2016] observe that stretching the sarcomere induces a structural change in the thin filament that is different from the structural change observed with the binding of calcium. They also observe that this structural change is not present for cardiomyocyte having a mutant titin. The role of titin is also highlighted by some other works which show that the replacement of titin with a longer isoform reduces the maximal force developed by the cardiomyocyte in saturated calcium conditions [Ait-Mou et al., 2016, ref 9, 13, 21 & 24]. The implication of titin in the variation of calcium sensitivity with sarcomere length thus seems well established.

Moreover, Ait-Mou et al. [2016] state that the binding affinity of $Ca^{2+}$to TnC is not affected by changes in sarcomere length. The variation of sensitivity has thus its origin in a mechanism occurring after the binding of calcium in the signal transduction.

Although the underlying principle of the change in sensitivity with sarcomere length are not well elucidated, the implication of titin has been considered as a vector of the modulation of the mechanisms involved in the thin filament activation [Farman et al., 2010] and is now more strongly established [Ait-Mou et al., 2016].

Impact of sarcomere length on the twitch contraction dynamics Comparing the twitch contractions obtained at different level of calcium supply in Figure 1.31(a), it appears that the duration of the relaxation is correlated with the sarcomere length but not

with the absolute force. Moreover, comparing two twitch contractions reaching the same peak force but obtained at different sarcomere lengths (by also varying the level of calcium supply) we also observe that the relaxation duration increases with increasing sarcomere length.

These two observations suggest that the longer relaxation duration is not related to the bound myosin heads but could be directly induced by the sarcomere length. In the same way as for the variations of the thin filament calcium sensitivity with sarcomere length, one can envision that the stretch of the sarcomere induces structural changes that prolongate the activation of the actin sites.

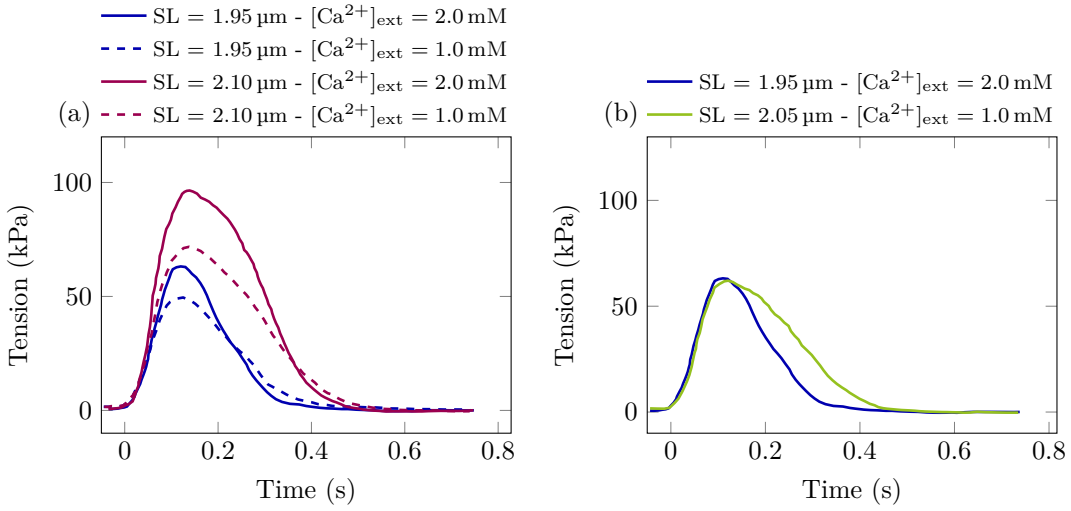

Figure 1.31 – (a) Comparison of twitch contractions at the same sarcomere length with different levels of calcium supply. Two sets of data are presented. (b) Comparison of twitch contraction reaching the same peak force but obtained at different sarcomere lengths and levels of calcium supply. (a) & (b) Data from [Janssen and Hunter, 1995] obtained with intact rat cardiac cells at 23–24 °C. In these experiments, the sarcomere length is carefully maintained constant throughout the measurement.

1.4.2.4 Conclusion on the origin of the force-length relation

The force-length relation originates from a variation of the number of attached myosin heads but not of the force that an individual cross-bridge develops. The fundamental origin of this regulation has been identified to be intrinsic to both the actin and myosin filaments but the exact mechanisms remain partially unknown. This intrinsic regulation also impact the dynamics of the force in a twitch contraction

Titin plays a fundamental role in the emergence of a force-length relation. Indeed, it is believed to contribute to the alterations of both the thick and the thin filament that lead to the variations of the number of available myosin heads and of the sensitivity to calcium of the actin sites, respectively.

1.4.3 Regulation by the neuroendocrine system

The developed force can also be modulated extrinsically by the neuroendocrine system. This regulation is of great important physiologically but constitutes in itself a broad topic of research that is out of the scope of this work. We will only present a brief overview of some of its effects.

This regulation path acts through the modulation of the protein activity. It may thus potentially an effect all aspects of the activation-contraction coupling.

It increases the amount of calcium release in the cell by changing the properties of the calcium ion channels and the ATP-powered Ca^{2+}-pumps [Silverthorn et al., 2009]. The neuroendocrine system also modulates the thin filament activation, and in particular, the behavior of the troponin complex and the tropomyosin [Solaro and Rarick, 1998] and it may affect the myosin heads cycling rate as well [de Tombe, 2003].

Moreover, the regulation of the activation-contraction coupling driven by the variation of the sarcomere length (see Section 1.4.2) is also affected. On the one hand, the responsiveness of the thin filament to calcium is modulated [Solaro, 2001; Kumar et al., 2015]. On the other hand, the "length sensor" is affected by the neuroendocrine regulation through its phosphorylation [Komukai and Kurihara, 1997; Hanft et al., 2013] (although the exact nature of this element has not been elucidated at this time).

1.4.4 Link with the Frank-Starling mechanism

The original works of Otto Frank [Frank, 1895] and Ernest Starling [Patterson and Starling, 1914] report a regulation mechanism in the heart allowing to adapt the output pressure (and thus the stroke volume) to the end diastolic ventricular volume. This mechanism, now termed Frank-Starling mechanism, is essential because it allows the cardiac output to be adapted to the venous return so that no blood is stored in the heart.

It consists in an increase in the left ventricle "strength" when the ventricle is dilated. If the venous return increases, the left ventricle end-diastolic volume increases as well. As a result, the contraction capability of the heart is enhanced, which allows the heart to eject this larger volume. The Frank-Starling regulation can trivially be summarized by the following statement: there is a monotone relation between the volume of blood that enters the heart and the ejected volume.

A modern formulation of the Frank-Starling effect, as stated by [de Tombe et al., 2010], reads as follows: the heart has a unique end-systolic pressure-volume relation (ESPVR) for each contractile state. Note that the ESPVR gives the maximal static pressure that can be generated inside a ventricle contracting at constant volume. The Frank-Starling mechanism thus ensures that the developed pressure in the ventricle directly depends on the volume.

At the microscopic level, the Frank-Starling effect originates from the variation of the force with sarcomere length. Indeed, increasing the ventricle volume stretches the sarcomere leading to a higher developed force and thus an enhanced ventricle contracting capability.

An increase in the contractile state at the organ level is induced through the neuroendocrine regulation either by an increase of the calcium supply or the modification of proteins involved in the activation-contraction coupling. It partially corresponds to the variations of the calcium supply in the *ex vivo* experiments.

The link between the microscopic and the macroscopic Frank-Starling mechanism is illustrated in Figure 1.32. Two heart cycles are represented at both sarcomere and organ level. The force length relation limits the active-force and translate to the ESPVR, which gives the range of reachable pressures (region below the curve). An element supporting the direct link between the is the following: the changes in convexity of the force-length relation with the level of calcium supply at the sarcomere level are also observed at the organ level in the ESPVR with varying level of contractility [Burkhoff et al., 1987; Sato et al., 1998] (note that the level of contractility is driven by the neuroendocrine regulation, which amongst others varies the level of calcium supply).

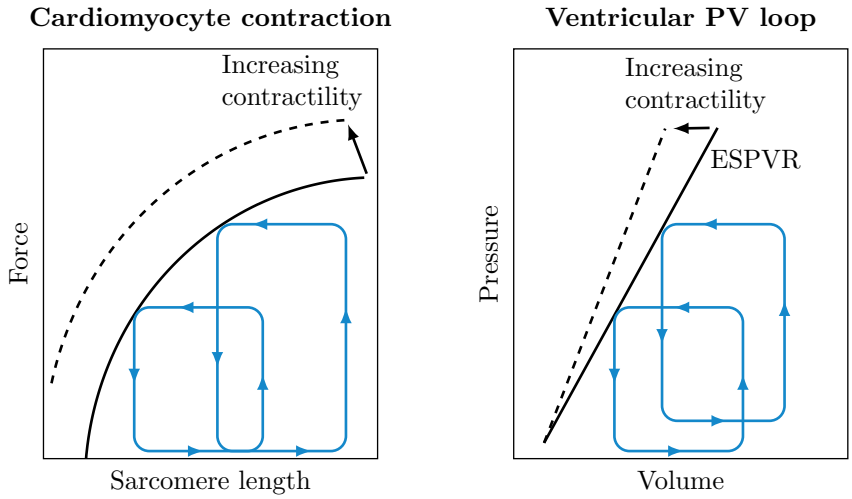

Figure 1.32 – (Left) Force-length relation at sarcomere level. (Right) End-systolic pressure-volume relation of the left ventricle. The blue lines schematically represent the physiological heart cycle from two different initial volumes at both sarcomere and organ level. Inspired from [de Tombe et al., 2010].

Note that the Frank-Starling effect is not the only way for the heart to adjust the output flow. It can alternatively change its beating rate — possibly simultaneously with a change in stroke volume.

1.5 Limitations of our presentation

The conclusions from this presentation of the contraction physiology suffers from limitations. Here we list a series of topics that are not covered by the above review.

First, the experiments are performed at 25–27 °C and not at body temperature for technical reasons. A second aspect lies in the fact that all experiments present in this review are performed on muscle cells that are disconnected from the neuroendocrine system although the latter is known to have a significant impact on the behavior of cardiac muscles. Our models will therefore not be calibrated to reproduce *in vivo* physiological behavior but the experimental behavior observed *ex vivo*. Finally, the actin-myosin interaction quantitative properties vary between species. Experiments performed on animal samples will therefore not give precise information about the behavior of human cardiac muscles.

In this section, we will briefly present some (non-exhaustive) illustrations of the three points mentioned above.

1.5.1 Influence of temperature

A strong limitation of all the experimental works presented here and of their applicability to the calibration of physiological models is that they are not performed at body temperature. Most of the experiments are performed around room temperature (usually between 22 °C and 27 °C). The reason for that is manyfold:

- the first reason is historical. Since many studies have been performed at room temperature, using the same range of temperature allows to position the new results with respect to the literature.

- the second reason is technical. Indeed, biological and chemical processes are sped up by an increase in temperature. For instance, [Gao et al., 1998] state that "the calcium indicators were quickly lost at 37 °C" (note that Janssen et al. [2002] using the same fluorescent protein write that it has a very little sensitivity to temperature). Furthermore, Janssen et al. [2002] observed that they could not obtain a tetanised state for intact cardiac cells at 37 °C presumably because of a too strong activity of the Ca^{2+}-pumps of the sarcoplasmic reticulum. Conversely, at 22 °C they obtain a tetanus state at high activation frequencies due to the slowdown in the detachment and Ca^{2+}re-uptake mechanisms.

A significant effect of temperature has been reported for many aspects of the excitation-contraction mechanism: the myosin head attachment-detachment dynamics [de Tombe and Stienen, 2007], the sarcoplasmic reticulum calcium release [Puglisi et al., 1999], the intracellular calcium transient in a twitch contraction [Janssen et al., 2002], the thin filament sensitivity to calcium (unlike the level of cooperativity in the thin filament activation which seems to be independent of temperature) [de Tombe and Stienen, 2007].

The impact of temperature on the intracellular calcium transient is illustrated in Figure 1.33. At higher temperature, the calcium concentration evolutions in the decreasing phase occur at a higher pace, while the peak occurs approximately at the same time. The force twitch is also affected with a reduction of the duration of both the tension rise and the relaxation. These experimental results on the calcium concentration may indicate an enhanced activity of the Ca^{2+}-pumps, which will speed up the calcium flux from the cytosol toward the sarcoplasmic reticulum and the exterior of the cell and thus reduce the duration of the calcium concentration decreasing phase. A faster uptake of calcium, combined with the previously suspected increase of the attachment and detachment rates, would naturally lead to a reduction of the twitch duration. The duration reduction is more pronounced in the relaxation, where the effect of a faster calcium uptake and faster detachment potentially add up, than in the tension rise where the faster attachment does not play a role because it is not the limiting reaction (see Section 1.3.3.3).

The analysis of the influence of temperature on the power-stroke dynamics has not been investigated yet (to the best of my knowledge) but it is likely that it will be affected.

These changes in the activation-contraction coupling mechanism have impact on the indicators used to characterize the muscle behavior. In steady-state shortening, the force developed at a given sliding velocity increases with temperature affecting the whole shape of the force-velocity curve. The unloaded shortening velocity V_0 is particularly changed (see Figure 1.34). Moreover, the rate of tension redevelopment is also increased with temperature (see Figure 1.35). These two observations suggest that the attachment and detachment rates are enhanced with increasing temperature.

The isometric peak force is also affected is a non monotone manner. Indeed, the variation of the peak force in a twitch contraction obtained by de Tombe and ter Keurs [1990] (Figure 1.36) first increases with temperature at "low" level of calcium supply but then decreases with temperature at "high" level of calcium supply. Note that other papers observe either a monotone increase of the peak force, for instance [Fujita and Kawai, 2002] with skinned bovine cardiac cells or a non-monotone variation with intact rat cells [Janssen et al., 2002] (note however that the experiments are performed without a proper sarcomere length control).

The origin of isometric force variation with temperature remains subject to debate. Indeed, Linari et al. [2005] conclude that the increase of force with temperature is linked with a myosin head structural change leading to think that the force per attached head is modified in frog skeletal muscle. On the contrary, Kawai et al. [2006] state that the force

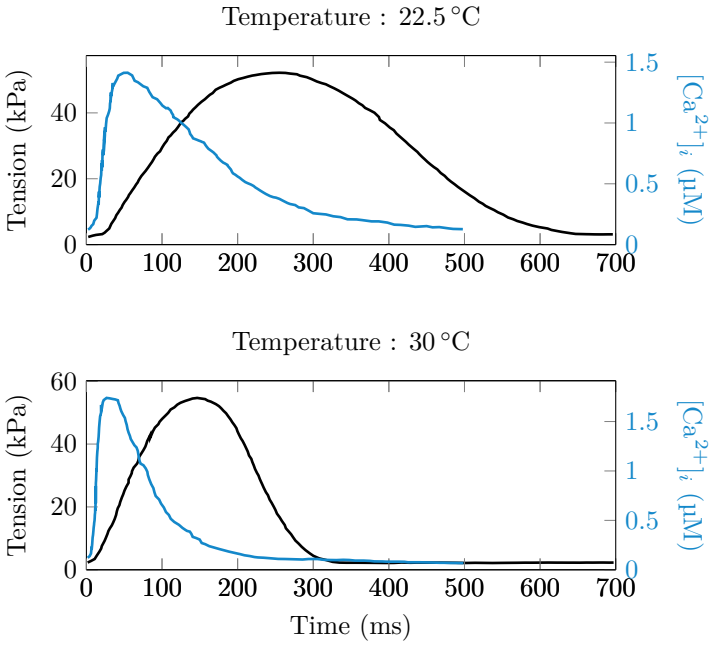

Figure 1.33 – Impact of temperature on the force and intracellular calcium concentration evolution in twitch contractions. Note that the sarcomere length is not properly maintained constant. Data from [Janssen et al., 2002] obtained with intact rat cardiac cells.

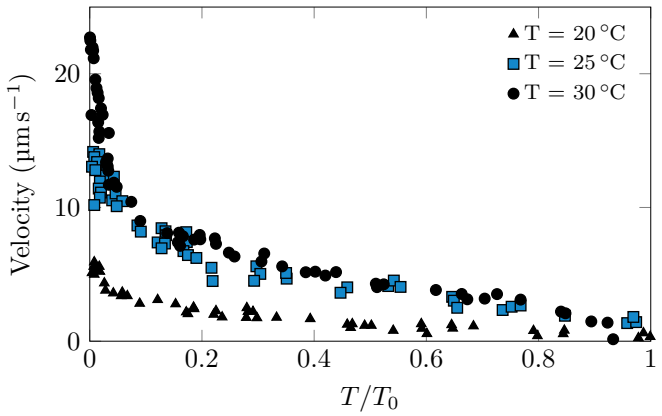

Figure 1.34 – Impact of the temperature on the force-velocity relation for intact rat cardiomyocyte. Data from [de Tombe and ter Keurs, 1990].

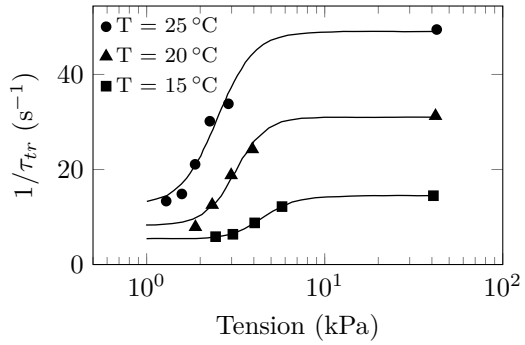

Figure 1.35 – Rate of tension redevelopment as a function of the isometric force at various temperature. Data measured from skinned rat cardiac cells, the various level of force are obtained by varying the environment calcium concentration. Data from [de Tombe and Stienen, 2007].

per cross-bridge is constant while the number of attached heads increases with temperature for rabbit skeletal muscle.

The non-monotonicity of the force variation with temperature shows that competing effect underlying the observed behavior have a different dependency on temperature. It is thus not straightforward to extrapolate the outcomes of experimental work at different temperatures.

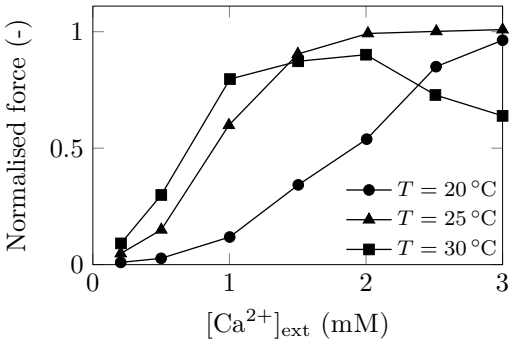

Figure 1.36 – Variation of the peak force with the cellular calcium concentration for various temperatures. The initial sarcomere length is 1.9 µm and is maintained constant throughout the experiment. Data from [de Tombe and ter Keurs, 1990] obtained with intact rat cardiac cells.

Note that a first set of data gathered on human skinned myocardium cells at body temperature has recently been presented in [Land et al., 2017]. Steady-state shortening and force development experiment are performed, as well as the observation of the steady-state force variation with the calcium supply. However, the very high discrepancy between the different cells characterized makes it difficult to draw definitive conclusions from these data.

Moreover, to the best of my knowledge, the only range of temperature at which all types of quantitative characterization of the cardiac muscle behavior are available is around 25 °C. We will therefore perform the calibration of our models with data measured at this temperature. However, using data obtained at non physiological temperature we are running the risk of misevaluating the relative contribution of the different ingredients in our models.

1.5.2 Variability between species

Variations in the activation-contraction coupling appear between species, even among mammals. We mention here several differences but the list is surely not exhaustive.

The method used for the adaption of the cardiac output varies among species [Shiels and White, 2008]. Mammals heart tissue experiences a higher passive tension for a similar stretch than for instance fish's tissue, which therefore can adapt their volume within a larger range. Mammals compensate the "lack of adaptability" of the ventricle volume by a greater ability to adjust their heart rate. Thus the relative importance of the Frank-Starling effect varies among species. We therefore expect the sarcomere length-tension relationship to also vary among species. In particular, Shiels and White [2008] report that amphibian myocardium has a broader and shifted sarcomere length working range compared to mammals (2 µm - 3 µm for amphibians against 1.85 µm - 2.3 µm for mammals).

Variations have also been reported in the calcium uptake by the sarcoplasmic reticulum and the membrane ion channels and exchangers [Bers, 2002] or the energy exchanges involved during contraction [Loiselle and Gibbs, 1979]. In mammals, the average heart beat is inversely correlated with the body size (data for various species can be found in [Noujaim et al., 2004]). The transition rate are also varying as suggested by results obtained by [Milani-Nejad et al., 2013] showing that rat and rabbit cardiac cells display different force redevelopment rates.

All of these results reflect the fact that there exist differences between species at many stages of the activation-contraction coupling. Therefore, the muscle contraction characterization with animal data should be considered with caution when aiming at obtaining quantitative data for human hearts.

1.5.3 Isolation from the neuroendocrine regulation

In vivo, the heart muscle contraction is regulated by the neuroendocrine system, which enhances or reduces the activity of the heart (contractility, beating pace, ...), see Section 1.1.5. The experiments however are performed *ex vivo* and thus isolated from the nervous system. Therefore, they only characterize a baseline behavior (without the action of the neuroendocrine system), which does not reflect the whole spectrum of physiological conditions.

An example of the difficulties that can appear when working with isolated cells is presented in what follows. Various twitch contractions obtained at varying level of calcium supply display an increase of the twitch duration when the extracellular calcium concentration increases (see Figure 1.37). In physiological conditions, the amount of calcium released inside the cell is increased as a result of the activation of the sympathetic nervous system to strengthen the contraction, by increasing the activity of the Ca^{2+}-pump of the sarcoplasmic reticulum. The result of this is twofold: it increases the developed force but simultaneously reduces the twitch duration. Hence, the experimental conditions do not reproduce the physiological conditions.

The response observed in the experiments is surely of great importance to understand the functioning of muscle cells but we should be aware that it may not correspond to the physiological *in vivo* behavior.

1.5.4 Conclusion of the limitations

The above-mentioned experimental works suffer from some limitations in the context of building models to simulate a human heart. Indeed, they are mostly performed at non-physiological temperature, with non-human samples isolated from the neural system.

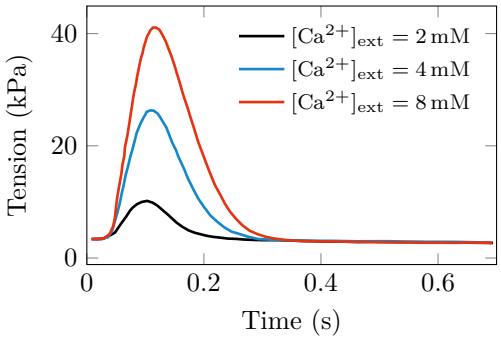

Figure 1.37 – Twitch contraction at different levels of external calcium concentration. Data from [Gao et al., 1998] from mouse cardiac cells at 20–22 °C. Note that these experiments are performed without a proper sarcomere length control system.

These three factors are been proven to strongly affect the experiment outputs. Therefore, there shouldn't be too much expectation that the models exclusively calibrated with *ex vivo* experimental data directly reproduce the physiological behavior at organ level. These data provide qualitative and semi-quantitative information only.

1.6 Appendix

1.6.1 Hill's cooperativity models

A classical way of describing cooperativity consist in using the phenomenological model of Hill originally designed to express the fraction of binding sites of a macromolecule saturated by ligand [Hill, 1910]. In this framework, we consider the following formal chemical reaction between an actin site with n_H calcium ion Ca^{2+}forming an activated actin site ACa_n:

$$\mathrm{A} + \mathrm{n_H}\,\mathrm{Ca}^{2+} \underset{\mathrm{k_-}}{\overset{\mathrm{k_+}}{\rightleftharpoons}} \mathrm{ACa_{n_H}},$$

with the hypothesis that the calcium concentration is buffered. At equilibrium, we have

$$K = \frac{k_+}{k_-} = \frac{[\mathrm{ACa}_{n_H}]}{[A][\mathrm{Ca}^{2+}]^{n_H}}$$

with K the reaction constant. The mass conservation gives that $[\mathrm{A}] + [\mathrm{ACa}_{n_H}] = C_{\mathrm{st}}$ is a constant. The dynamics of the system is given by

$$\begin{aligned}\frac{\mathrm{d}}{\mathrm{d}t}[\mathrm{ACa}_{n_H}] &= k_+[\mathrm{A}][\mathrm{Ca}^{2+}]^{n_H} - k_-[\mathrm{ACa}_{n_H}] \\ &= -(k_+ + k_-[\mathrm{Ca}^{2+}]^n)[\mathrm{ACa}_{n_H}] + k_+ C_{\mathrm{st}}[\mathrm{Ca}^{2+}]^{n_H}.\end{aligned}$$

Solving this ordinary differential equation with the initial condition $[\mathrm{ACa}_n](t=0) = 0$ for each calcium concentration $[\mathrm{Ca}^{2+}]$, we obtain the fraction of activated actin sites

$$n_a([\mathrm{Ca}^{2+}]) \overset{\mathrm{def}}{=\!=} \frac{\lim\limits_{t\to\infty}[\mathrm{ACa}_{n_H}]([\mathrm{Ca}^{2+}], t)}{C_{\mathrm{st}}} = \frac{k_+[\mathrm{Ca}^{2+}]^{n_H}}{k_- + k_+[\mathrm{Ca}^{2+}]^n}.$$

Note that $n_a([\mathrm{Ca}^{2+}] \to \infty) = 1$ and we can compute $[\mathrm{Ca}^{2+}]_{50}$, the calcium concentration which allows an equilibrium at half the saturation ratio. We obtain $[\mathrm{Ca}^{2+}]_{50} = \big(1/K\big)^{1/n_H}$.

The fraction of activated actin sites is given by

$$n_a([\mathrm{Ca}^{2+}]) = \frac{[\mathrm{ACa}_{n_H}]}{[\mathrm{ACa}_{n_H}] + [\mathrm{A}]} = \frac{K[A][\mathrm{Ca}^{2+}]^{n_H}}{K[\mathrm{A}][\mathrm{Ca}^{2+}]^{n_H} + [\mathrm{A}]} = \frac{[\mathrm{Ca}^{2+}]^{n_H}}{[\mathrm{Ca}^{2+}]^{n_H} + 1/K}.$$

Thus, we obtain the classical Hill's equation

$$n_a([\mathrm{Ca}^{2+}]) = \frac{[\mathrm{Ca}^{2+}]^{n_H}}{[\mathrm{Ca}^{2+}]_{50}^{n_H} + [\mathrm{Ca}^{2+}]^{n_H}}.$$

The coefficient n_H represents the level of cooperativity and is called the *Hill coefficient*. Note that in the case of calcium binding to troponin, it is rather an analogy with the Hill's model because there is only one regulatory binding site on TnC. However, since the macroscopic behavior (force measurement) shows cooperativity, we can use Hill's equation to fit the experimental curve and use the Hill coefficient as a measure of the level of cooperativity although it has, unlike Hill's model, no direct link with the underlying mechanism.

Bibliography

Adhikari, B., Regnier, M., Rivera, A., Kreutziger, K., and Martyn, D. (2004). Cardiac length dependence of force and force redevelopment kinetics with altered cross-bridge cycling. *Biophysj*, 87(3):1784–1794.

Ait-Mou, Y., Hsu, K., Farman, G., Kumar, M., Greaser, M., Irving, T., and de Tombe, P. (2016). Titin strain contributes to the Frank–Starling law of the heart by structural rearrangements of both thin- and thick-filament proteins. *Proceedings of the National Academy of Sciences*, 113(8):2306–2311.

Allen, D. (1977). On the relationship between action potential duration and tension in cat papillary muscle. *Cardiovascular Research*, 11(3):210–218.

Allen, D. and Kentish, J. (1985). The cellular basis of the length-tension relation in cardiac muscle. *Journal of molecular and cellular cardiology*, 17(9):821–840.

Allen, D. and Kurihara, S. (1982). The effects of muscle length on intracellular calcium transients in mammalian cardiac muscle. *The Journal of physiology*, 327(1):79–94.

Amiad Pavlov, D. and Landesberg, A. (2016). The cross-bridge dynamics is determined by two length-independent kinetics: Implications on muscle economy and Frank–Starling Law. *Journal of molecular and cellular cardiology*, 90:94–101.

Backx, P., Gao, W., Azan-Backx, M., and Marban, E. (1995). The relationship between contractile force and intracellular [Ca2+] in intact rat cardiac trabeculae. *The Journal of General Physiology*, 105(1):1–19.

Backx, P. and ter Keurs, H. (1993). Fluorescent properties of rat cardiac trabeculae microinjected with fura-2 salt. *The American journal of physiology*, 264(4):H1098–110.

Barclay, C. (2015). Energetics of contraction. *Comprehensive Physiology*, 5(2):961–995.

Bers, D. (2002). Cardiac excitation-contraction coupling. *Nature*, 415(6868):198–205.

Burkhoff, D., Sugiura, S., Yue, D., and Sagawa, K. (1987). Contractility-dependent curvilinearity of end-systolic pressure-volume relations. *The American journal of physiology*, 252(6):H1218–27.

Campbell, K. (2014). Dynamic coupling of regulated binding sites and cycling myosin heads in striated muscle. *The Journal of General Physiology*, 143(3):387–399.

Caputo, C., Edman, K., Lou, F., and Sun, Y. (1994). Variation in myoplasmic Ca2+ concentration during contraction and relaxation studied by the indicator fluo-3 in frog muscle fibres. *The Journal of Physiology*, 478(1):137–148.

Caremani, M., Pinzauti, F., Reconditi, M., Piazzesi, G., Stienen, G., Lombardi, V., and Linari, M. (2016). Size and speed of the working stroke of cardiac myosin in situ. *Proceedings of the National Academy of Sciences*, 113(13):3675–3680.

Caruel, M., Chabiniok, R., Moireau, P., Lecarpentier, Y., and Chapelle, D. (2013). Dimensional reductions of a cardiac model for effective validation and calibration. *Biomechanics and Modeling in Mechanobiology*, 13(4):897–914.

Cingolani, H., Pérez, N., Cingolani, O., and Ennis, I. (2013). The Anrep effect: 100 years later. *American journal of physiology. Heart and circulatory physiology*, 304(2):H175–82.

Cooke, R. and Franks, K. (1980). All myosin heads form bonds with actin in rigor rabbit skeletal muscle. *Biochemistry*, 19(10):2265–2269.

Craig, R. and Padrón, R. (2004). Molecular structure of the sarcomere. *Myology*, 3:129–144.

Craig, R. and Woodhead, J. (2006). Structure and function of myosin filaments. *Current opinion in structural biology*, 16(2):204–212.

Daniels, M., Noble, M., ter Keurs, H., and Wohlfart, B. (1984). Velocity of sarcomere shortening in rat cardiac muscle: relationship to force, sarcomere length, calcium and time. *The Journal of Physiology*, 355:367–381.

Davis, J., Norman, C., Kobayashi, T., Solaro, R., Swartz, D., and Tikunova, S. (2007). Effects of Thin and Thick Filament Proteins on Calcium Binding and Exchange with Cardiac Troponin C. *Biophysical Journal*, 92(9):3195–3206.

de Tombe, P. (2003). Cardiac myofilaments: mechanics and regulation. *Journal of Biomechanics*, 36(5):721–730.

de Tombe, P., Belus, A., Piroddi, N., Scellini, B., Walker, J., Martin, A., Tesi, C., and Poggesi, C. (2006). Myofilament calcium sensitivity does not affect cross-bridge activation-relaxation kinetics. *AJP: Regulatory, Integrative and Comparative Physiology*, 292(3):R1129–R1136.

de Tombe, P., Mateja, R., Tachampa, K., Mou, Y., Farman, G., and Irving, T. (2010). Journal of Molecular and Cellular Cardiology. *Journal of molecular and cellular cardiology*, 48(5):851–858.

de Tombe, P. and Stienen, G. (2007). Impact of temperature on cross-bridge cycling kinetics in rat myocardium. *The Journal of Physiology*, 584(2):591–600.

de Tombe, P. and ter Keurs, H. (1990). Force and velocity of sarcomere shortening in trabeculae from rat heart. Effects of temperature. *Circulation Research*, 66(5):1239–1254.

de Tombe, P. and ter Keurs, H. (1992). An internal viscous element limits unloaded velocity of sarcomere shortening in rat myocardium. *The Journal of Physiology*, 454(1):619–642.

de Tombe, P. and ter Keurs, H. (2016). Cardiac muscle mechanics: Sarcomere length matters. *Journal of molecular and cellular cardiology*, 91(C):148–150.

Dobesh, D., Konhilas, J., and de Tombe, P. (2002). Cooperative activation in cardiac muscle: impact of sarcomere length. *AJP: Heart and Circulatory Physiology*, 282(3):H1055–H1062.

Fabiato, A. (1983). Calcium-induced release of calcium from the cardiac sarcoplasmic reticulum. *American Journal of Physiology - Cell Physiology*, 245(1):C1–C14.

Fabiato, A. and Fabiato, F. (1975). Dependence of the contractile activation of skinned cardiac cells on the sarcomere length. *Nature*, 256(5512):54–56.

Farman, G., Allen, E., Schoenfelt, K., Backx, P., and de Tombe, P. (2010). The Role of Thin Filament Cooperativity in Cardiac Length-Dependent Calcium Activation. *Biophysical Journal*, 99(9):2978–2986.

Frank, O. (1895). *Zur Dynamik des Herzmuskels*, volume 32. Zeitschrift für Biologie.

Fuchs, F. and Wang, Y.-P. (1996). Sarcomere length versus interfilament spacing as determinants of cardiac myofilament ca2+ sensitivity and ca2+ binding. *Journal of molecular and cellular cardiology*, 28(7):1375–1383.

Fujita, H. and Kawai, M. (2002). Temperature effect on isometric tension is mediated by regulatory proteins tropomyosin and troponin in bovine myocardium. *The Journal of Physiology*, 539(Pt 1):267–276.

Fukuda, N., Granzier, H., Ishiwata, S., and Kurihara, S. (2008). Physiological functions of the giant elastic protein titin in mammalian striated muscle. *The Journal of Physiological Sciences*, 58(3):151–159.

Gao, W., Azan-Backx, M., Marban, E., and Backx, P. (1994). Myofilament Ca2+ sensitivity in intact versus skinned rat ventricular muscle. *Circulation Research*, 74(3):408–415.

Gao, W., Perez, N., and Marban, E. (1998). Calcium cycling and contractile activation in intact mouse cardiac muscle. *The Journal of Physiology*, 507(1):175–184.

Godt, R. and Maughan, D. (1981). Influence of osmotic compression on calcium activation and tension in skinned muscle fibers of the rabbit. *Pflügers Archiv - European Journal of Physiology*, 391(4):334–337.

Gordon, A., Huxley, A., and Julian, F. (1966). The variation in isometric tension with sarcomere length in vertebrate muscle fibres. *The Journal of Physiology*, 184(1):170.

Gordon, A. M., Homsher, E., and Regnier, M. (2000). Regulation of contraction in striated muscle. *Physiological reviews*, 80(2):853–924.

Hanft, L., Biesiadecki, B., and McDonald, K. (2013). Length dependence of striated muscle force generation is controlled by phosphorylation of cTnI at serines 23/24. *The Journal of Physiology*, 591(18):4535–4547.

Hill, A. (1938). The heat of shortening and the dynamic constants of muscle. *Proc. R. Soc. Lond. B*, 126(843):136–195.

Hill, A. V. (1910). The possible effects of the aggregation of the molecules of hæmoglobin on its dissociation curves. *The Journal of Physiology*, 40:i–vii.

Holzapfel, G. and Ogden, R. (2009). Constitutive modelling of passive myocardium: a structurally based framework for material characterization. *Philosophical transactions. Series A, Mathematical, physical, and engineering sciences*, 367(1902):3445–3475.

Houdusse, A. and Sweeney, H. (2016). How Myosin Generates Force on Actin Filaments. *Trends in Biochemical Sciences*, 41(12):989–997.

Huxley, A. and Simmons, R. (1971). Proposed mechanism of force generation in striated muscle. *Nature*.

Irving, M., Piazzesi, G., Lucii, L., Sun, Y., Harford, J., Dobbie, I., Ferenczi, M., Reconditi, M., and Lombardi, V. (2000). Conformation of the myosin motor during force generation in skeletal muscle. *Nature structural biology*, 7(6):482–485.

Janssen, P. and Hunter, W. (1995). Force, not sarcomere length, correlates with prolongation of isosarcometric contraction. *AJP: Heart and Circulatory Physiology*, 269(2):H676–H685.

Janssen, P., Stull, L., and Marban, E. (2002). Myofilament properties comprise the rate-limiting step for cardiac relaxation at body temperature in the rat. *AJP: Heart and Circulatory Physiology*, 282(2):H499–H507.

Kawai, M., Kido, T., Vogel, M., Fink, R., and Ishiwata, S. (2006). Temperature change does not affect force between regulated actin filaments and heavy meromyosin in single-molecule experiments. *The Journal of Physiology*, 574(Pt 3):877–887.

Kaya, M. and Higuchi, H. (2010). Nonlinear elasticity and an 8-nm working stroke of single myosin molecules in myofilaments. *Science*, 329(5992):686–689.

Kentish, J., Ter Keurs, H., Ricciardi, L., Bucx, J., and Noble, M. (1986). Comparison between the sarcomere length-force relations of intact and skinned trabeculae from rat right ventricle. influence of calcium concentrations on these relations. *Circulation research*, 58(6):755–768.

Kobayashi, T., Jin, L., and de Tombe, P. (2008). Cardiac thin filament regulation. *Pflügers Archiv - European Journal of Physiology*, 457(1):37–46.

Komukai, K. and Kurihara, S. (1997). Length dependence of ca (2+)-tension relationship in aequorin-injected ferret papillary muscles. *American Journal of Physiology-Heart and Circulatory Physiology*, 273(3):H1068–H1074.

Konhilas, J., Irving, T., and de Tombe, P. (2002a). Length-dependent activation in three striated muscle types of the rat. *The Journal of Physiology*, 544(1):225–236.

Konhilas, J., Irving, T., and deTombe, P. (2002b). Myofilament calcium sensitivity in skinned rat cardiac trabeculae: role of interfilament spacing. *Circulation Research*, 90(1):59–65.

Kumar, M., Govindan, S., Zhang, M., Khairallah, R., Martin, J., Sadayappan, S., and de Tombe, P. (2015). Cardiac Myosin-binding Protein C and Troponin-I Phosphorylation Independently Modulate Myofilament Length-dependent Activation. *The Journal of biological chemistry*, 290(49):29241–29249.

Land, S., Park-Holohan, S.-J., Smith, N., dos Remedios, C., Kentish, J., and Niederer, S. (2017). A model of cardiac contraction based on novel measurements of tension development in human cardiomyocytes. *Journal of molecular and cellular cardiology*, 106:68–83.

Lecarpentier, Y., Chuck, L., Housmans, P., De Clerck, N., and Brutsaert, D. (1979). Nature of load dependence of relaxation in cardiac muscle. *The American journal of physiology*, 237(4):H455–60.

Linari, M., Brunello, E., Reconditi, M., Fusi, L., Caremani, M., Narayanan, T., Piazzesi, G., Lombardi, V., and Irving, M. (2015). Force generation by skeletal muscle is controlled by mechanosensing in myosin filaments. *Nature*, 528(7581):276–279.

Linari, M., Brunello, E., Reconditi, M., Sun, Y., Panine, P., Narayanan, T., Piazzesi, G., Lombardi, V., and Irving, M. (2005). The structural basis of the increase in isometric force production with temperature in frog skeletal muscle. *The Journal of Physiology*, 567(Pt 2):459–469.

Linari, M., Caremani, M., and Lombardi, V. (2010). A kinetic model that explains the effect of inorganic phosphate on the mechanics and energetics of isometric contraction of fast skeletal muscle. *Proceedings. Biological sciences*, 277(1678):19–27.

Linari, M., Dobbie, I., Reconditi, M., Koubassova, N., Irving, M., Piazzesi, G., and Lombardi, V. (1998). The stiffness of skeletal muscle in isometric contraction and rigor: the fraction of myosin heads bound to actin. *Biophysj*, 74(5):2459–2473.

Loiselle, D. and Gibbs, C. (1979). Species differences in cardiac energetics. *The American journal of physiology*, 237(1):H90–8.

Lombardi, V., Piazzesi, G., and Linari, M. (1992). Rapid regeneration of the actin-myosin power stroke in contracting muscle. *Nature*.

Lymn, R. and Taylor, E. (1971). Mechanism of adenosine triphosphate hydrolysis by actomyosin. *Biochemistry*, 10(25):4617–4624.

Mateja, R. and de Tombe, P. (2012). Myofilament Length-Dependent Activation Develops within 5 ms in Guinea-Pig Myocardium. *Biophysical Journal*, 103(1):L13–L15.

Mateja, R., Greaser, M., and de Tombe, P. (2013). Impact of titin isoform on length dependent activation and cross-bridge cycling kinetics in rat skeletal muscle. *Biochimica et biophysica acta*, 1833(4):804–811.

Methawasin, M., Hutchinson, K., Lee, E., Smith, J., Saripalli, C., Hidalgo, C., Ottenheijm, C., and Granzier, H. (2014). Experimentally increasing titin compliance in a novel mouse model attenuates the Frank-Starling mechanism but has a beneficial effect on diastole. *Circulation …*, 129(19):1924–1936.

Milani-Nejad, N., Xu, Y., Davis, J., Campbell, K., and Janssen, P. (2013). Effect of muscle length on cross-bridge kinetics in intact cardiac trabeculae at body temperature. *The Journal of General Physiology*, 141(1):133–139.

Noble, M. (1977). The diastolic viscous properties of cat papillary muscle. *Circulation Research*, 40(3):288–292.

Noujaim, S., Lucca, E., Muñoz, V., Persaud, D., Berenfeld, O., Meijler, F. L., and Jalife, J. (2004). From mouse to whale: a universal scaling relation for the PR Interval of the electrocardiogram of mammals. *Circulation …*, 110(18):2802–2808.

Patterson, S. and Starling, E. (1914). On the mechanical factors which determine the output of the ventricles. *The Journal of Physiology*, 48(5):357–379.

Pery-Man, N., Chemla, D., Coirault, C., Suard, I., Riou, B., and Lecarpentier, Y. (1993). A comparison of cyclopiazonic acid and ryanodine effects on cardiac muscle relaxation. *The American journal of physiology*, 265(4 Pt 2):H1364–72.

Piazzesi, G., Caremani, M., Linari, M., Reconditi, M., and Lombardi, V. (2018). Thick filament mechano-sensing in skeletal and cardiac muscles: a common mechanism able to adapt the energetic cost of the contraction to the task. *Frontiers in Physiology*, 9.

Piazzesi, G. and Lombardi, V. (1995). A cross-bridge model that is able to explain mechanical and energetic properties of shortening muscle. *Biophysical Journal*, 68:1966–1979.

Piazzesi, G., Lucii, L., and Lombardi, V. (2002). The size and the speed of the working stroke of muscle myosin and its dependence on the force. *The Journal of Physiology*, 545(1):145–151.

Piazzesi, G., Reconditi, M., Linari, M., Lucii, L., Bianco, P., Brunello, E., Decostre, V., Stewart, A., Gore, D., Irving, T., Irving, M., and Lombardi, V. (2007). Skeletal muscle performance determined by modulation of number of myosin motors rather than motor force or stroke size. *Cell*, 131(4):784–795.

Pinzauti, F., Pertici, I., Reconditi, M., Narayanan, T., Stienen, G., Piazzesi, G., Lombardi, V., Linari, M., and Caremani, M. (2018). The force and stiffness of myosin motors in the isometric twitch of a cardiac trabecula and the effect of the extracellular calcium concentration. *The Journal of Physiology*, 596(13):2581–2596.

Puglisi, J., Yuan, W., Bassani, J., and Bers, D. (1999). Ca2+ influx through ca2+ channels in rabbit ventricular myocytes during action potential clamp: influence of temperature. *Circulation research*, 85(6):e7–e16.

Rayment, I., Holden, H., Whittaker, M., Yohn, C., Lorenz, M., Holmes, K., and Milligan, R. (1993). Structure of the actin-myosin complex and its implications for muscle contraction. *Science*, 261(5117):58–65.

Reconditi, M., Brunello, E., Linari, M., Bianco, P., Narayanan, T., Panine, P., Piazzesi, G., Lombardi, V., and Irving, M. (2011). Motion of myosin head domains during activation and force development in skeletal muscle. *Proceedings of the National Academy of Sciences*, 108(17):7236–7240.

Reconditi, M., Caremani, M., Pinzauti, F., Powers, J., Narayanan, T., Stienen, G., Linari, M., Lombardi, V., and Piazzesi, G. (2017). Myosin filament activation in the heart is tuned to the mechanical task. *Proceedings of the National Academy of Sciences*, pages 3240–3245.

Reconditi, M., Koubassova, N., Linari, M., Dobbie, I., Narayanan, T., Diat, O., Piazzesi, G., Lombardi, V., and Irving, M. (2003). The conformation of myosin head domains in rigor muscle determined by X-ray interference. *Biophysj*, 85(2):1098–1110.

Regnier, M., Martin, H., Barsotti, R., Rivera, A., Martyn, D., and Clemmens, E. (2004). Cross-Bridge versus Thin Filament Contributions to the Level and Rate of Force Development in Cardiac Muscle. *Biophysj*, 87(3):1815–1824.

Robinson, J., Dong, W.-J., Xing, J., and Cheung, H. (2004). Switching of troponin I: Ca(2+) and myosin-induced activation of heart muscle. *Journal of molecular biology*, 340(2):295–305.

Rodriguez, E., Hunter, W., Royce, M., Leppo, M., Douglas, A., and Weisman, H. (1992). A method to reconstruct myocardial sarcomere lengths and orientations at transmural sites in beating canine hearts. *The American journal of physiology*, 263(1 Pt 2):H293–306.

Sato, T., Shishido, T., Kawada, T., Miyano, H., Miyashita, H., Inagaki, M., Sugimachi, M., and Sunagawa, K. (1998). ESPVR of in situ rat left ventricle shows contractility-dependent curvilinearity. *The American journal of physiology*, 274(5):H1429–34.

Schouten, V. J., Bucx, J. J., de Tombe, P. P., and ter Keurs, H. E. (1990). Sarcolemma, sarcoplasmic reticulum, and sarcomeres as limiting factors in force production in rat heart. *Circulation Research*, 67(4):913–922.

Sequeira, V. and Velden, J. (2017). The Frank–Starling Law: a jigsaw of titin proportions. *Biophysical reviews*, 9(3):259–267.

Shiels, H. and White, E. (2008). The Frank–Starling mechanism in vertebrate cardiac myocytes. *Journal of Experimental Biology*, 211(13):2005–2013.

Silverthorn, D., Ober, W., Garrison, C., and Silverthorn, A. (2009). *Human physiology: an integrated approach*. Pearson.

Solaro, R. (2001). Modulation of cardiac myofilament activity by protein phosphorylation. *Handbook of Physiology: Section*, 2:264–300.

Solaro, R. and Rarick, H. M. (1998). Troponin and tropomyosin: proteins that switch on and tune in the activity of cardiac myofilaments. *Circulation research*, 83(5):471–480.

Sun, Y.-B. and Irving, M. (2010). The molecular basis of the steep force–calcium relation in heart muscle. *Journal of molecular and cellular cardiology*, 48(5):859–865.

Sun, Y.-B., Lou, F., and Irving, M. (2009). Calcium- and myosin-dependent changes in troponin structure during activation of heart muscle. *The Journal of Physiology*, 587(1):155–163.

Tachampa, K., Wang, H., Farman, G., and de Tombe, P. (2007). Cardiac troponin I threonine 144: role in myofilament length dependent activation. *Circulation Research*, 101(11):1081–1083.

ter Keurs, H. (1996). Heart failure and Starling's Law of the heart. *The Canadian journal of cardiology*, 12(10):1047–1057.

ter Keurs, H., Rijnsburger, W., Van Heuningen, R., and Nagelsmit, M. (1980). Tension Development and Sarcomere Length in Rat Cardiac Trabeculae: Evidence of Length-Dependent Activation. In *Cardiac Dynamics*, pages 25–36. Springer Netherlands, Dordrecht.

ter Keurs, H., Shinozaki, T., Zhang, Y., Zhang, M., Wakayama, Y., Sugai, Y., Kagaya, Y., Miura, M., Boyden, P., Stuyvers, B., and Landesberg, A. (2008). Sarcomere mechanics in uniform and non-uniform cardiac muscle: A link between pump function and arrhythmias. *Progress in biophysics and molecular biology*, 97(2-3):312–331.

van der Velden, J., de Jong, J., Owen, V., Burton, P., and Stienen, G. (2000). Effect of protein kinase A on calcium sensitivity of force and its sarcomere length dependence in human cardiomyocytes. *Cardiovascular Research*, 46(3):487–495.

Van Heuningen, R., Rijnsburger, W., and ter Keurs, H. (1982). Sarcomere length control in striated muscle. *The American journal of physiology*, 242(3):H411–20.

Wannenburg, T., Janssen, P., Fan, D., and de Tombe, P. (1997). The Frank-Starling mechanism is not mediated by changes in rate of cross-bridge detachment. *The American journal of physiology*, 273(5 Pt 2):H2428–35.

CHAPTER 2

Thermodynamic properties of muscle contraction models and associated discrete-time principles

Considering a large class of muscle contraction models accounting for actin-myosin interaction, we present a mathematical setting in which solution properties can be established, including fundamental thermodynamic balances. Moreover, we propose a complete discretization strategy for which we are also able to obtain discrete versions of the thermodynamic balances and other properties. Our major objective is to show how the thermodynamics of such models can be tracked after discretization, including when they are coupled to a macroscopic muscle formulation in the realm of continuum mechanics. Our approach allows to carefully identify the sources of energy and entropy in the system, and to follow them up to the numerical applications.

Contents

Thermodynamic properties of muscle contraction models and associated discrete-time principles

François Kimmig[1,2], Dominique Chapelle[2,1], Philippe Moireau[2,1]

[1]LMS, Ecole Polytechnique, CNRS, Université Paris-Saclay
[2]Inria, Université Paris-Saclay

AMSES, DOI:10.1186/s40323-019-0128-9

Abstract

Considering a large class of muscle contraction models accounting for actin-myosin interaction, we present a mathematical setting in which solution properties can be established, including fundamental thermodynamic balances. Moreover, we propose a complete discretization strategy for which we are also able to obtain discrete versions of the thermodynamic balances and other properties. Our major objective is to show how the thermodynamics of such models can be tracked after discretization, including when they are coupled to a macroscopic muscle formulation in the realm of continuum mechanics. Our approach allows to carefully identify the sources of energy and entropy in the system, and to follow them up to the numerical applications.

Keywords— muscle contraction, sliding filaments, thermodynamically consistent time-discretization, Clausius-Duhem inequality
Mathematics Subject Classification (2010)— 74F25, 74H15, 65M12, 35Q79 and 92C45

2.1 Introduction

The modeling of the active mechanical behavior of muscles has been the object of intense research since the seminal work of A.F. Huxley Huxley [1957] modeling the attachment-detachment process in the actin-myosin interaction responsible for sarcomere contraction. Then, numerous extensions – mostly based on refinements of the chemical process introduced by Huxley – of the previous model have been proposed in order to take into account different time scales of the actin-myosin interaction. In particular several models have been developed to account for the power stroke phenomenon Eisenberg and Hill [1978]; Eisenberg et al. [1980]; Huxley and Simmons [1971]; Piazzesi and Lombardi [1995]. In parallel, the question of the thermodynamic balances associated with the chemical machinery was intensively studied, notably with the fundamental contributions of T.L. Hill Hill [1977, 2004]. Note that these models are specific cases of molecular motors models without the natural diffusion introduced by the Fokker-Plank equation Julicher et al. [1997]; Chipot et al. [2004]; Mirrahimi and Souganidis [2012]; Chapelle et al. [2012]. In this paper, our objective is to develop a formalism allowing to derive these thermodynamic balances for Huxley's model and its extensions with an additional tracking of these balances at the discrete level after time-discretizing the model dynamics. Moreover, we present how these microscopic models can be incorporated into a macroscopic model of muscle fibers in the

spirit of Chapelle et al. [2012] with the aim of following these thermodynamic balances at the macroscopic level for the continuous-time dynamics but also after adequate time discretization. This last part is general with respect to the chemical microscopic model of interest and could also be extended to similar types of models Peskin [1975]; Chipot et al. [2004], or those mixing mechanical and chemical modeling elements, for instance Sheshka and Truskinovsky [2014]; Marcucci et al. [2016]; Caruel et al. [2019].

The outline of the paper is as follows. The first section presents the modeling ingredients of the microscopic models of actin-myosin interaction and we derive in a second section the fundamental properties of these models with the associated thermodynamic balances, up to the coupling with the macroscopic mechanical formulation. The third section then describes the discretization scheme and justifies its thermodynamic compatibility. Finally, the last section illustrates our results with numerical investigations.

2.2 Modeling of muscle contraction

2.2.1 Physiology of muscle contraction

Muscles are multi-scale structures in which motion is initiated at the cellular level by the relative sliding between two types of filaments: actin filaments and myosin filaments. At the surface of the myosin filament, myosin heads can bind to the actin filament. The actin filament has a periodic structure with regularly spaced attachment sites. The interaction between myosin heads and actin sites occurs in a cyclic manner Lymn and Taylor [1971], see Figure 2.1. The cycle includes attachment and detachment of the myosin head to and from an actin site and a conformation change of the attached myosin head called the power stroke. The detachment stage requires an energy input obtained from ATP molecules buffered inside the cell.

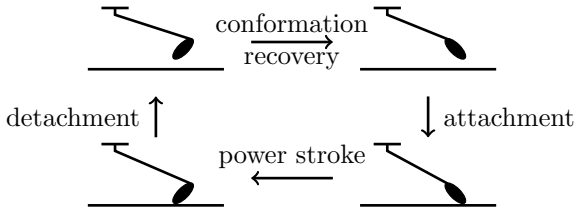

Figure 2.1 – Lymn-Taylor cycle representation. Each stage of the cycle can be seen as a change of chemical state.

Different levels of description of the actin-myosin interaction can be considered benefiting from the fact that the power stroke occurs much faster than the attachment and detachment processes.

2.2.2 Huxley'57 model

In his seminal work Huxley [1957], Huxley describes the myosin head with two chemical states representing the attached and detached configurations. Each myosin can interact with its closest actin site only. The transition rates – for attachment and detachment – depend only on the distance from the myosin head rest position to its nearest attachment site denoted by s. We denote by d_a the distance between two consecutive attachment sites. The distance s thus lies in an interval of width d_a, not necessarily symmetric but containing 0, that we denote by $[s^-, s^+]$ – see Figure 2.2.

Considering, in a population of myosin heads, the subset of heads with rest position located at distance s from their nearest attachment site, we define by $a(t, s)$ the ratio of

actually attached heads at time t. Equivalently, the ratio of detached heads is denoted by $d(s,t) = 1 - a(s,t)$, due to the assumption that both types of filaments are rigid. The sliding velocity $\dot{x}_c$ between the filaments is a macroscopic variable, hence independent of s and often quasi-static with respect to the microscopic time scales. We refer to Section 2.3.5 for an illustrating example of coupling between a macroscopic formulation and such a microscopic model.

The detached state is associated with a constant energy level w_0 and the attached state with an energy w_1 that depends on the distance s – the myosin head bound to actin is modeled as an elastic spring. This is where mechanics enters the model, and we point out that we extend here the original Huxley'57 model by allowing the spring to have a non-linear behavior. The myosin head is brought back to the initial detached energy level by the ATP energy input μ_T.

Transition rates between the states satisfy the detailed balance, i.e. for a transition i ($i = 1, 2$, see Figure 2.2) from a state of energy $w_j(s)$ to a state of energy $w_k(s)$, the forward and reverse rates – respectively denoted by k_i and k_{-i} – must satisfy the relation

$$\frac{k_i(s)}{k_{-i}(s)} = \exp\Big(\frac{w_k(s) - w_j(s)}{k_B T}\Big), \tag{2.1}$$

where k_B is the Boltzmann constant and T is the absolute temperature. A schematic of the model is presented in Figure 2.2.

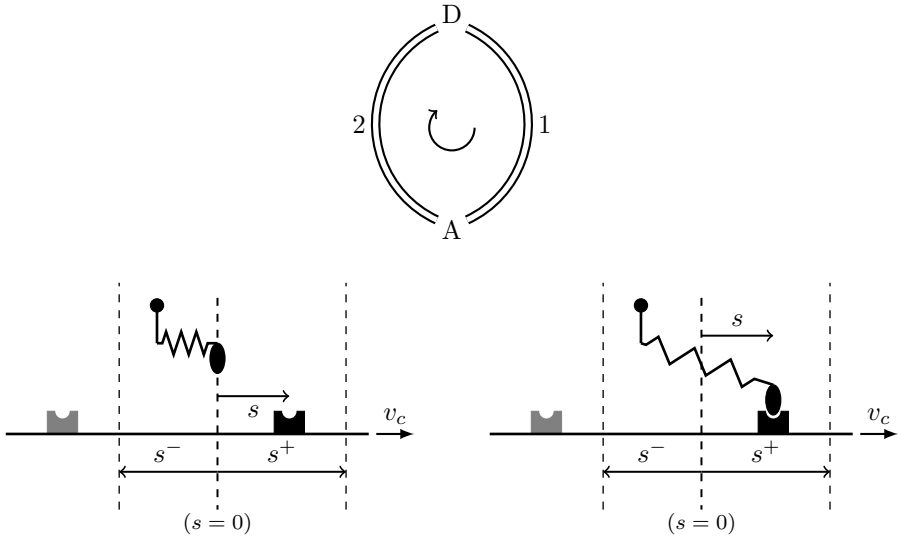

Figure 2.2 – Huxley'57 model representation. Top: definition of the transitions between the attached state (A) and the detached state (D). Bottom left: model parametrization, representation in the detached state. Bottom right: model parametrization, representation in the attached state. The position of the actin site corresponding to $s = 0$ is represented by a thick dashed line.

The conservation of matter, assuming that there is no coupling between the myosin heads, leads to the following dynamical system, for all $t > 0$ and all $s \in [s^-, s^+]$

$$\begin{cases} \dfrac{\partial a(s,t)}{\partial t} &= \Big(k_1(s) + k_{-2}(s)\Big)d(s,t) - \Big(k_2(s) + k_{-1}(s)\Big)a(s,t) - \dot{x}_c \dfrac{\partial a(s,t)}{\partial s} \\ \dfrac{\partial d(s,t)}{\partial t} &= \Big(k_2(s) + k_{-1}(s)\Big)a(s,t) - \Big(k_1(s) + k_{-2}(s)\Big)d(s,t) - \dot{x}_c \dfrac{\partial d(s,t)}{\partial s} \end{cases} \tag{2.2}$$

from adequate initial conditions $a(s,0) = a^0(s)$ and $d(s,0) = d^0(s)$, to be specified later. The assumption that the myosin head can only interact with its nearest actin site imposes

that the probability of being attached on the boundaries of the interval $[s^-, s^+]$ must be zero. Physically, the property $a(s^-, t) = a(s^+, t) = 0$ appears when the attachment rates $k_1(s)$ and $k_{-2}(s)$ vanish, while the detachment rates $k_{-1}(s)$ and $k_2(s)$ go to infinity on the boundaries of the interval $[s^-, s^+]$. Note that the energy levels and the transition rates are linked by the detailed balance (2.1), which implies that the energy of the attached level goes to infinity on the boundaries of the interval $[s^-, s^+]$. In a nutshell, the parameter functions must satisfy

$$\left|\begin{array}{l} \lim\limits_{s\to s^-} k_1(s) = \lim\limits_{s\to s^+} k_1(s) = \lim\limits_{s\to s^-} k_{-2}(s) = \lim\limits_{s\to s^+} k_{-2}(s) \quad = 0, \\ \lim\limits_{s\to s^-} \displaystyle\int_s^0 \big(k_{-1} + k_2\big)\mathrm{d}s = \lim_{s\to s^+} \int_0^s \big(k_{-1} + k_2\big)\mathrm{d}s = +\infty, \end{array}\right. \tag{2.3}$$

the second line enforcing that all heads are detached at the boundaries, see Section 2.3 (Equations (2.9) and (2.10)). This implies energetically that

$$\lim_{s\to s^-} w_1(s) = \lim_{s\to s^+} w_1(s) = +\infty.$$

Actin sites and myosin heads are located at discrete locations separated by regular intervals along their respective filaments. The spatial periodicities are, however, different on each filament. Therefore, for a large population of heads, the distribution of their distance to the nearest actin site can be assumed to be uniform in the interval $[s^-, s^+]$, and the average tension developed per myosin head is given by

$$\tau_c(t) = \frac{1}{d_a} \int_{s^-}^{s^+} a(s,t) \frac{\partial w_1}{\partial s}(s)\mathrm{d}s. \tag{2.4}$$

This force can then typically lead to a macroscopic active stress tensor and link to macroscale models of muscle tissue as presented in Chapelle et al. [2012] or in Section 2.3.5.

2.2.3 Extension of Huxley'57 model

To obtain a behavior closer to physiology, and in particular to capture the power stroke, various extensions of Huxley'57 model have been proposed Eisenberg and Hill [1978]; Eisenberg et al. [1980]; Huxley and Simmons [1971]; Piazzesi and Lombardi [1995]. These extensions can use more than two states to describe the myosin head and allow interactions with an arbitrary number of attachment sites. In this section, our objective is to present these models in a general form, albeit close to the initial 2-state Huxley's model, in particular concerning their general mathematical and mechanical properties.

Multi-state models – A general formulation of these models considers N_s chemical states $\{X_p\}_{1\leq p\leq N_s}$, that we can separate into two categories: attached states and detached states. The states are involved in N_r reactions between the states in the form

$$\mathrm{X_{p_i}} \underset{\mathrm{k_{-i}}}{\overset{\mathrm{k}_i}{\rightleftharpoons}} \mathrm{X_{q_i}}. \tag{2.5}$$

The collection of reactions between the states can be represented by a complete directed graph G. A complete directed graph is a set of vertices connected by edges, in which: edges have a direction; for each edge of the graph, the edge connecting the same vertices in the inverse direction also belongs to the graph; no vertex is connected to itself. We

respectively denote by V and E the sets of vertices and edges of the complete directed graph, and we write $G = (V, E)$. This graph is made of N_s vertices and $2N_r$ edges. A transition $X_{p_i} \to X_{q_i}$ is associated with the edge $E_{p_i q_i}$, whereas the reverse transition $X_{q_i} \to X_{p_i}$ is associated with the edge $E_{q_i p_i}$. The reaction presented in (2.5), which is bidirectional, is associated with the edges $E_{p_i q_i}$ and $E_{q_i p_i}$. The subsets of vertices corresponding to attached and detached states are respectively denoted by V_a and V_d.

The ratio of heads in state X_q located at s at time t is denoted by $x_q(s,t)$. We define the chemical flux between states X_{p_i} and X_{q_i} through transition i by

$$J_{p_i q_i}(s,t) = k_i(s) x_{p_i}(s,t) - k_{-i}(s) x_{q_i}(s,t).$$

Note that we have

$$J_{q_i p_i}(s,t) = -J_{p_i q_i}(s,t) = k_{-i}(s) x_{q_i}(s,t) - k_i(s) x_{p_i}(s,t).$$

The system dynamics is then governed by

$$\frac{\partial x_q}{\partial t}(s,t) = \sum_{p | E_{pq} \in G} J_{pq}(s,t) - \dot{x}_c \frac{\partial x_q}{\partial s}(s,t), \quad \forall q \in [\![1, N_s]\!].$$

The Huxley'57 model presented in Section 2.2.2 can naturally be seen as a particular case of multi-state models with only one attached state and one detached state. The graph G associated with the Huxley'57 model is given by

$$\begin{vmatrix} V = \{A, D\}, \\ V_\mathrm{a} = \{A\}, \\ V_\mathrm{d} = \{D\}, \\ E = \{E^1_{AD}, E^2_{AD}, E^1_{DA}, E^2_{DA}\}. \end{vmatrix}$$

Here, we use superscripts in the edges definition to denote that there are two reactions between the same vertices.

Multi-site models – In this further generalization, it is assumed that a myosin head can interact not only with its nearest actin site – located by definition at distance s – but also with all other actin sites located at distance $\{s + jd_a\}_{j \in \mathbb{Z}^*}$. A myosin head can thus be detached in state q – with a probability $x_q(s)$ – or attached in state q at a distance $s + jd_a$ of its rest position – with a probability $x_q(s + jd_a)$. We extend the definition of the ratio of heads in detached states by periodicity, i.e. if state q is a detached state $x_q(s + jd_a) = x_q(s)$, $\forall j$. We also refine the description of the graph defined for multi-site models, by splitting the set of edges E between the edges linking two detached states $\hat{E}$ and the remaining edges $\overline{E}$. We define the associated complete directed graphs $G_d = (V, \hat{E})$ and $G_a = (V, \overline{E})$. The system dynamics is governed by

$$\begin{cases} \dfrac{\partial x_q}{\partial t}(s + jd_a, t) = \displaystyle\sum_{p | E_{pq} \in G} J_{pq}(s + jd_a, t) - \dot{x}_c \frac{\partial x_q}{\partial s}(s + jd_a, t), \forall V_q \in V_\mathrm{a}, j \in \mathbb{Z}, \\ \dfrac{\partial x_q}{\partial t}(s, t) = \displaystyle\sum_{p | E_{pq} \in G_a} \sum_{j \in \mathbb{Z}} J_{pq}(s + jd_a, t) + \sum_{p | E_{pq} \in G_d} J_{pq}(s, t) - \dot{x}_c \frac{\partial x_q}{\partial s}(s, t), \forall V_q \in V_\mathrm{d}. \end{cases} \tag{2.6}$$

The ratios of attached head x_q for $V_q \in V_a$ are defined on $\mathbb{R}$ and must vanish at infinity. By contrast, the ratios of detached head x_q for $V_q \in V_d$ are defined on $[s^-, s^+]$ with periodic boundary conditions.

Example of a multi-state, multi-site model: Piazzesi-Lombardi'95 – A specific representative – denoted PL95 – of this family of models has been derived in Piazzesi and Lombardi [1995] with the aim of accounting for the energetics of muscle contraction. It describes the myosin head with five states arranged in two cycles of chemical reactions, see Figure 2.3. The five states are composed of three attached states A_1, A_2 and A_3 and two detached states D_1 and D_2. A first long cycle (cycle a) is meant to represent a complete power stroke, while a short cycle (cycle b) allows the myosin head to cycle at small or zero sliding velocity with incomplete power stroke.

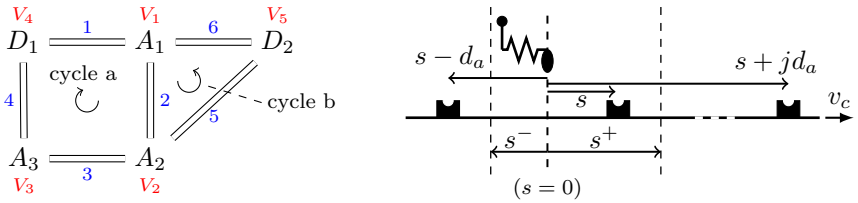

Figure 2.3 – Left: graph associated with the model Piazzesi-Lombardi'95. The vertex indices are given in red. The transition indices are given in blue. Right: Piazzesi-Lombardi'95 model parametrization. The position of the actin site corresponding to $s = 0$ is represented by a thick dashed line.

An energy μ_T is brought to the myosin head by ATP in the transitions $2 \to 5$ and $3 \to 4$.

The graph G associated with this model is given by

$$\begin{vmatrix} V = \{V_1, V_2, V_3, V_4, V_5\}, \\ V_{\mathrm{a}} = \{V_1, V_2, V_3\}, \\ V_{\mathrm{d}} = \{V_4, V_5\}, \\ E = \overline{E} = \{E_{12}, E_{21}, E_{23}, E_{32}, E_{34}, E_{43}, E_{41}, E_{14}, E_{25}, E_{52}, E_{51}, E_{15}\}. \end{vmatrix}$$

Moreover, it is assumed in this model that the myosin can attach to an arbitrary number of actin sites, hence it is also multi-site.

We denote by w_q the energy associated with the state of vertex q.

2.3 Model properties based on thermodynamics principles

2.3.1 From conservation of matter to boundary conditions and monotonicity properties

Let us consider the Huxley'57 model and derive its fundamental properties. System (2.2) was derived from the conservation of matter, hence we directly verify that for all (s,t), $a(s,t) + d(s,t) = 1$ as soon as we choose our initial condition $\forall s \in [s^-, s^+]$, $a^0(s) \in [0,1]$ and $d^0(s) = 1 - a^0(s)$, since

$$\forall s \in [s^-, s^+], \quad \frac{\mathrm{d}}{\mathrm{d}t}\big(a(s,t) + d(s,t)\big) = 0,$$

where we defined the total derivative by $\mathrm{d}/\mathrm{d}t(\bullet) = \partial/\partial t(\bullet) + \dot{x}_c \partial/\partial s(\bullet)$. Therefore, we can rewrite the system (2.2) in the form of a single equation

$$\frac{\partial a}{\partial t}(s,t) = k_+(s)\big(1 - a(s,t)\big) - k_-(s)a(s,t) - \dot{x}_c \frac{\partial a}{\partial s}(s,t), \tag{2.7}$$

where we denote the aggregated transition rates $k_+(s) = k_1(s) + k_{-2}(s)$ and $k_-(s) = k_2(s) + k_{-1}(s)$.

Boundary values – As explained in our model presentation, we expect the myosin head to only interact with the nearest actin site, which imposes that the probability of being attached must vanish on the boundaries of the interval $[s^-, s^+]$. However, the dynamics (2.2) is a first-order transport equation associated with only one boundary condition. Therefore, we can either consider one single Dirichlet boundary condition at one end of the interval – i.e., in s^- if $\dot{x}_c > 0$ and s^+ if $\dot{x}_c < 0$ – and then rely on the conditions (2.3) to obtain the proper value of the solution at the other end – as a property – or alternatively consider periodic boundary conditions. As the first option yields a periodic solution, it is clear that the two options are equivalent. However, they differ at the discrete level, in which case we will have to make a choice, see Section 2.4.1.

In fact, closed-form expressions can be obtained for the solution. To fix the ideas in this derivation, we consider the case $\dot{x}_c \geq 0$, although the same result can be obtained similarly for $\dot{x}_c < 0$. As $\dot{x}_c$ is assumed to be constant, the method of characteristic lines gives regular C^1 solutions from regular enough initial condition a^0. Considering $a(s,t)$ solution of (2.7), we define the function $\tilde{a}$ by

$$\tilde{a}(s,t) = a(s,t) \exp\Big(\frac{1}{\dot{x}_c} \int_0^s (k_+(\xi) + k_-(\xi))\, \mathrm{d}\xi\Big),$$

which satisfies the equation

$$\frac{\partial \tilde{a}}{\partial t}(s,t) + \dot{x}_c \frac{\partial \tilde{a}}{\partial s}(s,t) = k_+(s) e^{1/\dot{x}_c h(s)}, \tag{2.8}$$

where we define $h(s) = \int_0^s (k_+(\xi) + k_-(\xi))\, \mathrm{d}\xi$. Solving (2.8) along a characteristic line and pulling back the result to $a(s,t)$ we obtain, defining $t_0 = \max(0, t - \frac{s-s^-}{\dot{x}_c})$,

$$\begin{aligned} a(s,t) = a^0(s - \dot{x}_c t) \exp\Big(\frac{-1}{\dot{x}_c} \int_{s-\dot{x}_c t}^{s} \big(k_+(\xi) + k_-(\xi)\big)\, \mathrm{d}\xi\Big) \\ + \int_{t_0}^{t} k_+(s - \dot{x}_c t + \dot{x}_c \tau) \exp\Big(\frac{-1}{\dot{x}_c} \int_{s-\dot{x}_c t+\dot{x}_c\tau}^{s} \big(k_+(\xi) + k_-(\xi)\big)\, \mathrm{d}\xi\Big)\, \mathrm{d}\tau. \end{aligned} \tag{2.9}$$

We know that the aggregated attachment rate k_+ is a continuous function on $[s^-, s^+]$ and goes to zero on the boundaries of $[s^-, s^+]$. Therefore, under the condition on the aggregated detachment rate $\int_0^{s^+} k_-(\xi)\, \mathrm{d}\xi = \infty$, we deduce that

$$\lim_{s \to s^+} a(s,t) = 0 \tag{2.10}$$

using the dominated convergence theorem for the second term of (2.9). Likewise, the property $\lim_{s\to s^-} a(s,t) = 0$ is obtained for $\dot{x}_c < 0$, and a similar result can be obtained in a similar manner with periodic boundary conditions.

Positivity and boundedness properties – We want to check that the solution has values consistent with ratio quantities. More specifically, we want that, with an initial condition $a^0(s) \in [0,1]$, the property $a(s,t) \in [0,1]$ holds. Again, we rely on the solution obtained by the method of characteristic lines (2.9). As the transition rates and the initial condition are positive, we find that $a(s,t) \geq 0$. Then, noting that $1 - a(s,t)$ is governed by an equation of the same form as (2.7) with the initial condition $1 - a^0(s) \geq 0$, we similarly deduce that $a(s,t) \leq 1$.

2.3.2 First principle

We now want to establish a first thermodynamic property of the Huxley'57 system (2.2), namely, a first principle, and in this respect we follow the approach proposed by Hill [1977]. We consider a system made of a population of myosin heads and define the average energy per myosin head, namely

$$\mathcal{U}(t) = \frac{1}{d_a} \int_{s^-}^{s^+} \Big[w_1(s) a(s,t) + w_0 d(s,t) \Big] \, \mathrm{d}s. \tag{2.11}$$

We then define the chemical fluxes

$$\left| \begin{aligned} J_1(s,t) &= k_1(s) d(s,t) - k_{-1}(s) a(s,t), \\ J_2(s,t) &= k_2(s) a(s,t) - k_{-2}(s) d(s,t). \end{aligned} \right.$$

We will henceforth make the natural assumption that the reaction rates are chosen in order for $w_1 a$, $k_2 a$ and $k_{-1} a$ to tend to zero when s tends to s^- and s^+, with the physical interpretation that no finite energy ($w_1 a$) is stored and no detachment flux ($k_2 a$ and $k_{-1} a$) occurs at the ends of the interval. We will see in Section 2.5 that this assumption is easily satisfied in practice when (2.3) holds. Then, computing the time derivative, we obtain

$$\begin{aligned} \frac{\mathrm{d}}{\mathrm{d}t}\mathcal{U}(t) &= \frac{1}{d_a} \int_{s^-}^{s^+} \Big[w_1(s) \frac{\partial a(s,t)}{\partial t} + w_0 \frac{\partial d(s,t)}{\partial t} \Big] \, \mathrm{d}s \\ &= \frac{1}{d_a} \int_{s^-}^{s^+} \Big[\left(J_1(s,t) - J_2(s,t) \right) w_1(s) - w_1(s) \, \dot{x}_c \frac{\partial a(s,t)}{\partial s} \\ &\qquad + \left(J_2(s,t) - J_1(s,t) \right) w_0 - w_0 \dot{x}_c \frac{\partial d(s,t)}{\partial s} \Big] \, \mathrm{d}s. \end{aligned}$$

Using integrations by parts for the transport terms, the boundary properties of the solution – $w_1(s)a(t,s^-) = w_1(s)a(t,s^+) = 0$ and $d(t,s^-) = d(t,s^+)$ – and considering that detachment is associated with the consumption of one ATP, we obtain

$$\begin{aligned} \frac{\mathrm{d}}{\mathrm{d}t}\mathcal{U}(t) = \frac{1}{d_a} \int_{s^-}^{s^+} \Big[&\left(w_1(s) - w_0 \right) J_1(s,t) + \left(w_0 - \left(w_1(s) + \mu_T \right) \right) J_2(s,t) \\ &+ \dot{x}_c \, a(s,t) \frac{\partial w_1(s)}{\partial s} \Big] \, \mathrm{d}s + \mu_T \overline{J_2}(t), \end{aligned}$$

where we denoted by

$$\overline{J_2}(t) = \frac{1}{d_a} \int_{s^-}^{s^+} J_2(s,t) \, \mathrm{d}s$$

the mean net influx of ATP. Finally, we derive the following formulation of the first principle

$$\dot{\mathcal{U}}(t) = \dot{\mathcal{W}}(t) + \dot{\mathcal{E}}(t) + \dot{\mathcal{Q}}(t),$$

where

$$\left|\begin{aligned}\dot{\mathcal{W}}(t) &= \dot{x}_c \tau_c(t), && \text{(2.12a)}\\ \dot{\mathcal{E}}(t) &= \mu_T \overline{J_2}(t), && \text{(2.12b)}\\ \dot{\mathcal{Q}}(t) &= \frac{1}{d_a}\int_{s^-}^{s^+} \Big[\left(w_1(s) - w_0\right) J_1(s,t) + \left(w_0 - \left(w_1(s) + \mu_T\right)\right) J_2(s,t) \Big] \,\mathrm{d}s, && \text{(2.12c)}\end{aligned}\right.$$

with the active force τ_c defined in (2.4). The quantity $\dot{\mathcal{W}}$ is the rate of work given to the system and $\dot{\mathcal{E}}(t) = \mu_T \overline{J_2}(t)$ corresponds to the input flux in energy brought by ATP hydrolysis. The remaining term $\dot{\mathcal{Q}}$ can be identified with a heat flux. In steady-state shortening ($\tau_c > 0$ and $\dot{x}_c < 0$), the work is negative and in physiological conditions, we expect the energy input term to be positive, and the heat transfer to be negative (see numerical illustrations in Section 2.5). The energy balance can be interpreted as follows: the energy brought by ATP is for one part converted into work, the other part being dissipated as heat production.

2.3.3 Second principle

Let us now derive a second principle thermodynamic balance. We introduce the system entropy as

$$\mathcal{S}(t) = -\frac{k_B}{d_a}\int_{s^-}^{s^+} \Big[a(s,t)\ln(a(s,t)) + d(s,t)\ln(d(s,t)) \Big] \,\mathrm{d}s,$$

where k_B is the Boltzmann constant. The system remains at a constant temperature, the outside environment playing the role of a thermostat. We introduce the Helmholtz free energy

$$\mathcal{F}(t) = \mathcal{U}(t) - T\mathcal{S}(t),$$

which therefore corresponds to

$$\mathcal{F}(t) = \frac{1}{d_a}\int_{s^-}^{s^+} \Big[\mu_1(s,t)a(s,t) + \mu_0(s,t)d(s,t) \Big] \,\mathrm{d}s. \tag{2.13}$$

where

$$\left|\begin{aligned}\mu_1(s,t) &= w_1(s) + k_B T \ln(a(s,t)),\\ \mu_0(s,t) &= w_0 + k_B T \ln(d(s,t)),\end{aligned}\right.$$

are the chemical potentials. Computing the time derivative, we get

$$\begin{aligned}\frac{\mathrm{d}}{\mathrm{d}t}\mathcal{F}(t) = \frac{1}{d_a}\int_{s^-}^{s^+} \Big[&\Big(J_1(s,t) - J_2(s,t) - \dot{x}_c \frac{\partial}{\partial s} a(s,t) \Big) \cdot \left[w_1(s) + k_B T \ln(a(s,t)) + k_B T \right]\\ &+ \Big(J_2(s,t) - J_1(s,t) - \dot{x}_c \frac{\partial}{\partial s} d(s,t) \Big) \cdot \left[w_0 + k_B T \ln(d(s,t)) + k_B T \right] \Big] \,\mathrm{d}s. \end{aligned} \tag{2.14}$$

Using again integrations by part for the transport terms and the boundary properties of the solution, we obtain

$$\frac{\mathrm{d}}{\mathrm{d}t}\mathcal{F}(t) = \tau_c(t)\dot{x}_c + \mu_T\overline{J_2}(t) + \frac{1}{d_a}\int_{s^-}^{s^+}\Big[J_2(s,t)\Big(\mu_0(s,t) - \big(\mu_1(s,t)+\mu_T\big)\Big) + J_1(s,t)\Big(\mu_1(s,t)-\mu_0(s,t)\Big)\Big]\,\mathrm{d}s. \quad (2.15)$$

Independently, we also have

$$\frac{\mathrm{d}}{\mathrm{d}t}\mathcal{F}(t) = \frac{\mathrm{d}}{\mathrm{d}t}\mathcal{U}(t) - T\frac{\mathrm{d}}{\mathrm{d}t}\mathcal{S}(t). \quad (2.16)$$

Combining equations (2.15) and (2.16) and the first principle, we can write

$$\frac{\mathrm{d}}{\mathrm{d}t}\mathcal{S}(t) = \frac{\dot{\mathcal{Q}}(t)}{T} - \frac{1}{T}\frac{1}{d_a}\int_{s^-}^{s^+} J_2(s,t)\Big(\mu_0(s,t) - \big(\mu_1(s,t)+\mu_T\big)\Big) + J_1(s,t)\Big(\mu_1(s,t)-\mu_0(s,t)\Big)\,\mathrm{d}s. \quad (2.17)$$

The second principle then reads

$$\frac{\mathrm{d}}{\mathrm{d}t}\mathcal{S}(t) = \frac{\dot{\mathcal{Q}}(t)}{T} + \dot{\mathcal{S}}_{\mathrm{prod}}(t), \quad (2.18)$$

where we naturally associate the second term of (2.17) with the entropy production $\dot{\mathcal{S}}_{\mathrm{prod}}(t)$.

The model will be compatible with the second principle if this entropy production is always positive. Using the relation (2.1) deduced from the detailed balance, we recall that

$$\frac{k_1(s,t)}{k_{-1}(s,t)} = \exp\Big(\frac{w_0 - w_1(s,t)}{k_BT}\Big) \qquad \frac{k_2(s,t)}{k_{-2}(s,t)} = \exp\Big(\frac{w_1(s,t)+\mu_T - w_0}{k_BT}\Big). \quad (2.19)$$

Thus, when introducing the ratio of the one-way fluxes for transition 1, J_{1+} and J_{1-}, defined by $J_{1+}(s,t) = k_1(s,t)d(s,t)$ and $J_{1-}(s,t) = k_{-1}(s,t)a(s,t)$, we find

$$\begin{aligned}\frac{J_{1+}}{J_{1-}} &= \frac{k_1(s)d(s,t)}{k_{-1}(s)a(s,t)} \\ &= \exp\Big(\frac{w_0 - w_1(s,t)}{k_BT}\Big)\cdot\exp\Big(k_BT\Big[\frac{\ln(d(s,t)) - \ln(a(s,t))}{k_BT}\Big]\Big) \\ &= \exp\Big(\frac{\mu_0(s,t)-\mu_1(s,t)}{k_BT}\Big).\end{aligned} \quad (2.20)$$

As a consequence, we have two cases. If $\mu_1(s,t) \geq \mu_0(s,t)$, we find that

$$\frac{J_{1+}}{J_{1-}}(s,t) \leq 1 \Rightarrow J_1(s,t) = J_{1+}(s,t) - J_{1-}(s,t) \leq 0.$$

Conversely, $\mu_1(s,t) \leq \mu_0(s,t)$ implies that $J_1(s,t) \geq 0$. Proceeding in the same way for the second reaction, we finally have

$$\begin{vmatrix} J_1(s,t)\big(\mu_1(s,t)-\mu_0(s,t)\big) \leq 0, \\ J_2(s,t)\big(\mu_0(s,t)-\mu_1(s,t)-\mu_T\big) \leq 0. \end{vmatrix} \quad (2.21)$$

We thus obtain the conclusion that the entropy production term

$$\dot{\mathcal{S}}_{\text{prod}}(t) = -\frac{1}{Td_a}\int_{s^-}^{s^+} J_2(s,t)\Big(\mu_0(s,t) - \big(\mu_1(s,t)+\mu_T\big)\Big) + J_1(s,t)\Big(\mu_1(s,t)-\mu_0(s,t)\Big)\,\mathrm{d}s \geq 0, \quad (2.22)$$

hence that the model is compatible with the second principle. We can summarize this property using (2.15) by the free energy balance

$$\frac{\mathrm{d}}{\mathrm{d}t}\mathcal{F}(t) = \tau_c(t)\dot{x}_c + \mu_T\overline{J_2}(t) - T\dot{\mathcal{S}}_{\text{prod}}(t) \leq \tau_c(t)\dot{x}_c + \mu_T\overline{J_2}(t). \quad (2.23)$$

2.3.4 Extension to multi-state, multi-site models

Let us now consider the Piazzesi-Lombardi'95 model. We want to establish the thermodynamic balances associated with this model.

Fundamental properties of the solution – in particular the monotonicity properties of the results established for the Huxley'57 model, see Section 2.3.1 – can be extended to this model. In particular, conservation of matter here reads

$$\forall s \in [s^-, s^+]\ \ \frac{\mathrm{d}}{\mathrm{d}t}\left[\sum_{V_q\in V_\mathrm{a}}\sum_{j\in\mathbb{Z}} x_q(s+jd_a,t) + \sum_{V_q\in V_\mathrm{d}} x_q(s,t)\right] = 0. \quad (2.24)$$

First principle – We define the energy as

$$\mathcal{U}(t) = \frac{1}{d_a}\int_{s^-}^{s^+}\left[\sum_{V_q\in V_\mathrm{a}}\sum_{j\in\mathbb{Z}} x_q(s+jd_a,t)w_q(s+jd_a) + \sum_{V_q\in V_\mathrm{d}} x_q(s,t)w_q\right]\mathrm{d}s.$$

The time derivative reads, after integrating by parts the transport term

$$\frac{\mathrm{d}}{\mathrm{d}t}\mathcal{U}(t) = \frac{1}{d_a}\int_{s^-}^{s^+}\sum_{E_{pq}\in G}\sum_{j\in\mathbb{Z}} J_{pq}(s+jd_a,t)W_{pq}(s+jd_a)\,\mathrm{d}s + \dot{x}_c\tau_c(t),$$

with $W_{pq} = w_q - w_p$ and the active force defined as

$$\tau_c(t) = \frac{1}{d_a}\int_{s^-}^{s^+}\sum_{V_q\in V_\mathrm{a}}\sum_{j\in\mathbb{Z}} x_q(s+jd_a,t)\frac{\partial w_q}{\partial s}(s+jd_a)\,\mathrm{d}s.$$

We then obtain

$$\frac{\mathrm{d}}{\mathrm{d}t}\mathcal{U}(t) = \mu_T\big(\overline{J_{25}}(t) + \overline{J_{34}}(t)\big) + \dot{x}_c\tau_c(t) + \frac{1}{d_a}\int_{s^-}^{s^+}\sum_{E_{pq}\in G}\sum_{j\in\mathbb{Z}} J_{pq}(s+jd_a,t)\tilde{W}_{pq}(s+jd_a)\,\mathrm{d}s,$$

where the mean fluxes are given by

$$\overline{J_{pq}}(t) = \frac{1}{d_a} \int_{s^-}^{s^+} \sum_{j\in\mathbb{Z}} J_{pq}(s + jd_a, t)\,\mathrm{d}s,$$

and $\tilde{W}_{pq} = W_{pq} - \mu_T \delta_{pq=\{25,34\}}$ as an energy μ_T is brought to the myosin head by ATP during the transitions $2 \to 5$ and $3 \to 4$. Note that the introduction of the modified energy increments $\tilde{W}$ brings out the input energy fluxes $\mu_T\big(\overline{J_{25}}(t) + \overline{J_{34}}(t)\big)$. The first principle then naturally reads

$$\dot{U}(t) = \dot{\mathcal{W}}(t) + \dot{\mathcal{E}}(t) + \dot{\mathcal{Q}}(t), \tag{2.25}$$

with

$$\left|\begin{array}{l} \dot{\mathcal{W}}(t) = \dot{x}_c \tau_c(t), \\ \dot{\mathcal{E}}(t) = \mu_T\big(\overline{J_{25}}(t) + \overline{J_{34}}(t)\big), \\ \dot{\mathcal{Q}}(t) = \dfrac{1}{d_a} \displaystyle\int_{s^-}^{s^+} \sum_{E_{pq}\in G} \sum_{j\in\mathbb{Z}} J_{pq}(s + jd_a, t)\tilde{W}_{pq}(s + jd_a)\,\mathrm{d}s. \end{array}\right.$$

Second principle – Following the work done for the Huxley'57 model, we here define the entropy of the system as

$$\mathcal{S}(t) = -\frac{k_B}{d_a} \int_{s^-}^{s^+} \sum_{V_q\in V_\mathrm{a}} \sum_{j\in\mathbb{Z}} x_q(s + jd_a, t) \ln(x_q(s + jd_a, t)) + \sum_{V_q\in V_\mathrm{d}} x_q(s, t) \ln(x_q(s, t))\,\mathrm{d}s.$$

Then, we define the Helmholtz free energy as $\mathcal{F}(t) = \mathcal{U}(t) - T\mathcal{S}(t)$, which can be written as

$$\mathcal{F}(t) = \frac{1}{d_a} \int_{s^-}^{s^+} \sum_{V_q\in V_\mathrm{a}} \sum_{j\in\mathbb{Z}} \mu_q(s + jd_a, t) x_q(s + jd_a, t) + \sum_{V_q\in V_\mathrm{d}} \mu_q(s, t) x_q(s, t)\,\mathrm{d}s,$$

with the definitions

$$\left|\begin{array}{l} \mu_q(s + jd_a, t) = w_q(s + jd_a) + k_B T \ln(x_q(s + jd_a, t)),\ \forall V_q \in V_\mathrm{a},\ j \in \mathbb{Z}, \\ \mu_q(s, t) = w_q(s) + k_B T \ln(x_q(s, t)),\ \forall V_q \in V_\mathrm{d}. \end{array}\right.$$

We here define the entropy production as

$$\dot{\mathcal{S}}_\mathrm{prod}(t) = -\frac{1}{Td_a} \int_{s^-}^{s^+} \sum_{E_{pq}\in G} \sum_{j\in\mathbb{Z}} J_{pq}(s + jd_a, t)\tilde{M}_{pq}(s + jd_a, t)\,\mathrm{d}s,$$

where $\tilde{M}_{pq} = \mu_q - \mu_p - \mu_T \delta_{pq=\{34,25\}}$. Then, combining the first principle (2.25) with the identity $\dot{F} = \dot{U} - T\dot{S}$, we finally obtain the second principle

$$\frac{\mathrm{d}}{\mathrm{d}t}\mathcal{S}(t) = \frac{\dot{\mathcal{Q}}(t)}{T} + \dot{\mathcal{S}}_\mathrm{prod}(t).$$

Similarly as in the Huxley'57 model, the detailed balance ensures that the entropy production is always positive and the model is thus thermodynamically compatible. We have, as in (2.23), the free energy balance

$$\frac{\mathrm{d}}{\mathrm{d}t}\mathcal{F}(t) = \tau_c(t)\dot{x}_c + \mu_T\big(\overline{J_{25}}(t) + \overline{J_{34}}(t)\big) - T\dot{\mathcal{S}}_{\mathrm{prod}}(t)$$
$$\leq \tau_c(t)\dot{x}_c + \mu_T\big(\overline{J_{25}}(t) + \overline{J_{34}}(t)\big). \quad (2.26)$$

2.3.5 Coupling with a macroscopic model of muscle fiber

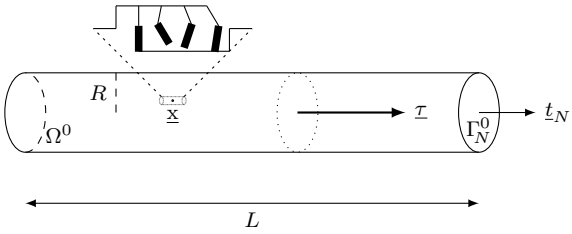

Figure 2.4 – Muscle fiber configuration.

The thermodynamic properties of these classes of models are very useful when coupling them with a macroscopic model, typically to represent a muscle fiber, as it will ensure a global consistent thermodynamic balance between macroscopic and microscopic contributions. Let us consider, indeed, a macroscopic model of muscle fiber modeled in the realm of non-linear continuum mechanics, as large deformations frequently occur in muscle fibers. The material points coordinates are denoted by $\underline{\mathrm{x}} \in \Omega^0$ in the reference configuration. The displacement field associated with the deformation map is denoted by $\underline{y}$. We denote by $\underline{\underline{e}}$ the Green-Lagrange strain tensor, i.e.

$$\underline{\underline{e}} = \frac{1}{2}\Big(\nabla\underline{y} + (\nabla\underline{y})^{\mathsf{T}} + (\nabla\underline{y})^{\mathsf{T}} \cdot \nabla\underline{y}\Big),$$

and the second Piola-Kirchhoff stress tensor is denoted by $\underline{\underline{\Sigma}}$. The fiber as shown in Figure 2.4 is subjected to a boundary force $\underline{t}_N$ on a boundary Γ_N^0. The principle of virtual work (PVW) then reads: for any admissible virtual displacement field $\underline{w} \in \mathscr{V}_{\mathrm{ad}}$,

$$\int_{\Omega^0} \rho_0 \ddot{\underline{y}} \cdot \underline{w}\,\mathrm{d}\Omega + \int_{\Omega^0} \underline{\underline{\Sigma}} : \mathrm{d}_{\underline{y}}\underline{\underline{e}} \cdot \underline{w}\,\mathrm{d}\Omega = \int_{\Gamma_N^0} \underline{t}_N \cdot \underline{w}\,\mathrm{d}\Gamma,$$

where the differential of the Green-Lagrange strain tensor with respect to the displacement field is given by

$$\mathrm{d}_{\underline{y}}\underline{\underline{e}} \cdot \underline{w} = \frac{1}{2}\Big(\nabla\underline{w} + (\nabla\underline{w})^{\mathsf{T}} + (\nabla\underline{y})^{\mathsf{T}} \cdot \nabla\underline{w} + (\nabla\underline{w})^{\mathsf{T}} \cdot \nabla\underline{y}\Big).$$

In this formulation, we want to associate with each material point an active microscopic model based on the Huxley'57 model or its extensions. Typically, we want to incorporate the microscopic model into a 3D visco-hyperelastic constitutive behavior of hyperelastic potential Ψ and viscous pseudo-potential Ψ^v – taken here as $\Psi^v(\underline{\underline{\dot{e}}}) = \frac{\eta}{2}\mathrm{tr}(\underline{\underline{\dot{e}}}^2)$ – where η denotes a viscosity modulus – to simplify the presentation. Following Chapelle et al. [2012], which extends the classical Hill-Maxwell scheme Hill [1938] to nonlinear behavior, we gather all the constitutive ingredients by defining an adequate rheological scheme – presented in Figure 2.5 – valid for large deformations. The upper branch represents

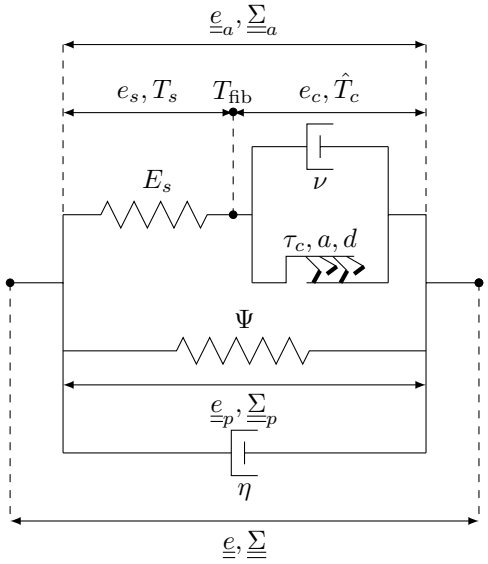

Figure 2.5 – Fiber rheology combining a 1D active element (upper branch) and a 3D visco-hyperelastic element (lower branch).

the sarcomere – including the above active behavior visualized by the collection of myosin heads in the figure – namely, constituents acting in the muscle fibre direction $\underline{\tau}$. The lower branch represents a 3D passive matrix, associated with the cellular envelope and the extracellular matrix. Each branch contains elastic and viscous constituents, respectively visualized by springs and dashpots, with specific constitutive equations given below.

We consider the following natural rheological rule for the parallel branch

$$\text{3D parallel law} : \underline{\underline{e}} = \underline{\underline{e}}_p = \underline{\underline{e}}_a, \quad \underline{\underline{\Sigma}} = \underline{\underline{\Sigma}}_p + \underline{\underline{\Sigma}}_a, \tag{2.27}$$

where $\underline{\underline{e}}$, $\underline{\underline{e}}_a$, $\underline{\underline{e}}_p$ denote Green-Lagrange tensors (global, active and passive) and $\underline{\underline{\Sigma}}$, $\underline{\underline{\Sigma}}_a$, $\underline{\underline{\Sigma}}_p$ second Piola-Kirchhoff stress tensors (global, active and passive). However, we will depart from Chapelle et al. [2012] for the series branch.

In fact, the natural view of muscle fibers made of a succession of active and passive segments points to a one-dimensional homogenization type of rheological interpretation. Let us denote by e_{fib} the total (local) extension of a fiber, i.e the ratio of length change over initial length

$$e_{\text{fib}} = \frac{\delta \ell_{hs}}{\ell_{hs}},$$

where we will take for ℓ_{hs} the length of a half-sarcomere at rest and $\delta \ell_{hs}$ the variation thereof. Then, the length change of the half-sarcomere can be decomposed into

$$\delta \ell_{hs} = x_c + \delta \ell_s,$$

where x_c and $\delta \ell_s$ respectively denote the contributions of the active (rigid filaments) and passive parts in this length change. Note that x_c then represents the relative displacement of the actin and myosin filaments considered above, indeed. We also introduce the corresponding dimensionless extension quantities $e_c = x_c/\ell_{hs}$ and $e_s = x_c/\ell_{hs}$, so that $e_{\text{fib}} = e_c + e_s$. Of course, the two components carry the same tension, which we denote by T_{fib} and define as the force – in the fiber direction – per unit area of transverse cross-section of tissue considered in the reference configuration. Therefore, we can summarize as

$$\text{1D series law} : e_{\text{fib}} = e_c + e_s, \quad T_{\text{fib}} = \hat{T}_c = T_s. \tag{2.28}$$

Note that the reason why such a simple additive rule holds for e_{fib} in this nonlinear framework is that we are considering extension quantities – scaled in an ad hoc manner – and not Green-Lagrange strains. Moreover, (2.28) must be complemented by relationships between 3D and 1D quantities. Considering the component of the Green-Lagrange strain tensor in the fiber direction, we directly have

$$1 + e_{\text{fib}} = \left(1 + 2\underline{\tau} \cdot \underline{\underline{e}} \cdot \underline{\tau}\right)^{\frac{1}{2}}. \tag{2.29}$$

Then, the tension T_{fib} corresponds to a contribution in the first Piola-Kirchhoff stress tensor given by

$$\underline{\underline{T}}_a = T_{\text{fib}} \frac{\underline{\underline{F}} \cdot \underline{\tau}}{\|\underline{\underline{F}} \cdot \underline{\tau}\|} \otimes \underline{\tau}, \tag{2.30}$$

where $\underline{\underline{F}} = \underline{\underline{1}} + \nabla \underline{y}$ is the classical deformation gradient tensor, as can be easily verified by computing the resulting traction in the fiber direction $\underline{\underline{T}}_a \cdot \underline{\tau}$. Hence, the associated contribution in the second Piola-Kirchhoff stress tensor reads

$$\underline{\underline{\Sigma}}_a = \underline{\underline{F}}^{-1} \cdot \underline{\underline{T}}_a = \frac{T_{\text{fib}}}{1 + e_{\text{fib}}} \underline{\tau} \otimes \underline{\tau}, \tag{2.31}$$

since $\|\underline{\underline{F}} \cdot \underline{\tau}\| = 1 + e_{\text{fib}}$.

Finally, the constitutive equations considered are

$$\underline{\underline{\Sigma}}_p = \frac{\partial \Psi}{\partial \underline{\underline{e}}} + \frac{\partial \Psi^v}{\partial \dot{\underline{\underline{e}}}}, \quad T_s = E_s e_s, \quad \hat{T}_c = \nu \dot{e}_c + T_c, \tag{2.32}$$

where $\check{T}_c$ represents the aggregation of forces contributed by actin-myosin cross-bridges as described above, i.e. $\check{T}_c = \rho_{\text{surf}} \tau_c$ with ρ_{surf} the number of myosin heads in a layer of thickness ℓ_{hs} per unit of cross-section area. The series elastic element is here assumed to have a linear constitutive equation of elasticity modulus E_s. Note that a nonlinear hyperelastic behavior could be considered, at the price of having to deal with the dimensionless extension e_s as an additional internal variable. Nevertheless, in physiological conditions the extension e_s remains small and a linear behavior is adequate Caruel et al. [2019]. As regards viscosity, we here incorporate a simple component of viscous modulus ν in parallel with the active part in the sarcomere branch, and we recall that viscosity is also present in the parallel branch as provided by the term $\frac{\partial \Psi^v}{\partial \dot{\underline{\underline{e}}}} = \eta \dot{\underline{\underline{e}}}$.

We can now summarize the 3D equations as

$$\begin{cases} \displaystyle\int_{\Omega^0} \rho_0 \ddot{\underline{y}} \cdot \underline{w} \, \mathrm{d}\Omega + \int_{\Omega^0} \underline{\underline{\Sigma}} : \mathrm{d}_{\underline{y}} \underline{\underline{e}} \cdot \underline{w} \, \mathrm{d}\Omega = \int_{\Gamma_N^0} \underline{t}_N \cdot \underline{w} \, \mathrm{d}\Gamma, \quad \forall \underline{w} \in \mathscr{V}_{\text{ad}} & \text{(2.33a)} \\ \quad \text{with } \underline{\underline{\Sigma}} = \dfrac{\partial \Psi}{\partial \underline{\underline{e}}} + \eta \dot{\underline{\underline{e}}} + \dfrac{T_{\text{fib}}}{(1 + 2\underline{\tau} \cdot \underline{\underline{e}} \cdot \underline{\tau})^{\frac{1}{2}}} \underline{\tau} \otimes \underline{\tau} & \\ T_{\text{fib}} = \nu \dot{e}_c + T_c = E_s e_s & \text{(2.33b)} \\ \quad \text{with } T_c(\underline{\mathrm{x}}, t) = \dfrac{\rho_{\text{surf}}}{d_a} \displaystyle\int_{s^-}^{s^+} a(\underline{\mathrm{x}}, s, t) \frac{\partial w_1}{\partial s}(s, t) \mathrm{d}s & \\ \dfrac{\partial a}{\partial t}(\underline{\mathrm{x}}, s, t) = k_+(s)\big(1 - a(\underline{\mathrm{x}}, s, t)\big) - k_-(s) a(\underline{\mathrm{x}}, s, t) - \ell_{hs} \dot{e}_c(\underline{\mathrm{x}}, t) \dfrac{\partial a}{\partial s}(\underline{\mathrm{x}}, s, t) & \text{(2.33c)} \end{cases}$$

where (2.33c) is based on the Huxley'57 model with sliding velocity $\dot{x}_c = \ell_{hs} \dot{e}_c$. This velocity is independent of the microscopic variable s, which justifies our above study. Note, however, the dependency of $a(\underline{\mathrm{x}}, s, t)$ on $\underline{\mathrm{x}}$, which means that the microscopic model must

be solved everywhere in the domain, i.e. at all numerical quadrature points in numerical simulations.

In order to establish a macroscopic energy balance for the system (2.33), we take the velocity field $\underline{\dot{y}}$ as an admissible virtual displacement field in (2.33a). We thus get

$$\frac{\mathrm{d}\mathcal{K}}{\mathrm{d}t} + \int_{\Omega^0} \underline{\underline{\Sigma}} : \underline{\underline{\dot{e}}}\,\mathrm{d}\Omega = \mathcal{P}_{\text{ext}},$$

where $\mathcal{K} = \frac{1}{2}\int_{\Omega^0} \rho_0 |\underline{\dot{y}}|^2\,\mathrm{d}\Omega$ stands for the kinetic energy and $\mathcal{P}_{\text{ext}} = \int_{\Gamma_N^0} \underline{t}_N \cdot \underline{\dot{y}}\,\mathrm{d}\Gamma$ is the power of external forces. Then, we decompose

$$\int_{\Omega^0} \underline{\underline{\Sigma}} : \underline{\underline{\dot{e}}}\,\mathrm{d}\Omega = \frac{\mathrm{d}}{\mathrm{d}t}\left[\int_{\Omega^0} \Psi\,\mathrm{d}\Omega\right] + \int_{\Omega^0} \eta |\underline{\underline{\dot{e}}}|^2\,\mathrm{d}\Omega + \int_{\Omega^0} T_{\text{fib}} \frac{\underline{\tau}\cdot\underline{\underline{\dot{e}}}\cdot\underline{\tau}}{(1+2\underline{\tau}\cdot\underline{\underline{e}}\cdot\underline{\tau})^{\frac{1}{2}}}\,\mathrm{d}\Omega,$$

where the first term is associated with the stored hyperelastic energy, the second term is a macroscopic viscous dissipation, and the last term – denoted $\mathcal{P}_{\text{fib}}$ – is the power of internal forces in the sarcomere. Then, using the rheological rules we find

$$\begin{aligned}
\mathcal{P}_{\text{fib}} &= \int_{\Omega^0} T_{\text{fib}} \frac{\underline{\tau}\cdot\underline{\underline{\dot{e}}}\cdot\underline{\tau}}{(1+2\underline{\tau}\cdot\underline{\underline{e}}\cdot\underline{\tau})^{\frac{1}{2}}}\,\mathrm{d}\Omega \\
&= \int_{\Omega^0} T_{\text{fib}}\dot{e}_{\text{fib}}\,\mathrm{d}\Omega = \int_{\Omega^0} \left[T_s\dot{e}_s + \hat{T}_c\dot{e}_c\right]\mathrm{d}\Omega = \int_{\Omega^0} \left[E_s e_s \dot{e}_s + \nu\dot{e}_c^2 + T_c\dot{e}_c\right]\mathrm{d}\Omega \\
&= \underbrace{\frac{\mathrm{d}}{\mathrm{d}t}\left[\int_{\Omega^0} \frac{E_s}{2} e_s^2\,\mathrm{d}\Omega\right]}_{(1)} + \underbrace{\int_{\Omega^0} \nu\dot{e}_c^2\,\mathrm{d}\Omega}_{(2)} + \underbrace{\int_{\Omega^0} T_c\dot{e}_c\,\mathrm{d}\Omega}_{(3)},
\end{aligned}$$

where we recognize (1) an elastic energy stored in the series element of the sarcomere, (2) a viscous dissipation term in the sarcomere, and (3) the mechanical work of the actin-myosin bridges. Therefore, combining this energy balance with the free energy balance (2.23) computed from the Huxley'57 model – or identically from (2.26) for the extensions – we finally obtain a form of macroscopic Clausius-Duhem relation

$$\begin{aligned}
\frac{\mathrm{d}}{\mathrm{d}t}\left[\mathcal{K} + \int_{\Omega^0} \Psi + \frac{E_s}{2} e_s^2 \; + \rho_v \mathcal{F}\,\mathrm{d}\Omega\right] \\
= \mathcal{P}_{\text{ext}} - \int_{\Omega^0} \left[\eta|\underline{\underline{\dot{e}}}|^2 + \nu\dot{e}_c^2\right]\mathrm{d}\Omega - \int_{\Omega^0} \rho_v T \dot{\mathcal{S}}_{\text{prod}}\,\mathrm{d}\Omega + \int_{\Omega^0} \rho_v \dot{\mathcal{E}}\,\mathrm{d}\Omega, \quad (2.34)
\end{aligned}$$

where $\rho_v = \rho_{\text{surf}}/\ell_{hs}$ is the density of myosin head per unit volume in the reference configuration, and where we recall that $\mathcal{F}$ is the internal free energy of the bridges introduced in (2.13), $\dot{\mathcal{S}}_{\text{prod}}$ is the entropy production term defined in (2.22) corresponding to energy dissipation associated with chemical transitions, and $\dot{\mathcal{E}} = \mu_T \bar{J}_2$ as defined in (2.12b) corresponds to the input flux in energy provided by ATP hydrolysis.

2.4 Discretization and thermodynamic principles at discrete level

We now present the proposed discretization scheme for the muscle contraction models. Classical schemes are sufficient for our purposes, and the main originality of this work is to show their compatibility with discrete versions of the thermodynamical principles. Nevertheless, for the sake of completeness, some basic properties of the schemes are quickly re-established before focusing on thermodynamics.

2.4.1 A numerical scheme for Huxley'57 model

To discretize the dynamics (2.2), we consider a regular grid for the simulation range $[s^-, s^+]$ of discretization length δs and with the convention $s_0 = s^-$ and $s_\ell = s^+$. We then choose an upwind implicit scheme, that for the sake of simplicity we only present for a positive sliding velocity $\dot{x}_c$, with a natural extension to negative sliding velocities $\dot{x}_c$ by inverting the shift in space for the transport term to keep an upwind scheme. We initiate the discretization from an initial condition such that $a_0^0 = a_\ell^0 = 0$ and with the natural condition $a_i^0 \in [0, 1]$. The discretization scheme then reads

$$\begin{cases} \dfrac{a_i^{n+1} - a_i^n}{\delta t} = k_{+,i} d_i^{n+1} - k_{-,i} a_i^{n+1} - \dot{x}_c \dfrac{a_i^{n+1} - a_{i-1}^{n+1}}{\delta s}, & \forall i \in [\![1, \ell]\!] \\ d_i^{n+1} = 1 - a_i^{n+1}, & \forall i \in [\![1, \ell]\!] \end{cases} \tag{2.35}$$

with the definition

$$\begin{vmatrix} k_{+,i} = k_+(s^- + i\delta s), & i \in [\![1, \ell]\!], & \text{(2.36a)} \\ k_{-,i} = k_-(s^- + i\delta s), & i \in [\![1, \ell - 1]\!], & \text{(2.36b)} \\ k_{-,\ell} = 2k_{-,\ell-1}. & & \text{(2.36c)} \end{vmatrix}$$

Note that the exact aggregated detachment rate goes to infinity on the boundary of the interval $[s^-, s^+]$. Numerically, we use a finite value defined as given in (2.36c), and we prove in the following section that this choice does not affect the convergence of the scheme.

For the numerical scheme (2.35), we also need to prescribe adequate boundary conditions. As the analytical solution of (2.7) vanishes on the boundaries of the interval $[s^-, s^+]$, we here again can choose: either a Dirichlet condition on one side, and check the consistency on the other side, or choose periodic boundary conditions and again ensure the consistency on the boundary of the interval $[s^-, s^+]$. From a numerical point of view, it is in fact more convenient for energy estimates to choose periodic boundary conditions for a, i.e. $a_0^n = a_\ell^n$. Note that, with this choice, we do not strictly have $a_0^n = a_\ell^n = 0$. This property is only satisfied approximately, or asymptotically when the spatial discretization length goes to zero.

Defining $\alpha = \dot{x}_c \delta t / \delta s$ and $k_i = k_{+,i} + k_{-,i}$, the scheme can be written in a matrix form on the state vector $\boldsymbol{a}^n = \begin{bmatrix} a_1^n & \dots & a_\ell^n \end{bmatrix}^\mathsf{T}$

$$\mathbb{D}\boldsymbol{a}^{n+1} = \boldsymbol{a}^n + \delta t \mathbf{k}_+,$$

where

$$\mathbb{D} = \begin{bmatrix} 1 + \delta t k_1 + \alpha & & & -\alpha \\ -\alpha & 1 + \delta t k_2 + \alpha & & \\ & \ddots & \ddots & \\ & & -\alpha & 1 + \delta t k_\ell + \alpha \end{bmatrix}, \quad \mathbf{k}_+ = \begin{bmatrix} k_{+,1} \\ k_{+,2} \\ \vdots \\ k_{+,\ell} \end{bmatrix}.$$

2.4.2 Some fundamentals properties

We first present the basic – but essential – properties of the proposed scheme. This is done using classical strategies for the analysis of transport equations schemes (see for instance Richtmyer and Morton [1967]).

Uniform positivity and boundedness – One first important property that must be satisfied by the discretization is that the natural bounds for ratio quantities be preserved at the discrete level, namely $\forall n, \forall i \in [\![1,\ell]\!], a_i^n \in [0,1]$. To obtain this property, we need $\mathbb{D}$ to preserve the positivity – *i.e.* for $\boldsymbol{a} \in \mathbb{R}^\ell, \mathbb{D}\boldsymbol{a} \geq 0 \Rightarrow \boldsymbol{a} \geq 0$ (where we use the convention that a vector is positive if all its coefficients a_i are positive). Let us then take $\boldsymbol{a} \in \mathbb{R}^\ell$ such that $\mathbb{D}\boldsymbol{a} \geq 0$. We have $\forall i \in [\![1,\ell]\!]$

$$\big(1 + \delta t\, k_i + \alpha\big)a_i - \alpha a_{i-1} \geq 0, \tag{2.37}$$

with the boundary condition $a_0 = a_\ell$. Multiplying (2.37) by α^{l-1} for $i = 1$ and by $\alpha^{\ell-i}\prod_{j=1}^{i-1}\big(1 + k_j + \alpha\big)$ for $i \in [\![2,\ell]\!]$, and summing, we obtain

$$\begin{aligned}
&\sum_{i=2}^{\ell}\Big[\alpha^{\ell-i}\prod_{j=1}^{i}\big(1+k_j+\alpha\big)a_i - \alpha^{\ell-i+1}\prod_{j=1}^{i-1}\big(1+k_j+\alpha\big)a_{i-1}\Big] \\
&\qquad + \alpha^{l-1}\big(1+k_1+\alpha\big)a_1 - \alpha^l a_l \geq 0 \\
&\Leftrightarrow \prod_{j=1}^{\ell}\big(1+k_j+\alpha\big)a_\ell + \sum_{i=3}^{\ell}\alpha^{\ell-i+1}\Big[\prod_{j=1}^{i-1}\big(1+k_j+\alpha\big)a_{i-1}\Big] \\
&\quad - \sum_{i=2}^{\ell}\alpha^{\ell-i+1}\Big[\prod_{j=1}^{i-1}\big(1+k_j+\alpha\big)a_{i-1}\Big] + \alpha^{l-1}\big(1+k_1+\alpha\big)a_1 - \alpha^l a_l \geq 0.
\end{aligned}$$

Noting that the middle term is a telescoping series, we obtain as expected

$$\underbrace{\Big[\prod_{j=1}^{\ell}\big(1+k_j+\alpha\big) - \alpha^\ell\Big]}_{\geq 0} a_\ell \geq 0.$$

Then, recursively from (2.37), we get $\forall i \in [\![1,\ell]\!],\ a_i \geq 0$, which shows that the matrix operator $\mathbb{D}$ preserves the positivity. Knowing that the initial condition and the transition rates are positive, we obtain $\forall n \geq 0, \forall i \in [\![1,\ell]\!], a_i^n \geq 0$. Writing the numerical scheme for the variable $1 - a_i^n$ from (2.35), we similarly obtain that $\forall n \geq 0, \forall i \in [\![1,\ell]\!], a_i^n \leq 1$. Therefore, the proposed numerical scheme preserves the adequate positivity and boundedness.

Consistency – Let us here denote $\overline{a}$ a sufficiently regular solution of (2.7). Note that this solution satisfies a Dirichlet boundary condition on one side of the simulation interval (i.e. $\overline{a}(s^-,t) = 0$) and that we showed in (2.10) that $\lim_{s\to s^+}\overline{a}(s,t) = 0$. We denote by $\overline{\boldsymbol{a}}$ the vector of the values of $\overline{a}$ at the spatial discretization points at time $n\,\delta t$, $\overline{\boldsymbol{a}}^n = \Big[\overline{a}(\delta s, n\,\delta t) \quad \dots \quad \overline{a}(\ell\,\delta s, n\,\delta t)\Big]^{\mathsf{T}}$. We define, as usual, the convergence error by

$$e^n = \boldsymbol{a}^n - \overline{\boldsymbol{a}}^n.$$

We have $\mathbb{D}e^{n+1} = e^n - \delta t\,\eta^n$, where the consistency error η^n is given by

$$\eta^n = \frac{1}{\delta t}\big[\mathbb{D}\overline{\boldsymbol{a}}^{n+1} - \big(\overline{\boldsymbol{a}}^n + \delta t \mathbf{k}_+\big)\big].$$

Evaluating the continuous equation (2.7) at $s = s^- + i\delta s$ and $t = (n+1)\delta t$, we obtain

$$\frac{\partial \bar{a}}{\partial t}\big(s^- + i\delta s, (n+1)\delta t\big) = k_{+,i} - k_i \bar{a}_i^{n+1} - \dot{x}_c\frac{\partial \bar{a}}{\partial s}\big(s^- + i\delta s, (n+1)\delta t\big),$$

and this also holds for $i = \ell$ with the finite numerical value chosen for k_ℓ, due to the fact that $\bar{a}(s^+) = 0$ and $k_-(s)\bar{a}(s)$ tends to zero in s^+. We directly infer, $\forall i \in [\![1, \ell]\!]$,

$$\begin{aligned}\eta_i^n &= \frac{\bar{a}\big(s^- + i\delta s, (n+1)\delta t\big) - \bar{a}\big(s^- + i\delta s, n\delta t\big)}{\delta t} - \frac{\partial \bar{a}}{\partial t}\big(s^- + i\delta s, (n+1)\delta t\big) \\ &\quad + \dot{x}_c\Big\{\frac{\bar{a}\big(s^- + i\delta s, (n+1)\delta t\big) - \bar{a}\big(s^- + (i-1)\delta s, (n+1)\delta t\big)}{\delta s} \\ &\qquad - \frac{\partial \bar{a}}{\partial s}\big(s^- + i\delta s, (n+1)\delta t\big)\Big\} = O(\delta s + \delta t).\end{aligned}$$

The numerical scheme is thus consistent at the first order with the continuous equation (2.7), although different – but compatible – boundary conditions are used. Note that a well-known result by Godunov states that we cannot have more than first-order convergence in time with a discrete scheme that satisfies the positivity and boundedness property Godunov [1959].

L^2-Stability – We now analyze the L^2-stability by justifying the ℓ^2-stability of the operator $\mathbb{D}^{-1}$. Multiplying (2.35) without the source term by a_i^{n+1}, we have

$$\frac{a_i^{n+1} - a_i^n}{\delta t} a_i^{n+1} + \dot{x}_c \frac{a_i^{n+1} - a_{i-1}^{n+1}}{\delta s} a_i^{n+1} = -k_i (a_i^{n+1})^2.$$

Using the identity $-ab = \frac{1}{2}\big(a - b\big)^2 - \frac{1}{2}a^2 - \frac{1}{2}b^2$, we obtain

$$\begin{aligned}&\frac{1}{2\delta t}\Big((a_i^{n+1})^2 - (a_i^n)^2\Big) + \frac{1}{2\delta t}\Big(a_i^{n+1} - a_i^n\Big)^2 \\ &\qquad = -\frac{\dot{x}_c}{2\delta s}\big((a_i^{n+1})^2 - (a_{i-1}^{n+1})^2\big) - \frac{\dot{x}_c}{2\delta s}\Big(a_i^{n+1} - a_{i-1}^{n+1}\Big)^2 - k_i (a_i^{n+1})^2.\end{aligned}$$

Summing over i, and using the periodic boundary conditions $(a_\ell^{n+1})^2 = (a_0^{n+1})^2$, we find

$$\big\|\mathbb{D}^{-1}\boldsymbol{a}^n\big\|_{\ell^2} \leq \|\boldsymbol{a}^n\|_{\ell^2}\,.$$

Note that this stability property is just a mathematical property.

Convergence – The stability analysis coupled to the consistency analysis gives directly the convergence error. Indeed, we find

$$e^n = \big(\mathbb{D}^{-1}\big)^n e_0 - \delta t \sum_{k=0}^{n-1} \big(\mathbb{D}^{-1}\big)^{n-k-1} \eta^k,$$

so that there exist $C, T > 0$ such that

$$\|e^n\|_{\ell^2} \leq C\delta t \sum_{k=0}^{n-1} (\delta s + \delta t) = CT\big(\delta s + \delta t\big).$$

2.4.3 First principle

Our objective is more ambitious than numerical convergence, as we want *in fine* to establish thermodynamic balances at the discrete level. In this respect, let us first consider the energy balance. We recall that the average energy of a myosin head is given at the

continuous level by (2.11). Similarly to (2.36), we assign a finite value to the energy of the attached state on the boundary of the interval $[s^-, s^+]$. With the notation

$$\left|\begin{aligned} &w_{1,i} = w_1(s^- + i\delta s),\ \forall i \in [\![1, l-1]\!], \\ &w_{1,l} = 2w_{1,l-1}, \end{aligned}\right.$$

the energy is discretized as

$$\mathcal{U}^n = \frac{\delta s}{d_a}\sum_{i=1}^{\ell} w_{1,i}a_i^n + w_0 d_i^n.$$

Then, defining the fluxes as

$$\left|\begin{aligned} &J_{1,i}^n = k_{1,i}d_i^n - k_{-1,i}a_i^n, \\ &J_{2,i}^n = k_{2,i}a_i^n - k_{-2,i}d_i^n, \end{aligned}\right.$$

we have

$$\begin{aligned} \frac{\mathcal{U}^{n+1}-\mathcal{U}^n}{\delta t} &= \frac{\delta s}{d_a}\sum_{i=1}^{\ell}\left[w_{1,i}\left(\frac{a_i^{n+1}-a_i^n}{\delta t}\right) + w_0\left(\frac{d_i^{n+1}-d_i^n}{\delta t}\right)\right] \\ &= \frac{\delta s}{d_a}\sum_{i=1}^{\ell}\left[w_{1,i}\left(J_{1,i}^{n+1} - J_{2,i}^{n+1} - \dot{x}_c\frac{a_i^{n+1}-a_{i-1}^{n+1}}{\delta s}\right)\right. \\ &\qquad\qquad \left. + w_0\left(J_{2,i}^{n+1} - J_{1,i}^{n+1} + \dot{x}_c\frac{a_i^{n+1}-a_{i-1}^{n+1}}{\delta s}\right)\right] \\ &= \frac{\delta s}{d_a}\sum_{i=1}^{\ell}\left[J_{1,i}^{n+1}\left(w_{1,i}-w_0\right) + J_{2,i}^{n+1}\left(w_0 - w_{1,i} - \mu_T\right)\right. \\ &\qquad \left. + \mu_T J_{2,i}^{n+1}\right] - \frac{\dot{x}_c\delta s}{d_a}\sum_{i=1}^{\ell-1}\frac{w_{1,i}-w_{1,i+1}}{\delta s}a_i^{n+1} + \frac{\delta s}{d_a}\frac{\dot{x}_c}{\delta s}a_0^{n+1}w_{1,1} \\ &\qquad - \frac{\delta s}{d_a}\frac{\dot{x}_c}{\delta s}a_\ell^{n+1}w_{1,\ell} + \frac{\delta s}{d_a}\frac{\dot{x}_c}{\delta s}w_0(a_\ell^{n+1} - a_0^{n+1}). \end{aligned} \tag{2.38}$$

With the definition of the discrete force

$$\tau_c^{n+1} = \frac{\delta s}{d_a}\sum_{i=1}^{\ell}\frac{w_{1,i+1}-w_{1,i}}{\delta s}a_i^{n+1},$$

where we define $w_{1,\ell+1} = w_{1,1}$, and using the periodicity of the solution, (2.38) becomes

$$\begin{aligned} \frac{\mathcal{U}^{n+1}-\mathcal{U}^n}{\delta t} &= \dot{x}_c\tau_c^{n+1} \\ &\quad + \frac{\delta s}{d_a}\sum_{i=1}^{\ell}\left[J_{1,i}^{n+1}\left(w_{1,i}-w_0\right) + J_{2,i}^{n+1}\left(w_0 - w_{1,i} - \mu_T\right) + \mu_T J_{2,i}^{n+1}\right]. \end{aligned}$$

We thus obtain the discretized version of the first principle, namely

$$\frac{\mathcal{U}^{n+1}-\mathcal{U}^n}{\delta t} = \frac{\mathcal{W}^{n+1}-\mathcal{W}^n}{\delta t} + \frac{\mathcal{Q}^{n+1}-\mathcal{Q}^n}{\delta t} + \frac{\mathcal{E}^{n+1}-\mathcal{E}^n}{\delta t}, \tag{2.39}$$

with

$$\left|\begin{array}{l} \dfrac{\mathcal{W}^{n+1}-\mathcal{W}^n}{\delta t} = \dot{x}_c \tau_c^{n+1}, \\ \dfrac{\mathcal{Q}^{n+1}-\mathcal{Q}^n}{\delta t} = \dfrac{\delta s}{d_a}\displaystyle\sum_{i=1}^{\ell}\Big[J_{1,i}^{n+1}\Big(w_{1,i}-w_0\Big)+J_{2,i}^{n+1}\Big(w_0-w_{1,i}-\mu_T\Big)\Big], \\ \dfrac{\mathcal{E}^{n+1}-\mathcal{E}^n}{\delta t} = \mu_T\dfrac{\delta s}{d_a}\displaystyle\sum_{i=1}^{\ell} J_{2,i}^{n+1}. \end{array}\right.$$

2.4.4 Second principle

Let us now establish a discrete entropy balance. In this respect, we introduce the discrete entropy

$$\mathcal{S}^n = -k_B\frac{\delta s}{d_a}\sum_{i=1}^{\ell}\big(a_i^n\ln a_i^n + d_i^n\ln d_i^n\big),$$

and the free energy $\mathcal{F}^n = \mathcal{U}^n - T\mathcal{S}^n$, which can be rewritten as

$$\mathcal{F}^n = \frac{\delta s}{d_a}\sum_{i=1}^{\ell}\big(\mu_{1,i}^n a_i^n + \mu_{0,i}^n d_i^n\big),$$

by introducing the discrete chemical potentials

$$\left|\begin{array}{l} \mu_{1,i}^n = w_{1,i} + k_B T\ln a_i^n, \\ \mu_{0,i}^n = w_0 + k_B T\ln d_i^n. \end{array}\right.$$

We then rewrite the previous calculation in a manner that closely follows the calculation in the continuous case. We have

$$\begin{aligned} \frac{\mathcal{F}^{n+1}-\mathcal{F}^n}{\delta t} &= \frac{1}{\delta t}\frac{\delta s}{d_a}\sum_{i=1}^{\ell}\Big[\mu_{1,i}^{n+1}a_i^{n+1}-\mu_{1,i}^n a_i^n+\mu_{0,i}^{n+1}d_i^{n+1}-\mu_{0,i}^n d_i^n\Big] \\ &= \frac{\delta s}{d_a}\sum_{i=1}^{\ell}\Big[\mu_{1,i}^{n+1}\Big(\frac{a_i^{n+1}-a_i^n}{\delta t}\Big)+a_i^n\Big(\frac{\mu_{1,i}^{n+1}-\mu_{1,i}^n}{\delta t}\Big) \\ &\qquad + \mu_{0,i}^{n+1}\Big(\frac{d_i^{n+1}-d_i^n}{\delta t}\Big)+d_i^n\Big(\frac{\mu_{0,i}^{n+1}-\mu_{0,i}^n}{\delta t}\Big)\Big]. \end{aligned}$$

Hence,

$$\begin{aligned} \frac{\mathcal{F}^{n+1}-\mathcal{F}^n}{\delta t} = \frac{\delta s}{d_a}\sum_{i=1}^{\ell}\Big[&\mu_{1,i}^{n+1}\Big(J_{1,i}^{n+1}-J_{2,i}^{n+1}-\dot{x}_c\frac{a_i^{n+1}-a_{i-1}^{n+1}}{\delta s}\Big) \\ &+ a_i^n\Big(\frac{w_{1,i}+k_BT\ln(a_i^{n+1})-\big(w_{1,i}+k_BT\ln(a_i^n)\big)}{\delta t}\Big) \\ &+ \mu_{0,i}^{n+1}\Big(J_{2,i}^{n+1}-J_{1,i}^{n+1}+\dot{x}_c\frac{a_i^{n+1}-a_{i-1}^{n+1}}{\delta s}\Big) \\ &+ d_i^n\Big(\frac{w_0+k_BT\ln(d_i^{n+1})-\big(w_0+k_BT\ln(d_i^n)\big)}{\delta t}\Big)\Big]. \end{aligned}$$

Developing the expression of the chemical potentials, performing Abel transformations and using the periodic boundary conditions, we obtain

$$\begin{aligned}\frac{\mathcal{F}^{n+1}-\mathcal{F}^{n}}{\delta t} &= \dot{x}_c\tau_c^{n+1}\\ &+\frac{\delta s}{d_a}\sum_{i=1}^{\ell}\left[J_{1,i}^{n+1}\Big(\mu_{1,i}^{n+1}-\mu_{0,i}^{n+1}\Big)+J_{2,i}^{n+1}\Big(\mu_{0,i}^{n+1}-\mu_{1,i}^{n+1}-\mu_T\Big)+\mu_T J_{2,i}^{n+1}\right]\\ &+\frac{\dot{x}_c}{d_a}k_BT\sum_{i=1}^{\ell}\left[a_i^{n+1}\Big(\ln(a_{i+1}^{n+1})-\ln(a_i^{n+1})\Big)\right]\\ &\qquad+\frac{\dot{x}_c}{d_a}k_BT\sum_{i=1}^{\ell}\left[d_i^{n+1}\Big(\ln(d_{i+1}^{n+1})-\ln(d_i^{n+1})\Big)\right]\\ &+\frac{k_BT\delta s}{d_a}\sum_{i=1}^{\ell}\left[a_i^{n}\Big(\frac{\ln(a_i^{n+1})-\ln(a_i^{n})}{\delta t}\Big)\right]+\frac{k_BT\delta s}{d_a}\sum_{i=1}^{\ell}\left[d_i^{n}\Big(\frac{\ln(d_i^{n+1})-\ln(d_i^{n})}{\delta t}\Big)\right].\end{aligned}$$

Since $x\mapsto \ln x$ is a concave function, we have $\ln a_j-\ln a_i\le \ln'(a_i)\big(a_j-a_i\big)$ so that

$$\begin{aligned}\frac{\mathcal{F}^{n+1}-\mathcal{F}^{n}}{\delta t} &\le \dot{x}_c\tau_c^{n+1}\\ &+\frac{\delta s}{d_a}\sum_{i=1}^{\ell}\left[J_{1,i}^{n+1}\Big(\mu_{1,i}^{n+1}-\mu_{0,i}^{n+1}\Big)+J_{2,i}^{n+1}\Big(\mu_{0,i}^{n+1}-\mu_{1,i}^{n+1}-\mu_T\Big)+\mu_T J_{2,i}^{n+1}\right]\\ &\qquad+\frac{\dot{x}_c}{d_a}k_BT\sum_{i=1}^{\ell}\Big[a_{i+1}^{n+1}-a_i^{n+1}\Big]+\frac{\dot{x}_c}{d_a}k_BT\sum_{i=1}^{\ell}\Big[d_{i+1}^{n+1}-d_i^{n+1}\Big]\\ &\qquad\qquad+\frac{k_BT\delta s}{d_a\,\delta t}\sum_{i=1}^{\ell}\Big[a_i^{n+1}-a_i^{n}\Big]+\frac{k_BT\delta s}{d_a\,\delta t}\sum_{i=1}^{\ell}\Big[d_i^{n+1}-d_i^{n}\Big].\end{aligned}$$

Using the fact that the scheme imposes $\forall n,\ \forall i\in[\![1,\ell]\!],\ a_i^n+d_i^n=1$, the sums vanish two by two. We finally find

$$\begin{aligned}\frac{\mathcal{F}^{n+1}-\mathcal{F}^{n}}{\delta t} &\le \dot{x}_c\tau_c^{n+1}\\ &\qquad\frac{\delta s}{d_a}\sum_{i=1}^{\ell}\left[J_{1,i}^{n+1}\Big(\mu_{1,i}^{n+1}-\mu_{0,i}^{n+1}\Big)+J_{2,i}^{n+1}\Big(\mu_{0,i}^{n+1}-\mu_{1,i}^{n+1}-\mu_T\Big)+\mu_T J_{2,i}^{n+1}\right].\end{aligned}$$

As a point-wise evaluation of the continuous expression (2.21), we have $\forall i\in[\![1,\ell]\!]$

$$\left|\begin{aligned}J_{1,i}^{n+1}\Big(\mu_{1,i}^{n+1}-\mu_{0,i}^{n+1}\Big)&\le 0,\\ J_{2,i}^{n+1}\Big(\mu_{0,i}^{n+1}-\mu_{1,i}^{n+1}-\mu_T\Big)&\le 0.\end{aligned}\right.$$

Hence, in our case where $\dot{x}_c>0$, we finally obtain

$$\frac{\mathcal{F}^{n+1}-\mathcal{F}^{n}}{\delta t}-\dot{x}_c\tau_c^{n+1}-\mu_T\frac{\delta s}{d_a}\sum_{i=1}^{\ell}J_{2,i}^{n+1}\le 0. \tag{2.40}$$

To relate the decrease of the free energy to the creation of entropy, we first note

$$\begin{aligned}\frac{\mathcal{F}^{n+1}-\mathcal{F}^{n}}{\delta t}-\dot{x}_c\tau_c^{n+1}-\mu_T\frac{\delta s}{d_a}\sum_{i=1}^{\ell}J_{2,i}^{n+1}&=\frac{\mathcal{F}^{n+1}-\mathcal{F}^{n}}{\delta t}\\&\quad-\Big[\frac{\mathcal{U}^{n+1}-\mathcal{U}^{n}}{\delta t}-\frac{\mathcal{Q}^{n+1}-Q^{n}}{\delta t}\Big]\\&=-T\frac{\mathcal{S}^{n+1}-\mathcal{S}^{n}}{\delta t}+\frac{\mathcal{Q}^{n+1}-Q^{n}}{\delta t}.\end{aligned}\tag{2.41}$$

Comparing (2.41) with the formal expression of the second principle (2.18), we define the discrete entropy creation by

$$\frac{\mathcal{S}_{\text{prod}}^{n+1}-\mathcal{S}_{\text{prod}}^{n}}{\delta t}=\frac{\mathcal{S}^{n+1}-\mathcal{S}^{n}}{\delta t}-\frac{1}{T}\frac{\mathcal{Q}^{n+1}-Q^{n}}{\delta t}\geq 0.\tag{2.42}$$

Note that the entropy creation is formally given by

$$\begin{aligned}\frac{\mathcal{S}_{\text{prod}}^{n+1}-\mathcal{S}_{\text{prod}}^{n}}{\delta t}=-\frac{1}{T}\Bigg(&\frac{\delta s}{d_a}\sum_{i=1}^{\ell}\Big[J_{1,i}^{n+1}\Big(\mu_{1,i}^{n+1}-\mu_{0,i}^{n+1}\Big)+J_{2,i}^{n+1}\Big(\mu_{0,i}^{n+1}-\mu_{1,i}^{n+1}-\mu_T\Big)\Big]\\&+\frac{\dot{x}_c k_B T}{d_a}\sum_{i=1}^{\ell}\Big[\Big(\ln(d_i^{n+1})-\ln(a_i^{n+1})\Big)\Big[a_i^{n+1}-a_{i-1}^{n+1}\Big]\Big]\\&+\frac{k_B T\delta s}{d_a}\sum_{i=1}^{\ell}\Big[a_i^{n}\Big(\frac{\ln(a_i^{n+1})-\ln(a_i^{n})}{\delta t}\Big)\Big]\\&+\frac{k_B T\delta s}{d_a}\sum_{i=1}^{\ell}\Big[d_i^{n}\Big(\frac{\ln(d_i^{n+1})-\ln(d_i^{n})}{\delta t}\Big)\Big]\Bigg).\end{aligned}$$

and finally combining (2.40),(2.41) and (2.42) we have the time-discrete counterpart of the free energy balance (2.23)

$$\begin{aligned}\frac{\mathcal{F}^{n+1}-\mathcal{F}^{n}}{\delta t}&=\dot{x}_c\tau_c^{n+1}+\mu_T\frac{\delta s}{d_a}\sum_{i=1}^{\ell}J_{2,i}^{n+1}-T\frac{\mathcal{S}_{\text{prod}}^{n+1}-\mathcal{S}_{\text{prod}}^{n}}{\delta t}\\&\leq\dot{x}_c\tau_c^{n+1}+\mu_T\frac{\delta s}{d_a}\sum_{i=1}^{\ell}J_{2,i}^{n+1}.\end{aligned}\tag{2.43}$$

2.4.5 Extension to multi-state, multi-site models

The case of multiple states and sites derives from the same principles, hence justifying that we developed precisely the computations for the Huxley'57 model. The developments are, however, not straightforward because the multi-site assumption implies an infinite number of attachment and detachment fluxes, which has to be properly integrated into the discrete thermodynamical balances. Indeed, in the case of a positive sliding velocity $\dot{x}_c$, we discretize the system (2.6) with the following implicit upwind numerical scheme

$$\begin{cases}\dfrac{x_{q,i+j\ell}^{n+1}-x_{q,i+j\ell}^{n}}{\delta t}=\displaystyle\sum_{p|E_{pq}\in G}J_{pq,i+j\ell}^{n+1}-\dot{x}_c\frac{x_{q,i+j\ell}^{n+1}-x_{q,i+j\ell-1}^{n+1}}{\delta s},\forall V_q\in V_{\text{a}},\\ \qquad\qquad\qquad\qquad\qquad\qquad\qquad\qquad\forall i\in[\![1,\ell]\!],\ j\in\mathbb{Z}\\ \dfrac{x_{q,i}^{n+1}-x_{q,i}^{n}}{\delta t}=\displaystyle\sum_{p|E_{pq}\in G}\sum_{j\in\mathbb{Z}}J_{pq,i+j\ell}^{n+1}-\dot{x}_c\frac{x_{q,i}^{n+1}-x_{q,i-1}^{n+1}}{\delta s},\forall V_q\in V_{\text{d}},\ i\in[\![1,\ell]\!]\end{cases}\tag{2.44}$$

with the notation $x^n_{q,i+j\ell} = x_q(s^- + (i+j\ell)\delta s, n\delta t)$ for $V_q \in V_a$, $x^n_{q,i} = x_q(s^- + i\delta s, n\delta t)$ for $V_q \in V_d$ and $J^n_{pq,i+j\ell} = J_{pq}(s^- + (i+j\ell)\delta s, n\delta t)$. Note that x_q for $V_q \in V_d$ has periodic boundary conditions and thus $x_{q,i+j\ell} = x_{q,i},\ \forall j \in \mathbb{Z}$, and we keep $j \in \mathbb{Z}$, albeit in practice we will bound the attachment zone, introducing a boundary consistency error.

Mass conservation – Defining the total quantity of matter

$$m^n_i = \sum_{V_q \in V_\mathrm{a}} \sum_{j\in\mathbb{Z}} x^n_{q,i+j\ell} + \sum_{V_q \in V_\mathrm{d}} x^n_{q,i},$$

– which has the periodicity $m^n_0 = m^n_\ell$ – and using the scheme (2.44), we find the classical implicit transport equation

$$\frac{m^{n+1}_i - m^n_i}{\delta t} = -\dot{x}_c \frac{m^{n+1}_i - m^{n+1}_{i-1}}{\delta s},$$

hence, we retrieve, as in the Huxley'57 model, the conservation of matter

$$\sum_{V_q \in V_\mathrm{a}} \sum_{j\in\mathbb{Z}} x^n_{q,i+j\ell} + \sum_{V_q \in V_\mathrm{d}} x^n_{q,i} = 1 \ \ \forall n,\ \forall i \in [\![1,\ell]\!]. \tag{2.45}$$

First principle – Concerning the energy balance, the internal energy is now defined as

$$\mathcal{U}^n = \frac{\delta s}{d_a} \sum_{i=1}^{\ell} \Big[\sum_{V_q \in V_\mathrm{a}} \sum_{j\in\mathbb{Z}} w_{q,i+j\ell} x^n_{q,i+j\ell} + \sum_{V_q \in V_\mathrm{d}} w_q x^n_{q,i} \Big].$$

and we find this time, with the notation $\tilde{W}_{pq,i+j\ell} = \tilde{W}_{pq}(s^- + (i+j\ell)\delta s)$, that

$$\begin{aligned}
\frac{\mathcal{U}^{n+1} - \mathcal{U}^n}{\delta t} = \frac{\delta s}{d_a} \Bigg[& \sum_{i=1}^{\ell} \sum_{E_{pq}\in G} \sum_{j\in\mathbb{Z}} J^{n+1}_{pq,i+j\ell} \tilde{W}_{pq,i+j\ell} \\
& + \mu_T \sum_{i=1}^{\ell} \sum_{j\in\mathbb{Z}} \Big(J_{25,i+j\ell} + J_{34,i+j\ell} \Big) \Bigg] \\
& - \frac{\dot{x}_c \delta s}{d_a} \sum_{i=1}^{\ell} \sum_{V_q \in V_\mathrm{a}} \sum_{j\in\mathbb{Z}} w_{q,i+j\ell} \frac{x^{n+1}_{q,i+j\ell} - x^{n+1}_{q,i+j\ell-1}}{\delta s} \\
& - \frac{\dot{x}_c \delta s}{d_a} \sum_{i=1}^{\ell} \sum_{V_q \in V_\mathrm{d}} w_q \frac{x^{n+1}_{q,i} - x^{n+1}_{q,i-1}}{\delta s}.
\end{aligned}$$

The last term vanishes with the periodic boundary conditions. Performing an Abel transformation on the penultimate term and defining the discrete force as

$$\tau^{n+1}_c = \frac{\delta s}{d_a} \sum_{i=1}^{\ell} \sum_{V_q \in V_\mathrm{a}} \sum_{j\in\mathbb{Z}} x_{q,i+j\ell} \frac{w^{n+1}_{q,i+j\ell+1} - w^{n+1}_{q,i+j\ell}}{\delta s},$$

we obtain the discrete first principle

$$\frac{\mathcal{U}^{n+1} - \mathcal{U}^n}{\delta t} = \frac{\mathcal{W}^{n+1} - \mathcal{W}^n}{\delta t} + \frac{\mathcal{Q}^{n+1} - \mathcal{Q}^n}{\delta t} + \frac{\mathcal{E}^{n+1} - \mathcal{E}^n}{\delta t},$$

with

$$\left|\begin{array}{l} \dfrac{\mathcal{W}^{n+1}-\mathcal{W}^n}{\delta t} = \dot{x}_c \tau_c^{n+1}, \\ \dfrac{\mathcal{Q}^{n+1}-\mathcal{Q}^n}{\delta t} = \dfrac{\delta s}{d_a}\displaystyle\sum_{i=1}^{\ell}\sum_{E_{pq}\in G}\sum_{j\in\mathbb{Z}} J^{n+1}_{pq,i+j\ell}\tilde{W}_{pq,i+j\ell}, \\ \dfrac{\mathcal{E}^{n+1}-\mathcal{E}^n}{\delta t} = \mu_T\dfrac{\delta s}{d_a}\displaystyle\sum_{i=1}^{\ell}\sum_{j\in\mathbb{Z}}\Big(J_{25,i+j\ell}+J_{34,i+j\ell}\Big). \end{array}\right.$$

Second principle – We now define the discrete entropy as

$$\mathcal{S}^n = -k_B\frac{\delta s}{d_a}\sum_{i=1}^{\ell}\Big[\sum_{V_q\in V_{\rm a}}\sum_{j\in\mathbb{Z}} x^n_{q,i+j\ell}\ln x^n_{q,i+j\ell} + \sum_{V_q\in V_{\rm d}} x^n_{q,i}\ln x^n_{q,i}\Big],$$

and the free energy $\mathcal{F}^n = \mathcal{U}^n - T\mathcal{S}^n$, that we rewrite as

$$\mathcal{F}^n = \frac{\delta s}{d_a}\sum_{i=1}^{\ell}\Big[\sum_{V_q\in V_{\rm a}}\sum_{j\in\mathbb{Z}} \mu^n_{q,i+j\ell}x^n_{q,i+j\ell} + \sum_{V_q\in V_{\rm d}} \mu^n_{q,i}x^n_{q,i}\Big],$$

using discrete chemical potentials

$$\left|\begin{array}{l} \mu^n_{q,i+j\ell} = w_{q,i+j\ell} + k_BT\ln x^n_{q,i+j\ell},\ V_q\in V_{\rm a}, \\ \mu^n_{p,i} = w_q + k_BT\ln x^n_{q,i},\ V_q\in V_{\rm d}. \end{array}\right.$$

The discrete time derivative of the free energy is

$$\begin{aligned}\frac{\mathcal{F}^{n+1}-\mathcal{F}^n}{\delta t} = \frac{\delta s}{d_a}\sum_{i=1}^{\ell}\sum_{V_q\in V_{\rm a}}\sum_{j\in\mathbb{Z}}\Big[&\mu^{n+1}_{q,i+j\ell}\Big(\frac{x^{n+1}_{q,i+j\ell}-x^n_{q,i+j\ell}}{\delta t}\Big) \\ &+ x^n_{q,i+j\ell}\Big(\frac{\mu^{n+1}_{q,i+j\ell}-\mu^n_{q,i+j\ell}}{\delta t}\Big)\Big] + \sum_{i=1}^{\ell}\sum_{V_q\in V_{\rm d}}\Big[\mu^{n+1}_{q,i}\frac{x^{n+1}_{q,i}-x^n_{q,i}}{\delta t} + x^n_{q,i}\frac{\mu^{n+1}_{q,i}-\mu^n_{q,i}}{\delta t}\Big].\end{aligned}$$

Using the notation $\tilde{M}^n_{pq,i+j\ell} = \mu^n_{q,i+j\ell} - \mu^n_{p,i+j\ell} - \mu_T\delta_{pq=\{25,34\}}$ and the results of the first principle, we get

$$\begin{aligned}\frac{\mathcal{F}^{n+1}-\mathcal{F}^n}{\delta t} = \frac{\delta s}{d_a}\Bigg[&\sum_{i=1}^{\ell}\sum_{E_{pq}\in G}\sum_{j\in\mathbb{Z}} J^{n+1}_{pq,i+j\ell}\tilde{M}^{n+1}_{pq,i+j\ell} \\ &+ \mu_T\sum_{i=1}^{\ell}\sum_{j\in\mathbb{Z}}\Big(J_{25,i+j\ell}+J_{34,i+j\ell}\Big)\Bigg] \\ &- \dot{x}_c\frac{\delta s}{d_a}\sum_{i=1}^{\ell}\sum_{V_q\in V_{\rm a}}\sum_{j\in\mathbb{Z}} k_BT\ln\big(x^{n+1}_{q,i+j\ell}\big)\frac{x^{n+1}_{q,i+j\ell}-x^{n+1}_{q,i+j\ell-1}}{\delta s} \\ &- \dot{x}_c\frac{\delta s}{d_a}\sum_{i=1}^{\ell}\sum_{V_q\in V_{\rm d}} k_BT\ln\big(x^{n+1}_{q,i}\big)\frac{x^{n+1}_{q,i}-x^{n+1}_{q,i-1}}{\delta s} \\ &+ \frac{k_BT\delta s}{d_a}\sum_{i=1}^{\ell}\sum_{V_q\in V_{\rm a}}\sum_{j\in\mathbb{Z}}\Big[x^n_{q,i+j\ell}\Big(\frac{\ln(x^{n+1}_{q,i+j\ell})-\ln(x^n_{q,i+j\ell})}{\delta t}\Big)\Big] \\ &+ \frac{k_BT\delta s}{d_a}\sum_{i=1}^{\ell}\sum_{V_q\in V_{\rm d}}\Big[x^n_{q,i}\Big(\frac{\ln(x^{n+1}_{q,i})-\ln(x^n_{q,i})}{\delta t}\Big)\Big] + \dot{x}_c\tau_c^{n+1}.\end{aligned}$$

Performing an Abel transformation on the transport terms, we obtain

$$\begin{aligned}\frac{\mathcal{F}^{n+1}-\mathcal{F}^n}{\delta t} = \frac{\delta s}{d_a}\Bigg[&\sum_{i=1}^{\ell}\sum_{E_{pq}\in G}\sum_{j\in\mathbb{Z}} J^{n+1}_{pq,i+j\ell}\tilde{M}^{n+1}_{pq,i+j\ell}\\ &+\mu_T\sum_{i=1}^{\ell}\sum_{j\in\mathbb{Z}}\Big(J_{25,i+j\ell}+J_{34,i+j\ell}\Big)\Bigg]\\ &+\frac{\dot{x}_c}{d_a}k_BT\sum_{i=1}^{\ell}\sum_{V_q\in V_{\mathrm{a}}}\sum_{j\in\mathbb{Z}}\Bigg[x^{n+1}_{q,i+j\ell}\Big(\ln(x^{n+1}_{q,i+j\ell+1})-\ln(x^{n+1}_{q,i+j\ell})\Big)\Bigg]\\ &+\frac{\dot{x}_c}{d_a}k_BT\sum_{i=1}^{\ell}\sum_{V_q\in V_{\mathrm{d}}}\Bigg[x^{n+1}_{q,i}\Big(\ln(x^{n+1}_{q,i+1})-\ln(x^{n+1}_{q,i})\Big)\Bigg]\\ &+\frac{k_BT\delta s}{d_a}\sum_{i=1}^{\ell}\sum_{V_q\in V_{\mathrm{a}}}\sum_{j\in\mathbb{Z}}\Bigg[x^{n}_{q,i+j\ell}\Big(\frac{\ln(x^{n+1}_{q,i+j\ell})-\ln(x^{n}_{q,i+j\ell})}{\delta t}\Big)\Bigg]\\ &+\frac{k_BT\delta s}{d_a}\sum_{i=1}^{\ell}\sum_{V_q\in V_{\mathrm{d}}}\Bigg[x^{n}_{q,i}\Big(\frac{\ln(x^{n+1}_{q,i})-\ln(x^{n}_{q,i})}{\delta t}\Big)\Bigg]+\dot{x}_c\tau_c^{n+1}.\end{aligned}$$

Using again that $\ln x_j-\ln x_i\le \ln'(x_i)\big(x_j-x_i\big)$, the detailed balance and the conservation of matter (2.45), we finally obtain

$$\frac{\mathcal{F}^{n+1}-\mathcal{F}^n}{\delta t}-\dot{x}_c\tau_c^{n+1}-\mu_T\sum_{i=1}^{\ell}\sum_{j\in\mathbb{Z}}\Big(J_{25,i+j\ell}+J_{34,i+j\ell}\Big)\le 0. \tag{2.46}$$

As in Section (2.4.4) this property is equivalent to

$$\frac{\mathcal{S}^{n+1}_{\mathrm{prod}}-\mathcal{S}^{n}_{\mathrm{prod}}}{\delta t}=\frac{\mathcal{S}^{n+1}-\mathcal{S}^{n}}{\delta t}-\frac{1}{T}\frac{\mathcal{Q}^{n+1}-Q^{n}}{\delta t}\ge 0. \tag{2.47}$$

Moreover, the entropy production is in fact given by

$$\begin{aligned}\frac{\mathcal{S}^{n+1}_{\mathrm{prod}}-\mathcal{S}^{n}_{\mathrm{prod}}}{\delta t} = -\frac{1}{T}\Bigg(&\frac{\delta s}{d_a}\sum_{i=1}^{\ell}\sum_{E_{pq}\in G}\sum_{j\in\mathbb{Z}} J^{n+1}_{pq,i+j\ell}\tilde{M}^{n+1}_{pq,i+j\ell}\\ &-\frac{\dot{x}_ck_BT}{d_a}\sum_{i=1}^{\ell}\sum_{V_q\in V_{\mathrm{a}}}\sum_{j\in\mathbb{Z}}\Bigg[\ln(x^{n+1}_{q,i+j\ell})\Big[x^{n+1}_{q,i+j\ell}-x^{n+1}_{q,i+j\ell-1}\Big]\Bigg]\\ &-\frac{\dot{x}_ck_BT}{d_a}\sum_{i=1}^{\ell}\sum_{V_q\in V_{\mathrm{d}}}\Bigg[\ln(x^{n+1}_{q,i})\Big[x^{n+1}_{q,i}-x^{n+1}_{q,i-1}\Big]\Bigg]\\ &+\frac{k_BT\delta s}{d_a}\sum_{i=1}^{\ell}\sum_{V_q\in V_{\mathrm{a}}}\sum_{j\in\mathbb{Z}}\Bigg[x^{n}_{q,i+j\ell}\Big(\frac{\ln(x^{n+1}_{q,i+j\ell})-\ln(x^{n}_{q,i+j\ell})}{\delta t}\Big)\Bigg]\\ &+\frac{k_BT\delta s}{d_a}\sum_{i=1}^{\ell}\sum_{V_q\in V_{\mathrm{d}}}\Bigg[x^{n}_{q,i}\Big(\frac{\ln(x^{n+1}_{q,i})-\ln(x^{n}_{q,i})}{\delta t}\Big)\Bigg]\Bigg).\end{aligned}$$

and, by recombining (2.46) and (2.47), we finally get

$$\frac{\mathcal{F}^{n+1}-\mathcal{F}^n}{\delta t}-\dot{x}_c\tau_c^{n+1}-\mu_T\sum_{i=1}^{\ell}\sum_{j\in\mathbb{Z}}\Big(J_{25,i+j\ell}+J_{34,i+j\ell}\Big)+T\frac{\mathcal{S}^{n+1}_{\mathrm{prod}}-\mathcal{S}^{n}_{\mathrm{prod}}}{\delta t}=0. \tag{2.48}$$

2.4.6 Discretization of the macroscopic model coupling

We can derive a full discretized version of the macroscopic model presented in Figure 2.4 and modeled by the dynamics (2.33). Here, we will rely – as in Chapelle et al. [2012] – on mid-point rules for the discretization of the PVW, with additional corrections in order to guarantee the energy balance. Therefore, we will typically denote $\underline{v}^{n+\frac{1}{2}} = \frac{\underline{v}^{n+1}+\underline{v}^{n}}{2}$ for any variable $\underline{v}$ and the notation $n+\frac{1}{2}\sharp$ will allow to indicate when we depart from this classical rule. First, as recommended in Gonzales [2000]; Le Tallec and Hauret [2003]; Hauret and Le Tallec [2006]; Chapelle et al. [2012], we will consider the following non-standard – albeit classical – mid-point quantities

$$\underline{\underline{e}}^{n+\frac{1}{2}\sharp} = \underline{\underline{e}}(\underline{y}^{n+\frac{1}{2}}), \quad \dot{\underline{\underline{e}}}^{n+\frac{1}{2}\sharp} = \frac{\underline{\underline{e}}^{n+1} - \underline{\underline{e}}^{n}}{\delta t},$$
$$\mathrm{d}_{\underline{y}}\,\underline{\underline{e}}^{n+\frac{1}{2}\sharp} \cdot \underline{w} = \frac{1}{2}\Big(\nabla \underline{w} + (\nabla \underline{w})^{\mathsf{T}} + (\nabla \underline{y}^{n+\frac{1}{2}})^{\mathsf{T}} \cdot \nabla \underline{w} + (\nabla \underline{w})^{\mathsf{T}} \cdot \nabla \underline{y}^{n+\frac{1}{2}}\Big),$$

and a passive hyperelastic stress law discretization that includes an energy correction term, namely

$$\frac{\partial \Psi}{\partial \underline{\underline{e}}}\Big|^{n+\frac{1}{2}\sharp} = \frac{\partial \Psi}{\partial \underline{\underline{e}}}(\underline{\underline{e}}^{n+\frac{1}{2}\sharp}) + \left(\frac{\Psi(\underline{\underline{e}}^{n+1}) - \Psi(\underline{\underline{e}}^{n})}{\delta t} - \frac{\partial \Psi}{\partial \underline{\underline{e}}}(\underline{\underline{e}}^{n+\frac{1}{2}\sharp}) : \dot{\underline{\underline{e}}}^{n+\frac{1}{2}\sharp}\right) \frac{\dot{\underline{\underline{e}}}^{n+\frac{1}{2}\sharp}}{\dot{\underline{\underline{e}}}^{n+\frac{1}{2}\sharp} : \dot{\underline{\underline{e}}}^{n+\frac{1}{2}\sharp}}. \tag{2.49}$$

Then, we propose the following discretization of (2.33)

$$\begin{cases}
\dfrac{\underline{y}^{n+1} - \underline{y}^{n}}{\delta t} = \underline{v}^{n+\frac{1}{2}} = \dfrac{\underline{v}^{n+1} + \underline{v}^{n}}{2} & \text{(2.50a)} \\
\displaystyle\int_{\Omega^0} \rho_0 \frac{\underline{v}^{n+1} - \underline{v}^{n}}{\delta t} \cdot \underline{w}\,\mathrm{d}\Omega + \int_{\Omega^0} \underline{\underline{\Sigma}}^{n+\frac{1}{2}\sharp} : \mathrm{d}_{\underline{y}}\underline{\underline{e}}^{n+\frac{1}{2}\sharp} \cdot \underline{w}\,\mathrm{d}\Omega = \mathcal{P}_{\mathrm{ext}}^{n+\frac{1}{2}}(\underline{w}),\ \forall \underline{w} \in \mathscr{V}_{\mathrm{ad}} & \text{(2.50b)} \\
\qquad \text{with } \underline{\underline{\Sigma}}^{n+\frac{1}{2}\sharp} = \dfrac{\partial \Psi}{\partial \underline{\underline{e}}}\Big|^{n+\frac{1}{2}\sharp} + \eta \dfrac{\underline{\underline{e}}^{n+1} - \underline{\underline{e}}^{n}}{\delta t} + \dfrac{T_{\mathrm{fib}}^{n+\frac{1}{2}\sharp}}{(1 + 2\underline{\tau} \cdot \underline{\underline{e}}^{n} \cdot \underline{\tau})^{\frac{1}{2}}} \underline{\tau} \otimes \underline{\tau} & \\
T_{\mathrm{fib}}^{n+\frac{1}{2}\sharp} = \nu \dfrac{e_c^{n+1} - e_c^{n}}{\delta t} + T_c^{n+1} = E_s e_s^{n+\frac{1}{2}} & \text{(2.50c)} \\
\qquad \text{with } T_c^{n+1} = \rho_{\mathrm{surf}} \dfrac{\delta s}{d_a} \displaystyle\sum_{i=1}^{\ell} \frac{w_{1,i+1} - w_{1,i}}{\delta s} a_i^{n+1} & \\
\dfrac{a_i^{n+1} - a_i^{n}}{\delta t} = k_{+,i}(1 - a_i^{n+1}) - k_{-,i} a_i^{n+1} - \ell_{hs} \dfrac{e_c^{n+1} - e_c^{n}}{\delta t} \dfrac{a_i^{n+1} - a_{i-1}^{n+1}}{\delta s} & \text{(2.50d)}
\end{cases}$$

Note here that (2.50c) and (2.50d) are defined at each quadrature point $\underline{\mathrm{x}}_m$, albeit we omit – for the sake of brevity – this explicit dependence in the equations. If the 1D elastic element is chosen nonlinear hyperelastic, the corresponding term in (2.50c) has to be treated as proposed for the 3D elastic element in (2.49).

To obtain a complete energy balance, we now proceed as in Chapelle et al. [2012] by considering the mid-point velocity $\underline{v}^{n+\frac{1}{2}}$ as an admissible displacement field and recalling that $\mathrm{d}_{\underline{y}}\,\underline{\underline{e}}^{n+\frac{1}{2}\sharp} \cdot \underline{v}^{n+\frac{1}{2}} = \frac{\underline{\underline{e}}^{n+1} - \underline{\underline{e}}^{n}}{\delta t}$. The balance associated with the hyperelastic contribution is handled by our choice in (2.49), and the viscous part directly gives a negative

contribution, so that we have

$$\frac{\mathcal{K}^{n+1}-\mathcal{K}^n}{\delta t}+\int_{\Omega^0}\frac{\Psi^{n+1}-\Psi^n}{\delta t}\,\mathrm{d}\Omega + \frac{1}{\delta t}\int_{\Omega^0} T_{\mathrm{fib}}^{n+\frac{1}{2}\sharp}\frac{\underline{\tau}\cdot(\underline{\underline{e}}^{n+1}-\underline{\underline{e}}^n)\cdot\underline{\tau}}{(1+2\underline{\tau}\cdot\underline{\underline{e}}^n\cdot\underline{\tau})^{\frac{1}{2}}}\,\mathrm{d}\Omega=\mathcal{P}_{\mathrm{ext}}^{n+\frac{1}{2}}-\int_{\Omega^0}\eta\frac{|\underline{\underline{e}}^{n+1}-\underline{\underline{e}}^n|^2}{\delta t^2}\,\mathrm{d}\Omega.$$

The function $x\mapsto(1+2x)^{\frac{1}{2}}$ is concave of derivative $(1+2x)^{-\frac{1}{2}}$, hence

$$\frac{\underline{\tau}\cdot\underline{\underline{e}}^{n+1}\cdot\underline{\tau}-\underline{\tau}\cdot\underline{\underline{e}}^n\cdot\underline{\tau}}{(1+2\underline{\tau}\cdot\underline{\underline{e}}^n\cdot\underline{\tau})^{\frac{1}{2}}}\geq(1+2\underline{\tau}\cdot\underline{\underline{e}}^{n+1}\cdot\underline{\tau})^{\frac{1}{2}}-(1+2\underline{\tau}\cdot\underline{\underline{e}}^n\cdot\underline{\tau})^{\frac{1}{2}}=e_{\mathrm{fib}}^{n+1}-e_{\mathrm{fib}}^n.$$

Therefore we have, recalling that we have defined e_s such that $e_{\mathrm{fib}}=e_s+e_c$,

$$\begin{aligned}\mathcal{P}_{\mathrm{fib}}&=\frac{1}{\delta t}\int_{\Omega^0}T_{\mathrm{fib}}^{n+\frac{1}{2}\sharp}\frac{\underline{\tau}\cdot(\underline{\underline{e}}^{n+1}-\underline{\underline{e}}^n)\cdot\underline{\tau}}{(1+2\underline{\tau}\cdot\underline{\underline{e}}^{n+1}\cdot\underline{\tau})^{\frac{1}{2}}}\,\mathrm{d}\Omega\\&\geq\int_{\Omega^0}T_{\mathrm{fib}}^{n+\frac{1}{2}\sharp}\frac{e_{\mathrm{fib}}^{n+1}-e_{\mathrm{fib}}^n}{\delta t}\,\mathrm{d}\Omega=\int_{\Omega^0}T_{\mathrm{fib}}^{n+\frac{1}{2}\sharp}\left[\frac{e_s^{n+1}-e_s^n}{\delta t}+\frac{e_c^{n+1}-e_c^n}{\delta t}\right]\mathrm{d}\Omega\\&\geq\int_{\Omega^0}E_s e_s^{n+\frac{1}{2}}\frac{e_s^{n+1}-e_s^n}{\delta t}\,\mathrm{d}\Omega+\int_{\Omega^0}\left[\nu\frac{(e_c^{n+1}-e_c^n)^2}{\delta t^2}+T_c^{n+1}\frac{e_c^{n+1}-e_c^n}{\delta t}\right]\mathrm{d}\Omega.\end{aligned}$$

We now incorporate the Huxley'57 discrete-time free energy balance (2.43) – and we could proceed identically with the other models using (2.48) – to get

$$\begin{aligned}&\frac{\mathcal{K}^{n+1}-\mathcal{K}^n}{\delta t}+\int_{\Omega^0}\left[\frac{\Psi^{n+1}-\Psi^n}{\delta t}+E_s\frac{|e_s^{n+1}|^2-|e_s^n|^2}{2\delta t}+\rho_v\frac{\mathcal{F}^{n+1}-\mathcal{F}^n}{\delta t}\right]\mathrm{d}\Omega\\&\quad\leq\mathcal{P}_{\mathrm{ext}}^{n+\frac{1}{2}}-\int_{\Omega^0}\left[\eta\frac{|\underline{\underline{e}}^{n+1}-\underline{\underline{e}}^n|^2}{\delta t^2}+\nu\frac{(e_c^{n+1}-e_c^n)^2}{\delta t^2}+T\rho_v\frac{\mathcal{S}_{\mathrm{prod}}^{n+1}-\mathcal{S}_{\mathrm{prod}}^n}{\delta t}\right]\mathrm{d}\Omega\\&\qquad+\int_{\Omega^0}\rho_v\mu_T\frac{\delta s}{d_a}\sum_{i=1}^{\ell}J_{2,i}^{n+1}\,\mathrm{d}\Omega,\end{aligned}\tag{2.51}$$

which is the discrete-time counterpart of the Clausius-Duhem relation (2.34), with here an inequality only due to numerical dissipation and consistent in δt. Note finally that in the case of models capturing the power stroke dynamics such as Piazzesi-Lombardi'95, time sub-iterations may be required. In this case it can be shown that the energy balance is preserved provided the active tension T_c^{n+1} is redefined by weighing the intermediate states over all sub-iterations.

2.5 Numerical results and discussion

In this section, our goal is to illustrate the analysis of the discrete system presented in the previous section for the Huxley'57 model and the Piazzesi-Lombardi'95 model, which we chose as a representative of the multi-site, multi-state models. These illustrations serve several purposes. We first want to demonstrate that the thermodynamics identities established at the discrete level are satisfied in the numerical simulations. Then, we want to show that the ability to compute the thermodynamical balances numerically allows to gain additional insight into the physiology of muscle contraction. Additionally, for the Piazzesi-Lombardi'95 model, we compare our simulation results with that obtained in the original paper as a further validation of our approach.

2.5.1 Huxley'57 model

The choice of model parameters must satisfy the conditions (2.3) and the assumption that $w_1 a$ and $k_- a$ tend to zero when s tends to s^- and s^+. We choose the energy levels and transition rates as follows

$$\begin{cases} w_1(s) = \kappa_w (s - s^*)^2 + \dfrac{\alpha_w}{s^+ - s} + \dfrac{\alpha_w}{s - s^-}, \\ k_1(s) = k_{\max} \exp\Big(- \lambda_1 \Big[(s - \bar{s})^8 + \dfrac{\alpha_{k_1}}{(s^+ - s)^2} + \dfrac{\alpha_{k_1}}{(s - s^-)^2} \Big] \Big), \\ k_2(s) = k_{\mathrm{mid}} - \big(k_{\mathrm{mid}} - k_{\min} \big) \exp\big(- \lambda_2 (s - \bar{s})^8 \big) \\ \qquad\qquad + \dfrac{\alpha_{k_2}}{(s^+ - s)^2} + \dfrac{\alpha_{k_2}}{(s - s^-)^2}. \end{cases} \tag{2.52}$$

We choose here to prescribe k_1 and k_2 in addition to the energies w_1 and w_0. The reverse rates k_{-1} and k_{-2} are then derived from the detailed balance (2.1). The energy levels parametrization is shown in Figure 2.6. The transition rates are depicted in Figure 2.7. The models parameters used in the following simulations are presented in Table 2.1.

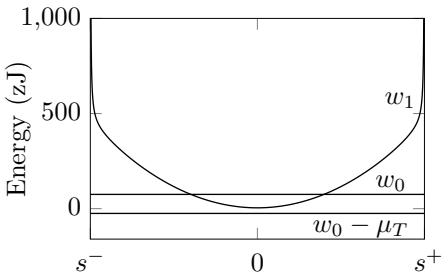

Figure 2.6 – Energy levels parametrization for the Huxley'57 model.

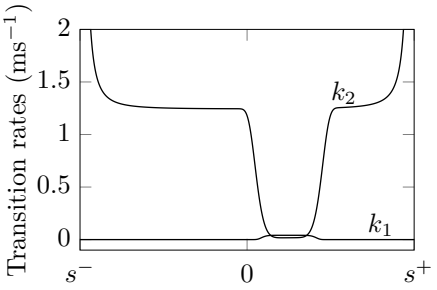

Figure 2.7 – Transition rates parametrization for the Huxley'57 model.

Model parameters	
μ_{T}	100 zJ
s^+	20 nm
s^-	−20 nm
s^*	0
$\tilde{s}$	9 nm
$\bar{s}$	5 nm
κ_w	1.1 pN nm^{-1}
$k_{\max}$	41.3×10^{-3} ms^{-1}
$k_{\min}$	10×10^{-3} ms^{-1}
k_{mid}	30 $k_{\max}$
λ_1	6.21×10^{-5} nm^{-8}
λ_2	3 λ_1
α_w	$\frac{1}{2}\kappa_w(\tilde{s} - \bar{s})^2$
α_{k_1}	$k_{\mathrm{mid}}/\lambda_1$
α_{k_2}	k_{mid}

Table 2.1 – Model parameters used in the simulations with the Huxley'57 model.

The asymptotic properties of the chosen transition rates and of the associated solutions

can be easily obtained using the analytical solution (2.9) and the theorem of dominated convergence.

We consider two simulation cases. First, we simulate the tension rise in isometric conditions ($\dot{x}_c = 0$). Then, we compute the muscle response in contraction at constant shortening velocity ($\dot{x}_c < 0$) starting from the isometric steady-state solution.

Validation of the thermodynamical identities at discrete level – We first want to verify that the discrete versions of the first principle (2.39) and the second principles (2.43) are satisfied numerically. To do so, we compute respectively the expressions

$$\frac{\mathcal{U}^{n+1} - \mathcal{U}^n}{\delta t} - \left[\frac{\mathcal{W}^{n+1} - \mathcal{W}^n}{\delta t} + \frac{\mathcal{Q}^{n+1} - \mathcal{Q}^n}{\delta t} + \frac{\mathcal{E}^{n+1} - \mathcal{E}^n}{\delta t}\right],$$

and

$$\frac{\mathcal{F}^{n+1} - \mathcal{F}^n}{\delta t} - \frac{\mathcal{W}^{n+1} - \mathcal{W}^n}{\delta t} - \frac{\mathcal{E}^{n+1} - \mathcal{E}^n}{\delta t}.$$

The results for both simulation cases is presented in Figure 2.8. We notice that the first expression is ten orders of magnitude smaller that the individual terms that compose it (see Figures 2.9 and 2.10), showing that the first principle is satisfied at discrete level. The second expression is always negative showing the validity of the discrete second principle.

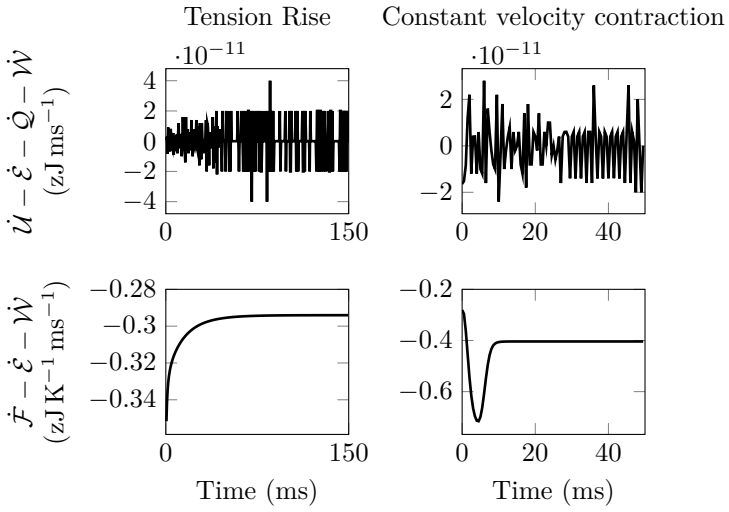

Figure 2.8 – Validation of the discrete thermodynamical balances in two test cases for the Huxley'57 model.

Tension rise – In our first illustration of the results obtained for the Huxley'57 model, we simulate the tension rise in isometric conditions ($\dot{x}_c = 0$). We initialize all heads in the detached state and let the myosin heads evolve. Along the usual tension evolution, our scheme allows us to compute the thermodynamic fluxes associated with muscle contraction – see Figure 2.9. In the steady-state regime, the energy input remains positive and heat is dissipated. The force is sustained through the continuous cycling of the myosin heads in interaction with the actin filament. This process is fueled by the energy brought by ATP. We see here the active nature of muscle contraction. Force is produced when the muscle is supplied with energy. Naturally, as the velocity is zero no work is produced.

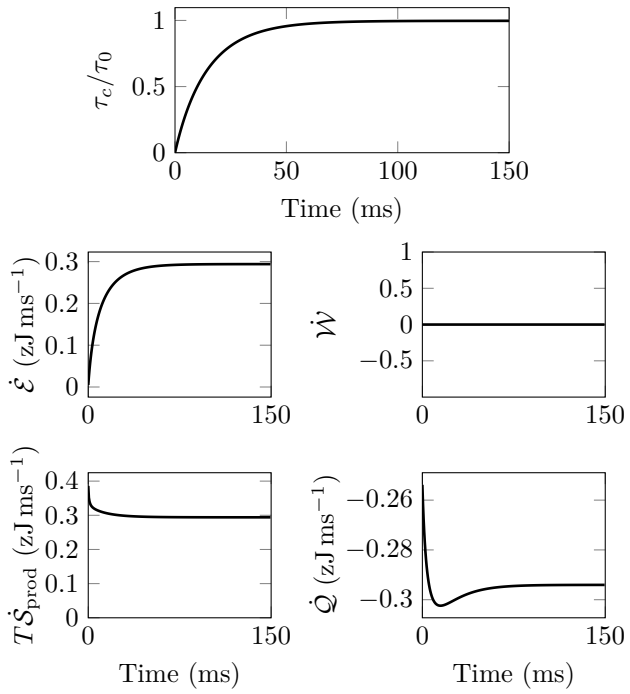

Figure 2.9 – Average tension and thermodynamic fluxes per myosin head in an isometric tension rise simulation with the Huxley'57 model. The isometric tension is denoted by τ_0.

Constant velocity contraction – We now show a second illustrative example with a contraction at constant shortening velocity ($\dot{x}_c < 0$) starting from the isometric steady-state solution. The simulation results are presented in Figure 2.10. After a transient phase, the system reaches a permanent regime in which the classical force-velocity curve is measured Hill [1938] (note that in the original experimental protocol force and not length is controlled). In this regime, we observe the energy mechano-transduction performed by the molecular motors: the energy input brought by ATP is for one part converted into work produced by the system ($\mathcal{W} < 0$), and for the other part dissipated by entropy production.

2.5.2 Piazzesi-Lombardi'95 model

The Piazzesi-Lombardi'95 model reproduces the physiology of muscle contraction more precisely. In particular, it is able to capture the power stroke fast dynamics observed in length step experiments.

We simulate such an experiment starting from the isometric steady state with a length step of 8 nm. As in the experimental conditions, the length step is made by a ramp of duration 100 µs. Note that, here, the compliance of the myosin and actin filaments is neglected as in the original paper. We choose the energy levels as defined in Piazzesi and Lombardi [1995]. We use modified transition rates to ensure that detachment rates diverge at infinity. The energy brought by ATP is set to 50 zJ following the model assumption that an ATP molecule can be used for the detachment of several myosin heads.

The results are presented in Figure 2.11. They match the results presented in the original paper Piazzesi and Lombardi [1995], which shows the consistency of our approach with the original model, hence completed with thermodynamic balances.

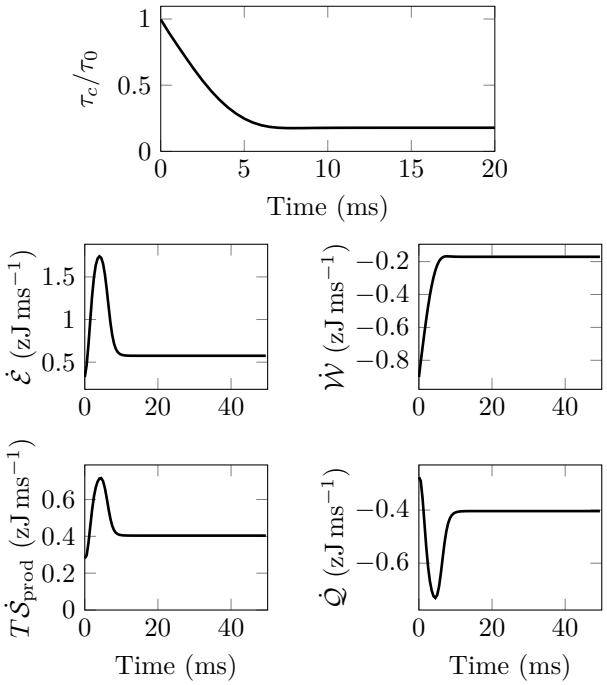

Figure 2.10 – Average tension and thermodynamic fluxes per myosin head for constant shortening velocity simulation with the Huxley'57 model. The isometric tension is denoted by τ_0.

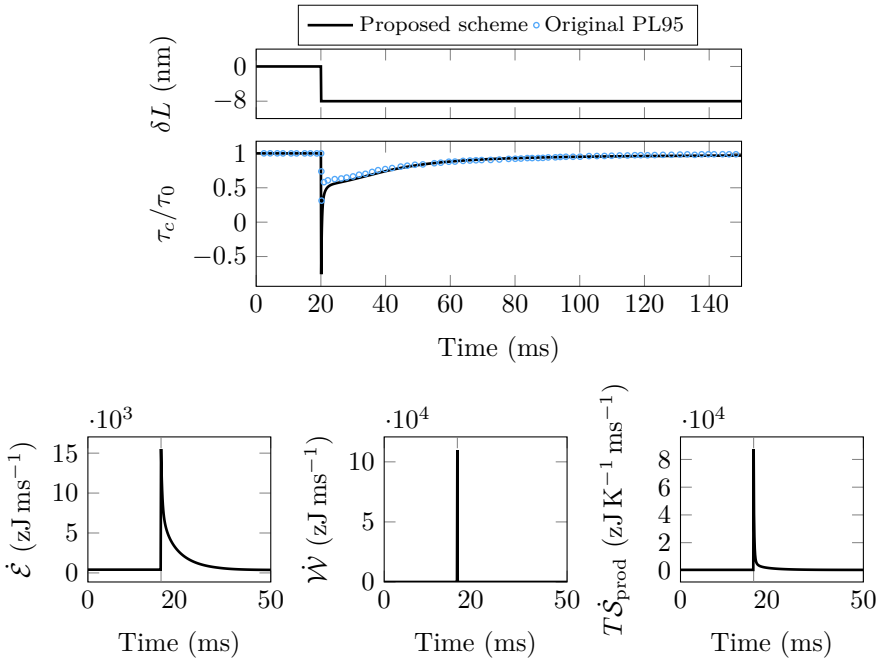

Figure 2.11 – Tension evolution and thermodynamic fluxes per myosin head in a length step experiment simulation with Piazzesi-Lombardi'95 model. The isometric tension is denoted by τ_0.

2.6 Concluding remarks

Considering a large class of muscle contraction models based on actin-myosin interaction – i.e. the Huxley'57 model and various extensions thereof, including the Piazzesi-Lombardi'95 model – we have presented a mathematical setting in which solution properties can be established, including fundamental thermodynamic balances. Moreover, we have proposed a complete discretization strategy for which we were also able to obtain discrete versions of the thermodynamic balances and other properties. In addition, we have also shown how these models can be coupled with a macroscopic continuum mechanics formulation in such a way that these balances carry over to the macroscopic level, including for the discrete versions of the models. As muscle energetics are of major relevance in physiology, this is an important achievement, both from a fundamental and numerical point of view. This paves the way, indeed, for detailed numerical studies of energy exchanges in various applications, such as with a complete realistic heart model.

2.7 Appendix

2.7.1 Numerical scheme for negative sliding velocities

In this section, we present the discrete thermodynamical balances obtained with negative sliding velocities without developing the proofs.

2.7.1.1 The Huxley'57 model

We first consider the Huxley'57 model. With negative sliding velocities $\dot{x}_c$, the numerical scheme reads

$$\begin{cases} \dfrac{a_i^{n+1}-a_i^n}{\delta t} = \underbrace{\left(k_{1,i}+k_{-2,i}\right)}_{k_{+,i}} d_i^{n+1} - \underbrace{\left(k_{2,i}+k_{-1,i}\right)}_{k_{-,i}} a_i^{n+1} - \dot{x}_c \dfrac{a_{i+1}^{n+1}-a_i^{n+1}}{\delta s} & \forall i \in [\![1,p]\!] \\ d_i^n = 1 - a_i^n \qquad \forall i \in [\![1,p]\!]. \end{cases}$$

First principle We still define the energy as

$$U^n = \frac{\delta s}{d_a}\sum_{i=1}^{p} w_{1,i}a_i^n + w_0 d_i^n = \frac{\delta s}{d_a}\sum_{i=0}^{p-1} w_{1,i}a_i^n + w_0 d_i^n.$$

and the fluxes as

$$\begin{cases} J_{1,i}^n = k_{1,i}d_i^n - k_{-1,i}a_i^n, \\ J_{2,i}^n = k_{2,i}a_i^n - k_{-2,i}d_i^n. \end{cases}$$

We obtain the the discretized version of the first principle

$$\frac{U^{n+1}-U^n}{\delta t} = \frac{W^{n+1}-W^n}{\delta t} + \frac{Q^{n+1}-Q^n}{\delta t} + \frac{E_{\text{int}}^{n+1}-E_{\text{int}}^n}{\delta t}$$

with

$$\begin{cases} \dfrac{W^{n+1}-W^n}{\delta t} = \dot{x}_c \tau_c^{n+1} \\ \dfrac{Q^{n+1}-Q^n}{\delta t} = \dfrac{\delta s}{d_a}\displaystyle\sum_{i=1}^{p}\Big[J_{1,i}^{n+1}\Big(w_{1,i}-w_0\Big) + J_{2,i}^{n+1}\Big(w_0 - w_{1,i} - \mu_T\Big)\Big] \\ \dfrac{E_{\text{int}}^{n+1}-E_{\text{int}}^{n}}{\delta t} = \mu_T \dfrac{\delta s}{d_a}\displaystyle\sum_{i=1}^{p} J_{2,i}^{n+1}. \end{cases}$$

and the definition of the discrete force

$$\tau_c^{n+1} = \frac{\delta s}{d_a}\sum_{i=1}^{p}\frac{w_{1,i}-w_{1,i-1}}{\delta s}a_i^{n+1},$$

which is adapted to the numerical scheme for negative sliding velocities.

Second principle To establish a discrete entropy balance, we define the discrete entropy

$$S^n = -k_B\sum_{i=1}^{p} a_i^n \ln a_i^n + d_i^n \ln d_i^n$$

and the free energy $F^n = U^n - TS^n$. The free energy can be rewritten

$$F^n = \sum_{i=1}^{p}\mu_{1,i}^n a_i^n + \mu_{0,i}^n d_i^n$$

by introducing the discrete chemical potentials

$$\mu_{1,i}^n = w_{1,i} + k_B T \ln a_i^n$$
$$\mu_{0,i}^n = w_0 + k_B T \ln d_i^n.$$

We obtain

$$\frac{F^{n+1}-F^n}{\delta t} - \dot{x}_c\tau_c^{n+1} - \mu_T\frac{\delta s}{d_a}\sum_{i=1}^{p} J_{2,i}^{n+1} \le 0.$$

or in terms of an entropy balance

$$\frac{S_{\text{prod}}^{n+1}-S_{\text{prod}}^n}{\delta t} = \frac{S^{n+1}-S^n}{\delta t} - \frac{1}{T}\frac{Q^{n+1}-Q^n}{\delta t},$$

where the entropy creation is formally given by

$$\begin{aligned} \frac{S_{\text{prod}}^{n+1}-S_{\text{prod}}^n}{\delta t} = & \\ -\frac{1}{T}\Bigg(&\frac{\delta s}{d_a}\sum_{i=1}^{p}\Big[J_{1,i}^{n+1}\Big(\mu_{1,i}^{n+1}-\mu_{0,i}^{n+1}\Big) + J_{2,i}^{n+1}\Big(\mu_{0,i}^{n+1}-\mu_{1,i}^{n+1}-\mu_T\Big)\Big] \\ &+ \frac{\dot{x}_c k_B T}{d_a}\sum_{i=1}^{p}\Big[\Big(\ln(d_i^{n+1})-\ln(a_i^{n+1})\Big)\Big[a_{i+1}^{n+1}-a_i^{n+1}\Big]\Big] \\ &+ \frac{k_B T\delta s}{d_a}\sum_{i=1}^{p}\Big[a_i^n\Big(\frac{\ln(a_i^{n+1})-\ln(a_i^n)}{\delta t}\Big)\Big] + \frac{k_B T\delta s}{d_a}\sum_{i=1}^{p}\Big[d_i^n\Big(\frac{\ln(d_i^{n+1})-\ln(d_i^n)}{\delta t}\Big)\Big]\Bigg), \end{aligned}$$

and satisfies the inequality

$$T\frac{S_{\text{prod}}^{n+1}-S_{\text{prod}}^n}{\delta t} \ge 0.$$

2.7.1.2 Piazzesi-Lombardi'95 model

We now consider the Piazzesi-Lombardi'95 model.

Numerical scheme The numerical scheme with $\dot{x}_c \leq 0$ is given by

$$\begin{cases} \dfrac{x_{q,i+j\ell}^{n+1} - x_{q,i+j\ell}^{n}}{\delta t} = \displaystyle\sum_{p|E_{pq}\in G} J_{pq,i+j\ell}^{n+1} - \dot{x}_c \frac{x_{q,i+j\ell+1}^{n+1} - x_{q,i+j\ell}^{n+1}}{\delta s}, \forall V_q \in V_{\mathrm{a}}, \\ \qquad\qquad\qquad\qquad\qquad\qquad\qquad\qquad \forall i \in [\![1,\ell]\!],\ j \in \mathbb{Z} \\ \dfrac{x_{q,i}^{n+1} - x_{q,i}^{n}}{\delta t} = \displaystyle\sum_{p|E_{pq}\in G} \sum_{j\in\mathbb{Z}} J_{pq,i+j\ell}^{n+1} - \dot{x}_c \frac{x_{q,i+1}^{n+1} - x_{q,i}^{n+1}}{\delta s}, \forall V_q \in V_{\mathrm{d}},\ i \in [\![1,\ell]\!]. \end{cases}$$

First principle We define the internal by the same expression as with positive sliding velocitites

$$\mathcal{U}^n = \frac{\delta s}{d_a} \sum_{i=1}^{\ell} \Big[\sum_{V_q\in V_{\mathrm{a}}} \sum_{j\in\mathbb{Z}} w_{q,i+j\ell} x_{q,i+j\ell}^n + \sum_{V_q\in V_{\mathrm{d}}} w_q x_{q,i}^n \Big].$$

The discrete force is defined by

$$\tau_c^{n+1} = \frac{\delta s}{d_a} \sum_{i=1}^{\ell} \sum_{V_q\in V_{\mathrm{a}}} \sum_{j\in\mathbb{Z}} x_{q,i+j\ell} \frac{w_{q,i+j\ell}^{n+1} - w_{q,i+j\ell-1}^{n+1}}{\delta s}.$$

and we obtain the discrete first principle

$$\frac{\mathcal{U}^{n+1} - \mathcal{U}^n}{\delta t} = \frac{\mathcal{W}^{n+1} - \mathcal{W}^n}{\delta t} + \frac{\mathcal{Q}^{n+1} - \mathcal{Q}^n}{\delta t} + \frac{\mathcal{E}^{n+1} - \mathcal{E}^n}{\delta t},$$

with

$$\left| \begin{array}{l} \dfrac{\mathcal{W}^{n+1} - \mathcal{W}^n}{\delta t} = \dot{x}_c \tau_c^{n+1}, \\ \dfrac{\mathcal{Q}^{n+1} - \mathcal{Q}^n}{\delta t} = \dfrac{\delta s}{d_a} \displaystyle\sum_{i=1}^{\ell} \sum_{E_{pq}\in G} \sum_{j\in\mathbb{Z}} J_{pq,i+j\ell}^{n+1} \tilde{W}_{pq,i+j\ell}, \\ \dfrac{\mathcal{E}^{n+1} - \mathcal{E}^n}{\delta t} = \mu_T \dfrac{\delta s}{d_a} \displaystyle\sum_{i=1}^{\ell} \sum_{j\in\mathbb{Z}} \Big(J_{25,i+j\ell} + J_{34,i+j\ell} \Big). \end{array} \right.$$

Second principle As before, we define the discrete entropy as

$$\mathcal{S}^n = -k_B \frac{\delta s}{d_a} \sum_{i=1}^{\ell} \Big[\sum_{V_q\in V_{\mathrm{a}}} \sum_{j\in\mathbb{Z}} x_{q,i+j\ell}^n \ln x_{q,i+j\ell}^n + \sum_{V_q\in V_{\mathrm{d}}} x_{q,i}^n \ln x_{q,i}^n \Big].$$

The free energy $\mathcal{F}^n = \mathcal{U}^n - T\mathcal{S}^n$ can be rewritten as

$$\mathcal{F}^n = \frac{\delta s}{d_a} \sum_{i=1}^{\ell} \Big[\sum_{V_q\in V_{\mathrm{a}}} \sum_{j\in\mathbb{Z}} \mu_{q,i+j\ell}^n x_{q,i+j\ell}^n + \sum_{V_q\in V_{\mathrm{d}}} \mu_{q,i}^n x_{q,i}^n \Big],$$

using discrete chemical potentials

$$\left| \begin{array}{l} \mu_{q,i+j\ell}^n = w_{q,i+j\ell} + k_B T \ln x_{q,i+j\ell}^n,\ V_q \in V_{\mathrm{a}}, \\ \mu_{p,i}^n = w_q + k_B T \ln x_{q,i}^n,\ V_q \in V_{\mathrm{d}}. \end{array} \right.$$

We finally obtain

$$\frac{\mathcal{F}^{n+1}-\mathcal{F}^{n}}{\delta t}-\dot{x}_c\tau_c^{n+1}-\mu_T\sum_{i=1}^{\ell}\sum_{j\in\mathbb{Z}}\Big(J_{25,i+j\ell}+J_{34,i+j\ell}\Big)\leq 0.$$

As in Section (2.4.4) this property is equivalent to

$$\frac{\mathcal{S}_{\text{prod}}^{n+1}-\mathcal{S}_{\text{prod}}^{n}}{\delta t}=\frac{\mathcal{S}^{n+1}-\mathcal{S}^{n}}{\delta t}-\frac{1}{T}\frac{\mathcal{Q}^{n+1}-Q^{n}}{\delta t}\geq 0,$$

with the entropy production given by

$$\begin{aligned}\frac{\mathcal{S}_{\text{prod}}^{n+1}-\mathcal{S}_{\text{prod}}^{n}}{\delta t}=-\frac{1}{T}\Bigg(&\frac{\delta s}{d_a}\sum_{i=1}^{\ell}\sum_{E_{pq}\in G}\sum_{j\in\mathbb{Z}}J_{pq,i+j\ell}^{n+1}\tilde{M}_{pq,i+j\ell}^{n+1}\\&-\frac{\dot{x}_c k_B T}{d_a}\sum_{i=1}^{\ell}\sum_{V_q\in V_{\text{a}}}\sum_{j\in\mathbb{Z}}\Big[\ln(x_{q,i+j\ell}^{n+1})\Big)\Big[x_{q,i+j\ell+1}^{n+1}-x_{q,i+j\ell}^{n+1}\Big]\Big]\\&-\frac{\dot{x}_c k_B T}{d_a}\sum_{i=1}^{\ell}\sum_{V_q\in V_{\text{d}}}\Big[\ln(x_{q,i}^{n+1})\Big)\Big[x_{q,i+1}^{n+1}-x_{q,i}^{n+1}\Big]\Big]\\&+\frac{k_B T\delta s}{d_a}\sum_{i=1}^{\ell}\sum_{V_q\in V_{\text{a}}}\sum_{j\in\mathbb{Z}}\Big[x_{q,i+j\ell}^{n}\Big(\frac{\ln(x_{q,i+j\ell}^{n+1})-\ln(x_{q,i+j\ell}^{n})}{\delta t}\Big)\Big]\\&+\frac{k_B T\delta s}{d_a}\sum_{i=1}^{\ell}\sum_{V_q\in V_{\text{d}}}\Big[x_{q,i}^{n}\Big(\frac{\ln(x_{q,i}^{n+1})-\ln(x_{q,i}^{n})}{\delta t}\Big)\Big]\Bigg).\end{aligned}$$

Bibliography

Caruel, M., Moireau, P., and Chapelle, D. (2019). Stochastic modeling of chemical-mechanical coupling in striated muscles. *Biomechanics and Modeling in Mechanobiology*, 18(3):563–587.

Chapelle, D., Le Tallec, P., Moireau, P., and Sorine, M. (2012). Energy-preserving muscle tissue model: formulation and compatible discretizations. *Journal for Multiscale Computational Engineering*.

Chipot, M., Hastings, S., and Kinderlehrer, D. (2004). Transport in a molecular motor system. *ESAIM: M2AN*, 38(6):1011–1034.

Eisenberg, E. and Hill, T. (1978). A cross-bridge model of muscle contraction. *Progress in biophysics and molecular biology*, 33(1):55–82.

Eisenberg, E., Hill, T., and Chen, Y. (1980). Cross-bridge model of muscle contraction. Quantitative analysis. *Biophysical Journal*, 29(2):195–227.

Godunov, S. (1959). A difference method for numerical calculation of discontinuous solutions of the equations of hydrodynamics. *Matematicheskii Sbornik*, 89(3):271–306.

Gonzales, O. (2000). Exact energy and momentum conserving algorithm for general models in nonlinear elasticity. *Comput. Meth. Appl. Mech. Eng.*, 190(13-14):1763–1783.

Hauret, P. and Le Tallec, P. (2006). Energy controlling time integration methods for nonlinear elastodynamics and low velocity impact. *Comput. Meth. Appl. Mech. Eng.*, 195:4890–4916.

Hill, A. (1938). The heat of shortening and the dynamic constants of muscle. *Proc. R. Soc. Lond. B*, 126(843):136–195.

Hill, T. (1977). *Free Energy Transduction in Biology*. Academic Press.

Hill, T. (2004). *Free Energy Transduction And Biochemical Cycle Kinetics*. Dover.

Huxley, A. (1957). Muscle structures and theories of contraction. *Progr. Biophys. Chem.*

Huxley, A. and Simmons, R. (1971). Proposed mechanism of force generation in striated muscle. *Nature*.

Julicher, F., Ajdari, A., and Prost, J. (1997). Modeling molecular motors. *Rev. Mod. Phys.*, 69(4):1269–1281.

Le Tallec, P. and Hauret, P. (2003). Energy conservation in fluid structure interactions. In Kuznetsov, Y., Neittanmaki, P., and Pironneau, O., editors, *Numerical Methods for Scientific Computing - Variational Problems and Applications*.

Lymn, R. and Taylor, E. (1971). Mechanism of adenosine triphosphate hydrolysis by actomyosin. *Biochemistry*, 10(25):4617–4624.

Marcucci, L., Washio, T., and Yanagida, T. (2016). Including thermal fluctuations in actomyosin stable states increases the predicted force per motor and macroscopic efficiency in muscle modelling. *PLoS Computational Biology*, 12(9).

Mirrahimi, S. and Souganidis, P. (2012). A homogenization approach for the motion of motor proteins. *Nonlinear Differ. Equ. Appl.*, 20(1):129–147.

Peskin, C. (1975). *Mathematical Aspects of Heart Physiology*. Courant Institute of Mathematical Sciences - NYU.

Piazzesi, G. and Lombardi, V. (1995). A cross-bridge model that is able to explain mechanical and energetic properties of shortening muscle. *Biophysical Journal*, 68:1966–1979.

Richtmyer, R. and Morton, K. (1967). *Difference methods for initial-value problems*. Interscience tracts in pure and applied mathematics. Interscience Publishers.

Sheshka, R. and Truskinovsky, L. (2014). Power-stroke-driven actomyosin contractility. *Physical review. E, Statistical, nonlinear, and soft matter physics*, 89(1):012708.

CHAPTER 3

Hierarchical modeling of force generation in cardiac muscle

Chemico-mechanical models are commonly used to describe the myosin heads within the sarcomeres of cardiac muscles. Our main objective is to propose a hierarchy of cardiac muscle contraction models that are rigorously and systematically related with each other. Starting from a refined model, which considers the stochastic dynamics of the myosin heads and, in particular, captures the power stroke, we propose two stages of simplification. We first perform the asymptotic elimination of the fast degrees of freedom, which are associated with the myosin internal configuration. This transforms the governing stochastic differential equation into a partial differential equation and allows us to derive a formulation that falls into the family of the Huxley'57 model, while embedding some ingredients of power stroke description. Then, making assumptions on the attachment and detachment rates and the cross-bridge mechanical energy, the model is further reduced to a set of ordinary differential equations. These models are validated with the experimental data corresponding to their range of validity. A particular emphasis is put on the calibration process, which takes advantage of the tight links between the models. The calibration is indeed an essential element for the use of models in clinical applications. The proposed modeling framework offers a way to select, for a specific application, the model that yields the best trade-off between the fidelity of the model, the associated computational cost and the availability of the data that are required for the model calibration.

Contents

Hierarchical modeling of force generation in cardiac muscle

François Kimmig[1,2], Matthieu Caruel[3]

[1]LMS, Ecole Polytechnique, CNRS, Université Paris-Saclay
[2]Inria, Université Paris-Saclay
[3]MSME, Université Paris-Est Créteil Val de Marne

to be submitted

Abstract

Chemo-mechanical models are commonly used to describe the myosin heads within the sarcomeres of cardiac muscles. Our main objective is to propose a hierarchy of cardiac muscle contraction models that are rigorously and systematically related with each other. Starting from a refined model, which considers the stochastic dynamics of the myosin heads and, in particular, captures the power stroke, we propose two stages of simplification. We first perform the asymptotic elimination of the fast degrees of freedom, which are associated with the myosin internal configuration. This transforms the governing stochastic differential equation into a partial differential equation and allows us to derive a formulation that falls into the family of the Huxley'57 model, while embedding some ingredients of power stroke description. Then, making assumptions on the attachment and detachment rates and the cross-bridge mechanical energy, the model is further reduced to a set of ordinary differential equations. Theses models are validated with the experimental data corresponding to their range of validity. A particular emphasis is put on the calibration process, which takes advantage from the tight links between the models. The calibration is indeed an essential element for the use of models in clinical applications. The proposed modeling framework offers a way to select, for a specific application, the model that yields the best trade-off between the fidelity of the model, the associated computational cost and the availability of the data that are required for the model calibration.

Keywords— muscle modeling; sarcomere; sliding filament; cross-bridge; power stroke; model reduction

3.1 Introduction

Mechanical modeling of micro-scale muscle contraction mechanisms is an essential step towards the implementation of patient-specific physiologically relevant *in silico* heart simulations, providing an effective diagnosis and treatment planning tool. The effectiveness of the developed models relies primarily on their ability to reproduce the biological processes at the origin of muscle contraction with a level of detail adapted to the clinical situation. The usual approach is to design a multi-scale and multi-physics framework that establishes the coupling between the microscopic active force production and regulation mechanisms at the molecular scale with the macroscopic, organ scale, indicators that can be utilized in a clinical context.

The active force to be modeled results from the conversion of the metabolic energy extracted from ATP hydrolysis into mechanical work [Alberts, 2015]. This operation is done

through the cyclic enzymatic interaction between groups of ATPase Myosin II molecular motors forming a thick filament and the surrounding parallel (thin) actin filaments. The force is produced while Myosin heads are attached to actin, via a large conformational change, the power stroke, which induces a relative displacement ($\sim$10 nm at zero load) between the Myosin filament and the actin filament. The energy necessary to recock the power-stroke mechanism is provided by ATP hydrolysis within the myosin molecule.

The thick and thin filaments are spatially organized in parallel within micrometer-sized contractile units called sarcomeres [Huxley, 1957, 1969].

The sarcomeres themselves are arranged in series along the longitudinal direction of the muscle cells forming a dense elastic fibers network which transmits force to the whole tissue.

The active force production is subjected to physiological mechanisms that regulate the degree of activation of the force producing units. The main regulation pathways are the actin filament activation (through the calcium sensitive troponin-tropomyosin complex) and the availability of myosin heads. Both pathways have been shown to be modulated by the degree of sarcomere stretch [Kentish et al., 1986; de Tombe et al., 2010]. The activation of actin sites is, in addition, sensitive to the level of calcium supply in the cell.

These regulations are at the core of the so-called Franck-Starling effect at the macroscopic scale [Allen & Kentish, 1985; de Tombe et al., 2010]. Notice that, at the organ level, the intracellular calcium concentration and many other aspects of the muscle contraction are also controlled by the neuroendocrine system.

Even though both contraction and regulation mechanisms are essential for the physiological heart contraction, recent experimental studies have demonstrated that these regulation mechanisms do not affect the characterization of the intrinsic mechanical properties of the actomyosin system [Caremani et al., 2016; Pinzauti et al., 2018]. Indeed, the regulation mechanisms only affect the number of attached myosin heads. Hence the basal contraction mechanism can presumably be studied at any nominal sarcomere length and any level of calcium activation by properly normalizing the experimental results. In particular, this finding allows to study in detail the force generation molecular mechanisms on ex-vivo preparations disconnected from the regulation apparatus. In this paper, we focus on of the force production mechanism alone (without regulation), and use the results of these experimental studies for calibration of the proposed models.

The most widely used experiment of this type allowing to characterize the mechanical output of the contractile system – and calibrate the model parameters – consists in measuring at the sarcomere level, the transient isotonic shortening in response to a sudden force step applied within $\sim 100\,\mu$s from an isometric state [Caremani et al., 2016]. Remarkably, the reaction to this perturbation allows to identify, from a single experiment, the contribution of three essential physical characteristics of the actomyosin system – namely elasticity, conformational change and actomyosin attachment and detachment processes – by using the fact that they operate at three different timescales: 100 µs, 1 ms and 30 ms, respectively [Caremani et al., 2016]. To reproduce this benchmark experiment, theoretical models should be built from ingredients representing all the involved processes.

Most of the available modeling attempts derive from the seminal work of A.F. Huxley [Huxley, 1957] later thermodynamically formalized by T.L. Hill [Hill, 1977]. The framework is a spatially unidimensional system where myosin II is modeled as a spring that can reversibly attach to specific binding sites on the surrounding actin filaments. The spring itself has internal – discrete or continuous – degrees of freedom that represent the conformational – and ligand-binding – state of the protein. A single motor is therefore characterized by (i) its position relative to the binding sites (strain) (ii) its internal conformation and (iii) its attachment state. The force generated by the motor directly derives

from the energy of the spring, which then depends on the distance to the binding site and the internal conformation. The myofilaments themselves are usually modeled as an independent spring in series with the motor system [Linari et al., 1998]. The molecular motors then effectively bridge two rigid backbones.

In this context, the thermodynamics properties of the system depend on three categories of model parameters. The first category characterizes the intrinsic mechanical properties of the myosin motor system such as the geometric lengths, the transition rates between discrete attached states, the stiffnesses and more generally the energy landscapes associated with the degrees of freedom representing the protein state. The second category contains the model input that determine the kinetic properties of the contraction mechanism. This set includes the attachment and detachment rates, and the viscosity-type parameters characterizing the dynamics of continuous internal degrees of freedom [Marcucci & Truskinovsky, 2010]. The last category concerns the energetic properties of the system related to both the intrinsic energy landscapes (mechanical properties) and the free energy changes associated with the metabolic reactions among which the most important one is the ATP hydrolysis.

A major challenge faced by all modeling attempts is to calibrate these parameters. We point out that since some of them may be functions (in the case of transition rates), the number of parameters is virtually infinite, and the calibration of complex models is likely not unique. Therefore, the space of function should be chosen such as to leave a minimal number of free parameters and the available data that the model intends to reproduce would ideally impose strong constraints on them.

Moreover, increasingly complex models are inevitably accompanied by higher CPU costs. Hence, their use in finite elements simulations of heart contraction on realistic geometries, may reveal inefficient, for instance, when real-time simulation are required, indeed. The use of theoretical modeling of heart contraction should then results from a compromise between a high degree of model refinement – to reproduce the micro-scale physiology – and the possibility to identify – in a reasonable time – the effects of the modeling assumptions on the observable macro-scale. For instance, a model that is capable of reproducing the physiological phenomena occurring at the molecular level at a sub-millisecond timescale in the isotonic shortening in-vitro experiments is likely to be unnecessarily detailed and too difficult to calibrate to simulate the $\sim 1\,\mathrm{s}$ heart beat of a specific outpatient.

In this paper, we propose a hierarchical approach to this problem by formulating a series of interrelated models, from the more refined, calibrated on single cell experiments, to the more coarse grained aimed at efficient organ simulation. Each coarse graining step is obtained from simplifications of the more refined model, such that the loss of information is well controlled. All models are calibrated using the benchmark isotonic shortening experiment, which again provide the essential mechanical information about the micro-scale contractile apparatus. For each model of our hierarchy, we discuss its ability to reproduce the experimental data and its relevance for heart simulations as a guidance for appropriate model choosing depending on the application sought.

Our starting point is the stochastic model formulated in [Caruel et al., 2019] to reproduce the fundamental four steps of the force generating Lymn-Taylor cycle [Lymn & Taylor, 1971] *i.e.* (i) the attachment of myosin to actin, (ii) the myosin conformational change that corresponds to the force generating power-stroke, (iii) the detachment from actin, and (iv) the re-cocking of the power-stroke while the myosin is detached from actin. This model combines a standard Hill-type approach to describe the attachment and detachment processes with a more recently developed continuous stochastic dynamics for the internal conformational variables [Marcucci & Truskinovsky, 2010].

We show that our model can be almost univocally calibrated using available isotonic shortening experimental data from rat cardiomyocytes [Caremani et al., 2016], by restricting the space of function describing the energy landscapes of the conformational variables and the strain dependence of the transition rates.

The first level of simplification is obtain by adiabatically eliminating the internal variable characterizing the force-generating conformational change (power-stroke). The relaxation of this internal rearrangement towards equilibrium has been shown to be at the origin of the milli-second timescale phase of the response to sudden force changes [Huxley & Simmons, 1971; Lombardi et al., 1992], which can be considered to be fast compared to the $\sim 30\,\mathrm{ms}$ timescale associated with the completion of the ATPase cycle [Caremani et al., 2015]. Hence at each time one can make the approximation approximate that internal degrees of freedom are in thermal equilibrium.

This procedure has already been used in [Zahalak, 2000; Hill, 1977; Caruel et al., 2019]. The obtained power-stroke equilibrated mode (PSE model) is a simple two-state model that can be viewed as an instance of the Huxley'57 framework. This model can be calibrated alongside the stochastic model. Our procedure allows to put the calibration into perspective and illustrate that the experimental constraints define the calibration almost uniquely for this type of model. We show that the PSE model is able to reproduce the most relevant markers of the mechanical performance of cardiac fibers Caremani et al. [2016]; Pertici et al. [2018]; de Tombe & Stienen [2007]. A particular emphasis is put on the fact that the ATP consumption is not calibrated but predicted by the model.

Both the stochastic and the PSE models describe the evolution of the population of the available myosin motors – either from stochastic differential equations (SDE) or deterministic partial differential equations (PDE) – from which the mechanical macroscopic outputs such as force, stiffness, thermodynamic yield, can be derived by direct statistical averaging. In the context of 3D finite element simulations of the heart, these equations have to be solved at each integration points of the mesh, which dramatically increases the computational time.

The next level of simplification is based on the classical expansion of the population densities into an infinite series of *macroscopic* moments, whose dynamics are obtained by solving an infinite set of coupled Ordinary Differential Equation (ODE) [Chapelle et al., 2012; Zahalak, 2000, 1981]. Simple closure relations can be formulated in order to limit the size of the system at an arbitrary – ideally low – number of equations. Solving ODEs instead of PDEs at each integration point leads to a dramatic decrease on the computational time, which makes this type of coarse-grained models particularly fit for 3D heart simulation in clinical context [Chapelle et al., 2012; Chabiniok et al., 2011]. We propose two simplifying assumptions of the PSE model allowing to derive two moment based "macroscopic models". These models are derived by restraining the PSE model space of functions for the attachment-detachment process and for the internal equilibrium energy landscape. These restrictions are on the model parameters rather than on the form of the solution as it was done in [Zahalak, 1981].

Finally, our method is not restricted to a single refined model, it can be applied to any state-of-the-art chemico-mechanical models [Smith et al., 2008; Smith & Mijailovich, 2008; Månsson, 2010; Mijailovich et al., 2016]. We show that the obtained macroscopic models are in good agreement with the PSE model over the range of loading conditions that is relevant for the heart functioning during a typical PV loop, the differences becoming significant only in regimes that are non-physiological. Hence, despite their simplicity and the fact that they are not able to fully reproduce the behavior of the contractile system as observed *ex vivo*, the macroscopic models appears to be an adequate tool for an efficient simulation of the basal contraction mechanics at the macro-scale. The originality of our

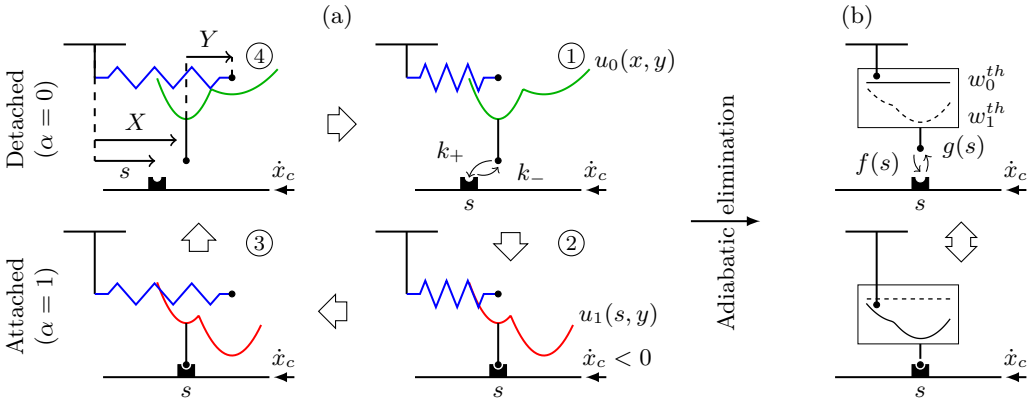

Figure 3.1 – Summary of the full model and its reduction to a two state model. (a) Stochastic model. The states are indexed as follows. 1 detached pre-power stroke; 2 attached pre-power stroke, 3 attached post-power stroke, 4 detached post-power stroke. (b) PSE model obtained by the adiabatic elimination of the stochastic model power stroke degrees of freedom.

approach is that the loss of information brought by the sequence of simplifying assumptions is well controlled, so that the simpler models can be consistently enriched if need be.

The paper is organized as follows. In Section 3.2 we derive our hierarchy of models, starting with the population models. Note that we only give here a summary of the stochastic model, which is presented in full detail in [Caruel et al., 2019]. Section 3.3 presents the calibration and the comparison of the models using the isotonic shortening experimental data. First, the two population models, namely the stochastic model and the PSE model are discussed, before the PSE model is compared with the macroscopic models. Sections 3.4 and 3.5 present a discussion of the results and our conclusion, respectively.

3.2 Hierarchy of models

3.2.1 Population models

3.2.1.1 Stochastic model

Our core model on which our hierarchy is built was already formulated in [Caruel et al., 2019], and calibrated using data from frog skeletal muscle experiments. The model relies on the sliding filament theory introduced by [Huxley, 1957], based on the hypothesis that the myosin heads and actin sites are regularly distributed along their respective filaments within a sarcomere and that the distance to their neighbors is constant. The compliance of the myofilaments is assumed to be lumped into an effective linear elastic element in series with a set of myosin motors interacting with two rigid backbones [Ford et al., 1981]. We consider a single actin site model, meaning that the myosin head can bind to the nearest actin site only, which is located at a distance s from the anchor point of the head in the myosin filament. In this framework, the description of the actomyosin interaction can be reduced to that of a single representative myosin head because of the high number of myosin heads in a sarcomere.

The state of the myosin head is parametrized by three dynamical variables (see Figure 3.1(a)):

- X^t, a continuous variable representing the displacement between the position of tip of the head in the current state and at rest;

- Y^t, a continuous internal variable representing the internal conformation of the head (power-stroke)
- α^t, a discrete variable accounting for the attachment state of the head, taking the value $\alpha^t = 1$ when the myosin head is attached, and the value $\alpha^t = 0$ when it is detached.

Following [Marcucci & Truskinovsky, 2010] the myosin head is modeled as a bistable snap-spring comprising an elastic spring representing the compliance of the macromolecule in series with a bi-stable element accounting for the power-stroke conformational change, see Figure 3.1(a). The internal energy of the head in state α is then defined as

$$w(x, y, \alpha) = w_\alpha(x, y) = \frac{\kappa}{2}(x + y)^2 + u_\alpha(y), \tag{3.1}$$

where κ is the stiffness of the macromolecule and u_α is a double well potential associated with the bistable element. The force developed by the attached myosin head on the thin filament is thus $\tau_c(x, y) = \partial_x w_1(x, y) = \kappa(x+y)$. Undergoing the power stroke is equivalent to stretching this elastic element, see Figure 3.1(a). When the myosin is detached, no force is developed.

In the over-damped regime, the dynamics of an individual myosin head is governed by the following system of stochastic equations [Caruel et al., 2019]

$$\begin{cases} \mathrm{d}X^t = \left[\alpha^t \dot{x}_c - (1-\alpha^t)\eta^{-1}\partial_x w_\alpha(X^t, Y^t)\right]\mathrm{d}t \\ \qquad\qquad + \delta(t - t_s)[s(t) - X^t]\mathrm{d}t + (1-\alpha^t)\sqrt{2D}\mathrm{d}B_x^t & \text{(3.2a)} \\ \mathrm{d}Y^t = -\eta^{-1}\partial_y w_\alpha(X^t, Y^t)\mathrm{d}t + \sqrt{2D}\mathrm{d}B_y^t & \text{(3.2b)} \\ \mathbb{P}\left[\alpha^{t+\mathrm{d}t} = 1 | \alpha^t = 0\right] = k_+(X^t, Y^t, s, t)\mathrm{d}t & \text{(3.2c)} \\ \mathbb{P}\left[\alpha^{t+\mathrm{d}t} = 0 | \alpha^t = 1\right] = k_-(X^t, Y^t, s, t)\mathrm{d}t & \text{(3.2d)} \end{cases}$$

where η is a drag coefficient, $\dot{x}_c$ is the sliding velocity ($\dot{x}_c$ being positive for an extending sarcomere) and $D = k_B T/\eta$ is a diffusion coefficient. Here T is the absolute temperature and k_B is the Boltzmann constant[1]. In (3.2a), t_s denotes the time where a transition from the detached to the attached state occurs and the term $\delta(t - t_s)[s(t) - X^t]\mathrm{d}t$ ensures that between t_s and $t_s + \mathrm{d}t$, the variable X^t jumps from its current value X^{t_s} to the value $s(t_s + \mathrm{d}t)$.

Following the approach presented in [Caruel et al., 2019], we now consider the population of heads in a section that has the thickness of half-sarcomere. The density of myosin heads in such a section is $1.25 \times 10^{17}\,\mathrm{m}^{-2}$ [Pinzauti et al., 2018], a statistical description of the system can thus be used. We denote by $p(x, y, \alpha; s, t)$ the probability distribution of the myosin head state for a subpopulation of the heads located at distance s of the nearest actin site at time t. This probability distribution mixing continuous and discrete variables is normalized in the following way

$$\sum_{\alpha=\{0,1\}} \iint p(x, y, \alpha; s, t)\,\mathrm{d}x\mathrm{d}y = 1, \quad \forall t\ \forall s. \tag{3.3}$$

Since, in the attached state, the tip of the myosin head can only be located at the position of the actin site ($X^t = s(t)$), the probability distribution $p(x, y, \alpha = 1; s, t)$ is degenerated and becomes

$$p(x, y, \alpha = 1; s, t) = \delta(x - s)\overline{p}(y; s, t). \tag{3.4}$$

[1] $k_B = 1.38 \times 10^{-23}\,\mathrm{J\,K}^{-1}$

The Fokker-Planck equations associated to the system of SDEs (3.2) are (see [Caruel et al., 2019] for the detailed derivation of the equations)

$$\begin{cases} \partial_t p(x,y,0;s,t) + \dot{x}_c \partial_s p(x,y,0;s,t) = \\ \qquad \partial_y \Big[\eta^{-1} \partial_y w_0(x,y) p(x,y,0;s,t) + D \partial_y p(x,y,0;s,t) \Big] \\ \qquad + \partial_x \Big[\eta^{-1} \partial_x w_0(x,y) p(x,y,0;s,t) + D \partial_x p(x,y,0;s,t) \Big] \\ \qquad + k_-(y,s) \delta(x-s) \overline{p}(y;s,t) - k_+(x,y,s) p(x,y,0;s,t), \\ \partial_t \overline{p}(y;s,t) + \dot{x}_c \partial_s \overline{p}(y;s,t) = \\ \qquad \partial_y \Big[\eta^{-1} \partial_y w_1(x,y) \overline{p}(y;s,t) + D \partial_y \overline{p}(y;s,t) \Big] \\ \qquad + \int k_+(x,y,s) p(x,y,0;s,t) \, \mathrm{d}x - k_-(y,s) \overline{p}(y;s,t). \end{cases} \tag{3.5}$$

In this framework, the active force is given by

$$\tau_c(t) = \frac{1}{d_a} \int_{s^-}^{s^+} \int_{-\infty}^{+\infty} \partial_s w_1(s,y) \overline{p}(y;s,t) \, \mathrm{d}y \mathrm{d}s, \tag{3.6}$$

where d_a is the distance between two consecutive actin sites. The interval of reachable actin sites is denoted by $[s^-, s^+]$ with $s^+ - s^- = d_a$. The cross-bridges working in parallel in the sarcomere, the macroscopic tension developed by a muscle fiber is given by

$$T_c(t) = \rho_{\mathrm{surf}} \tau_c(t), \tag{3.7}$$

where ρ_{surf} is the number of myosin heads in a layer that has a thickness equal to the half-sarcomere length ℓ_{hs} per cross-section area.

As noted by T.L. Hill [Hill, 1977], the assumption of a single actin site available at a given time for each myosin head imposes that the probability that a myosin head is attached on the boundary of the interval $[s^-, s^+]$ vanishes. We should thus have

$$\iint p(x,y,\alpha;s^-,t) \, \mathrm{d}x \mathrm{d}y = \iint p(x,y,\alpha;s^+,t) \, \mathrm{d}x \mathrm{d}y = 0, \text{ for } \alpha \in \{0,1\}. \tag{3.8}$$

This property is ensured by a proper choice of the attachment and detachment rates k_+ and k_-, respectively.

Note that this model does not take into account the calcium-induced thin filament activation [Kobayashi et al., 2008]. The recently observed OFF-state in which the myosin head is folded on the back bone of the thick filament and do not undergo the Lymn-Taylor cycle [Linari et al., 2015], [Reconditi et al., 2017] is also not considered. All myosin heads are supposed to be available for attachment and all actin sites are activated, meaning that they can form cross-bridges with myosin heads.

The main purpose of the the stochastic model is to capture all the timescales of the response of a fiber submitted to rapid load changes, see Section 3.3. In particular, the rapid transient corresponding to the second phase will be associated with the relaxation of the internal degree of freedom Y towards its equilibrium distribution, which will allow to calibrate the energy $w_1(x,y)$.

In the following section, we formulate a simplified model whose formulation is obtained by eliminating the dynamics of this relaxation.

3.2.1.2 Adiabatic elimination of the power stroke: the PSE model

The first level of simplification of the stochastic model can be obtained by considering the experimental evidence of a separation of timescale between the power-stroke transition ($\sim$ 1 ms) and the characteristic timescale for the completion of the Lymn-Taylor cycle ($\sim$ 100 ms). A detailed analysis of the response of a muscle fiber to rapid change in loading condition revealed the ability for the contractile apparatus to quickly adjust to the new load through the synchronization of the power-stroke transitions of attached cross-bridges [Huxley & Simmons, 1971]. After this fast transient the attachment-detachment process gets involved and the system eventually reaches a steady state.

Building on this separation of timescale, one can adiabatically eliminate the internal degrees of freedom X and Y – characterizing the power-stroke conformational change – by assuming that their dynamics is infinitely fast compared to the timescale associated with the other variable dynamics (α^t). In this limit, the distribution of the random variable X and Y follows the classical Boltzmann equilibrium distribution

$$\begin{cases} p_0^{th}(x,y) = \dfrac{\exp\Big(-w_0(x,y)/(k_BT)\Big)}{\iint \exp\Big(-w_0(x,y)/(k_BT)\Big)\,\mathrm{d}y\mathrm{d}x}, & \text{(3.9a)} \\ p_1^{th}(y;s) = \dfrac{\exp\Big(-w_1(s,y)/(k_BT)\Big)}{\int \exp\Big(-w_1(s,y)/(k_BT)\Big)\,\mathrm{d}y}. & \text{(3.9b)} \end{cases}$$

The probability densities $p(x,y,\alpha;s,t)$ can then be decomposed as follows

$$\begin{cases} p(x,y,0;s,t) = P_0(s,t)p_0^{th}(x,y), & \text{(3.10a)} \\ p(x,y,1;s,t) = P_1(s,t)\delta(s-x)p_1^{th}(y;s), & \text{(3.10b)} \end{cases}$$

where

$$\left| \begin{aligned} P_0(s,t) &= \iint p(x,y,0;s,t)\,\mathrm{d}x\mathrm{d}y, && \text{(3.11)} \\ P_1(s,t) &= \iint p(x,y,1;s,t)\,\mathrm{d}x\mathrm{d}y = 1 - P_0(s,t) && \text{(3.12)} \end{aligned} \right.$$

are the population probabilities for a myosin head to be detached and attached respectively. We name them the population probability of being attached and detached, respectively. The resulting models have only two states corresponding to $\alpha = \{1,0\}$, characterized by the equilibrium free energies

$$\begin{cases} w_0^{th}(s) = \iint \Big[w_0(x,y)p_0^{th}(x,y) + k_BTp_0^{th}(x,y)\ln\Big(a^2\,p_0^{th}(x,y)\Big)\Big]\,\mathrm{d}x\mathrm{d}y, & \text{(3.13a)} \\ w_1^{th}(s) = \int \Big[w_1(s,y)p_1^{th}(y;s) + k_BTp_1^{th}(y;s)\ln\Big(a\,p_1^{th}(y;s)\Big)\Big]\,\mathrm{d}y, & \text{(3.13b)} \end{cases}$$

where we remind that a is the size of the power stroke and is used as the reference length in our system.

To obtain the dynamics of the transition between the two states, we integrate the Fokker-Planck equation (3.5) with the explicit definition of the internal energy levels (3.1) and the equilibrium distributions (3.9). We obtain

$$\begin{cases} \partial_t P_1(s,t) + \dot{x}_c\partial_s P_1(s,t) = f^{th}(s)\big(1 - P_1(s,t)\big) - g^{th}(s)P_1(s,t), & \text{(3.14)} \\ P_0(s,t) = 1 - P_1(s,t) & \text{(3.15)} \end{cases}$$

where (3.14) corresponds to the classical Huxley [Huxley, 1957] conservation equation with the averaged transition rates

$$\begin{cases} f^{th}(s) = \iint k_+(x,y,s)p_0^{th}(x,y)\,\mathrm{d}y\mathrm{d}x, & \text{(3.16a)} \\ g^{th}(s) = \int k_-(y,s)p_1^{th}(y;s)\,\mathrm{d}y. & \text{(3.16b)} \end{cases}$$

Note that the transition rates (3.16) are not defined *per se* but are instead derived from the rates k_+ and k_- defined within the stochastic framework.

The average force per head generated by a population of myosin heads (3.6) is now given by

$$\tau_c^{th}(t) = \frac{1}{d_a}\int_{s^-}^{s^+} P_1(s,t)\tau^{th}(s)\,\mathrm{d}s. \tag{3.17}$$

The term $\tau^{th}(s)$ is the average equilibrium tension which derives from the thermal equilibrium free energy in the attached state w_1^{th}:

$$\tau^{th}(s) = \frac{\mathrm{d}w_1^{th}}{\mathrm{d}s}(s).$$

With the assumption of a linear neck elasticity used in our model, we simply have

$$\tau^{th}(s) = \int \kappa(y+s)p_1^{th}(y;s)\,\mathrm{d}y. \tag{3.18}$$

The equivalence between the two formulation is given in Appendix (3.6.4).

We can also define the equilibrium stiffness per head, which is given by

$$\kappa_c^{th}(t) = \frac{1}{d_a}\int_{s^-}^{s^+} P_1(y,t)\partial_s\tau^{th}(s),\ \mathrm{d}s.$$

The boundary conditions requirement (3.8) becomes here

$$P_1(s^-,t) = P(s^+,t) = 0. \tag{3.19}$$

This property is ensured by a suitable choice of the transition rates f^{th} and g^{th} or their antecedent k_+ and k_-. A more detailed assessment of the mathematical properties of the Huxley'57 equation solutions is presented in [Kimmig et al., 2019] (Chapter 2).

Similarly to (3.7), the tension developed by a muscle fiber is

$$T_c(t) = \rho_{\text{surf}}\tau_c^{th}(t). \tag{3.20}$$

3.2.1.3 Generalized Huxley'57 model

The PSE model can be seen as an instance of a larger family of models within the Huxley'57 framework. These models are characterized by only two states associated with the free energies $w_{1,0}^h$ and the transition rates f and g, which are the inputs of the model. The probability of being attached is ruled by the PDE

$$\partial_t P_1(s,t) + \dot{x}_c\partial_s P_1(s,t) = f(s)\big(1 - P_1(s,t)\big) - g(s)P_1(s,t), \tag{3.21}$$

and the active tension is given by

$$\tau_c(t) = \frac{1}{d_a}\int \frac{\mathrm{d}w_1^h}{\mathrm{d}s}(s)P_1(s,t)\,\mathrm{d}s. \tag{3.22}$$

We see that our PSE model pertains to this larger family with the inputs derived from a more refined model and not prescribed directly as parameters.

Finally, we mention that the more widely used modeling approach can be retrieved by replacing the continuous internal degree of freedom y by a discrete variable i that is defined only in the attached state, the detached state being characterized by a constant (space independent) energy [Hill, 1977; Eisenberg et al., 1980]. In that case, the internal energy of state i is usually written as

$$w_1^h(x,i) = \frac{\kappa_{\text{xb}}}{2}(x+x_i)^2 + u_1(i).$$

The original Huxley'57 model has only one of such state.

In this framework, the adiabatic elimination of the fast variable i leads to the definition of the equilibrium probabilities

$$a^{th}(i;s) = \frac{\exp[-w_1(s,i)/(k_BT)]}{\sum_i \exp[-w_1(s,i)/(k_BT)]},$$

The resulting two state model is then characterized by the free energy

$$w_1^{th}(s) = \sum_i \Big[w_1(s,i)a^{th}(y;s) + k_BTa^{th}(i;s)\ln\Big(a\cdot a^{th}(i;s)\Big)\Big],$$

as an analog to (3.13b) and the tension

$$\tau^{th}(t) = \sum_i \kappa_{\text{xb}}(x+x_i)\, a^{th}(i;s)$$

as an analog to (3.18).

3.2.2 Macroscopic models

A further reduction of the model from Huxley'57 equations has been proposed in [Bestel et al., 2001; Chapelle et al., 2012] and reused in [Caruel et al., 2019]. It aims at establishing dynamics equations for relevant macroscopic quantities such as the tension developed by the population of myosin heads in a half-sarcomere. It has the advantage of reducing the partial differential equation (3.14) of Huxley'57 model into a set of ordinary differential equations, thus strongly reducing the computational cost. We give here a brief summary of the steps required to obtain these equations following [Caruel et al., 2019].

We consider in all generality a multi-site model, i.e. the myosin head can bind to any actin sites, which are regularly located along the thin filament at distances $s+jd_a\ \forall j\in\mathbb{Z}$. The geometry of the system is defined by the half-sarcomere of length ℓ_{hs} and the surface myosin head density ρ_{surf}, both defined in the reference configuration. We define the moment

$$M_p(t) = \frac{1}{d_a}\int_{s^-}^{s^+}\sum_{j\in\mathbb{Z}}(s+jd_a)^pP_1(s+jd_a,t)\,\mathrm{d}s. \tag{3.23}$$

Integrating (3.14) and performing an integration by parts – with the boundary conditions (3.19) – , we have for $p\geq 1$

$$\dot{M}_p(t) = p\dot{x}_cM_{p-1}(t) + f_p - \frac{1}{d_a}\int_{s^-}^{s^+}\sum_{j\in\mathbb{Z}}\Big(f(s+jd_a)+g(s+jd_a)\Big)(s+jd_a)^pP_1(s+jd_a,t)\,\mathrm{d}s, \tag{3.24}$$

with

$$f_p = \frac{1}{d_a}\int_{s^-}^{s^+} \sum_{j\in\mathbb{Z}} (s+jd_a)^p f(s+jd_a)\,\mathrm{d}s.$$

Assuming that the sum of the transition rates $f(s)+g(s)$ does not depend on the space variable s, we can close the moment equation (3.24) and we obtain

$$\begin{cases} \dot{M}_0(t) = -\big(f+g\big)M_0(t) + f_0, \\ \dot{M}_p(t) = p\dot{x}_c M_{p-1}(t) - \big(f+g\big)M_p(t) + f_p \quad \text{for } p>0. \end{cases} \tag{3.25}$$

3.2.2.1 Linear elastic cross-bridge : BCS model

Assuming that the cross-bridges can be modeled as a linear spring, it has a quadratic energy of the form

$$w_1^h(s) = w_1^L(s) = \frac{\kappa_{\mathrm{xb}}}{2}(s+s_0)^2. \tag{3.26}$$

where s_0 is the length of the unloaded spring. We retrieve here the original the Bestel-Clément-Sorine model (BCS). The macroscopic first Piola-Kirchhoff stress developed by the muscle fiber is given by

$$T_c(t) = \frac{\rho_{\mathrm{surf}}}{d_a}\int_{s^-}^{s^+} \sum_{j\in\mathbb{Z}} \kappa_{\mathrm{xb}}(s+jd_a+s_0)P_1(s+jd_a,t)\,\mathrm{d}s = \rho_{\mathrm{surf}}\kappa_{\mathrm{xb}}\big(s_0M_0(t)+M_1(t)\big). \tag{3.27}$$

The macroscopic stiffness per unit surface is similarly given by

$$K_c(t) = \frac{\rho_{\mathrm{surf}}}{d_a}\int_{s^-}^{s^+} \sum_{j\in\mathbb{Z}} \kappa_{\mathrm{xb}}P_1(s+jd_a,t)\,\mathrm{d}s = \rho_{\mathrm{surf}}\kappa_{\mathrm{xb}}M_0(t). \tag{3.28}$$

From the moment dynamics (3.25), we obtain

$$\begin{cases} \dot{K}_c(t) = -\big(f+g\big)K_c(t) + f_0K_\infty, \\ \dot{T}_c(t) = -\big(f+g\big)T_c(t) + \dot{x}_cK_c(t) + (s_0f_0+f_1)K_\infty, \end{cases} \tag{3.29}$$

with $K_\infty = \rho_{\mathrm{surf}}\kappa_{\mathrm{xb}}$ the stiffness in the rigor state where all cross-bridges are attached.

The relation between the force and the sliding velocity in steady-state shortening is classically measured by experimentalists and is usually termed *force-velocity relation*. With the macroscopic models, a closed form expression of the force-velocity relation can be given. The steady-state tension is given by

$$T_c^\infty = \frac{f_0K_\infty}{(f+g)^2}\dot{x}_c + \frac{s_0f_0+f_1}{f+g}K_\infty. \tag{3.30}$$

The force velocity curve is thus a straight line whose slope is a balance between the stiffness of the cross-bridges and the transition rates of the myosin heads. A high stiffness of the cross-bridge results in a high tension when the myosin head attaches since the myosin head attaches in a stretched state. Similarly, a larger rate of attachment and detachment decreases the slope. Indeed, with a higher cycling rate, the myosin head will detach faster from the state where it develops a low or negative force and reattach on another actin site where it will develop a high positive force.

3.2.2.2 Non-linear cross-bridge : extended BCS model

We now consider a non linear spring, associated with a polynomial internal energy. The related model is named extended BCS model. The energy of the cross-bridge is defined by

$$w_1^h(s) = w_1^{NL}(s) = \sum_{i=0}^{n} \frac{c_i}{\max(i,1)} s^i.$$

The force is then given by

$$\begin{aligned} T_c(t) &= \frac{\rho_{\text{surf}}}{d_a} \int_{s^-}^{s^+} \sum_{j\in\mathbb{Z}} \frac{\mathrm{d}}{\mathrm{d}s} w_1^{NL}(s) P_1(s + jd_a, t)\,\mathrm{d}s, \\ &= \frac{\rho_{\text{surf}}}{d_a} \int_{s^-}^{s^+} \sum_{j\in\mathbb{Z}} \sum_{i=1}^{n} c_i s^{i-1} P_1(s + jd_a, t)\,\mathrm{d}s, \\ &= \sum_{i=0}^{n-1} C_{i+1} M_i(t), \end{aligned} \tag{3.31}$$

where we defined

$$C_i = \rho_{\text{surf}} c_i.$$

The dynamics of the force is given by

$$\dot{T}_c(t) = \sum_{i=0}^{n-1} C_{i+1} \dot{M}_i(t).$$

In the permanent regime, and using the moment dynamics (3.25), we obtain the relation

$$0 = C_1 \Big[-(f+g) M_0^\infty + f_0 \Big] + \sum_{i=1}^{n-1} C_{i+1} \Big[i\dot{x}_c M_{i-1}^\infty - (f+g) M_i^\infty + f_i \Big],$$

where M_i^∞ is the steady-state value of the moments given by the recursive relation deduced from (3.25). They are given by

$$\begin{cases} M_0^\infty = \dfrac{f_0}{f+g}, \\ M_i^\infty(\dot{x}_c) = \dfrac{i}{f+g} \Big[\dot{x}_c M_{i-1}^\infty(\dot{x}_c) + f_i \Big], \text{ for } i \geq 1. \end{cases} \tag{3.32}$$

Applying recursively (3.32), we obtain a general form of the steady-state moment value

$$M_i^\infty(\dot{x}_c) = \sum_{j=0}^{i} \frac{\frac{i!}{j!} f_i}{(f+g)^{i+1-j}} \dot{x}_c^{i-j}. \tag{3.33}$$

Noting that the steady-state is defined from (3.31) by $T_c^\infty = \sum_{i=1}^{n} C_i M_{i-1}^\infty$, we have

$$T_c^\infty = \frac{1}{f+g} \Big[\dot{x}_c \sum_{i=1}^{n-1} i C_{i+1} M_{i-1}^\infty(\dot{x}_c) + \sum_{i=0}^{n-1} C_{i+1} f_i \Big]. \tag{3.34}$$

which gives the explicit expression of force-velocity curve as a function of the model parameters using (3.33). Note that the steady-state force is a polynomial function of the shortening velocity.

3.3 Results

In this section we show to what extend the different models of our hierarchy succeed in reproducing the experimental results.

We have derived two classes of models: the population models containing our most refined stochastic model (see Section 3.2.1.1) and the PSE model (see Section 3.2.1.2) and the macro-models containing the BCS model and its extensions (see Section 3.2.2). In what follows, we will first present the calibration and the results for the population models and compare the stochastic model to the PSE model; then we will present the calibration of the macro model and study how they compare to the PSE model, the latter being considered at the pivot of the whole model hierarchy.

3.3.1 Population models

3.3.1.1 Calibration

The model calibration procedure based here on cardiac experimental data is extensively described in [Caruel et al., 2019]. It uses the hierarchical link between the stochastic and the PSE model – the PSE model being an approximation of the stochastic model for external loads of slow time scale. The calibration of the two models is thus performed simultaneously and in a consistent manner.

The behavior of the population models relies on the definition of two families of functions: the energy landscapes (w_α, see (3.1)) and the attachment-detachment transition rates (k_+ and k_- for the stochastic model or f^{th} and g^{th} for the PSE model).

Having functions as model parameter leaves, in general, a lot of freedom to calibrate the model with the experimental data. However, we will show that within the function family that we will choose and with the set of data used, there is actually not much leeway for changes in the calibration.

For the energy landscapes, w_α we will consider a simple bi-quadratic form in combination with an elastic element which, in addition to being analytically simple, have proven efficient in reproducing the fast transient response of skeletal muscle fibers, see [Marcucci & Truskinovsky, 2010; Caruel et al., 2013a] and Table 3.5.

For attachment and detachment transitions, kinetics are described by (minimally) regularized piece-wise constant functions over the interior of the $[s^-, s^+]$ interval. Near the boundaries, the transitions rates either tend to zero or grow to infinity, exponentially to ensure that the boundary property (3.8) and (3.19) are satisfied (see Table 3.5).

The most widely used experimental setup from which most of the currently used models are calibrated consist in measuring the sarcomere shortening in response to a sudden force step applied on an isometrically contracting muscle cell.

We first show that our choice of parameter functions allows to simplify the calibration of the isometric population probability of being attached $\check{P}_1$, which is the cornerstone of the PSE model calibration, to the tuning of a reduced set of parameters only. Then, we detail how each element of the isotonic response brings strong constraints on the model calibration due to the direct relationship between the stochastic and the PSE model, the constraints on the parameters of one model directly transpose to the other model.

Note that the calibration elements are general and can apply to any model derived from the seminal Huxley'57 model. In particular, for model representing the power stroke as a transition between several discrete chemical states [Eisenberg et al., 1980; Piazzesi & Lombardi, 1995; Caremani et al., 2015], one can also compute the power stroke thermal equilibrium tension τ^{th} and use the same calibration procedure.

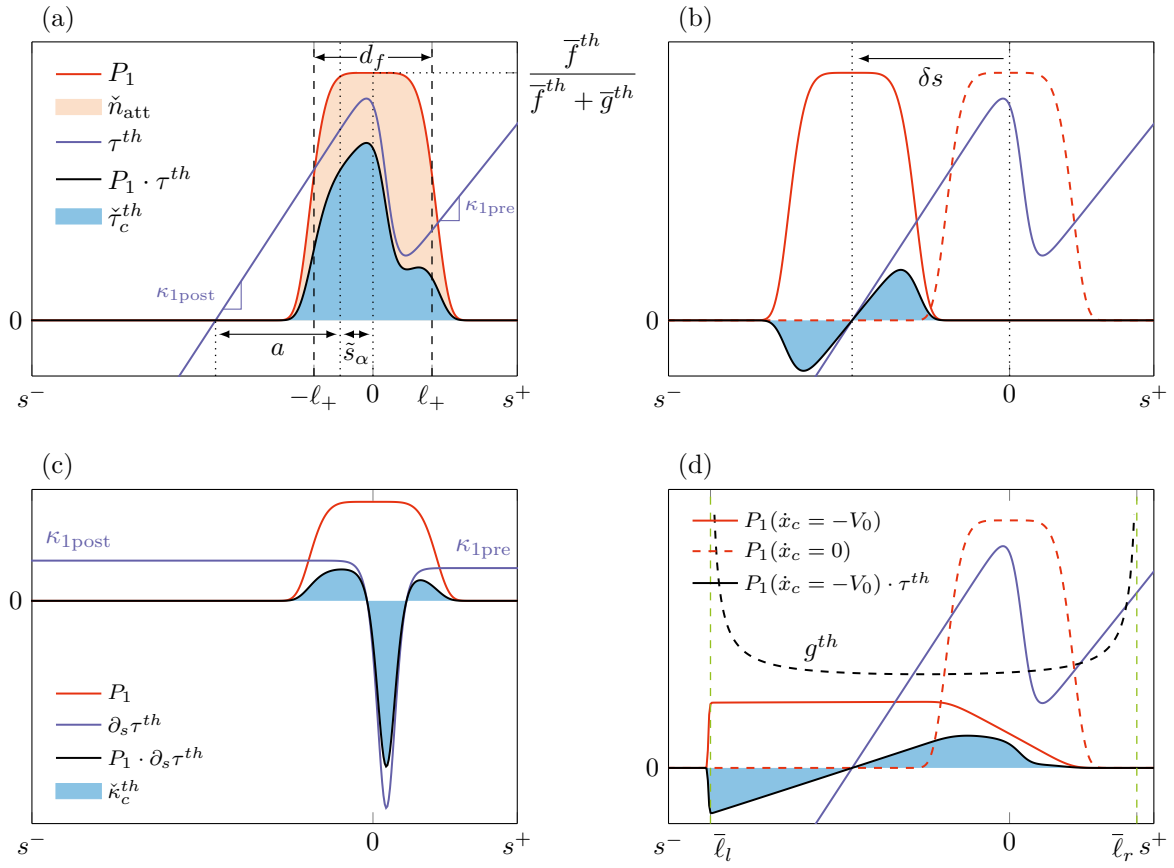

Figure 3.2 – Illustration of the calibration ground principles. Note that the model elements represented here are chosen for illustration purposes and do not reflect the actual calibration. (a) Isometric conditions. The ratio of attached heads $\check{n}_{\text{att}}$ depends on the width and the height of the isometric population probability $\check{P}_1$ (see orange area). The force per attached head $\check{\tau}_c^{th}$ is a function of the isometric population probability $\check{P}_1$ and the equilibrium tension τ^{th}. (b) Illustration of the situation at the end of phase-II. The isometric distribution is shifted due to the applied step in length. Note that the legend is the same as in panel (a). (c) Computation of the stiffness in isometric conditions. The stiffness depends on the width of the isometric population probability $\check{P}_1$ and the asymptotic stiffnesses of the two potential wells $\kappa_{1\text{pre}}$ and $\kappa_{1\text{post}}$. (d) When the filaments slide past each other, the population probability population probability P_1 is spread towards negative values of s (see solid red curve). For the PSE model, the force is then given by the integral of $P_1(s)$ against the thermal equilibrium tension $\tau^{th}(s)$ (see area in blue).

Isometric indicators for cardiomyocytes	symbol	Value	Reference
Power stroke characteristic length	a	11 nm	[Holmes and Geeves, 2000]
Distance between two actin sites	d_a	40 nm	[Craig and Padrón, 2004]
Cross-bridge stiffness	κ	$1.07\,\text{pN}\,\text{nm}^{-1}$	[Pinzauti et al., 2018]
Density of thick filament in the cross-section of thickness ℓ_{hs}	ρ_{surf}	$1.25 \times 10^{17}\,\text{m}^{-2}$	[Pinzauti et al., 2018]
Myofilament compliance	C_m	$17\,\text{nm}\,\text{MPa}^{-1}$	[Pinzauti et al., 2018]

Table 3.1 – Parameters whose value is not adjusted in the calibration process but directly taken from the literature.

Fixed parameters Before turning to the calibration procedure per se, we mention that some of the model parameters are not chosen through a calibration process but are directly taken from experimental measurements. These parameters are listed in Table 3.1.

Isometric indicators The initial state of the fiber, in isotonic shortening experiments is the so-called steady state isometric contraction. As we have already mentioned in the introduction, at the heart level, the developed force is subjected to regulation mechanisms, which, in particular prevents tetanization hence a sustained isometric contraction in physiological conditions. Indeed, the heart acts as a blood pump alternating ejection and filling phases corresponding to the contraction and relaxation of the cardiac muscles, respectively. A sustained contraction would interrupt this cycle and is thus prevented in physiological conditions. We refer to isometric conditions when the developed force reaches its peak in a twitch contraction in which the length of the fiber is maintained constant (specific experimental apparatus have been designed for that purpose [ter Keurs et al., 1980; Van Heuningen et al., 1982; Caremani et al., 2016]

The main indicator of the isometric state is the maximal isometric tension (or stress) T_0 generated by the fraction $\check{n}_{\text{att}}$ of the myosin motors bound to actin. In maximal activation conditions, it has been experimentally shown that this tension can reach the value 118 kPa and that it corresponds to a maximal ratio of attached heads $\check{n}_{\text{att}} = 0.15$ and to a tension per head of 6.14 pN [Caremani et al., 2016; Pinzauti et al., 2018].

For the PSE model, the isometric population probability $\check{P}_1$ is the steady state solution of (3.14) with $\dot{x}_c = 0$,

$$\check{P}_1(s) = \frac{f^{th}(s)}{f^{th}(s) + g^{th}(s)} = \frac{f^{th}(s)/g^{th}(s)}{1 + f^{th}(s)/g^{th}(s)}, \tag{3.35}$$

which only depends on the ratio $f^{th}(s)/g^{th}(s)$.

Our strategy consists in a parallel and interdependent calibration of the transition rates k_+ and k_- and the attached energy landscape $w_1(s, y)$, or their PSE model counterparts the equilibrium transition rates f^{th} and g^{th} and the equilibrium tension τ^{th}.

To limit the number of parameters that characterize this ratio, we assume, first that the attachment rate k_+ is non-zero only in an interval $S_f = [-\ell_+, \ell_+]$ around the nearest binding site; second, that k_+ is almost constant in this interval; and third that the detachment rate k_- is strictly constant on this interval. Using these hypotheses in the definitions of f^{th} and g^{th} (see Equation (3.16)) together with the (regularized) piecewise constant shapes proposed in Table 3.5 leads to the following approximations: for the attachment rate

$$f^{th}(s) \approx \begin{cases} \overline{f}^{th} = k_{\max}\alpha_{0\text{pre}} & \text{if } s \in [-\ell_+, \ell_+], \\ 0 & \text{otherwise,} \end{cases}$$

where $\alpha_{0\text{pre}}$ denotes the fraction of detached myosin heads in the pre-power-stroke conformation, which is independent of s but depends on the energy landscape w_0. For the detachment rate we have $g^{th}(s) \approx \overline{g}^{th} = k_{\min}$ for $s \in [-\ell_+, \ell_+]$. These two approximations illustrate the direct link between the calibration of the two models. In summary, to define the isometric population probability $\check{P}_1$, it is sufficient to prescribe directly the ratio $\overline{f}^{th}/\overline{g}^{th}$ and the support width $d_f = 2\ell_+$ (see illustration in Figure 3.2(a)). If we carry on with these assumption, we obtain the following approximation: (i) for the isometric ratio of attached heads $\check{n}_{\text{att}} = \dfrac{1}{d_a}\displaystyle\int_{s^-}^{s^+} \check{P}_1(s)\,\mathrm{d}s \approx \dfrac{d_f}{d_a}\dfrac{\overline{f}^{th}/\overline{g}^{th}}{1 + \overline{f}^{th}/\overline{g}^{th}}$

[see the orange area in Figure 3.2(a] and (ii) for the isometric force per attached head $\frac{\tau_c^{th}}{\check{n}_{\text{att}}} = \frac{1}{\check{n}_{\text{att}}}\frac{1}{d_a}\int_{s^-}^{s^+} \tau^{th}(s)\check{P}_1(s)\,\mathrm{d}s \approx \frac{1}{d_f}\int_{-\ell_+}^{\ell_+} \tau^{th}(s)\,\mathrm{d}s$.

Given the bi-quadratic form postulated for the energy landscapes, the equilibrium tension τ^{th} basically depends on three parameters (see Figure 3.2(a)): the asymptotic stiffnesses $\kappa_{1\text{pre}}$ and $\kappa_{1\text{post}}$ and the position of the negative slope part, which is directly linked to the position of the potential barrier ℓ_1 of the attached energy landscape, see Table 3.5. Note that the stiffness $\kappa_{1\text{post}}$ will be univocally determined from the fast isotonic transients (see next paragraph), which leaves only 3 parameters (ℓ_+, $\kappa_{1\text{pre}}$ and ℓ_1) to adjust in order to obtained the measured tension per attached heads. Once ℓ_+ is fixed, the ratio $\overline{f}^{th}/\overline{g}^{th}$ is calibrated to obtain the measured fraction of attached heads, see Table 3.2.

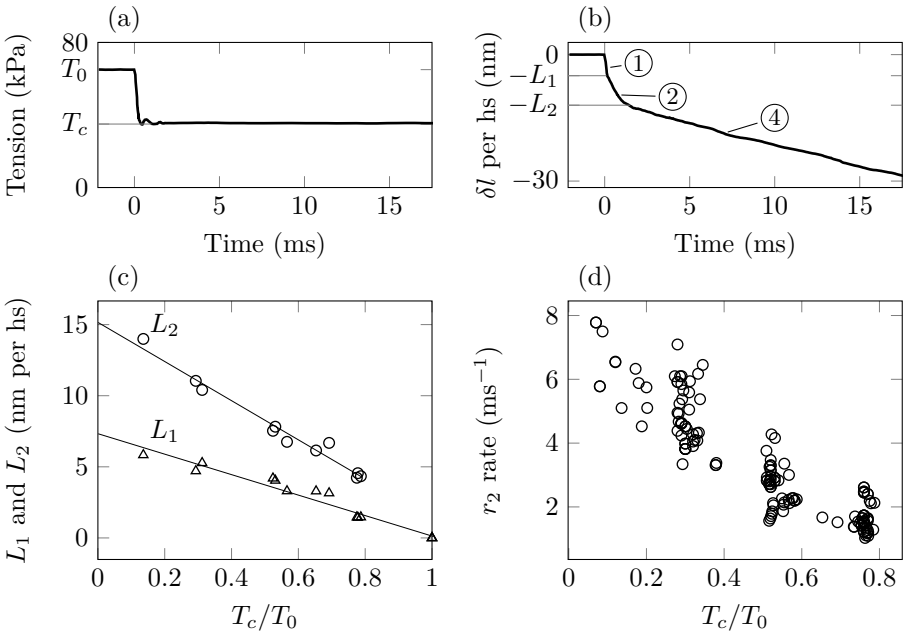

Figure 3.3 – Experimental data from fast transient experiments in force control conditions. (a) Imposed sample tension. (b) Transient response following the tension drop. The response display three different phases indexed by 1, 2 and 4 (see text for more explanations). (c) Signature of phase I and phase II. The amount of shortening at the end of phase I and phase II, denoted respectively by L_1 and L_2 is reported as a function of the relative tension drop. (d) Rate of shortening in phase II as a function of the relative tension drop. Data from [Caremani et al., 2016] obtained with rat cardiac muscle at 27 °C.

Fast isotonic transients A typical response of a cardiac muscle fiber to a sudden force drop applied at the peak force T_0 of an isometric twitch contraction is illustrated in Figure 3.3(a) & (b). The step in force is applied within $\sim 200\,\mu\text{s}$, and the length response is measured afterwards [Caremani et al., 2016].

The response displays three phases. First (phase I) an instantaneous shortening – L_1 – is observed alongside the load step itself. Second (phase II), after the force has stabilized to its new value, a second shortening – up to L_2 – happens within the next $\sim 2\,\text{ms}$. After this second phase, the system enters a steady state characterized by a constant load-dependent shortening velocity (phase IV). In frog skeletal muscle at 4 °C, a pause in the

shortening is observed between phase II and phase IV [Piazzesi et al., 2002]. This phase is named phase III but is not observed with rat cardiac muscles at 27 °C.

The signature of phase I and phase II, namely the curves $L_1(T_c)$ and $L_2(T_c)$, are presented in Figure 3.3(c). Observe that the measured amount of shortening after both phases depends linearly on the load step.

To reproduce these experimental results, we exploit the fact that experimental studies have shown that the relation $L_1(T_c)$ and $L_2(T_c)$ can also be obtained following a dual protocol where the sarcomere length ℓ_{hs} is controlled while the tension T_c is recorded [Piazzesi et al., 2002]. In this case a step in length $\delta\ell_{hs}$ is applied and the fast transient responses are characterized by the relations $T_1(\delta\ell_{hs})$ (phase I) and $T_2(\delta\ell_{hs})$ (phase II), which are identical to $L_1(T_c)$ and $L_2(T_c)$, respectively.

To reproduce $L_1(T_c)$ and $L_2(T_c)$ with our model we will then compute the response of our system to a rapid change in the filament relative position δs and compute $T_1(\delta s)$ (phase 1) and $T_2(\delta s)$ (phase II).

Note however, that due to the filament compliance, the length displacement per half sarcomere seen by the cross-bridges δs is different from the length displacement per half-sarcomere $\delta\ell_{hs}$ that is measured or imposed in experiments. To account for this difference, we map the length displacement δs applied in our simulations for phase 1 and phase 2 to its $\delta\ell_{hs}$ counterpart, which corresponds to the measured L_1 and L_2, using $L_{1,2}(\delta s) = \delta s + C_m[T_{1,2}(\delta s) - T_0]$ [Caruel et al., 2019], where the filament compliance C_m is given in Table 3.1.

The first phase (from $\delta\ell_{hs} = 0$ to $\delta\ell_{hs} = L_1$) happens along with the applied load step. At this timescale, all internal conformational degrees of freedom can be considered "frozen", and the fraction of attached heads is assumed constant. Hence phase I is a purely elastic response to which both the myofilament and the cross-bridges contribute to. Therefore, we model the tension $T_1(\delta s)$ as $T_1(\delta s) \sim T_0 + \kappa\rho_{\text{surf}}\check{n}_{\text{att}}\delta s$, (see Appendix 3.6.2 for the details about how to obtain this approximation), which allows to calibrate the parameter κ, [Linari et al., 1998].

The duration of the second phase immediately following the step is of about 1 ms which can be considered to be much faster than the ATPase cycle timescale (~ 30 ms). Hence, one can assume that the amount of detachment and attachment events is low during phase II before the shortening has reached the length L_2. Consequently, the observed rapid shortening in phase II is attributed to the thermal relaxation of the internal degrees of freedom parametrizing the conformational change [Huxley & Simmons, 1971; Lombardi et al., 1992] and so the tension at the end of this phase can be computed by shifting the population of attached heads approximated by δs, (see Figure 3.2(b)).

$$T_2(\delta s) \approx \frac{\rho_{\text{surf}}}{d_a}\int_{s^-}^{s^+} \check{P}_1(s-\delta s)\tau^{th}(s)\,\mathrm{d}s = \frac{\rho_{\text{surf}}}{d_a}\int_{s^-}^{s^+} \check{P}_1(s)\tau^{th}(s+\delta s)\,\mathrm{d}s. \tag{3.36}$$

For large shortening, one can further assume that the whole population of attached cross-bridges are in the post-power-stroke conformation. The fact that the observed relation $L_2(T_c)$ is linear (see Figure 3.3(c)) suggests that the energy characterizing this state is harmonic, hence the choice of the bi-quadratic form of u_1, see (3.1) and Table 3.5. Using the parametrization of Table 3.5, we can then derive the following large shortening approximation (see Appendix 3.6.3 for the details about how to obtain this approximation)

$$T_2(\delta s) = \frac{\rho_{\text{surf}}}{d_a}\int_{s^-}^{s^+} \check{P}_1(s)\tau^{th}(s+\delta s)\,\mathrm{d}s \approx \rho_{\text{surf}}\check{n}_{\text{att}}\frac{\kappa\kappa_{1\text{post}}}{\kappa+\kappa_{1\text{post}}}(\delta s + \tilde{s}_1 + a), \tag{3.37}$$

which allows to univocally calibrate both $\kappa_{1\text{post}}$ and $\tilde{s}_1$. The direct connexion between

the two models is again fully explicit here through the link between τ^{th} and the stiffnesses defining the attached energy potential w_1.

Note importantly that the above calibration on the linear portion of the $L_2(T_c)$ is independent of the form of the population probability $\check{P}_1$.

The slope of the $T_2(\delta\ell_{hs})$ curve at the origin, which is given by $\frac{\rho_{\text{surf}}}{d_a}\int_{s^-}^{s^+}\check{P}_1(y)\partial_s\tau^{th}(s)\,\mathrm{d}s = \rho_{\text{surf}}\check{\kappa}_c^{th}$, aggregates the contributions of the isometric population probability $\check{P}_1$ and the attached energy landscape through the equilibrium average tension τ^{th}. Its value results from the balance between heads contributing with a negative stiffness and heads contributing with a positive stiffness, see Figure 3.2(c).

Increasing the width (d_f) of $\check{P}_1$ leads to an increase in the stiffness while decreasing the width of $\check{P}_1$ decreases the stiffness, possibly to negative values. This puts a constraint on the support of the attachment rate d_f and thus indirectly helps choosing a value of the ratio $\overline{f}^{th}/\overline{g}^{th}$ through the constraint on the isometric ratio of attached heads $\check{n}_{\text{att}}$, see above. Furthermore, an increase of the stiffnesses $\kappa_{1\text{pre}}$ and $\kappa_{1\text{post}}$ has a positive impact on the slope at origin.

An additional element characterizing the response in phase II is the rate of tension recovery r_2 (in length control conditions). The rate of phase II is determined by the shape of the attached energy landscape w_1 and the viscosity η. The former being fully constrained by the T_2-curve and the isometric indicators, we use the information about the rate of force recovery to adjust the value of the parameter η.

At this stage, the isometric population probability $\check{P}_1$ is fully defined. The energy landscape associated with the attached state parametrized by κ, $\kappa_{1\text{pre}}$, $\kappa_{1\text{post}}$, $\tilde{s}$, ℓ_1, is also completely determined. If the ratio $\overline{f}^{th}/\overline{g}^{th}$ is fixed, a particularization of the attachment rates $\overline{f}^{th}$ and $\overline{g}^{th}$ is still to be done. The shape of the detachment rate g^{th} for value of s non close to the origin $s = 0$, along with the detached energy landscape $w_0(x, y)$ also remain to the calibrated.

The parameters of $w_0(x, y)$ are less constrained than the other parameters of the model. Indeed, only few data characterizing the behavior of the detached myosin heads are available, most of them being obtained with solutions of myosin heads and actin sites *ex vivo*, whose applicability in the context of modeling the actin-myosin interaction in the sarcomere may not be straightforward. We choose to calibrate the detached double well potential positions $y_{0\text{post}}$ and $y_{0\text{pre}}$ so that they correspond to that of the attached double well potential $y_{1\text{post}}$ and $y_{1\text{pre}}$, respectively. The stiffness of the two wells $\kappa_{0\text{post}}$ and $\kappa_{0\text{pre}}$ and the position of the barrier between the two wells ℓ_0 is set such that the jumps occurring between the attached and detached state are associated with a "maximal" energy loss given the constraint that w_1 is now fixed and that the energy brought by ATP in the detachment process μ_T is equal to 100 zJ [Barclay, 2015].

Shape of the force-velocity relation The force-velocity curve is the last element that will allow to close the calibration. This data is obtained with a high certainty; it has indeed been registered for decades with a great consistency in the results (see Figure 3.4). There three main components in this data: the general shape, the high shortening velocity behavior and the near isometric behavior (stall force).

The global shape of the force-velocity curve is mainly the result of a balance between two effects. First, the shortening of the sarcomere reduces the force generated by attached myosin heads. We call this effect the "stiffness effect". Second, the ability of the myosin heads to cycle regenerate the force generation capability – the myosin heads can detach from a position where they exert low or even negative force and to reattach somewhere else on the thin filament where they generate a positive force; we call this effect the "cycling

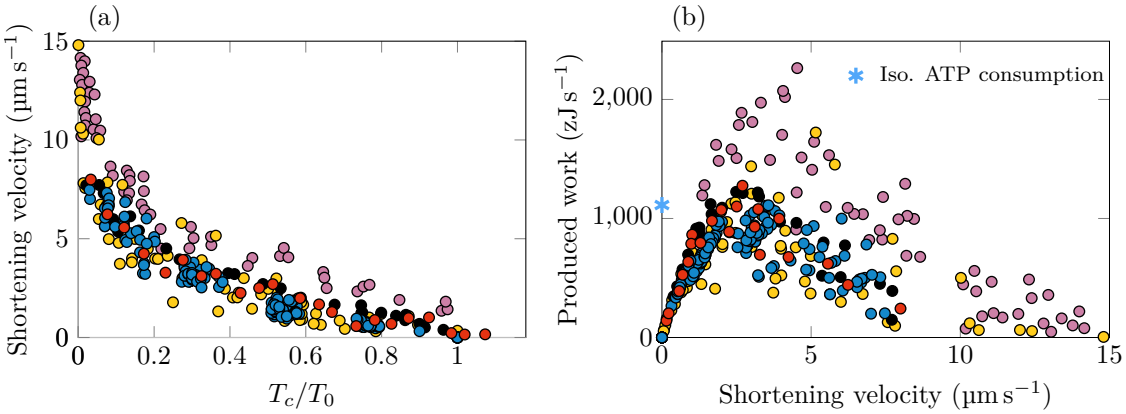

Figure 3.4 – Summary of steady-state shortening experimental data measured on rat cardiac muscles. We collect here all data point obtained in various sarcomere stretch and thin filament activation conditions. All experiments are performed on trabeculae. (a) Force-velocity curve. (b) Produced work. (Black) Data from [Van Heuningen et al., 1982] at 25 °C. (Yellow) Data from [Daniels et al., 1984] at 25 °C. (Lilac) Data from [de Tombe & ter Keurs, 1990] at 25 °C. (Orange) Data from [de Tombe & ter Keurs, 1992] at 25 °C. (Blue) Data from [Caremani et al., 2016] at 27 °C.

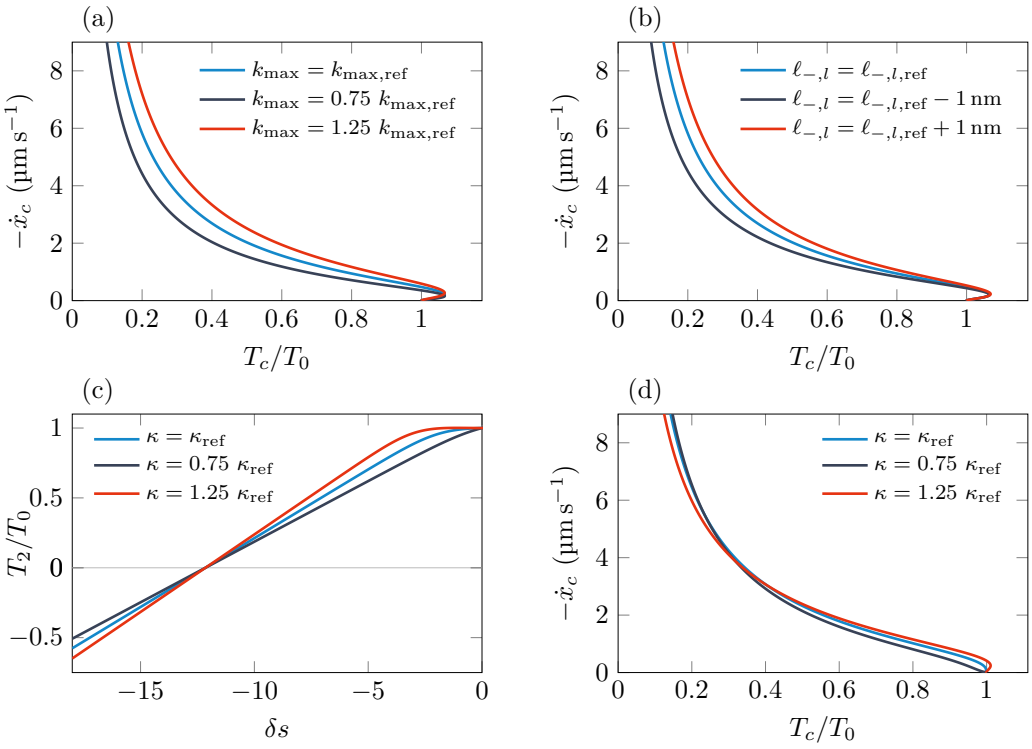

Figure 3.5 – Parametric study on the force-velocity curve predicted by the PSE model. (a) & (b) Illustration of the "cycling effect". (a) The attachment rate k_{max} is varied while the ratio k_{max}/k_{min} is maintained constant. The condition k_{max}/k_{min} constant also implies that $\overline{f}^{th}/\overline{g}^{th}$ is constant. (b) Variation of the position $\ell_{-,l}$, which varies in the same way as the position of g^{th} pseudo-asymptote $\overline{\ell}_l$ (see Figure 3.2(d)). (c) & (d) Illustration of the "stiffness effect". Variation of the stiffness κ and subsequent effects on the T_2-curve (c) and the force-velocity curve (d). The slope of the T_2-curve constitutes the apparent stiffness for slow time scale responses (as it is the case in steady-state shortening).

effect". Both effects are illustrated in Figure 3.5.

The cycling effect (see Figure 3.5(a)), is illustrated by the force-velocity curves predicted by the PSE model for varying the isometric attachment and detachment rates $k_{\max}$ and $k_{\min}$ (thus augmenting the cycling rate) while maintaining the ratio $k_{\max}/k_{\min}$ constant. Note that these variations also translate into a variation of the thermal equilibrium transition rates f^{th} and g^{th} with a ratio $\overline{f}^{th}/\overline{g}^{th}$ that remains constant. Notice that since the heads always bind in a region where they exert a high force (see Figure 3.2(a)), increasing the cycling rate increases the steady-state force produced at a given velocity.

In the PSE model, the equilibrium state in the energy potentials w_α is assumed to be always reached. Therefore the apparent force-shortening relation is thus always given by the $T_2(\delta s)$ curve whose slope is an apparent stiffness, see (3.36) and Figure 3.2(a). To illustrate the "stiffness effect", we vary this apparent stiffness by changing the cross-bridge neck stiffness κ, see Figure 3.5(c). Since the value $\delta s = -(a + \tilde{s}_1)$ corresponding to $T_2(\delta s) = 0$ (see Equation (3.37)) is independent from κ, increasing κ increases the tension for low shortening ($\delta s > -(a+\tilde{s}_1)$) and decreases the tension for large shortening ($\delta s < -(a + \tilde{s}_1)$).

At low shortening velocity, the heads experience a moderate displacement before detachment and therefore exert a higher force at higher macromolecule stiffnesses. Conversely for high shortening velocity, the attached heads can reach a region where they start to be under compression (negative forces) before they detach, and a higher macromolecule stiffness then lowers the average force. These tendencies are illustrated in Figure 3.5(d).

In the calibration process, the stiffness parameters are already fixed, we can only adjust the transition rates to make the model prediction of the force-velocity curve match the experimental data. In particular, the global shape of the force-velocity curve is used to particularize the parameters $\overline{f}^{th}$ and $\overline{g}^{th}$.

Large shortening velocity behavior In steady state isotonic shortening, while the myosin and actin filaments slide pass each other, the population probability $P_1(s)$ is spread towards negative values of s. A zero force is obtained when the contributions of heads exerting a negative force and that of heads exerting a positive force balance. This behavior is illustrated in Figure 3.2(d).

In the PSE model, unloaded shortening sliding velocity is determined mainly by the position $\overline{\ell}_l$ of the vertical pseudo-asymptote of the detachment rate g^{th} for negative values of s, see illustration in Figure 3.2(d). The value of $\overline{\ell}_l$ itself depends the position of the detachment rate k_- pseudo-asymptote – denoted $\ell_{-,l}$ – and on the reciprocal spatial characteristic length λ_3 for the stochastic model (see Table 3.5). Hence, different couples $(\ell_{-,l}, \lambda_3)$ may lead to the same force-velocity relation, and we present here only the effect of $\ell_{-,l}$, see Figure 3.5(b). When the vertical pseudo-asymptote of the detachment rate is located at a higher position $\ell_{-,l}$, the detachment rate is increased for all value of s at the vicinity of s^-. This results in an increase in the cycling rate, which, as presented in Figure 3.5(b), leads to an increase of the developed force. Hence the maximum shortening velocity is increased by increasing $\overline{\ell}_l$ through an increase of $\ell_{-,l}$.

Similarly, the position $\overline{\ell}_r$of the vertical pseudo-asymptote of the detachment rate g^{th} for positive values of s – parametrized by $\ell_{-,r}$ and λ_3 – is chosen such that we can numerically ensure that $P_1(s = s^+) \approx 0$ when the sliding velocity is positive and corresponds to the maximal physiological value observed in the filling phase of the heart or in the relaxation phase of a fiber twitch contraction ($\dot{x}_c \sim 2\,\mu\mathrm{m\,s}^{-1}$).

Near isometric behavior – The shape of the force-velocity curve in near isometric conditions – ie. for shortening with characteristic time $\ell_{hs}/\dot{x}_c$ that is small with respect

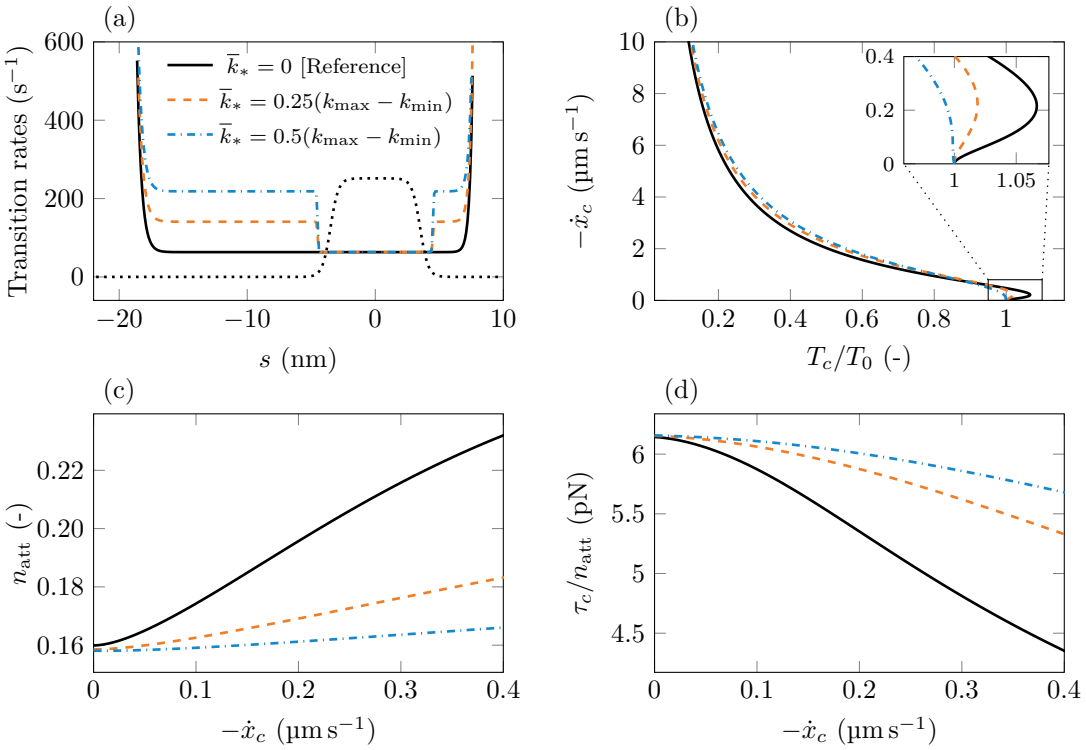

Figure 3.6 – Investigation of the force-velocity curve in near isometric conditions obtained with the PSE model. We compare three values of k_* – black line: $k_* = 0$, orange dashed line: $k_* = 0.25(k_{\max} - k_{\min})$ and blue dashed line: $k_* = 0.5(k_{\max} - k_{\min})$. (a) Transition rates for the considered value of k_*. (b) Global force-velocity curve with focus on the near isometric region of the force-velocity curve. (c) Ratio of attached heads as a function of the shortening velocity. (d) Force per attached head as a function of the shortening velocity.

to the transition rates – is determined by a balance between two effects : a change in the number of attached heads and a change in the averaged force per attached head. This balance can lead to an increase or a decrease of the force at slow sliding velocities with respect to the isometric force. In our calibration, the near isometric properties of the force-velocity curve are adjusted with the function $\overline{k}_*$, which is part of the detachment rate k_- definition (see Table 3.5).

In our reference model ($\overline{k}_* = 0$), the detachment function $g^{th} = k_{\min}$ is constant over the whole $[s^+, s^+]$ except near the boundary where where it diverges. With this detachment function, we observe that the tension actually increases at slow shortening velocities compared to the isometric configuration, see Figure 3.5 and Figure 3.6(b, black line). This behavior is not visible in the experimental data because of a lack at very slow shortening velocities. Therefore, the introduction of such a feature in the model would only be speculative. We thus present a variation of the transition rate that allows to modulate the model behavior in this region.

The influence of a possible variation of the function $\overline{k}_*$ is presented in Figure 3.6. The function $\overline{k}_*$ has three parameters: the position of the transition between the two detachment rate regions ℓ_*, the reciprocal characteristic length λ_* and the detachment rate value k_*.

In Figure 3.6, we show the effect of $\overline{k}_*$. Increasing the detachment rate compared to the attachment rate f^{th} has two effects: it reduces the fraction of attached heads (see Figure 3.6(c)) but it also increases the tension per attached heads (see Figure 3.6(d)). The first effect has to be stronger than the second to eliminate the increase of the overall tension at low shortening velocity. Furthermore, this increase of the detachment rate only marginally affects the rest of the F-V curve, as shown in Figure 3.6(b). Therefore this introduction of a s-dependence in the detachment rate can be adjusted only at the end of the calibration procedure. Note that similar effect can be obtained by adjusting the parameters ℓ_* and λ_*, also without affecting the global shape of the F-V curve.

In summary, the isometric indicators and the fast transients allow to unambiguously determine the isometric population probability $\check{P}_1$ and the attached energy landscape w_1. Adding information from the force-velocity curve leads to the unique definition of the transition rates f^{th} and g^{th}. Only the detached potential w_0 remains subjected to variability in the calibration. More experimental data targeting the detached state would be needed to reduce this variability.

3.3.1.2 PSE model vs Stochastic model

The list of functions and parameters obtained after the calibration procedure presented in the previous section are listed and illustrated in Section 3.6.1. The detailed model calibration is given in Table 3.5.

The PSE model is derived as the asymptotic limit of the stochastic model by performing the adiabatic elimination of the fastest time scales. We analyze here in detail the consequences of this adiabatic elimination and the differences between the two population models.

Isometric indicators We first consider isometric and energetics indicators. In isometric condition, the PSE model and the stochastic model are almost equivalent as already observed in [Caruel et al., 2019] with skeletal muscles indicator. We show in Table 3.2 that similar results are obtained in the case of cardiac data. The force per attached head obtained in both models are consistent with the experimental data. The ratio of attached head is over-estimated by 5%, leading also to a slight over-evaluation of the maximal

Isometric indicators	symbol	Exp. value	PSE model value
Ratio of attached heads	$\check{n}_{\text{att}}$	0.15	0.158
Force per attached head	$\check{\tau}_c^{th}$ / $\check{n}_{\text{att}}$	6.14 pN	6.16 pN
Maximal total stress	T_0	118 kPa	121 kPa
ATP tension cost	A_T	0.0928 /s/head/kPa	0.0835 /s/head/kPa

Table 3.2 – Target isometric physiological indicators for the calibration on cardiac data. Furthermore, knowing that the relationship between the developed force and the ratio of attached heads is linear on the one hand, the force [Caremani et al., 2016] in maximal activation conditions and the ratio of attached heads in several activation conditions [Pinzauti et al., 2018] on the other hand, maximal ratio of attached heads $\check{n}_{\text{att}} = 0.15$ can be derived.

isometric stress.

In addition to the force and fraction of attached motors, our model can be used to predict the energetic properties of the contractile system in isometric condition. We chose as an indicator of the energetic performance the "ATP tension cost", which is defined by the ATP consumption rate per myosin head in the sarcomere per unit of produced force. From the data of [de Tombe & Stienen, 2007] measured on rat cardiac cells at 25 °C, which give the ATP consumption per unit volume and geometrical data of Reconditi et al. [2017], which allow to derive a density of myosin heads per unit volume of 1.246×10^{23} heads/m^3 (choosing a reference length of 1 µm for the half sarcomere), we obtain a experimental tension cost of 0.0928 /s/head/kPa. Note that the ATP consumption obtained experimentally is indeed only linked to the cycling myosin heads since experiments are performed on skinned cells (in intact cells 30% to 40% of the energy is used to transfer ions through membranes [Barclay, 2015]). In the Lymn-Taylor cycle, the ATP is consumed when the detachment of the myosin head occurs. The ATP consumption rate per myosin head is therefore equal to the flux of detachment per myosin head. For the PSE model, the tension cost is given by

$$A_T = \frac{\text{detachment flux per myosin head}}{\text{produced force}} = \frac{\dfrac{1}{d_a}\displaystyle\int_{s^-}^{s^+} g^{th}(s)\check{P}_1(s)\,\mathrm{d}s}{\dfrac{\rho_{\text{surf}}}{d_a}\displaystyle\int_{s^-}^{s^+} \tau^{th}(s)\check{P}_1(s)\,\mathrm{d}s},$$

and we obtain a value of 0.0835 /s/head/kPa in relatively good agreement with the experimental data. It is important to note that in our calibration framework, the ATP tension cost is not calibrated but predicted by the model. The fact that the model reproduces this indicator without further adjustments confirms that our parametrization is well constrained.

Fast isotonic transients We continue by comparing the calibrated models predictions of the fast transient response with experimental data. The calibration results are presented in Figure 3.7.

While the relation $T_2(\delta\ell_{hs})$ is explicitly defined in the PSE model (see Equation (3.36)), it has to be inferred from the average trajectory of the stochastic model internal variables X^t, Y^t and α^t. We used the method proposed in [Ford et al., 1981; Caruel et al., 2019] to reconstruct the $T_2(\delta\ell_{hs})$ relation.

The fundamental assumption underlying the derivation of the PSE model is precisely to neglect the time required for the equilibration of the internal mechanical degrees of freedom corresponding to the power stroke. There is thus a theoretical equivalence between

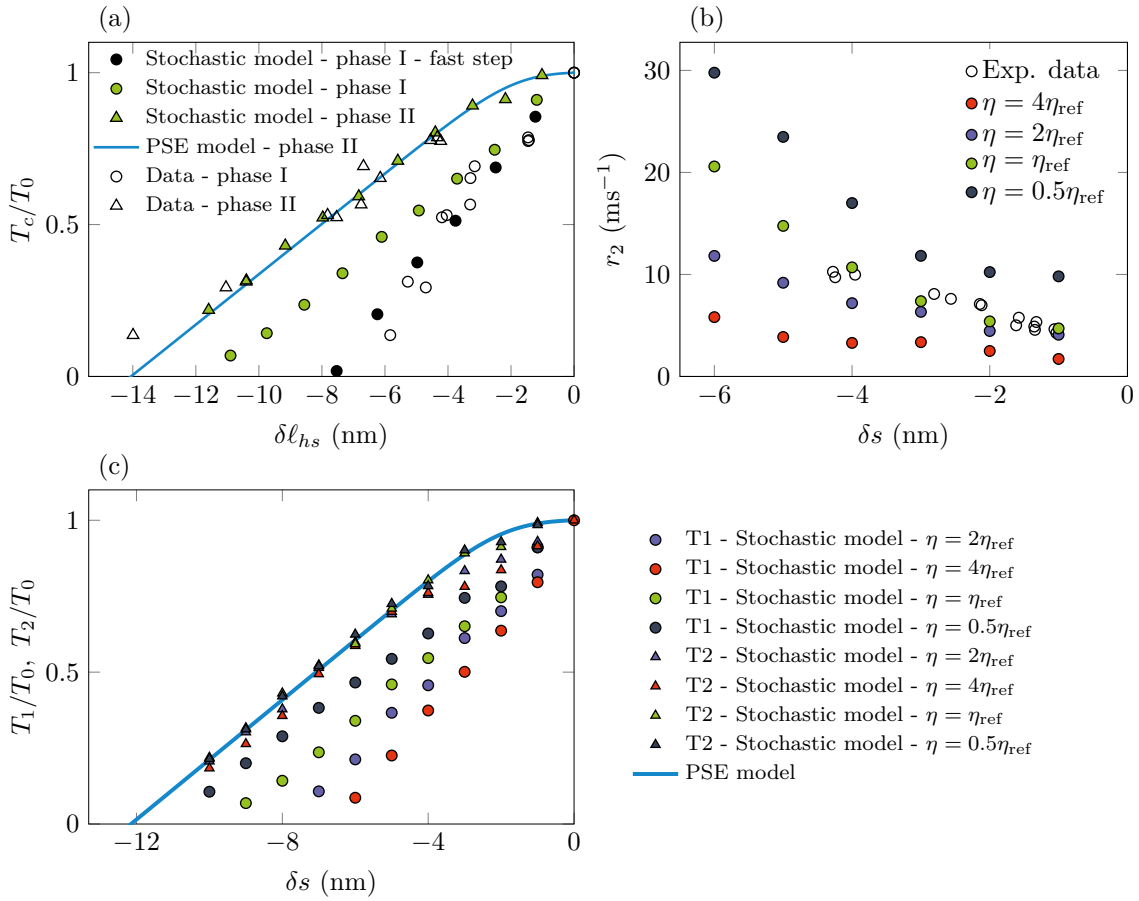

Figure 3.7 – Comparison of the calibrated model prediction and experimental data for the fast transient response. (a) Signature of the transient response in phases 1 and 2 in length control conditions. The model predictions are obtained with a length step applied in 100 µs (marks in green). We also present the relation between the length step and the force T_1 with a fast step of 10 µs (marks in black). (b) Recovery rate in phase 2 in length control conditions. Experimental data and stochastic model prediction for various values of the viscosity. The experimental data are extrapolated from force control conditions data (see Appendix 3.6.5 for a detailed explanation). (c) Influence of viscosity on the force T_1- and T_2-curves predicted by the stochastic model.

the end of phase II for the stochastic model and the PSE model. This translates into the numerical simulations (see Figure 3.7) showing that the $(\delta\ell_{hs}, T_2)$-curves obtained with the stochastic and the PSE models are the same. As a result, the elastic response of the PSE model aggregates the dynamics of these two – fast – elements into a single – instantaneous – non-linear elastic dynamics.

The accordance between the predictions of the calibrated PSE model (blue line in Figure 3.7(a)) and the predictions of the stochastic model (green triangles in Figure 3.7(a)) validates the hypotheses of the PSE model, that the force length relation characterizing the end of phase II corresponds to the thermal relaxation of the internal degrees of freedom.

The response in phase I, which corresponds to the fastest time scale, can only be captured by the stochastic model. Indeed, the linear elastic element, which models this initial response phase in the stochastic model, is incorporated into the equilibrium non-linear elastic element of the PSE model (blue line in Figure 3.7(a)). Note that with a length step of 100 µs the model predictions match the experimental for short steps only (up to -3 nm). The complete experimental data trend can nevertheless be obtained with a fast length step. This discrepancy is due to viscosity effect and is discussed in Section 3.4.1.1.

The relation $T_1(\delta\ell_{hs})$ is obtained simply by reporting the value of the tension at the end of the applied length step. In Figure 3.7(c), we show different $T_1(\delta\ell_{hs})$ obtained with the stochastic model for different values of η. The reference value is chosen so that the rate of recovery – from phase I to phase II – matches the experimental observations (green symbols Figure 3.7(b), see Table 3.5). We see that with this reference value, the $T_1(\delta\ell_{hs})$ relation does not match the experimental data, which means that the timescale of phase II is not large enough compared to the timescale of the elastic response. To increase the timescale separation, one can increase the viscosity parameter. The results presented in Figure 3.7(c) show that the experimental $T_1(\delta\ell_{hs})$ relation can be recovered by increasing 4-fold the viscosity, but this deteriorate the fit of the rate of phase II. Notice however that modifying the viscosity marginally affects the $T_2(\delta\ell_{hs})$ relation.

Isotonic shortening velocity The force-velocity relations obtained with both the stochastic model and the PSE model are shown in Figure 3.8(a).

In phase IV, the developed force is the result of the balance between the "stiffness effect" and the "cycling effect" as presented in Section 3.3.1.1.

In the stochastic model, the "cycling effect" mentioned in Section 3.3.1.1 is limited by the ability of the myosin heads that detach to regain the power stroke capability. This corresponds to the transition from the post-power stroke state to the pre-power stroke state in the detached energy landscape. The time scale of this transition is defined by the energy landscape itself (mainly through the sharpness of the energy barrier) and the viscosity. With a lower viscosity, the transition time between the energy wells is reduced and the myosin heads recover their power stroke capability faster, thus reinforcing their ability to cycle.

The PSE model corresponds to the limit of this process with an instantaneous power-stroke capability recovery. It implies that the heads that detach are immediately available for reattachment. Therefore, the thermal equilibrium assumption strengthens the "cycling effect". For this reason, the force developed in phase IV by the PSE model at a given shortening velocity is always higher than that of the stochastic model, as illustrated in Figure 3.8((a) and (d)). This effect is reduced by a decrease in the internal viscosity η, see Figure 3.8(d).

Note that at the time scale of a cardiac contraction twitch – about 100 ms – , the time to reach the end of phase II – on average 0.1 ms – is negligible. Moreover, the physiological load in vivo ranges between 45 % and 65 % of the maximal load (see Section 3.3.2.2). In

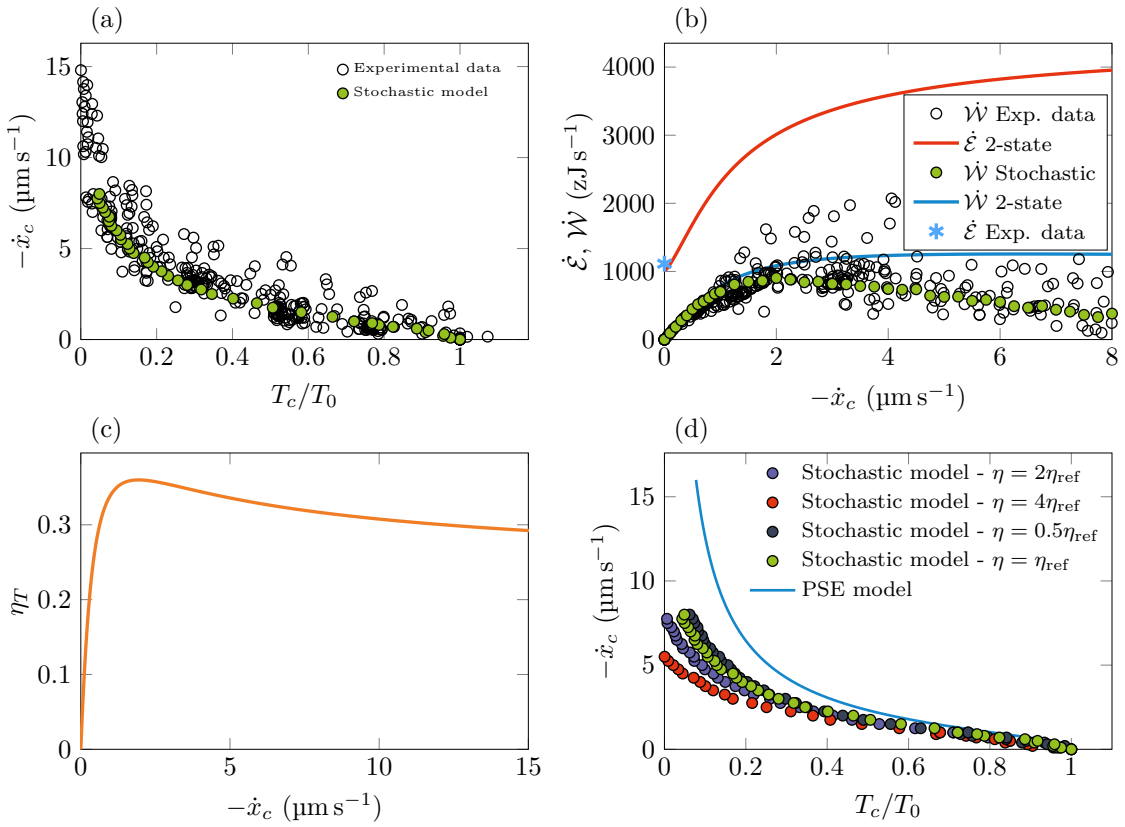

Figure 3.8 – Steady state isotonic shortening response. (a) Force-velocity curve for the stochastic model and the PSE model. (b) Produced work rate and energy input rate per myosin head in steady state shortening conditions. (c) Efficiency of the transduction of ATP energy into work for the PSE model in steady state shortening conditions. (d) Influence of the viscosity on the force-velocity curve computed with the stochastic model.

this region, the force-velocity curve of the stochastic model and the PSE model are similar, see Figure 3.8(a).

Finally, as in isometric contraction, we are able to predict the mechanical power and the ATP consumption rate during the steady state isotonic shortening, see Figure 3.8(b). The work production rate and the associated ATP energy consumption rate per myosin head can straightforwardly be computed from the steady state isotonic shortening response. They are defined respectively by

$$\begin{cases} \dot{\mathcal{W}} = \dot{x}_c \tau_c, \\ \dot{\mathcal{E}} = \dfrac{\mu_T}{d_a} \displaystyle\int_{s^-}^{s^+} g^{th}(s) \check{P}_1(s) \, \mathrm{d}s, \end{cases}$$

where μ_T is the chemical potential brought by ATP. From the latter the yield $\eta_T = \dot{\mathcal{W}}/\dot{\mathcal{E}}$ can be calculated (see Figure 3.8(c)).

Again without any particular adjustment of the parameter and using the validated ATP hydrolysis energy $\mu_T = 100\,\mathrm{zJ}$, our model recovers the ATP consumption rate in isometric conditions. Our prediction of the consumption rate and the yield during shortening remains to be validated experimentally.

Equilibration time As observed in the previous paragraphs, the accuracy of the PSE model relies principally on the assumption of an ultra-fast relaxation of the internal degrees of freedom, which means assuming that the variables X^t and Y^t are distributed according to the thermal equilibrium distribution at any time. Qualitatively, this assumption is valid if the "external effects" vary with a time scale that is longer than that requested to reach the thermal equilibrium. We have shown in particular that decreasing the value of the internal viscosity η tends to reduce the differences between the two population models, see Figure 3.7 and 3.8.

To quantitatively test the limit of validity of the thermal equilibrium assumption, we numerically estimate the equilibration time in the attached and detached potentials for the calibration proposed in Table 3.5. We perform this estimation with the convergence time of the first and second moments of the probability distributions $p(x, y, 0; s, t)$ and $p(x, y, 1; s, t)$ computed for a population of myosin heads evolving in the attached and detached energy landscapes w_α without jumps from a initial random distribution. The detached energy landscape is the same for all value of s and we thus compute a single estimate. On the contrary, the attached energy landscape depends on s. We therefore estimate the equilibration time for different values of this parameter.

The numerical results are presented in Figure 3.9. They show that the equilibration is faster in the attached potential than in the detached potential, the latter is therefore the limiting reaction in the global equilibration process.

We can then use the equilibration time in the detached potential to estimate that the global equilibration time τ_{eq} is $\tau_{eq} = 3.4\,\mathrm{ms}$ (see Figure 3.9). We can then define a limit shortening velocity v_t at the scale of the myosin head taking the power stroke distance a as characteristic length by $v_t = a/\tau_{eq} = 3.24\,\mu\mathrm{m\,s^{-1}}$. A comparison of the force-velocity curves for the PSE model and the stochastic model (Figure 3.8(a)) shows indeed that the two curves diverge from one another around the limit shortening velocity v_t.

For shortening velocities $\dot{x}_c$ lower than v_t, the contraction rate $\dot{x}_c/a$ is slow compared to the equilibration rate in the energy landscape. A myosin head that detaches has time to recover its power stroke capability and to attach to the next actin site (head can only attach when they are in the pre-power stroke configuration). For shortening velocities higher than v_t, the contraction rate is higher and a myosin head that detaches may not recovery its

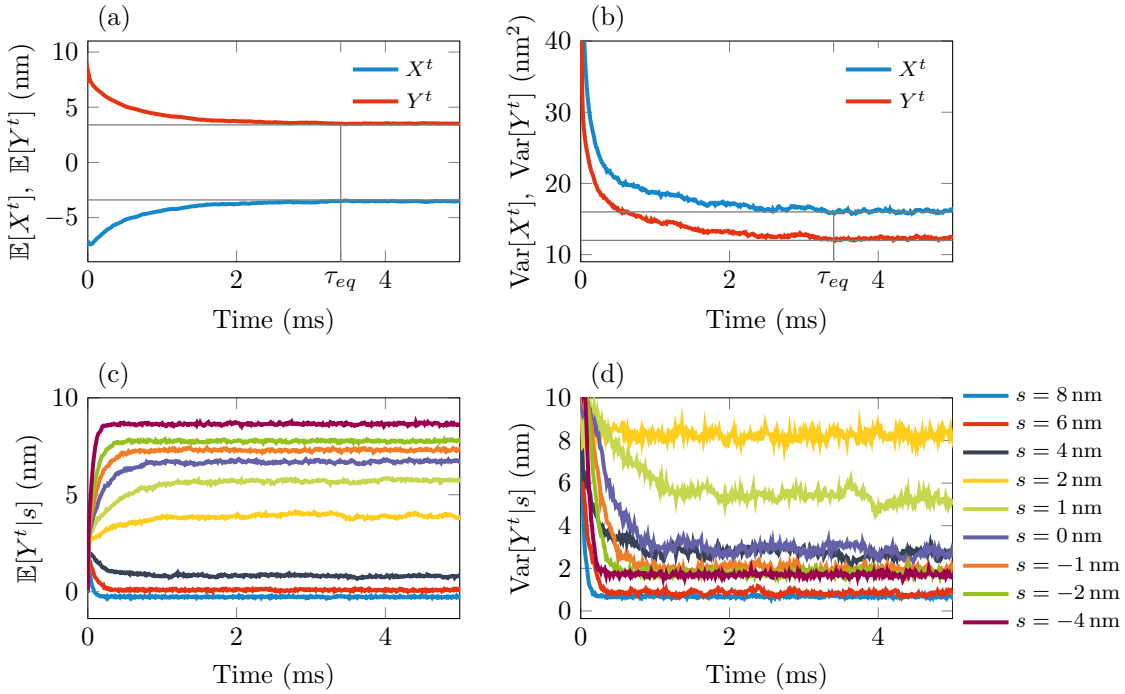

Figure 3.9 – Estimation of the equilibration time in the attached and detached potentials with the first and second moments of the respective probability distributions. (a) & (b) Detached potential. (c) & (d) Attached potential.

ability to reattach fast enough to bind to the next actin. It thus loses opportunity to attach, reducing the apparent cycling rate.

The discrepancy between the force-velocity curve of the PSE model and that of the stochastic model at high shortening velocities is thus due to a lower relative cycling capability in the stochastic model compared to the PSE model.

3.3.2 Macro models

3.3.2.1 Calibration

We recall that the main assumption made to obtain the simplified "macro models" was to consider that the sum $f(s)+g(s)$ was constant over the whole $[s^-, s^+]$ interval. To compare the PSE model with the macro-models we thus need to define "equivalent" transition rates for the different versions of the macroscopic models.

We chose the attachment rates of the macro models such that the maximal value $\overline{f}$ of the attachment rate is equal to $\overline{f}^{th}$ of the PSE model and we adjusted the width of region where the attachment function $f(s)$ does not vanish, such that the isometric ratio of attached heads $\check{n}_{\mathrm{att}}$ matches the data while verifying the condition that $f+g$ is constant (see Figure 3.10(a)). The minimal value of the detachment rate g is denoted by $\overline{g}$.

The first macro-model (BCS model) assumes a linear elastic cross-bridges characterized by two parameters: a stiffness κ_{xb} and a reference length s_0. We consider two cases for the definition of these constants. In the first cases, we chose the value of the stiffness measured experimentally $\kappa_{\mathrm{xb}} = \kappa = 1.07\,\mathrm{pN\,nm^{-1}}$ and the pre-strain $\tilde{s} = 5.74\,\mathrm{nm}$ that leads to an isometric force per attached head of 6.14 pN (see free energy profile in Figure 3.10(b)). In the second case, we aim at approximating the response at the end of phase II $(\delta s, T_2)$ with a linear elastic response. The cross-bridge stiffness is then taken equal to $\kappa_{\mathrm{xb}} = 0.52\,\mathrm{pN\,nm^{-1}}$

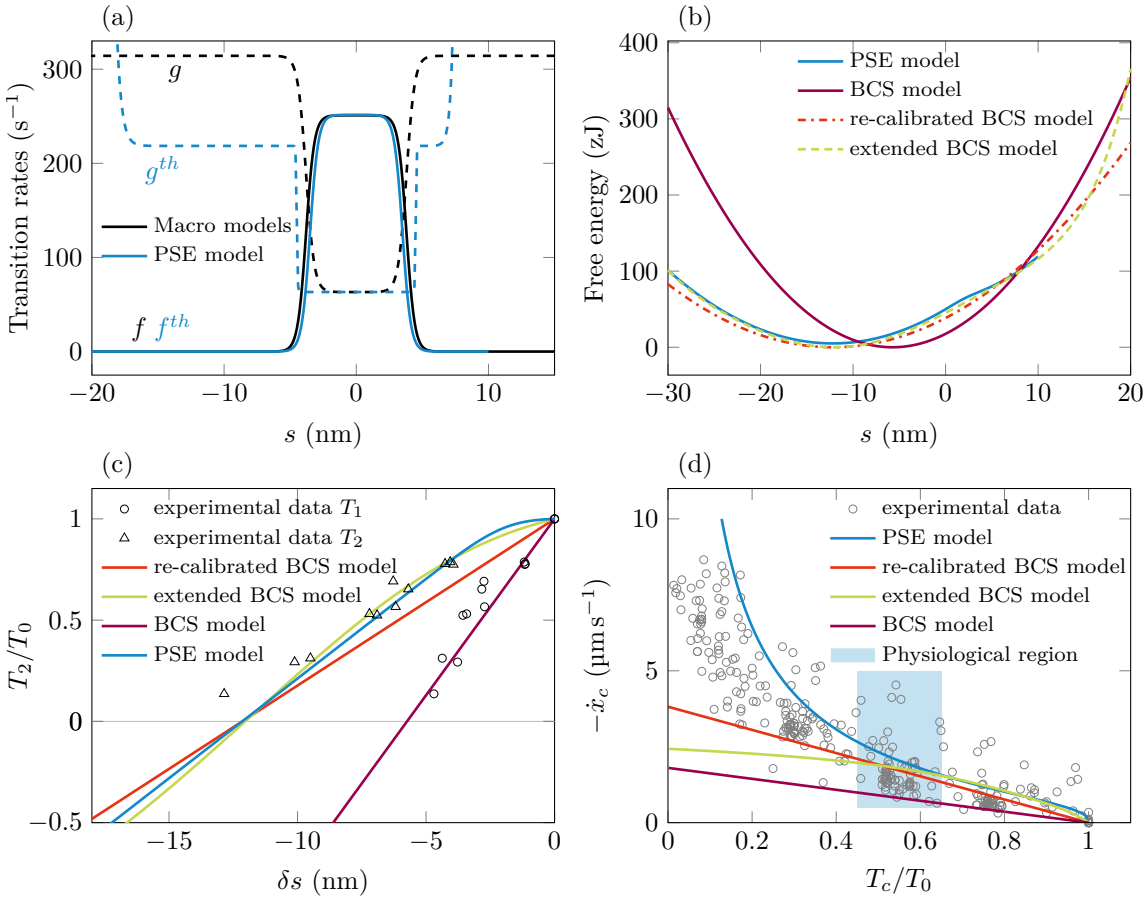

Figure 3.10 – (a) Transition rates used for the macroscopic models. (b) Free energy of the cross-bridge for the various macroscopic models considered. Note that the energy levels are defined up to a constant. (c) Elastic response of the different macroscopic models considered and the PSE model. (d) Force-velocity relation for the the different macroscopic models considered along with experimental data (same data as in Figure 3.4).

Isometric indicators	Symbol	PSE model	BCS model	recalibrated BCS model	extended BCS model
Ratio of attached head	$\check{n}_{\text{att}}$	0.158	0.152	0.152	0.152
Force per attached head	$\check{\tau}_c^{th} \ / \ \check{n}_{\text{att}}$	6.16 pN	6.14 pN	6.32 pN	6.14 pN
Maximal total stress	T_0	121 kPa	116 kPa	120 kPa	116 kPa
ATP tension cost (/s/head/kPa)	A_T	0.0835	0.110	0.106	0.110

Table 3.3 – Target isometric physiological indicators for the calibration on cardiac data of the PSE model and the macro models.

and the pre-strain $\tilde{s}$ is then set to 12.15 nm to obtain an isometric force per attached head of 6.31 pN (see free energy profile in Figure 3.10(b)). We call this model the re-calibrated BCS model.

The second macroscopic model (extended BCS model) assumes a non-linear elastic energy for the cross-bridge. We choose to define the free energy of the attached state with a polynomial of order 6 ($n = 6$) and calibrate the model so that the elastic response follows the $(\delta s, T_2)$ response (the model parameters are given in Table 3.6), see Figure 3.10((b) and (c)).

3.3.2.2 PSE model vs macro models

Isometric indicators The isometric indicators are presented in Table 3.3. With the proposed calibrations, all models are able to reproduce the key isometric indicators.

Effective elastic response By construction, the PSE model and the macro-models cannot reproduce the fast transients. The parameters of the stochastic model has been chosen such that the effective elastic response of the PSE model reproduces the $(\delta \ell_{hs}, T_2)$ relation obtained from the isotonic fast transients.

With the calibration choices made in the previous section, the elastic response of the BCS model corresponds to the $(\delta s, T_1)$-curve, while the elastic response of the re-calibrated BCS model corresponds to a linear approximation of the $(\delta s, T_2)$-curve (see Figure 3.10(c)). As expected the extended BCS model best reproduces the results of the PSE model as regards to the effective elasticity.

Steady state isotonic shortening We compare the steady-state isotonic behavior of the macro-models in Figure 3.10(d). The force-velocity relation corresponding to both BCS models are straight lines given by (3.30), see Figure 3.10(d, purple and green lines). In accordance with the "stiffness effect", the force of the re-calibrated BCS model (green dashed line) is larger at any fixed shortening velocity than that of the BCS model, which has a larger stiffness. Note that with linear macroscopic models, the "stiffness effect" appears straightforwardly in the equation (3.30).

For the non-linear model (extended BCS model), the force-velocity curve is given by (3.34). It remains close to the PSE model at low shortening velocity as expected from the higher force at small displacements. However the polynomial approximation leads to a dramatic force drop for $s < 20$ nm therefore, as the velocity increases, the non-linear

BCS model rapidly looses force and thus has a low maximum shortening velocity, again because of the "stiffness effect".

Macro-models as effective heart contraction models To put the development of the macro models into perspective, we compare the implication of the behavior differences between the two proposed versions (linear elastic and non-linear elastic) in the context of heart modeling. Within the heart cycle, the active contraction takes place during the ejection phase.

Considering experimental pressure-volume loop and end-systolic pressure-volume relation obtained on rats [Sato et al., 1998; Pacher et al., 2004], the range of physiological loads can be estimated to be between 45 % and 65 % of the maximal load (the physiological region is indicated in blue in Figure 3.10(d)). In this region the shortening velocity measured experimentally has an average value of $2\,\mu\mathrm{m\,s^{-1}}$. The same value is predicted by the PSE model and the re-calibrated BCS model, whereas the BCS model predicts a shortening velocity of $0.6\,\mu\mathrm{m\,s^{-1}}$.

Denoting the duration of ejection τ_e and assuming that the heart cavity is spherical and that the thickness is negligible, we obtain a end-systolic volume V_{ES} of

$$V_{\mathrm{ES}} = V_{\mathrm{ED}}\left(1 + \dot{x}_c \frac{\tau_e}{\ell_{hs}}\right)^3.$$

The ejection fraction being defined by $(V_{\mathrm{ED}} - V_{\mathrm{ES}})/V_{\mathrm{ED}}$ and taking a duration of ejection equal to 45 ms and an end-diastolic volume of 200 mL, the BCS model would predict an ejection fraction of 8 % whereas the re-calibrated BCS model would give a value of 35 %. Note that the ejection fractions estimated with the PSE model and the re-calibrated BCS model are outside of the physiological range at 37 °C, which is 50–65 % [Pacher et al., 2004]. This is because the models are calibrated on data obtained at 25 °C, the results can thus not be physiological. Considering the data measured by de Tombe & ter Keurs [1990] at 30 °C, we see that the shortening speed in the physiological range is approximately $5\,\mu\mathrm{m\,s^{-1}}$, which leads to an ejection fraction of 53 %.

The BCS model is thus not applicable in the context of heart modeling. On the contrary, the re-calibrated BCS model has good properties to be used in heart simulations. Its force-velocity curve presents a good match with the data over the whole physiological range and the elastic response is in good agreement with the experimental $(\delta s, T_2)$-curve.

The PSE model has the capability of reproducing the end of phase 2 response and the whole force-velocity curve. The computational complexity is further increased because the dynamics is governed by a partial differential equation. Note that a curved force-velocity relation can also be obtained with a macroscopic model using a linear elastic cross-bridge with the addition of a velocity dependent term in the definition of the detachment rate [Chapelle et al., 2012; Månsson, 2010].

The use of one or other of the models will naturally depend on the goal of the simulation. For a heart simulation in which a default physiological active behavior is sufficient, the re-calibrated BCS model is probably the best trade-off between the physiological consistency and the computational cost. However, if the heart simulation is targeting the active behavior of the cardiac tissue, the PSE model should be recommended. Indeed, with its tighter link to the physiology, the PSE model main advantage is to be able to give a better physiological interpretation of the simulated behavior. Moreover, it can consistently transfer properties across time and space scales, for instance the impact of a cardiomyopathy that affect the actin-myosin interaction can then be incorporated in the model by an adjustment of the calibration and then brought to the macroscopic space scale.

3.4 Discussion

Building macroscopic mechanical models of the heart contraction that are compatible with the micro-scale physiology is a major step toward the use of numerical simulation in clinical situations. Achieving this goal requires overcoming two difficulties. First, formulating comprehensive models of the molecular mechanisms necessarily requires to define an increasing number of model parameters that cannot be unambiguously calibrated. Second, implementing these complex models into a standard finite element simulation framework implies solving the classical continuum mechanics dynamic equations coupled with the local equation of the micro-scale physiological models. Since the local equations have to be solved at each integration points of the macroscopic structure (finite element mesh), increasing the contraction models complexity can dramatically increase the CPU time, making the simulation tool impractical.

We proposed a method to circumvent these drawbacks by formulating a hierarchy of interconnected mechanical models of the actomyosin contractile system. At the base of this hierarchy are two population based models, which we have shown to be almost univocally calibrated using data from classical benchmark experiment. We put forward that these models, once calibrated, can reproduce the most important mechanical indicators (isometric force, force-velocity relation, ...) of the actomyosin system.

In this section we put our results in perspective with other theoretical and experimental works.

3.4.1 Limitations of the models

As we have shown in Section 3.3, our model is able to reproduce the most fundamental physiological indicators of muscle contraction with a rather limited number of parameters compared to other models. However, our models face some limitations.

3.4.1.1 Viscoelasticity

Internal viscous damping controlling the kinetics of the relaxation of the conformational variables Y is the essential link between the stochastic model and the PSE model. The lower the internal viscosity parameter η, the more valid the PSE approximation. With our calibrated model the characteristic time of the relaxation of Y towards equilibrium is $\gamma_{\text{stoch}} = \eta/\kappa = 45\,\mu\text{s}$ (see Table 3.5), a value obtained by adjusting the parameter η to match the timescale of the rapid force recovery following a length step (see Section 3.3.1.1 and Figure 3.7). This value is smaller than the duration of the force step used in experiments [Caremani et al., 2016], which suggest that the T_1 response is viscoelastic rather than elastic, partially involving the internal damping. We checked that a good agreement with the experimental points can be recovered either by reducing the step duration or increasing η, see Figure 3.7.

Two comments can be made in light of these results. First, the data we used to calibrate our parameter η are extrapolated from measurement performed in force controlled conditions [Caremani et al., 2016], while our simulations are done in length controlled conditions. There is a known difference between the two rates of phase II, which has been linked to the nonequivalence of the two loading protocols [Caruel et al., 2013a]. It is thus possible that our extrapolation is not accurate.

Second, and more importantly, the assumption that phase I is a purely elastic response may be erroneous, which implies that the stiffness $\kappa \sim 1\,\text{pN}\,\text{nm}^{-1}$ obtained in [Caremani et al., 2016; Pinzauti et al., 2018] is underestimated, because it includes viscosity effects.

New experiments with faster load changes, typically about twice as fast, would be needed to confirm or contradict this value.

This conclusion is also supported by the fact that the myosin stiffness in skeletal muscle is larger, about $2.7\,\mathrm{pN\,nm^{-1}}$ [Piazzesi et al., 2007]. A new calibration is required to assess how a higher value of κ would affect the results obtained with our models.

However, we mention that experiments on rat cardiomyocytes are performed at 25 °C while skeletal muscles are tested at 4 °C, and therefore such comparison of the stiffnesses is not straightforward. It is expected that all physiological processes are speeded up by an increase of temperature and, indeed, the measured rate of phase 2 is about four times larger on cardiac sample than on skeletal samples, and the transition rates needed with our model to match the measured power-output of a fiber are about six times larger on cardiac sample than on skeletal samples [Caruel et al., 2019].

3.4.1.2 Rate of tension redevelopment

In the calibration process, we adjust the transition rates k_+ and k_- to fit the experimental force-velocity curve. In particular, the parameters $k_{\max}$ and $k_{\min}$, or equivalently the value of the equilibrium transition rate $\overline{f}^{th}$ and $\overline{g}^{th}$, influence the global shape of the force-velocity curve (see Section 3.3.1.1).

de Tombe & Stienen [2007] propose an alternative way to calibrate these model parameters. They measure the tension redevelopment characteristic time in isometric conditions after applying a fast release-restretch maneuver to force the detachment of some myosin heads. With this loading protocol, the dynamics of the tension rise is supposedly not affected by the thin filament activation process. For the family of models derived from the Huxley'57 model, this characteristic time τ_{tr} is given by $\tau_{tr} = \dfrac{1}{\overline{f}+\overline{g}}$. Coupling these data with the ATP consumption measurement, which is linked to the detachment rate g, they obtain an estimation of the transition rates f and g. For rat cardiac muscle at 25 °C, they obtain $\overline{f} = 35.0\,\mathrm{s^{-1}}$ and $\overline{g} = 14.4\,\mathrm{s^{-1}}$. These values are different from the ones obtained after our calibration. We have $\overline{f}^{th} = 251\,\mathrm{s^{-1}}$ and $\overline{g}^{th} = 63.2\,\mathrm{s^{-1}}$, which means that our model would fail to reproduce the kinetics of force redevelopment reported in de Tombe & Stienen [2007]. Nevertheless, if we use the value proposed by [de Tombe & Stienen, 2007] – all other things remaining equal – , we obtain the force-velocity curve presented in Figure 3.11, which does not match the experimental data. This comparison illustrates one

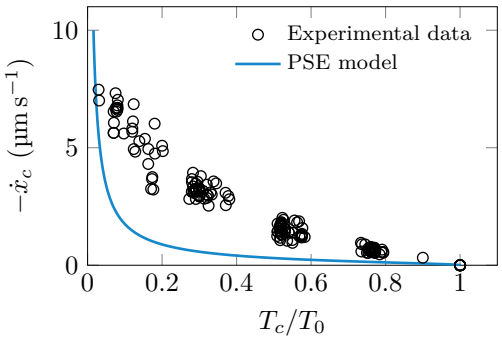

Figure 3.11 – Force-velocity curve using the transition rate values given in [de Tombe & Stienen, 2007], all other model parameters remain as given in Table 3.5.

of the current challenges in the understanding and modeling of muscle contraction: How a given model can match both the observed power-output of the fiber – which necessitates

a high cycling rate – and the rather low rate of force redevelopment – which necessitates low cycling rate? For a discussion of this conundrum, we refer to Mansson et al. [2015].

To resolve this issue Pertici et al. [2018] (simplified version of Caremani et al. [2015]) proposed a model that is able to capture the physiological cardiac force-velocity curve without involving a cycling rate as high as in our calibration. To do so, they introduce the possibility for the attached myosin heads to slide to a neighbor actin site without detaching, thus restoring a part of their force generation capability without consuming ATP. Another attempt consisting in prescribing a phenomenological dependence of the attachment rate on the shortening velocity is considered in Månsson [2010]. While both attempts successfully reconcile the two apparently contradicting observations within a single model, to our best knowledge, further studies are required to assess the validity of their assumptions.

3.4.1.3 Compatibility with X-ray diffraction

As we discussed in Section 3.3.1.1, the width d_f of the equilibrium attachment rate support S_f (see Figure 3.2) is adjusted to match the indicators of the isometric contraction. We have $d_f \approx 8\,\text{nm}$, which is larger to values reported for instance in [Piazzesi & Lombardi, 1995; Caremani et al., 2015; Mansson et al., 2015] but comparable to the values reported in [Smith et al., 2008]. According to [Reconditi, 2006], the dispersion of the projected mass of the attached myosin heads on the actin filament in isometric contraction is about 5 nm, which is incompatible with a wide distribution of the attachment rate. To reconcile our model with these observations, one can consider a chain of half-sarcomeres as the elementary unit of the contraction instead of a single representative motor as it is done most of the time. While the tension-elongation relation $\tau_c^{th}(s)$ of a single motor shows a region of negative slope, Caruel & Truskinovsky [2018] have shown that, with the same parameters, the tension-elongation relation of a series arrangement of half-sarcomere is necessarily larger or equal to 0. If we take such a relation as a "constitutive behavior" of the PSE model, we would need a much lower value of d_f to match the isometric contraction indicators, indeed.

3.4.1.4 Comparison with other models

Our model can be compared to two other Huxley'57-type models, the first one developed in [Pertici et al., 2018] and the other in [de Tombe & Stienen, 2007], see Table 3.4.

One of the major differences is that our models consider the actin periodicity to be $d_a = 38\,\text{nm}$, which corresponds to the periodicity of the double helix, whereas the other models consider the distance between monomers: $d_a = 5.5\,\text{nm}$. To match the experimental indicators of the isometric contraction both Pertici et al. [2018] and de Tombe & Stienen [2007] define a positive attachment rate over the interval $d_f = d_a$ whereas our model has $d_f < d_a$. The consequence of this choice is that the fraction of the heads that are attached in isometric contraction $\check{n}_{\text{att}}$ can, in the PSE model, be decorrelated from the duty ratio r, *i.e.* the fraction of the cycle that a motor spends bound to actin. Indeed, the fraction

Table 3.4 – Model comparison in isometric conditions. Note that we consider in this table the model proposed by Pertici et al. [2018] without the possibility of actin shifting so that we can compare the calibration of the transition.

	Pertici et al. [2018]	PSE model	de Tombe & Stienen [2007]
d_a	5.5 nm	40 nm	5.5 nm
d_f	5.5 nm	8 nm	5.5 nm
$\overline{f}$	$15\,\mathrm{s}^{-1}$	$250\,\mathrm{s}^{-1}$	$35\,\mathrm{s}^{-1}$
$\overline{g}$	$40\,\mathrm{s}^{-1}$	$60\,\mathrm{s}^{-1}$	$14\,\mathrm{s}^{-1}$
$\check{n}_{\mathrm{att}}$	0.3	0.2	0.7
r	0.3	0.8	0.7
$\frac{J_{\mathrm{ATP}}}{\mu_T}$	$12\,\mathrm{s}^{-1}$	$12\,\mathrm{s}^{-1}$	$9.8\,\mathrm{s}^{-1}$
τ_{tr}	2×10^{-2} s ✔	3×10^{-3} s ✖	2×10^{-2} s ✔
F-V curve	✖	✔	✖

of attached heads and the duty ratio are given by

$$\check{n}_{\mathrm{att}} = \frac{1}{d_a}\int_{s^-}^{s^+} \check{P}_1(s)\,\mathrm{d}s = \frac{d_f}{d_a}\frac{\overline{f}}{\overline{f}+\overline{g}}$$

$$r = \frac{\frac{1}{d_a}\int_{s^-}^{s^+} \frac{1}{g(s)}\check{P}_1(s)\,\mathrm{d}s}{\frac{1}{d_a}\int_{s^-}^{s^+} \left(\frac{1}{f(s)}+\frac{1}{g(s)}\right)\check{P}_1(s)\,\mathrm{d}s} = \frac{\overline{f}}{\overline{f}+\overline{g}},$$

so that having $d_f = d_a$ necessarily implies $r = \check{n}_{\mathrm{att}}$. Another consequence of having $d_f \neq d_a$ is that, a significant fraction of heads cannot attach and therefore do not consume energy. The consumption of ATP is defined by

$$\frac{J_{\mathrm{ATP}}}{\mu_T} = \frac{1}{d_a}\int_{s^-}^{s^+} g(s)\check{P}_1(s)\,\mathrm{d}s = \overline{g}\,\check{n}_{\mathrm{att}} = \overline{g}\frac{d_f}{d_a}\frac{\overline{f}}{\overline{f}+\overline{g}}$$

which shows that, even with high attachment/detachment frequencies, the energy consumption of the PSE model can be kept low, again by tuning the ratio d_f/d_a.

As explained above the two-state models presented in Table 3.4 cannot reproduce both the rate of force recovery τ_{tr} and the force velocity relation at the same time. In the case of Pertici et al. [2018], the two state model as to be supplemented by the addition of the possibility for actin shifting without detachment in order to reproduce the power output. We chose to concentrate on reproducing the force-velocity relation assuming that other physiological mechanisms may play a role in the specific kinetics of the force redevelopment.

3.4.2 Limitations of our calibration

First, the isotonic shortening protocols target either rapid transient or steady state dynamics. One can also consider the protocols aiming at the transient dynamics such as the

response to applied shortening and immediate restretch to study the kinetics of the non-steady-state force development [de Tombe & Stienen, 2007]. We have shown show that the classical models cannot both reproduce this force redevelopment dynamics and the steady state force-velocity relation without adding new still experimentally unvalidated modeling assumptions.

Second, the experiments are performed at 25–27 °C and not at body temperature for technical reasons. Temperature is known to affect the shape of the force-velocity curve, the value of the unloaded shortening velocity V_0 and the value of the force developed in isometric conditions [de Tombe & ter Keurs, 1990], but also the apparent cycling rates of the cross-bridges [de Tombe & Stienen, 2007]. However, the only range of temperature, at which all types of quantitative characterization of the cardiac muscle behavior are available, is around 25 °C. We will therefore perform the calibration of our models with data measured at this temperature.

Finally, the actin-myosin interaction quantitative properties vary between species. Experiments performed on rat trabeculae will therefore not give precise information and the behavior of human cardiac muscles.

3.5 Conclusion

The acto-myosin interaction is a fundamental force generation mechanism, present in a wide range of biological processes, from cell motility to muscle contraction. Its physical modeling has been the object of intense research activities over the last decades, resulting in increasingly comprehensive simulations of its physiology. In parallel, the development of numerical medicine and the associated patient-specific simulations, now open the way to enriched clinical procedures, where adequate models of the microscopic physiological mechanisms play a crucial role.

To be fully operational in practice, patient specific simulations need to be computationally efficient to obtain results in real time, which is usually incompatible with a high degree of model refinement. Increasing computational cost is, on the one hand, a direct consequence of the multi-scale – in time and space – nature of the physical phenomena, requiring sophisticated and time consuming algorithms for their simulation. On the other hand, comprehensive model usually require finely calibrating a large number of parameters, based on a limited set of data. Even though substantial progresses have been made in data assimilation techniques [Moireau & Chapelle, 2011], the identifiability of complex active models with data obtained from current standard acquisition technics remains limited.

In this paper we have addressed this issue in the context of the modeling of the actomyosin mechanical behavior in heart contraction. Our approach is to develop a hierarchy of interconnected models of the actomyosin system, from the more refined, accounting for a large number of physiological indicators, to the more coarse-grained, allowing for fast simulation at the organ scale.

We started with a stochastic mechanical model of a population of molecular motors constitutive of a sarcomere, which was developed in [Caruel et al., 2019] but only validated for skeletal muscle. We have shown that this model can be calibrated to reproduce essential mechanical indicators of the cardiac contractile unit that can be obtained experimentally. The calibration procedure leads to a robust definition of the parameters value, which allow, in particular, for specifically identifying the effect of a parameter value on the output of the model.

The stochastic model is formulated to reproduce the fastest molecular processes involved in the transient isotonic shortening of cardiomyocytes *ex vivo*, providing essential

information about the mechanical characteristics of the cross-bridges. Since theses processes are characterized by timescales of the order of 1 ms, their direct simulation will dramatically impair the computational efficiency of a 3D organ simulation.

We propose a first coarse graining step by building on the separation of timescales between the power-stroke mechanism, playing a major role in the isotonic fast transient, and the attachment-detachment process of the myosin motor on actin, whose timescale is at least one order of magnitude larger than that of the power stroke. By assuming that the internal stochastic variables parametrizing the power-stroke conformational change quickly relax towards their equilibrium distribution, we formulated the PSE model, which appears as an instance of the landmark Huxley'57 family of models whose parameters are directly inherited from the stochastic model and not postulated *a priori*. This model however requires solving a population density, whose dynamics still takes the form of a local PDE in a finite element simulation environment.

The contraction model can be further simplified by considering that the quantities of interest at the macro-scale are only the moments of this density, representing average physiological indicators (force, stiffness, ATP consumption rate etc...) over a large population of motors. By imposing specific constrains on the parameters of the PSE model, we derived the system of ordinary differential equations, accounting for the moments dynamics. This type of moment-based approach can be combined with standard geometrical simplification of the heart to construct reduced dimensional models of the organ that can be simulated in real time and therefore used as a primary estimation tool or for rapid pre-calibration purposes [Caruel et al., 2013b] or in clinical contexts [Le Gall et al., 2019].

The advantage of our approach is that the hierarchical relation between the models allow to predict the consequences of microscopic actin-myosin constitutive behavior variations, for instance as a result of a disease, at the larger time and spaces scales. In addition the coarse graining approach is well controlled *i.e.* the loss of information inherent to the simplifications is quantified and the associated hypothesis can always be tested. Therefore, a more refined model can be called upon if needed for a specific application, without having to start over a tedious calibration procedure. Moreover, the method is not specific to our starting stochastic model: it can be applied to the widely used chemical-mechanical modeling framework [Eisenberg et al., 1980], which, through elimination of the fastest chemical-like reaction, can be also reduced to simple population model and further to moment-based model [Zahalak, 1981].

Finally, we recall that only the basal mechanical behavior of the actomyosin system have been addressed in this work. In particular, all the regulation aspects, essential for a relevant simulation of the organ behavior, remain out of the scope of our study. Detailed activation models also involve the simulation of the dynamics of populations of active and inactive agents – actin sites or myosin heads – using similar chemical analogy. Therefore building a similar model hierarchy, might also be a solution for an organ-scale simulation of the microscopic activation and regulation physiology.

3.6 Appendices

3.6.1 Reference calibration

The double quadratic well potentials u_α are presented in Figure 3.12. Combining them with the myosin neck potential energy, we obtain the energy landscapes w_α of the attached and detached states. They are depicted in Figure 3.13. The transition rates k_+ and k_- are presented in Figure 3.14.

From these calibration choices, we derive the constitutive elements of the PSE model.

The energy landscapes u_α allow to compute the equilibrium probability densities p_0^{th} and p_1^{th}. Then, the integration against the transition rates k_+ and k_- leads to the derivation of the thermal equilibrium transition rates f^{th} and g^{th}. The elements of the PSE model are presented in Figure 3.15.

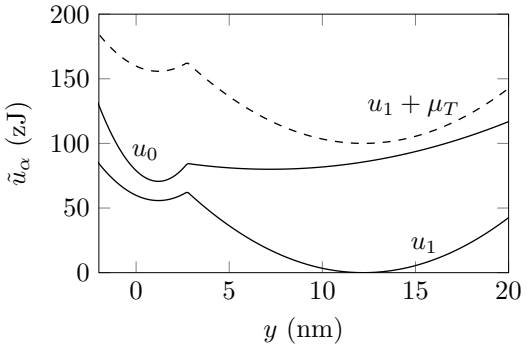

Figure 3.12 – Double well potential in both attached (u_1) and detached state (u_0) in our calibration for cardiac fibers.

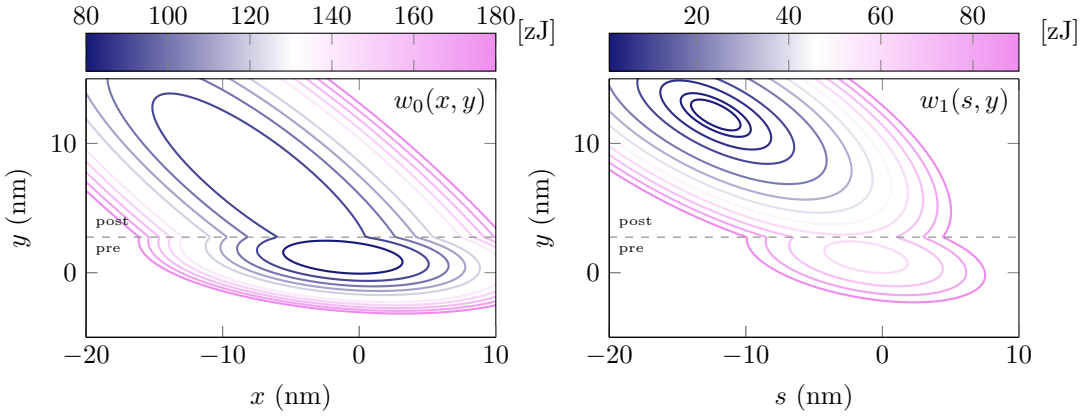

Figure 3.13 – Contour lines of the myosin head energy landscape. The thin dashed line represent the separation between the pre-power stroke and post-power stroke conformations. (Left) Detached potential $w_0(x, y)$. (Right) Attached potential $w_1(s, y)$.

3.6.2 Asymptotic calculation of the T_1-curve

At the time scale of the phase I (assuming that this phase is instantaneous), the force predicted by the stochastic model (3.6) becomes

$$T_1(\delta s) = \frac{\rho_{\text{surf}}}{d_a} \int_{s^-}^{s^+} \int_{-\infty}^{+\infty} \kappa(s + \delta s + y) \breve{\bar{p}}(y; s) \, \mathrm{d}y \mathrm{d}s, \tag{3.38}$$

where $\breve{\bar{p}}(y; s)$ is the isometric probability density of being attached. Equation (3.38) becomes

$$T_1(\delta s) = T_0 + \kappa \rho_{\text{surf}} \delta s \frac{1}{d_a} \int_{s^-}^{s^+} \int_{-\infty}^{+\infty} \breve{\bar{p}}(y; s) \, \mathrm{d}y \mathrm{d}s.$$

Parameter	Symbol	Value
Power stroke potentials		
Power stroke characteristic length	a	11 nm
Bistable element in attached state ($\alpha = 1$)		
$\overline{u}_1(y) = \begin{cases} \kappa_{1\text{pre}}/2\,(y - y_{1\text{pre}})^2 + v_1 & \text{if } y < \ell_1, \\ \kappa_{1\text{post}}/2\,(y - y_{1\text{post}})^2 & \text{otherwise,} \end{cases}$	$\kappa_{1\text{pre}}$	5.60 pN nm^{-1}
	$\kappa_{1\text{post}}$	1.40 pN nm^{-1}
	ℓ_1	1.55 nm
$v_1 = \kappa_{1\text{post}}/2\,(\ell_1 - y_{1\text{post}})^2 - \kappa_{1\text{pre}}/2\,(\ell_1 - y_{1\text{pre}})^2$	$y_{1\text{post}}$	a
	$y_{1\text{pre}}$	0
Bistable element in detached state ($\alpha = 0$)		
$\overline{u}_0(y) = \begin{cases} \kappa_{0\text{pre}}/2\,(y - y_{0\text{pre}})^2 + v_0 + E & \text{if } y < \ell_0, \\ \kappa_{0\text{post}}/2\,(y - y_{0\text{post}})^2 + E & \text{otherwise,} \end{cases}$	$\kappa_{0\text{pre}}$	2.72 pN nm^{-1}
	$\kappa_{0\text{post}}$	1.54 pN nm^{-1}
	ℓ_0	1.55 nm
$v_0 = \kappa_{0\text{post}}/2\,(\ell_0 - y_{0\text{post}})^2 - \kappa_{0\text{pre}}/2\,(\ell_0 - y_{1\text{pre}})^2$	$y_{0\text{post}}$	6 nm
	$y_{0\text{pre}}$	0
	E	80 zJ
Energy landscapes $w_\alpha(y) = u_\alpha(y) + \frac{1}{2}\kappa(x+y)^2$ (see Figure 3.12)		
$u_\alpha(y) = \overline{u}_\alpha(y + \tilde{s}_\alpha)$	κ	1.07 pN nm^{-1}
	$\tilde{s}_0$	1.2 nm
	$\tilde{s}_1$	1.2 nm
	μ_T	100 zJ
Stochastic dynamics		
Drag coefficient	η	0.0486 ms pN nm^{-1}
Microscopic timescale	$\gamma_{\text{stoch}} = \eta/\kappa$	0.0454 ms
Temperature	T	298 K
Attachment / detachment rates (Figure 3.14)		
$\psi_{0\alpha}(y) = 1/2\,\{1 + \tanh[\lambda_1\,(\ell_\alpha - y)]\}, \quad \psi_{1\alpha} = 1 - \psi_{0\alpha}$		
$k_+(s,y) = \psi_{00}\,(y)\,\overline{k}_+(s)$		
$k_-(s,y) = \psi_{01}\,(y)\,\overline{k}_{\text{pre}}\,(s,y) + \psi_{11}\,(y)\,\overline{k}_{\text{post}}\,(s,y) + \overline{k}_*\,(s,y)$	λ_1	7.28 nm^{-1}
	$k_{\max}$	374 s^{-1}
	λ_2	1.60 nm^{-1}
$\bar{k}_+(s) = \frac{k_{\max}}{2}\Big[\tanh\big(\lambda_2(s+\ell_+)\big)\,\mathbb{1}_{]-\infty,0]}(s) + \tanh\big(\lambda_2(s-\ell_+)\big)\,\mathbb{1}_{]0,\infty[}(s)\Big]$	ℓ_+	3.5 nm
	k_0	1400 s^{-1}
	λ_3	5 nm^{-1}
$\overline{k}_{\text{post}}\,(s,y) = k_0 \exp\big(-\lambda_3(s+y-\ell_{-,l})\big)$	λ_4	5 nm^{-1}
$\overline{k}_{\text{pre}}\,(s,y) = k_0 \exp\big(\lambda_4(s+y-\ell_{-,r})\big)$	$\ell_{-,l}$	−8 nm
$\overline{k}_*\,(s,y) = k_{\min} + \frac{k_*}{2}\Big[2 + \tanh\big(\lambda_*(s-\ell_*)\big) - \tanh\big(\lambda_*(s+\ell_*)\big)\Big]$	$\ell_{-,r}$	9 nm
	$k_{\min}$	63.3 s^{-1}
	k_*	155 s^{-1}
	λ_*	72.8 nm^{-1}
	ℓ_*	4.5 nm^{-1}
Scaling parameter		
Reference length of a half sarcomere	ℓ_{hs}	0.925 µm
Lower bound of the reachable actin sites interval	s^-	−30 nm
Upper bound of the reachable actin sites interval	s^+	10 nm

Table 3.5 – Calibration of the model for cardiac data.

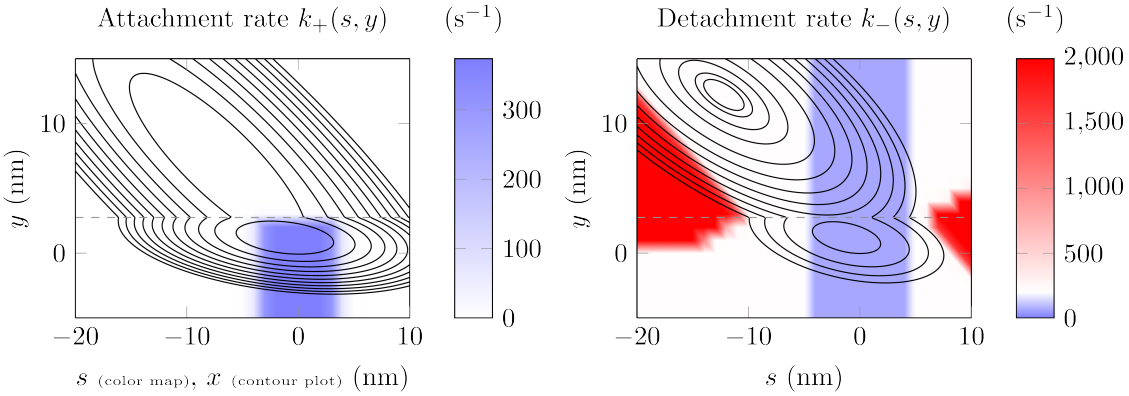

Figure 3.14 – Transition rates $k_+(s,y)$ and $k_-(s,y)$. The contours represent the energy landscape of the myosin head. The thin dashed line represent the separation between the pre-power stroke and post-power stroke conformations. (Left) Attachment rate k_+ (color map) and detached energy landscape (contour line). (Right) Detachment rate k_- (color map) and attached energy landscape (contour line).

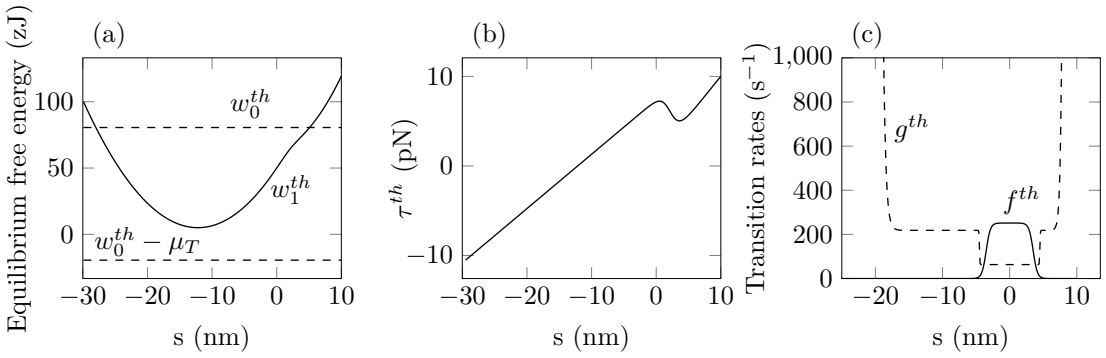

Figure 3.15 – Constitutive elements of the PSE model. (a) Equilibrium energy levels. (b) Equilibrium average tension. (c) Equilibrium transition rates.

Model parameter	Value	Model parameter	Value
c_0	$0.349\ \kappa a^2$	c_4	$0.213\ \kappa a^2/a^4$
c_1	$0.534\ \kappa a^2/a$	c_5	$0.234\ \kappa a^2/a^5$
c_2	$0.155\ \kappa a^2/a^2$	c_6	$0.0511\ \kappa a^2/a^6$
c_3	$-0.286\ \kappa a^2/a^3$		

Table 3.6 – Model parameter of the extended BCS model.

By definition, we have

$$\frac{1}{d_a}\int_{s^-}^{s^+}\int_{-\infty}^{+\infty}\check{\bar{p}}(y;s)\,\mathrm{d}y\mathrm{d}s = \check{n}_{\mathrm{att}},$$

and thus the tension T_1 is given by

$$T_1(\delta s) = T_0 + \kappa\rho_{\mathrm{surf}}\check{n}_{\mathrm{att}}\delta s.$$

3.6.3 Asymptotic calculation of the T_2-curve

We want to establish the equation of the asymptotic branch of τ^{th} for large and negative s. We consider the energy landscape w_1 defined with the quadratic double well potential u_1 by $w_1(s,y) = \kappa/2(s+y)^2 + u_1(y)$. We have

$$\begin{aligned}\tau^{th}(s) &\approx \int_{-\infty}^{\infty}\kappa(s+y)p_1^{th}(y;s)\,\mathrm{d}y = \int_{-\infty}^{\infty}\kappa(s+y)\frac{e^{-w_1(s,y)/k_BT}}{\int_{-\infty}^{\infty}e^{-w_1(s,y')/k_BT}\,\mathrm{d}y'}\,\mathrm{d}y,\\ &= \kappa s + \frac{\kappa}{\int_{-\infty}^{\infty}e^{-w_1(y',s)/k_BT}\,\mathrm{d}y'}\int_{-\infty}^{\infty}ye^{-w_1(y,s)/k_BT}\,\mathrm{d}y. \end{aligned} \tag{3.39}$$

The integral over the internal variable y can be split into two parts, one for each well of the attached potential. For large and negative s, all the heads are concentrated in the post-power stroke well of the energy landscape (see Figure 3.13). Therefore, we can neglect the contribution of the pre-power stroke well to the integral and we approximate the whole bistable potential by the post power stroke well. We have

$$\begin{aligned}\int_{-\infty}^{\infty}e^{-w_1(s,y')/k_BT}\,\mathrm{d}y' &\approx \int_{\ell_1}^{\infty}e^{-w_1(s,y')/k_BT}\,\mathrm{d}y',\\ &\approx \int_{-\infty}^{\infty}\exp\left[-\frac{1}{k_BT}\left[\frac{\kappa}{2}(s+y')^2 + \frac{\kappa_{1\mathrm{post}}}{2}(y'-y_{1\mathrm{post}})^2\right]\right]\mathrm{d}y'.\end{aligned}$$

Writing the quadratic potential in the canonical form, we have

$$\begin{aligned}
&\int_{-\infty}^{\infty} e^{-w_1(s,y')/k_BT}\,\mathrm{d}y' \approx \\
&\qquad \int_{-\infty}^{\infty} \exp\left[-\frac{\kappa+\kappa_{1\text{post}}}{2k_BT}\left[(y'+\frac{\kappa s-\kappa_{1\text{post}}y_{1\text{post}}}{\kappa+\kappa_{1\text{post}}})^2-(\frac{\kappa s-\kappa_{1\text{post}}y_{1\text{post}}}{\kappa+\kappa_{1\text{post}}})^2\right]\right] \\
&\qquad\qquad \cdot\exp\left[-\frac{1}{2k_BT}\left[\kappa s^2+\kappa_{1\text{post}}y_{1\text{post}}^2\right]\right]\mathrm{d}y', \\
&\qquad = \exp\left[\frac{\kappa+\kappa_{1\text{post}}}{2k_BT}(\frac{\kappa s-\kappa_{1\text{post}}y_{1\text{post}}}{\kappa+\kappa_{1\text{post}}})^2\right]\exp\left[-\frac{1}{2k_BT}\left[\kappa s^2+\kappa_{1\text{post}}y_{1\text{post}}^2\right]\right] \\
&\qquad\qquad \cdot\int_{-\infty}^{\infty}\exp\left[-\frac{\kappa+\kappa_{1\text{post}}}{2k_BT}(y'+\frac{\kappa s-\kappa_{1\text{post}}y_{1\text{post}}}{\kappa+\kappa_{1\text{post}}})^2\right]\mathrm{d}y', \\
&\qquad = \exp\left[-\frac{1}{2k_BT}\frac{\kappa_{1\text{post}}\kappa}{\kappa_{1\text{post}}+\kappa}(s+y_{1\text{post}})^2\right]\sqrt{\frac{2\pi k_BT}{\kappa+\kappa_{1\text{post}}}}.
\end{aligned}$$

We define the stiffness $\overline{\kappa}$ and the two lengths $y_0'(s)$ and L_{ref} by

$$\overline{\kappa}=\frac{\kappa\kappa_{1\text{post}}}{\kappa+\kappa_{1\text{post}}},\quad y_0'(s)=\frac{\kappa s-\kappa_{1\text{post}}y_{1\text{post}}}{\kappa+\kappa_{1\text{post}}},\quad\text{and}\quad L_{\text{ref}}=\sqrt{\frac{k_BT}{\kappa+\kappa_{1\text{post}}}}.$$

Using the previous calculation and its result, (3.39) becomes

$$\begin{aligned}
\tau^{th}(s)\approx\kappa s+&\frac{\kappa}{\exp\left[-\frac{1}{2k_BT}\overline{\kappa}(s+y_{1\text{post}})^2\right]\sqrt{2\pi}L_{\text{ref}}} \\
&\cdot\exp\left[-\frac{1}{2k_BT}\overline{\kappa}(s+y_{1\text{post}})^2\right]\int_{-\infty}^{\infty}y\exp\left[-\frac{1}{2L_{\text{ref}}^2}\big(y+y_0'(s)\big)^2\right]\mathrm{d}y.
\end{aligned}$$

With the change of variable $u=\frac{1}{L_{\text{ref}}}(y+y_0'(s))$, we obtain

$$\tau^{th}(s)\approx\kappa s+\frac{\kappa}{\sqrt{2\pi}L_{\text{ref}}}\int_{-\infty}^{\infty}\big(L_{\text{ref}}u-y_0'(s)\big)\exp\left[-\frac{u^2}{2}\right]L_{\text{ref}}\,\mathrm{d}u.$$

Noting that

$$\int_{-\infty}^{\infty}u\exp\left[-\frac{u^2}{2}\right]\mathrm{d}u=0,$$

and expanding $y_0'(s)$, we obtain

$$\tau^{th}(s)\approx\kappa s-\frac{\kappa}{\sqrt{2\pi}}\sqrt{2\pi}\frac{\kappa s-\kappa_{1\text{post}}y_{1\text{post}}}{\kappa+\kappa_{1\text{post}}}.$$

Finally, the asymptotic expression of $\tau^{th}(s)$ for large and negative values of s is

$$\tau^{th}(s)\underset{s\to-\infty}{\sim}\frac{\kappa\kappa_{1\text{post}}}{\kappa+\kappa_{1\text{post}}}(s+y_{1\text{post}}).$$

Similarly, we obtain the asymptotic branch for large and positive values of s, neglecting the contribution of myosin heads in the post-power stroke conformation, as

$$\tau^{th}(s) \underset{s\to+\infty}{\sim} \frac{\kappa\kappa_{1\mathrm{pre}}}{\kappa+\kappa_{1\mathrm{pre}}}(s+y_{1\mathrm{pre}}).$$

In a nutshell, the T_2-curve being given by

$$T_2(\delta s) = \frac{\rho_{\mathrm{surf}}}{d_a}\int_{s^-}^{s^+} \check{P}_1(s)\tau^{th}(s+\delta s)\,\mathrm{d}s,$$

the its asymptotic slopes are given by

$$\left|\frac{\partial T_2}{\partial \delta s}\right|_{\delta s\to-\infty} = \rho_{\mathrm{surf}}\check{n}_{\mathrm{att}}\frac{\kappa\kappa_{1\mathrm{post}}}{\kappa+\kappa_{1\mathrm{post}}},$$
$$\left|\frac{\partial T_2}{\partial \delta s}\right|_{\delta s\to+\infty} = \rho_{\mathrm{surf}}\check{n}_{\mathrm{att}}\frac{\kappa\kappa_{1\mathrm{pre}}}{\kappa+\kappa_{1\mathrm{pre}}}.$$

3.6.4 Computation of the PSE tension

To show the equivalence of the two expression of the equilibrium tension $\tau^{th}(s)$, let us compute the derivation of the equilibrium attached free energy $w_1^{th}(s)$.

$$\frac{\mathrm{d}w_1^{th}}{\mathrm{d}s}(s) = \int \partial_s w_1(s,y)p_1^{th}(y;s)\,\mathrm{d}y + \underbrace{\int \partial_s p_1^{th}(y;s)\Big[w_1(s,y)+k_BT\Big(\ln\big(a\,p_1^{th}(y;s)\big)+1\Big)\Big]\,\mathrm{d}y}_{\equiv A(s)}.$$

Defining $Z_1(s)=\int \exp\big(-w_1(s,y)/(k_BT)\big)\,\mathrm{d}y$, we have

$$\begin{aligned}
A(s) &= \int\Bigg[\Big[-\frac{1}{k_BT}\partial_s w_1(s,y)\frac{e^{-w_1(s,y)/(k_BT)}}{Z_1(s)} \\
&\qquad + \frac{1}{k_BT}\frac{e^{-w_1(s,y)/(k_BT)}}{Z_1(s)}\int \partial_s w_1(s,y')\frac{e^{-w_1(s,y')/(k_BT)}}{Z_1(s)}\,\mathrm{d}y'\Big] \\
&\qquad \cdot\Big[\cancel{w_1(s,y)} + k_BT\Big(-\frac{\cancel{w_1(s,y)}}{\cancel{k_BT}} - \ln\big(Z_1(s)/a\big)+1\Big)\Big]\Bigg]\,\mathrm{d}y, \\
&= k_BT\Big(1-\ln\big(Z_1(s)/a\big)\Big)\Big[-\int \partial_s w_1(s,y)\frac{e^{-w_1(s,y)/(k_BT)}}{Z_1(s)}\,\mathrm{d}y \\
&\qquad + \int \partial_s w_1(s,y')\frac{e^{-w_1(s,y')/(k_BT)}}{Z_1(s)}\,\mathrm{d}y'\underbrace{\int p_1^{th}(y,s)\,\mathrm{d}y}_{=1}\Big], \\
&= 0.
\end{aligned}$$

From the expression (3.1) of w_1, we thus finally obtain

$$\tau^{th}(s) = \int \kappa(y+s)p_1^{th}(y;s)\,\mathrm{d}y = \int \partial_s w_1(s,y)p_1^{th}(y;s)\,\mathrm{d}y = \frac{\mathrm{d}w_1^{th}}{\mathrm{d}s}(s).$$

Note that, naturally, a calculation with the free energy $\mathcal{F}(s) = -k_BT\ln(Z(s))$, the partition function defined as $Z(s)=\int e^{-w_1(s,y)/(k_BT)}\,\mathrm{d}y$ and a definition of τ^{th} as $\tau^{th}(s) = -\partial_s\mathcal{F}(s)$ leads to the same result.

3.6.5 Extrapolation of the rate of phase II in length control conditions for cardiac cells

The rate of force development and of shortening in phase II have been measured for frog skeletal muscles at 4 °C in length control [Huxley & Simmons, 1971; Piazzesi & Lombardi, 1995; Linari et al., 2009] and force control conditions [Piazzesi et al., 2002], respectively. On the contrary, for cardiac muscles, experiments have only been performed in force control conditions (at 27 °C) [Caremani et al., 2016]. Tough non-equivalent, the dynamics in phase II in the two setups are nevertheless linked. We will use an analogy between them to extrapolate the behavior of cardiac muscle cells in length control conditions, which is important for our calibration process. We first compare the rate in force control conditions for cardiac and skeletal muscle cells (see Figure 3.16(a)). The experimental data show that, in their respective experimental conditions, the rate of shortening in phase II is four times faster for rat cardiac muscle cells at than for frog skeletal muscle. We apply the same proportionality factor to extrapolate the rate of force recovery in phase II for rat cardiac fibers at 27 °C from measurements of the same rate of recovery for frog skeletal muscles at 4 °C. The results are presented in Figure 3.16(b).

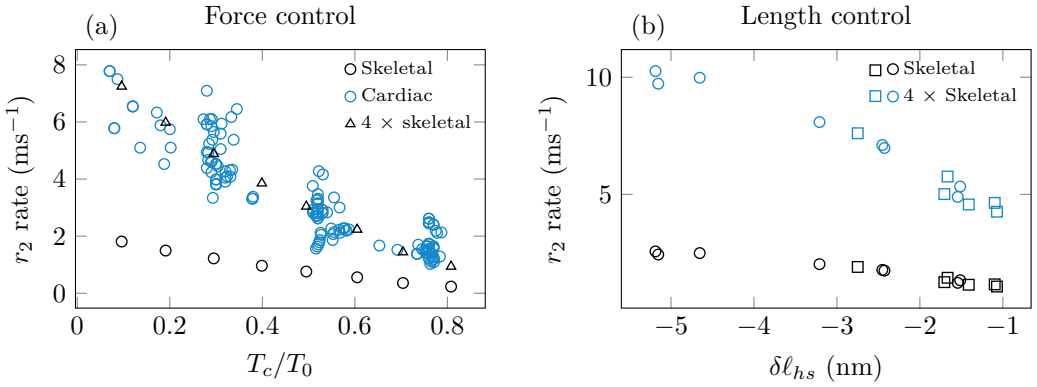

Figure 3.16 – Extrapolation of the rate of force recovery in phase 2 in length control conditions for cardiac muscle cell from the comparison of the rate of shortening in phase 2 in force control conditions between cardiac and skeletal experimental data. (a) Rate of shortening in phase II in force control conditions. (Black circles) Frog skeletal muscle cells at 4 °C, data from [Piazzesi et al., 2002]. (Blue circles) Rat cardiac muscle cells at 27 °C, data from [Caremani et al., 2016]. (Black triangles) Rate measured for frog skeletal muscle cells at 4 °C multiplied by 4. (b) Rate of force recovery in phase II in length control conditions. (Black symbols) Frog skeletal muscle cells at 4 °C. (Black circles) Data from [Piazzesi & Lombardi, 1995]. (Black squares) Data from [Linari et al., 2009]. (Blue symbols) Extrapolation of the rate of force recovery in phase 2 in length control conditions for cardiac muscle cells. The data measured for skeletal muscle cells are multiplied by 4

Bibliography

Alberts, B. (2015). *Molecular Biology of the Cell*. Garland Science, Taylor and Francis Group, 6th ed.

Allen, D.G., & Kentish, J.C. (1985). The cellular basis of the length-tension relation in cardiac muscle. *Journal of molecular and cellular cardiology*, *17*(9), 821–840.

Barclay, C.J. (2015). Energetics of contraction. *Comprehensive Physiology*, *5*(2), 961–995.

Bestel, J, Clément, F, & Sorine, M (2001). A Biomechanical Model of Muscle Contraction. In *Medical Image Computing and Computer-Assisted Intervention – MICCAI 2001*, (pp. 1159–1161). Berlin, Heidelberg: Springer, Berlin, Heidelberg.

Caremani, M., Melli, L., Dolfi, M., Lombardi, V., & Linari, M. (2015). Force and number of myosin motors during muscle shortening and the coupling with the release of the ATP hydrolysis products. *The Journal of Physiology*, *593*(15), 3313–3332.

Caremani, M., Pinzauti, F., Reconditi, M., Piazzesi, G., Stienen, G.J.M., Lombardi, V., & Linari, M. (2016). Size and speed of the working stroke of cardiac myosin in situ. *Proceedings of the National Academy of Sciences*, *113*(13), 3675–3680.

Caruel, M., Allain, J.-M., & Truskinovsky, L. (2013a). Muscle as a Metamaterial Operating Near a Critical Point. *Physical review letters*, *110*(24), 248103.

Caruel, M., Chabiniok, R., Moireau, P., Lecarpentier, Y., & Chapelle, D. (2013b). Dimensional reductions of a cardiac model for effective validation and calibration. *Biomechanics and Modeling in Mechanobiology*, *13*(4), 897–914.

Caruel, M., Moireau, P., & Chapelle, D. (2019). Stochastic modeling of chemical-mechanical coupling in striated muscles. *Biomechanics and Modeling in Mechanobiology*, *18*(3), 563–587.

Caruel, M., & Truskinovsky, L. (2018). Physics of muscle contraction. *Reports on Progress in Physics*, (pp. 1–98).

Chabiniok, Radomir, Moireau, Philippe, Moireau, Philippe, Lesault, P-F, Rahmouni, Alain, Deux, J-F, & Chapelle, Dominique (2011). Estimation of tissue contractility from cardiac cine-MRI using a biomechanical heart model. *Biomech. Model Mechanobiol.*, *11*(5), 609–630.

Chapelle, D., Le Tallec, P., Moireau, P., & Sorine, M. (2012). Energy-preserving muscle tissue model: formulation and compatible discretizations. *Journal for Multiscale Computational Engineering*.

Craig, R., & Padrón, R. (2004). Molecular structure of the sarcomere. *Myology*, *3*, 129–144.

Daniels, M., Noble, M.I., ter Keurs, H.E.D.J., & Wohlfart, B. (1984). Velocity of sarcomere shortening in rat cardiac muscle: relationship to force, sarcomere length, calcium and time. *The Journal of Physiology*, *355*, 367–381.

de Tombe, P.P., Mateja, R.D., Tachampa, K., Mou, YA, Farman, G.P., & Irving, T.C. (2010). Journal of Molecular and Cellular Cardiology. *Journal of molecular and cellular cardiology*, *48*(5), 851–858.

de Tombe, P.P., & Stienen, G.J.M. (2007). Impact of temperature on cross-bridge cycling kinetics in rat myocardium. *The Journal of Physiology*, *584*(2), 591–600.

de Tombe, P.P., & ter Keurs, H.E.D.J. (1990). Force and velocity of sarcomere shortening in trabeculae from rat heart. Effects of temperature. *Circulation Research*, *66*(5), 1239–1254.

de Tombe, P.P., & ter Keurs, H.E.D.J. (1992). An internal viscous element limits unloaded velocity of sarcomere shortening in rat myocardium. *The Journal of Physiology*, *454*(1), 619–642.

Eisenberg, E., Hill, T.L., & Chen, Y. (1980). Cross-bridge model of muscle contraction. Quantitative analysis. *Biophysical Journal*, *29*(2), 195–227.

Ford, L.E., Huxley, A.F., & Simmons, R.M. (1981). The relation between stiffness and filament overlap in stimulated frog muscle fibres. *The Journal of physiology*, *311*(1), 219–249.

Hill, T.L. (1977). *Free Energy Transduction in Biology*. Academic Press.

Holmes, K.C., & Geeves, M.A. (2000). The structural basis of muscle contraction. *Philosophical transactions of the Royal Society of London. Series B, Biological sciences*, *355*(1396), 419–431.

Huxley, A.F. (1957). Muscle structures and theories of contraction. *Progr. Biophys. Chem.*.

Huxley, A.F., & Simmons, R.M. (1971). Proposed mechanism of force generation in striated muscle. *Nature*.

Huxley, H.E. (1969). The mechanism of muscular contraction. *Science*, *164*(3886), 1356–1365.

Kentish, J.C., Ter Keurs, H.E.D.J., Ricciardi, L., Bucx, J.J., & Noble, M.I. (1986). Comparison between the sarcomere length-force relations of intact and skinned trabeculae from rat right ventricle. influence of calcium concentrations on these relations. *Circulation research*, *58*(6), 755–768.

Kimmig, F., Chapelle, D., & Moireau, P. (2019). Thermodynamic properties of muscle contraction models and associated discrete-time principles. *Advanced Modeling and Simulation in Engineering Sciences*, *6*(1), 6.

Kobayashi, T., Jin, L., & de Tombe, P.P. (2008). Cardiac thin filament regulation. *Pflügers Archiv - European Journal of Physiology*, *457*(1), 37–46.

Le Gall, A., Vallée, F., Mebazaa, A., Chapelle, D., Gayat, E., & Chabiniok, R. (2019). Monitoring of cardiovascular physiology augmented by a patient-specific biomechanical model during general anaesthesia. a proof of concept study. *submitted*.

Linari, M., Brunello, E., Reconditi, M., Fusi, L., Caremani, M., Narayanan, T., Piazzesi, G., Lombardi, V., & Irving, M. (2015). Force generation by skeletal muscle is controlled by mechanosensing in myosin filaments. *Nature*, *528*(7581), 276–279.

Linari, M., Dobbie, I., Reconditi, M., Koubassova, N., Irving, M., Piazzesi, G., & Lombardi, V. (1998). The stiffness of skeletal muscle in isometric contraction and rigor: the fraction of myosin heads bound to actin. *Biophysj*, *74*(5), 2459–2473.

Linari, M., Piazzesi, G., & Lombardi, V. (2009). The Effect of Myofilament Compliance on Kinetics of Force Generation by Myosin Motors in Muscle. *Biophysj*, *96*(2), 583–592.

Lombardi, V., Piazzesi, G., & Linari, M. (1992). Rapid regeneration of the actin-myosin power stroke in contracting muscle. *Nature*.

Lymn, R.W., & Taylor, E.W. (1971). Mechanism of adenosine triphosphate hydrolysis by actomyosin. *Biochemistry*, *10*(25), 4617–4624.

Månsson, Alf (2010). Actomyosin-ADP states, interhead cooperativity, and the force-velocity relation of skeletal muscle. *Biophysical Journal*, *98*(7), 1237–1246.

Mansson, A., Rassier, D., & Tsiavaliaris, G. (2015). Poorly Understood Aspects of Striated Muscle Contraction. *BioMed Research International*, *2015*(1), 1–28.

Marcucci, L., & Truskinovsky, L. (2010). Mechanics of the power stroke in myosin II. *Physical Review E*, *81*(5), 051915–8.

Mijailovich, S.M., Kayser-Herold, O., Stojanovic, B., Nedic, D., Irving, T.C., & Geeves, M.A. (2016). Three-dimensional stochastic model of actin–myosin binding in the sarcomere lattice. *The Journal of General Physiology*, *148*(6), 459–488.

Moireau, Philippe, & Chapelle, Dominique (2011). Reduced-order Unscented Kalman Filtering with application to parameter identification in large-dimensional systems. *ESAIM: Control, Optimisation and Calculus of Variations*, *17*(2), 380–405.

Pacher, P., Mabley, J.G., Liaudet, L., Evgenov, O.V., Marton, A., Haskó, G., Kollai, M., & Szabó, C. (2004). Left ventricular pressure-volume relationship in a rat model of advanced aging-associated heart failure. *AJP: Heart and Circulatory Physiology*, *287*(5), H2132–7.

Pertici, I., Bongini, L., Melli, L., Bianchi, G., Salvi, L., Falorsi, G., Squarci, C., Bozó, T., Cojoc, D., Kellermayer, M.S.Z., Lombardi, V., & Bianco, P. (2018). A myosin II nanomachine mimicking the striated muscle. *Nature Communications*, (pp. 1–10).

Piazzesi, G., & Lombardi, V. (1995). A cross-bridge model that is able to explain mechanical and energetic properties of shortening muscle. *Biophysical Journal*, *68*, 1966–1979.

Piazzesi, G., Lucii, L., & Lombardi, V. (2002). The size and the speed of the working stroke of muscle myosin and its dependence on the force. *The Journal of Physiology*, *545*(1), 145–151.

Piazzesi, G., Reconditi, M., Linari, M., Lucii, L., Bianco, P., Brunello, E., Decostre, V., Stewart, A., Gore, D.B., Irving, T.C., Irving, M., & Lombardi, V. (2007). Skeletal muscle performance determined by modulation of number of myosin motors rather than motor force or stroke size. *Cell*, *131*(4), 784–795.

Pinzauti, F., Pertici, I., Reconditi, M., Narayanan, T., Stienen, G.J.M., Piazzesi, G., Lombardi, V., Linari, M., & Caremani, M. (2018). The force and stiffness of myosin motors in the isometric twitch of a cardiac trabecula and the effect of the extracellular calcium concentration. *The Journal of Physiology*, *596*(13), 2581–2596.

Reconditi, Massimo (2006). Recent improvements in small angle x-ray diffraction for the study of muscle physiology. *Reports on Progress in Physics*, *69*(10), 2709.

Reconditi, M., Caremani, M., Pinzauti, F., Powers, J.D., Narayanan, T., Stienen, G.J.M., Linari, M., Lombardi, V., & Piazzesi, G. (2017). Myosin filament activation in the heart is tuned to the mechanical task. *Proceedings of the National Academy of Sciences*, (pp. 3240–3245).

Sato, T., Shishido, T., Kawada, T., Miyano, H., Miyashita, H., Inagaki, M., Sugimachi, M., & Sunagawa, K. (1998). ESPVR of in situ rat left ventricle shows contractility-dependent curvilinearity. *The American journal of physiology*, *274*(5), H1429–34.

Smith, D.A., Geeves, M.A., Sleep, J., & Mijailovich, S.M. (2008). Towards a unified theory of muscle contraction. I: foundations. *Annals of Biomedical Engineering*, *36*(10), 1624–1640.

Smith, D A, & Mijailovich, S M (2008). Toward a Unified Theory of Muscle Contraction. II: Predictions with the Mean-Field Approximation. *Annals of Biomedical Engineering*, *36*(8), 1353–1371.

ter Keurs, H.E.D.J., Rijnsburger, W.H., Van Heuningen, R., & Nagelsmit, M.J. (1980). Tension Development and Sarcomere Length in Rat Cardiac Trabeculae: Evidence of Length-Dependent Activation. In *Cardiac Dynamics*, (pp. 25–36). Dordrecht: Springer Netherlands.

Van Heuningen, R., Rijnsburger, W.H., & ter Keurs, H.E.D.J. (1982). Sarcomere length control in striated muscle. *The American journal of physiology*, *242*(3), H411–20.

Zahalak, G.I. (1981). A distribution-moment approximation for kinetic theories of muscular contraction. *Elsevier*, *55*(1-2), 89–114.

Zahalak, G I (2000). The two-state cross-bridge model of muscle is an asymptotic limit of multi-state models. *Journal of Theoretical Biology*.

CHAPTER 4

Activation-contraction coupling in a multiscale heart model capturing the Frank-Starling effect

In the context of cardiac muscle modeling, the availability of the myosin heads in the sarcomeres varies over the heart cycle contributing to the Frank-Starling mechanism at the organ level. In this paper, we propose a new approach that allows to incorporate this variation into the Huxley'57 muscle contraction model equations in a thermodynamically consistent way. We also develop adapted numerical methods enabling to follow-up the thermodynamical balances at the discrete level. Coupling our model with a previously developed simplified heart model, this simulation framework displays its ability to capture the essential features of the Frank-Starling mechanism.

Contents

Activation-contraction coupling in a multiscale heart model capturing the Frank-Starling effect

François Kimmig[1,2], Philippe Moireau[2,1], Dominique Chapelle[2,1]

[1]LMS, Ecole Polytechnique, CNRS, Université Paris-Saclay
[2]Inria, Université Paris-Saclay

to be submitted

Abstract

In the context of cardiac muscle modeling, the availability of the myosin heads in the sarcomeres varies over the heart cycle contributing to the Frank-Starling mechanism at the organ level. In this paper, we propose a new approach that allows to extend the Huxley'57 muscle contraction model equations to incorporate this variation. This extension is built in a thermodynamically consistent way. We also develop adapted numerical methods enabling to follow-up the thermodynamical balances at the discrete level. Coupling our model with a previously developed simplified heart model, this simulation framework displays its ability to capture the essential features of the Frank-Starling mechanism.

Keywords— muscle contraction, sliding filaments, Frank-Starling effect, thermodynamically consistent time-discretization, Clausius-Duhem inequality

4.1 Introduction

Cardiac muscles are made of a set of fibers themselves composed of sarcomeres in series. The sarcomeres are the elementary units of contraction. They are mainly made of two types of protein filaments: myosin filaments (also called thick filaments) and actin filaments (also called thin filaments). The myosin heads of the thick filaments interact with the actin sites of the thin filament in a cycle that involves, among other stages, the attachment of the myosin head on an actin site, the production of force and the detachment of the myosin heads that can then enter in a new cycle [Lymn & Taylor, 1971]. The macroscopic muscle shortening is then the result of the microscopic relative sliding between the myosin and actin filaments. At rest, the binding of the myosin heads on the actin sites is prevented. The contraction is triggered by a release of calcium ions in the muscle cell cytosol that bind to the actin sites and activate them. This ultimately allows the attachment of myosin heads. The thin filament activation is a transient process. When calcium is released, the actin sites are activated by the calcium ions and the myosin heads can attach. Then, the calcium ions are taken from the cytosol, the actin sites deactivate and the myosin heads detach.

In cardiac muscles, not all myosin heads are available for attachment (we also say that the thick filament is not fully activated) and the release of calcium may not be sufficient to activate all actin sites (even at the maximum of the transient activation). The variation of these levels of activation is affected by the length of the sarcomeres and can be used to regulate the value of the developed force. Note that both the myosin heads availability and

the actin sites activation contribute simultaneously to this regulation (see Section 4.2). It is an essential element of the contraction since it allows the emergence at the organ level of the Frank-Starling mechanism [de Tombe et al., 2010].

Muscle contraction is often described by a family of models deriving from the seminal Huxley'57 model [Huxley, 1957; Eisenberg et al., 1980; Caruel et al., 2019; Kimmig & Caruel, 2019]. To account for the regulation mechanisms involving the variation of the thick and thin filament level of activation, modifications of the Huxley'57 model equations have been previously proposed [Zahalak & Motabarzadeh, 1997; Chapelle et al., 2012]. It consists in modifying the expression of the law of mass action that describes the attachment-detachment process. However, this approach suffers from some limitations, in particular, it fails to be thermodynamically compatible. An alternative approach has been proposed by Marcucci et al. [2017] to model the varying thick filament activation. It considers the newly discovered myosin head state called off-state (as opposed to the classical on-state) in which the myosin head is folded back on the thick filament backbone. The on- and off- states are related by chemical transitions. A myosin head in the off-state cannot participate in the attachment-detachment process; to do so it must first transition to the on-state. In the model, the transition rates between the on- and off-states are modulated by the force exerted in the thick filament, a higher force favoring the transition to the on-state. Variations of the sarcomere length change the value of the passive force in the thick filament through the contribution of titin (a giant protein linked with both the thick and thin filament). These variations thus affect the transition rates between the on- and off-states and therefore change the availability of the myosin heads. This mechanism theoretically allows to account for the thick filament activation level variations with the sarcomere length. It remains nevertheless unclear, because of a lack of data for cardiac muscle, whether the time scale of the on-off transition is compatible with the time scale of the length dependent thick filament activation.

In this paper, we propose a new paradigm that extend the Huxley'57 model equations to include the varying myosin heads availability. We introduce two groups of myosin heads and deduce the governing equations from conservation laws. The consistency with the thermodynamic principles of this modeling framework is then demonstrated and associated numerical methods are developed. Note that we focus on the modeling of the thick filament activation mechanism, the thin filament activation being phenomenologically represented. Some elements of validation of our model are presented with the simulation of heart beats. These results are obtained through the coupling of our model with a simplified heart model [Caruel et al., 2013].

This paper is organized as follows. We first present in Section 4.2 the experimental results that support the assumption chosen for the development of our model. Section 4.3 briefly recalls the Huxley'57 model and presents the derivation of our new paradigm. The thermodynamic principles associated with this new model are established in Section 4.4. In Section 4.5, we explore the limits of our model and its relation with the previously proposed formulations. The numerical methods developed for our model are presented in Section 4.6 and the thermodynamic compatibility of the discretization scheme is justified. The model calibration and the numerical results illustrating the ability of the model to reproduce the Frank-Starling mechanism are finally presented in Section 4.7.

4.2 Physiological review

In living conditions, the heart contraction is regulated by two main regulation pathways: an *intrinsic* pathway, which varies the force as a function of the sarcomere stretch – a higher sarcomere length being associated with a higher force – and an *extrinsic* pathway

corresponding the control of the nervous system through neuroendocrine mediators [Silverthorn et al., 2009]. These two regulations modulate the force developed by the muscle tissues ultimately impacting the volume of blood ejected by the heart (called *stroke volume*). At the organ level, this regulation is called the *Frank-Starling effect*. Note that the neuroendocrine regulation also affects the proteins involved in the intrinsic regulation. Note also that varying the muscle contraction level is not the only option to vary the cardiac output. Variations of the heart beating rate also affect the average stroke volume.

4.2.1 Frank-Starling effect

The Frank-Starling effect has been discovered more than a century ago [Frank, 1895; Patterson & Starling, 1914]. It is a regulation at the heart level that ensures that no blood is stored inside the heart by increasing the contractile capability of the muscle tissues when the filling volume is increased. This regulation originates from the variations, at the sarcomere (micro-metric) level, of the force with the sarcomere length defining the force-length relation (see Figure 4.1) [de Tombe et al., 2010]. The force increases with increasing sarcomere lengths up to a certain extension. The shape of the force-length relation is affected by the extrinsic regulation through a variation of the calcium supply or the change of some proteins functioning through phosphorylation.

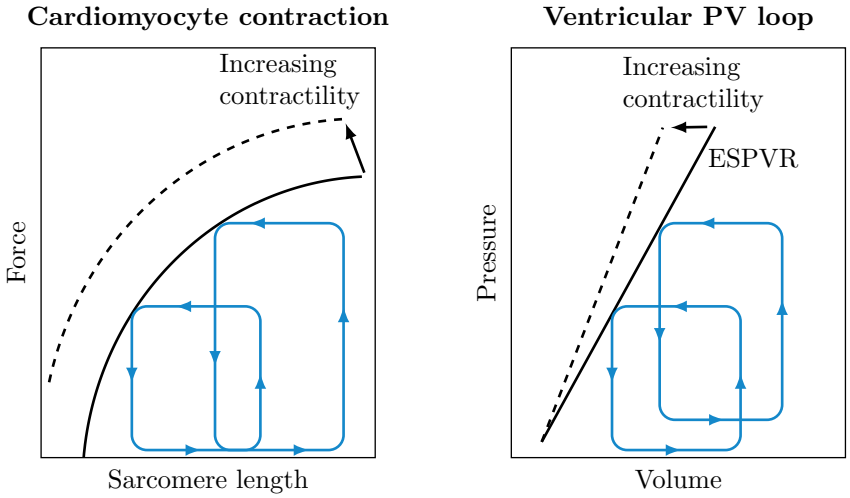

Figure 4.1 – Illustration of the Frank-Starling mechanism and its microscopic origin. Figure inspired by [de Tombe et al., 2010].

The exact origin of these variations still remains partially unknown despite large research efforts [de Tombe & ter Keurs, 2016; Sequeira & Velden, 2017]. In all generality, the variation of the force with the sarcomere length may result either from an increase of the force generated by each cross-bridge or from an increase of the number of attached cross-bridges (or from both mechanisms combined). The works of Wannenburg et al. [1997], Amiad Pavlov & Landesberg [2016], Caremani et al. [2016] and Pinzauti et al. [2018] show that the cross-bridge properties are not affected by variations of the sarcomere length or the level of calcium supply leading to the conclusion that neither is the force developed by each cross-bridge. Note that a direct assessment of the non-variation of the cross-bridge force with the level of thin filament activation has been performed by Pinzauti et al. [2018].

As a result, the force variation with the sarcomere length is only due to a change in the number of formed cross-bridges. This effect itself may have two distinct origins: a

variation of the number of available myosin heads or a change in the level of the thin filament activation.

4.2.2 Evidence of a regulation mechanism intrinsic to the thick filament

In this paper, we focus on the variation of the number of available myosin heads as a function of the sarcomere length.

To justify that this regulation exists, we present experimental data in which the possibility of a variation of the thin filament activation is eliminated. To create these conditions, experimentalists either used skinned cells so that they can artificially maintain the "intracellular" calcium concentration at a high value ensuring that all actin sites are activated [Kentish et al., 1986; Dobesh et al., 2002], or force a large enough release of calcium in intact cells and maintain this state [ter Keurs et al., 2008], in which case the cells are said to be in a tetanised state.

The experimental results showing the variation of the developed force in these two experimental conditions are presented in Figure 4.2. They indeed show that the contraction force is modulated as a function of the sarcomere length. Note that the force is obtained in a steady-state isometric state that may not exist in physiological conditions if the force does not have enough time to reach its maximum value in a transient contraction. The origin of the number of available myosin heads variation as a function of the sarcomere length is not elucidated.

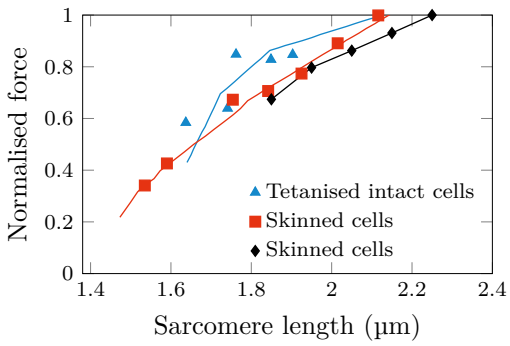

Figure 4.2 – Variation of the force with the sarcomere length. The data are obtained in maximal thin filament activation. The variation observed is thus solely due to the thick filament activation variation. Closed diamonds: experimental data from skinned rat cells [Dobesh et al., 2002]. Closed triangles: experimental data from intact tetanised rat cardiac muscle cells [ter Keurs et al., 2008]. Closed square: experimental data from skinned rat ventricular trabeculae [Kentish et al., 1986]. The solid lines represent a fit of the data.

4.2.3 Dynamics of the regulation

The time scale of the force adaptation to the sarcomere length is a critical element for the development of models. It has been studied by [Mateja & de Tombe, 2012] with the measurement of the force development dynamics in contractions triggered after change of muscle length with various waiting durations between the length change maneuver and the initiation of the contraction. They establish an upper bound of 5 ms for the time scale of this regulation. The attachment and detachment time scale can be estimated in the light of Huxley'57 model family [Huxley, 1957]. A debate remains about the calibration of these models depending which experimental data are used for the calibration. If the focus is put on the tension rise rate, experimental data yield a time scale of 25 ms for attachment and

100 ms for detachment [de Tombe & Stienen, 2007]. In contrast, if the estimation is made on the force-velocity curve, which is a typical indicator of the muscle behavior relating the force developed by the muscle in a steady-state shortening at various speed of shortening (see for instance [de Tombe & ter Keurs, 1990; Caremani et al., 2016]), we obtain time scales of 4 ms and 16 ms for attachment and detachment, respectively [Kimmig & Caruel, 2019] (see Chapter 3). In the first case, the fastest time scale is significantly higher than the upper bound for the regulation mechanism time scale provided by [Mateja & de Tombe, 2012]. In the second case, they are of the same order. However, the established upper bound is not a maximum, meaning that it does not correspond to the time scale from which the dynamics of the regulation started to be visible but it is simply the fastest time scale that could be tested. Therefore, we can confidently estimate that the regulation occurs actually at an even faster time scale and is possibly instantaneous. Note that the same conclusion is drawn by Mateja & de Tombe [2012]. We will thus assume that the regulation mechanism time scale is much faster than that of attachment and detachment and that it can be considered as instantaneous. Therefore, the relations presented in Figure 4.2 will be supposed to hold at all time.

4.3 Model presentation

Our goal is to propose a modeling framework that is able to incorporate the variation of myosin heads availability into the classical equations describing the actin-myosin interaction. We first shortly present the muscle contraction models based on the seminal work of A.F. Huxley [Huxley, 1957]. Then, we introduce our formalism and derive the equations governing the dynamics of the system from the conservation of matter. Finally, we put our new approach into perspective by comparing it to existing formulations.

4.3.1 Contraction model - Huxley'57 model family

The mathematical description of muscle contraction has its origin in the seminal work of Huxley [1957], which has been abundantly extended since then [Huxley & Simmons, 1971; Eisenberg & Hill, 1978; Eisenberg et al., 1980; Piazzesi & Lombardi, 1995; Zahalak, 2000] but remains the standard framework of modern models [Caremani et al., 2015; Marcucci et al., 2016]. In particular, this approach has proven to be well-adapted to the modeling of mammals cardiac muscles [Månsson, 2010; Pertici et al., 2018; Kimmig & Caruel, 2019]. This family of models considers a collection of chemical states representing attached and detached myosin heads, interacting with each other according to the law of mass action. A general presentation of the Huxley'57 model and its extensions can be found in [Kimmig et al., 2019] (see Chapter 3).

We will restrict our presentation to a two-state model – with one attached state and one detached state – , which is sufficiently refined to capture the essential features of cardiac muscle contraction [Kimmig & Caruel, 2019] (see Chapter 3). However, the modeling ingredient presented in this work could be easily extended to any model derived from the Huxley'57 model. The dynamics of attachment and detachment is described in the framework of the so-called *sliding filament theory*. The myosin and actin filaments are assumed to be rigid, meaning that the distance between consecutive myosin heads or consecutive actin sites is constant. We assume moreover that each myosin head interacts with its nearest actin site only. Actin sites are uniformly distributed along the actin filament and are separated by a distance d_a. Myosin heads are also uniformly distributed along the myosin filament but with a different spatial periodicity. The approach is centered on the myosin heads and a myosin head is characterized by the distance between its rest

position and its nearest actin site. This distance is denoted by s (see Figure 4.3) and we denote the interval of possible values of s by $[s^-, s^+]$ with $s^+ - s^- = d_a$. Note that this interval may be non-symmetric. Due to the difference in spatial periodicity between the actin and the myosin filaments, all positions $s \in [s^-, s^+]$ of the myosin heads are equiprobable in the population.

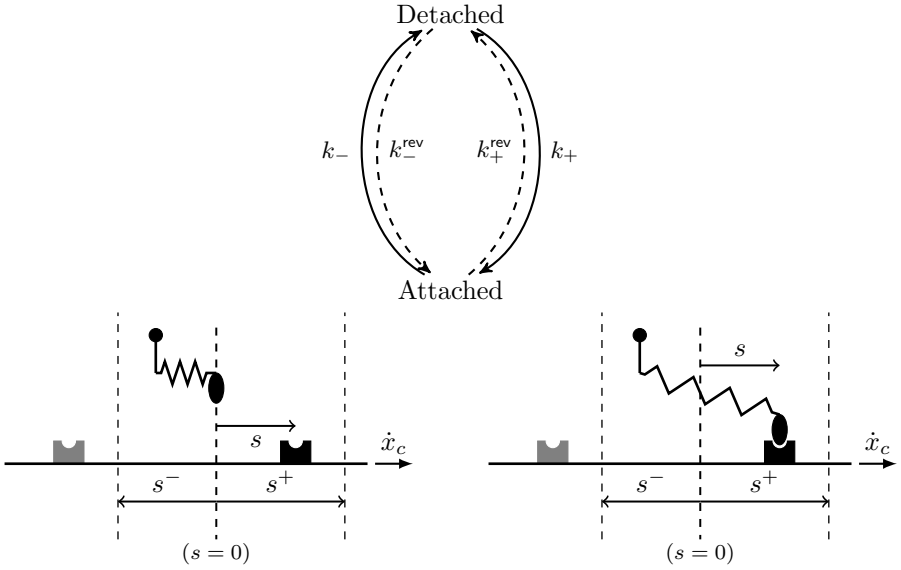

Figure 4.3 – Presentation of the two-state model. Top: transitions between the attached state and the detached state and the associated transition rates. Bottom left: detached state model parametrization. Bottom right: attached state model parametrization.

We now consider the subset of myosin heads located at distance s to their nearest actin site. The energy of the attached heads is given by $w_1(s)$ and that of the detached heads by w_0, which does not depend on the spatial variable. When a myosin head detaches, it uses an energy input μ_T brought by ATP to retrieve its original energy level. The transitions between the attached and the detached states are governed by the transition rate $k_+(s)$ for the attachment and $k_-(s)$ for the detachment. We assume that these two transitions are associated respectively with a reverse transition (see Figure 4.3) whose rate is given by the detailed balance

$$\frac{k_+(s)}{k_+^{\text{rev}}(s)} = \exp\left[\frac{w_0 - w_1(s)}{k_B T}\right], \qquad \frac{k_-(s)}{k_-^{\text{rev}}(s)} = \exp\left[\frac{w_1(s) + \mu_T - w_0}{k_B T}\right], \tag{4.1}$$

where T is the temperature and k_B is the Boltzmann constant.

The probability of being attached for a head in this subset at time t is given by $P_1(s,t)$ and we denote by $P_0(s,t)$, the probability of being detached. The conservation of matter leads to the following dynamics equations, for all $t > 0$ and all $s \in [s^-, s^+]$

$$\begin{cases} \partial_t P_1(s,t) + \dot{x}_c \partial_s P_1(s,t) = \big(k_+(s) + k_-^{\text{rev}}(s)\big) P_0(s,t) - \big(k_-(s) + k_+^{\text{rev}}(s)\big) P_1(s,t), \\ \partial_t P_0(s,t) + \dot{x}_c \partial_s P_0(s,t) = \big(k_+(s) + k_-^{\text{rev}}(s)\big) P_0(s,t) - \big(k_-(s) + k_+^{\text{rev}}(s)\big) P_1(s,t). \end{cases} \tag{4.2}$$

Note that the Eulerian nature of this description leads to the presence of transport terms which take into account the change in position when the myosin and actin filaments slide pass each other with a velocity $\dot{x}_c$.

The single actin site assumption implies that the probability of being attached must vanish on the boundaries of the interval $[s^-, s^+]$. As proposed by Kimmig et al. [2019] (see

Chapter 2), we choose periodic boundary conditions $P_1(s^-,t) = P_1(s^+,t)$ and enforce the property $P_1(s^-,t) = P_1(s^+,t) = 0$ through an appropriate choice of the transition rates.

Choosing the initial conditions $P_1(s,t=0) + P_0(s,t=0) = 1,\ \forall s \in [s^-,s^+]$, the probability P_0 is given by $P_0(s,t) = 1 - P_1(s,t),\ \forall s \in [s^-,s^+], \forall t > 0$ and (4.2) becomes

$$\begin{cases} \partial_t P_1(s,t) + \dot{x}_c \partial_s P_1(s,t) = \big(k_+(s) + k_-^{\text{rev}}(s)\big) P_0(s,t) - \big(k_-(s) + k_+^{\text{rev}}(s)\big) P_1(s,t), \\ P_0(s,t) = 1 - P_1(s,t). \end{cases} \tag{4.3}$$

Note that the original Huxley'57 model equations can be straightforwardly retrieved by defining the aggregated attachment rate f and detachment rate g by

$$\begin{vmatrix} f(s) = k_+(s) + k_-^{\text{rev}}(s), \\ g(s) = k_-(s) + k_+^{\text{rev}}(s). \end{vmatrix}$$

4.3.2 Incorporation of the variations in myosin availability level in the model equations

As shown in Section 4.2.2, the sarcomere stretch directly influences the level of availability of the myosin heads and this regulation mechanism occurs instantaneously.

To build our model, we extend the two-state model presented in Section 4.3.1. In addition to its natural assumptions, we assume that a part of the myosin heads population is available for attachment, while the remaining part is not and that the ratio of heads belonging to each pool depends on the sarcomere stretch. For thermodynamical reasons, heads that are not available for attachment are not strictly prevented from attaching, but their attachment rate is much reduced compared to heads available for attachment. We also assume that heads can change from one pool to the other independently of their attachment state (attached or detached). Since we know that the thick filament regulation occurs at a fast time scale compared to the cycling time scale, the transfers between pools are supposed to take place instantaneously. We do not track the myosin heads individually but instead focus on average quantities. We thus proposed a homogenized description of the myosin heads within the pools.

Note that this modeling framework is not specific to the mechanism underlying the regulation of the myosin heads availability.

To describe the state of a myosin head, we introduce an additional – discrete and deterministic – internal variable γ that is equal to one if the head is available for attachment and equal to zero if it is not. As a consequence, we are now considering the probability $P_1(s,t,\gamma)$. Note that γ is somewhat comparable to s meaning that both can change when following actual myosin heads, albeit γ is discrete while s is continuous. The constraint of normalization becomes

$$P_1(s,t,\gamma) + P_0(s,t,\gamma) = 1 \quad \forall s \ \in [s^-,s^+],\ \forall t > 0,\ \forall \gamma \in \{0,1\}. \tag{4.4}$$

The ratio of available heads is denoted by $n_0(e_c)$. It solely depends on the active extension e_c, which is linked to the relative displacement of the rigid filaments x_c by $x_c = \ell_{hs} e_c$, where ℓ_{hs} is the *half-sarcomere slack length*. The latter is defined as the half-sarcomere length corresponding to zero passive force in the sarcomere. The total ratio of attached heads is obtained as the average between the two pools. It is given by

$$P_1(s,t) = n_0 P_1(s,t,1) + (1 - n_0) P_1(s,t,0). \tag{4.5}$$

The energy levels of the attached and detached states are the same in each pool because the transfer of a myosin head from one pool to the other is not associated with any energy

input. The attached state and detached state energy levels are still denoted w_1 and w_0, respectively. However, myosin heads experience two distinct chemical cycles in the two pools. The transitions rates are still defined as in Figure 4.3 but are now indexed by the variable γ. They satisfy the detailed balance in each pool, i.e.

$$\frac{k_{+,\gamma}(s)}{k^{\text{rev}}_{+,\gamma}(s)} = \exp\Big[\frac{w_0 - w_1(s)}{k_B T}\Big], \quad \frac{k_{-,\gamma}(s)}{k^{\text{rev}}_{-,\gamma}(s)} = \exp\Big[\frac{w_1(s) + \mu_T - w_0}{k_B T}\Big], \ \forall \gamma \in \{0,1\}. \tag{4.6}$$

To model the non-availability of the myosin heads in the pool $\gamma = 0$, we choose $k_{+,1} \gg k_{+,0}$.

To describe the dynamics of the system, we write the conservation of matter on a closed system. For that purpose, we consider the sub-ensemble of heads that, in each pool, are located at a distance s to their nearest actin site. We describe the dynamics of these heads following them in their "motion". We obtain the following dynamics for all $s \in [s^-, s^+]$

$$\begin{cases} \dfrac{\mathrm{d}}{\mathrm{d}t} P_1(s,t,1) = \big(k_{+,1}(s) + k^{\text{rev}}_{-,1}(s)\big) P_0(s,t,1) - \big(k_{-,1}(s) + k^{\text{rev}}_{+,1}(s)\big) P_1(s,t,1), \\ \dfrac{\mathrm{d}}{\mathrm{d}t} P_1(s,t,0) = \big(k_{+,0}(s) + k^{\text{rev}}_{-,0}(s)\big) P_0(s,t,0) - \big(k_{-,0}(s) + k^{\text{rev}}_{+,0}(s)\big) P_1(s,t,0), \\ \quad P_0(s,t,\gamma) = 1 - P_1(s,t,\gamma). \end{cases} \tag{4.7}$$

The equation (4.7) uses total derivatives, which follow the myosin heads in their evolution. To fully establish the system dynamics, we need to explicit these total derivatives. Note that γ is a discrete parameter and it thus cannot be treated with the classical chain rule formula. We consider the ensemble of head located at distance s of the nearest actin site, and that are in the pool $\gamma = 1$. The probability of being attached for the ensemble of heads at time t is given by $P_1(s,t,1)$.

At time $t + \mathrm{d}t$, we denote by $\hat{P}_1$ the probability of being attached for this very same ensemble of heads. Because of the system evolution happening between t and $t + \mathrm{d}t$, some of the heads in the considered ensemble, which are in the pool of available heads ($\gamma = 1$) at time t may move to the pool of unavailable heads ($\gamma = 0$) at time $t + \mathrm{d}t$. This has to be taken into account in the computation of $\hat{P}_1$.

We define

$$|x|_+ = \begin{cases} x & \text{if } x \geq 0, \\ 0 & \text{otherwise,} \end{cases} \qquad \text{and} \qquad |x|_- = \begin{cases} -x & \text{if } x \leq 0, \\ 0 & \text{otherwise.} \end{cases}$$

Note that, from the definition of $|\bullet|_\pm$, we can directly derive the following property

$$x = |x|_+ - |x|_-. \tag{4.8}$$

The ratio of heads in the considered ensemble that are in the pool $\gamma = 1$ being given by n_0, the ratio of heads switching from the pool $\gamma = 0$ to the pool $\gamma = 1$ between the times t and $t + \mathrm{d}t$ is given by $|\dot{n}_0|_+ \mathrm{d}t$ and the ratio of heads switching from the pool $\gamma = 1$ to the pool $\gamma = 0$ in the same time interval is given by $-|\dot{n}_0|_- \mathrm{d}t$.

We first consider the case where $\dot{n}_0 > 0$ – note that we assume that there is no head switching from the pool $\gamma = 1$ to the pool $\gamma = 0$. At time $t + \mathrm{d}t$, the myosin heads in the considered ensemble are the heads of the pool $\gamma = 1$ minus the heads that switched from the pool $\gamma = 0$ in the time interval $\mathrm{d}t$. We thus have

$$n_0 \hat{P}_1 = \big[n_0 + |\dot{n}_0|_+ \mathrm{d}t\big] P_1(s + \mathrm{d}s, t + \mathrm{d}t, 1) - |\dot{n}_0|_+ \mathrm{d}t P_1(s,t,0). \tag{4.9}$$

At first order, (4.9) becomes

$$n_0\hat{P}_1 = n_0 P_1(s+\mathrm{d}s, t+\mathrm{d}t, 1) + |\dot{n}_0|_+ \mathrm{d}t\big[P_1(s,t,1) - P_1(s,t,0)\big]. \tag{4.10}$$

We now consider the case where $\dot{n}_0 < 0$. At time $t+\mathrm{d}t$, the myosin heads in the considered ensemble are the heads of the pool $\gamma = 1$ plus the heads that switched to the pool $\gamma = 0$ in the time interval $\mathrm{d}t$. We thus have

$$n_0\hat{P}_1 = \big[n_0 - |\dot{n}_0|_-\mathrm{d}t\big]P_1(s+\mathrm{d}s, t+\mathrm{d}t, 1) + |\dot{n}_0|_-\mathrm{d}t P_1(s,t,1). \tag{4.11}$$

At first order, (4.11) becomes

$$\hat{P}_1 = P_1(s+\mathrm{d}s, t+\mathrm{d}t, 1). \tag{4.12}$$

Altogether, (4.10) and (4.12) yield

$$\hat{P}_1 = P_1(s+\mathrm{d}s, t+\mathrm{d}t, 1) + \frac{|\dot{n}_0|_+}{n_0}\mathrm{d}t\big[P_1(s,t,1) - P_1(s,t,0)\big]$$

Defining $\dfrac{\mathrm{d}P_1(s,t,1)}{\mathrm{d}t}$ by $\lim\limits_{\mathrm{d}t\to 0}\dfrac{\hat{P}_1(s,t) - P_1(s,t,1)}{\mathrm{d}t}$, we obtain

$$\frac{\mathrm{d}P_1(s,t,1)}{\mathrm{d}t} = \partial_t P_1(s,t,1) + \dot{x}_c\partial_s P_1(s,t,1) + \frac{|\dot{n}_0|_+}{n_0}\big[P_1(s,t,1) - P_1(s,t,0)\big].$$

Considering the sub-ensemble of heads that are located at distance s, at time t and in the pool $\gamma = 0$, we similarly establish that

$$\frac{\mathrm{d}P_1(s,t,1)}{\mathrm{d}t} = \partial_t P_1(s,t,1) + \dot{x}_c\partial_s P_1(s,t,1) + \frac{|\dot{n}_0|_-}{1-n_0}\big[P_1(s,t,0) - P_1(s,t,1)\big].$$

Altogether, we obtain

$$\begin{cases} \dfrac{\mathrm{d}}{\mathrm{d}t}P_1(s,t,1) = \partial_t P_1(s,t,1) + \dot{x}_c\,\partial_s P_1(s,t,1) + \dfrac{|\dot{n}_0|_+}{n_0}\big[P_1(s,t,1) - P_1(s,t,0)\big], \\ \dfrac{\mathrm{d}}{\mathrm{d}t}P_1(s,t,0) = \partial_t P_1(s,t,0) + \dot{x}_c\,\partial_s P_1(s,t,0) + \dfrac{|\dot{n}_0|_-}{1-n_0}\big[P_1(s,t,0) - P_1(s,t,1)\big], \end{cases} \tag{4.13}$$

Finally, combining (4.7) and (4.13), we obtain the complete system of evolution equations

$$\begin{cases} \partial_t P_1(s,t,1) + \dot{x}_c\,\partial_s P_1(s,t,1) + \dfrac{|\dot{n}_0|_+}{n_0}\big[P_1(s,t,1) - P_1(s,t,0)\big] = \\ \qquad\qquad \big(k_{+,1}(s) + k^{\mathrm{rev}}_{-,1}(s)\big)P_0(s,t,1) - \big(k_{-,1}(s) + k^{\mathrm{rev}}_{+,1}(s)\big)P_1(s,t,1), \\ \partial_t P_1(s,t,0) + \dot{x}_c\,\partial_s P_1(s,t,0) + \dfrac{|\dot{n}_0|_-}{1-n_0}\big[P_1(s,t,0) - P_1(s,t,1)\big] = \\ \qquad\qquad \big(k_{+,0}(s) + k^{\mathrm{rev}}_{-,0}(s)\big)P_0(s,t,0) - \big(k_{-,0}(s) + k^{\mathrm{rev}}_{+,0}(s)\big)P_1(s,t,0), \\ P_0(s,t,\gamma) = 1 - P_1(s,t,\gamma). \end{cases} \tag{4.14}$$

Note that, as in the original two-state mode, the boundary conditions are chosen periodic for both pools, i.e. $P_1(s^-,t,\gamma) = P_1(s^+,t,\gamma)$. The property that no head should be attached on the boundaries of interval $[s^-, s^+]$, which intrinsically comes with the assumption that the myosin heads can only attach to their nearest actin site, is ensured by

the choice of appropriate transition rate parameter functions satisfying the conditions for all $\gamma \in \{0,1\}$ [Kimmig et al., 2019] (see Chapter 2)

$$\left|\begin{array}{l} \lim\limits_{s\to s^-} k_{+,\gamma}(s) = \lim\limits_{s\to s^+} k_{+,\gamma}(s) = \lim\limits_{s\to s^-} k^{\mathrm{rev}}_{-,\gamma}(s) = \lim\limits_{s\to s^+} k^{\mathrm{rev}}_{-,\gamma}(s) = 0, \\ \lim\limits_{s\to s^-} \displaystyle\int_s^0 \big(k_{-,\gamma}(s) + k^{\mathrm{rev}}_{+,\gamma}(s)\big) = \lim\limits_{s\to s^+} \int_0^s \big(k_{-,\gamma}(s) + k^{\mathrm{rev}}_{+,\gamma}(s)\big) = +\infty. \end{array}\right. \tag{4.15}$$

The active force per myosin head developed by the system aggregates the contributions of the myosin heads in the two pools. It is given by

$$\tau_c(t) = \frac{1}{d_a} \int_{s^-}^{s^+} \big[n_0 P_1(s,t,1) + (1-n_0)P_1(s,t,0)\big]\partial_s w_1(s)\,\mathrm{d}s.$$

Note that, in the framework presented here, we do not track the availability of the myosin heads individually, but we consider instead an average behavior for the population of myosin heads. Moreover, we assume that the heads switch pools randomly, i.e. all heads have the same probability to switch from one pool to another. A comparison with such models is presented in Section 4.5.

4.3.3 Comparison with previous formulations

In this section, we compare our model with previous attempts of incorporating the thick filament activation mechanisms into the Huxley'57 model equation. Since it is the original choice made by the authors, we will write the two-state model equations with the aggregated transition rates, i.e.

$$\left|\begin{array}{ll} f_\gamma(s) = k_{+,\gamma}(s) + k^{\mathrm{rev}}_{-,\gamma}(s), & (4.16) \\ g_\gamma(s) = k_{-,\gamma}(s) + k^{\mathrm{rev}}_{+,\gamma}(s). & (4.17) \end{array}\right.$$

As in our model, Zahalak & Motabarzadeh [1997] and Chapelle et al. [2012] consider that the fraction of myosin heads that are available for attachment is n_0. In the matter conservation, the flux of attachment is then assumed to be $f\big[n_0 - P_1\big]$. The model dynamics is thus governed by the equation

$$\partial_t P_1(s,t) + \dot{x}_c \frac{\partial}{\partial s} P_1(s,t) = f(s)\big[n_0(e_c) - P_1(s,t)\big] - g(s)P_1(s,t). \tag{4.18}$$

We can first note that the modeling assumption underlying the definition of the attachment flux is only valid if $n_0 - P_1$ represents the apparent activity of the myosin heads, i.e. $n_0 - P_1 \geq 0$. However, the latter property may not be ensured by the dynamics (4.18) (see Appendix 4.9.1) possibly leading to the non-validity of the model in phases of the simulated contraction.

We assume that the property $n_0 \geq P_1$ holds in the rest of this section. The probability of attachment P_1 is given by (4.5) in our proposed formulation using two pools of myosin heads. We differentiate P_1 with respect to time. We obtain

$$\partial_t P_1(s,t) = \dot{n}_0\Big[P_1(s,t,1) - P_1(s,t,0)\Big] + n_0\partial_t P_1(s,t,1) + (1-n_0)\partial_t P_1(s,t,0).$$

Substituting the time derivatives from (4.14), we obtain

$$\begin{aligned}\partial_t P_1(s,t) + \dot{x}_c \frac{\partial}{\partial s} P_1(s,t) = \dot{n}_0 \Big[P_1(s,t,1) - P_1(s,t,0)\Big] \\ + n_0 \Big(f_1(s)\big(1 - P_1(s,t,1)\big) - g_1(s) P_1(s,t,1) \\ - \frac{|\dot{n}_0|_+}{n_0}\big[P_1(s,t,1) - P_1(s,t,0)\big]\Big) \\ + (1-n_0)\Big(f_0(s)\big(1 - P_1(s,t,0)\big) - g_0(s) P_1(s,t,0) \\ - \frac{|\dot{n}_0|_-}{1-n_0}\big[P_1(s,t,0) - P_1(s,t,1)\big]\Big).\end{aligned} \tag{4.19}$$

Using the property (4.8), (4.19) becomes

$$\begin{aligned}\partial_t P_1(s,t) + \dot{x}_c \frac{\partial}{\partial s} P_1(s,t) = n_0 \Big(f_1(s)\big(1 - P_1(s,t,1)\big) - g_1(s) P_1(s,t,1)\Big) \\ + (1-n_0)\Big(f_0(s)\big(1 - P_1(s,t,0)\big) - g_0(s) P_1(s,t,0)\Big).\end{aligned} \tag{4.20}$$

The spirit of our model is that the myosin heads belonging to the pool $\gamma = 0$ have a reduced probability of being attached, i.e. $P_1(s,t,0) \approx 0$. This property can be obtained with various choices of the transition rates, for instance with $f_1 = f$, $f_0 = 0$ and $g_1 = g_0 = g$ or with $f_1 = f_0 = f$ and $g_1 = g \ll g_0$.

With the approximation $P_1(s,t,0) \approx 0$, we have $P_1(s,t) \approx n_0 P_1(s,t,1)$. Equation (4.20) yields

$$\partial_t P_1(s,t) + \dot{x}_c \frac{\partial}{\partial s} P_1(s,t) \approx f(s)\big(n_0 - P_1(s,t)\big) + g(s) P_1(s,t), \tag{4.21}$$

and we retrieve the origin modified Huxley equation (4.18).

The previously proposed formulations are thus enclosed in our model and are equivalent at the limit when $P_1(s,t,0)$ goes to zero. Our approach provides a more rigorous modeling framework having all apparent activities of the myosin heads considered in the flux of matter unconditionally positive. Moreover, as we will see in the next section, it is thermodynamically consistent, whereas previously proposed formulations do not satisfy the second principle because they break the detailed balance. Another interpretation of the last comment is the following: decreasing n_0 from the value one puts a fraction of myosin heads in a state where they are not allowed to attach. They are constrained in a single state: the detached state. Putting the heads in this situation increases the level of information on the system and is thus associated with a negative entropy creation, which is in contradiction with the second principle.

4.4 Thermodynamics

We now want to derive, from the proposed evolution equations, the first and second thermodynamic balances for our system, which shows the coherence of the newly introduced modeling ingredients. For that, we extend, for equations containing the pool exchange term, the approach proposed by Hill [1977] for the original family of Huxley'57 models.

We emphasize on a property that is fundamental in our analysis: the choice of transitions rates (4.15) ensures that

$$P_1(s = s^-, t, \gamma) = P_1(s = s^+, t, \gamma) = 0 \ \forall t, \ \forall \gamma \in \{0,1\}.$$

4.4.1 Myosin heads conservation

The model equations (4.14) have been derived from the conservation of the myosin heads being thus equivalent to the latter. However, because of the unusual form of the equations in (4.14), we recall the myosin heads conservation identities of the model before exhibiting its thermodynamical properties.

From (4.7), we have the conservation of matter in each pool

$$P_1(s,t,\gamma) + P_0(s,t,\gamma) = 1,\ \forall s \in [s^-, s^+],\ \forall t > 0,\ \forall \gamma \in \{0,1\}. \tag{4.22}$$

It directly ensures the conservation of the total quantity of matter

$$m(s,t) = n_0\big(P_1(s,t,1) + P_0(s,t,1)\big) + (1-n_0)\big(P_1(s,t,0) + P_0(s,t,0)\big).$$

Moreover, the pool exchange operator alone does not alter the total probability of being attached $P(s,t) = n_0 P(s,t,1) + (1-n_0)P(s,t,0)$, as it only transfers attached and detached heads from one pool to another. Indeed, in the absence of attachment and detachment, i.e. with $k_{+,\gamma}(s) = k_{-,\gamma}(s) = 0,\ \forall s \in [s^-, s^+],\ \forall t > 0,\ \forall \gamma \in \{0,1\}$, we obtain from (4.18)

$$\frac{\partial}{\partial t} P_1(s,t) + \dot{x}_c \frac{\partial}{\partial s} P_1(s,t) = 0.$$

4.4.2 First principle

To establish the thermodynamic balances, we consider a population of myosin heads. The average energy per myosin head is defined by

$$\begin{aligned}
\mathcal{U}(t) &= \frac{1}{d_a} \int_{s^-}^{s^+} \Big[w_1(s) P_1(s,t) + w_0 P_0(s,t) \Big] \,\mathrm{d}s, \\
&= \frac{1}{d_a} \int_{s^-}^{s^+} \Big[w_1(s) \Big(n_0(t) P_1(s,t,1) + \big(1-n_0(t)\big) P_1(s,t,0) \Big) \\
&\qquad\qquad + w_0 \Big(n_0(t) P_0(s,t,1) + \big(1-n_0(t)\big) P_0(s,t,0) \Big) \Big] \,\mathrm{d}s.
\end{aligned}$$

We have

$$\begin{aligned}
\frac{\mathrm{d}}{\mathrm{d}t}\mathcal{U}(t) = \frac{1}{d_a} \int_{s^-}^{s^+} \Big(& \dot{n}_0 \Big[w_1(s) \big[P_1(s,t,1) - P_1(s,t,0) \big] + w_0 \big[P_0(s,t,1) - P_0(s,t,0) \big] \Big] \\
& + n_0(t) \Big[w_1(s)\, \partial_t P_1(s,t,1) + w_0\, \partial_t P_0(s,t,1) \Big] \\
& + \big(1-n_0(t)\big) \Big[w_1(s)\, \partial_t P_1(s,t,0) + w_0\, \partial_t P_0(s,t,0) \Big] \Big) \,\mathrm{d}s.
\end{aligned} \tag{4.23}$$

The treatment of the chemical reaction and the transport terms arising from $\partial_t P_1(s,t,\gamma)$ and $\partial_t P_0(s,t,\gamma)$ is given in [Hill, 1977] (see also [Kimmig et al., 2019] in Chapter 2 for the detailed calculation). Therefore, we just detail here the contribution arising from the pool

exchange term. Equation (4.23) becomes

$$\begin{aligned}\frac{\mathrm{d}}{\mathrm{d}t}\mathcal{U}(t) = \mu_T \overline{J}_-(t) + \dot{x}_c \tau_c(t) \\ + \frac{1}{d_a}\int_{s^-}^{s^+} \Big(n_0 \Big[(w_1(s) - w_0) J_+(s,t,1) + (w_0 - (w_1(s) + \mu_T)) J_-(s,t,1) \Big] \\ + (1-n_0)\Big[(w_1(s) - w_0) J_+(s,t,0) + (w_0 - (w_1(s) + \mu_T)) J_-(s,t,0) \Big] \Big)\, \mathrm{d}s \\ + \frac{1}{d_a}\int_{s^-}^{s^+} \dot{n}_0 \Big[w_1(s)\big[P_1(s,t,1) - P_1(s,t,0)\big] + w_0\big[P_0(s,t,1) - P_0(s,t,0)\big] \Big]\, \mathrm{d}s \\ - \frac{1}{d_a}\int_{s^-}^{s^+} \Big(n_0 \Big[w_1(s) \frac{|\dot{n}_0|_+}{n_0}\big[P_1(s,t,1) - P_1(s,t,0)\big] \\ + w_0 \frac{|\dot{n}_0|_+}{n_0}\big[P_0(s,t,1) - P_0(s,t,0)\big] \Big] \\ + (1-n_0)\Big[w_1(s) \frac{|\dot{n}_0|_-}{1-n_0}\big[P_1(s,t,0) - P_1(s,t,1)\big] \\ + w_0 \frac{|\dot{n}_0|_-}{1-n_0}\big[P_0(s,t,0) - P_0(s,t,1)\big] \Big] \Big)\, \mathrm{d}s.\end{aligned} \tag{4.24}$$

where we defined

$$\left|\begin{aligned} J_+(s,t,\gamma) &= k_{+,\gamma}(s) P_0(s,t,\gamma) - k^{\mathrm{rev}}_{+,\gamma}(s) P_1(s,t,\gamma), \\ J_-(s,t,\gamma) &= k_{-,\gamma}(s) P_1(s,t,\gamma) - k^{\mathrm{rev}}_{-,\gamma}(s) P_0(s,t,\gamma), \\ \overline{J}_-(t) &= \frac{1}{d_a}\int_{s^-}^{s^+} \Big[n_0(t) J_-(s,t,1) + \big(1 - n_0(t)\big) J_-(s,t,0) \Big]\, \mathrm{d}s. \end{aligned}\right.$$

Using the property (4.8), the last two integrals in (4.24) cancel out. We finally have

$$\dot{\mathcal{U}}(t) = \dot{\mathcal{W}}(t) + \dot{\mathcal{E}}(t) + \dot{\mathcal{Q}}(t), \tag{4.25}$$

with

$$\left|\begin{aligned} \dot{\mathcal{W}}(t) &= \dot{x}_c \tau_c(t), && \text{(4.26a)} \\ \dot{\mathcal{E}}(t) &= \mu_T \overline{J}_-(t), && \text{(4.26b)} \\ \dot{\mathcal{Q}}(t) &= \frac{1}{d_a}\int_{s^-}^{s^+} \Big(n_0 \Big[(w_1(s) - w_0) J_+(s,t,1) + (w_0 - (w_1(s) + \mu_T)) J_-(s,t,1) \Big] \\ &\qquad + (1-n_0)\Big[(w_1(s) - w_0) J_+(s,t,0) \\ &\qquad\qquad + (w_0 - (w_1(s) + \mu_T)) J_-(s,t,0) \Big] \Big)\, \mathrm{d}s. && \text{(4.26c)} \end{aligned}\right.$$

The variation of energy is thus separated into different contributions: a flux of work $\dot{\mathcal{W}}$, a flux of chemical energy brought by ATP $\dot{\mathcal{E}}$ and a thermal transfer flux $\dot{\mathcal{Q}}$. Note that all the terms are counted positive when the flux of energy is entering the system. As expected, the pool exchange terms do not contribute in the energy balance since the state energy levels are the same in both pools.

4.4.3 Second principle

The establishment of the second principle requires convexity inequalities that we present first.

Lemma 4.4.1 (Convexity inequalities) *For all $(x, y) \in]0,1[^2$, we have the classical convexity inequalities*

$$\left|\begin{aligned} &\ln y - \ln x \leq \frac{1}{x}\big[y - x\big] && \text{(4.27a)}\\ &\ln y - \ln x \geq \frac{1}{y}\big[y - x\big] && \text{(4.27b)}\end{aligned}\right.$$

Moreover, using (4.27b) we also have

$$\ln(1-y) - \ln(1-x) \geq \frac{1}{1-y}\big[x - y\big] \tag{4.28}$$

Multiplying (4.27b) by y and (4.28) by $1-y$ and summing, we obtain

$$y \ln\left(\frac{y}{x}\right) + (1-y)\ln\left(\frac{1-y}{1-x}\right) \geq 0 \tag{4.29}$$

or equivalently

$$y \ln\left(\frac{x}{y}\right) + (1-y)\ln\left(\frac{1-x}{1-y}\right) \leq 0. \tag{4.30}$$

The average entropy per myosin head is defined by the weighted average between the entropy in each pool. It is given by

$$\begin{aligned}\mathcal{S}(t) = -\frac{k_B}{d_a}\int_{s^-}^{s^+}\Big(&n_0\Big[P_1(s,t,1)\ln P_1(s,t,1) + P_0(s,t,1)\ln P_0(s,t,1)\Big]\\ &+ (1-n_0)\Big[P_1(s,t,0)\ln P_1(s,t,0) + P_0(s,t,0)\ln P_0(s,t,0)\Big]\Big)\,\mathrm{d}s.\end{aligned}$$

Our system is maintained at constant temperature by the environment, it can thus be more easily described by the adapted thermodynamics potential: the Helmholtz free energy. It is given by

$$\mathcal{F}(t) = \mathcal{U}(t) - T\mathcal{S}(t),$$

We thus formally have

$$\frac{\mathrm{d}}{\mathrm{d}t}\mathcal{F}(t) = \frac{\mathrm{d}}{\mathrm{d}t}\mathcal{U}(t) - T\frac{\mathrm{d}}{\mathrm{d}t}\mathcal{S}(t). \tag{4.31}$$

The free energy can be also expressed in terms of the chemical potentials

$$\left|\begin{aligned}&\mu_1(s,t,\gamma) = w_1(s) + k_B T\ln[P_1(s,t,\gamma)],\ \forall\gamma\in\{0,1\}\\ &\mu_0(s,t,\gamma) = w_0 + k_B T\ln[P_0(s,t,\gamma)],\ \forall\gamma\in\{0,1\}.\end{aligned}\right.$$

as

$$\begin{aligned}\mathcal{F}(t) = \frac{1}{d_a}\int_{s^-}^{s^+}\Big(&n_0\Big[P_1(s,t,1)\mu_1(s,t,1) + P_0(s,t,1)\mu_0(s,t,1)\Big]\\ &+ (1-n_0)\Big[P_1(s,t,0)\mu_1(s,t,0) + P_0(s,t,0)\mu_0(s,t,0)\Big]\Big)\,\mathrm{d}s.\end{aligned}$$

We have

$$\begin{aligned}\frac{\mathrm{d}}{\mathrm{d}t}\mathcal{F}(t) = \frac{1}{d_a}\int_{s^-}^{s^+}\Big(&\dot{n}_0\Big[P_1(s,t,1)\mu_1(s,t,1) + P_0(s,t,1)\mu_0(s,t,1)\\ &\qquad - P_1(s,t,0)\mu_1(s,t,0) - P_0(s,t,0)\mu_0(s,t,0)\Big]\\ &+ n_0\Big[P_1(s,t,1)\,\partial_t\mu_1(s,t,1) + \mu_1(s,t,1)\,\partial_t P_1(s,t,1)\\ &\qquad + P_0(s,t,1)\,\partial_t\mu_0(s,t,1) + \mu_0(s,t,1)\,\partial_t P_0(s,t,1)\Big]\\ &+ (1-n_0)\Big[P_1(s,t,0)\,\partial_t\mu_1(s,t,0) + \mu_1(s,t,0)\,\partial_t P_1(s,t,0)\\ &\qquad + P_0(s,t,0)\,\partial_t\mu_0(s,t,0) + \mu_0(s,t,0)\,\partial_t P_0(s,t,0)\Big]\Big)\,\mathrm{d}s.\end{aligned} \tag{4.32}$$

The time derivative of the chemical potentials times the probability P_α being given by

$$P_\alpha(s,t,\gamma)\,\partial_t\mu_\alpha(s,t,\gamma) = k_B T\,\partial_t P_\alpha(s,t,\gamma)\,\forall\alpha\in\{0,1\}\text{ and }\forall\gamma\in\{0,1\}.$$

We obtain that

$$\begin{aligned}&n_0\Big[P_1(s,t,1)\,\partial_t\mu_1(s,t,1) + P_0(s,t,1)\,\partial_t\mu_0(s,t,1)\Big]\\ &\qquad + (1-n_0)\Big[P_1(s,t,0)\,\partial_t\mu_1(s,t,0) + P_0(s,t,0)\,\partial_t\mu_0(s,t,0)\Big]\\ &= n_0 k_B T\,\partial_t\Big[P_1(s,t,1) + P_0(s,t,1)\Big] + (1-n_0)k_B T\,\partial_t\Big[P_1(s,t,0) + P_0(s,t,0)\Big]\\ &= 0,\end{aligned}$$

from the matter conservation (4.22). The time derivative of the free energy becomes

$$\begin{aligned}\frac{\mathrm{d}}{\mathrm{d}t}\mathcal{F}(t) = \frac{1}{d_a}\int_{s^-}^{s^+}\Big(&\dot{n}_0\Big[P_1(s,t,1)\mu_1(s,t,1) + P_0(s,t,1)\mu_0(s,t,1)\\ &\qquad - P_1(s,t,0)\mu_1(s,t,0) - P_0(s,t,0)\mu_0(s,t,0)\Big]\\ &+ n_0\Big[\mu_1(s,t,1)\Big(-\dot{x}_c\partial_s P_1(s,t,1) - \frac{|\dot{n}_0|_+}{n_0}\big[P_1(s,t,1) - P_1(s,t,0)\big]\\ &\qquad + \big(k_{+,1}(s) + k^{\mathrm{rev}}_{-,1}(s)\big)\big(1 - P_1(s,t,1)\big) - \big(k_{-,1}(s) + k^{\mathrm{rev}}_{+,1}(s)\big)P_1(s,t,1)\Big)\\ &\qquad + \mu_0(s,t,1)\Big(\dot{x}_c\partial_s P_1(s,t,1) + \frac{|\dot{n}_0|_+}{n_0}\big[P_1(s,t,1) - P_1(s,t,0)\big]\\ &\qquad - \big(k_{+,1}(s) + k^{\mathrm{rev}}_{-,1}(s)\big)\big(1 - P_1(s,t,1)\big)\\ &\qquad\qquad + \big(k_{-,1}(s) + k^{\mathrm{rev}}_{+,1}(s)\big)P_1(s,t,1)\Big)\Big]\\ &+ (1-n_0)\Big[\mu_1(s,t,0)\Big(-\dot{x}_c\partial_s P_1(s,t,0) - \frac{|\dot{n}_0|_-}{1-n_0}\big[P_1(s,t,0) - P_1(s,t,1)\big]\\ &\qquad + \big(k_{+,0}(s) + k^{\mathrm{rev}}_{-,0}(s)\big)\big(1 - P_1(s,t,0)\big) - \big(k_{-,0}(s) + k^{\mathrm{rev}}_{+,0}(s)\big)P_1(s,t,0)\Big)\\ &\qquad + \mu_0(s,t,0)\Big(\dot{x}_c\partial_s P_1(s,t,0) + \frac{|\dot{n}_0|_-}{1-n_0}\big[P_1(s,t,0) - P_1(s,t,1)\big]\\ &\qquad - \big(k_{+,0}(s) + k^{\mathrm{rev}}_{-,0}(s)\big)\big(1 - P_1(s,t,0)\big)\\ &\qquad\qquad + \big(k_{-,0}(s) + k^{\mathrm{rev}}_{+,0}(s)\big)P_1(s,t,0)\Big)\Big]\Big)\,\mathrm{d}s.\end{aligned} \tag{4.33}$$

Adapting the calculation performed in [Kimmig et al., 2019] (Chapter 2) for the derivation of the second principle in the usual family of Huxley'57 models, we obtain

$$
\begin{aligned}
&\frac{1}{d_a}\int_{s^-}^{s^+}\Big(n_0\Big[\mu_1(s,t,1)\Big(\big(k_{+,1}(s)+k_{-,1}^{\mathrm{rev}}(s)\big)\big(1-P_1(s,t,1)\big)\\
&\qquad\qquad -\big(k_{-,1}(s)+k_{+,1}^{\mathrm{rev}}(s)\big)P_1(s,t,1)-\dot{x}_c\,\partial_s P_1(s,t,1)\Big)\\
&\qquad +\mu_0(s,t,1)\Big(-\big(k_{+,1}(s)+k_{-,1}^{\mathrm{rev}}(s)\big)\big(1-P_1(s,t,1)\big)\\
&\qquad\qquad +\big(k_{-,1}(s)+k_{+,1}^{\mathrm{rev}}(s)\big)P_1(s,t,1)+\dot{x}_c\,\partial_s P_1(s,t,1)\Big)\Big]\\
&+(1-n_0)\Big[\mu_1(s,t,0)\Big(\big(k_{+,0}(s)+k_{-,0}^{\mathrm{rev}}(s)\big)\big(1-P_1(s,t,0)\big)\\
&\qquad\qquad -\big(k_{-,0}(s)+k_{+,0}^{\mathrm{rev}}(s)\big)P_1(s,t,0)-\dot{x}_c\,\partial_s P_1(s,t,0)\Big)\\
&\qquad +\mu_0(s,t,0)\Big(-\big(k_{+,0}(s)+k_{-,0}^{\mathrm{rev}}(s)\big)\big(1-P_1(s,t,0)\big)\\
&\qquad\qquad +\big(k_{-,0}(s)+k_{+,0}^{\mathrm{rev}}(s)\big)P_1(s,t,0)+\dot{x}_c\,\partial_s P_1(s,t,0)\Big)\Big]\Big)\,\mathrm{d}s\\
&=\dot{\mathcal{W}}(t)+\dot{\mathcal{E}}(t)\\
&\qquad+\frac{1}{d_a}\int_{s^-}^{s^+}\Big(n_0\Big[J_-(s,t,1)\big[\mu_0(s,t,1)-\big(\mu_1(s,t,1)+\mu_T\big)\big]\\
&\qquad\qquad +J_+(s,t,1)\big[\mu_1(s,t,1)-\mu_0(s,t,1)\big]\Big]\\
&\qquad+(1-n_0)\Big[J_-(s,t,0)\big[\mu_0(s,t,0)-\big(\mu_1(s,t,0)+\mu_T\big)\big]\\
&\qquad\qquad +J_+(s,t,0)\big[\mu_1(s,t,0)-\mu_0(s,t,0)\big]\Big]\Big)\,\mathrm{d}s.
\end{aligned}
$$

Using the calculation made for the derivation of the energy balance, we have

$$
\begin{aligned}
&\dot{n}_0\Big[P_1(s,t,1)w_1(s)+P_0(s,t,1)w_0-P_1(s,t,0)w_1(s)-P_0(s,t,0)w_0\Big]\\
&\quad-\Big(n_0\Big[w_1(s)\frac{|\dot{n}_0|_+}{n_0}\big[P_1(s,t,1)-P_1(s,t,0)\big]-w_0\frac{|\dot{n}_0|_+}{n_0}\big[P_1(s,t,1)-P_1(s,t,0)\big]\Big]\\
&+(1-n_0)\Big[w_1(s)\frac{|\dot{n}_0|_-}{1-n_0}\big[P_1(s,t,0)-P_1(s,t,1)\big]-w_0\frac{|\dot{n}_0|_-}{1-n_0}\big[P_1(s,t,0)-P_1(s,t,1)\big]\Big]\Big)=0.
\end{aligned}
$$

Finally, we have using the property (4.8)

$$
\begin{aligned}
&\dot{n}_0 k_B T\Big[P_1(s,t,1)\ln\big[P_1(s,t,1)\big] + P_0(s,t,1)\ln\big[P_0(s,t,1)\big] \\
&\qquad\qquad - P_1(s,t,0)\ln\big[P_1(s,t,0)\big] - P_0(s,t,0)\ln\big[P_0(s,t,0)\big]\Big] \\
&- n_0 k_B T\Big[\ln\big[P_1(s,t,1)\big]\frac{|\dot{n}_0|_+}{n_0}\big[P_1(s,t,1)-P_1(s,t,0)\big] \\
&\qquad\qquad + \ln\big[P_0(s,t,1)\big]\frac{|\dot{n}_0|_+}{n_0}\big[P_0(s,t,1)-P_0(s,t,0)\big]\Big] \\
&- (1-n_0)k_B T\Big[\ln\big[P_1(s,t,0)\big]\frac{|\dot{n}_0|_-}{1-n_0}\big[P_1(s,t,0)-P_1(s,t,1)\big] \\
&\qquad\qquad + \ln\big[P_0(s,t,0)\big]\frac{|\dot{n}_0|_-}{1-n_0}\big[P_0(s,t,0)-P_0(s,t,1)\big]\Big] \\
&= k_B T\Big(P_1(s,t,1)|\dot{n}_0|_-\Big[-\ln\big[P_1(s,t,1)\big]+\ln\big[P_1(s,t,0)\big]\Big] \\
&\qquad\qquad + P_0(s,t,1)|\dot{n}_0|_-\Big[-\ln\big[P_0(s,t,1)\big]+\ln\big[P_0(s,t,0)\big]\Big] \\
&\qquad\qquad + P_1(s,t,0)|\dot{n}_0|_+\Big[-\ln\big[P_1(s,t,0)\big]+\ln\big[P_1(s,t,1)\big]\Big] \\
&\qquad\qquad + P_0(s,t,0)|\dot{n}_0|_+\Big[-\ln\big[P_0(s,t,0)\big]+\ln\big[P_0(s,t,1)\big]\Big]\Big) \\
&= -k_B T\Big[|\dot{n}_0|_+\Big[\ln\Big(\frac{P_1(s,t,0)}{P_1(s,t,1)}\Big)P_1(s,t,0)+\ln\Big(\frac{1-P_1(s,t,0)}{1-P_1(s,t,1)}\Big)\big(1-P_1(s,t,0)\big)\Big] \\
&\qquad + |\dot{n}_0|_-\Big[\ln\Big(\frac{P_1(s,t,1)}{P_1(s,t,0)}\Big)P_1(s,t,1)+\ln\Big(\frac{1-P_1(s,t,1)}{1-P_1(s,t,0)}\Big)\big(1-P_1(s,t,1)\big)\Big]\Big].
\end{aligned}
$$

Altogether, (4.33) becomes

$$
\begin{aligned}
\frac{\mathrm{d}}{\mathrm{d}t}\mathcal{F}(t) &= \dot{\mathcal{W}}(t)+\dot{\mathcal{E}}(t) \\
&\quad + \frac{1}{d_a}\int_{s^-}^{s^+}\Big(n_0\Big[J_-(s,t,1)\big[\mu_0(s,t,1)-\big(\mu_1(s,t,1)+\mu_T\big)\big] \\
&\qquad\qquad + J_+(s,t,1)\big[\mu_1(s,t,1)-\mu_0(s,t,1)\big]\Big] \\
&\quad + (1-n_0)\Big[J_-(s,t,0)\big[\mu_0(s,t,0)-\big(\mu_1(s,t,0)+\mu_T\big)\big] \\
&\qquad\qquad + J_+(s,t,0)\big[\mu_1(s,t,0)-\mu_0(s,t,0)\big]\Big]\Big)\,\mathrm{d}s \\
&\quad - \frac{k_B T}{d_a}\int_{s^-}^{s^+}\Big[|\dot{n}_0|_+\Big[\ln\Big(\frac{P_1(s,t,0)}{P_1(s,t,1)}\Big)P_1(s,t,0) \\
&\qquad\qquad + \ln\Big(\frac{1-P_1(s,t,0)}{1-P_1(s,t,1)}\Big)\big(1-P_1(s,t,0)\big)\Big] \\
&\qquad + |\dot{n}_0|_-\Big[\ln\Big(\frac{P_1(s,t,1)}{P_1(s,t,0)}\Big)P_1(s,t,1) \\
&\qquad\qquad + \ln\Big(\frac{1-P_1(s,t,1)}{1-P_1(s,t,0)}\Big)\big(1-P_1(s,t,1)\big)\Big]\Big]\,\mathrm{d}s.
\end{aligned}
\tag{4.34}
$$

Joining (4.34) with (4.31) and the first principle (4.25), we obtain second principle

$$\frac{\mathrm{d}}{\mathrm{d}t}\mathcal{S}(t) = \frac{\dot{\mathcal{Q}}}{T} + \dot{\mathcal{S}}_{\mathrm{prod}}(t), \tag{4.35}$$

defining the rate of entropy production as

$$\begin{aligned}
\dot{\mathcal{S}}_{\mathrm{prod}}(t) = -\frac{1}{T}\frac{1}{d_a}\int_{s^-}^{s^+} \Big(& n_0 \Big[J_-(s,t,1)\big[\mu_0(s,t,1) - \big(\mu_1(s,t,1)+\mu_T\big)\big] \\
& \qquad + J_+(s,t,1)\big[\mu_1(s,t,1) - \mu_0(s,t,1)\big]\Big] \\
& + (1-n_0)\Big[J_-(s,t,0)\big[\mu_0(s,t,0) - \big(\mu_1(s,t,0)+\mu_T\big)\big] \\
& \qquad + J_+(s,t,0)\big[\mu_1(s,t,0) - \mu_0(s,t,0)\big]\Big]\Big)\,\mathrm{d}s \\
+ \frac{k_B}{d_a}\int_{s^-}^{s^+} & \Big[|\dot{n}_0|_+ \Big[\ln\left(\frac{P_1(s,t,0)}{P_1(s,t,1)}\right) P_1(s,t,0) + \ln\left(\frac{1-P_1(s,t,0)}{1-P_1(s,t,1)}\right)\big(1-P_1(s,t,0)\big)\Big] \\
& + |\dot{n}_0|_- \Big[\ln\left(\frac{P_1(s,t,1)}{P_1(s,t,0)}\right) P_1(s,t,1) + \ln\left(\frac{1-P_1(s,t,1)}{1-P_1(s,t,0)}\right)\big(1-P_1(s,t,1)\big)\Big]\Big]\,\mathrm{d}s.
\end{aligned} \tag{4.36}$$

The second principle is thus satisfied if the above defined entropy production rate is always positive. As was shown in [Hill, 1977], the integrand of the first integral term of $\dot{\mathcal{S}}_{\mathrm{prod}}$ is always positive if the transition rates satisfy the detailed balance (4.6). Indeed, we have

$$\begin{aligned}
\frac{k_{+,\gamma}(s)P_0(s,t,\gamma)}{k^{\mathrm{rev}}_{+,\gamma}(s)P_1(s,t,\gamma)} &= \exp\left(\frac{w_0 - w_1(s)}{k_BT}\right)\exp\left(k_BT\frac{\ln\big[P_0(s,t,\gamma)-P_1(s,t,\gamma)\big]}{k_BT}\right) \\
&= \exp\left(\frac{\mu_0(s,t,\gamma) - \big(\mu_1(s,t,\gamma)+\mu_T\big)}{k_BT}\right).
\end{aligned} \tag{4.37}$$

Since we have $J_-(s,t,\gamma) = k_{-,\gamma}(s)P_1(s,t,\gamma) - k^{\mathrm{rev}}_{-,\gamma}(s)P_0(s,t,\gamma)$, we conclude from (4.37) that J_- and $\mu_0(s,t,1) - \big(\mu_1(s,t,1)+\mu_T\big)$ are of opposite sign. Therefore, the product of these two factors is negative and contribute positively to the entropy production with the minus sign in front of the integral. Similarly, the product of J_+ and $\mu_1(s,t,1) - \mu_0(s,t,1)$ is also always negative and contributes positively to the entropy production. Moreover, using the convexity inequality (4.29), we deduce that the second integral term of $\dot{\mathcal{S}}_{\mathrm{prod}}$ is always positive. As a consequence, we have $\dot{\mathcal{S}}_{\mathrm{prod}} \geq 0$ and the model is compatible with the second principle.

One can note that the entropy creation is composed of two contributions. The first one involves the attachment and detachment fluxes and corresponds to the physical creation of entropy. The second one is an entropy creation term induced by the averaging process introduced in our model by the pool exchange terms. Indeed, at each time, we mix the probability of being attached (resp. detached) of the heads switching from one pool to another and the heads remaining in their initial pool. There is a loss of information on the system and thus a creation of entropy. An illustration of this phenomenon is presented in Section 4.5.1.

4.4.4 Coupling with a macroscopic model

We now want to couple our model describing the microscopic interaction between actin and myosin to the macroscopic model of a muscle fibre. Let us define a domain Ω^0 for the

reference configuration. We assume that the domain is subjected to a boundary traction $\underline{t}_N$ on the subpart of the boundary Γ_N. We introduce the rheology proposed in [Kimmig et al., 2019] (Chapter 2) in the realm of finite strains as presented in Figure 4.4. The upper branch models the one dimensional half-sarcomere of direction $\underline{\tau}$. The displacement x_c represent the relative sliding between the actin and the myosin filaments considered rigid. The length change of the filaments due to their passive properties is accounted for by e_s. Defining the extensions

$$e_c = \frac{x_c}{\ell_{hs}} \qquad \text{and} \qquad e_s = \frac{\ell_s}{\ell_{hs}},$$

the rheology assumes the following additive law to define the total 1D extension $e_{\text{fib}} = e_s + e_c$. The tension in the branch is naturally given by

$$T_{\text{fib}} = E_s e_s = T_c + \nu \dot{e}_c.$$

In this context, the filament sliding velocity $\dot{x}_c$, which appear in microscopic dynamic equation, is given by $\ell_{hs}\dot{e}_c$.

The remaining part of the rheology models the 3D visco-hyperelastic passive properties of the tissue. The total second Piola-Kirchhoff stress tensor is given by $\underline{\underline{\Sigma}} = \underline{\underline{\Sigma}}_p + \underline{\underline{\Sigma}}_a$ with

$$\underline{\underline{\Sigma}}_p = \frac{\partial \Psi}{\partial \underline{\underline{e}}} + \eta \dot{\underline{\underline{e}}} \qquad \text{and} \qquad \underline{\underline{\Sigma}}_a = \frac{T_{\text{fib}}}{1 + e_{\text{fib}}} \underline{\tau} \otimes \underline{\tau},$$

where Ψ is the constitutive hyperelastic potential, η the 3D viscosity coefficient, $\underline{\underline{e}}$ is the Green-Lagrange deformation tensor and $\underline{\tau}$ the local fiber direction. Note that the 1D extension and the 3D Green-Lagrange tensor are linked through the relation

$$1 + e_{\text{fib}} = (1 + 2\underline{\tau} \cdot \underline{\underline{e}} \cdot \underline{\tau})^{\frac{1}{2}}. \tag{4.38}$$

The principle of virtual work written on Ω^0 yields the macro-micro coupled model

$$\begin{cases} \displaystyle\int_{\Omega^0} \rho_0 \ddot{\underline{y}} \cdot \underline{w}\,\mathrm{d}\Omega + \int_{\Omega^0} \underline{\underline{\Sigma}} : \mathrm{d}_{\underline{y}}\underline{\underline{e}} \cdot \underline{w}\,\mathrm{d}\Omega = \int_{\Gamma_N} \underline{t}_N \cdot \underline{w}\,\mathrm{d}\Gamma, \quad \forall \underline{w} \in \mathscr{V}_{\mathrm{ad}}, \\ \qquad \text{with } \underline{\underline{\Sigma}} = \dfrac{\partial \Psi}{\partial \underline{\underline{e}}} + \eta \dot{\underline{\underline{e}}} + \dfrac{T_{\mathrm{fib}}}{(1 + 2\underline{\tau} \cdot \underline{\underline{e}} \cdot \underline{\tau})^{\frac{1}{2}}} \underline{\tau} \otimes \underline{\tau}, \end{cases} \tag{4.39a}$$

$$\begin{cases} T_{\mathrm{fib}} = \nu \dot{e}_c + T_c = E_s e_s, \\ \qquad \text{with } T_c(\underline{x}, t) = \dfrac{\rho_{\mathrm{surf}}}{d_a} \displaystyle\int_{s^-}^{s^+} \Big[n_0(\underline{x}, e_c) P_1(\underline{x}, s, t, 1) \\ \qquad\qquad + \big(1 - n_0(\underline{x}, e_c)\big) P_1(\underline{x}, s, t, 0) \Big] \dfrac{\partial w_1}{\partial s}(s, t) \mathrm{d}s, \ \forall \underline{x} \in \Omega^0, \end{cases} \tag{4.39b}$$

$$\begin{cases} \dfrac{\partial P_1}{\partial t}(\underline{x}, s, t, 1) = -\dfrac{|\dot{n}_0|_+}{n_0} \big[P_1(\underline{x}, s, t, 1) - P_1(\underline{x}, s, t, 0) \big] \\ \qquad\qquad - \ell_{hs} \dot{e}_c(\underline{x}, t) \dfrac{\partial P_1}{\partial s}(\underline{x}, s, t, 1) \\ \qquad + \big(k_{+,1}(s) + k^{\mathrm{rev}}_{-,1}(s)\big)\big(1 - P_1(\underline{x}, s, t, 1)\big) \\ \qquad\qquad - \big(k_{-,1}(s) + k^{\mathrm{rev}}_{+,1}(s)\big) P_1(\underline{x}, s, t, 1) \\ \dfrac{\partial P_1}{\partial t}(\underline{x}, s, t, 0) = -\dfrac{|\dot{n}_0|_-}{1 - n_0} \big[P_1(\underline{x}, s, t, 0) - P_1(\underline{x}, s, t, 1) \big] \\ \qquad\qquad - \ell_{hs} \dot{e}_c(\underline{x}, t) \dfrac{\partial P_1}{\partial s}(\underline{x}, s, t, 0) \\ \qquad + \big(k_{+,0}(s) + k^{\mathrm{rev}}_{-,0}(s)\big)\big(1 - P_1(\underline{x}, s, t, 0)\big) \\ \qquad\qquad - \big(k_{-,0}(s) + k^{\mathrm{rev}}_{+,0}(s)\big) P_1(\underline{x}, s, t, 0) \end{cases} \tag{4.39c}$$

4.5 Range of validity and limitations

We want to gain a deeper understanding of our model and in particular of the consequences of the homogenized myosin heads description in the pools instead of an individual description. For that, we first numerically investigate the behavior of the pool exchange term in our equations. Then, to put our model in perspective, we compare our formulation with two ways of treating the myosin heads individually. Finally, we numerically compare our newly proposed formulation to the state of the art integration of the thick filament activation into the Huxley'57 model equations [Zahalak & Motabarzadeh, 1997; Chapelle et al., 2012].

To put the focus on the variations of myosin head availability, we assume that the filaments do not slide past each other ($\dot{x}_c = 0$). In these conditions, the distance to the nearest actin site s is a parameter. We consider the representative subset of the myosin heads population that is located at distance s to its nearest actin site and the reference to the parameter s will be omitted in the rest of this section.

4.5.1 Impact of the homogenized description in the pool model

We first want to isolate the effect of the pool exchange operator, We thus assume that the attachment-detachment dynamics is prevented ($k_{+,\gamma}(s) = k_{-,\gamma}(s) = 0, \ \forall \alpha \in \{0, 1\}, \ \forall \gamma \in \{0, 1\}$).

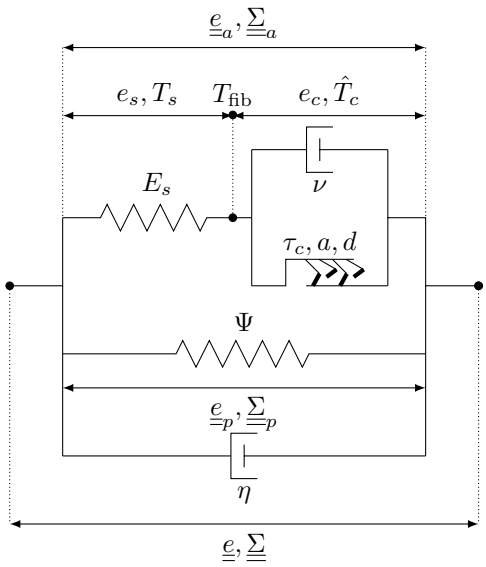

Figure 4.4 – Tissue rheology. The upper branch represents the 1D filaments inside the sarcomere, which comprises the active cross-bridges represented here by the attached myosin heads. The lower branch represents the 3D passive visco-hyperelastic contribution of the remaining muscle cell constituents to the mechanical behavior. The rheology is constructed in the framework of finite strains, the constitutive elements are thus assembled together in a non-linear way.

The only effect at play is a transfer between the two pools when n_0 varies. We will assume here that n_0 has an explicit dependency on time. We choose that, in the initial situation, $P_1(t,1) = 0.90$ and $P_1(t,0) = 0.10$.

We impose a periodic oscillatory evolution for n_0 (see Figure 4.5), i.e. in each period, we alternatively transfer heads from one pool to the other. The simulation results are presented in Figure 4.5.

When n_0 increases, heads are transferred from the pool $\gamma = 0$ to the pool $\gamma = 1$. Since $P_1(s,t,0) \leq P_1(s,t,1)$, the heads arriving in the pool $\gamma = 1$ have a lower probability of being attached than the myosin heads that they join in the pool. As a result the average probability of being attached in the pool $\gamma = 1$ decreases. Heads remaining in the pool $\gamma = 0$ are not mixed with any transferring myosin heads. Their probability of being attached $P_1(s,t,0)$ is left unchanged. When n_0 increases, the opposite effect takes place. Heads are transferred from the pool $\gamma = 1$ to the pool $\gamma = 0$ and $P_1(s,t,0)$ increases. Since the attachment-detachment dynamics is prevented, the total probability of being attached $P_1(t) = n_0(t)P_1(s,t,1) + \big(1 - n_0(t)\big)P_1(s,t,0)$ remains constant over a period.

Repeating this process, the probability of being attached in the two pools converges to the total probability of being attached $P_1(t)$. The exchanges between the pools tend to homogenize the probability of being attached between the two pools. This mixing effect is associated with a loss of information that is revealed in the thermodynamic second balance.

4.5.2 Comparison with individual description of the myosin heads

Our formulation (4.14) proposes an homogenized description of the myosin heads within the pools. To assess the impact of this assumption, we compare this homogenized formulation with stochastic individual descriptions of the myosin heads when the myosin heads availability varies. The heads are still separated in two pools, which defines their attachment-detachment dynamics, but their probability of being attached is tracked indi-

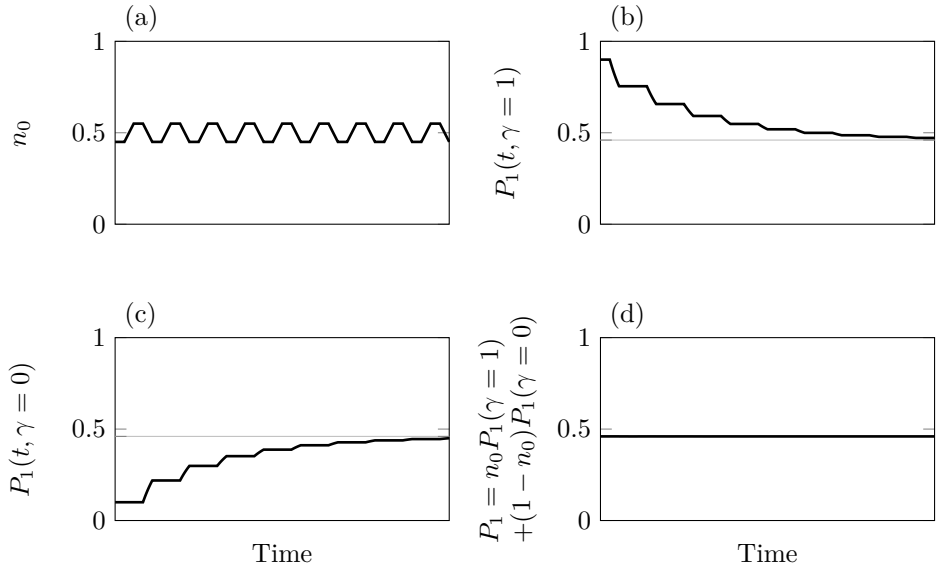

Figure 4.5 – Illustration of the homogenization effect of the pool model. We consider here that the sliding velocity $\dot{x}_c$ vanishes and the attachment-detachment dynamics is blocked $k_{+,\gamma}(s) = k_{-,\gamma}(s) = 0$. (a) Imposed evolution for n_0. (b), (c) & (d) Model outputs.

vidually.

This is not only an opportunity to put our modeling assumptions into perspective but also a way to determine if the distinction between different potential underlying mechanisms matters in physiological conditions.

Note that, for the sake of compactness, we will use the aggregated transition rates f_γ and g_γ in this section.

4.5.2.1 Heads switching pool chosen randomly

We first assume that the heads switching from one pool to the other are randomly chosen (i.e. all heads in the pool have the same probability to switch pool). The heads in the sarcomere therefore do not interact with each other. Any myosin head in the considered subset can attach and detach (the internal variable α is equal to one when the myosin head is attached, and to zero if it is detached) and switch between the pool of available head ($\gamma = 1$) and the pool of non-available myosin heads ($\gamma = 0$). Its state at time t is described by (α^t, γ^t).

In our modeling framework, we want the ratio of heads in the pool $\gamma = 1$ to be controlled and equal to $n_0(t)$. In this stochastic model, this translates into the expected property $\mathbb{P}\big[\gamma^t = 1\big] = n_0(t)$.

Let us assume that this property holds and examine the resulting requirements on transition probabilities for the variable γ^t. We would have

$$\mathbb{P}\big[\gamma^{t+\mathrm{d}t} = 1 | \gamma^t = 0\big] = \frac{\mathbb{P}\big[\gamma^{t+\mathrm{d}t} = 1, \gamma^t = 0\big]}{\mathbb{P}\big[\gamma^t = 0\big]} = \frac{|\dot{n}_0(t)|_+}{1 - n_0(t)} \mathrm{d}t.$$

Similarly, we would also obtain

$$\mathbb{P}\big[\gamma^{t+\mathrm{d}t} = 0 | \gamma^t = 1\big] = \frac{\mathbb{P}\big[\gamma^{t+\mathrm{d}t} = 0, \gamma^t = 1\big]}{\mathbb{P}\big[\gamma^t = 0\big]} = \frac{|\dot{n}_0(t)|_-}{n_0(t)} \mathrm{d}t.$$

We choose these transition probabilities for the variable γ so that the property $\mathbb{P}\big[\gamma^t = 1\big] = n_0(t)$ holds and we choose the initial condition $\mathbb{P}\big[\gamma^0 = 1\big] = n_0(0)$.

The complete system of probability transitions for the state of the myosin head is given by

$$\left|\begin{aligned}
&\mathbb{P}\big[\alpha^{t+\mathrm{d}t} = 1, \gamma^{t+\mathrm{d}t} = 1 | \alpha^t = 0, \gamma^t = 1\big] = f_1\,\mathrm{d}t,\\
&\mathbb{P}\big[\alpha^{t+\mathrm{d}t} = 0, \gamma^{t+\mathrm{d}t} = 1 | \alpha^t = 1, \gamma^t = 1\big] = g_1\,\mathrm{d}t,\\
&\mathbb{P}\big[\alpha^{t+\mathrm{d}t} = 1, \gamma^{t+\mathrm{d}t} = 0 | \alpha^t = 0, \gamma^t = 0\big] = f_0\,\mathrm{d}t,\\
&\mathbb{P}\big[\alpha^{t+\mathrm{d}t} = 0, \gamma^{t+\mathrm{d}t} = 0 | \alpha^t = 1, \gamma^t = 0\big] = g_0\,\mathrm{d}t,\\
&\mathbb{P}\big[\alpha^{t+\mathrm{d}t} = 1, \gamma^{t+\mathrm{d}t} = 1 | \alpha^t = 1, \gamma^t = 0\big] = \frac{|\dot{n}_0(t)|_+}{1-n_0(t)}\,\mathrm{d}t,\\
&\mathbb{P}\big[\alpha^{t+\mathrm{d}t} = 0, \gamma^{t+\mathrm{d}t} = 1 | \alpha^t = 0, \gamma^t = 0\big] = \frac{|\dot{n}_0(t)|_+}{1-n_0(t)}\,\mathrm{d}t,\\
&\mathbb{P}\big[\alpha^{t+\mathrm{d}t} = 1, \gamma^{t+\mathrm{d}t} = 0 | \alpha^t = 1, \gamma^t = 1\big] = \frac{|\dot{n}_0(t)|_-}{n_0(t)}\,\mathrm{d}t,\\
&\mathbb{P}\big[\alpha^{t+\mathrm{d}t} = 0, \gamma^{t+\mathrm{d}t} = 0 | \alpha^t = 0, \gamma^t = 1\big] = \frac{|\dot{n}_0(t)|_-}{n_0(t)}\,\mathrm{d}t.
\end{aligned}\right. \tag{4.40}$$

The various states, in which a myosin heads can be, and the transitions between them are summarised in Figure 4.6.

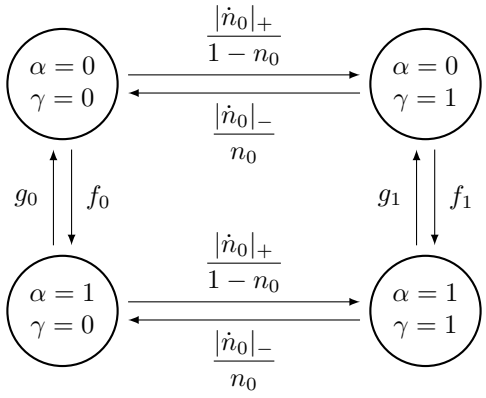

Figure 4.6 – Diagram representation of the stochastic model tracking the myosin heads individually in the pools and using the random exchange paradigm.

We now want to analytically compare this model and the homogenized pool model. For this, we establish a Kolmogorov-forward-like equation associated with (4.40) (the detailed calculus are presented in Appendix (4.9.2)).

Noting that the probabilities of the random exchange stochastic model states $\mathbb{P}\big[\alpha^t, \gamma^t\big]$ can be related to the homogenized pool model probabilities $P_\alpha(t, \gamma)$ by

$$\left|\begin{aligned}
&\mathbb{P}\big[\alpha^t = 1, \gamma^t = 1\big] = \mathbb{P}\big[\alpha^t = 1 | \gamma^t = 1\big]\mathbb{P}\big[\gamma^t = 1\big] = P_1(t,1)n_0(t),\\
&\mathbb{P}\big[\alpha^t = 1, \gamma^t = 0\big] = \mathbb{P}\big[\alpha^t = 1 | \gamma^t = 0\big]\mathbb{P}\big[\gamma^t = 0\big] = P_1(t,0)\cdot\big(1-n_0(t)\big),\\
&\mathbb{P}\big[\alpha^t = 0, \gamma^t = 1\big] = \mathbb{P}\big[\alpha^t = 0 | \gamma^t = 1\big]\mathbb{P}\big[\gamma^t = 1\big] = P_0(t,1)n_0(t),\\
&\mathbb{P}\big[\alpha^t = 0, \gamma^t = 0\big] = \mathbb{P}\big[\alpha^t = 0 | \gamma^t = 0\big]\mathbb{P}\big[\gamma^t = 0\big] = P_0(t,0)\cdot\big(1-n_0(t)\big).
\end{aligned}\right.$$

the system (4.40) is associated with the partial differential equations

$$\left|\begin{aligned}
\frac{\partial}{\partial t}P_1(1) &= -\frac{|\dot{n}_0(t)|_+}{n_0(t)}\Big[P_1(1) - P_1(0)\Big] - g_1 P_1(1) + f_1 P_0(1),\\
\frac{\partial}{\partial t}P_1(0) &= -\frac{|\dot{n}_0(t)|_-}{1-n_0(t)}\Big[P_1(0) - P_1(1)\Big] - g_0 P_1(0) + f_0 P_0(0),\\
P_0(1) &= 1 - P_1(1),\\
P_0(0) &= 1 - P_1(0),
\end{aligned}\right.$$

which are identical to (4.14) in the considered conditions (no filament sliding). The random exchange stochastic model and the homogenized pool model are thus equivalent.

4.5.2.2 Last-in first-out

It is also possible to consider that the heads are switching from one pool to the other in a last-in first-out manner. This would be a natural mechanism if the overlap effect is at the origin of the variations of myosin heads availability. In this case, the heads are, in some ways, interacting with each other through the memory of the transition order.

We assume that the considered subset of myosin heads contains N elements indexed by i of state (α_i^t, γ_i^t). They are shared in the two pools in the following manner

$$\gamma_i^t = \begin{cases} 1, & \text{if } i \leq \left\lfloor \dfrac{n_0(t)}{N} \right\rfloor \\ 0, & \text{otherwise,} \end{cases} \tag{4.41}$$

where $\lfloor \bullet \rfloor$ denotes the floor function. Then, in each pool, we have the dynamics

$$\left|\begin{aligned}
\mathbb{P}\big[\alpha_i^{t+\mathrm{d}t} = 1 | \alpha_i^t = 0, \gamma_i^t = 1\big] &= f_1\,\mathrm{d}t,\\
\mathbb{P}\big[\alpha_i^{t+\mathrm{d}t} = 0 | \alpha_i^t = 1, \gamma_i^t = 1\big] &= g_1\,\mathrm{d}t,\\
\mathbb{P}\big[\alpha_i^{t+\mathrm{d}t} = 1 | \alpha_i^t = 0, \gamma_i^t = 0\big] &= f_0\,\mathrm{d}t,\\
\mathbb{P}\big[\alpha_i^{t+\mathrm{d}t} = 0 | \alpha_i^t = 1, \gamma_i^t = 0\big] &= g_0\,\mathrm{d}t.
\end{aligned}\right. \tag{4.42}$$

4.5.2.3 Numerical simulation

We have formally proven the equivalence between the homogenized description of the myosin heads availability and the individual description with a random pool exchange paradigm. In this section, we will additionally numerically compare the homogenized pool descriptions with the individual description of the myosin head availability using the last-in first-out exchange paradigm.

To simulate stochastically the latter model with an individual description of the myosin heads, we consider N myosin heads. We approximate the probabilities $\mathbb{P}_t\big[\overline{\alpha}, \overline{\gamma}\big] = \mathbb{P}\big[\alpha^t = \overline{\alpha}, \gamma^t = \overline{\gamma}\big]$ with the empirical probabilities

$$\overline{\mathbb{P}}_t\big[\overline{\alpha}, \overline{\gamma}\big] = \frac{1}{N}\sum_{i=1}^{N} \mathbb{1}_{\{\alpha^t = \overline{\alpha}, \gamma^t = \overline{\gamma}\}}(\alpha_i^t, \gamma_i^t).$$

We impose the time evolution of n_0 with variations that reproduce that of a heart beat with physiological time scales. Starting from a steady-state where n_0 is constant with a value of 0.80 – heads are mainly available for attachment – , the ratio of available myosin heads is decreased to the value 0.20 – heads are mainly not available for attachment – in

0.1 s corresponding to the stystole. This phase is then followed by a plateau in which n_0 is maintained constant for 0.2 s. The thick filament activation n_0 is then brought back to its original value in 0.1 s. This corresponds to the diastole.

For a physiological simulation, we also need to select meaningful values for the transition rates. The physiological values of the attachment f and detachment g rates for cardiac muscle remain subject to debate [Månsson, 2010; Kimmig & Caruel, 2019] (see Chapter 3). Indeed, classically, muscle contraction models – deriving from Huxley'57 model – cannot reproduce at the sarcomere level both the force-velocity relation and the tension rise dynamics, showing that this description of the cycling process actually encompasses other molecular mechanisms whose dynamics is aggregated to the attachment and detachment rates. Depending on which physiological indicators is privileged for the model calibration, different values of the transition rates are obtained with a factor six difference. In this section, we will here test both possibilities.

On the one hand, we have the transition rates proposed by [Kimmig et al., 2019] when favoring the force-velocity curve. The attachment rate is $f_1(s) = \overline{f}_1 = 250\,\mathrm{s}^{-1}$ and the detachment rate is $g_1(s) = \overline{g}_1 = 60\,\mathrm{s}^{-1}$. To take into account that heads in the pool $\gamma = 0$ attach with a lower probability, we use $\overline{f}_0 = 0.01\overline{f}_1$ and $\overline{g}_0 = \overline{g}_1$. We call this choice of parameters the reference. On the other hand, if we focus on the tension rise dynamics, we typically have $f_1(s) = \overline{f}_1/6 = 41.6\,\mathrm{s}^{-1}$ and the detachment rate is $g_1(s) = \overline{g}_1/6 = 10\,\mathrm{s}^{-1}$ (see for instance [de Tombe & Stienen, 2007]) and again with the assumption $\overline{f}_0 = 0.01\overline{f}_1$ and $\overline{g}_0 = \overline{g}_1$. We additionally consider a non-physiological calibration for illustration purposes with $f_1(s) = \overline{f}_1/50 = 5\,\mathrm{s}^{-1}$ and $g_1(s) = \overline{g}_1/50 = 1.2\,\mathrm{s}^{-1}$ The simulation results for the two models considered and the three tested calibrations are presented in Figure 4.7.

We first comment on the evolution of the system with the two sets of physiological rates (Figure 4.7 left and middle columns). In the initial state, heads in both pools are attached with the steady-state probability $P_1(\gamma, t) = \overline{f}_\gamma/(\overline{f}_\gamma + \overline{g}_\gamma)$. In the systole, some heads switch from the pool $\gamma = 1$ to the pool $\gamma = 0$. Since the probability of being attached is higher in the pool $\gamma = 1$ than in the pool $\gamma = 0$, $P_1(\gamma = 0)$ increases. The probability of being attached in the pool $\gamma = 1$ remains unchanged. For both models, heads that change pool are equivalent, therefore, the way of choosing them does not matter and the evolution of $P_1(\gamma = 0)$ is the same for the two models. As soon as the heads are transferred in the other pool, the attachment-detachment dynamics leads to a return to the steady-state value of $P_1(\gamma = 0)$. Here, the time scale of the attachment-detachment dynamics is short compared to the duration of the plateau, at the end of the latter phase the heads thus have a probability of being attached in both pools that is almost equal to the steady-state probability. There is no memory of the "pool of origin". In the diastole, heads switch from the pool $\gamma = 0$ to the pool $\gamma = 1$. We have $P_1(\gamma = 1) > P_1(\gamma = 0)$, which implies that $P_1(\gamma = 1)$ decreases while $P_1(\gamma = 0)$ is almost constant (it is only varied by the attachment-detachment process). Since the state in the two models were the same at the end of the plateau, the evolution of $P_1(\gamma = 1)$ is the same for the two models.

The situation is different with the non-physiological transition rates (Figure 4.7 right column). The attachment-detachment dynamics time scale is not short compared to the plateau duration. Therefore, in the pool $\gamma = 0$ heads that swapped pools during the systole have a higher probability of being attached than the other heads of the pool. With the homogenized model, the probability $P_1(\gamma = 0)$ is not affected by the pool exchange in the diastole, since heads that leave the pool have the average probability of being attached and it is governed solely by the attachment-detachment dynamics. With the last-in first-out paradigm, the heads that switch from the pool $\gamma = 0$ to the pool $\gamma = 1$ are exactly those that were in the pool $\gamma = 1$ at the beginning of the simulation, they are precisely the heads that have a higher probability of being attached. As a result, the probabilities $P_1(\gamma = 1)$

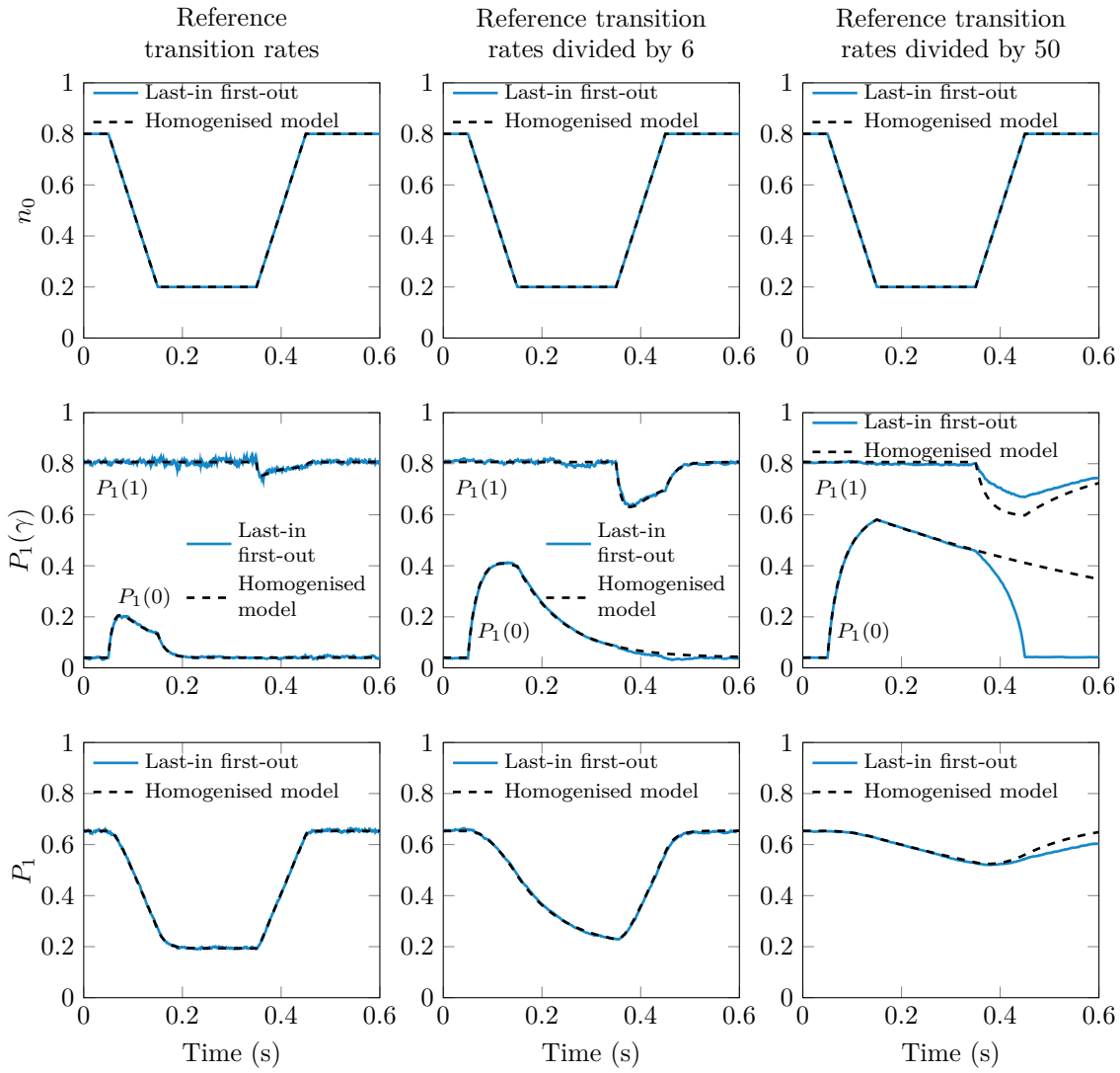

Figure 4.7 – Model comparison between the homogenized treatment of the myosin heads changing pool, and individual tracking of those head with the last-in first-out paradigm (quantities computed from 10000 stochastic trajectories). Note that the time scale of the transition between the pools is 0.15 s. The time scale of the attachment-detachment process is given by the duration of a cycle, which is given by $f^{-1} + g^{-1}$. Left column: simulation with reference transition rates targeting the force-velocity curve [Kimmig & Caruel, 2019] (Chapter 3). The time scale of the attachment-detachment process is 0.02 s. Center column: reference transition rates divided by a factor six to mimic the calibration proposed by [de Tombe & Stienen, 2007] aiming at capturing the force rise dynamics. The time scale of the attachment-detachment process is 0.12 s. Right column: reference transition rates divided by a factor fifty to illustrate the competition between the attachment-detachment time scale and the pool exchange time scale in the model. The time scale of the attachment-detachment process is 1 s.

and $P_1(\gamma = 0)$ retrieve their initial level – up to attachment-detachment transitions that have occurred in the plateau. In this configuration, the last-in first-out paradigm and the homogenized pool model provide different outputs that affect the total probability of being attached P_1 which will lead variations of the ultimate quantity of interest: the active force.

In a nutshell, the last-in first-out pool exchange paradigm differs from the homogenized model (or equivalently the random pool exchange paradigm) when the dynamics of the exchanges between the pools is fast compared to the attachment-detachment dynamics. The two paradigms are equivalent otherwise. It is *a priori* not possible to know which exchange paradigm – random, last-in first-out, or another paradigm – is at play at the microscopic level. However, this does not harm our modeling approach because the two pools are equivalent when physiological values of the transition rates and physiological variation time scales of the parameter function n_0 are considered. Therefore, our homogenized formulation is fully valid in the context of cardiac muscle modeling, independently of the uncertainty on the physiological transition rates.

In another situation where the difference between both paradigms may matter, additional experimental data should be sought. It would require structural experimental measurements that are capable of distinguishing the behavior of neighboring heads in a dynamical manner. To the best of our knowledge, state of the art structural measurements for cardiac muscle cells can only deal with steady states and describe the global behavior of the myosin heads population [Reconditi et al., 2017].

4.5.3 Comparison with previously proposed formulation

We now compare our formulation (4.14), aiming at a proper treatment of the myosin heads availability in the realm of the Huxley'57 contraction model family, with standard previous attempts (4.18) [Zahalak & Motabarzadeh, 1997; Chapelle et al., 2012].

We consider again a system where n_0 is imposed and we use the same time evolution of this input function as in Section 4.5.2.3. The results are presented in Figure 4.8. We can note that the two formulations depart from each other when $P_1(\gamma = 0)$ becomes significant.

With the model proposed by [Chapelle et al., 2012], a fraction $1-n_0$ of myosin heads is not allowed to attach. In the new formulation, it is equivalent to assume that $P_1(\gamma = 0) = 0$. When the attachment-detachment dynamics is fast compared to the pool dynamics, the myosin heads in the pool $\gamma = 0$ quickly detach and this assumption is approximately valid (see Figure 4.8(a)). The two formulations provide results that differ by about 10% at mid-end-systole.

However, when the cycling time scale is large compared to the myosin availability variations, we may have $P_1(\gamma = 0)$ significantly different from 0. In this case, the two formulation differ (see Figure 4.8(b)).

4.6 Discretization

To simulate numerically our model, we propose a dedicated discretization scheme. We base our analysis on the work done by Kimmig et al. [2019] (see Chapter 2) for the usual family of Huxley'57 models. The originality here is the addition of the pool exchange term in the numerical scheme and the introduction of a multi-step time scheme. As in [Kimmig et al., 2019], we establish a discretized version of the thermodynamical principles (4.25) and (4.35).

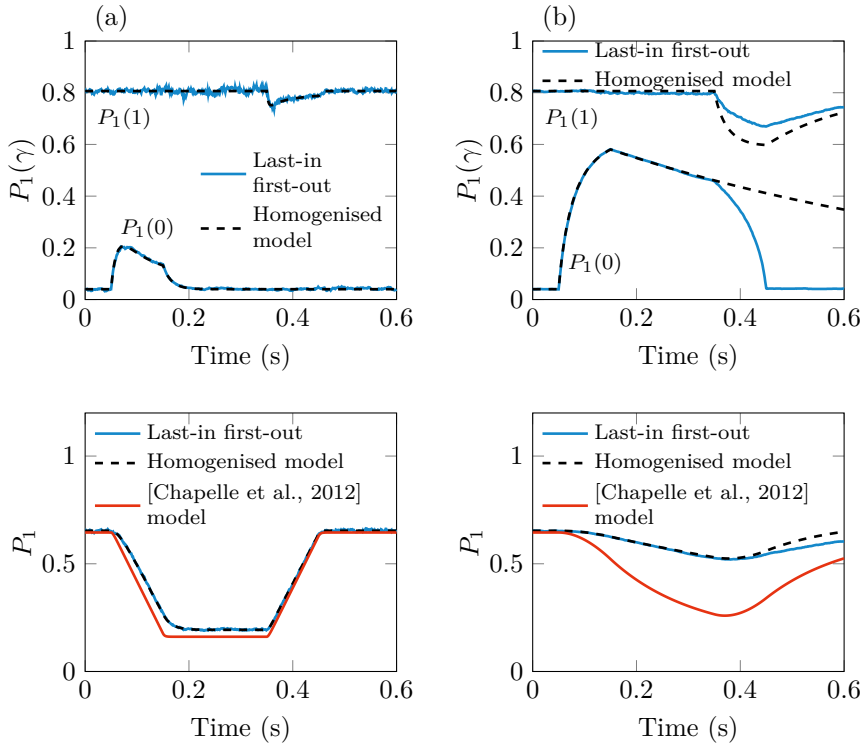

Figure 4.8 – Comparison between the proposed thick filament activation description and the literature standard. (a) Transition rates given by [Kimmig & Caruel, 2019] (Chapter 3). (b) Non-physiological transition rates that are 50 times slower than that of [Kimmig & Caruel, 2019].

To account for the different time scale in the muscle contraction, we propose here a multi-time-step numerical scheme. We consider here two time steps: a global time step Δt and a intermediate time step δt with $N\delta t = \Delta t$. The small time step is used at the microscopic level while the large time step is used to discretize the macroscopic dynamics. We index the global time iterations with n and, inside a global iteration, we index the intermediate iteration by k with the convention

$$a^{n,k=0} = a^n \quad \text{and} \quad a^{n,k=N} = a^{n+1},$$

for any variable a. The macroscopic internal variables – the variables of equations (4.39a) and (4.39b) – are only defined at the global time steps. The microscopic variables – the variables of equations (4.39c) – are defined at local time steps.

Note that we apply the following general notation rule: for any physical quantity, exponents designate discrete time instant and indices designate discrete space location.

4.6.1 Microscopic numerical scheme

We first present the numerical scheme for the microscopic dynamics.

The simulation range $[s^-, s^+]$ is discretized by a regular grid of discretization length δs and with the choice $s_0 = s^-$ and $s_\ell = s^+$. For the sake of compactness of the notation, we approximate $P_1(s^- + i\delta s, n\Delta t + k\delta t, 1)$ by $a_i^{n,k}$ and $P_1(s^- + i\delta s, n\Delta t + k\delta t, 0)$ by $b_i^{n,k}$.

For the chemical reaction term we use an implicit scheme, and an upwind implicit scheme for the transport term as proposed by [Kimmig et al., 2019] (Chapter 2). The pool exchanges terms are treated with a semi-explicit, semi-implicit scheme. The choice of such

a scheme is justified by the fact that it allows to establish a discrete energy balance (see Section (4.6.1.2)).

Note that the presentation will be restricted to positive sliding velocities $\dot{x}_c$ but the results can be straightforwardly extended to negative sliding velocities by reversing the space shift in the transport term so that the scheme keeps its upwind nature. The results for negative sliding velocities are given in Appendix (4.9.4).

We denote the discrete sliding velocity by

$$v_c^{n+\frac{1}{2}\sharp} = \ell_{hs}(e_c^{n+1} - e_c^n)/\Delta t \tag{4.43}$$

and we assume that it is positive (i.e. $e_c^{n+1} - e_c^n \geq 0$). We define $n_0^n = n_0(e_c^n)$.

The discretization scheme then reads

$$\begin{cases} \dfrac{a_i^{n,k+1} - a_i^{n,k}}{\delta t} = -\dfrac{|n_0^{n+1} - n_0^n|_+}{n_0^{n,k+1}\Delta t}\Big[a_i^{n,k} - b_i^{n,k}\Big] + (k_{+,1,i} + k_{-,1,i}^{\mathrm{rev}})(1 - a_i^{n,k+1}) \\ \qquad\qquad - (k_{-,1,i} + k_{+,1,i}^{\mathrm{rev}})a_i^{n,k+1} - v_c^{n+\frac{1}{2}\sharp}\dfrac{a_i^{n,k+1} - a_{i-1}^{n,k+1}}{\delta s}, \forall i \in [\![1, \ell]\!] \\ \dfrac{b_i^{n,k+1} - b_i^{n,k}}{\delta t} = -\dfrac{|n_0^{n+1} - n_0^n|_-}{(1 - n_0^{n,k+1})\Delta t}\Big[b_i^{n,k} - a_i^{n,k}\Big] + (k_{+,0,i} + k_{-,0,i}^{\mathrm{rev}})(1 - b_i^{n,k+1}) \\ \qquad\qquad - (k_{-,0,i} + k_{+,0,i}^{\mathrm{rev}})b_i^{n,k+1} - v_c^{n+\frac{1}{2}\sharp}\dfrac{b_i^{n,k+1} - b_{i-1}^{n,k+1}}{\delta s}, \forall i \in [\![1, \ell]\!] \end{cases} \tag{4.44}$$

with the definition

$$\begin{vmatrix} k_{+,1,i} = k_{+,1}(s^- + i\delta s) & \text{and} & k_{+,1,i}^{\mathrm{rev}} = k_{+,1}^{\mathrm{rev}}(s^- + i\delta s), & \forall i \in [\![1, \ell]\!] \\ k_{+,0,i} = k_{+,0}(s^- + i\delta s) & \text{and} & k_{+,0,i}^{\mathrm{rev}} = k_{+,0}^{\mathrm{rev}}(s^- + i\delta s), & \forall i \in [\![1, \ell]\!] \\ k_{-,1,i} = k_{-,1}(s^- + i\delta s) & \text{and} & k_{-,1,i}^{\mathrm{rev}} = k_{-,1}^{\mathrm{rev}}(s^- + i\delta s), & \forall i \in [\![1, \ell - 1]\!] \\ k_{-,0,i} = k_{-,0}(s^- + i\delta s) & \text{and} & k_{-,0,i}^{\mathrm{rev}} = k_{-,0}^{\mathrm{rev}}(s^- + i\delta s), & \forall i \in [\![1, \ell - 1]\!] \\ k_{-,1,\ell} = 2k_{-,1,\ell-1} & \text{and} & k_{+,1,\ell}^{\mathrm{rev}} = 2k_{+,1,\ell-1}^{\mathrm{rev}}, & \\ k_{-,0,\ell} = 2k_{-,0,\ell-1} & \text{and} & k_{+,0,\ell}^{\mathrm{rev}} = 2k_{+,0,\ell-1}^{\mathrm{rev}}, & \end{vmatrix} \tag{4.45}$$

and

$$n_0^{n,k} = n_0^n + k\frac{\delta t}{\Delta t}\Big(n_0^{n+1} - n_0^n\Big).$$

We define the aggregated attachment and detachment rate by $f_{\gamma,i} = k_{+,\gamma,i} + k_{-,\gamma,i}^{\mathrm{rev}}$ and $g_{\gamma,i} = k_{-,\gamma i} + k_{+,\gamma,i}^{\mathrm{rev}}$, respectively. Note that the numerical aggregated detachment rates differ from their analytical counterparts, which go to infinity on the boundaries of the interval $[s^-, s^+]$. Indeed, as proposed by Kimmig et al. [2019] (Chapter 2), we use instead a consistent finite approximation. The choice of the boundary conditions follows that of Kimmig et al. [2019] as well. We impose periodic boundary conditions for $a^{n,k}$ and $b^{n,k}$. We have $a_0^{n,k} = a_\ell^{n,k}$ and $b_0^{n,k} = b_\ell^{n,k}$. The initialisation of the discretization is done such that $a_0^0 = a_\ell^0 = 0$ and $b_0^0 = b_\ell^0 = 0$. Moreover, we impose that a_i^0 and $b_i^0 \in [0, 1],\ \forall n, \forall i \in [\![1, \ell]\!]$ to be consistent with the definition of a_i^0 and b_i^0 as probabilities.

Defining

$$\begin{vmatrix} \alpha^{n+\frac{1}{2}\sharp} = \ell_{hs}(e_c^{n+1} - e_c^n)/\Delta t \cdot \delta t/\delta s, \\ \beta_{1,i}^{n+\frac{1}{2}\sharp} = \delta t\big(k_{+,1,i} + k_{+,1,i}^{\mathrm{rev}} + k_{-,1,i} + k_{-,1,i}^{\mathrm{rev}}\big) + \alpha^{n+\frac{1}{2}\sharp}, \\ \beta_{0,i}^{n+\frac{1}{2}\sharp} = \delta t\big(k_{+,0,i} + k_{+,0,i}^{\mathrm{rev}} + k_{-,0,i} + k_{-,0,i}^{\mathrm{rev}}\big) + \alpha^{n+\frac{1}{2}\sharp}, \end{vmatrix}$$

the numerical scheme can be written in a vectorial form using the state vector

$$\underline{P}^{n,k} = \begin{bmatrix} a_1^{n,k} & \dots & a_\ell^{n,k} & b_1^{n,k} & \dots & b_\ell^{n,k} \end{bmatrix}^\mathsf{T}.$$

The system (4.45) becomes

$$(\mathbb{I}_d + \mathbb{I}^{n+\frac{1}{2}\sharp})\underline{P}^{n,k+1} = (\mathbb{I}_d - \mathbb{E}^{n,k+1})\underline{P}^{n,k} + \delta t \underline{f},$$

where $\mathbb{I}_d$ is the $2\ell \times 2\ell$ identity matrix

$$\mathbb{I}^{n+\frac{1}{2}\sharp} = \left[\begin{array}{cccc|cccc} \beta_{1,1}^{n+\frac{1}{2}\sharp} & & & -\alpha^{n+\frac{1}{2}\sharp} & & & & \\ -\alpha^{n+\frac{1}{2}\sharp} & \beta_{1,2}^{n+\frac{1}{2}\sharp} & & & & & & \\ & \ddots & \ddots & & & & & \\ & & -\alpha^{n+\frac{1}{2}\sharp} & \beta_{1,\ell}^{n+\frac{1}{2}\sharp} & & & & \\ \hline & & & & \beta_{0,1}^{n+\frac{1}{2}\sharp} & & & -\alpha^{n+\frac{1}{2}\sharp} \\ & & & & -\alpha^{n+\frac{1}{2}\sharp} & \beta_{0,2}^{n+\frac{1}{2}\sharp} & & \\ & & & & & \ddots & \ddots & \\ & & & & & & -\alpha^{n+\frac{1}{2}\sharp} & \beta_{0,\ell}^{n+\frac{1}{2}\sharp} \end{array}\right],$$

$$\mathbb{E}_1 = \left[\begin{array}{cccc|cccc} 1 & & & & -1 & & & \\ & 1 & & & & -1 & & \\ & & 1 & & & & -1 & \\ & & & 1 & & & & -1 \\ \hline & & & & & & & \\ & & & & & & & \\ & & & & & & & \\ & & & & & & & \end{array}\right], \quad \mathbb{E}_0 = \left[\begin{array}{cccc|cccc} & & & & & & & \\ & & & & & & & \\ & & & & & & & \\ & & & & & & & \\ \hline -1 & & & & 1 & & & \\ & -1 & & & & 1 & & \\ & & -1 & & & & 1 & \\ & & & -1 & & & & 1 \end{array}\right],$$

$$\underline{f} = \begin{bmatrix} f_{1,1}, f_{1,2}, \dots, f_{1,\ell}, f_{0,1}, f_{0,2}, \dots, f_{0,\ell} \end{bmatrix}^\mathsf{T},$$

$$\text{and } \mathbb{E}^{n,k+1} = \frac{|n_0^{n+1} - n_0^n|_+}{n_0^{n,k+1}} \frac{\delta t}{\Delta t} \mathbb{E}_1 + \frac{|n_0^{n+1} - n_0^n|_-}{1 - n_0^{n,k+1}} \frac{\delta t}{\Delta t} \mathbb{E}_0.$$

4.6.1.1 Uniform positivity and - boundness

We want to ensure that, at all time steps and all spatial positions, the numerical solutions $a_i^{n,k}$ and $b_i^{n,k}$ satisfy the property

$$0 \le a_i^{n,k} \le 1 \quad \text{and} \quad 0 \le b_i^{n,k} \le 1 \quad \Longleftrightarrow \quad 0 \le \underline{P}^{n,k} \le 1, \ \forall n \in \mathbb{N}, \forall k \in [\![0, N]\!],$$

with the convention that a vector is positive if each of its components are positive. This property allows to keep the interpretation of $a_i^{n,k}$ and $b_i^{n,k}$ as probabilities but it is also essential from a numerical point of view since some thermodynamic quantities that are involves in thermodynamic, requires to evaluate the logarithm of the probabilities of being attached. We proceed recursively and we assume that

$$0 \le \underline{P}^{n,k} \le 1. \tag{4.46}$$

We introduce the vector $\underline{1} - \underline{P}^{n,k}$, whose dynamics is governed by

$$(\mathbb{I}_d + \mathbb{I}^{n+\frac{1}{2}\sharp})(\underline{1} - \underline{P}^{n,k+1}) = (\mathbb{I}_d - \mathbb{E}^{n,k+1})(\underline{1} - \underline{P}^{n,k}) + \delta t \underline{g}.$$

We want to show that

$$\left| \begin{array}{l} 0 \leq \underline{P}^{n,k+1}, \\ 0 \leq \underline{1} - \underline{P}^{n,k+1}. \end{array} \right. \tag{4.47}$$

We know from [Kimmig et al., 2019] (Chapter 2), that the matrix $\mathbb{I}_d + \mathbb{I}^{n+\frac{1}{2}\sharp}$ preserves the positivity – ie. $\forall \underline{P} \in \mathbb{R}^{2\ell}$, $(\mathbb{I}_d + \mathbb{I}^{n+\frac{1}{2}\sharp})\underline{P} \geq 0 \Rightarrow \underline{P} \geq 0$. Therefore, the desired property $0 \leq \underline{P}^{n,k+1} \leq 1$ is obtained if

$$(\mathbb{I}_d - \mathbb{E}^{n,k+1})\underline{P}^{n,k} + \delta t \underline{f} \geq 0 \quad \text{and} \quad (\mathbb{I}_d - \mathbb{E}^{n,k+1})(\underline{1} - \underline{P}^{n,k}) + \delta t \underline{g} \geq 0.$$

A sufficient condition is given by

$$\left| \begin{array}{l} 0 \leq \Big(1 - \delta t \dfrac{|n_0^{n+1} - n_0^n|_+}{n_0^{n,k+1}\Delta t}\Big) a_i^{n,k} + \delta t \dfrac{|n_0^{n+1} - n_0^n|_+}{n_0^{n,k+1}\Delta t} b_i^{n,k} + \delta t f_{1,i} \\ 0 \leq \delta t \dfrac{|n_0^{n+1} - n_0^n|_+}{n_0^{n,k+1}\Delta t} a_i^{n,k} + \Big(1 - \delta t \dfrac{|n_0^{n+1} - n_0^n|_-}{(1 - n_0^{n,k+1})\Delta t}\Big) b_i^{n,k} + \delta t f_{0,i} \\ 0 \leq \Big(1 - \delta t \dfrac{|n_0^{n+1} - n_0^n|_+}{n_0^{n,k+1}\Delta t}\Big)(1 - a_i^{n,k}) + \delta t \dfrac{|n_0^{n+1} - n_0^n|_+}{n_0^{n,k+1}\Delta t}(1 - b_i^{n,k}) + \delta t g_{1,i} \\ 0 \leq \delta t \dfrac{|n_0^{n+1} - n_0^n|_+}{n_0^{n,k+1}\Delta t}(1 - a_i^{n,k}) + \Big(1 - \delta t \dfrac{|n_0^{n+1} - n_0^n|_-}{(1 - n_0^{n,k+1})\Delta t}\Big)(1 - b_i^{n,k}) + \delta t g_{0,i}. \end{array} \right. \tag{4.48}$$

Knowing that $0 \leq a_i^{n,k} \leq 1$ and $0 \leq b_i^{n,k} \leq 1$ from (4.46), we have the property (4.48) if δt satisfies the (not optimal) CFL-like condition

$$\delta t \leq \min\Big(\frac{n_0^{n+1}}{|n_0^{n+1} - n_0^n|_+}\Delta t, \frac{1 - n_0^{n+1}}{|n_0^{n+1} - n_0^n|_-}\Delta t\Big). \tag{4.49}$$

In all numerical results presented in what follows, we will make sure that this conditions is satisfied.

4.6.1.2 First principle

We now aim at establishing a discrete counterpart to the continuous first principle (4.25). We only present here the main results; their detailed proof is given in Section 4.9.3.1. We discretise the attached state energy level on $[s^-, s^+]$ by

$$\left| \begin{array}{l} w_{1,i} = w_1(s^- + i\delta s), \ \forall i \in [\![1, \ell - 1]\!] \\ w_{1,\ell} = 2w_{1,\ell-1}. \end{array} \right.$$

We define the discrete average energy per myosin head by

$$\mathcal{U}^{n,k} = \frac{\delta s}{d_a} \sum_{i=1}^{\ell} \Big[w_{1,i}\big(n_0^{n,k} a_i^{n,k} + (1 - n_0^{n,k}) b_i^{n,k}\big) + w_0\big(n_0^{n,k}(1 - a_i^{n,k}) + (1 - n_0^{n,k})(1 - b_i^{n,k})\big)\Big]. \tag{4.50}$$

Defining the attachment-detachment fluxes as

$$\left|\begin{aligned} J^{n,k}_{+,1,i} &= k_{+,1,i} a_i^{n,k} - k^{\text{rev}}_{+,1,i}(1-a_i^{n,k}),\\ J^{n,k}_{+,0,i} &= k_{+,0,i} b_i^{n,k} - k^{\text{rev}}_{+,0,i}(1-b_i^{n,k}),\\ J^{n,k}_{-,1,i} &= k_{-,1,i}(1-a_i^{n,k}) - k^{\text{rev}}_{-,1,i} a_i^{n,k},\\ J^{n,k}_{-,1,i} &= k_{-,0,i}(1-b_i^{n,k}) - k^{\text{rev}}_{-,0,i} b_i^{n,k}, \end{aligned}\right. \tag{4.51}$$

we obtain the first principle formulation at local time steps

$$\frac{\mathcal{U}^{n,k+1}-\mathcal{U}^{n,k}}{\delta t} = \frac{\mathcal{W}^{n,k+1}-\mathcal{W}^{n,k}}{\delta t} + \frac{\mathcal{Q}^{n,k+1}-\mathcal{Q}^{n,k}}{\delta t} + \frac{\mathcal{E}^{n,k+1}-\mathcal{E}^{n,k}}{\delta t}, \tag{4.52}$$

with

$$\left|\begin{aligned} \frac{\mathcal{W}^{n,k+1}-\mathcal{W}^{n,k}}{\delta t} &= v_c^{n+\frac{1}{2}\sharp}\tau_c^{n,k+1}, && (4.53)\\ \frac{\mathcal{Q}^{n,k+1}-\mathcal{Q}^{n,k}}{\delta t} &= \frac{\delta s}{d_a}\sum_{i=1}^{\ell}\Big[\Big(n_0^{n,k+1}J^{n,k+1}_{+,1,i} + (1-n_0^{n,k+1})J^{n,k+1}_{+,0,i}\Big)(w_{1,i}-w_0)\\ &\qquad + \Big(n_0^{n,k+1}J^{n,k+1}_{-,1,i} + (1-n_0^{n,k+1})J^{n,k+1}_{-,0,i}\Big)\big(w_0-(w_{1,i}+\mu_T)\big)\Big], && (4.54)\\ \frac{\mathcal{E}^{n,k+1}-\mathcal{E}^{n,k}}{\delta t} &= \mu_T\frac{\delta s}{d_a}\sum_{i=1}^{\ell}\Big(n_0^{n,k+1}J^{n,k+1}_{-,1,i} + (1-n_0^{n,k+1})J^{n,k+1}_{-,0,i}\Big), && (4.55) \end{aligned}\right.$$

where the force per myosin head $\tau_c^{n,k+1}$ is defined by

$$\tau_c^{n,k+1} = \frac{\delta s}{d_a}\sum_{i=1}^{\ell}\frac{w_{1,i+1}-w_{1,i}}{\delta s}\Big(n_0^{n,k+1}a^{n,k+1} + (1-n_0^{n,k+1})b^{n,k+1}\Big).$$

4.6.1.3 Second principle

As for the first principle, we only present here the results; their detailed proof is given in Section 4.9.3.2.

To derive a discrete version of the second principle, we first define the chemical potentials in each pool

$$\left|\begin{aligned} \mu^{n,k}_{\alpha=1,\gamma=1,i} &= \mu^{n,k}_{1,1,i} = w_{1,i} + k_B T \ln a_i^{n,k}, && (4.56a)\\ \mu^{n,k}_{\alpha=1,\gamma=0,i} &= \mu^{n,k}_{1,0,i} = w_{1,i} + k_B T \ln b_i^{n,k}, && (4.56b)\\ \mu^{n,k}_{\alpha=0,\gamma=1,i} &= \mu^{n,k}_{0,1,i} = w_0 + k_B T \ln(1-a_i^{n,k}), && (4.56c)\\ \mu^{n,k}_{\alpha=0,\gamma=0,i} &= \mu^{n,k}_{0,0,i} = w_0 + k_B T \ln(1-b_i^{n,k}). && (4.56d) \end{aligned}\right.$$

We define the entropy per myosin head as

$$\frac{\mathcal{S}^{n,k}}{k_B} = -\frac{\delta s}{d_a}\sum_{i=1}^{\ell}\Big[n_0^{n,k}\Big(a_i^{n,k}\ln a_i^{n,k} + (1-a_i^{n,k})\ln(1-a_i^{n,k})\Big) + (1-n_0^{n,k})\Big(b_i^{n,k}\ln b_i^{n,k} + (1-b_i^{n,k})\ln(1-b_i^{n,k})\Big)\Big].$$

Note that the entropy is well defined for $a^{n,k} \in [0,1]$ and $b^{n,k} \in [0,1]$.

Using the numerical scheme (4.44), we obtain the second principle inequality

$$\frac{\mathcal{S}^{n,k+1}-\mathcal{S}^{n,k}}{\delta t} \geq \frac{1}{T}\frac{\mathcal{Q}^{n,k+1}-\mathcal{Q}^{n,k}}{\delta t}, \text{ for } a^{n,k}\in[0,1] \text{ and } b^{n,k}\in[0,1],\ \forall n,\forall k. \tag{4.57}$$

If the property $a^{n,k}\in]0,1[$ and $b^{n,k}\in]0,1[,\ \forall n,\forall k$ holds, we can give an explicit expression of the the entropy creation and we have

$$\frac{\mathcal{S}^{n,k+1}-\mathcal{S}^{n,k}}{\delta t} = \frac{\mathcal{S}^{n,k+1}_{\text{prod}}-\mathcal{S}^{n,k}_{\text{prod}}}{\delta t} + \frac{1}{T}\frac{\mathcal{Q}^{n,k+1}-\mathcal{Q}^{n,k}}{\delta t}, \tag{4.58}$$

with

$$\begin{aligned}
\frac{\mathcal{S}^{n,k+1}_{\text{prod}}-\mathcal{S}^{n,k}_{\text{prod}}}{\delta t} =& \\
&- \left(n_0^{n,k+1}\frac{1}{T}\frac{\delta s}{d_a}\sum_{i=1}^{\ell}\left[J^{n,k+1}_{+,1,i}\left(\mu^{n,k+1}_{1,1,i}-\mu^{n,k+1}_{0,1,i}\right) + J^{n,k+1}_{-,1,i}\left(\mu^{n,k+1}_{0,1,i}-\mu^{n,k+1}_{1,1,i}-\mu_T\right)\right]\right. \\
&\quad + (1-n_0^{n,k+1})\frac{1}{T}\frac{\delta s}{d_a}\sum_{i=1}^{\ell}\left[J^{n,k+1}_{+,0,i}\left(\mu^{n,k+1}_{1,0,i}-\mu^{n,k+1}_{0,0,i}\right)\right. \\
&\quad\quad \left.\left. + J^{n,k+1}_{-,0,i}\left(\mu^{n,k+1}_{0,0,i}-\mu^{n,k+1}_{1,0,i}-\mu_T\right)\right]\right) \\
&- v_c^{n,k+\frac{1}{2}\sharp}k_B\left(n_0^{n,k+1}\frac{1}{d_a}\sum_{i=1}^{\ell}\left[a_i^{n,k+1}\ln\left(\frac{a_{i+1}^{n,k+1}}{a_i^{n,k+1}}\right) + (1-a_i^{n,k+1})\ln\left(\frac{1-a_{i+1}^{n,k+1}}{1-a_i^{n,k+1}}\right)\right]\right. \\
&\quad \left.\left. + (1-n_0^{n,k+1})\frac{1}{d_a}\sum_{i=1}^{\ell}\left[b_i^{n,k+1}\ln\left(\frac{b_{i+1}^{n,k+1}}{b_i^{n,k+1}}\right) + (1-b_i^{n,k+1})\ln\left(\frac{1-b_{i+1}^{n,k+1}}{1-b_i^{n,k+1}}\right)\right]\right) \\
&- \frac{k_B}{\delta t}\left(n_0^{n,k+1}\frac{\delta s}{d_a}\sum_{i=1}^{\ell}\left[a_i^{n,k}\ln\left(\frac{a_i^{n,k+1}}{a_i^{n,k}}\right) + (1-a_i^{n,k})\ln\left(\frac{1-a_i^{n,k+1}}{1-a_i^{n,k}}\right)\right]\right) \\
&\quad + (1-n_0^{n,k+1})\frac{\delta s}{d_a}\sum_{i=1}^{\ell}\left[b_i^{n,k}\ln\left(\frac{b_i^{n,k+1}}{b_i^{n,k}}\right) + (1-b_i^{n,k})\ln\left(\frac{1-b_i^{n,k+1}}{1-b_i^{n,k}}\right)\right]\Big) \\
&- k_B\frac{|n_0^{n,k+1}-n_0^{n,k}|_+}{\delta t}\frac{\delta s}{d_a}\sum_{i=1}^{\ell}\left[b_i^{n,k}\ln\left(\frac{a_i^{n,k+1}}{b_i^{n,k}}\right) + (1-b_i^{n,k})\ln\left(\frac{1-a_i^{n,k+1}}{1-b_i^{n,k}}\right)\right] \\
&- k_B\frac{|n_0^{n,k+1}-n_0^{n,k}|_-}{\delta t}\frac{\delta s}{d_a}\sum_{i=1}^{\ell}\left[a_i^{n,k}\ln\left(\frac{a_i^{n,k}}{b_i^{n,k+1}}\right) + (1-a_i^{n,k})\ln\left(\frac{1-a_i^{n,k}}{1-b_i^{n,k+1}}\right)\right]
\end{aligned}$$

satisfying the inequality

$$\frac{\mathcal{S}^{n,k+1}_{\text{prod}}-\mathcal{S}^{n,k}_{\text{prod}}}{\delta t} \geq 0.$$

If we re-write the second principle under the form of an inequality on the free energy, we have for $a^{n,k}\in[0,1]$ and $b^{n,k}\in[0,1]$

$$\begin{aligned}
\frac{\mathcal{F}^{n,k+1}-\mathcal{F}^{n,k}}{\delta t} &= \frac{\mathcal{U}^{n,k+1}-\mathcal{U}^{n,k}}{\delta t} - T\frac{\mathcal{S}^{n,k+1}-\mathcal{S}^{n,k}}{\delta t} \\
&\leq \frac{\mathcal{W}^{n,k+1}-\mathcal{W}^{n,k}}{\delta t} + \frac{\mathcal{E}^{n,k+1}-\mathcal{E}^{n,k}}{\delta t}.
\end{aligned} \tag{4.59}$$

4.6.2 Numerical illustration

To illustrate the discrete thermodynamic balance, we perform a simulation of the equations (4.44) in a single time step scheme, i.e. $\delta t = \Delta t$. The evolution of the sliding velocity is imposed over time. Note that this is equivalent to imposing the extension e_c^n from an initial condition e_c^0 because these two quantities are linked through (4.43). We choose here the initial condition $e_c^0 = 0.06$ and a time step $\Delta t = 0.01\,\mathrm{ms}$. The myosin head population is initially in a configuration in which all heads are detached.

The simulation starts with an isometric tension rise phase; the extension e_c^n remains constant. After a duration that is sufficient for the active force to reach its peak isometric value, the sarcomere is progressively shortened until reaching a steady-state shortening velocity of $-1\,\mu\mathrm{m\,s}^{-1}$.

The dependency between the ratio of available heads n_0 and the extension e_c is the same as the function that will be used for the simulation of physiological heart beats, which is presented in Figure 4.11(a). For the simulation, we use the transition rates and energy levels presented in Figure 4.9. Note that these input parameters function are not meant to match experimental data characterizing the physiological behavior of cardiac muscles. They are only designed to provide reasonable input parameters.

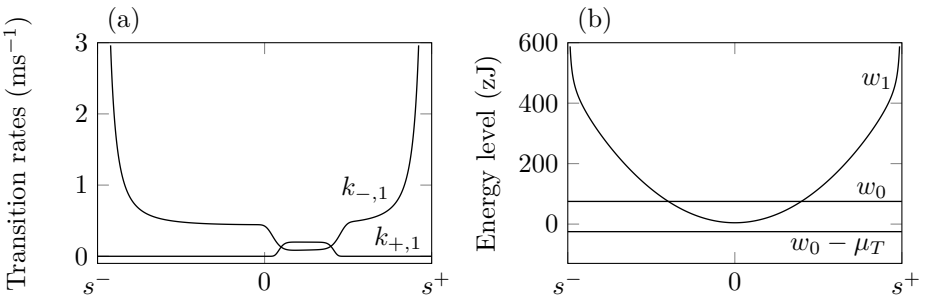

Figure 4.9 – Input parameter functions for the numerical illustration. (a) Forward transition rates for the pool $\gamma = 1$. The reverse transition rates are determined from the forward transition rate along with the energy levels by the detailed balance (4.6). The transition rates in the pool $\gamma = 0$ are obtained with the relations $k_{+,0} = 0.01 k_{+,1}$ and $k_{-,0} = k_{-,1}$. (b) Energy levels of the attached and detached states.

The results are presented in Figure 4.10. It can first be checked that the CFL condition (4.49) is satisfied in this simulation. In the initial isometric phase, myosin heads attach and the developed force increases. In the shortening phase, the tension decreases due to two factors. When the sarcomere shortens, the force is reduced compared to isometric conditions following the classical force-velocity relation. Simultaneously, the decreases of the sarcomere extension implies a decrease in the number of available myosin heads (as shown by the decrease of $n_0(e_c)$) and thus of the force.

Being able to write consistent thermodynamical balances at discrete level allows to investigate the elements of the energy transduction performed by the molecular motors. The work production, which is zero in the absence of displacement, grows as the muscle starts to shorten. Note that the work rate is negative because, in our length controlled numerical experiment, the mechanical energy is transferred from the system to the environment. We now consider the consumption of chemical energy brought by ATP. As myosin heads start to cycle in the tension rise phase, the consumption of ATP increases. In the shortening phase, myosin heads are transported in a region where the detachment rate is higher. The cycling rate increases, leading to a higher consumption of ATP. We can note that the consumption of ATP is always strictly positive, even when no work is

produced. This highlights the active nature of muscle contraction, i.e. the force is developed "in exchange" of a continuous supply in chemical energy. One can also note that, as expected, the entropy production term is always positive. Note that with the initial conditions ($a_i^0 = b_i^0 = 0,\ \forall i \in [\![1, \ell]\!]$) and the entropy creation term is thus not defined. After the first time step, the numerical noise combined with the non-divergence of the detachment rates on the boundaries of the interval $[s^-, s^+]$ induce that we have, for all $n > 0$ and all $i \in [\![0, \ell]\!]$, the property $a_i^n \in]0, 1[$ and $b_i^n \in]0, 1[$. The entropy creation term is thus defined for $n > 0$.

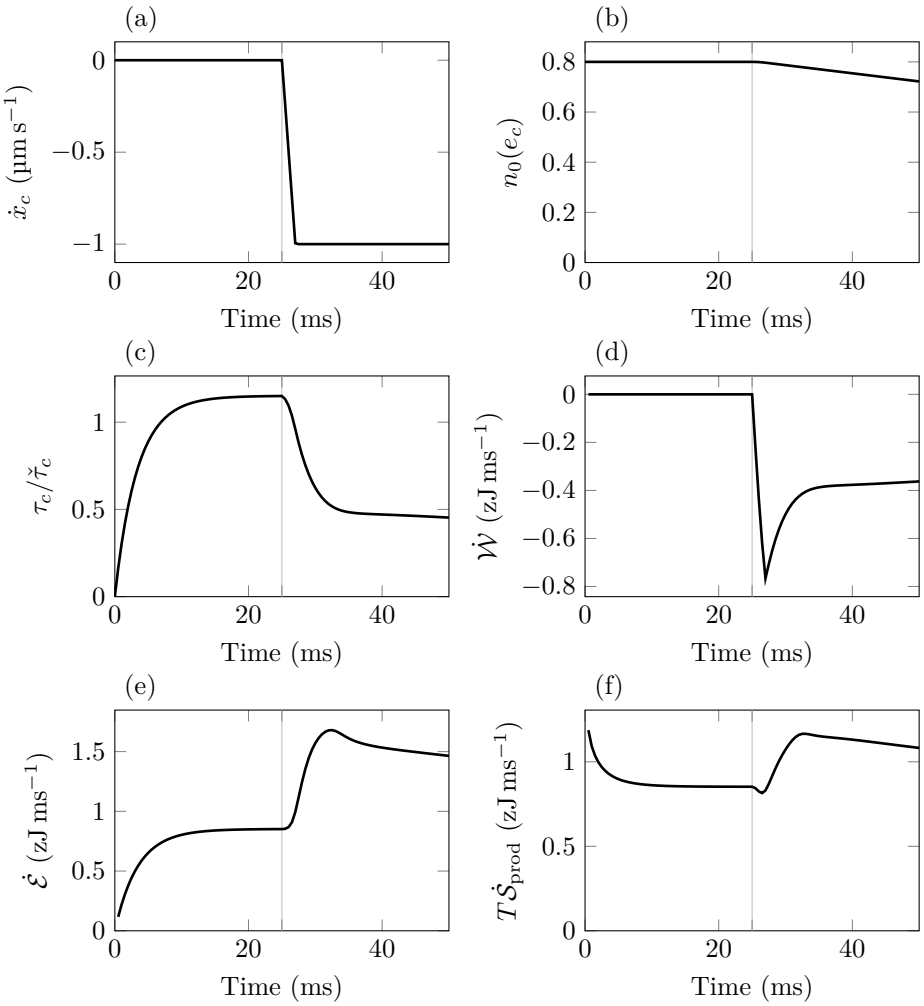

Figure 4.10 – Simulation of the microscopic contraction model (4.14) with an imposed extension e_c^n time evolution. (a) Sliding velocity. (b) Ratio of heads in the pool $\gamma = 1$. (c) Normalized average force per myosin head. (d) Work rate per myosin head. (e) Energy input rate per myosin head. (f) Entropy production rate per myosin head multiplied by the temperature.

Note that a validation of the established discrete thermodynamic principles is presented in Appendix 4.9.5.

4.6.3 Link with discrete macro model: a multi-time step strategy

4.6.3.1 Macroscopic time scheme

We recall here the time scheme proposed in Kimmig et al. [2019] (Chapter 2) to discretize the macroscopic part of the system (4.39) and we extend it to embed the microscopic time scale dynamics in a multi-time step manner.

The numerical scheme reads

$$\begin{cases} \dfrac{\underline{y}^{n+1}-\underline{y}^{n}}{\Delta t} = \underline{v}^{n+\frac{1}{2}} = \dfrac{\underline{v}^{n+1}+\underline{v}^{n}}{2} & \text{(4.60a)} \\[2ex] \displaystyle\int_{\Omega^0} \rho_0 \frac{\underline{v}^{n+1}-\underline{v}^{n}}{\Delta t}\cdot\underline{w}\,\mathrm{d}\Omega + \int_{\Omega^0} \underline{\underline{\Sigma}}^{n+\frac{1}{2}\sharp} : \mathrm{d}_{\underline{y}}\underline{\underline{e}}^{n+\frac{1}{2}\sharp}\cdot\underline{w}\,\mathrm{d}\Omega = \mathcal{P}_{\mathrm{ext}}^{n+\frac{1}{2}}(\underline{w}),\ \forall \underline{w}\in\mathscr{V}_{\mathrm{ad}} \\ \qquad \text{with } \underline{\underline{\Sigma}}^{n+\frac{1}{2}\sharp} = \dfrac{\partial\Psi}{\partial\underline{\underline{e}}}\Big|^{n+\frac{1}{2}\sharp} + \eta\dfrac{\underline{\underline{e}}^{n+1}-\underline{\underline{e}}^{n}}{\Delta t} + \dfrac{T_{\mathrm{fib}}^{n+\frac{1}{2}\sharp}}{(1+2\underline{\tau}\cdot\underline{\underline{e}}^{n}\cdot\underline{\tau})^{\frac{1}{2}}}\underline{\tau}\otimes\underline{\tau} & \text{(4.60b)} \\[2ex] T_{\mathrm{fib}}^{n+\frac{1}{2}\sharp} = \nu\dfrac{\dot{e}_c^{n+1}-\dot{e}_c^{n}}{\Delta t} + T_c^{n+1} = E_s e_s^{n+\frac{1}{2}} \\ \qquad \text{with } T_c^{n+1} = \rho_{\mathrm{surf}}\dfrac{\delta t}{\Delta t}\displaystyle\sum_{k=0}^{N-1}\tau_c^{n,k+1} & \text{(4.60c)} \end{cases}$$

where we define

$$\underline{v}^{n+\frac{1}{2}} = \frac{v^{n+1}-v^{n}}{\delta t},\quad \underline{\underline{e}}^{n+\frac{1}{2}\sharp} = \underline{\underline{e}}(\underline{y}^{n+\frac{1}{2}}),\quad \dot{\underline{\underline{e}}}^{n+\frac{1}{2}\sharp} = \frac{\underline{\underline{e}}^{n+1}-\underline{\underline{e}}^{n}}{\delta t},$$
$$\mathrm{d}_{\underline{y}}\underline{\underline{e}}^{n+\frac{1}{2}\sharp}\cdot\underline{w} = \frac{1}{2}\Big(\nabla\underline{w} + (\nabla\underline{w})^{\mathsf{T}} + (\nabla\underline{y}^{n+\frac{1}{2}})^{\mathsf{T}}\cdot\nabla\underline{w} + (\nabla\underline{w})^{\mathsf{T}}\cdot\nabla\underline{y}^{n+\frac{1}{2}}\Big),$$

and

$$\frac{\partial\Psi}{\partial\underline{\underline{e}}}\Big|^{n+\frac{1}{2}\sharp} = \frac{\partial\Psi}{\partial\underline{\underline{e}}}(\underline{\underline{e}}^{n+\frac{1}{2}\sharp}) + \left(\frac{\Psi(\underline{\underline{e}}^{n+1})-\Psi(\underline{\underline{e}}^{n})}{\delta t} - \frac{\partial\Psi}{\partial\underline{\underline{e}}}(\underline{\underline{e}}^{n+\frac{1}{2}\sharp}) : \dot{\underline{\underline{e}}}^{n+\frac{1}{2}\sharp}\right)\frac{\dot{\underline{\underline{e}}}^{n+\frac{1}{2}\sharp}}{\dot{\underline{\underline{e}}}^{n+\frac{1}{2}\sharp} : \dot{\underline{\underline{e}}}^{n+\frac{1}{2}\sharp}}.$$

The question that arises, when linking the time micro- and macro-dynamics, is how to properly define the macroscopic active tension T_c^{n+1} as a function of the microscopic variables. The choice made in (4.60c) will be motivated in Section (4.6.3.2) with a use of the discrete thermodynamic balance to tackle this issue.

It is important to note that the equations in (4.60) must be written at each quadrature point. For the sake of compactness, this spatial dependency is omitted here.

4.6.3.2 First principle at global time steps

At global time step, we have

$$\frac{\mathcal{U}^{n+1}-\mathcal{U}^{n}}{\Delta t} = \frac{\delta t}{\Delta t}\sum_{k=0}^{N-1}\frac{\mathcal{U}^{n,k+1}-\mathcal{U}^{n,k}}{\delta t}$$

Using the micro time step energy balance (4.52), we have

$$\begin{aligned}\frac{\mathcal{U}^{n+1}-\mathcal{U}^{n}}{\Delta t} &= \frac{\delta t}{\Delta t}\sum_{k=0}^{N-1} v_c^{n+\frac{1}{2}\sharp}\tau_c^{n,k+1} + \frac{\delta t}{\Delta t}\sum_{k=0}^{N-1}\left[\frac{\mathcal{Q}^{n,k+1}-\mathcal{Q}^{n,k}}{\delta t}+\frac{\mathcal{E}^{n,k+1}-\mathcal{E}^{n,k}}{\delta t}\right]\\ &= \frac{\mathcal{W}^{n+1}-\mathcal{W}^{n}}{\Delta t}+\frac{\mathcal{Q}^{n+1}-\mathcal{Q}^{n}}{\Delta t}+\frac{\mathcal{E}^{n+1}-\mathcal{E}^{n}}{\Delta t}\end{aligned}$$

where we define the macroscopic force by

$$T_c^{n+1} = \frac{\delta t}{\Delta t}\sum_{k=0}^{N-1}\tau_c^{n,k+1} = \frac{\delta t}{\Delta t}\sum_{k=0}^{N-1}\frac{\delta s}{d_a}\sum_{i=1}^{\ell}\frac{w_{1,i+1}-w_{1,i}}{\delta s}\left(n_0^{n,k+1}a^{n,k+1}+(1-n_0^{n,k+1})b^{n,k+1}\right) \tag{4.61}$$

and the global time step work flux per myosin head by

$$\frac{\mathcal{W}^{n+1}-\mathcal{W}^{n}}{\Delta t} = v_c^{n+\frac{1}{2}\sharp}T_c^{n+1}.$$

We can note that the force at macro time instant is not the force corresponding to the simultaneous microscopic time instant but the time average of the microscopic time force over the macro time step. The energy balance allows to properly perform the link between time scales.

4.6.3.3 Second principle at global time steps

At global time step, we have

$$\frac{\mathcal{F}^{n+1}-\mathcal{F}^{n}}{\Delta t} = \frac{\delta t}{\Delta t}\sum_{k=0}^{N-1}\frac{\mathcal{F}^{n,k+1}-\mathcal{F}^{n,k}}{\delta t}.$$

Using the micro time step free energy inequality (4.57), we have

$$\begin{aligned}\frac{\mathcal{F}^{n+1}-\mathcal{F}^{n}}{\Delta t} &\leq \frac{\delta t}{\Delta t}\sum_{k=0}^{N-1}\frac{\mathcal{W}^{n,k+1}-\mathcal{W}^{n,k}}{\delta t}+\frac{\delta t}{\Delta t}\sum_{k=0}^{N-1}\frac{\mathcal{E}^{n,k+1}-\mathcal{E}^{n,k}}{\delta t}\\ &\leq \frac{\mathcal{W}^{n+1}-\mathcal{W}^{n}}{\Delta t}+\frac{\mathcal{E}^{n+1}-\mathcal{E}^{n}}{\Delta t},\end{aligned} \tag{4.62}$$

with the definition of the global time step energy input flux

$$\frac{\mathcal{E}^{n+1}-\mathcal{E}^{n}}{\Delta t} = \frac{\delta t}{\Delta t}\sum_{k=0}^{N-1}\frac{\mathcal{E}^{n,k+1}-\mathcal{E}^{n,k}}{\delta t}.$$

The inequality on the free-energy is thus straightforwardly transferred to the macroscopic time scale.

4.6.3.4 Discrete time Clausius-Duhem relation for the complete model

Having a discrete model, which satisfies the global time step inequality (4.62), we can apply and adapt the thermodynamic balance obtained in [Kimmig et al., 2019] (Chapter 2) for the micro-macro coupled model. We have

$$\begin{aligned}&\frac{\mathcal{K}^{n+1}-\mathcal{K}^{n}}{\delta t}+\int_{\Omega^0}\left[\frac{\Psi^{n+1}-\Psi^{n}}{\delta t}+E_s\frac{|e_s^{n+1}|^2-|e_s^{n}|^2}{2\delta t}+\rho_v\frac{\mathcal{F}^{n+1}-\mathcal{F}^{n}}{\delta t}\right]\mathrm{d}\Omega\\ &\quad\leq \mathcal{P}_{\text{ext}}^{n+\frac{1}{2}}-\int_{\Omega^0}\left[\eta\frac{|\underline{\underline{e}}^{n+1}-\underline{\underline{e}}^{n}|^2}{\delta t^2}+\nu\frac{(e_c^{n+1}-e_c^{n})^2}{\delta t^2}\right]\mathrm{d}\Omega+\int_{\Omega^0}\rho_v\frac{\mathcal{E}^{n+1}-\mathcal{E}^{n}}{\delta t},\end{aligned} \tag{4.63}$$

where the density of myosin head per unit volume is defined as $\rho_v = \rho_{\text{surf}}/\ell_{hs}$.

In summary, the proposed numerical scheme satisfies discrete thermodynamical balances at the local time step. A definition of the macroscopic active force guided by the thermodynamics allows to extend this discrete thermodynamic balances to the micro-macro coupled model.

4.7 Physiological simulation of a heart beat

We now want to show the ability of our model to produce a physiologically relevant behavior in the context of cardiovascular system modeling. To this end, we incorporate our model in a heart model with a simplified geometry [Caruel et al., 2013].

We first need to embed into the model the regulation of the thin filament activation. It is done here in a phenomenological way. Then, we present the physiological calibration used in our simulations and the simulation results.

In this section, we use the aggregated transition rates f and g because we want to use the calibration given in papers proposing models of the cardiac muscle contraction, which is generally provided with this convention [Pertici et al., 2018; Kimmig & Caruel, 2019].

4.7.1 Modification to account for the thin filament activation

We have presented here a model allowing to capture the varying levels of thick filament activation in the sarcomere. However, it is not the only regulation mechanism in a physiological contraction. The thin filament activation level is also varied as a function of the sarcomere stretch and the intracellular calcium dynamics depends on the inputs of the neuroendocrine system [de Tombe et al., 2010].

In this paper, we focus our modeling effort on the activation of the thick filament and we treat the activation of the thin filament phenomenologically. Following the idea proposed by Zahalak & Motabarzadeh [1997] and Chapelle et al. [2012], we place the impact of this regulation on the transition rates. We assume that the aggregated attachment rate $f(s)$ is modulated multiplicatively by a phenomenological activation function u. The complexity of the underlying mechanisms is incorporated into the freedom in the choice of the activation function u. This function varies between zero and one, representing a level of activation that modulates the rate of attachment. The model dynamics equation (4.14) becomes

$$\begin{cases} \partial_t P_1(s,t,1) + \dot{x}_c\,\partial_s P_1(s,t,1) + \dfrac{|\dot{n}_0|_+}{n_0}\big[P_1(s,t,1) - P_1(s,t,0)\big] = \\ \qquad\qquad u(t)\big(k_{+,1}(s) + k^{\text{rev}}_{-,1}(s)\big)P_0(s,t,1) - \big(k_{-,1}(s) + k^{\text{rev}}_{+,1}(s)\big)P_1(s,t,1), \\ \partial_t P_1(s,t,0) + \dot{x}_c\,\partial_s P_1(s,t,0) + \dfrac{|\dot{n}_0|_-}{1-n_0}\big[P_1(s,t,0) - P_1(s,t,1)\big] = \\ \qquad\qquad u(t)\big(k_{+,0}(s) + k^{\text{rev}}_{-,0}(s)\big)P_0(s,t,0) - \big(k_{-,0}(s) + k^{\text{rev}}_{+,0}(s)\big)P_1(s,t,0), \\ P_0(s,t,\gamma) = 1 - P_1(s,t,\gamma). \end{cases} \tag{4.64}$$

Naturally, multiplying the attachment rate without modifying the detachment rate breaks the detailed balance (4.6). The modified model is thus no more compatible with the second principle.

Note that an alternative choice has been proposed by Zahalak [1981] consisting in applying the activation as a multiplicative factor of the force.

4.7.2 Model calibration

We now want to calibrate our model. Our objective is to show the ability of the model to qualitatively capture the Frank-Starling mechanism and not to precisely match physiological pressure-volume data for a given individual. We thus allow ourselves to use data coming from different species. The heart model parameters, except for the active element, and the blood circulation parameters are calibrated to represent a human physiological behavior (patient specific calibrations can be found in [Le Gall et al., 2019]). The proposed micro-scale model of the actin-myosin interaction and its regulation provided a detailed description of the involved mechanisms. The model calibration thus requires accurate data obtained *ex vivo* targeting the short time and space scales of the muscle contraction. These data are not available for human to the best of our knowledge and we will use instead measurements from rats obtained at sub-physiological temperatures. For the actin-myosin interaction model, we rely on the calibration proposed in [Kimmig & Caruel, 2019] (Chapter 3) based on data obtained by Caremani et al. [2016] for the pool $\gamma = 1$. For the pool $\gamma = 0$, we use the modeling assumption $f_0 = 0.01 f_1$ and $g_0 = g_1$. Note that to get a calibration that satisfies the detailed balance, it would be easier to make assumptions and the non-aggregated transition rates instead of then having to solve an inverse problem to obtain the non-aggregated rates from the aggregated transition rates. However, the aggregated rates are easier to link with the physiology and that is why we use this formalism here. We then calibrate the input function $n_0(e_c)$. For that, we compare our model with experimental data coming from *ex vivo* muscle cells, which are either intact tetanised cells or skinned cells, displaying the variations of the isometric force with variations of the sarcomere length. We make sure to use only data obtained in conditions where the thin filament is fully activated. In this way, the variation of force is solely due to variations in the thick filament level of activation. Finally, we define the thin filament activation function $u(t)$.

4.7.2.1 Myosin activation function

To relate the measured force to the ratio of available myosin heads n_0, we use experiments measuring the relation between the steady-state isometric peak force and the sarcomere length in full thin filament activation conditions, so that the variation in force can be attributed solely to variations in the myosin heads availability. We aggregate here data collected by Kentish et al. [1986], ter Keurs et al. [2008] and Dobesh et al. [2002].

Note the extension e_c, which we consider as the argument of the thick filament activation function n_0, adds up to the filament self extension e_s, which depends on the developed active force, to give the sarcomere extension e_{fib}. The latter quantity is the extension that can be directly linked to the sarcomere length. We thus need to consider the experimental data in the light of the rheology model. The range of sarcomere length that is used in experimental conditions spans between 1.65 µm and 2.25 µm. In this range, the passive force is small compared to the active force (see for instance [ter Keurs et al., 2008, Fig. 2] or [Caremani et al., 2016, Fig. 1B]). We thus interpret the measured force as resulting solely from the upper branch of the rheology (the rheology is presented in Figure 4.4). Recalling the sarcomere length corresponding to zero passive force – called *slack length* – is denoted by ℓ_{hs}, the half-sarcomere length in steady-state contraction conditions is given by $\ell_{hs}(e_{\text{fib}}) = \ell_{hs}\big(1 + e_{\text{fib}}\big)$ with

$$\begin{cases} e_{\text{fib}} = e_c + e_s, \\ E_s e_s = T_c\big(n_0(e_c)\big), \end{cases} \tag{4.65}$$

denoting by $\check{T}_c$ the steady state value of T_c given by

$$\check{T}_c\big(n_0(e_c)\big) = \rho_{\text{surf}} \frac{1}{d_a} \int_{s^-}^{s^+} \big[n_0 \check{P}_1(s,1) + (1-n_0)\check{P}_1(s,0)\big] \partial_s w_1(s)\,\mathrm{d}s,$$

where $\check{P}_1(\gamma) = \frac{f_\gamma}{f_\gamma + g_\gamma}$ is the steady-state solution of (4.64) with $\dot{x}_c = 0$ and in maximal activation conditions ($n_0 = 1$ and $u = 1$). Normalising the tensions by the maximal isometric tension

$$T_0 = \rho_{\text{surf}} \frac{1}{d_a} \int_{s^-}^{s^+} \check{P}_1(s,1) \partial_s w_1(s)\,\mathrm{d}s,$$

we seek a function $n_0(e_c)$ such that the model predicted $\big(\ell_{hs}(e_{\text{fib}}), \check{T}_c\big(n_0(e_c)\big)/T_0\big)$-curve matches the experimental data. This data corresponding to a complete thin filament activation, the corresponding function u is maintain equal to one here and we simulate the steady-state response in force of the model. As for the most elements of the rheology, the slack length is taken from measurements on human cardiac cells. We use the value $\ell_{hs} = 1.7\,\mu\text{m}$ [van der Velden et al., 2000]. The calibration results and the validation are presented in Figure 4.11.

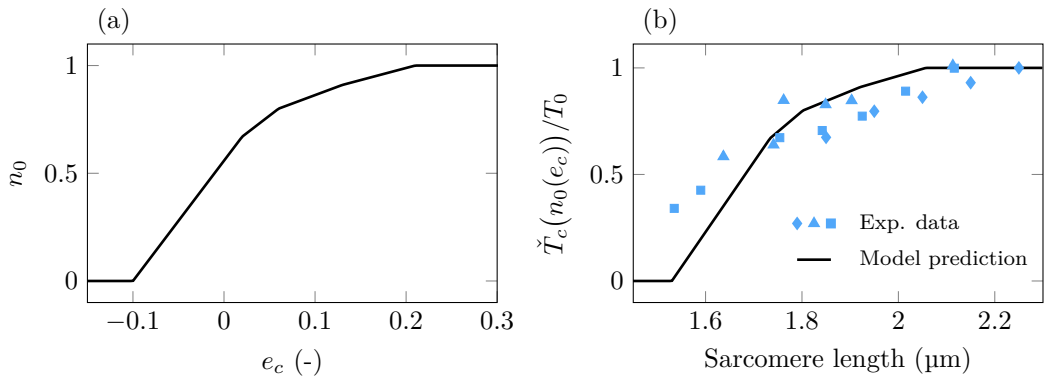

Figure 4.11 – (a) Calibrated input parameter function $n_0(e_c)$. (b) Validation of the calibration with the relation between the sarcomere length and the isometric force in maximal thin filament activation conditions. Solid line: model prediction. Closed diamonds: experimental data from skinned rat cells [Dobesh et al., 2002]. Closed triangles: experimental data from intact tetanised rat cardiac muscle cells [ter Keurs et al., 2008]. Closed square: experimental data from skinned rat ventricular trabeculae [Kentish et al., 1986].

4.7.2.2 Actin activation function

The actin activation function u is phenomenologically defined to mimic the transient activation of the thin filament following the triggering of the action potential in the cell. In a first phase, calcium is released from the sarcoplasmic reticulum and transiently adsorbed by the thin filament, the level of activation increases and reaches its maximal value – assumed here to be equal to one. The calcium ions are then re-uptaken by the sarcoplasmic reticulum and the level of activation decreases until it vanishes. The liberation of calcium is then prevented during a so-called *refractory period*, which ensures that the ventricle has time to relax before the next contraction. The proposed function $u(t)$ is presented in Figure 4.12.

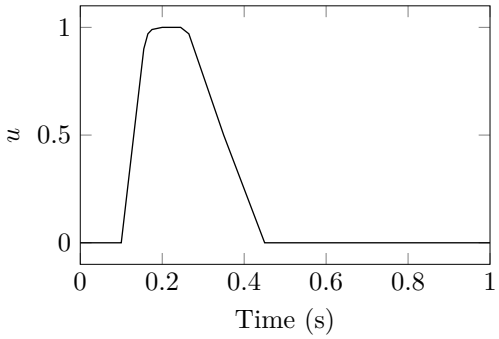

Figure 4.12 – Phenomenological thin filament activation function.

4.7.3 Numerical results

At the macroscopic level, de Tombe et al. [2010] characterize the Frank-Starling mechanism by two features: the stroke volume is increasing with an increase of the end-diastolic volume and the stroke volume can be maintained in case of an increased after-load by increasing the end-diastolic volume (i.e. increasing the pre-load). Altogether, they state that a comprehensive view of this mechanism is to say that there is a single end-systolic pressure-volume relation (EVPVR).

4.7.3.1 Physiological pressure-volume loop

The simulation results with the previously calibrated thick and thin filament activation functions are presented in Figure 4.13. We see in the panel (a) that an increase in the pre-load results in an increase of the ejected blood volume. Our model thus captures the first feature of the Frank-Starling mechanism. In the panel (b), we show that the second feature is also encompassed in our model.

Additionally, we plot the static (ESPVR) that can be computed from the simplified 0D-model equation in static case (see [Caruel et al., 2013]). The ESPRV (V, P_V) is given in a parametric form by

$$\begin{cases} V = \dfrac{4}{3}\pi R_0^3\Big(1 + e_{\text{fib}} - \dfrac{h(1+e_{\text{fib}})^{-2}}{2R_0}\Big)^3, \\ \Big(1 + e_{\text{fib}} - \dfrac{\epsilon}{2}(1+e_{\text{fib}})^{-2}\Big)^2\Big(1 + \epsilon(1+e_{\text{fib}})^{-3}\Big)P_V = \epsilon\Big(1+e_{\text{fib}}\Big)\Sigma_{\text{sph}}, \\ \Sigma_{\text{sph}} = \dfrac{\check{T}_c\big(n_0(e_c)\big)}{1+e_{\text{fib}}} + 4\big(1-(1+e_{\text{fib}})^{-6}\big)\dfrac{\partial \Psi}{\partial J_1} + 2\dfrac{\partial \Psi}{\partial J_4}, \\ J_1 = 2(1+e_{\text{fib}})^2 + (1+e_{\text{fib}})^{-4}, \\ J_4 = (1+e_{\text{fib}})^2, \\ e_{\text{fib}} = e_c + e_s, \\ E_s e_s = T_c\big(n_0(e_c)\big), \end{cases}$$

where R_0 is the radius of the ventricle in rest conditions, e_{fib} is the local homogeneous stretch of the muscle tissue (as defined in (4.38)), h is the ventricle wall thickness in the reference configuration, Σ_{sph} the local stress in the heart wall, J_1 and J_4 are the first and fourth reduced invariant of the Cauchy-Green strain tensor, respectively, and ϵ is the ratio between the ventricle wall thickness and the ventricle radius. The first equation gives the volume of the spherical ventricle as a function of the fiber extension accounting for the wall

thickness variation, the second one is the relation between the pressure inside the ventricle and the stress in the ventricular wall (it is a sort of Laplace's Law), the third equation gives the total – active and passive – stress as prescribed by the rheology, the fourth and fifth equations yield the tensor invariants for the chosen kinematics assumptions, and the sixth and seven equations reflect the kinematical assumptions and the mechanical equilibrium introduced by the one dimensional half-sarcomere part of the rheology, respectively.

Note that due to inertia, the ESPVR is slightly exceeded by the PV-loop but it shows that the dynamic ESPVR almost coincides with the static ESPVR and is thus unique

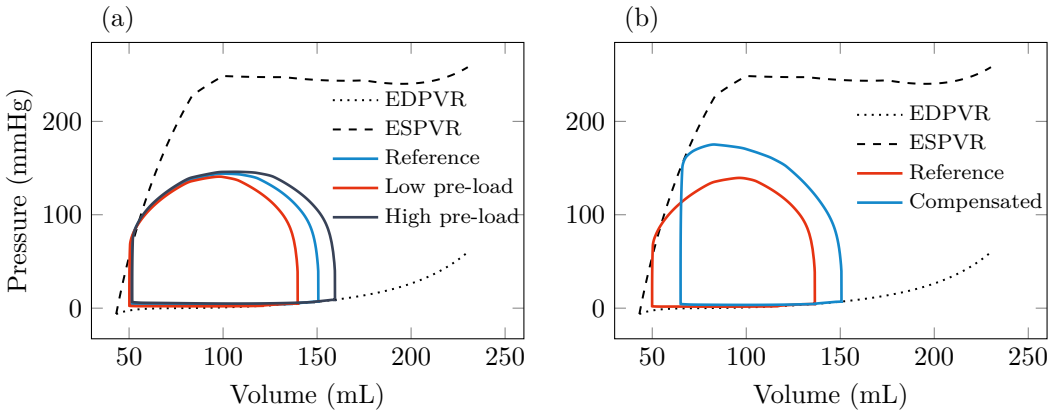

Figure 4.13 – Relation between the ventricular pressure and the ventricular volume during a simulated heart beat (PV-loop). (a) Variation of the pre-load, which increases the end-diastolic volume. (b) Comparison between a reference and a case where a higher after-load is compensated by an increased pre-load to maintain the ejected blood volume constant. (a) & (b) The dashed line represents the static End-Systolic Pressure Volume Relation (ESPVR). The dotted line represents the End-Diastolic Pressure Volume Relation (EDPVR).

In a nutshell, our model based on a microscopic description of the actin-myosin interaction coupled with a macroscopic description of the muscle tissue and embedded into a cardiovascular model is able to capture the key features of the Frank-Starling mechanism at the macroscopic level.

4.7.3.2 Impact of the micro models on the macroscopic physiology

In this section, we want to highlight the impact of the force-velocity captured by the model on a physiological heart beat.

We compare the simulations of a heart beat with two different calibrations of the transition rates. The isometric values of the transitions rates are either taken from [Kimmig & Caruel, 2019] (Chapter 3) or mimic that proposed in [de Tombe & Stienen, 2007] (see Figure 4.14(a) & (b)). The force-velocity relation associated with this two model calibrations are presented in Figure 4.14(c). With the calibration from [Kimmig & Caruel, 2019], the steady-state force is higher for all velocities than the same relation computed with the calibration inspired by [de Tombe & Stienen, 2007]. We thus denote this first calibration *high force-velocity* (HFV) and as opposed to the *low force-velocity* calibration (LFV).

Note that both simulations use the calibration of n_0 and u presented in Section 4.7.2.1. In the early contraction phase, the aortic valve is closed and the muscle works in isometric conditions. As soon as the valve opens, the heart cavity volume decreases and the sarcomere shortens. This shortening results in a decrease in the force following the force-velocity curve, under the approximation that the population probability $P_1(s,t)$ quickly converges

to its steady-state counterpart (this is true if the cycling time scale is shorter than the duration of the systole).

We now compare the pressure-volume loops obtained with the two calibrations. When the force-velocity relation predicts a strong decrease of the force with increasing shortening velocities, the opening of the valve (and the beginning of the sarcomere shortening) leads to a drastic decrease of the active force. As a result, the pressure that can be created in the heart cavity is limited due to the limited time of activation (see Figure 4.14(d)). This further leads to a reduction of the stroke volume because the heart is not able to oppose the aortic pressure long enough.

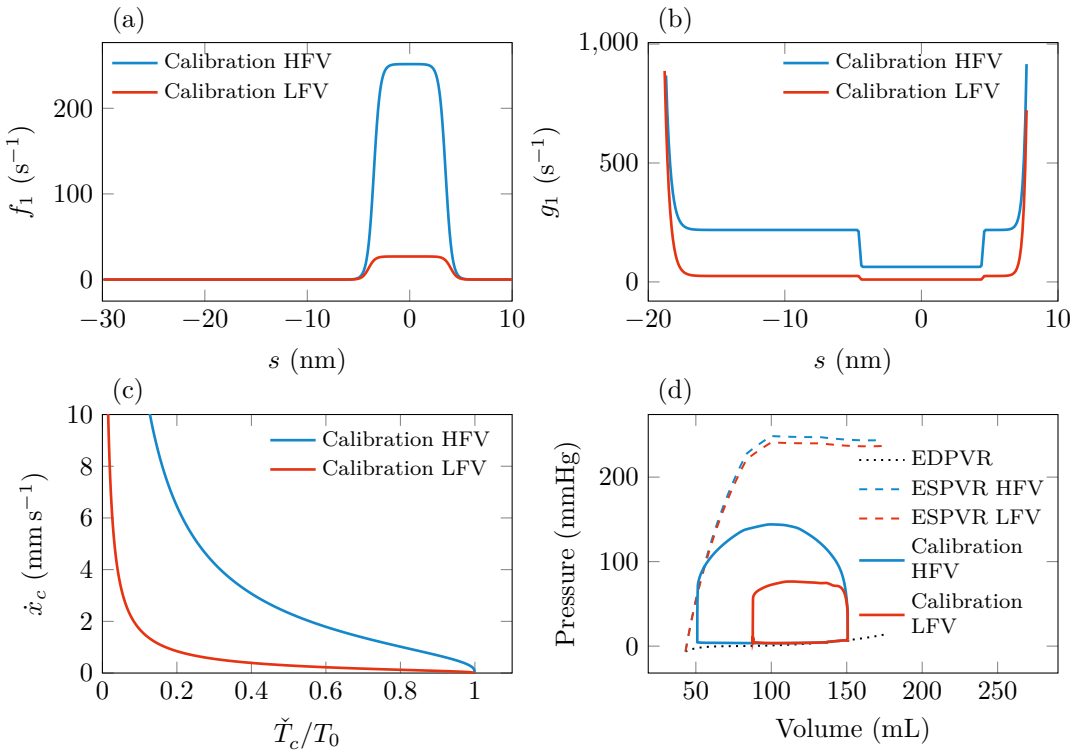

Figure 4.14 – Comparison of high force-velocity calibration (HFV) with low force-velocity calibration (LFV). The two calibrations only differ by the choice of the transition rates. (a) Aggregated attachment rates for both calibrations. (b) Aggregated detachment rates for both calibrations. (c) Resulting force-velocity relation with both calibrations. (d) Force-velocity relation obtained in a heart beat simulation with both calibrations.

The force-velocity is thus important in the calibration to allow the heart to eject blood while maintaining a high enough blood pressure to avoid the closing of the aortic valve.

4.8 Conclusion

In this paper, we have presented a new paradigm that extend the family of models derived from the seminal work of A.F. Huxley [Huxley, 1957] to take into account the activation of the thick filament. The thermodynamical compatibility of the newly proposed model is established. A discrete counterpart of the thermodynamics balances is also obtained with a dedicated discretization scheme.

As a consequence of the investigation of our model limits, we showed that the inclusion of a memory effect in the transition between the available and non-available states for the

myosin heads is not useful in physiological conditions. Indeed, the attachment-detachment process occurs fast enough to eliminate this memory effect.

This work suffers from two main limitations in the context of physiological heart modeling. First, the activation of the thin filament has been incorporated in a phenomenological way. There remains a need for the development of a rigorous thin filament activation modeling. Secondly, the extrinsic regulation controlled by the the neuroendocrine system is not considered in this model. A limitation in this regards is the difficulty to obtain sarcomere level data – on which the microscopic level model can be calibrated – that also consider the impact of the neuroendocrine system, because extraction of muscle samples from the body separate them from this system. In our approach, we get around these two limitations by incorporating these effects phenomenologically into the activation function u. We are then able to display the ability of our model to capture the two essential features of the Frank-Starling mechanism.

Note that a physiological pressure-volume relation can also be obtained with less refined models of the actomyosin interaction, for instance models that only track the first two moments of the population probability P_1 [Chapelle et al., 2012]. This is because the heartbeat time scale is long compared to the actin-myosin interaction time scales and thus capturing the details of this interaction is enough to produce physiological results at the heartbeat time scale. However, our framework allows to better describe the physical mechanisms underlying the contraction and thus allows to take into account changes of these mechanisms – for instance as a result of pathologies – more easily.

4.9 Appendix

4.9.1 Some properties of the Chapelle'12 Frank-Starling model

The modified two-state model equation as proposed by [Zahalak & Motabarzadeh, 1997; Chapelle et al., 2012] defines the attachment flux by $f(n_0 - P_1)$, thus assuming that $n_0 - P_1) \geq 0$. In this section, we investigate whether this property is indeed satisfied.

We consider the modified two-state model equation in the case where there is no filament sliding ($\dot{x}_c = 0$)

$$\partial_t P_1(s,t) = f(s)\Big(n_0(t) - P_1(s,t)\Big) - g(s)P_1(s,t), \tag{4.66}$$

where the ratio n_0 depends explicitly on time and not on the active fibre stretch. The distance to the nearest actin site appears here as a parameters (and not a variable). We choose a value of this parameter such that $f \neq 0$ and we then omit this parameters in the equations in what follows. There exist an analytical solution to the equation (4.66) given by

$$P_1(t) = P_1(t = t_0)e^{-(f+g)(t-t_0)} + f\int_{t_0}^{t} n_0(\tau)e^{-(f+g)(t-\tau)}\,\mathrm{d}\tau$$

If n_0 is fixed, and with the initial condition $P_1(t = t_0) < n_0$, we have the property

$$P_1(t) \leq n_0, \quad \forall t \geq t_0.$$

However, the latter property is not ensured if $n_0(t)$ varies. Let us consider the initial condition $P_1(t = 0) = 1$ and a linearly decreasing ratio

$$n_0(t) = \begin{cases} 1 - \dfrac{t}{T} & \text{if } t \in [0, T], \\ 0 & \text{otherwise.} \end{cases}$$

For $t \in [0,T]$, the function $P_1(t)$ is given by

$$\begin{aligned} P_1(t) &= e^{-(f+g)t} + f\int_0^t \Big(1-\frac{\tau}{T}\Big)e^{-(f+g)(t-\tau)}\,\mathrm{d}\tau, \\ &= \Big(1-\frac{f}{f+g}\Big)e^{-(f+g)t} + \frac{1}{T}\frac{f}{(f+g)^2}\Big(1-e^{-(f+g)t}\Big) + \frac{f}{f+g}\Big(1-\frac{\tau}{T}\Big). \end{aligned}$$

We thus have

$$P_1(t) - n_0(t) = \Big(1-\frac{f}{f+g}\Big)e^{-(f+g)t} + \frac{1}{T}\frac{f}{(f+g)^2}\Big(1-e^{-(f+g)t}\Big) + \Big(\frac{f}{f+g}-1\Big)\Big(1-\frac{\tau}{T}\Big).$$

We consider short evolutions times such that $t(f+g) \ll 1$, we have

$$P_1(t) - n_0(t) = \Big(\frac{1}{T} - g\Big)t + O(t^2). \tag{4.67}$$

For short evolution times, we thus have the desired property $P_1(t) \leq n_0(t)$ if and only if $g \geq 1/T$, namely when the detachment characteristic time is lower than the characteristic time of the variation of n_0.

We have thus shown that the property $P_1(t) \leq n_0(t)$ underlying the establishment of Equation (4.66) is not self-contained in the dynamics prescribed by this equation and most be ensured by a suitable choice of the model parameters.

4.9.2 Proof of the equivalence between the random exchange model and the homogenized pool model

We detail here the proof that the stochastic model described by (4.40) and the homogenized pool model (4.14).

Let $\phi(\alpha,\gamma)$ be a test function. Denoting the joint probability $\mathbb{P}\big[\alpha^t = \overline{\alpha}, \gamma^t = \overline{\gamma}\big]$ by $\mathbb{P}_t\big[\overline{\alpha},\overline{\gamma}\big]$, we have

$$\begin{aligned} \frac{\mathrm{d}}{\mathrm{d}t}\mathbb{E}\big[\phi(\alpha^t,\gamma^t)\big] = {} & \big[\phi(0,1)-\phi(1,1)\big]g_1\mathbb{P}_t\big[1,1\big] + \big[\phi(1,1)-\phi(0,1)\big]f_1\mathbb{P}_t\big[0,1\big] \\ & + \big[\phi(0,0)-\phi(1,0)\big]g_0\mathbb{P}_t\big[1,0\big] + \big[\phi(1,0)-\phi(0,0)\big]f_0\mathbb{P}_t\big[0,0\big] \\ & + \big[\phi(1,0)-\phi(1,1)\big]\frac{|\dot{n}_0(t)|_-}{n_0(t)}\mathbb{P}_t\big[1,1\big] + \big[\phi(0,0)-\phi(0,1)\big]\frac{|\dot{n}_0(t)|_-}{n_0(t)}\mathbb{P}_t\big[0,1\big] \\ & + \big[\phi(1,1)-\phi(1,0)\big]\frac{|\dot{n}_0(t)|_+}{1-n_0(t)}\mathbb{P}_t\big[1,0\big] \\ & + \big[\phi(0,1)-\phi(0,0)\big]\frac{|\dot{n}_0(t)|_+}{1-n_0(t)}\mathbb{P}_t\big[0,0\big]. \end{aligned} \tag{4.68}$$

Furthermore, the time derivative of the expectation is also given by

$$\frac{\mathrm{d}}{\mathrm{d}t}\mathbb{E}\big[\phi(\alpha^t,\gamma^t)\big] = \sum_{\alpha=\{0,1\}}\sum_{\gamma=\{0,1\}}\Big(\phi(\alpha^t,\gamma^t)\frac{\partial}{\partial t}\mathbb{P}\big[\alpha^t,\gamma^t\big]\Big). \tag{4.69}$$

Since the test function can be chosen arbitrary, we can identify the coefficients of (4.68)

and (4.69). We obtain

$$\begin{cases} \dfrac{\partial}{\partial t}\mathbb{P}_t\big[1,1\big] = -g_1\mathbb{P}_t\big[1,1\big] + f_1\mathbb{P}_t\big[0,1\big] + \dfrac{|\dot{n}_0(t)|_+}{1-n_0(t)}\mathbb{P}_t\big[1,0\big] - \dfrac{|\dot{n}_0(t)|_-}{n_0(t)}\mathbb{P}_t\big[1,1\big], \\ \dfrac{\partial}{\partial t}\mathbb{P}_t\big[1,0\big] = -g_0\mathbb{P}_t\big[1,0\big] + f_0\mathbb{P}_t\big[0,0\big] - \dfrac{|\dot{n}_0(t)|_+}{1-n_0(t)}\mathbb{P}_t\big[1,0\big] + \dfrac{|\dot{n}_0(t)|_-}{n_0(t)}\mathbb{P}_t\big[1,1\big], \\ \dfrac{\partial}{\partial t}\mathbb{P}_t\big[0,1\big] = g_1\mathbb{P}_t\big[1,1\big] - f_1\mathbb{P}_t\big[0,1\big] + \dfrac{|\dot{n}_0(t)|_+}{1-n_0(t)}\mathbb{P}_t\big[0,0\big] - \dfrac{|\dot{n}_0(t)|_-}{n_0(t)}\mathbb{P}_t\big[0,1\big], \\ \dfrac{\partial}{\partial t}\mathbb{P}_t\big[0,0\big] = g_0\mathbb{P}_t\big[1,0\big] - f_0\mathbb{P}_t\big[0,0\big] - \dfrac{|\dot{n}_0(t)|_+}{1-n_0(t)}\mathbb{P}_t\big[0,0\big] + \dfrac{|\dot{n}_0(t)|_-}{n_0(t)}\mathbb{P}_t\big[0,1\big]. \end{cases} \tag{4.70}$$

Noting that we have

$$\begin{cases} \mathbb{P}_t\big[1,1\big] = \mathbb{P}_t\big[1|1\big]\mathbb{P}_t\big[\gamma=1\big] = P_1(t,1)n_0(t), \\ \mathbb{P}_t\big[1,0\big] = \mathbb{P}_t\big[1|0\big]\mathbb{P}_t\big[\gamma=0\big] = P_1(t,0)\cdot\big(1-n_0(t)\big), \\ \mathbb{P}_t\big[0,1\big] = \mathbb{P}_t\big[0|1\big]\mathbb{P}_t\big[\gamma=1\big] = P_0(t,1)n_0(t), \\ \mathbb{P}_t\big[0,0\big] = \mathbb{P}_t\big[0|0\big]\mathbb{P}_t\big[\gamma=0\big] = P_0(t,0)\cdot\big(1-n_0(t)\big). \end{cases}$$

and with the property

$$\dot{n}_0(t) = |\dot{n}_0(t)|_+ - |\dot{n}_0(t)|_-,$$

the system (4.70) becomes

$$\begin{cases} \dfrac{\partial}{\partial t}P_1(t,1) = -g_1P_1(t,1) + f_1P_0(t,1) + \dfrac{|\dot{n}_0(t)|_+}{n_0(t)}P_1(t,0) - \dfrac{|\dot{n}_0(t)|_+}{n_0(t)}P_1(t,1), \\ \dfrac{\partial}{\partial t}P_1(t,0) = -g_0P_1(t,0) + f_0P_0(t,0) - \dfrac{|\dot{n}_0(t)|_-}{1-n_0(t)}P_1(t,0) + \dfrac{|\dot{n}_0(t)|_-}{1-n_0(t)}P_1(t,1), \\ \dfrac{\partial}{\partial t}P_0(t,1) = g_1P_1(t,1) - f_1P_0(t,1) + \dfrac{|\dot{n}_0(t)|_+}{n_0(t)}P_0(t,0) - \dfrac{|\dot{n}_0(t)|_+}{n_0(t)}P_0(t,1), \\ \dfrac{\partial}{\partial t}P_0(t,0) = g_0P_1(t,0) - f_0P_0(t,0) - \dfrac{|\dot{n}_0(t)|_-}{1-n_0(t)}P_0(t,0) + \dfrac{|\dot{n}_0(t)|_-}{1-n_0(t)}P_0(t,1). \end{cases} \tag{4.71}$$

Moreover, we also have

$$\begin{aligned} P_1(t,1) + P_0(t,1) &= \frac{\mathbb{P}_t\big[1,1\big] + \mathbb{P}_t\big[0,1\big]}{n_0(t)} = 1, \\ P_1(t,0) + P_0(t,0) &= \frac{\mathbb{P}_t\big[1,0\big] + \mathbb{P}_t\big[0,0\big]}{1-n_0(t)} = 1. \end{aligned}$$

The system (4.71) becomes

$$\begin{cases} \dfrac{\partial}{\partial t}P_1(t,1) = -\dfrac{|\dot{n}_0(t)|_+}{n_0(t)}\Big[P_1(t,1) - P_1(t,0)\Big] - g_1P_1(t,1) + f_1P_0(t,1), \\ \dfrac{\partial}{\partial t}P_1(t,0) = -\dfrac{|\dot{n}_0(t)|_-}{1-n_0(t)}\Big[P_1(t,0) - P_1(t,1)\Big] - g_0P_1(t,0) + f_0P_0(t,0), \\ P_0(t,1) = 1 - P_1(t,1), \\ P_0(t,0) = 1 - P_1(t,0). \end{cases}$$

and we retrieve the equation system (4.14) in the absence of filament sliding. Our averaging assumption in the homogenized pool formulation is thus equivalent to an individual description of the myosin heads if the myosin heads that change pool are selected randomly.

4.9.3 Proof of the discrete thermodynamics identities

In this section, we detailed the proof of the discrete thermodynamic balances presented in Section 4.6.

4.9.3.1 First principle

We now aim at establishing a discrete counterpart to the continuous first principle (4.25). We discretise the attached state energy level on $[s^-, s^+]$ by

$$\begin{vmatrix} w_{1,i} = w_1(s^- + i\delta s), \ \forall i \in [\![1, \ell - 1]\!] \\ w_{1,\ell} = 2w_{1,\ell-1}. \end{vmatrix}$$

We define the discrete average energy per myosin head by

$$\mathcal{U}^{n,k} = \frac{\delta s}{d_a} \sum_{i=1}^{\ell} \Big[w_{1,i} \big(n_0^{n,k} a_i^{n,k} + (1 - n_0^{n,k}) b_i^{n,k} \big) + w_0 \big(n_0^{n,k} (1 - a_i^{n,k}) + (1 - n_0^{n,k})(1 - b_i^{n,k}) \big) \Big].$$

We have at local time steps

$$\begin{aligned} \frac{\mathcal{U}^{n,k+1} - \mathcal{U}^{n,k}}{\delta t} = \frac{\delta s}{d_a} \sum_{i=1}^{\ell} \Bigg(& w_{1,i} \Bigg[n_0^{n,k+1} \left(\frac{a_i^{n,k+1} - a_i^{n,k}}{\delta t} \right) + a_i^{n,k} \left(\frac{n_0^{n,k+1} - n_0^{n,k}}{\delta t} \right) \\ & + (1 - n_0^{n,k+1}) \left(\frac{b_i^{n,k+1} - b_i^{n,k}}{\delta t} \right) + b_i^{n,k} \left(\frac{(1 - n_0^{n,k+1}) - (1 - n_0^{n,k})}{\delta t} \right) \Bigg] \\ & + w_0 \Bigg[n_0^{n,k+1} \left(\frac{(1 - a_i^{n,k+1}) - (1 - a_i^{n,k})}{\delta t} \right) + (1 - a_i^{n,k}) \left(\frac{n_0^{n,k+1} - n_0^{n,k}}{\delta t} \right) \\ & + (1 - n_0^{n,k+1}) \left(\frac{(1 - b_i^{n,k+1}) - (1 - b_i^{n,k})}{\delta t} \right) \\ & \qquad + (1 - b_i^{n,k}) \left(\frac{(1 - n_0^{n,k+1}) - (1 - n_0^{n,k})}{\delta t} \right) \Bigg] \Bigg). \end{aligned}$$

With the fluxes defined in (4.51) and the calculations done in [Kimmig et al., 2019] (Chap-

ter 2) we obtain, using the periodicity of the solution to handle the discrete transport term,

$$
\begin{aligned}
\frac{\mathcal{U}^{n,k+1}-\mathcal{U}^{n,k}}{\delta t} = \\
&\frac{\delta s}{d_a}\sum_{i=1}^{\ell}\Bigg(w_{1,i}\Bigg[n_0^{n,k+1}\Big(-\frac{|n_0^{n+1}-n_0^n|_+}{n_0^{n,k+1}\Delta t}\Big[a_i^{n,k}-b_i^{n,k}\Big]\Big)+a_i^{n,k}\left(\frac{n_0^{n,k+1}-n_0^{n,k}}{\delta t}\right)\\
&\quad+(1-n_0^{n,k+1})\Big(-\frac{|n_0^{n+1}-n_0^n|_-}{(1-n_0^{n,k+1})\Delta t}\Big[b_i^{n,k}-a_i^{n,k}\Big]\Big)+b_i^{n,k}\left(\frac{n_0^{n,k+1}-n_0^{n,k}}{\delta t}\right)\Bigg]\\
&\quad+w_0\Bigg[n_0^{n,k+1}\Big(\frac{|n_0^{n+1}-n_0^n|_+}{n_0^{n,k+1}\Delta t}\Big[a_i^{n,k}-b_i^{n,k}\Big]\Big)+(1-a_i^{n,k})\left(\frac{n_0^{n,k+1}-n_0^{n,k}}{\delta t}\right)\\
&\quad+(1-n_0^{n,k+1})\Big(\frac{|n_0^{n+1}-n_0^n|_-}{(1-n_0^{n,k+1})\Delta t}\Big[a_i^{n,k}-b_i^{n,k}\Big]\Big)\\
&\qquad\qquad+(1-b_i^{n,k})\left(\frac{n_0^{n,k+1}-n_0^{n,k}}{\delta t}\right)\Bigg]\Bigg)\\
&+v_c^{n+\frac{1}{2}\sharp}\frac{\delta s}{d_a}\sum_{i=1}^{\ell}\frac{w_{1,i+1}-w_{1,i}}{\delta s}\Big(n_0^{n,k+1}a^{n,k+1}+(1-n_0^{n,k+1})b^{n,k+1}\Big)\\
&+\frac{\delta s}{d_a}\sum_{i=1}^{\ell}\Big[\Big(n_0^{n,k+1}J_{+,1,i}^{n,k+1}+(1-n_0^{n,k+1})J_{+,0,i}^{n,k+1}\Big)(w_{1,i}-w_0)\\
&+\Big(n_0^{n,k+1}J_{-,1,i}^{n,k+1}+(1-n_0^{n,k+1})J_{-,0,i}^{n,k+1}\Big)\big(w_0-(w_{1,i}+\mu_T)\big)\Big]\\
&+\mu_T\frac{\delta s}{d_a}\sum_{i=1}^{\ell}\Big(n_0^{n,k+1}J_{-,1,i}^{n,k+1}+(1-n_0^{n,k+1})J_{-,0,i}^{n,k+1}\Big).
\end{aligned}
$$

Noting that

$$\frac{n_0^{n,k+1}-n_0^{n,k}}{\delta t}=\frac{n_0^{n+1}-n_0^n}{\Delta t}$$

and with the property (4.8), the pool exchange terms cancel out. We define the force per myosin head by

$$\tau_c^{n,k+1}=\frac{\delta s}{d_a}\sum_{i=1}^{\ell}\frac{w_{1,i+1}-w_{1,i}}{\delta s}\Big(n_0^{n,k+1}a^{n,k+1}+(1-n_0^{n,k+1})b^{n,k+1}\Big).$$

It is the average of the force between the two pools weighted by n_0. We finally obtain the first principle formulation at local time steps

$$\frac{\mathcal{U}^{n,k+1}-\mathcal{U}^{n,k}}{\delta t}=\frac{\mathcal{W}^{n,k+1}-\mathcal{W}^{n,k}}{\delta t}+\frac{\mathcal{Q}^{n,k+1}-\mathcal{Q}^{n,k}}{\delta t}+\frac{\mathcal{E}^{n,k+1}-\mathcal{E}^{n,k}}{\delta t},\tag{4.72}$$

with

$$\left|\begin{aligned}
&\frac{\mathcal{W}^{n,k+1}-\mathcal{W}^{n,k}}{\delta t}=v_c^{n+\frac{1}{2}\sharp}\tau_c^{n,k+1},&(4.73)\\
&\frac{\mathcal{Q}^{n,k+1}-\mathcal{Q}^{n,k}}{\delta t}=\frac{\delta s}{d_a}\sum_{i=1}^{\ell}\Big[\Big(n_0^{n,k+1}J_{+,1,i}^{n,k+1}+(1-n_0^{n,k+1})J_{+,0,i}^{n,k+1}\Big)(w_{1,i}-w_0)\\
&\qquad\qquad+\Big(n_0^{n,k+1}J_{-,1,i}^{n,k+1}+(1-n_0^{n,k+1})J_{-,0,i}^{n,k+1}\Big)\big(w_0-(w_{1,i}+\mu_T)\big)\Big],&(4.74)\\
&\frac{\mathcal{E}^{n,k+1}-\mathcal{E}^{n,k}}{\delta t}=\mu_T\frac{\delta s}{d_a}\sum_{i=1}^{\ell}\Big(n_0^{n,k+1}J_{-,1,i}^{n,k+1}+(1-n_0^{n,k+1})J_{-,0,i}^{n,k+1}\Big).&(4.75)
\end{aligned}\right.$$

4.9.3.2 Second principle

To derive a discrete version of the second principle, we recall the definition of the chemical potentials in each pool

$$\begin{vmatrix}
\mu^{n,k}_{\alpha=1,\gamma=1,i} = \mu^{n,k}_{1,1,i} = w_{1,i} + k_B T \ln a^{n,k}_i, \\
\mu^{n,k}_{\alpha=1,\gamma=0,i} = \mu^{n,k}_{1,0,i} = w_{1,i} + k_B T \ln b^{n,k}_i, \\
\mu^{n,k}_{\alpha=0,\gamma=1,i} = \mu^{n,k}_{0,1,i} = w_0 + k_B T \ln(1 - a^{n,k}_i), \\
\mu^{n,k}_{\alpha=0,\gamma=0,i} = \mu^{n,k}_{0,0,i} = w_0 + k_B T \ln(1 - b^{n,k}_i).
\end{vmatrix}$$

We define the entropy per myosin head as

$$\frac{\mathcal{S}^{n,k}}{k_B} = -\frac{\delta s}{d_a} \sum_{i=1}^{\ell} \Big[n_0^{n,k} \Big(a_i^{n,k} \ln a_i^{n,k} + (1 - a_i^{n,k}) \ln(1 - a_i^{n,k}) \Big) + (1 - n_0^{n,k}) \Big(b_i^{n,k} \ln b_i^{n,k} + (1 - b_i^{n,k}) \ln(1 - b_i^{n,k}) \Big) \Big].$$

Note that the entropy is well defined for $a^{n,k} \in [0,1]$ and $b^{n,k} \in [0,1]$. For the derivation of the discrete second principle, we first assume that $a^{n,k} \in]0,1[$ and $b^{n,k} \in]0,1[$. We have

$$\begin{aligned}
-\frac{1}{k_B} \frac{\mathcal{S}^{n,k+1} - \mathcal{S}^{n,k}}{\delta t} = \frac{\delta s}{d_a} \sum_{i=1}^{\ell} \Bigg[& n_0^{n,k+1} \Big(\frac{a_i^{n,k+1} - a_i^{n,k}}{\delta t} \ln a_i^{n,k+1} + a_i^{n,k} \frac{\ln a_i^{n,k+1} - \ln a_i^{n,k}}{\delta t} \Big) \\
& + a_i^{n,k} \ln a_i^{n,k} \frac{n_0^{n,k+1} - n_0^{n,k}}{\delta t} \\
& + n_0^{n,k+1} \Big(\frac{(1 - a_i^{n,k+1}) - (1 - a_i^{n,k})}{\delta t} \ln(1 - a_i^{n,k+1}) \\
& + (1 - a_i^{n,k}) \frac{\ln(1 - a_i^{n,k+1}) - \ln(1 - a_i^{n,k})}{\delta t} \Big) \\
& + (1 - a_i^{n,k}) \ln(1 - a_i^{n,k}) \frac{n_0^{n,k+1} - n_0^{n,k}}{\delta t} \\
& + (1 - n_0^{n,k+1}) \Big(\frac{b_i^{n,k+1} - b_i^{n,k}}{\delta t} \ln b_i^{n,k+1} + b_i^{n,k} \frac{\ln b_i^{n,k+1} - \ln b_i^{n,k}}{\delta t} \Big) \\
& + b_i^{n,k} \ln b_i^{n,k} \frac{(1 - n_0^{n,k+1}) - (1 - n_0^{n,k})}{\delta t} \\
& + (1 - n_0^{n,k+1}) \Big(\frac{(1 - b_i^{n,k+1}) - (1 - b_i^{n,k})}{\delta t} \ln(1 - b_i^{n,k+1}) \\
& + (1 - b_i^{n,k}) \frac{\ln(1 - b_i^{n,k+1}) - \ln(1 - b_i^{n,k})}{\delta t} \Big) \\
& + (1 - b_i^{n,k}) \ln(1 - b_i^{n,k}) \frac{(1 - n_0^{n,k+1}) - (1 - n_0^{n,k})}{\delta t} \Bigg].
\end{aligned} \tag{4.76}$$

We now introduce the numerical scheme (4.44). Using the calculation made in [Kimmig

et al., 2019] (Chapter 2), we have

$$
\begin{aligned}
-\frac{1}{k_B}\frac{\mathcal{S}^{n,k+1}-\mathcal{S}^{n,k}}{\delta t} = & \\
&-\frac{1}{k_B}\frac{\tilde{\mathcal{S}}^{n,k+1}_{\text{prod}}-\tilde{\mathcal{S}}^{n,k}_{\text{prod}}}{\delta t}-\frac{1}{k_B T}\frac{\mathcal{Q}^{n,k+1}-\mathcal{Q}^{n,k}}{\delta t} \\
&+\frac{n_0^{n,k+1}-n_0^{n,k}}{\delta t}\frac{\delta s}{d_a}\sum_{i=1}^{\ell}\Big[a_i^{n,k}\ln a_i^{n,k}+(1-a_i^{n,k})\ln(1-a_i^{n,k}) \\
&\qquad -b_i^{n,k}\ln b_i^{n,k}-(1-b_i^{n,k})\ln(1-b_i^{n,k})\Big] \\
&-\frac{|n_0^{n,k+1}-n_0^{n,k}|_+}{\delta t}\frac{\delta s}{d_a}\sum_{i=1}^{\ell}\Big[\big[a_i^{n,k}-b_i^{n,k}\big]\ln a_i^{n,k+1} \\
&\qquad +\big[(1-a_i^{n,k})-(1-b_i^{n,k})\big]\ln(1-a_i^{n,k+1})\Big] \\
&-\frac{|n_0^{n,k+1}-n_0^{n,k}|_-}{\delta t}\frac{\delta s}{d_a}\sum_{i=1}^{\ell}\Big[\big[b_i^{n,k}-a_i^{n,k}\big]\ln b_i^{n,k+1} \\
&\qquad +\big[(1-b_i^{n,k})-(1-a_i^{n,k})\big]\ln(1-b_i^{n,k+1})\Big] \\
&+\frac{n_0^{n,k+1}\delta s}{d_a\delta t}\sum_{i=1}^{\ell}\left[a_i^{n,k}\ln\left(\frac{a_i^{n,k+1}}{a_i^{n,k}}\right)+(1-a_i^{n,k})\ln\left(\frac{1-a_i^{n,k+1}}{1-a_i^{n,k}}\right)\right] \\
&+\frac{(1-n_0^{n,k+1})\delta s}{d_a\delta t}\sum_{i=1}^{\ell}\left[b_i^{n,k}\ln\left(\frac{b_i^{n,k+1}}{b_i^{n,k}}\right)+(1-b_i^{n,k})\ln\left(\frac{1-b_i^{n,k+1}}{1-b_i^{n,k}}\right)\right],
\end{aligned}
$$

with

$$
\begin{aligned}
\frac{\tilde{\mathcal{S}}^{n,k+1}_{\text{prod}}-\tilde{\mathcal{S}}^{n,k}_{\text{prod}}}{\delta t} = & \\
&-\frac{n_0^{n,k+1}}{T}\left(\frac{\delta s}{d_a}\sum_{i=1}^{\ell}\left[J^{n,k+1}_{+,1,i}\left(\mu^{n,k+1}_{1,1,i}-\mu^{n,k+1}_{0,1,i}\right)+J^{n,k+1}_{-,1,i}\left(\mu^{n,k+1}_{0,1,i}-\mu^{n,k+1}_{1,1,i}-\mu_T\right)\right]\right. \\
&\qquad \left.+\frac{v_c^{n+\frac{1}{2}\sharp}k_BT}{d_a}\sum_{i=1}^{\ell}\left[a_i^{n,k+1}\ln\left(\frac{a_{i+1}^{n,k+1}}{a_i^{n,k+1}}\right)+(1-a_i^{n,k+1})\ln\left(\frac{1-a_{i+1}^{n,k+1}}{1-a_i^{n,k+1}}\right)\right]\right) \\
&-\frac{1-n_0^{n,k+1}}{T}\left(\frac{\delta s}{d_a}\sum_{i=1}^{\ell}\left[J^{n,k+1}_{+,0,i}\left(\mu^{n,k+1}_{1,0,i}-\mu^{n,k+1}_{0,0,i}\right)\right.\right. \\
&\qquad \left.\left.+J^{n,k+1}_{-,0,i}\left(\mu^{n,k+1}_{0,0,i}-\mu^{n,k+1}_{1,0,i}-\mu_T\right)\right]\right. \\
&\qquad \left.+\frac{v_c^{n+\frac{1}{2}\sharp}k_BT}{d_a}\sum_{i=1}^{\ell}\left[b_i^{n,k+1}\ln\left(\frac{b_{i+1}^{n,k+1}}{b_i^{n,k+1}}\right)+(1-b_i^{n,k+1})\ln\left(\frac{1-b_{i+1}^{n,k+1}}{1-b_i^{n,k+1}}\right)\right]\right)
\end{aligned}
$$

which is positive from the calculation made in [Kimmig et al., 2019] (Chapter 2), given that $1-n_0^{n,k+1}\geq 0$ and $n_0^{n,k+1}\geq 0$.

We first assume that $n_0^{n,k+1} \geq n_0^{n,k}$. We have

$$\begin{aligned}
\frac{1}{k_B}\frac{\mathcal{S}^{n,k+1}-\mathcal{S}^{n,k}}{\delta t} = & \\
& \frac{1}{k_B}\frac{\tilde{\mathcal{S}}_{\text{prod}}^{n,k+1}-\tilde{\mathcal{S}}_{\text{prod}}^{n,k}}{\delta t} + \frac{1}{k_B T}\frac{\mathcal{Q}^{n,k+1}-\mathcal{Q}^{n,k}}{\delta t} \\
& - \frac{n_0^{n,k+1}-n_0^{n,k}}{\delta t}\frac{\delta s}{d_a}\sum_{i=1}^{\ell}\left[b_i^{n,k}\ln\left(\frac{a_i^{n,k+1}}{b_i^{n,k}}\right) + (1-b_i^{n,k})\ln\left(\frac{1-a_i^{n,k+1}}{1-b_i^{n,k}}\right)\right] \\
& + \frac{n_0^{n,k+1}}{\delta t}\frac{\delta s}{d_a}\sum_{i=1}^{\ell}\left[a_i^{n,k}\ln\left(\frac{a_i^{n,k}}{a_i^{n+1,k}}\right) + (1-a_i^{n,k})\ln\left(\frac{1-a_i^{n,k}}{1-a_i^{n,k+1}}\right)\right] \\
& + \frac{1-n_0^{n,k+1}}{\delta t}\frac{\delta s}{d_a}\sum_{i=1}^{\ell}\left[b_i^{n,k+1}\ln\left(\frac{b_i^{n,k+1}}{b_i^{n,k}}\right)\right. \\
& \qquad \left. + (1-b_i^{n,k+1})\ln\left(\frac{1-b_i^{n,k+1}}{1-b_i^{n,k}}\right)\right].
\end{aligned}$$

With the property that $a^{n,k} \in]0,1[$ and $b^{n,k} \in]0,1[$, we can use the convexity inequalities (4.29) and (4.30), and, noting that we have

$$\left|\begin{aligned} n_0^{n,k+1}-n_0^{n,k} &\geq 0, \\ 1-n_0^{n,k+1} &\geq 0, \\ n_0^{n,k+1} &\geq 0, \end{aligned}\right.$$

we obtain

$$\frac{\mathcal{S}^{n,k+1}-\mathcal{S}^{n,k}}{\delta t} = \frac{\mathcal{S}_{\text{prod}}^{n,k+1}-\mathcal{S}_{\text{prod}}^{n,k}}{\delta t} + \frac{1}{T}\frac{\mathcal{Q}^{n,k+1}-\mathcal{Q}^{n,k}}{\delta t}, \tag{4.77}$$

with the entropy creation term

$$\begin{aligned}
\frac{1}{k_B}\frac{\mathcal{S}_{\text{prod}}^{n,k+1}-\mathcal{S}_{\text{prod}}^{n,k}}{\delta t} & \\
& = \frac{1}{k_B}\frac{\tilde{\mathcal{S}}_{\text{prod}}^{n,k+1}-\tilde{\mathcal{S}}_{\text{prod}}^{n,k}}{\delta t} \\
& \quad - \frac{n_0^{n,k+1}-n_0^{n,k}}{\delta t}\frac{\delta s}{d_a}\sum_{i=1}^{\ell}\left[b_i^{n,k}\ln\left(\frac{a_i^{n,k+1}}{b_i^{n,k}}\right) + (1-b_i^{n,k})\ln\left(\frac{1-a_i^{n,k+1}}{1-b_i^{n,k}}\right)\right] \\
& \quad + \frac{n_0^{n,k+1}}{\delta t}\frac{\delta s}{d_a}\sum_{i=1}^{\ell}\left[a_i^{n,k}\ln\left(\frac{a_i^{n,k}}{a_i^{n,k+1}}\right) + (1-a_i^{n,k})\ln\left(\frac{1-a_i^{n,k}}{1-a_i^{n,k+1}}\right)\right] \\
& \quad - \frac{1-n_0^{n,k+1}}{\delta t}\frac{\delta s}{d_a}\sum_{i=1}^{\ell}\left[b_i^{n,k+1}\ln\left(\frac{b_i^{n,k+1}}{b_i^{n,k}}\right) + (1-b_i^{n,k+1})\ln\left(\frac{1-b_i^{n,k+1}}{1-b_i^{n,k}}\right)\right]
\end{aligned}$$

satisfying the inequality

$$\frac{\mathcal{S}_{\text{prod}}^{n,k+1}-\mathcal{S}_{\text{prod}}^{n,k}}{\delta t} \geq 0. \tag{4.78}$$

Similarly, we have, for $n_0^{n,k+1} < n_0^{n,k}$, the second principle (4.77) with

$$\begin{aligned}\frac{1}{k_B}\frac{\mathcal{S}_{\text{prod}}^{n,k+1}-\mathcal{S}_{\text{prod}}^{n,k}}{\delta t} = &\\ &\frac{1}{k_B}\frac{\tilde{\mathcal{S}}_{\text{prod}}^{n,k+1}-\tilde{\mathcal{S}}_{\text{prod}}^{n,k}}{\delta t}\\ &-\frac{n_0^{n,k+1}-n_0^{n,k}}{\delta t}\frac{\delta s}{d_a}\sum_{i=1}^{\ell}\left[a_i^{n,k}\ln\left(\frac{a_i^{n,k}}{b_i^{n,k+1}}\right)+(1-a_i^{n,k})\ln\left(\frac{1-a_i^{n,k}}{1-b_i^{n,k+1}}\right)\right]\\ &-\frac{n_0^{n,k+1}}{\delta t}\frac{\delta s}{d_a}\sum_{i=1}^{\ell}\left[a_i^{n,k}\ln\left(\frac{a_i^{n,k+1}}{a_i^{n,k}}\right)+(1-a_i^{n,k})\ln\left(\frac{1-a_i^{n,k+1}}{1-a_i^{n,k}}\right)\right]\\ &-\frac{1-n_0^{n,k+1}}{\delta t}\frac{\delta s}{d_a}\sum_{i=1}^{\ell}\left[b_i^{n,k}\ln\left(\frac{b_i^{n,k+1}}{b_i^{n,k}}\right)+(1-b_i^{n,k})\ln\left(\frac{1-b_i^{n,k+1}}{1-b_i^{n,k}}\right)\right],\end{aligned}$$

which satisfies the positivity of the entropy creation property (4.78). In summary, we have

$$\frac{\mathcal{S}^{n,k+1}-\mathcal{S}^{n,k}}{\delta t}\geq\frac{1}{T}\frac{\mathcal{Q}^{n,k+1}-\mathcal{Q}^{n,k}}{\delta t},\ \text{for } a^{n,k}\in]0,1[\text{ and } b^{n,k}\in]0,1[,\ \forall n,\forall k. \tag{4.79}$$

Noting that the heat transfer rate term and the entropy rate term are properly defined for $a^{n,k}\in[0,1]$ and $b^{n,k}\in[0,1]$, we pass to the limit the inequality (4.79) and we obtain

$$\frac{\mathcal{S}^{n,k+1}-\mathcal{S}^{n,k}}{\delta t}\geq\frac{1}{T}\frac{\mathcal{Q}^{n,k+1}-\mathcal{Q}^{n,k}}{\delta t},\ \text{for } a^{n,k}\in[0,1]\text{ and } b^{n,k}\in[0,1],\ \forall n,\forall k. \tag{4.80}$$

4.9.4 Numerical scheme for negative sliding velocities

In this section, we present the results of the numerical analysis for negative sliding velocities.

4.9.4.1 Numerical scheme

The numerical scheme is the same as that for positive velocities with the exception of the transport term. To keep an upwind treatment of the transport term, we shift the spatial discretization by one spatial increment. The discretization scheme becomes

$$\begin{cases}\dfrac{a_i^{n,k+1}-a_i^{n,k}}{\delta t} = -\dfrac{|n_0^{n+1}-n_0^n|_+}{n_0^{n,k+1}\Delta t}\left[a_i^{n,k}-b_i^{n,k}\right]+(k_{+,1,i}+k_{-,1,i}^{\text{rev}})(1-a_i^{n,k+1})\\ \qquad\qquad -(k_{-,1,i}+k_{+,1,i}^{\text{rev}})a_i^{n,k+1}-v_c^{n+\frac{1}{2}\sharp}\dfrac{a_{i+1}^{n,k+1}-a_i^{n,k+1}}{\delta s},\forall i\in[\![1,\ell]\!]\\ \dfrac{b_i^{n,k+1}-b_i^{n,k}}{\delta t} = -\dfrac{|n_0^{n+1}-n_0^n|_-}{(1-n_0^{n,k+1})\Delta t}\left[b_i^{n,k}-a_i^{n,k}\right]+(k_{+,0,i}+k_{-,0,i}^{\text{rev}})(1-b_i^{n,k+1})\\ \qquad\qquad -(k_{-,0,i}+k_{+,0,i}^{\text{rev}})b_i^{n,k+1}-v_c^{n+\frac{1}{2}\sharp}\dfrac{b_{i+1}^{n,k+1}-b_i^{n,k+1}}{\delta s},\forall i\in[\![1,\ell]\!]\end{cases} \tag{4.81}$$

4.9.4.2 First principle

The energy remains defined by (4.50). Computing the time increment between two local time steps, we obtain the first principle

$$\frac{\mathcal{U}^{n,k+1}-\mathcal{U}^{n,k}}{\delta t}=\frac{\mathcal{W}^{n,k+1}-\mathcal{W}^{n,k}}{\delta t}+\frac{\mathcal{Q}^{n,k+1}-\mathcal{Q}^{n,k}}{\delta t}+\frac{\mathcal{E}^{n,k+1}-\mathcal{E}^{n,k}}{\delta t}, \tag{4.82}$$

with

$$\left|\begin{aligned}
\frac{\mathcal{W}^{n,k+1}-\mathcal{W}^{n,k}}{\delta t} &= v_c^{n+\frac{1}{2}\sharp}\tau_c^{n,k+1},\\
\frac{\mathcal{Q}^{n,k+1}-\mathcal{Q}^{n,k}}{\delta t} &= \frac{\delta s}{d_a}\sum_{i=1}^{\ell}\Big[\Big(n_0^{n,k+1}J_{+,1,i}^{n,k+1}+(1-n_0^{n,k+1})J_{+,0,i}^{n,k+1}\Big)(w_{1,i}-w_0)\\
&\qquad +\Big(n_0^{n,k+1}J_{-,1,i}^{n,k+1}+(1-n_0^{n,k+1})J_{-,0,i}^{n,k+1}\Big)\big(w_0-(w_{1,i}+\mu_T)\big)\Big],\\
\frac{\mathcal{E}^{n,k+1}-\mathcal{E}^{n,k}}{\delta t} &= \mu_T\frac{\delta s}{d_a}\sum_{i=1}^{\ell}\Big(n_0^{n,k+1}J_{-,1,i}^{n,k+1}+(1-n_0^{n,k+1})J_{-,0,i}^{n,k+1}\Big),
\end{aligned}\right.$$

where the force is now defined by

$$\tau_c^{n,k+1}=\frac{\delta s}{d_a}\sum_{i=1}^{\ell}\frac{w_{1,i}-w_{1,i-1}}{\delta s}\Big(n_0^{n,k+1}a^{n,k+1}+(1-n_0^{n,k+1})b^{n,k+1}\Big).$$

4.9.4.3 Second principle

The inequality still holds (4.80) with negative sliding velocities.

If we have the property $a^{n,k}\in]0,1[$ and $b^{n,k}\in]0,1[,\ \forall n,\forall k$, we can give an explicit expression of the the entropy creation and we have

$$\frac{\mathcal{S}^{n,k+1}-\mathcal{S}^{n,k}}{\delta t}=\frac{\mathcal{S}_{\text{prod}}^{n,k+1}-\mathcal{S}_{\text{prod}}^{n,k}}{\delta t}+\frac{1}{T}\frac{\mathcal{Q}^{n,k+1}-\mathcal{Q}^{n,k}}{\delta t},$$

with a new definition of the entropy creation term by

$$
\begin{aligned}
&\frac{\mathcal{S}_{\text{prod}}^{n,k+1}-\mathcal{S}_{\text{prod}}^{n,k}}{\delta t} = \\
&\quad -\left(n_0^{n,k+1}\frac{1}{T}\frac{\delta s}{d_a}\sum_{i=1}^{\ell}\left[J_{+,1,i}^{n,k+1}\left(\mu_{1,1,i}^{n,k+1}-\mu_{0,1,i}^{n,k+1}\right)+J_{-,1,i}^{n,k+1}\left(\mu_{0,1,i}^{n,k+1}-\mu_{1,1,i}^{n,k+1}-\mu_T\right)\right]\right. \\
&\qquad\quad +(1-n_0^{n,k+1})\frac{1}{T}\frac{\delta s}{d_a}\sum_{i=1}^{\ell}\left[J_{+,0,i}^{n,k+1}\left(\mu_{1,0,i}^{n,k+1}-\mu_{0,0,i}^{n,k+1}\right)\right. \\
&\qquad\qquad\qquad\left.\left.+J_{-,0,i}^{n,k+1}\left(\mu_{0,0,i}^{n,k+1}-\mu_{1,0,i}^{n,k+1}-\mu_T\right)\right]\right) \\
&\quad -v_c^{n,k+\frac{1}{2}\sharp}k_B\left(n_0^{n,k+1}\frac{1}{d_a}\sum_{i=1}^{\ell}\left[a_i^{n,k+1}\ln\left(\frac{a_{i+1}^{n,k+1}}{a_i^{n,k+1}}\right)+(1-a_i^{n,k+1})\ln\left(\frac{1-a_{i+1}^{n,k+1}}{1-a_i^{n,k+1}}\right)\right]\right. \\
&\qquad\quad \left.+(1-n_0^{n,k+1})\frac{1}{d_a}\sum_{i=1}^{\ell}\left[b_i^{n,k+1}\ln\left(\frac{b_{i+1}^{n,k+1}}{b_i^{n,k+1}}\right)+(1-b_i^{n,k+1})\ln\left(\frac{1-b_{i+1}^{n,k+1}}{1-b_i^{n,k+1}}\right)\right]\right) \\
&\quad -\frac{k_B}{\delta t}\left(n_0^{n,k+1}\frac{\delta s}{d_a}\sum_{i=1}^{\ell}\left[a_i^{n,k}\ln\left(\frac{a_i^{n,k+1}}{a_i^{n,k}}\right)+(1-a_i^{n,k})\ln\left(\frac{1-a_i^{n,k+1}}{1-a_i^{n,k}}\right)\right]\right) \\
&\qquad\quad +(1-n_0^{n,k+1})\frac{\delta s}{d_a}\sum_{i=1}^{\ell}\left[b_i^{n,k}\ln\left(\frac{b_i^{n,k+1}}{b_i^{n,k}}\right)+(1-b_i^{n,k})\ln\left(\frac{1-b_i^{n,k+1}}{1-b_i^{n,k}}\right)\right]\Big) \\
&\quad -k_B\frac{|n_0^{n,k+1}-n_0^{n,k}|_+}{\delta t}\frac{\delta s}{d_a}\sum_{i=1}^{\ell}\left[b_i^{n,k}\ln\left(\frac{a_i^{n,k+1}}{b_i^{n,k}}\right)+(1-b_i^{n,k})\ln\left(\frac{1-a_i^{n,k+1}}{1-b_i^{n,k}}\right)\right] \\
&\quad -k_B\frac{|n_0^{n,k+1}-n_0^{n,k}|_-}{\delta t}\frac{\delta s}{d_a}\sum_{i=1}^{\ell}\left[a_i^{n,k}\ln\left(\frac{a_i^{n,k}}{b_i^{n,k+1}}\right)+(1-a_i^{n,k})\ln\left(\frac{1-a_i^{n,k}}{1-b_i^{n,k+1}}\right)\right],
\end{aligned}
$$

satisfying the inequality

$$
\frac{\mathcal{S}_{\text{prod}}^{n,k+1}-\mathcal{S}_{\text{prod}}^{n,k}}{\delta t}\geq 0.
$$

This expressions contains terms that are consistent with the continuous formulation (4.36) for the attachment and detachment fluxes and the pool averaging process contributions and additional terms corresponding to positive numerical entropy creation.

4.9.5 Validation of the discrete thermodynamics balance illustration

We present in this section the numerical computation of the residual corresponding to the discrete thermodynamics balances (4.52) and (4.58) defined as

$$
\left|\begin{aligned}
&\frac{\mathcal{U}^{n,k+1}-\mathcal{U}^{n,k}}{\delta t}-\frac{\mathcal{W}^{n,k+1}-\mathcal{W}^{n,k}}{\delta t}-\frac{\mathcal{Q}^{n,k+1}-\mathcal{Q}^{n,k}}{\delta t}-\frac{\mathcal{E}^{n,k+1}-\mathcal{E}^{n,k}}{\delta t},\\
&\frac{\mathcal{F}^{n+1}-\mathcal{F}^{n}}{\delta t}-\frac{\mathcal{W}^{n+1}-\mathcal{W}^{n}}{\delta t}-\frac{\mathcal{E}^{n+1}-\mathcal{E}^{n}}{\delta t}-T\frac{\mathcal{S}_{\text{prod}}^{n+1}-\mathcal{S}_{\text{prod}}^{n}}{\delta t}.
\end{aligned}\right. \tag{4.83}
$$

It may serve as a validation of the algebraic derivation of the first and second thermodynamic balances, as well as a validation of the correct implementation of the proposed numerical scheme. The results are presented in Figure 4.15.

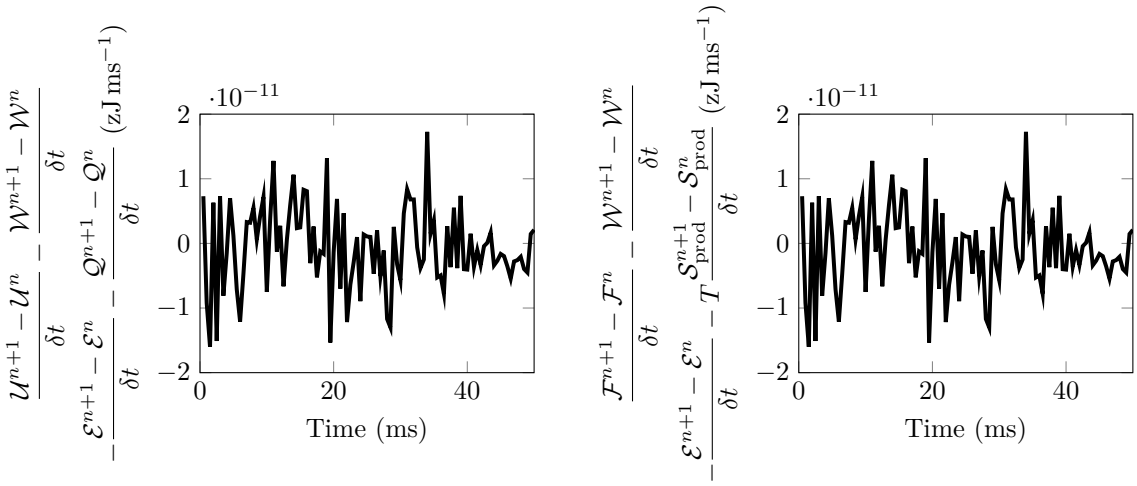

Figure 4.15 – Numerical evaluation of the discrete thermodynamic residuals (4.83) during the simulation presented in Figure 4.10. For this simulation, we used $\Delta t = 0.001\,\text{s}$ and $\delta t = \Delta t$.

We can notice that the value of the residuals is eight orders of magnitude lower that the various terms that composed them (see Figure 4.10). We conclude that the observed oscillations solely reflect the numerical noise. It therefore validates our derivation of the discrete thermodynamics principles.

4.9.6 Moment equation

We have seen in Section 3.2.2, that under a simple mathematical assumption, the active force associated with Huxley'57 models can be obtained from the resolution of a finite set of ordinary differential equations. In this section, we extend this approach to the system (4.14). As in Chapter 3, we use the aggregated transition rates f_γ and g_γ defined in (4.16). Moreover, we will restrict to the case of a quadratic energy potential for the attached state $w_1 = \frac{\kappa_{\text{xb}}}{2}(s+s_0)^2$ but the results can be extended to any polynomial energy potential. For that, we derive the dynamics of the moment of the distributions $P_1(s,t,1)$ and $P_1(s,t,0)$. We define the moments of order p as $M_p(t,\gamma) = \frac{1}{d_a}\int_{-\infty}^{+\infty} s^p P_\gamma(s,t,\gamma)\,\mathrm{d}s$.

Using the dynamic equations (4.14) we obtain

$$\begin{cases}
\dot{M}_0(t,1) = -\dfrac{|\dot{n}_0(t)|_+}{n_0}\left[M_0(t,1) - M_0(t,0)\right] + f_{0,1} \\
\qquad\qquad - \dfrac{1}{d_a}\displaystyle\int_{-\infty}^{+\infty}\left[f_1(s) + g_1(s)\right] P_1(s,t,1)\,\mathrm{d}s, \\
\dot{M}_0(t,0) = -\dfrac{|\dot{n}_0(t)|_-}{1-n_0}\left[M_0(t,0) - M_0(t,1)\right] + f_{0,0} \\
\qquad\qquad - \dfrac{1}{d_a}\displaystyle\int_{-\infty}^{+\infty}\left[f_0(s) + g_0(s)\right] P_1(s,t,0)\,\mathrm{d}s, \\
\dot{M}_p(t,1) = \dot{x}_c\, p\, M_{p-1}(t,1) - \dfrac{|\dot{n}_0(t)|_+}{n_0}\left[M_p(t,1) - M_p(t,0)\right] + f_{p,1} \\
\qquad\qquad - \dfrac{1}{d_a}\displaystyle\int_{-\infty}^{+\infty}\left[f_1(s) + g_1(s)\right] s^p P_1(s,t,1)\,\mathrm{d}s, \\
\dot{M}_p(t,0) = \dot{x}_c\, p\, M_{p-1}(t,0) - \dfrac{|\dot{n}_0(t)|_-}{1-n_0}\left[M_p(t,0) - M_p(t,1)\right] + f_{p,0} \\
\qquad\qquad - \dfrac{1}{d_a}\displaystyle\int_{-\infty}^{+\infty}\left[f_0(s) + g_0(s)\right] s^p P_1(s,t,0)\,\mathrm{d}s,
\end{cases}$$

with $f_{p,\gamma} = \frac{1}{d_a}\int_{-\infty}^{+\infty} s^p f_\gamma\,\mathrm{d}s$. If we use the usual assumption $f_\gamma + g_\gamma$ is independent of s, we have

$$\begin{cases}
\dot{M}_0(t,1) = -\dfrac{|\dot{n}_0(t)|_+}{n_0}\left[M_0(t,1) - M_0(t,0)\right] + f_{0,1} - \left[f_1 + g_1\right] M_0(t,1), \\
\dot{M}_0(t,0) = -\dfrac{|\dot{n}_0(t)|_-}{1-n_0}\left[M_0(t,0) - M_0(t,1)\right] + f_{0,0} - \left[f_0 + g_0\right] M_0(t,0), \\
\dot{M}_p(t,1) = \dot{x}_c\, p\, M_{p-1}(t,1) - \dfrac{|\dot{n}_0(t)|_+}{n_0}\left[M_p(t,1) - M_p(t,0)\right] + f_{p,1} - \left[f_1 + g_1\right] M_p(t,1), \\
\dot{M}_p(t,0) = \dot{x}_c\, p\, M_{p-1}(t,0) - \dfrac{|\dot{n}_0(t)|_-}{1-n_0}\left[M_p(t,0) - M_p(t,1)\right] + f_{p,0} - \left[f_0 + g_0\right] M_p(t,0).
\end{cases}$$

As for the original Huxley'57 model, the dynamics of any moment give by a closed system of ordinary differential equations.

The dynamics of the fraction of attached cross-bridges $n_{\mathrm{att}}(t) = n_0 M_0(t,1) + (1-n_0)M_0(t,0)$ is directly given by that of the moments of order zero

$$\begin{aligned}
\dot{n}_{\mathrm{att}}(t) &= n_0(t)\Big(f_{0,1} - \left[f_1 + g_1\right] M_0(t,1)\Big) + \big(1 - n_0(t)\big)\Big(f_{0,0} - \left[f_0 + g_0\right] M_0(t,0)\Big), \\
&= -\Big(n_0(t)\left[f_1 + g_1\right] M_0(t,1) + \big(1 - n_0(t)\big)\left[f_0 + g_0\right] M_0(t,0)\Big) + f_0(t).
\end{aligned}$$

defining f_p by $f_p(t) = n_0(t) f_{p,1}(t) + \big(1 - n_0(t)\big) f_{p,0}(t)$.

The active force reads

$$\begin{aligned}\tau_c(t) &= \frac{1}{d_a}\int_{s^-}^{s^+}\Big[n_0(t)P_1(s,t,1) + \big(1-n_0(t)\big)P_0(s,t,0)\Big]\kappa_{\mathrm{xb}}(s+s_0)\,\mathrm{d}s,\\ &= \kappa_{\mathrm{xb}}\Big(n_0(t)M_1(t,1) + \big(1-n_0(t)\big)M_1(t,0)\Big)\\ &\qquad + \kappa_{\mathrm{xb}}s_0\Big(n_0(t)M_0(t,1) + \big(1-n_0(t)\big)M_0(t,0)\Big).\end{aligned}$$

Its dynamics is given by

$$\begin{aligned}\dot{\tau}_c(t) = &-n_0(t)\big[f_1+g_1\big]\Big(\kappa_{\mathrm{xb}}M_1(t,1) + \kappa_{\mathrm{xb}}s_0M_0(t,1)\Big)\\ &- \big(1-n_0(t)\big)\big[f_0+g_0\big]\Big(\kappa_{\mathrm{xb}}M_1(t,0) + \kappa_{\mathrm{xb}}s_0M_0(t,0)\Big)\\ &+ \dot{x}_c\kappa_{\mathrm{xb}}n_{\mathrm{att}}(t) + \kappa_{\mathrm{xb}}\big(s_0f_0(t) + f_1(t)\big)\end{aligned}$$

and can therefore be computed from that of the moments of order zero and one only.

Bibliography

Amiad Pavlov, D., & Landesberg, A. (2016). The cross-bridge dynamics is determined by two length-independent kinetics: Implications on muscle economy and Frank–Starling Law. *Journal of molecular and cellular cardiology*, *90*, 94–101.

Caremani, M., Melli, L., Dolfi, M., Lombardi, V., & Linari, M. (2015). Force and number of myosin motors during muscle shortening and the coupling with the release of the ATP hydrolysis products. *The Journal of Physiology*, *593*(15), 3313–3332.

Caremani, M., Pinzauti, F., Reconditi, M., Piazzesi, G., Stienen, G.J.M., Lombardi, V., & Linari, M. (2016). Size and speed of the working stroke of cardiac myosin in situ. *Proceedings of the National Academy of Sciences*, *113*(13), 3675–3680.

Caruel, M., Allain, J.-M., & Truskinovsky, L. (2013). Muscle as a Metamaterial Operating Near a Critical Point. *Physical review letters*, *110*(24), 248103.

Caruel, M., Moireau, P., & Chapelle, D. (2019). Stochastic modeling of chemical-mechanical coupling in striated muscles. *Biomechanics and Modeling in Mechanobiology*, *18*(3), 563–587.

Chapelle, D., Le Tallec, P., Moireau, P., & Sorine, M. (2012). Energy-preserving muscle tissue model: formulation and compatible discretizations. *Journal for Multiscale Computational Engineering*.

de Tombe, P.P., Mateja, R.D., Tachampa, K., Mou, YA, Farman, G.P., & Irving, T.C. (2010). Journal of Molecular and Cellular Cardiology. *Journal of molecular and cellular cardiology*, *48*(5), 851–858.

de Tombe, P.P., & Stienen, G.J.M. (2007). Impact of temperature on cross-bridge cycling kinetics in rat myocardium. *The Journal of Physiology*, *584*(2), 591–600.

de Tombe, P.P., & ter Keurs, H.E.D.J. (1990). Force and velocity of sarcomere shortening in trabeculae from rat heart. Effects of temperature. *Circulation Research*, *66*(5), 1239–1254.

de Tombe, P.P., & ter Keurs, H.E.D.J. (2016). Cardiac muscle mechanics: Sarcomere length matters. *Journal of molecular and cellular cardiology*, *91*(C), 148–150.

Dobesh, D.P., Konhilas, J.P., & de Tombe, P.P. (2002). Cooperative activation in cardiac muscle: impact of sarcomere length. *AJP: Heart and Circulatory Physiology*, *282*(3), H1055–H1062.

Eisenberg, E., & Hill, T.L. (1978). A cross-bridge model of muscle contraction. *Progress in biophysics and molecular biology*, *33*(1), 55–82.

Eisenberg, E., Hill, T.L., & Chen, Y. (1980). Cross-bridge model of muscle contraction. Quantitative analysis. *Biophysical Journal*, *29*(2), 195–227.

Frank, O. (1895). *Zur Dynamik des Herzmuskels*, vol. 32. Zeitschrift für Biologie.

Hill, T.L. (1977). *Free Energy Transduction in Biology*. Academic Press.

Huxley, A.F. (1957). Muscle structures and theories of contraction. *Progr. Biophys. Chem.*.

Huxley, A.F., & Simmons, R.M. (1971). Proposed mechanism of force generation in striated muscle. *Nature*.

Kentish, J.C., Ter Keurs, H.E.D.J., Ricciardi, L., Bucx, J.J., & Noble, M.I. (1986). Comparison between the sarcomere length-force relations of intact and skinned trabeculae from rat right ventricle. influence of calcium concentrations on these relations. *Circulation research*, *58*(6), 755–768.

Kimmig, F., & Caruel, M. (2019). Hierarchical modeling of muscle contraction. *submitted*.

Kimmig, F., Chapelle, D., & Moireau, P. (2019). Thermodynamic properties of muscle contraction models and associated discrete-time principles. *Advanced Modeling and Simulation in Engineering Sciences*, *6*(1), 6.

Le Gall, A., Vallée, F., Mebazaa, A., Chapelle, D., Gayat, E., & Chabiniok, R. (2019). Monitoring of cardiovascular physiology augmented by a patient-specific biomechanical model during general anaesthesia. a proof of concept study. *submitted*.

Lymn, R.W., & Taylor, E.W. (1971). Mechanism of adenosine triphosphate hydrolysis by actomyosin. *Biochemistry*, *10*(25), 4617–4624.

Månsson, Alf (2010). Actomyosin-ADP states, interhead cooperativity, and the force-velocity relation of skeletal muscle. *Biophysical Journal*, *98*(7), 1237–1246.

Marcucci, L., Washio, T., & Yanagida, T. (2016). Including thermal fluctuations in actomyosin stable states increases the predicted force per motor and macroscopic efficiency in muscle modelling. *PLoS Computational Biology*, *12*(9).

Marcucci, L., Washio, T., & Yanagida, T. (2017). Titin-mediated thick filament activation, through a mechanosensing mechanism, introduces sarcomere-length dependencies in mathematical models of rat trabecula and whole ventricle. *Scientific Reports*, (pp. 1–10).

Mateja, R.D., & de Tombe, P.P. (2012). Myofilament Length-Dependent Activation Develops within 5 ms in Guinea-Pig Myocardium. *Biophysical Journal*, *103*(1), L13–L15.

Patterson, S.W., & Starling, E.H. (1914). On the mechanical factors which determine the output of the ventricles. *The Journal of Physiology*, *48*(5), 357–379.

Pertici, I., Bongini, L., Melli, L., Bianchi, G., Salvi, L., Falorsi, G., Squarci, C., Bozó, T., Cojoc, D., Kellermayer, M.S.Z., Lombardi, V., & Bianco, P. (2018). A myosin II nanomachine mimicking the striated muscle. *Nature Communications*, (pp. 1–10).

Piazzesi, G., & Lombardi, V. (1995). A cross-bridge model that is able to explain mechanical and energetic properties of shortening muscle. *Biophysical Journal*, *68*, 1966–1979.

Pinzauti, F., Pertici, I., Reconditi, M., Narayanan, T., Stienen, G.J.M., Piazzesi, G., Lombardi, V., Linari, M., & Caremani, M. (2018). The force and stiffness of myosin motors in the isometric twitch of a cardiac trabecula and the effect of the extracellular calcium concentration. *The Journal of Physiology*, *596*(13), 2581–2596.

Reconditi, M., Caremani, M., Pinzauti, F., Powers, J.D., Narayanan, T., Stienen, G.J.M., Linari, M., Lombardi, V., & Piazzesi, G. (2017). Myosin filament activation in the heart is tuned to the mechanical task. *Proceedings of the National Academy of Sciences*, (pp. 3240–3245).

Sequeira, V., & Velden, J. (2017). The Frank–Starling Law: a jigsaw of titin proportions. *Biophysical reviews*, *9*(3), 259–267.

Silverthorn, D.U., Ober, W.C., Garrison, C.W., & Silverthorn, A.C. (2009). *Human physiology: an integrated approach*. Pearson.

ter Keurs, H.E.D.J., Shinozaki, T., Zhang, Y.M., Zhang, M.L., Wakayama, Y., Sugai, Y., Kagaya, Y., Miura, M., Boyden, P.A., Stuyvers, B.D.M., & Landesberg, A. (2008). Sarcomere mechanics in uniform and non-uniform cardiac muscle: A link between pump function and arrhythmias. *Progress in biophysics and molecular biology*, *97*(2-3), 312–331.

van der Velden, J., de Jong, J.W., Owen, V.J., Burton, P.B., & Stienen, G.J. (2000). Effect of protein kinase A on calcium sensitivity of force and its sarcomere length dependence in human cardiomyocytes. *Cardiovascular Research*, *46*(3), 487–495.

Wannenburg, T., Janssen, P.M., Fan, D., & de Tombe, P.P. (1997). The Frank-Starling mechanism is not mediated by changes in rate of cross-bridge detachment. *The American journal of physiology*, *273*(5 Pt 2), H2428–35.

Zahalak, G.I. (1981). A distribution-moment approximation for kinetic theories of muscular contraction. *Elsevier*, *55*(1-2), 89–114.

Zahalak, G.I., & Motabarzadeh, I. (1997). A Re-examination of Calcium Activation in the Huxley Cross-Bridge Model. *Journal of Biomechanical Engineering*, *119*(1), 20–29.

Zahalak, G I (2000). The two-state cross-bridge model of muscle is an asymptotic limit of multi-state models. *Journal of Theoretical Biology*.

CHAPTER 5

Varying thin filament activation in the framework of the Huxley'57 model

Muscle contraction is triggered by the activation of the actin sites of the thin filament by calcium ions. It results that the thin filament activation level varies over time. Moreover, this activation process is also used as a regulation mechanism of the force developed. Our main objective is to propose a rigorous framework to account for the varying actin sites activation level in chemico-mechanical models of the actin-myosin contraction. Our new model is obtained as an enhancement of our previously proposed formulation extending the Huxley'57 model, which considers the varying thick filament activation (presented in the previous chapter). We assume that the states of an actin site depends on whether it is activated or not and whether it forms a cross-bridge with the associated myosin head, resulting in four possible states or not. The transitions between the actin site states are controlled by the global actin sites activation level and the dynamics of these transitions is coupled to the attachment-detachment process. A preliminary validation of the model with experimental twitch contraction data obtained at varying sarcomere lengths is performed.

Contents

5.1 Abstract

5.2 Introduction

Cardiac muscle contraction originates from the interaction between two types of filaments: myosin filaments (also called thick filaments) and actin filaments (also called thin filaments). These two filaments are regrouped in sarcomeres that are the elementary contractile units of the muscle fibers. The myosin heads of the thick filaments attach on the actin sites of the thin filaments – forming the so-called *cross-bridges* – generate a force, and detach. At rest, the actin sites are blocked by the troponin-tropomyosin complex and the myosin heads cannot attach. When calcium ions are released inside the cell, these ions bind to the troponin-tropomyosin complex resulting in the unblocking of the actin sites. The myosin heads can attach and the tension can rise. The activation of the thin filament is a transient process, and shortly after the release, calcium ions are taken off the cytosol, which contributes to the detachment of the calcium ions from the thin filament. As the myosin heads detach (and because they cannot reattach) the force decreases. *In vivo*, this corresponds to a heartbeat. At the scale of the sarcomere we talk about a *twitch contraction*, which can be observed experimentally.

In physiological conditions, the availability of the myosin heads and the activation of the actin sites are regulated in order to modulate the developed force [de Tombe et al., 2010]. As a result of this regulation, not all myosin heads may be available and not all actin sites may be activated, even at the peak of the activation. We say that the thick and thin filaments have a varying activation level. The level of activation of the thick filament depends on the sarcomere extension only. The thin filament activation level is also impacted by the sarcomere extension – this effect is called the length dependent activation (LDA). For both filaments, an extension of the sarcomere is associated with an increase of the level of activation and thus an increase of the developed force. Note that *in vivo*, in addition to this intrinsic regulation with the sarcomere length, the thin filament is also subjected to an extrinsic regulation driven by the neuroendocrine system, which affects the way the thin filament responds to variations of the sarcomere length and modulates the supply of calcium ions. The latter regulation is not active in experiments performed *ex vivo* as the cells are separated from the neuroendocrine system.

To better understand the mechanisms of the thin filament activation, models have been developed. Two paths have been pursued: a phenomenological description of the thin filament state and description related to the thin filament structure.

The phenomenological description originate from the work of [Landesberg & Sideman, 1994a,b; Rice et al., 1999]. The actin sites are grouped into regulatory units (made of the seven consecutive actin sites that are covered by a single troponin-tropomyosin complex) and it is assumed that there is only one attachment site for the myosin heads per regulatory unit (RU). Having thus paired myosin heads and regulatory units, these formulations propose continuous-time Markov models mixing the description of the myosin heads (attached or not) and the description of the regulatory unit (linked with calcium or not, activated or not, state of associated proteins). They use a mean-field approach, representing the whole filaments with a single regulatory unit.

A major contribution is the model of Rice et al. [2003], which focuses on the description of the thin filament alone. They suppose that each regulatory unit can exist in four different states corresponding to the four combinations of the two following properties: *the regulatory unit is linked to a calcium ion or not* and the regulatory unit is activated (available for the attachment of a myosin head) or not. To account for the cooperativity effect observed experimentally – the fact the activation of some regulatory units has a

positive feedback effect on the other regulatory units, favoring their activation – Rice et al. [2003] propose to link the value of the transition rates between the states to the state of the direct neighbors regulatory units, with an increase of the probability of begin activated when the neighboring regulatory units are already activated. With this new modeling ingredient, the thin filament cannot be modeled by a representative regulatory unit anymore. Instead, all regulatory units must be considered. This model was extended by Rice & de Tombe [2004] to incorporate a simplified myosin attachment-detachment process that does not take into account the strain of the cross-bridges. A difficulty that arises with this modification of the model is the large number of possible states. Indeed, a thin filament is made of 26 regulatory units [Rice et al., 2003], which leads to a number of possible states of $4^{26} = 4.5 \times 10^{15}$.

A first method to overcome this difficulty (proposed in the original paper) consists in assuming that the thin filament is periodic (although it does not correspond to the actual structure). This assumption allows an analytical resolution of the system steady-state. Several other approaches have then been proposed to tackle the issue. They include simulating the whole system using high performance computing [Hussan et al., 2006] or a reduction of the model again a single representative regulatory unit but with adjusted transitions rate so that cooperativity effects can be reproduced [Rice et al., 2008]. Washio et al. [2011] have introduced an hypothesis assuming that the an level of overlap between the thick and thin filaments impacts the transition rates in the thin filament model. This hypothesis can lead to relevant model predictions and thus making mechanisms linked to the level of overlap between the thin and the thick filaments potential origin of the length-dependent activation. Recently, a novel and powerful technique for the efficient simulation of the latter model has been proposed along with an improvement of the model formalization [Regazzoni et al., 2018].

A large collection of models have been developed based on the model proposed by Rice et al. [2003] to simulate the force transient development and relaxation [Land & Niederer, 2015; Dupuis et al., 2016]. They can be grouped into three categories depending on whether they consider the thin filament only or they are linked to a model of myosin heads attachment and whether this model is reduced (the whole filament is represented by a single myosin head) or considers the various spatial positions of the myosin heads (which allows to take into account the relative sliding between the thick and thin filaments). For a review of the models proposed and a summary of their fundamental assumption, we refer to [Trayanova & Rice, 2011].

The inclusion of the actin-myosin dynamics with a contribution of the filament sliding is important for two reasons. First, the sliding of the filaments is a key phenomena of the cardiac muscle behavior, in particular – in the context of heart modeling – in the blood ejection phase when the left ventricle shrinks. Second, there does not exist experimental protocols capable of measuring the time transient variations of the thin filament activation happening in a twitch contraction. Therefore, models have to be calibrated from force transient measurements. There is thus an additional dynamics between the regulatory units activation and the myosin heads binding that has to be considered. Models that do not consider the actin-myosin interaction as a dynamical process and identify the level of thin filament activation with the developed force (up to a multiplicative factor) are thus calibrated on biased data.

An alternative approach to the phenomenological models has been proposed to model the thin filament activation. It consists in considering the proteins as a single long flexible chain whose deformations are associated with an elastic energy. This approach may seem more appealing than the phenomenological approach because it is related to the actual structure of the thin filament. However, since the origin of the length-dependent activation

remains partially unknown, the establishment of non-phenomenological models and their evaluation with respect to phenomenological models is difficult.

Our approach in this chapter is slightly alternative – and at the same time complementary – to that proposed in the works mentioned above. We are here interested in investigating how models targeting the level of thin filament activation can be linked with the family of the Huxley'57 model in a rigorous way in order to build a complete contraction model taking into account the actin-myosin and the regulations of the contraction. Our approach thus focuses on the description of the myosin whereas previously mentioned approaches are based on a description of the actin (or the regulatory unit). The thin filament activation is taken as a model input, which contains the effects of cooperativity, but could also potentially be given by the output of one of the above mentioned thin filament activation models.

This chapter focuses on the modeling of the twitch contraction observed in isolated cells. We do not consider a direct model input for the extrinsic regulation. First, the experiments performed on isolated cells do not allow to see this effect of this regulation. They can only mimic its effect by varying the level of calcium supply, which is one of the consequences of the extrinsic regulation. Secondly, there are potentially many other mechanisms in between the sarcomere-level contraction and the organ behavior. Therefore, the translation of microscopic level contraction models to the organ level is a research topic in itself that is beyond the scope of this work.

Several works have already followed that path but use a phenomenological approach; a limitation that we propose to overcome in this work. Classically, the thin filament activation is introduced as a multiplicative modulation of the attachment rate [Zahalak & Motabarzadeh, 1997; Chapelle et al., 2012; Kimmig et al., 2019] (see Chapter 4) or as an *ad hoc* modification directly put in factor of the active force [Zahalak, 1981]. However, these paradigms suffer from modeling limitations. In particular, formulations using a multiplicative modulation of the attachment rate disregard the fact that attachment induces a reduction of the number of activated actin sites that are actually available for attachment.

This chapter is organized as follows. Section 5.3 presents the experimental data that support modeling ingredient choices and on which the model calibration is performed. In Section 5.4, we first present a review of the Huxley'57 model and the previously proposed extension to account for the thick filament activation. Then, we present our description of the thin filament and we derive our further enhancement of these models from the conservation of conservation of matter. In Section 5.5, we exhibit a possible calibration of our model that we validate with experimental data.

5.3 Physiological review

We recall here the essential properties of the thin filament activation that we will need for the development of our model. A more detailed investigation is presented in Chapter 1. Note that in this chapter, we neglect the passive compliance of the thick and thin filaments. Therefore, the link between the sarcomere length SL and the active contribution to the sarcomere extension e_c is simply given by $\mathrm{SL} = 2\ell_{hs}(1 + e_c)$, where ℓ_{hs} is the reference half-sarcomere length taken equal to 0.925 µm for rat cardiac muscle [ter Keurs et al., 1980].

5.3.1 Activation of the thin filament

The baseline evolution of the thin filament activation is a transient process. It cannot be directly measured experimentally and must therefore be inferred from the force transient

measurement through models. The transient thin filament activation results in a transient variation of the force. The typical force evolution observed *ex vivo* is shown in Figure 5.1.

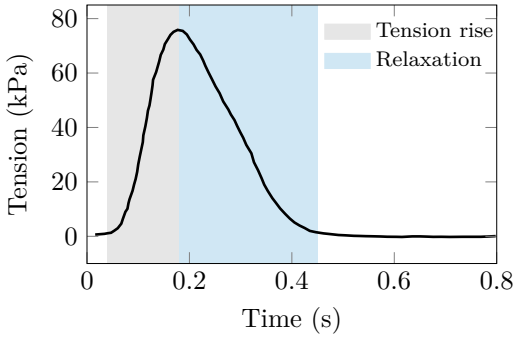

Figure 5.1 – Typical force transient evolution. In this experiment the sarcomere length is maintained constant. Data from [Janssen & Hunter, 1995].

5.3.2 Regulation mechanisms

In vivo, the basal force transient is regulated by the extension of the sarcomere (or equivalently the sarcomere length) and the neuroendocrine regulation. In experiments (*ex vivo*), the variation of the sarcomere length can be reproduced but not all the effects of the neuroendocrine regulation. One effect of the latter regulation that can be indirectly reproduced experimentally is the modulation of the calcium supply ultimately affecting the level of thin filament activation.

The sarcomere length regulation affects both the thick and thin filaments activation but leaves the properties of the cross-bridges unchanged and in particular does not affect the force generated by a cross-bridge. We present in Chapter 4 the effect of the sarcomere length on the thick filament activation and how to extend the Huxley'57 model to incorporate this regulation.

The regulation of the thin filament activation level by the sarcomere length and the level of calcium supply can in general affect both the maximum level of thin filament activation and the shape of the transient activation evolution. We first analyze the impact on the maximum level of activation. For that, we consider the steady-state conditions to remove the dynamics effects. In these conditions, the force is proportional to the level of thick filament activation and the level of thin filament activation. Therefore, to extract information on the thin filament activation from the force experimental data, the contribution of the varying thick filament activation must be eliminated.

We present in Figure 5.2(b), the variation of the thin filament activation with the sarcomere length at various levels of calcium supply for tetanised intact cells (see Chapter 1), assuming that the thick filament activation dependency on the sarcomere length extension e_c is given by the function $n_0(e_c)$ presented in Figure 5.2(a). Note that the variations of the calcium supply are obtained here by varying the extracellular calcium concentration. These data show that the thin filament activation level increases with the level of calcium supply. Moreover, the sarcomere length changes the manner in which the calcium ions are handled by the thin filament. The origin of this effect remains partially unknown [de Tombe & ter Keurs, 2016] but there are now evidences that it is a mechanism intrinsic to the thin filament [Ait-Mou et al., 2016].

The sarcomere length has also an impact on the time evolution of the thin filament

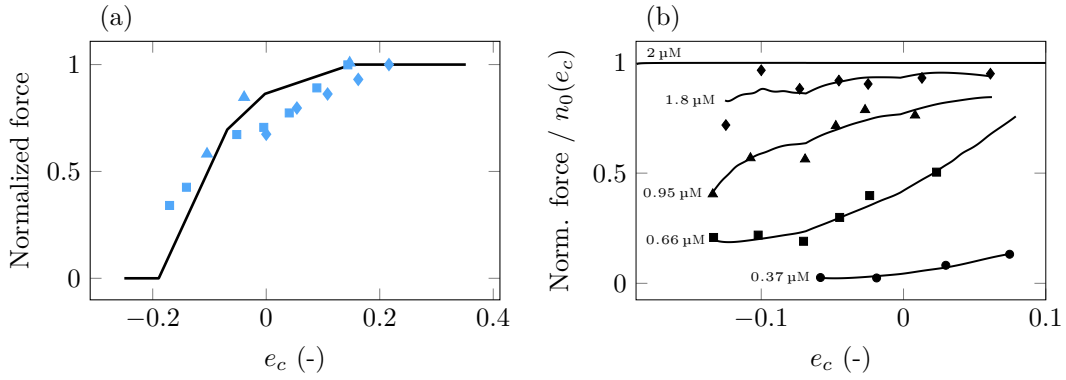

Figure 5.2 – (a) Steady-state force obtained in maximal thin filament activation. The force variation thus only depends on the variation of the thick filament activation and it allows to calibrate the function $n_0(e_c)$. (Triangle) intact tetanised rat cardiac cell at 26 °C [ter Keurs et al., 2008], (Square) skinned rat cardiac cells at 22–24 °C [Kentish et al., 1986], (Diamond) skinned rat cardiac cells at 15 °C [Dobesh et al., 2002]. (b) Variation of the thin filament activation with respect to the sarcomere extension for various levels of calcium supply obtained from intact tetanised rat cell force measurement using the function $n_0(e_c)$ presented in (a). In the experimental conditions, the latter parameter is varied by changing the extracellular calcium concentration. The resulting measured intracellular concentration is reported near the curves. Data from [ter Keurs et al., 2008].

activation as assessed by the observed variations of the force transient evolution presented in Figure 5.3 (we recall that the dynamics of the myosin heads is left unchanged by sarcomere length variations). The time to peak is not strongly affected by the sarcomere length but the relaxation duration is increased with increasing sarcomere lengths. These data also show that the level of calcium activation only affects a little the time evolution of force, in particular with a delay of the peak time at higher levels of calcium supply but this feature is not observed in all experimental data [Van Heuningen et al., 1982] (see Figure 1.20).

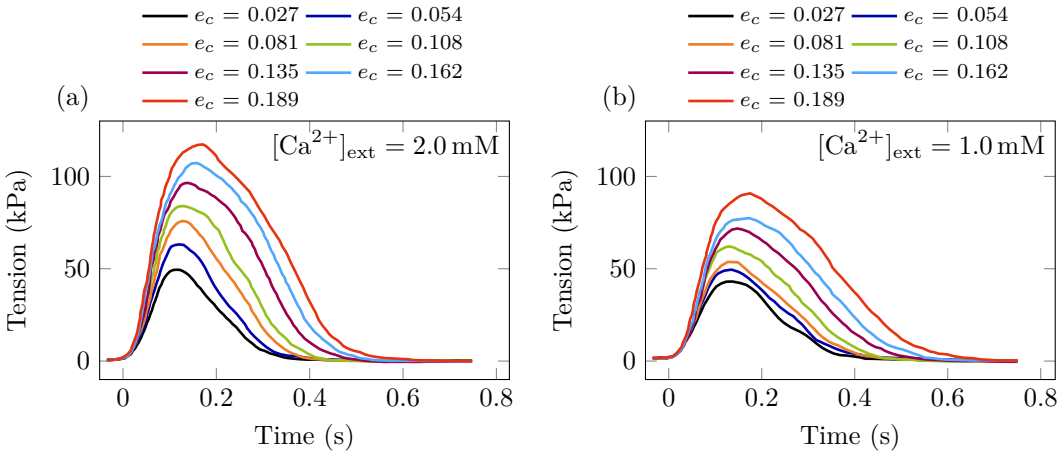

Figure 5.3 – Twitch contraction of rat cardiac cells at 25 °C at various level of calcium supply (controlled through the extracellular concentration $[Ca^{2+}]_{ext}$). The sarcomere length is maintained constant throughout the experiment. Data from [Janssen & Hunter, 1995].

Note that the transient activation may not have time to reach a full level of activation in a twitch contraction. Indeed, comparing the peak force obtained in a twitch contraction

in high level of calcium supply and the steady-state force obtained in similar condition a discrepancy appears (see Figure 5.4).

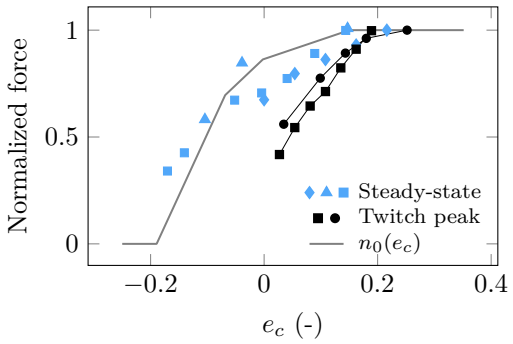

Figure 5.4 – Comparison of the twitch peak force and the steady-state force in high level of calcium supply. In steady-state conditions, the variation of the force originates from the variation of the thick filament activation. All experiments are performed on rats cardiac cells around 25 °C unless otherwise stated. (Black closed symbols) Peak force in twitch contractions for intact cells at high external calcium concentration; data from [Caremani et al., 2016] (circles) and [Janssen & Hunter, 1995] (squares). (Gray line) Estimation of the thick filament activation function n_0 with respect to the sarcomere extension. (Blue triangle) intact tetanised cell [ter Keurs et al., 2008], (blue square) skinned cells with data from [Kentish et al., 1986], (blue diamond) skinned cells at 15 °C with data from [Dobesh et al., 2002].

From the experiment analysis of Mateja & de Tombe [2012], we conclude, as for the thick filament activation, that the thin filament activation variation due to changes in the sarcomere length are assumed to be instantaneous (see more details in Section 4.2.3).

5.4 Model presentation

We start our model presentation by briefly presenting the models that serve as a basis for the building of our actin-myosin interaction formulation that considers a varying level of thin filament activation. The seminal Huxley'57 model and the extension accounting for the thick filament activation have been presented in more detail in Chapter 2 and 4, respectively.

5.4.1 Actine-myosin interaction and thick filament activation

The original Huxley'57 model considers that all myosin heads and all actin sites are activated. Describing a group of myosin heads located at distance s from their nearest actin site, the ratio of these heads that are attached at time t is denoted $P_1(s,t)$. The actin sites accessible for the myosin heads are supposed to be regularly located along the thin filament with a spatial period d_a, and therefore the value of the parameter s can vary in a possibly non-symmetric interval $[s^-, s^+]$ with $s^+ - s^- = d_a$. The dynamics of the system is given by

$$\partial_t P_1(s,t) + \dot{x}_c \partial_s P_1(s,t) = f(s)\big(1 - P_1(s,t)\big) - g(s)P_1(s,t),$$

where $\dot{x}_c$ is the relative sliding velocity between the myosin and actin filaments (taken positive when the sarcomere length increases), f and g are the attachment and detachment rates, respectively. The active stress developed in a muscle cross section of thickness ℓ_{hs}

is given by

$$T_c = \frac{\rho_{\text{surf}}}{d_a} \int_{s^-}^{s^+} \frac{\mathrm{d}w_1}{\mathrm{d}s}(s) P_1(s,t)\,\mathrm{d}s,$$

where w_1 is the free energy of the attached state and ρ_{surf} is the surface myosin head density in a muscle cross section of thickness ℓ_{hs}.

The availability of the myosin heads is then introduced by considering two pools of heads: heads that are available for attachment and those that are not. Heads that are not available can still attach but with a much slower rate. The fraction of heads that are available is given by n_0. In each pool, the probability of being attached is denoted $P_1(s,t,\gamma)$, where an additional discrete parameter γ describing the belonging to one of the two pools that has been introduced. The parameter γ takes the value 1 in the pool of the available heads and takes the value 0 in the other pool. We also define the attachment and detachment rates in each pool by f_γ and g_γ, respectively. Defining

$$|x|_+ = \begin{cases} x, & \text{if } x \geq 0, \\ 0, & \text{otherwise,} \end{cases} \qquad \text{and} \qquad |x|_- = \begin{cases} -x, & \text{if } x \leq 0, \\ 0, & \text{otherwise,} \end{cases}$$

the dynamics of the system is now given by

$$\begin{cases} \partial_t P_1(s,t,1) + \dot{x}_c \partial_s P_1(s,t,1) + \dfrac{|\dot{n}_0|_+}{n_0}\Big[P_1(s,t,1) - P_1(s,t,0)\Big] = \\ \qquad\qquad f_1(s)\big(1 - P_1(s,t,1)\big) - g_1(s) P_1(s,t,1), \\ \partial_t P_1(s,t,0) + \dot{x}_c \partial_s P_1(s,t,0) + \dfrac{|\dot{n}_0|_-}{1-n_0}\Big[P_1(s,t,0) - P_1(s,t,1)\Big] = \\ \qquad\qquad f_0(s)\big(1 - P_1(s,t,0)\big) - g_0(s) P_1(s,t,0). \end{cases}$$

On can note that additional terms appear in the equation to account for the transfer of myosin heads from one pool to the other as the thick filament activation function n_0 varies. In our modeling framework, the latter is assumed to depend only on the sarcomere extension e_c. The active tension is given as the weighted average between the two pools, hence we have

$$T_c = \frac{\rho_{\text{surf}}}{d_a} \int_{s^-}^{s^+} \frac{\mathrm{d}w_1}{\mathrm{d}s}(s) \Big[n_0 P_1(s,t,1) + (1-n_0) P_1(s,t,0)\Big]\,\mathrm{d}s.$$

5.4.2 Thin filament activation

We now extend this model to rigorously incorporate the variation of the thin filament activation.

A first step is to describe the geometry of our system. The longitudinal periodicity of the myosin heads along the thick filament is 43 nm while the periodicity along the helix direction is 14.3 nm [Craig & Padrón, 2004] (see Figure 5.5). Similarly, the thin filament also has two types of periodicity: the longitudinal periodicity is 38.5 nm while the periodicity along the helix direction is 5.5 nm. The thin filament is organized in regulatory units of length 38.5 nm. Note that the regulatory unit length corresponds to the distance d_a that was considered for the distance between accessible actin sites.

The thick and thin filament are organized in a pseudo-crystalline structure (see Figure 5.6). Possibly, a myosin head could interact with several different actin filaments and,

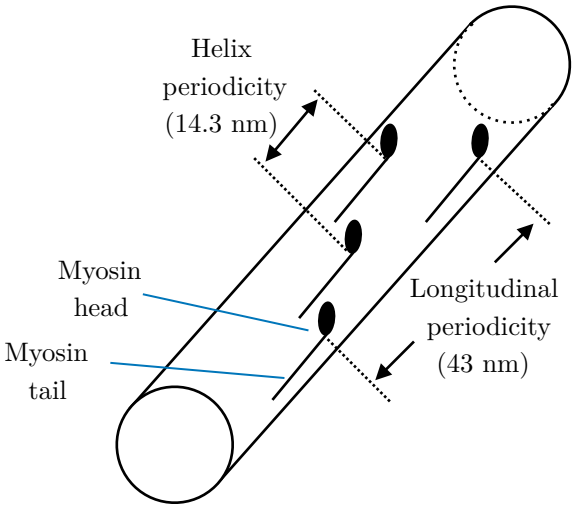

Figure 5.5 – Myosin filament

conversely, an actin filament could be linked to multiple myosin filaments. In these conditions, it is not straightforward to define what are the relevant periodicity lengths that should be considered when describing a group of myosin heads and actin sites interacting with each other.

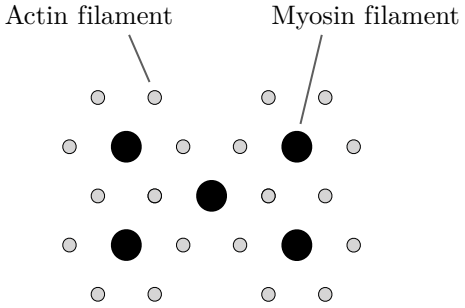

Figure 5.6 – Filaments array structure

In this work, we consider that for a group of actin sites and myosin heads interacting with each other, the periodicity of the myosin heads is 43 nm and that of the actin sites is 38.5 nm. Moreover, we consider that a myosin head can interact with its closest actin site only. Since the periodicity length is larger for the myosin heads some actin sites are not paired with any myosin head (see Figure 5.7). These actin sites do not interact with myosin heads, their states can thus be easily described. Indeed, they are necessarily not part of a cross-bridge and their probability of being activated is equal to the global thin filament activation level. It is therefore more convenient to centre our description on the myosin heads. Note that in this description, the number of considered actin sites is the same as the number of myosin heads although there are more actins site in the real physical system.

Note also that if it turns out that the relevant periodicity length is larger for actin sites than for myosin heads, the point of view of the description should be moved to the actin sites – as is done in [Regazzoni, 2020] – but the modeling principles would not change.

The signed distance between a myosin head rest position and its nearest actin site is still denoted by s. This relation pairs a myosin head and an actin site. The signed

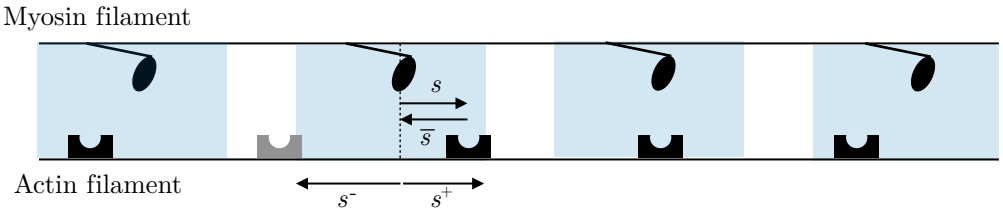

Figure 5.7 – Model parametrization. For each myosin head, the interval in which it can reach actin sites is represented in blue. Due to the difference in length of periodicity between myosin heads and actin sites, some actin actin sites are thus not paired with any myosin head (actin site represented in gray).

distance between the actin site and its paired myosin head is denoted by $\overline{s}$ and satisfies the relation $\overline{s} = -s$ (see Figure 5.7). Since we only considered actin sites that are paired with a myosin head, we can express every quantity as a function of the distance s.

To derive our model, we add to the dynamics of the myosin heads a description of the actin sites. We establish, in each pool of myosin heads, the governing system of equations. The actin site exists in four possible states

- it is non activated and non occupied by a myosin head,
- it is activated and non occupied,
- it is non activated but occupied a myosin head,
- it is activated and occupied.

For the subset of actin sites located at distance s of their paired myosin head, we denote the respective ratios of each state at time t: $\hat{n}_a(s,t,\gamma)$, $\overline{n}_a(s,t,\gamma)$, $\check{n}_a(s,t,\gamma)$ and $\tilde{n}_a(s,t,\gamma)$. Naturally, these ratios must satisfy the condition

$$\hat{n}_a(s,t,\gamma) + \overline{n}_a(s,t,\gamma) + \tilde{n}_a(s,t,\gamma) + \check{n}_a(s,t,\gamma) = 1, \ \forall t.$$

We represent the four states of our model and the fluxes between them in Figure 5.8.

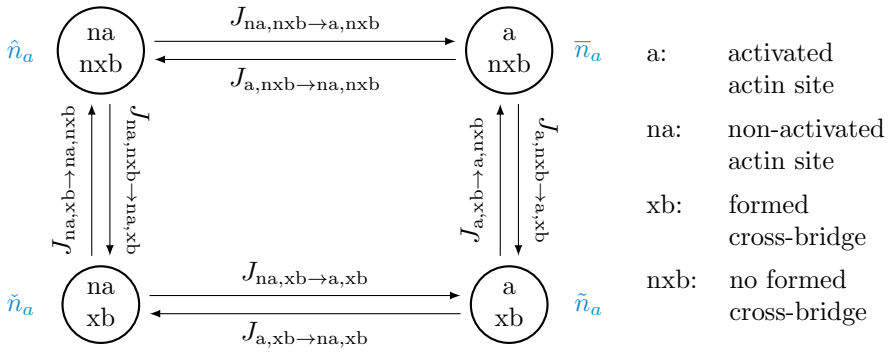

Figure 5.8 – Actin site representation. The ratio associated with each state is indicated in blue.

The ratio of activated actin sites is given by $n_a = \overline{n}_a(s,t,\gamma) + \tilde{n}_a(s,t,\gamma)\ \forall\gamma \in \{0,1\}$. It is the controlled input in our system and we assume that it is homogeneous over the whole filaments, that is $n_a(s,t,\gamma) = n_a(t)\ \forall s \in [-s^+, -s^-],\ \forall\gamma \in \{0,1\}$. Note that n_a may depend explicitly on time and on other macro-scale variables. We consider that when

$n_a(t)$ varies, the changes occur indistinctly between occupied and non-occupied actin sites. With this assumption, we have

$$\left|\begin{aligned} J_{\mathrm{na,xb}\to\mathrm{a,xb}}(s,t,\gamma) &= \frac{|\dot{n}_a|_+}{\check{n}_a(s,t,\gamma)+\hat{n}_a(s,t,\gamma)}\check{n}_a(s,t,\gamma),\\ J_{\mathrm{a,xb}\to\mathrm{na,xb}}(s,t,\gamma) &= \frac{|\dot{n}_a|_-}{\tilde{n}_a(s,t,\gamma)+\overline{n}_a(s,t,\gamma)}\tilde{n}_a(s,t,\gamma),\\ J_{\mathrm{na,nxb}\to\mathrm{a,nxb}}(s,t,\gamma) &= \frac{|\dot{n}_a|_+}{\check{n}_a(s,t,\gamma)+\hat{n}_a(s,t,\gamma)}\hat{n}_a(s,t,\gamma),\\ J_{\mathrm{a,nxb}\to\mathrm{na,nxb}}(s,t,\gamma) &= \frac{|\dot{n}_a|_-}{\tilde{n}_a(s,t,\gamma)+\overline{n}_a(s,t,\gamma)}\overline{n}_a(s,t,\gamma). \end{aligned}\right.$$

The remaining transition rates are linked to the attachment-detachment process. Similarly to the fact that it is possible for a myosin head to attach when it is in the pool $\gamma = 0$, we do not assume that is impossible to bind on a non-activated actin site. However, the rate of this transition is lower than when the actin site is activated. We define the attachment rates with an activated actin site by $f_{\gamma,\mathrm{a}}$ and by $f_{\gamma,\mathrm{na}}$ when the actin site is not activated.

We now consider the flux of actin sites changing from an activated non-occupied state to an activated occupied state. This flux is equal to the flux of myosin heads attaching to activated actin sites. Myosin heads that can undergo this transition are a subgroup of the detached heads (the detached heads represent a ratio of $1 - P_1$), that are paired with an activated actin site. The ratio of myosin heads that, among the detached heads, are paired with an activation actin site is denoted $r_{\mathrm{a|nxb}}$. We thus have

$$J_{\mathrm{a,nxb}\to\mathrm{a,xb}}(s,t,\gamma) = f_{\gamma,\mathrm{a}}\big(1-P_1(s,t,\gamma)\big)r_{\mathrm{a|nxb}} = f_{\gamma,\mathrm{a}}\big(1-P_1(s,t,\gamma)\big)\frac{\overline{n}_a(s,t,\gamma)}{\overline{n}_a(s,t,\gamma)+\hat{n}_a(s,t,\gamma)}.$$

Similarly, we obtain

$$\begin{aligned} J_{\mathrm{na,nxb}\to\mathrm{na,xb}}(s,t,\gamma) &= f_{\gamma,\mathrm{na}}\big(1-P_1(s,t,\gamma)\big)r_{\mathrm{na|nxb}}\\ &= f_{\gamma,\mathrm{na}}\big(1-P_1(s,t,\gamma)\big)\frac{\hat{n}_a(s,t,\gamma)}{\overline{n}_a(s,t,\gamma)+\hat{n}_a(s,t,\gamma)}. \end{aligned}$$

Using the same reasoning for the actin sites paired with attached myosin heads (the attached myosin heads represent a ratio of P_1), we have

$$\left|\begin{aligned} J_{\mathrm{a,xb}\to\mathrm{a,nxb}}(s,t,\gamma) &= g_{\gamma,\mathrm{a}}(s)P_1(s,t,\gamma)r_{\mathrm{a|xb}}\\ &= g_{\gamma,\mathrm{a}}(s)P_1(s,t,\gamma)\frac{\tilde{n}_a(s,t,\gamma)}{\tilde{n}_a(s,t,\gamma)+\check{n}_a(s,t,\gamma)},\\ J_{\mathrm{na,xb}\to\mathrm{na,nxb}}(s,t,\gamma) &= g_{\gamma,\mathrm{na}}(s)P_1(s,t,\gamma)r_{\mathrm{na|xb}}\\ &= g_{\gamma,\mathrm{na}}(s)P_1(s,t,\gamma)\frac{\check{n}_a(s,t,\gamma)}{\tilde{n}_a(s,t,\gamma)+\check{n}_a(s,t,\gamma)}. \end{aligned}\right.$$

Altogether, the system dynamics equation is

$$
\begin{cases}
\dfrac{\mathrm{d}}{\mathrm{d}t}P_1(s,t,\gamma) = f_{\gamma,\mathrm{a}}(s)\dfrac{\overline{n}_a(s,t,\gamma)}{\overline{n}_a(s,t,\gamma)+\hat{n}_a(s,t,\gamma)}\big(1-P_1(s,t,\gamma)\big) \\
\qquad\qquad + f_{\gamma,\mathrm{na}}(s)\dfrac{\hat{n}_a(s,t,\gamma)}{\overline{n}_a(s,t,\gamma)+\hat{n}_a(s,t,\gamma)}\big(1-P_1(s,t,\gamma)\big) \\
\qquad - g_{\gamma,\mathrm{a}}(s)P_1(s,t,\gamma)\dfrac{\tilde{n}_a(s,t,\gamma)}{\tilde{n}_a(s,t,\gamma)+\check{n}_a(s,t,\gamma)} \\
\qquad\qquad - g_{\gamma,\mathrm{na}}(s)P_1(s,t,\gamma)\dfrac{\check{n}_a(s,t,\gamma)}{\tilde{n}_a(s,t,\gamma)+\check{n}_a(s,t,\gamma)}, \qquad (5.1a) \\
\dfrac{\mathrm{d}}{\mathrm{d}t}\overline{n}_a(s,t,\gamma) = -f_{\gamma,\mathrm{a}}\big(1-P_1(s,t,\gamma)\big)\dfrac{\overline{n}_a(s,t,\gamma)}{\overline{n}_a(s,t,\gamma)+\hat{n}_a(s,t,\gamma)} \\
\qquad\qquad + g_{\gamma,\mathrm{a}}(s)P_1(s,t,\gamma)\dfrac{\tilde{n}_a(s,t,\gamma)}{\tilde{n}_a(s,t,\gamma)+\check{n}_a(s,t,\gamma)} \\
\qquad + \dfrac{|\dot{n}_a|_+}{\check{n}_a(s,t,\gamma)+\hat{n}_a(s,t,\gamma)}\hat{n}_a(s,t,\gamma) \\
\qquad\qquad - \dfrac{|\dot{n}_a|_-}{\tilde{n}_a(s,t,\gamma)+\overline{n}_a(s,t,\gamma)}\overline{n}_a(s,t,\gamma), \qquad (5.1b) \\
\dfrac{\mathrm{d}}{\mathrm{d}t}\tilde{n}_a(s,t,\gamma) = f_{\gamma,\mathrm{a}}\big(1-P_1(s,t,\gamma)\big)\dfrac{\overline{n}_a(s,t,\gamma)}{\overline{n}_a(s,t,\gamma)+\hat{n}_a(s,t,\gamma)} \\
\qquad\qquad - g_{\gamma,\mathrm{a}}(s)P_1(s,t,\gamma)\dfrac{\tilde{n}_a(s,t,\gamma)}{\tilde{n}_a(s,t,\gamma)+\check{n}_a(s,t,\gamma)} \\
\qquad + \dfrac{|\dot{n}_a|_+}{\check{n}_a(s,t,\gamma)+\hat{n}_a(s,t,\gamma)}\check{n}_a(s,t,\gamma) \\
\qquad\qquad - \dfrac{|\dot{n}_a|_-}{\tilde{n}_a(s,t,\gamma)+\overline{n}_a(s,t,\gamma)}\tilde{n}_a(s,t,\gamma), \qquad (5.1c) \\
\dfrac{\mathrm{d}}{\mathrm{d}t}\check{n}_a(s,t,\gamma) = f_{\gamma,\mathrm{na}}\big(1-P_1(s,t,\gamma)\big)\dfrac{\hat{n}_a(s,t,\gamma)}{\overline{n}_a(s,t,\gamma)+\hat{n}_a(s,t,\gamma)} \\
\qquad\qquad - g_{\gamma,\mathrm{na}}(s)P_1(s,t,\gamma)\dfrac{\check{n}_a(s,t,\gamma)}{\tilde{n}_a(s,t,\gamma)+\check{n}_a(s,t,\gamma)} \\
\qquad + \dfrac{|\dot{n}_a|_-}{\tilde{n}_a(s,t,\gamma)+\overline{n}_a(s,t,\gamma)}\tilde{n}_a(s,t,\gamma) \\
\qquad\qquad - \dfrac{|\dot{n}_a|_+}{\check{n}_a(s,t,\gamma)+\hat{n}_a(s,t,\gamma)}\check{n}_a(s,t,\gamma), \qquad (5.1d) \\
\dfrac{\mathrm{d}}{\mathrm{d}t}\hat{n}_a(s,t,\gamma) = -f_{\gamma,\mathrm{na}}\big(1-P_1(s,t,\gamma)\big)\dfrac{\hat{n}_a(s,t,\gamma)}{\overline{n}_a(s,t,\gamma)+\hat{n}_a(s,t,\gamma)} \\
\qquad\qquad + g_{\gamma,\mathrm{na}}(s)P_1(s,t,\gamma)\dfrac{\check{n}_a(s,t,\gamma)}{\tilde{n}_a(s,t,\gamma)+\check{n}_a(s,t,\gamma)} \\
\qquad + \dfrac{|\dot{n}_a|_-}{\tilde{n}_a(s,t,\gamma)+\overline{n}_a(s,t,\gamma)}\overline{n}_a(s,t,\gamma) \\
\qquad\qquad - \dfrac{|\dot{n}_a|_+}{\check{n}_a(s,t,\gamma)+\hat{n}_a(s,t,\gamma)}\hat{n}_a(s,t,\gamma). \qquad (5.1e)
\end{cases}
$$

From the dynamics equation, we obtain the, desired, relations

$$
\begin{cases}
\hat{n}_a(s,t,\gamma)+\overline{n}_a(s,t,\gamma)+\tilde{n}_a(s,t,\gamma)+\check{n}_a(s,t,\gamma)=1, \\
\tilde{n}_a(s,t,\gamma)+\overline{n}_a(s,t,\gamma)=n_a, \\
\tilde{n}_a(s,t,\gamma)+\check{n}_a(s,t,\gamma)=P_1(s,t,\gamma).
\end{cases}
$$

The first one is the conservation of actin sites. The second one corresponds to the definition that the ratio of activated actin sites (occupied or not) is given by n_a. The third one reflects the fact that the ratio of attached head and the ratio of occupied actin sites is the same.

The system (5.1) can thus be reduced to

$$\begin{cases} \dfrac{\mathrm{d}}{\mathrm{d}t}P_1(s,t,\gamma) = f_{\gamma,\mathrm{a}}(s)\overline{n}_a(s,t,\gamma) + f_{\gamma,\mathrm{na}}(s)\big(1 - P_1(s,t,\gamma) - \overline{n}_a(s,t,\gamma)\big) \\ \qquad\qquad - g_{\gamma,\mathrm{a}}(s)\big(n_a - \overline{n}_a(s,t,\gamma)\big) - g_{\gamma,\mathrm{na}}(s)\big(\overline{n}_a(s,t,\gamma) - n_a + P_1(s,t,\gamma)\big), & (5.2a) \\ \dfrac{\mathrm{d}}{\mathrm{d}t}\overline{n}_a(s,t,\gamma) = \dfrac{|\dot{n}_a|_+}{1-n_a}\big(1 - P_1(s,t,\gamma) - \overline{n}_a(s,t,\gamma)\big) + g_{\gamma,\mathrm{a}}(s)\big(n_a - \overline{n}_a(s,t,\gamma)\big) \\ \qquad\qquad - \dfrac{|\dot{n}_a|_-}{n_a}\overline{n}_a(s,t,\gamma) - f_{\gamma,\mathrm{a}}(s)\overline{n}_a(s,t,\gamma), & (5.2b) \\ \hat{n}_a(s,t,\gamma) = 1 - \overline{n}_a(s,t,\gamma) - P_1(s,t,\gamma), & (5.2c) \\ \tilde{n}_a(s,t,\gamma) = n_a - \overline{n}_a(s,t,\gamma), & (5.2d) \\ \check{n}_a(s,t,\gamma) = P_1(s,t,\gamma) - n_a - \overline{n}_a(s,t,\gamma). & (5.2e) \end{cases}$$

The derivative used here is a total time derivative, meaning that it describes the time variations following a group of myosin heads. To fully establish the system dynamics, these total time derivative needs to be made explicit. The system is described from the point of view of the myosin heads, therefore the pool exchange terms are written as in Chapter 4 and the total time derivatives in (5.2) are given by

$$\begin{cases} \dfrac{\mathrm{d}}{\mathrm{d}t}P_1(s,t,1) = \partial_t P_1(s,t,1) + \dot{x}_c\partial_s P_1(s,t,\gamma) + \dfrac{|\dot{n}_0|_+}{n_0}\Big[P_1(s,t,1) - P_1(s,t,0)\Big], \\ \dfrac{\mathrm{d}}{\mathrm{d}t}P_1(s,t,0) = \partial_t P_1(s,t,1) + \dot{x}_c\partial_s P_1(s,t,\gamma) + \dfrac{|\dot{n}_0|_-}{1-n_0}\Big[P_1(s,t,0) - P_1(s,t,1)\Big], \\ \dfrac{\mathrm{d}}{\mathrm{d}t}\overline{n}_a(s,t,1) = \partial_t \overline{n}_a(s,t,\gamma) + \dot{x}_c\partial_s\,\overline{n}_a(s,t,\gamma) + \dfrac{|\dot{n}_0|_+}{n_0}\Big[\overline{n}_a(s,t,1) - \overline{n}_a(s,t,0)\Big], \\ \dfrac{\mathrm{d}}{\mathrm{d}t}\overline{n}_a(s,t,1) = \partial_t \overline{n}_a(s,t,\gamma) + \dot{x}_c\partial_s\,\overline{n}_a(s,t,\gamma) + \dfrac{|\dot{n}_0|_-}{1-n_0}\Big[\overline{n}_a(s,t,0) - \overline{n}_a(s,t,1)\Big]. \end{cases}$$

The active tension is still given by

$$T_c = \frac{\rho_{\mathrm{surf}}}{d_a}\int_{s^-}^{s^+}\frac{\mathrm{d}w_1}{\mathrm{d}s}(s)\Big[n_0 P_1(s,t,1) + (1-n_0)P_1(s,t,0)\Big]\,\mathrm{d}s.$$

5.4.3 Model steady-state

To check the consistence of our modeling assumptions, we consider the steady-state regime of our model. We assume that $\dot{n}_0 = 0$ and $\dot{n}_a = 0$. We also suppose that $\dot{x}_c = 0$. The system (5.2) yields

$$\begin{cases} \overline{n}_a(s,\gamma) = \dfrac{g_{\gamma,\mathrm{a}}(s)}{f_{\gamma,\mathrm{a}}(s) + g_{\gamma,\mathrm{a}}(s)}n_a, \\ P_1(s,t,\gamma) = n_a\dfrac{f_{\gamma,\mathrm{a}}(s)}{f_{\gamma,\mathrm{a}}(s) + g_{\gamma,\mathrm{a}}(s)} + (1-n_a)\dfrac{f_{\gamma,\mathrm{na}}(s)}{f_{\gamma,\mathrm{na}}(s) + g_{\gamma,\mathrm{na}}(s)} \end{cases}$$

The global probability of being attached is then given by

$$\begin{aligned} P_1(s) &= n_0 P_1(s,1) + (1-n_0)P_1(s,0), \\ &= n_0\Big[n_a\frac{f_{1,\mathrm{a}}(s)}{f_{1,\mathrm{a}}(s)+g_{1,\mathrm{a}}(s)} + (1-n_a)\frac{f_{1,\mathrm{na}}(s)}{f_{1,\mathrm{na}}(s)+g_{1,\mathrm{na}}(s)}\Big] \\ &\qquad + (1-n_0)\Big[n_a\frac{f_{0,\mathrm{a}}(s)}{f_{0,\mathrm{a}}(s)+g_{0,\mathrm{a}}(s)} + (1-n_a)\frac{f_{0,\mathrm{na}}(s)}{f_{0,\mathrm{na}}(s)+g_{0,\mathrm{na}}(s)}\Big]. \end{aligned}$$

The probability of being attached is the weighted average of the probability of being attached in each configuration (actin site activated or not, myosin head attached or not). With the natural approximations

$$\frac{f_{0,\mathrm{a}}}{g_{0,\mathrm{a}}} \ll 1, \quad \frac{f_{0,\mathrm{na}}}{g_{0,\mathrm{na}}} \ll 1, \quad \frac{f_{1,\mathrm{na}}}{g_{1,\mathrm{na}}} \ll 1,$$

we obtain

$$P_1(s) = n_0 n_a \frac{f_{1,\mathrm{a}}(s)}{f_{1,\mathrm{a}}(s)+g_{1,\mathrm{a}}(s)}.$$

The ratio of attached heads is given by

$$n_{\mathrm{att}} = \frac{1}{d_a}\int_{s^-}^{s^+} P_1(s)\,\mathrm{d}s = n_0 n_a \int_{s^-}^{s^+} \frac{f_{1,\mathrm{a}}(s)}{f_{1,\mathrm{a}}(s)+g_{1,\mathrm{a}}(s)}\,\mathrm{d}s.$$

The number of attached heads is thus proportional to the the level of thick filament activation and the level of thin filament activation, which is consistent with our modeling objective.

5.5 Model calibration and validation

To validate our proposed model extension that take into account the variation of the thin filament activation level, we need to specify the form of the thin filament activation function n_a. We propose here a function n_a that mimics the physiology. To account for the experimental data, the thin filament activation must be a function of the time, the sarcomere extension and the level of calcium supply. In experiments, the extracellular or intracellular calcium concentrations may be controlled. Since we do not model here the interaction between the thin filament and the calcium ions, we cannot use these quantities as model variables. Instead, we introduce a variable C for the "level of calcium supply". This variable does not have a direct physical interpretation, and it indeed corresponds to an indicator between zero and one of the force variation that can be achieved with a variation of the calcium supply (when $C = 0$, there is no calcium supply and the force is zero; when $C = 1$, the calcium supply is maximal). It can however be related in a bijective manner to the contractility Σ_0, which is the relevant variable for the medical doctors. This link is done as follows: the contractility is defined as the maximal tension that can be developed for a given level of calcium supply – this tension is naturally obtained at the highest possible sarcomere extension and in steady-state conditions.

We assume that the thin filament activation can be multiplicatively decomposed as

$$n_a(e_c, t, C) = n_{a,\infty}(e_c, C) n_{a,t}(e_c, t)$$

where $n_{a,\infty}$ accounts for the steady-state variation of the thin filament activation with the sarcomere extension and the level of calcium supply, and where $n_{a,t}$ accounts for the

transient evolution, which is affected by the sarcomere extension. To avoid the overfitting of the twitch contraction data presented in Figure 5.3, we choose to have a time evolution that does not depend on the level of calcium supply.

Getting inspired from experiments on skinned cells showing that the force varies with a sigmoid shape with respect to the level of calcium supply [Kentish et al., 1986; Dobesh et al., 2002], we choose a family of sigmoid functions to represent the variation of the force with respect to the contractility, parametrized by the sarcomere extension. We have

$$\begin{cases} n_{a,\infty}(e_c, C) = \dfrac{(C)^{n_{\mathrm{Ha}}}}{(C)^{n_{\mathrm{Ha}}} + \left(C_{50}(e_c)\right)^{n_{\mathrm{Ha}}}}, \\ \\ C_{50}(e_c) = \dfrac{C_{50}^{\mathrm{H}} - C_{50}^{\mathrm{L}}}{e_{c,50}^{\mathrm{H}} - e_{c,50}^{\mathrm{L}}}(e_c - e_{c,50}^{\mathrm{L}}) + C_{50}^{\mathrm{L}}, \end{cases}$$

where C_{50} represents the effect of the sarcomere extension on the thin filament activation. It is assumed to vary linearly with e_c. The transient part of the thin filament activation function is defined by

$$\begin{cases} n_{a,t}(e_c, t) = n_{a,\mathrm{peak}}(e_c) n_{a,t,\mathrm{norm}}(e_c, t), \\ \\ n_{a,t,\mathrm{norm}}(e_c, t) = \begin{cases} \dfrac{1 - n_{a,0}}{2}\Big(\sin\big(\dfrac{\pi}{\tau_{\mathrm{rise}}}(t - t_0) - \dfrac{\pi}{2}\big) + 1\Big) + n_{a,0}, \\ \qquad \text{if } t_0 \le t \le t_0 + \tau_{\mathrm{rise}}, \\ \\ \dfrac{1 - n_{a,0}}{2}\Big(\sin\big(\dfrac{\pi}{\tau_{\mathrm{relax}}(e_c)}(t - t_0 - \tau_{\mathrm{rise}}) + \dfrac{\pi}{2}\big) + 1\Big) + n_{a,0}, \\ \qquad \text{if } t_0 + \tau_{\mathrm{rise}} \le t \le t_0 + \tau_{\mathrm{rise}} + \tau_{\mathrm{relax}}(e_c), \\ \\ 0, \ \text{otherwise}, \end{cases} \\ \\ \tau_{\mathrm{relax}}(e_c) = \dfrac{\tau_{\mathrm{relax}}^{\mathrm{H}} - \tau_{\mathrm{relax}}^{\mathrm{L}}}{e_{c,\mathrm{relax}}^{\mathrm{H}} - e_{c,\mathrm{relax}}^{\mathrm{L}}}(e_c - e_{c,\mathrm{relax}}^{\mathrm{L}}) + \tau_{\mathrm{relax}}^{\mathrm{L}}, \\ \\ n_{a,\mathrm{peak}}(e_c) = \begin{cases} \dfrac{n_{a,\mathrm{peak}}^{\mathrm{M}} - n_{a,\mathrm{peak}}^{\mathrm{L}}}{e_{c,t}^{\mathrm{M}} - e_{c,t}^{\mathrm{L}}}(e_c - e_{c,t}^{\mathrm{M}}) + n_{a,\mathrm{peak}}^{\mathrm{L}}, & \text{if } e_c < e_{c,t}^{\mathrm{M}}, \\ 1, & \text{if } e_c \ge e_{c,t}^{\mathrm{M}}, \end{cases} \end{cases}$$

where τ_{rise} it the constant activation rising time, τ_{relax} accounts for the varying relaxation duration, $n_{a,\mathrm{peak}}$ represents the fact that the thin filament may not have time to reach the complete activation state for non-maximal sarcomere extensions and $n_{a,0}$, satisfying $0 < n_{a,0} \ll 1$, ensures that n_a is never equal to zero, which is forbidden in the system (5.2).

We choose the transition rates and the attached free energy level as calibrated in [Kimmig & Caruel, 2019] (see Chapter 3). They are presented in Figure 5.9. Moreover, we choose the modeling assumption

$$\begin{cases} f_{\gamma,\mathrm{na}} = \dfrac{1}{500} f_{\gamma,\mathrm{a}} \ \forall \gamma \in \{0, 1\}, \ f_{1,\mathrm{a}} = \dfrac{1}{100} f_{0,\mathrm{a}}, \ f_{1,\mathrm{na}} = \dfrac{1}{100} f_{0,\mathrm{na}}, \\ g_{1,\mathrm{a}} = g_{1,\mathrm{na}} = g_{0,\mathrm{a}} = g_{0,\mathrm{na}}. \end{cases}$$

The parameters of the thin filament activation function are given in Appendix 5.7. The functions $n_{a,\infty}$, $n_{a,t,\mathrm{norm}}$ and $n_{a,\mathrm{peak}}$ defined with these parameters along with the link between the level of calcium supply C and the contractility Σ_0 are presented in Figure 5.10.

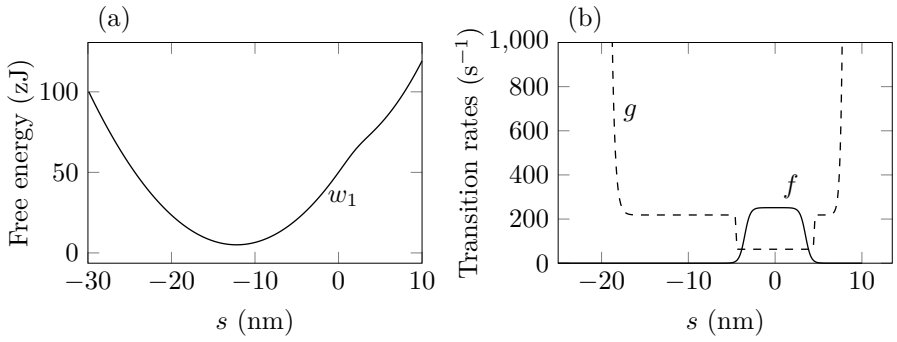

Figure 5.9 – (a) Attached state free energy level w_1. (b) Transition rates. The derivation of these parameters functions is presented in [Kimmig & Caruel, 2019] (Chapter 3).

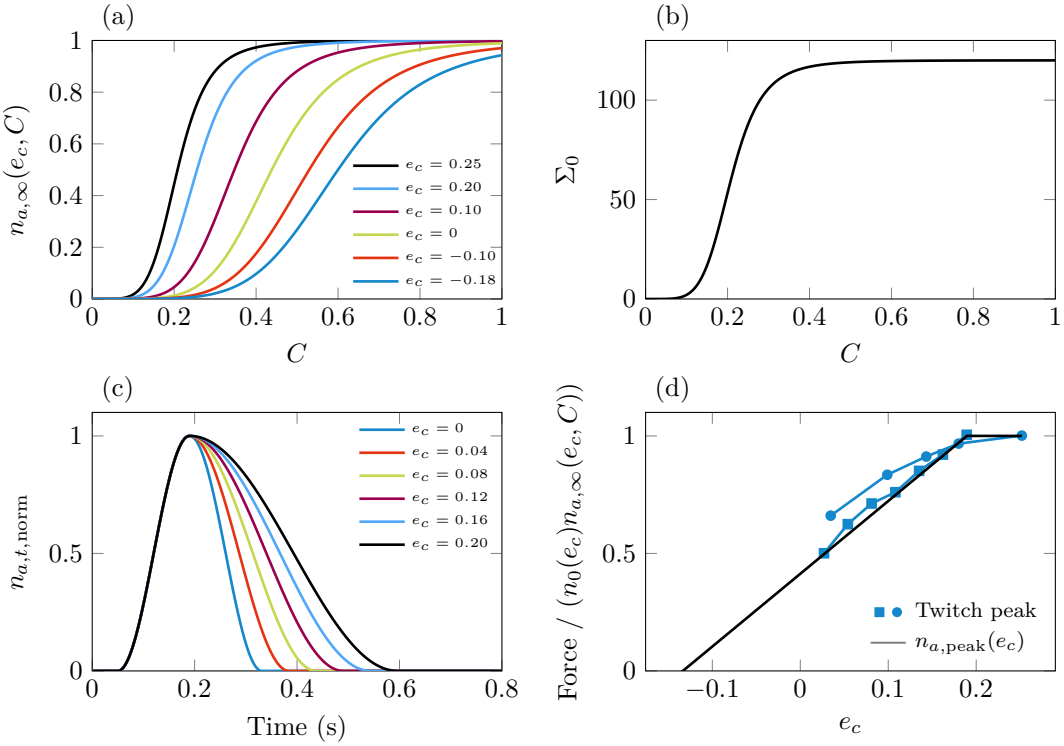

Figure 5.10 – (a) Steady-state thin filament activation function $n_{a,\infty}$ for various sarcomere extensions. (b) Relation between the contractility Σ_0 and the level of calcium supply C. (c) Normalized thin filament activation function $n_{a,t,\text{norm}}$ for various sarcomere extensions. (d) Function $n_{a,\text{peak}}$ compared with experimental data ($\tilde{C} = 0.95$ is the value of the level of calcium supply C calibrated to match the maximal tension developed in the experimental data in maximal calcium activation conditions). (Closed symbols) Peak twitch forces in high calcium supply conditions for cardiac rat cells; (circle) data from [Caremani et al., 2016], (square) data from [Janssen & Hunter, 1995].

We validate our model by comparing its outputs with the experimental data presented in Figures 5.2 and 5.3. We first compare the steady-state model prediction with experimental data (see Figure 5.11) and note that our model displays a good match with the data. We then simulate twitch contractions in "high" and "low" contractility conditions

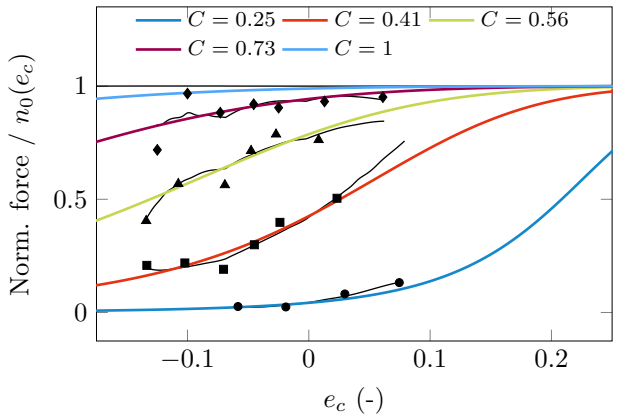

Figure 5.11 – Comparison between the model steady-state force predictions at various level of calcium supply as a function of the sarcomere extension and experimental data from [ter Keurs et al., 2008] (black symbols). Each symbol corresponds to a single level of extracellular calcium concentration; the black lines are fit of the data. Note that the values of the variable C chosen in the simulations are adjusted to match the data (there is not rule to link the experimental calcium concentration and the value of the level of calcium supply C).

(we use a level of calcium supply C of 0.95 and 0.33, respectively) in isometric conditions, i.e. with $\dot{x}_c = 0$. The results are presented in Figure 5.12. Note that with $C = 0.33$, the contractility is $\Sigma_0 = 110\,\text{kPa}$ but the peak maximal peak force is only equal to 94 kPa because the experimental conditions do not use the maximal sarcomere length and, at this level of calcium supply, the decrease of the force with the sarcomere length is steep. The results match well the experimental data in high contractility conditions. However, in low contractility conditions, the decreases of the peak force with the sarcomere extension is faster in the simulations than in the data. We see here a limitation of our calibration. One can note that the strong decrease of the force with the sarcomere extension originates from the constraints imposed on the function $n_{a,\infty}$ by the steady-state data (Figure 5.11). However these data are obtained on a range of sarcomere extensions between -0.15 and 0.05 whereas the twitch contractions are performed at sarcomere extensions between 0.02 and 0.19, i.e. in a region where the function $n_{a,\infty}$ extrapolates the data. The correspondence with the experimental data may thus be improved by adjusting the function $n_{a,\infty}$ such that the steady-state force varies more gently with the sarcomere extension in the latter region of sarcomere extensions for "low" values of C. Moreover, the data in steady-state conditions and the experimental twitch contractions have not been obtained in the same study, and there may thus be some intrinsic incompatibilities between them due to different experimental conditions.

We can now compare the dynamics of the thin filament activation and the tension development. There is no consensus on the calibration of the transition rates of the Huxley'57 model family [Kimmig & Caruel, 2019] (Chapter 3). If the calibration favors the match with the force-velocity relation observed in a steady-state shortening contraction, the transition rates are six times faster than if the tension development rate is favored. We test both cases here without changing the calibration of the thin filament activation n_a (the point is not to match experimental data). The results for a representative contraction are

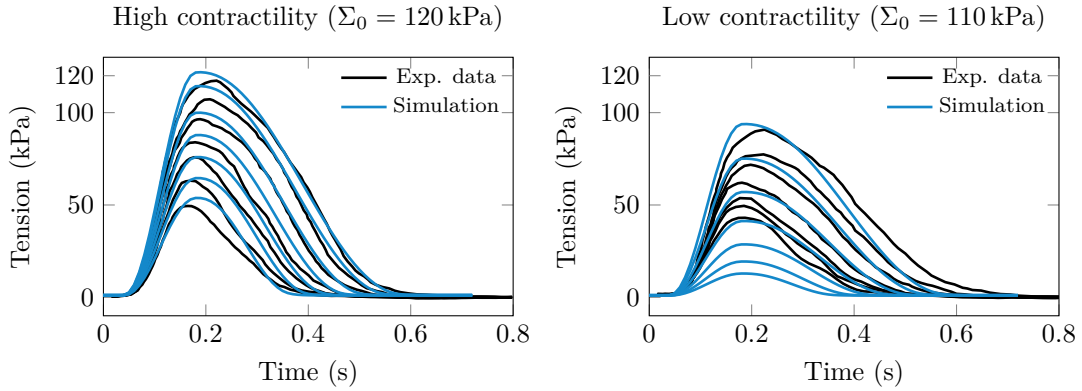

Figure 5.12 – Comparison of simulated twitch contractions at various sarcomere extension with experimental data (from top to bottom, $e_c = \{0.19, 0.162, 0.135, 0.108, 0.081, 0.054, 0.027\}$). (Left) high contractility conditions, (right) low contractility conditions. The experimental data are obtained with a strict sarcomere length control throughout the experiment [Janssen & Hunter, 1995].

presented in Figure 5.13. Not surprisingly, the delay between the thin filament activation and the active tension is longer when the attachment-detachment rate is slower. What we can conclude from this simulation is that, in physiological conditions, the delay between the thin filament activation and the force development is non-negligible and can even become significant depending on the choices made in the actin-myosin interaction model calibration. A rigorous incorporation of both dynamics in the model is thus necessary.

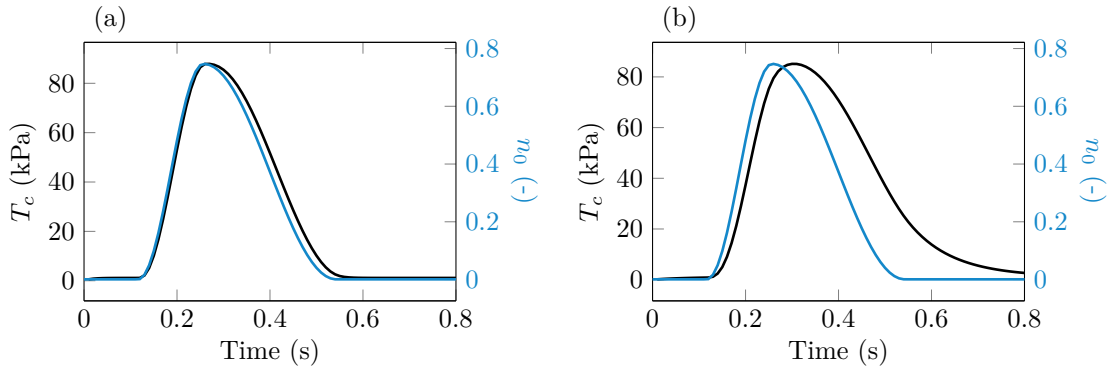

Figure 5.13 – Comparison of the time evolution of the thin filament activation function n_a and the active tension T_c. The simulation is performed in isometric conditions ($\dot{x}_c = 0$). We have $e_c = 0.108$ and $C = 0.33$. We choose two sets of transitions rates. (a) Transition rates based on the force-velocity calibration from [Kimmig & Caruel, 2019] (Chapter 3). (b) Transition rates divided by a factor six with respect to (a). These rates are similar to that proposed by [de Tombe & Stienen, 2007] that are calibrated on the tension development dynamics.

5.6 Conclusion

In this chapter, we proposed a novel framework to rigorously incorporate the varying actin sites activation level into the Huxley'57 model family. This framework may be coupled to a separately defined thin filament activation models or, as done in this work, used as

a standalone model with the time-dependent thin filament activation being provided as a model input. The model is calibrated on experimental twitch contractions obtained in controlled sarcomere length conditions and a preliminary validation is performed. However, additional validations are required to fully assess the capabilities of the model, in particular in conditions where the sarcomere extension varies during the contraction as it is the case in a heartbeat.

Our new framework opens new possibilities to develop thin filament activation models by allowing to couple them with an actin-myosin interaction model, therefore enabling a rigorous calibration. Moreover, in the context of heart simulation, our model may also prove to be an important element. It indeed bridges the electrophysiological part and the mechanical part of the description. Once properly calibrated and coupled within the heart simulation framework, our model may allow to investigate the relation between the force and calcium concentration measured *ex vivo* and that required *in vivo* in a normal functioning. If a discrepancy appears (potentially due to the absence of neuroendocrine regulation in the model apart from its effects on the level of calcium supply), it will encourage the development of new experimental protocols to understand this discrepancy and allow the development of the associated models.

5.7 Appendix

The model parameters used in this chapter are presented in Table 5.1.

Parameter	Value	Parameter	Value
n_{Ha}	5.5	$e^H_{c,relax}$	0.18
C^H_{50}	0.21	$e^L_{c,relax}$	6.5e-3
C^L_{50}	0.60	t_0	0.4
$e^H_{c,50}$	0.252	$e^L_{c,t}$	0.028
$e^L_{c,50}$	-0.177	$e^M_{c,t}$	0.1895
τ_{rise}	0.14	$n^M_{a,peak}$	1
τ^H_{relax}	0.38	$n^L_{a,peak}$	0.50
τ^L_{relax}	0.15	$n_{a,0}$	1e-3

Table 5.1 – Model parameters for the thin filament activation function.

Bibliography

Ait-Mou, Y., Hsu, K., Farman, G.P., Kumar, M., Greaser, M.L., Irving, T.C., & de Tombe, P.P. (2016). Titin strain contributes to the Frank–Starling law of the heart by structural rearrangements of both thin- and thick-filament proteins. *Proceedings of the National Academy of Sciences*, *113*(8), 2306–2311.

Caremani, M., Pinzauti, F., Reconditi, M., Piazzesi, G., Stienen, G.J.M., Lombardi, V., & Linari, M. (2016). Size and speed of the working stroke of cardiac myosin in situ. *Proceedings of the National Academy of Sciences*, *113*(13), 3675–3680.

Chapelle, D., Le Tallec, P., Moireau, P., & Sorine, M. (2012). Energy-preserving muscle tissue model: formulation and compatible discretizations. *Journal for Multiscale Computational Engineering*.

Craig, R., & Padrón, R. (2004). Molecular structure of the sarcomere. *Myology*, *3*, 129–144.

de Tombe, P.P., Mateja, R.D., Tachampa, K., Mou, YA, Farman, G.P., & Irving, T.C. (2010). Journal of Molecular and Cellular Cardiology. *Journal of molecular and cellular cardiology*, *48*(5), 851–858.

de Tombe, P.P., & Stienen, G.J.M. (2007). Impact of temperature on cross-bridge cycling kinetics in rat myocardium. *The Journal of Physiology*, *584*(2), 591–600.

de Tombe, P.P., & ter Keurs, H.E.D.J. (2016). Cardiac muscle mechanics: Sarcomere length matters. *Journal of molecular and cellular cardiology*, *91*(C), 148–150.

Dobesh, D.P., Konhilas, J.P., & de Tombe, P.P. (2002). Cooperative activation in cardiac muscle: impact of sarcomere length. *AJP: Heart and Circulatory Physiology*, *282*(3), H1055–H1062.

Dupuis, L. J, Lumens, J., Arts, T., & Delhaas, T. (2016). Mechano-chemical Interactions in Cardiac Sarcomere Contraction: A Computational Modeling Study. *PLOS Computational Biology*, *12*(10), e1005126–20.

Hussan, J., de Tombe, P.P., & Rice, J.J. (2006). A spatially detailed myofilament model as a basis for large-scale biological simulations. *IBM journal of research and …*, *50*(6), 583–600.

Janssen, P.M., & Hunter, W.C. (1995). Force, not sarcomere length, correlates with prolongation of isosarcometric contraction. *AJP: Heart and Circulatory Physiology*, *269*(2), H676–H685.

Kentish, J.C., Ter Keurs, H.E.D.J., Ricciardi, L., Bucx, J.J., & Noble, M.I. (1986). Comparison between the sarcomere length-force relations of intact and skinned trabeculae from rat right ventricle. influence of calcium concentrations on these relations. *Circulation research*, *58*(6), 755–768.

Kimmig, F., & Caruel, M. (2019). Hierarchical modeling of muscle contraction. *submitted*.

Kimmig, F., Moireau, P., & Chapelle, D. (2019). Activation-contraction coupling in a multiscale heart model, an element for capturing the frank-starling effect. *to be submitted*.

Land, S., & Niederer, S.A. (2015). A Spatially Detailed Model of Isometric Contraction Based on Competitive Binding of Troponin I Explains Cooperative Interactions between Tropomyosin and Crossbridges. *PLOS Computational Biology*, *11*(8), e1004376–28.

Landesberg, A., & Sideman, S. (1994a). Coupling calcium binding to troponin C and cross-bridge cycling in skinned cardiac cells. *The American journal of physiology*, *266*(3), H1260–71.

Landesberg, A., & Sideman, S. (1994b). Mechanical regulation of cardiac muscle by coupling calcium kinetics with cross-bridge cycling: a dynamic model. *The American journal of physiology*, *267*(2), H779–95.

Mateja, R.D., & de Tombe, P.P. (2012). Myofilament Length-Dependent Activation Develops within 5 ms in Guinea-Pig Myocardium. *Biophysical Journal*, *103*(1), L13–L15.

Regazzoni, Francesco (2020). *Mathematical modeling and efficient numerical simulation of the cardiac mechanical activation*. Ph.D. thesis, Politecnico di Milano.

Regazzoni, F., Dede', L., & Quarteroni, A. (2018). Active contraction of cardiac cells: a reduced model for sarcomere dynamics with cooperative interactions. *Biomechanics and Modeling in Mechanobiology*, (pp. 1–24).

Rice, J.J., & de Tombe, P.P. (2004). Approaches to modeling crossbridges and calcium-dependent activation in cardiac muscle. *Progress in biophysics and molecular biology*, *85*(2-3), 179–195.

Rice, J.J., Stolovitzky, G., Tu, Y., & de Tombe, P.P. (2003). Ising Model of Cardiac Thin Filament Activation with Nearest-Neighbor Cooperative Interactions. *Biophysical Journal*, *84*(2), 897–909.

Rice, J.J., Wang, F., Bers, D.M., & de Tombe, P.P. (2008). Approximate Model of Cooperative Activation and Crossbridge Cycling in Cardiac Muscle Using Ordinary Differential Equations. *Biophysical Journal*, *95*(5), 2368–2390.

Rice, J.J., Winslow, R.L., & Hunter, W.C. (1999). Comparison of putative cooperative mechanisms in cardiac muscle: length dependence and dynamic responses. *AJP: Heart and Circulatory Physiology*, *276*(5), H1734–H1754.

ter Keurs, H.E.D.J., Rijnsburger, W.H., Van Heuningen, R., & Nagelsmit, M.J. (1980). Tension Development and Sarcomere Length in Rat Cardiac Trabeculae: Evidence of Length-Dependent Activation. In *Cardiac Dynamics*, (pp. 25–36). Dordrecht: Springer Netherlands.

ter Keurs, H.E.D.J., Shinozaki, T., Zhang, Y.M., Zhang, M.L., Wakayama, Y., Sugai, Y., Kagaya, Y., Miura, M., Boyden, P.A., Stuyvers, B.D.M., & Landesberg, A. (2008). Sarcomere mechanics in uniform and non-uniform cardiac muscle: A link between pump function and arrhythmias. *Progress in biophysics and molecular biology*, *97*(2-3), 312–331.

Trayanova, N.A., & Rice, J.J. (2011). Cardiac electromechanical models: from cell to organ. *Frontiers in Physiology*, *2*, 43.

Van Heuningen, R., Rijnsburger, W.H., & ter Keurs, H.E.D.J. (1982). Sarcomere length control in striated muscle. *The American journal of physiology*, *242*(3), H411–20.

Washio, T., Okada, J.-I., Sugiura, S., & Hisada, T. (2011). Approximation for Cooperative Interactions of a Spatially-Detailed Cardiac Sarcomere Model. *Cellular and Molecular Bioengineering*, *5*(1), 113–126.

Zahalak, G.I. (1981). A distribution-moment approximation for kinetic theories of muscular contraction. *Elsevier*, *55*(1-2), 89–114.

Zahalak, G.I., & Motabarzadeh, I. (1997). A Re-examination of Calcium Activation in the Huxley Cross-Bridge Model. *Journal of Biomechanical Engineering*, *119*(1), 20–29.

Conclusions and perspectives

Conclusions

Digital medicine has raised a growing interest in the last decade due to the multiplication of data acquisition devices, allowing to better quantify the state of the patients, and the development of powerful tools to store and share the acquired data that make them easier to use. As a corollary, there is an increasing demand for the development of *predictive* models that are capable to help answer clinical questions. Models indeed enhance the amount of information that can be extracted from the data, allowing for instance to reconstruct non-measurable physiological quantities, to test and evaluate *in silico* different therapeutic strategies before an intervention, or to build medically relevant indicators. The cardiovascular system is naturally at the center of these new research efforts and this work has been done as part of it.

The main objective of this thesis was to propose a model of molecular motors that is relevant in the context of cardiac modeling, with a particular emphasis on the multi-scale aspects of this system. The interest in the fine description of the microscopic molecular motors is explained by the fact that they are at the core of the active force generation and their disfunction often leads to severe pathological conditions. Indeed, mutations of the myosin heads that induce variations of the cross-bridges force generation capability have been associated with the development of cardiomyopathies [Moore et al., 2012; Spudich, 2014]. In a more general point of view, being able to model the molecular motors contributes to better understand the physiology and the diseases, and may potentially help design more efficient treatments. In this regard, it is essential to be able to link the microscopic models with the whole heart description so that the effect of microscopic modifications can be evaluated on the heart performance, which is the ultimate objective to take care of.

In the last fifty years, great research efforts have been made to develop cardiovascular models [Peskin, 1975, 1977; Hunter & Smaill, 1988; Chapelle et al., 2012; Quarteroni et al., 2017] and meaningful simplifications [Caruel et al., 2013] on the one hand, and to create a vast variety of models with different level of refinements, from models capturing the finest time scales [Eisenberg et al., 1980; Piazzesi & Lombardi, 1995; Sheshka & Truskinovsky, 2014; Caruel et al., 2019] to coarser models [Hill, 1938; Bestel et al., 2001] on the other hand. Our work fell at the interface between these two areas of research with the aim of building a bridge between them to incorporate various levels of the microscopic actin-myosin interaction into a heart simulation framework.

More precisely, we aimed at deriving a hierarchy of models starting from a refined model [Caruel et al., 2019] by performing successive simplification stages. To integrate these descriptions into a heart simulation framework, the models needed to be extended to take into account the force regulation mechanisms that are of high significance *in vivo*. Then, the link between the microscopic contraction models and the macroscopic organ model had to be performed. To do so, we needed to deal with the multi-scale nature in time and space of the muscle tissue at the continuous and at the discrete level. We followed for that an approach based on the thermodynamical principles. The main results of this work can be grouped into the following categories.

Understanding of the actin-myosin interaction physiology

- We have first performed a literature review of the experimental works characterizing the actin-myosin interaction and its regulations to put information in a useable form for the development of models. Compiling the available experimental data in a comprehensive manner was important for the development of models and their validation.

Indeed, it allows to distinguish the general trend from the experiment-specific variations (due for instance to temperature differences or species differences). To the best of my knowledge, no review aggregating and presenting quantitative data has been published since the work of Allen & Kentish [1985]. Moreover, our work is broader than the latter paper because we have not restricted our presentation to the force regulation mechanisms.

Multi-scale modeling of the actomyosin interaction

- We have built a hierarchy of muscle contraction models starting from a refined stochastic model [Caruel et al., 2019], which was only validated for skeletal muscles. Performing the asymptotic elimination of the fastest time scale, we have derived a simplified model that falls into the Huxley'57 model family [Huxley, 1957]. With additional assumptions on the attachment and detachment rates and the attached state mechanical energy, we have further simplified this model using moment techniques proposed by Zahalak [1981]; Bestel et al. [2001]. These models have been validated on experimental data obtained on cardiac muscle cells. This model hierarchy provides a representative model – validated for the description of cardiac muscles – of the model families introduced by Caruel et al. [2019] for a complete model capturing all time scales of the microscopic contraction, by Huxley [1957] for an intermediate model describing the slower time scale only, and by Bestel et al. [2001] for a simplified model targeting the slow time scales in the range of validity that is relevant in physiological heart conditions. We have emphasized on the comparison between these models to rigorously highlight the loss of properties when performing the simplifying assumptions. Furthermore, a generic calibration procedure, which is fundamental to prove the validity of the model and for the use in patient-specific clinical applications, has been designed.

- We have proposed a first extension of the Huxley'57 model family to take into account the variation of the myosin heads availability. Following an original approach considering two pools of myosin heads, grouping available and non-available heads, we established a new partial differential equation governing the dynamics of a population of myosin heads. The fundamental thermodynamical balances are established. The validity of this new modeling ingredient has been demonstrated, with a phenomenologically modified model to add the calcium activation, by showing its ability to capture the essential features of the Frank-Starling effect.

- We have developed the last missing block in our modeling framework, i.e. the account of the activation of the thin filament. To be able to naturally integrate this extension into our modeling framework, we have chosen an original approach that centers the description on the myosin head, whereas alternative formulations are often written from the point of view of the actin site. This formulation can be used as a standalone model or be linked to a thin filament activation model. In the latter case, it provides a way to bridge the electrophysiology and the mechanical contraction.

Numerical methods

- We have proposed a discretization strategy, valid for a large class of microscopic chemico-mechanical contraction models extending the seminal Huxley'57 model [Huxley, 1957], that carries over to the discrete level the microscopic thermodynamical balances established at the continuous level. Furthermore, we have demonstrated that this property could be extended to the system coupling the microscopic contraction

model to a macroscopic muscle description derived in the framework of continuum mechanics. This ability to rigorously compute thermodynamical quantities at the discrete level could open the way to the use of thermodynamical measurements (such as the liberated heat) to further calibrate and validate the models.

- We have further extended these numerical methods by also considering the additional terms appearing in the partial differential equation governing the extended model that takes into account the thick filament activation. Moreover, we have proposed a thermodynamically consistent multi-time step numerical scheme taking advantage from the separation of time scales to perform numerical simulations in an efficient way.

Perspectives

These elements mostly meet the objectives that we set at the beginning of this work. However, many points could be improved to strengthen its significance.

- The main area to improve is the validation of the models incorporating the force regulation. This is due to the lack of comprehensive data set that would allow to confront the different parts of the models to data that should all be obtained in the same conditions (same temperature, same species, same part of the heart muscle tissue, same chemical environment, ...). We hope that this work could help raise the interest of the physiologists community in re-performing well established experiments to create a database for modeling purposes.

- Many questions remain open regarding the origin of the thick and thin filament activation. This limits the possibilities of developing physical models. To overcome this issue, collaborations with experimentalists are essential. Indeed, the data feed the model for calibration and validation, which in return helps identify the area where our understanding does not correspond to the reality and help design appropriate experiments to test new hypotheses.

- The thermodynamics properties of the model incorporating the thin filament activation have not been established yet. We believe however that our rigorous modeling framework should allow to naturally derive these properties. If the thermodynamics balances can indeed be obtained, a straightforward follow-up question is whether we could design a discretization strategy that would be able to derive a discrete counterpart to this continuous level thermodynamical properties.

This research work has also been an opportunity to identify some open subjects that may constitute future research topics.

- One of the goal of the fine molecular motors behavior modeling is to be able to follow-up modifications of the micro-scale behavior up to the organ behavior. These modifications may typically be related to diseases. A natural extension of our work could be to model abnormal myosin heads and to investigate whether the effects predicted at the heart level indeed correspond to that happening in living subjects. This project would require new experimental work to quantitively characterize the diseased myosin heads properties. In the same vein, the introduction of pharmacological inputs in the model to capture the effect of drugs is a promising research area. Together, these two topics may enable the development of a platform to select therapeutic strategies *in silico* and therefore to reduce the development time of new drugs or even allow the personalization of the treatment for each patient.

- Several theoretical questions are also opened by this work. The newly proposed equations for the extension of the Huxley'57 model may become the object of mathematical analysis. This may improve the level of understanding that we have on these models and bring new ideas to design model simplifications. Moreover, the asymptotic elimination of the stochastic model fast variables has been done here in a heuristic way only. A more formal derivation of the simplified model could be obtained by demonstrating the asymptotic convergence of the solution of one model to the other. The work of Tugaut [2018] may constitute a starting point to tackle this question.

- Finally, a major challenge concerns the identifiability of the model parameters. This question is essential for the use of these models in real clinical applications since it is a prerequisite for the development of automatic calibration algorithms. The associated issues are which type of data should be provided, can they be obtained minimally invasively, or up to which level of refinement can reasonably hope to identify parameters. The multi-scale and multi-physics nature of the cardiovascular system makes the resolution of inverse problems difficult. Classical approaches to solve them are data assimilation methods [Chapelle et al., 2009; Moireau & Chapelle, 2011] that have already proven their relevance in the framework of personalized medicine [Sermesant et al., 2012; Chabiniok et al., 2012].

From a broader point of view, this work brings new theoretical modeling elements that are, in part due to their lack of validation, not meant to be used in clinical applications in the coming years. However, it is perfectly in line with the challenges that digital medicine offers. The development of a model hierarchy having various levels of refinement meets the requirements of this research area. Building models for clinical applications is indeed not about developing the most comprehensive model but to identify and select the modeling elements that are at play in a given situation to design the relevant model for this particular question. Moreover, the focus on the numerical methods associated with the proposed models is also essential. The vision of making new numerical medical tools broadly available can indeed not be achieved if these tools only run on high performance computing clusters. Being able to design robust and efficient discretization strategies is therefore of major importance.

Today, a large scientific community is convinced by the potential of predictive models in clinical practice, as shown by the vast research efforts on this topic – we can mention in particular the VPH initiative [Viceconti & Dall'Ara, 2019]. Medical doctors, who are at the core of this topic, are joining the research efforts and the clinical world starts to be aware of the improvements that these techniques could bring, as shown by the progressive adoption of some early developed products making use of models. The conditions seem thus favorable for a broader development of these techniques and to move from the proof-of-concepts to the clinical reality.

Bibliography

Allen, D.G., & Kentish, J.C. (1985). The cellular basis of the length-tension relation in cardiac muscle. *Journal of molecular and cellular cardiology*, *17*(9), 821–840.

Bestel, J, Clément, F, & Sorine, M (2001). A Biomechanical Model of Muscle Contraction. In *Medical Image Computing and Computer-Assisted Intervention – MICCAI 2001*, (pp. 1159–1161). Berlin, Heidelberg: Springer, Berlin, Heidelberg.

Caruel, M., Chabiniok, R., Moireau, P., Lecarpentier, Y., & Chapelle, D. (2013). Dimensional reductions of a cardiac model for effective validation and calibration. *Biomechanics and Modeling in Mechanobiology*, *13*(4), 897–914.

Caruel, M., Moireau, P., & Chapelle, D. (2019). Stochastic modeling of chemical-mechanical coupling in striated muscles. *Biomechanics and Modeling in Mechanobiology*, *18*(3), 563–587.

Chabiniok, R, Moireau, Philippe, Lesault, P F, Rahmouni, A, Deux, J F, & Chapelle, Dominique (2012). Estimation of tissue contractility from cardiac cine-MRI using a biomechanical heart model. *Biomechanics and Modeling in Mechanobiology*, *11*(5), 609–630.

Chapelle, D., Le Tallec, P., Moireau, P., & Sorine, M. (2012). Energy-preserving muscle tissue model: formulation and compatible discretizations. *Journal for Multiscale Computational Engineering*.

Chapelle, Dominique, Moireau, Philippe, & Le Tallec, Patrick (2009). Robust filtering for joint state-parameter estimation in distributed mechanical systems. *Discrete & Continuous Dynamical Systems - A*, *23*(1&2), 65–84.

Eisenberg, E., Hill, T.L., & Chen, Y. (1980). Cross-bridge model of muscle contraction. Quantitative analysis. *Biophysical Journal*, *29*(2), 195–227.

Hill, A.V. (1938). The heat of shortening and the dynamic constants of muscle. *Proc. R. Soc. Lond. B*, *126*(843), 136–195.

Hunter, P.J., & Smaill, B.H. (1988). The analysis of cardiac function: a continuum approach. *Progress in biophysics and molecular biology*, *52*(2), 101–164.

Huxley, A.F. (1957). Muscle structures and theories of contraction. *Progr. Biophys. Chem.*.

Moireau, Philippe, & Chapelle, Dominique (2011). Reduced-order Unscented Kalman Filtering with application to parameter identification in large-dimensional systems. *ESAIM: Control, Optimisation and Calculus of Variations*, *17*(2), 380–405.

Moore, Jeffrey R, Leinwand, Leslie, & Warshaw, David M (2012). Understanding cardiomyopathy phenotypes based on the functional impact of mutations in the myosin motor. *Circulation Research*, *111*(3), 375–385.

Peskin, C.S. (1975). *Mathematical aspects of heart physiology*. Courant Institute of Mathematical Sciences.

Peskin, C.S. (1977). Numerical analysis of blood flow in the heart. *Journal of Computational Physics*, *25*(3), 220–252.

Piazzesi, G., & Lombardi, V. (1995). A cross-bridge model that is able to explain mechanical and energetic properties of shortening muscle. *Biophysical Journal*, *68*, 1966–1979.

Quarteroni, A., Lassila, T., Rossi, S., & Ruiz-Baier, R. (2017). Integrated Heart-Coupling multiscale and multiphysics models for the simulation of the cardiac function. *Computer Methods in Applied Mechanics and Engineering*, *314*, 345–407.

Sermesant, M., Chabiniok, R., Chinchapatnam, P., Mansi, T., Billet, F., Moireau, P., Peyrat, J.M., Wong, K., Relan, J., Rhode, K., Ginks, M., Lambiase, P., Delingette, H., Sorine, M., Rinaldi, C.A., Chapelle, D., Razavi, R., & Ayache, N. (2012). Patient-specific electromechanical models of the heart for the prediction of pacing acute effects in CRT: A preliminary clinical validation. *Medical Image Analysis*, *16*(1), 201–215.

Sheshka, R, & Truskinovsky, L (2014). Power-stroke-driven actomyosin contractility. *Physical review. E, Statistical, nonlinear, and soft matter physics*, *89*(1), 012708.

Spudich, James A (2014). Hypertrophic and dilated cardiomyopathy: four decades of basic research on muscle lead to potential therapeutic approaches to these devastating genetic diseases. *Biophysj*, *106*(6), 1236–1249.

Tugaut, Julian (2018). Convergence in Wasserstein distance for self-stabilizing diffusion evolving in a double-well landscape. *C. R. Acad. Sci. Paris, Ser. I*, *356*(6), 657–660.

Viceconti, M., & Dall'Ara, E. (2019). From bed to bench: How in silico medicine can help ageing research. *Mechanisms of Ageing and Development*, *177*, 103–108.

Zahalak, G.I. (1981). A distribution-moment approximation for kinetic theories of muscular contraction. *Elsevier*, *55*(1-2), 89–114.

université PARIS-SACLAY

ÉCOLE DOCTORALE
Sciences mécaniques et énergétiques, matériaux et géosciences (SMEMAG)

Titre : Modélisation multi-échelles de la contraction musculaire - De la dynamique stochastique des moteurs moléculaires à la mécanique des milieux continus.

Mots clés : Modélisation cardiovasculaire ; Biomécanique ; Multi-échelle; Médecine numérique ; Thermodynamique ; Analyse Numérique

Résumé : L'objectif de cette thèse est la modélisation mathématique des mécanismes de contraction musculaire à l'échelle microscopique dans le but de proposer et d'intégrer ces modèles dans un environnement de simulation cardiaque multi-échelle. Ce travail est réalisé dans le contexte de la médecine numérique, qui propose d'améliorer le traitement des patients par l'utilisation d'outils numériques. La première contribution de cette thèse est une analyse bibliographique des travaux expérimentaux caractérisant l'interaction actine-myosine et ses régulations afin de compiler les informations sous une forme utilisable pour le développement de modèles. Cette étape est une condition préalable essentielle à la modélisation. Nous proposons ensuite une hiérarchie de modèles de contraction musculaire à partir d'un modèle stochastique raffiné existant, mais validé uniquement pour les muscles squelettiques, en appliquant des hypothèses de simplification successives. Les étapes de simplification transforment l'équation différentielle stochastique initiale en une équation aux dérivées partielles avec une description qui fait partie de la famille de modèles dérivée du modèle Huxley'57. Une simplification supplémentaire conduit ensuite à un modèle décrit par un ensemble d'équations différentielles ordinaires. La pertinence des modèles proposés, qui ciblent différentes échelles de temps, est démontrée en les comparant aux données expérimentales obtenues avec des muscles cardiaques, et leur domaine de validité est étudié. Pour intégrer ces descriptions dans un environnement de simulation cardiaque, nous avons étendu ces modèles afin de prendre en compte les mécanismes de régulation de la force qui se produisent *in vivo*. Cela conduit à de nouvelles équations aux dérivées partielles. Ensuite, nous lions les modèles de contraction microscopiques à un modèle d'organe macroscopique. Nous suivons pour cela une approche fondée sur les principes thermodynamiques pour traiter la nature multi-échelle en temps et en espace du tissu musculaire aux niveaux continu et discret. La validité de cet environnement de simulation est démontrée en présentant sa capacité à reproduire le comportement du cœur et en particulier les caractéristiques essentielles de l'effet Frank-Starling.

Title: Multi-scale modeling of muscle contraction - From stochastic dynamics of molecular motors to continuum mechanics.

Keywords: Cardiovascular modeling; Biomechanics; Multi-scale; Digital medicine; Thermodynamics; Numerical analysis

Abstract: This PhD thesis deals with the mathematical description of the micro-scale muscle contraction mechanisms with the aim of proposing and integrating our models into a multiscale heart simulation framework. This research effort is made in the context of digital medicine, which proposes to improve the treatment of patients with the use of numerical tools. The first contribution of this thesis is a literature review of the experimental works characterizing the actin-myosin interaction and its regulations to compile information in a useable form for the development of models. This stage is an essential prerequisite to modeling. We then propose a hierarchy of muscle contraction models starting from a previously proposed refined stochastic model, which was only validated for skeletal muscles, and applying successive simplification assumptions. The simplification stages transform the initial stochastic differential equation into a partial differential equation with a model that is part of the Huxley'57 model family. A further simplification then leads to a description governed by a set of ordinary differential equations. The relevance of these models, targeting different time scales, is demonstrated by comparing them with experimental data obtained with cardiac muscles and their range of validity is investigated. To integrate these microscopic descriptions into a heart simulation framework, we extend the models to take into account the force regulation mechanisms that take place *in vivo*, leading to the derivation of new partial differential equations. Then, we link the microscopic contraction models to the macroscopic organ model. We follow for that an approach based on the thermodynamical principles to deal with the multi-scale nature in time and space of the muscle tissue at the continuous and at the discrete levels. The validity of this simulation framework is demonstrated by showing its ability to reproduce the heart behavior and in particular to capture the essential features of the Frank-Starling effect.

Université Paris-Saclay
Espace Technologique / Immeuble Discovery
Route de l'Orme aux Merisiers RD 128 / 91190 Saint-Aubin, France